NUREG/CR-6196
TMI V(93)EG01
EGG-2732

Calculations to Estimate the Margin to Failure in the TMI-2 Vessel

Prepared by L. A. Stickler, J. L. Rempe, S. A. Chávez, G. L. Thinnes, S. D. Snow, R. J. Witt, M. L. Corradini, J. A. Kos

Idaho National Engineering Laboratory
EG&G Idaho, Inc.

Prepared for
U.S. Nuclear Regulatory Commission

AVAILABILITY NOTICE

Availability of Reference Materials Cited in NRC Publications

Most documents cited in NRC publications will be available from one of the following sources:

1. The NRC Public Document Room, 2120 L Street, NW., Lower Level, Washington, DC 20555-0001

2. The Superintendent of Documents, U.S. Government Printing Office, Mail Stop SSOP, Washington, DC 20402-9328

3. The National Technical Information Service, Springfield, VA 22161

Although the listing that follows represents the majority of documents cited in NRC publications, it is not intended to be exhaustive.

Referenced documents available for inspection and copying for a fee from the NRC Public Document Room include NRC correspondence and internal NRC memoranda; NRC bulletins, circulars, information notices, inspection and investigation notices; licensee event reports; vendor reports and correspondence; Commission papers; and applicant and licensee documents and correspondence.

The following documents in the NUREG series are available for purchase from the GPO Sales Program: formal NRC staff and contractor reports, NRC-sponsored conference proceedings, international agreement reports, grant publications, and NRC booklets and brochures. Also available are regulatory guides, NRC regulations in the *Code of Federal Regulations*, and *Nuclear Regulatory Commission Issuances*.

Documents available from the National Technical Information Service include NUREG-series reports and technical reports prepared by other Federal agencies and reports prepared by the Atomic Energy Commission, forerunner agency to the Nuclear Regulatory Commission.

Documents available from public and special technical libraries include all open literature items, such as books, journal articles, and transactions. *Federal Register* notices, Federal and State legislation, and congressional reports can usually be obtained from these libraries.

Documents such as theses, dissertations, foreign reports and translations, and non-NRC conference proceedings are available for purchase from the organization sponsoring the publication cited.

Single copies of NRC draft reports are available free, to the extent of supply, upon written request to the Office of Administration, Distribution and Mail Services Section, U.S. Nuclear Regulatory Commission, Washington, DC 20555-0001.

Copies of industry codes and standards used in a substantive manner in the NRC regulatory process are maintained at the NRC Library, 7920 Norfolk Avenue, Bethesda, Maryland, for use by the public. Codes and standards are usually copyrighted and may be purchased from the originating organization or, if they are American National Standards, from the American National Standards Institute, 1430 Broadway, New York, NY 10018.

DISCLAIMER NOTICE

NUREG/CR-6196
TMI V(93)EG01
EGG-2733

Calculations to Estimate the Margin to Failure in the TMI-2 Vessel

Manuscript Completed: February 1994
Date Published: March 1994

Prepared by L. A. Stickler, J. L. Rempe, S. A. Chávez, G. L. Thinnes, S. D. Snow,
R. J. Witt,* M. L. Corradini,* J. A. Kos*

Idaho National Engineering Laboratory
Managed by the U.S. Department of Energy

EG&G Idaho, Inc.
Idaho Falls, ID 83415

Prepared for
Division of Systems Research
Office of Nuclear Regulatory Research
U.S. Nuclear Regulatory Commission
Washington, DC 20555-0001
NRC FIN A6899
Under DOE Contract No. DE-AC07-76ID0-1570

* University of Wisconsin-Madison
1500 Johnson Drive
Madison, WI 53706

ABSTRACT

As part of the OECD-sponsored Three Mile Island Unit 2 (TMI-2) Vessel Investigation Project (VIP), margin-to-failure calculations for mechanisms having the potential to threaten the integrity of the vessel were performed to improve understanding of events that occurred during the TMI-2 accident. Analyses considered four failure mechanisms: tube rupture, tube ejection, global vessel failure, and localized vessel failure. Calculational input was based on data from the TMI-2 VIP examinations of the vessel steel samples, the instrument tube nozzles, and samples of the hard layer of debris found on the TMI-2 vessel lower head. Sensitivity studies were performed to investigate the uncertainties in key parameters for these analyses.

CONTENTS

LIST OF FIGURES

LIST OF TABLES

EXECUTIVE SUMMARY

As part of the Three Mile Island Unit 2 (TMI-2) Vessel Investigation Project (VIP), margin-to-failure calculations were performed to increase understanding of events that occurred during the TMI-2 accident. Because there is considerable uncertainty in input parameters for these calculations, analyses relied upon methods with closed-form or simplified numerical solution techniques so that a large number of cases could be evaluated.

Calculations were performed to consider tube and vessel failure mechanisms. Results from these calculations illustrate uncertainties in the ability of current models to predict debris behavior and vessel response during a severe accident. Results from thermal and structural response calculations combined with the relatively rapid vessel cooling indicated by metallurgical examinations indicate that debris cooling occurred that was not evident from companion sample examinations and that is not currently considered in severe accident analysis models. In addition, analysis results suggest that a stress-based failure criterion may be too conservative for predicting failure. Furthermore, the large uncertainty in methods for predicting vessel failure precluded an accurate assessment of the margin to failure during the TMI-2 event. Little, if any, validation has been performed on methods used to predict melt/water interaction, molten pool behavior, cooling in debris that solidifies after relocation, and structural creep failure in a severe accident. Therefore, analysis results should only be viewed as providing insight into areas, such as assessing what failure mechanisms were plausible during the TMI-2 event, quantifying for which failure mode there existed the smallest margin during the TMI-2 event, and emphasizing areas where additional research is needed in severe accident analysis. Major conclusions and insights from these calculations are listed below.

- *Tube failures have been eliminated as potential failure mechanisms during the TMI-2 event.*

  Melt penetration calculations indicate that ceramic melt would not penetrate below the vessel head. Therefore, ex-vessel tube rupture calculations were performed assuming tube temperatures consistent with the vessel coolant temperatures. Because such temperatures were expected to result in very high margins to failure, a constant upper system pressure of 15 MPa was applied in the tube failure calculations. Results indicate that the margin to failure for this mechanism was very high.

  Prior to performing a tube ejection analysis, a weld failure analysis was performed to determine if the weld holding the nozzle to the vessel failed. Since it is not known if the hot spot temperatures occurred at the same time that the RCS was repressurized to 15 MPa, weld failure calculations were conservatively performed assuming that peak temperatures and pressures occurred simultaneously. Results indicate that even for these very conservative assumptions, there was considerable margin in the weld's integrity. Therefore, there was no need for a tube ejection analysis.

- *Debris cooling occurred within the first 2 hours after debris relocation.*

  Vessel thermal response calculation results indicate that only a case with "lower-bound" input assumptions for parameters, such as debris decay heat, vessel outer heat transfer

coefficient, and debris-to-vessel gap resistance resulted in global peak temperature predictions consistent with the boat sample examination data, namely that vessel temperatures remain below values where the material undergoes a transition from ferritic to austenitic steel. However, temperatures for this lower-bound case do not reflect the 10 to 100 K/min cooling rate deduced from boat sample examination data.

The potential for the vessel to experience a global failure was evaluated for vessel temperature distributions based upon nominal and lower-bound input assumptions consistent with companion sample data. Global failure was predicted to occur at 1.7 hours after relocation for the nominal case and 2.3 hours after relocation for the lower-bound case. Subsequent parametric studies indicate that failure will be predicted for global vessel temperatures above 700 to 800 K, if the reactor vessel is maintained at pressures near the operating pressure. Although the magnitude of cooling required was decreased when a stress-based failure criterion was replaced with a mechanical instability failure criterion, analyses indicate that debris cooling must have occurred within approximately 2 hours after debris relocation in order to prevent global failure.

Finally, an energy balance based on parameters directly measured or inferred from data measured during the accident indicates that the debris must have cooled after relocation. Calculations were conservatively performed by neglecting heat losses to the vessel and internal structures. Input parameters, such as debris decay heat, coolant injection rates, and relief valve flow rates were quantified based upon data measured during the accident or inferred from data measured during the accident. For all of the cases evaluated, which included upper-bound and lower-bound estimates on debris decay heat and mass flow rates, the debris is predicted to cool in the time period between debris relocation and vessel repressurization.

- *Enhanced debris cooling may have occurred via coolant traveling in channels within the debris and in channels between the debris and the vessel.*

Although there are insufficient TMI-2 data to determine the exact mechanisms that caused the debris to cool, scoping calculations were performed to quantify the magnitude of cooling needed in order to obtain results consistent with metallurgical examination data. Results indicate that both "slow" cooling (via coolant flowing through channels within the debris bed) and "rapid" cooling (via coolant flowing between the debris and the vessel) were needed in order for the vessel thermal response to be consistent with metallurgical examination data. Calculations indicate that coolant traveling through a negligible volume of channels within the debris bed (i.e., much less than 1% of the debris bed volume) and a very small gap thickness (e.g., as small as 1 mm) would provide sufficient cooling.

- *It is possible for the vessel to withstand the hot spot temperatures and durations inferred from the vessel metallurgical examinations if the balance of the vessel remains relatively cool.*

Jet impingement calculations indicate that the magnitude and duration of hot spot temperatures estimated in TMI vessel examinations were not due to debris from an

impinging jet. This is due to the fact that peak temperatures from an impinging jet could not be sustained for more than about 1 minute. The limited area estimated to have experienced hot spot temperature suggests that this region was subjected to a longer term localized heat source, such as might occur with a nonhomogeneous debris bed or a localized region with enhanced debris-to-vessel contact.

The potential for the vessel to experience a localized failure was evaluated by imposing hot spot temperatures on two background distributions, which were selected to bound possible background temperature distributions predicted by metallurgical examinations. Results for the background case with higher temperatures indicate that the presence of a hot spot reduces the predicted time to vessel failure. However, results from the case with lower background temperatures indicate that the vessel is capable of surviving local hot spots in the temperature range and of the duration inferred from the metallurgical examinations if the balance of the shell remains relatively cool.

Localized and global vessel failure calculations indicate that the background temperature behavior, which is highly dependent upon the heat load from relocated debris in the lower head, is key to predicting failure from either of these mechanisms. However, data from companion sample examinations were not sufficient to quantify the timing and rate of cooling that actually reduced this heat load.

The importance of results from these calculations may not be limited to TMI-2 specific applications. Rather, insights from these analyses provide another step toward answering severe accident questions.

ACKNOWLEDGMENTS

We would like to express our gratitude to several individuals who contributed to this report. First, we would like to thank Drs. A. Rubin and C. Serpan of the U.S. NRC for their helpful suggestions and guidance on this research project. We would also like to express our appreciation to members of the Structural Mecahanics Peer Review Group: Dr. Y. Rashid (chairman), Dr. R. Dodds, Dr. R. Huddleston, Dr. A. Combescure, Mr. K. Hashimoto, Dr. B. Turland, Dr. B. Sturm, and Prof. E. Vitale. As documented within this report, the comments received from this group were instrumental in completing this analysis effort.

ACRONYMS

ANL	Argonne National Laboratory
ANS	American Nuclear Society
DOE	U.S. Department of Energy
FCI	fuel-coolant interaction
HPI	high pressure injection
INEL	Idaho National Engineering Laboratory
L/D	jet length-to-jet diameter
LMP	Larsen-Miller parameter
MF	margin to failure
NRC	U.S. Nuclear Regulatory Commission
OECD	Organization for Economic Cooperation and Development
PORV	pilot operated relief valve
PWR	pressurized water reactor
RCS	reactor coolant system
SEM	scanning electron microscopy
SPND	self-powered neutron detector
SRM	source range monitor
TMI-2	Three Mile Island Unit 2
VIP	Vessel Investigation Project

NOMENCLATURE

a	Radius of debris on upper surface of hard layer (m)
b	Temperature-dependent constant used in Bailey-Norton creep equations (dimensionless)
c	Temperature-dependent constant used in Bailey-Norton creep equations (dimensionless)
c_p	Specific heat capacity; may be further designated by the subscript, d for debris, f for bulk coolant temperature, g for coolant in vapor phase, l for coolant in liquid phase, p for molten pool material, jet for impinging jet material, or v for pressure vessel steel (J/kg-K)
d_e	Effective diameter for melt flow (cm)
d_i	Nozzle inner diameter (cm)
d_{so}	Instrument string outer diameter (cm)
$f(\varphi)$	Function indicating variation of heat flux as function of angle, φ (dimensionless)
f_f	Fanning friction factor (dimensionless)
g	Acceleration due to gravity (m/s^2)
h	Heat transfer coefficient (W/m^2K)
h	Height of debris in lower head (m)
h_{cond}	Heat transfer coefficient through the outer half of the pressure vessel (W/m^2K)
h_{conv}	Component of the heat transfer coefficient on the outer surface of the vessel due to natural convection (W/m^2K)
h_{crust}	Heat transfer coefficient through the crust (W/m^2K)
h_{dir}	Heat transfer coefficient due to jet impingement (W/m^2K)
h_{dc}	Convective heat transfer coefficient from the molten pool to the lower crust (W/m^2K)
$h_{fb,r}$	Heat transfer coefficient for film boiling and radiation from the crust to the coolant (W/m^2K)
h_{fg}	Coolant latent heat of vaporization (J/kg)

h_{in} Coolant enthalpy at the inlet (J/kg)

h_{int} Debris to structure gap heat transfer coefficient (W/m^2K)

h_{out} Coolant enthalpy at the exit (J/kg)

h_{pv} Effective heat transfer coefficient for the pressure vessel (W/m^2K)

h_{pvo} Heat transfer coefficient on the outside of the pressure vessel (W/m^2K)

h_{rad} Radioactive component of the heat transfer coefficient on the outside of the vessel (W/m^2K)

h_{sat} Saturated liquid coolant enthalpy for a given pressure (J/kg)

h_{td} Heat transfer coefficient between tube wall and debris (W/m^2K)

h_{uc} Convective heat transfer coefficient from the molten pool to the upper crust (W/m^2K)

h_{wd} Heat transfer coefficient between coolant and debris (W/m^2K)

k Thermal conductivity; may be further designated by the subscript, *crust* for crust material, *d* for debris material, *f* for liquid coolant, *jet* for impinging jet material, *por* for porous material, *s* for nonporous material, or *v* for vessel material (W/mK)

l_t Distance melt must travel through nozzle to outer vessel surface (m)

m Temperature-dependent constant used in Bailey-Norton creep equations (dimensionless)

m Temperature-dependent material constant used in low temperature (<922 K) creep strain relations (dimensionless)

$\dot{m}$ Mass flow rate of impinging jet (kg/s)

$\dot{m}$ Coolant mass flow rate in Section 5, may be further designated by the subscript, *crack*, for flow through a crack, *in*, for flow entering the vessel, *out*, for flow exiting the vessel, and *tot*, for flow through all debris cracks

m_d Debris mass (kg)

m_{sat} Mass of saturated coolant (kg)

n Exponent used in power law hardening relation (dimensionless)

n Number of cracks in a debris bed (m)

p_i	Reactor system pressure (MPa)
q''	Heat flux from debris to vessel (W/m^2)
q''_{fb}	Film boiling heat flux (W/m^2)
q''_{fbr}	Combined film boiling and radiative heat flux up from the pool (W/m^2)
$q''_{fb,sub}$	Film boiling heat flux to subcooled coolant (W/m^2)
q''_{nom}	Heat flux for nominal case (W/m^2)
q''_{r}	Radiative heat flux to coolant (W/m^2)
q_{remove}	Heat that must be removed by coolant in the debris to vessel gap to obtain cooling rates consistent with metallurgical examinations (W)
q_{sink}	Heat that must be removed by coolant flowing through the cracks to prevent vessel failure (W)
q''_{NB}	Nucleate boiling heat flux to coolant (W/m^2)
q''_{NC}	Natural convection heat flux (W/m^2)
q'''	Volumetric heat generation rate (W/m^3)
r	Radial distance from the center of curvature of the vessel (m). In Hookes' Law equations, it specifies the radial direction.
r_h	Horizontal distance from the vertical axis/centerline of the spherical head for use in calculating x (m)
r_i	Inner vessel radius (m)
r_j	Mean radius of segment of vessel head (m)
r_m	Mean wall radius of vessel head (m)
r_o	Outer vessel radius (m)
t	Time (s or h)
t_{drain}	Time required for jet to drain (s)

t_{gap} Gap thickness, (m)

t_r Rupture time (s or h)

t_{sol} Time required for melt to solidify while traveling through tube (s)

t_v Vessel thickness (m)

u Radial displacement (m)

u_d Debris internal energy; may be further designated by the subscript, *1* or *2*, to denote an initial or final state, respectively (J/kg)

u_l Coolant internal energy; may be further designated by the subscript, 1 or 2, to denote an initial or final state, respectively (J/kg)

v_d Melt velocity (m/s, cm/s)

φ Angle between the vertical and point along the inner surface of the vessel in Appendix C and Appendix E; may be modified with subscript *o* to define undeformed configuration (radians)

x Fraction of the effective cross-section area covered by debris (dimensionless)

x Quality in the RCS (may be further designated by the subscript, *1* or *2* to denote an initial or final state, respectively)

x_p Melt penetration distance (cm)

z_{crack} Effective height for a crack in the debris (m)

z_{debris} Effective height for a crack in the debris (m)

A Temperature-dependent constant used in Bailey-Norton creep equations (dimensionless)

A Contact area; may be further designated by the subscript, *dcrust* for area between bottom of molten pool and crust; *pvi* for area between molten pool and vessel inner surface, *pvo* for outer surface area of the vessel, *td* for area between tube and debris, *top* for area between upper crust and coolant, *ucrust* for area between top of molten pool and crust, or *wd* for area between coolant and debris (m^2)

A_{crack} Surface area in a crack (m^2)

A_{down} Surface area of debris facing vessel (m^2)

A_{flow} Cross-sectional flow area (m^2)

C_i Structural capacity (N)

D Creep damage based on time to rupture (dimensionless)

D_e Effective diameter for a crack in the debris (m)

D_{jet} Jet diameter (m)

E Young's modulus (MPa)

F_d Deadweight load (N)

F_p Pressure load (N)

F_{total} Total force on weld (N)

Fo Fourier number (dimensionless)

Gr Grashof number (may be further designated with the subscript, f, to designate that it be evaluated at the bulk coolant temperature) (dimensionless)

J_1 First stress invariant (MPa)

K Entrance loss coefficient (dimensionless)

L Latent heat of fusion; may be further designated by the subscript, d in Section 3 for debris or the subscript, *crust* in Appendix C for debris crust (J/kg)

L_{char} Characteristic length (m)

L_i Applied load (N)

LMP Larson-Miller parameter (dimensionless)

M Mass; may be further designated by the subscript, p for pool material or v for pressure vessel material (kg)

M_c Coolant mass in the RCS (may be further designated by the subscript, *1* or *2* to denote an initial or final state, respectively) (kg)

M_d Debris mass in hard layer (may be further designated by the subscript, *1* or *2* to denote an initial or final state, respectively) (kg)

M_{dtot} Total debris mass in the vessel (kg)

MF	Margin to failure (dimensionless percentage)
Nu	Nusselt number; may be further designated by the subscript, *stag* to indicate value for stagnation region (dimensionless)
P	Pressure; may be further designated by the subscript, *init* to indicate initial value or max to indicate maximum value (MPa, Pa)
P_{crust}	Crust porosity (dimensionless)
Pe	Peclet number (dimensionless)
Pr	Prandtl number (may be further designated with the subscript, *f*, to indicate that it be evaluated at the bulk coolant temperature, or *w*, to indicate that it be evaluated at the debris surface temperature) (dimensionless)
P_{RCS}	RCS pressure (MPa)
Q_{decay}	Debris decay heat (W)
Q_{hg}	Volumetric internal heat generation within a molten pool (W/m^2)
Ra	Rayleigh number (dimensionless)
Re	Reynolds number; may be further designated with the subscript, *f*, to indicate that it is evaluated at the bulk coolant temperature (dimensionless)
R_{crust}	Radius of crust on upper surface of debris bed in lower head (m)
R_m	Length parameter for estimating convective heat transfer in a molten pool in Appendix C (m)
R_φ	Radius of curvature for the deformed surface (m).
$R_{\varphi o}$	Radius of curvature for the undeformed surface (m).
S_s	Modulus of principal stresses (MPa)
S_u	Ultimate strength at temperature (MPa)
S_y	Yield strength (MPa)
T	Temperature for Larson-Miller parameter calculation (°R)
T_a	Containment ambient temperature (K)

T_{bulk}	Bulk coolant temperature (K)
T_c	Coolant temperature (K)
T_d	Debris temperature (K)
T_{debris}	Initial debris temperature (K)
T_i	Initial coolant temperature (K)
T_{in}	Coolant inlet temperature (K)
T_{in}	Inside shell surface temperature (K)
T_{int}	Interface temperature between the coolant and the crust upper surface (K)
T_{jet}	Jet temperature (K)
T_{mp}	Debris melting temperature (K)
$T_{mp,p}$	Melting temperature of material within pool (K)
T_{out}	Coolant exit temperature (K)
T_{out}	Outside shell surface temperature (K)
T_p	Temperature within molten pool (K)
T_{peak}	Peak temperature for hot spot temperature definitions (K)
T_{sat}	Coolant saturation temperature (K)
T_{sub}	Subcooled coolant temperature (K)
T_{sup}	Superheated coolant temperature (K)
T_t	In-vessel tube temperature (K)
T_{tEV}	Ex-vessel tube temperature (K)
$T_{tinterface}$	Tube temperature at vessel/tube interface (K)
T_{RCS}	Reactor coolant system temperature (K)
T_v	Vessel temperature (K)
T_{wall}	Melt cup wall temperature (K)

U Overall heat transfer coefficient; may be further designated by the subscript *down* to indicate transfer from the pool downward to the vessel, *up* to indicated transfer from the pool upward to the coolant, or out to indicate transfer from the vessel to the surroundings (W/m^2K)

V Volume; may be further designated by the subscript, *dcrust* to indicate volume of crust on lower pool surface *ucrust* to indicate volume of curst on upper pool surface (m^3)

$V_{coolant}$ Reactor coolant system volume (may be further designated by the subscript, *1* or *2* to denote an initial or final state, respectively) (m^3)

X_s Solid fraction (dimensionless)

α Thermal expansion coefficient (K^{-1})

α_i Thermal diffusivity; may be further designated by the subscript *p* for pool material, *d* for melt; or v for vessel material (m^2/s)

α_{sf} Shape factor (dimensionless)

α_{tr} Vessel thermal diffusivity (m^2/s)

β Shell rotation relative to its original configuration (radians)

β Thermal expansion coefficient (may be further designated with the subscript, *f*, to designate that it be evaluated at the bulk coolant temperature) (K^{-1})

β_p Coefficient of thermal expansion of melt in a molten pool (K^{-1})

β_c Coefficient of thermal expansion for coolant (K^{-1})

γ Material rotation from normal to the deformed middle surface (radians)

γ' $d\gamma/d\xi$ (radians)

Δt_j Time increment used in creep damage calculations (h)

Δt_v Incremental width of a vessel segment (m)

Δt Time step; may be further designated by the subscript, *creep* to indicate that step was selected based upon creep strain rates, *press* to indicate time step to next time at which a pressure state is defined, or *temp* to indicate time step to next time at which a temperature distribution is defined (seconds)

ΔT Temperature increment; may be further designated by the subscript, p to indicate amount that pool temperature is incremented or v to indicate amount that vessel temperature is incremented (K)

Δx Mesh size (m)

δ Crust thickness; may be further designated by the subscript dcrust to indicate lower crust thickness or ucrust to indicate upper crust thickness (m)

ε Strain; maybe modified with the subscripts y, pl cr, T, av, m, ϕ, θ, and r to define yield, plastic, creep, thermal, average, at the middle surface, and/or strain component directions (dimensionless)

$\bar{\varepsilon}$ Effective, or equivalent, strain; may be modified with the subscript cr to define effective creep strain (m/m).

ε_{crust} Crust emissivity (dimensionless)

ε_{ves} Vessel emissivity (dimensionless)

ζ Distance between shell material and midplane, measured normal to the middle surface, between -t/2 and +t/2 (m)

λ_c Melt solidification constant (dimensionless)

μ Temperature-dependent material constant used in low temperature (<922 K) creep strain relations (dimensionless)

μ Viscosity; may be further designated by the subscript g for coolant vapor, jet for molten jet material, p for pool material, f for the bulk coolant temperature (Pa-s)

ν Poisson's ratio (dimensionless)

ν_p Melt kinematic viscosity in a molten pool (m^2/s)

ξ Parametric variable used to define the shell model meridian, $0 \leq \xi \leq 1$, $\xi^2 = r/b$ (dimensionless)

ρ Density; may be further designated by the subscript crust, to indicate crust density, d to indicate melt density, f to indicate liquid coolant density, g to indicate vapor coolant density, p to indicate pool material density, sat_g to indicate density for saturated vapor phase of coolant, sat_l to indicate density for saturated liquid phase of coolant, sub to indicate subcooled coolant density, or sup to indicate superheated coolant density (kg/m^3)

σ Stress; may be modified with the subscripts y, θ,$\hat{\theta}$, *r* or *1,2,3* to define yield, or stress co.nponent directions or principal stresses (MPa)

$\bar{\sigma}$ Effective or equivalent stress (MPa). Note: Mises effective stress (σ_{vm}) is defined separately

σ_c Crust thickness (cm)

σ_f Surface tension for liquid coolant (N/m)

σ_m Temperature-dependent material constant used in low temperature (<922 K) creep strain relations (dimensionless)

σ_{sb} Stefan Boltzmann constant (5.672×10^{-8} W/m^{2}K^4)

σ_{vm} Mises effective stress (MPa)

τ Characteristic time used in creep strain relationship (hours)

υ_l Saturated liquid specific volume (may be further designated by the subscript, *1* or *2* to denote an initial or final state, respectively) (m^3/kg)

υ_g Saturated vapor specific volume (may be further designated by the subscript, *1* or *2* to denote an initial or final state, respectively) (m^3/kg)

φ' $d\varphi/d\xi$ in Appendix E (radians)

FOREWORD

The contents of this report were developed as part of the Three Mile Island Unit 2 Vessel Investigation Project. This project is jointly sponsored by eleven countries under the auspices of the Nuclear Energy Agency of the Organization for Economic Cooperation and Development. The twelve sponsoring organizations are:

* The Centre d'Etudes d'Energie Nucléaires of Belgium,
* The Säteilyturvakeskus of Finland,
* The Institute de Protection et de Sûreté Nucléaire of the Commissariat à l'Energie Atomique of France,
* The Gesellschaft für Reaktorsicherheit mbH of Germany,
* The Comitato Nazionale per La Ricerca e per Lo Sviluppo Dell' Energia Nucleare e Delle Energie Alternative of Italy,
* The Japan Atomic Energy Research Institute,
* The Consejo de Seguridad Nuclear of Spain,
* The Statens Kärnkraftinspektion of Sweden,
* The Office Fédéral de l'Energie of Switzerland,
* AEA Technology of the United Kingdom,
* The United States Nuclear Regulatory Commission, and
* The Electric Power Research Institute.

The primary objectives of the Nuclear Energy Agency (NEA) are to promote cooperation between its Member governments on the safety and regulatory aspects of nuclear development, and on assessing the future role of nuclear energy as a contributor to economic progress.

This is achieved by:

- encouraging harmonisation of governments' regulatory policies and practices in the nuclear field, with particular reference to the safety of nuclear installations, protection of man against ionising radiation and preservation of the environment, radioactive waste management, and nuclear third party liability and insurance;

- keeping under review the technical and economic characteristics of nuclear power growth and of the nuclear fuel cycle, and assessing demand and supply for the different phases of the nuclear fuel cycle and the potential future contribution of nuclear power to overall energy demand;

- developing exchanges of scientific and technical information on nuclear energy, particularly through participation in common services;

- setting up international research and development programmes and undertakings jointly organized and operated by OECD countries.

In these and related tasks, NEA works in close collaboration with the International Atomic Energy Agency in Vienna, with which it has concluded a Cooperation Agreement, as well as with other international organizations in the nuclear field.

Calculations to Estimate the Margin to Failure in the TMI-2 Vessel

1. INTRODUCTION

1.1 Objective

This report describes the calculations performed to estimate the margin to failure (MF) of the Three Mile Island Unit-2 (TMI-2) pressure vessel lower head. Scoping calculations were performed to quantify the margin to failure of several mechanisms that might have caused failure of the lower head. These mechanisms include tube ejection, tube rupture, and localized or global vessel failure. Several models, using closed-form analytical or simplified numerical solution techniques, were used to determine the thermal and mechanical response of the lower head to the molten core material that relocated from the core to the lower plenum. Although it is recognized that the uncertainty in many input parameters for these calculations is large, an attempt was made to estimate the margin to failure for each failure mechanism, and results were compared to determine which mechanism had the smallest margin to failure.

Rather than obtaining a definitive answer related to the margin to failure that existed in the vessel during the TMI-2 accident, results from these calculations illustrate uncertainties in the ability of current models to predict debris behavior and vessel response during a severe accident. As will be discussed within this report, thermal response calculation results indicate that debris cooling occurred that was not evident from companion sample examinations and that is not currently considered in severe accident analysis models. Furthermore, the large uncertainty in methods for predicting vessel failure precluded an accurate assessment of the margin to failure during the TMI-2 event. Little, if any, validation has been performed on methods used to predict melt/water interaction, molten pool behavior, cooling in debris that solidifies after relocation, and structural creep failure in a severe accident. Therefore, analysis results should only be viewed as providing insight into areas, such as assessing what failure mechanisms were plausible during the TMI-2 event, quantifying the failure mode with the smallest margin during the TMI-2 event, and emphasizing areas where additional research is needed in severe accident analysis.

1.2 Methodology

Failure of the TMI-2 pressure vessel lower head due to relocation of approximately 19 tonnes of debris to the lower head could have resulted from one of several mechanisms. These failure mechanisms include tube ejection, tube rupture, localized vessel failure, and global vessel failure. Scoping calculations for each mechanism were performed to determine for which mechanism there existed the smallest margin to failure. Figure 1-1 presents a flow diagram of the scoping calculations performed to accomplish this task. Scoping calculations for failure mechanisms are shown in bold ellipses in Figure 1-1.

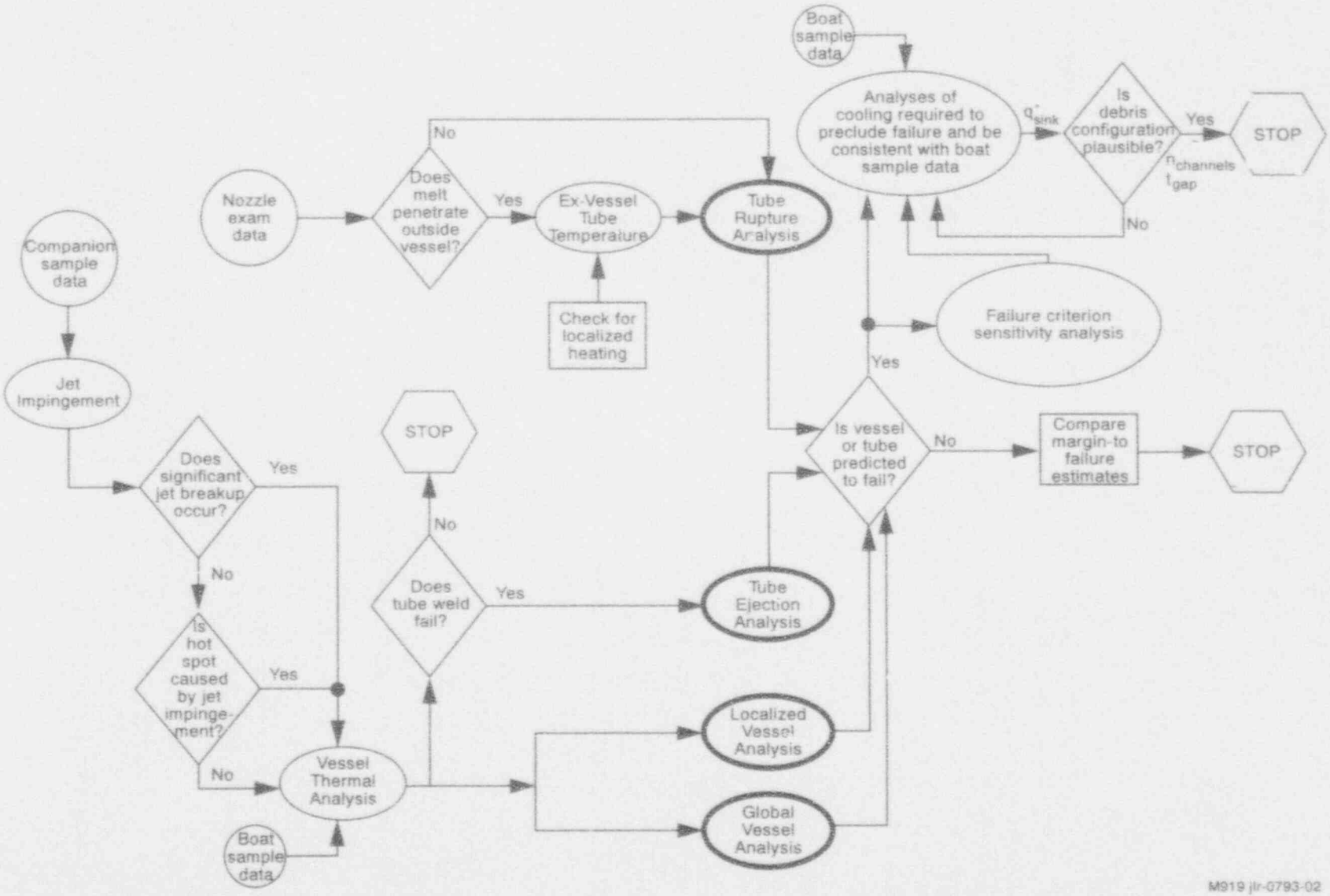

Figure 1-1. Flow diagram of scoping calculations.

The margin to failure for each of the mechanisms was quantified on the basis of both ultimate strength and creep effects. Failure of a nozzle or the vessel by exceeding the ultimate strength of the material reflects the instantaneous response of the material to temperature/load combinations over a given time period. Failure by creep reflects the cumulative damage of the temperature/load over the entire time period. Creep failure occurs at or before an ultimate-strength failure; thus, creep produces the lowest margin to failure.

As shown in Figure 1-1, several preliminary calculations provide input to the failure analyses. These calculations modeled melt penetration, jet impingement, and the thermal response of the vessel and vessel components. Melt penetration calculations were completed to determine if melt that penetrated into the instrument tubes traveled beyond the vessel lower head. Results provided a basis for determining the effective tube temperature to be used for a tube rupture analysis. Jet impingement calculations were used to determine if the thermal load from a coherent jet would cause the hot spot temperatures observed in Vessel Investigation Project (VIP) metallurgical examinations. This information was used in global vessel thermal response calculations. The vessel temperature distribution information was used in the weld failure analysis and the localized and global vessel failure analyses. Because the weld between the instrument tube nozzle and the vessel must fail prior to tube ejection occurring, results from a weld failure analysis determine the need for a tube ejection analysis.

As indicated in Figure 1-1, these calculations rely upon three major sources of VIP examination data: nozzle examination data for characterizing melt composition and penetration distances within instrument tubes; companion sample examination data for characterizing debris properties, such as decay heat and material composition; and reactor vessel steel, "boat sample," examination data for characterizing peak vessel temperatures, duration of peak temperatures, and vessel cooling rate. As will be illustrated by results within this report, calculation results indicate that some of the companion sample data were inconsistent with boat sample examination cooling rates (namely that the debris underwent a slow cooling). When results based upon companion sample data indicated that vessel failure would occur, irrespective of which failure criterion was selected, it was postulated that cooling, not indicated by companion sample data, needed to be modeled. Hence, calculations were performed to quantify the magnitude of this cooling and the debris configuration required to support this cooling. Calculations were also performed to verify the existence of this cooling based upon plant thermal-hydraulic parameters.

Many of the models used in the scoping calculations are extensions of models developed and/or applied under the U.S. Nuclear Regulatory Commission (NRC)-sponsored Lower Head Failure Analysis Program.[1] These models were modified according to the geometry of the TMI-2 vessel and operating conditions during the accident.

1.3 Report Content

Many of the parameters used in these calculations depend upon the manner, quantity, and timing of debris relocation to the lower head. Plant data available to quantify details related to accident progression are summarized in Section 2. In addition, Section 2 presents several possible scenarios for the manner in which molten debris relocated to the lower head. Sections 3 and 4 describe initial scoping calculations that were performed based upon VIP examination data. Section 3 describes results from thermal analyses that provide input to the failure analyses.

Failure analyses and margin-to-failure estimates for each failure mechanism are documented in Section 4. Results from these initial scoping calculations illustrate uncertainties in the ability of current models to predict debris behavior and vessel response during a severe accident. Two areas of uncertainty, the amount of cooling that occurred within the debris after relocation and the criterion used for predicting vessel failure, were investigated in more detail. Section 5 summarizes results from these additional scoping calculations. Conclusions from these calculations are discussed in Section 6.

1.4 Reference

1. J. L. Rempe et. al., *Light Water Reactor Lower Head Failure Analysis,* NUREG/CR-5642, EGG-2618, October 1993.

2. TMI-2 ACCIDENT DATA AND RELOCATION SCENARIO DESCRIPTION

Prior to performing the margin-to-failure analyses, it was necessary to have a clear understanding of the information available for reconstructing the TMI-2 event. To assist in this understanding, plant instrumentation data, previous examination data and TMI-2 Vessel Investigation Program (VIP) data were reviewed, with associated analyses of these data. Results from this review and a description of possible relocation scenarios based upon current understanding of these data are provided in this section.

2.1 Measured Plant Data and Examination Data

Data from online instrumentation and the subsequent analysis of these data assisted in identifying the possible sequence of events that took place within the reactor vessel during the accident. Instrumentation information was used to set input parameters in the thermal analyses and scoping calculations. Most data discussed in this section were used in margin-to-failure calculations. In some cases, additional data have been included for completeness.

2.1.1 Instrumentation Data

Online instrumentation recorded reactor coolant system (RCS) pressure, coolant temperatures, source range monitor (SRM) count rate, and self-powered neutron detector (SPND) response during the TMI-2 accident. Figure 2-1 shows the RCS pressure, with significant events overlaid up to the time when a major relocation was postulated to occur.[1] Figure 2-2 shows the pressure from reactor scram to 17 hours.[2] The pressurizer block valve was repeatedly cycled between 6 and 8 hours, in an attempt to establish RCS flow (see Figure 2-2). Figure 2-3 shows cold leg temperatures from 0 to 17 hours. Figure 2-4 shows the cold leg temperatures between 220 and 230 minutes.

2.1.2 SRM Data and Analysis

Source range monitors provided the only time-dependent data to estimate core liquid levels and changes in core geometry. Figure 2-5 shows the source range count rate during the accident with reactions to significant events highlighted. The data were interpreted using neutronic analysis and assumptions of the core configuration and coolant distribution in the core and downcomer.[2] Initial core uncovery occurred between 114 to 120 minutes. At 140 minutes, the coolant level was estimated to be at midcore. By 165 minutes, coolant covered approximately 1.0 m of the core. The core was completely covered with water after emergency cooling was injected at 200 minutes. The relocation of 10 to 19 tonnes of molten fuel is substantiated by the sharp increase in the count rate between 224 and 226 minutes. Based on analysis of the count rate, molten fuel continued to drain onto the upper control support assembly after the major relocation at 224 minutes, although in much smaller amounts.

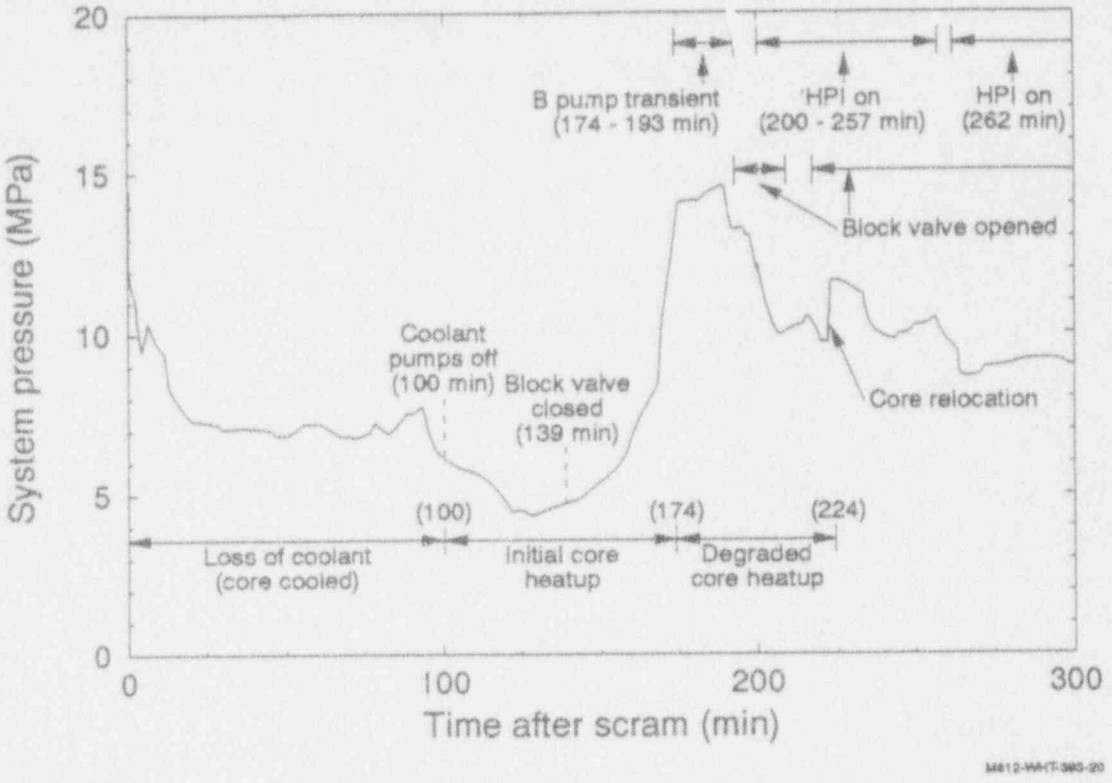

Figure 2-1. RCS pressure with timing of significant events noted.

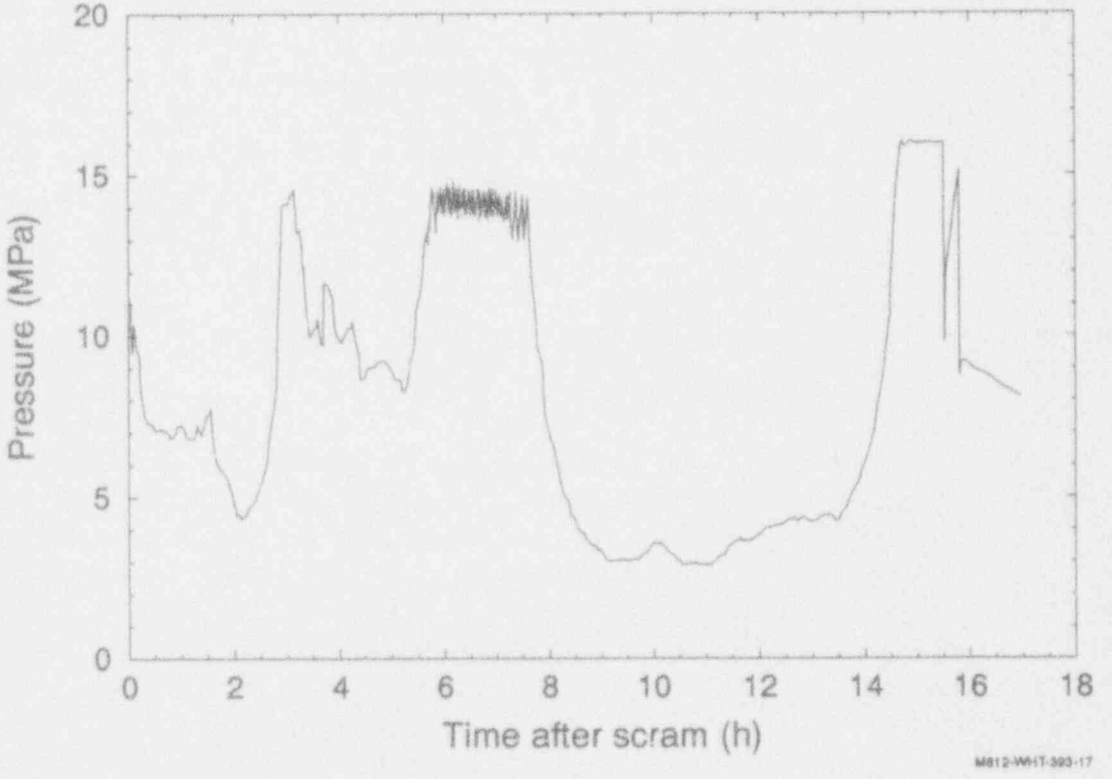

Figure 2-2. RCS pressure from reactor scram to 17 hours.

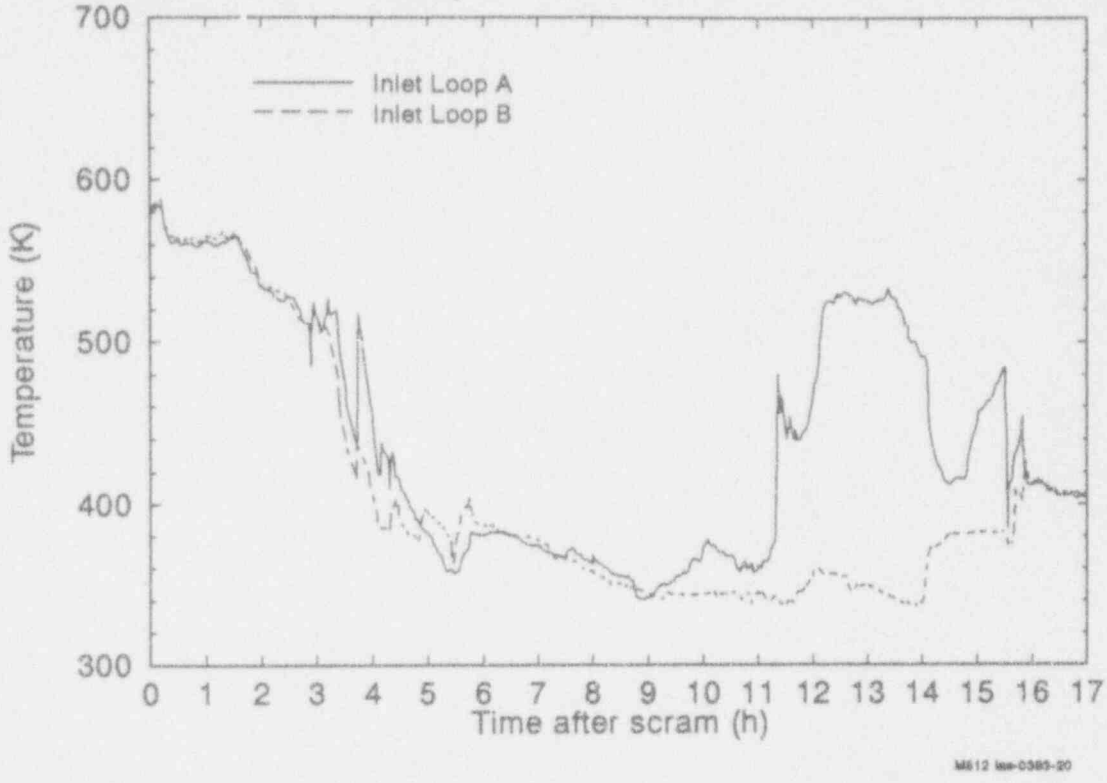

Figure 2-3. Cold leg temperatures from 0 to 17 hours.

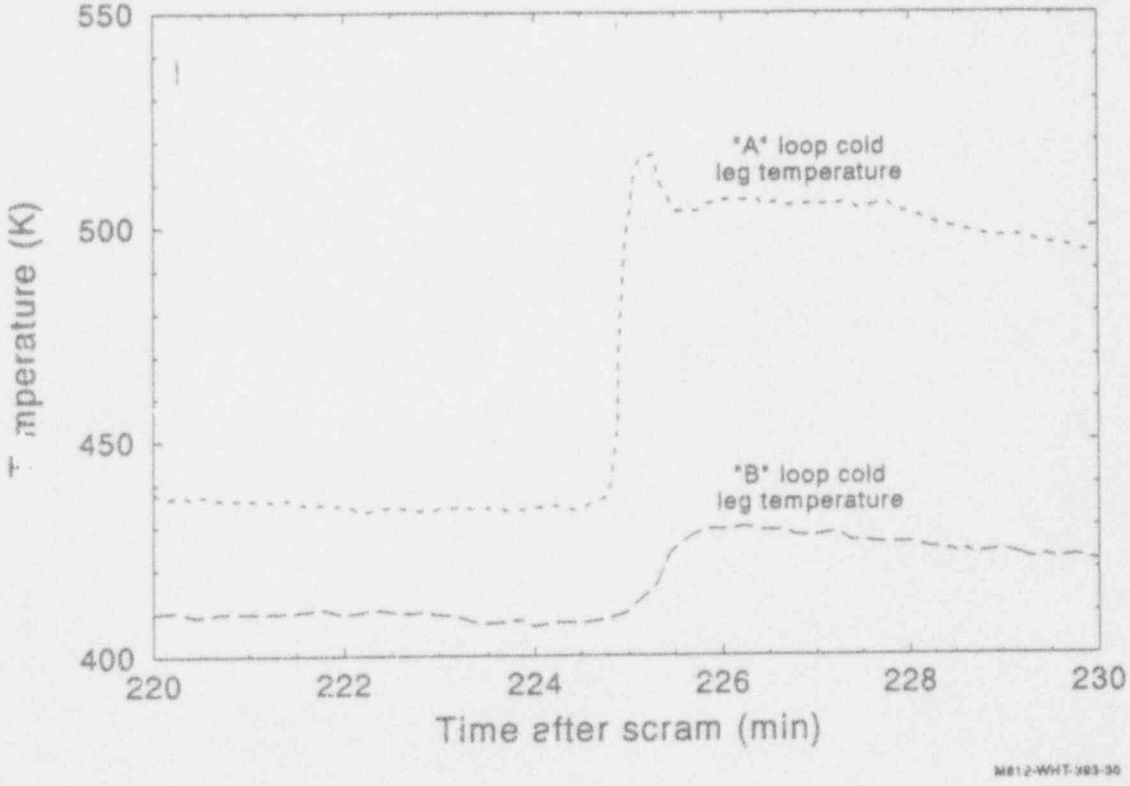

Figure 2-4. Cold leg temperatures between 220–230 minutes.

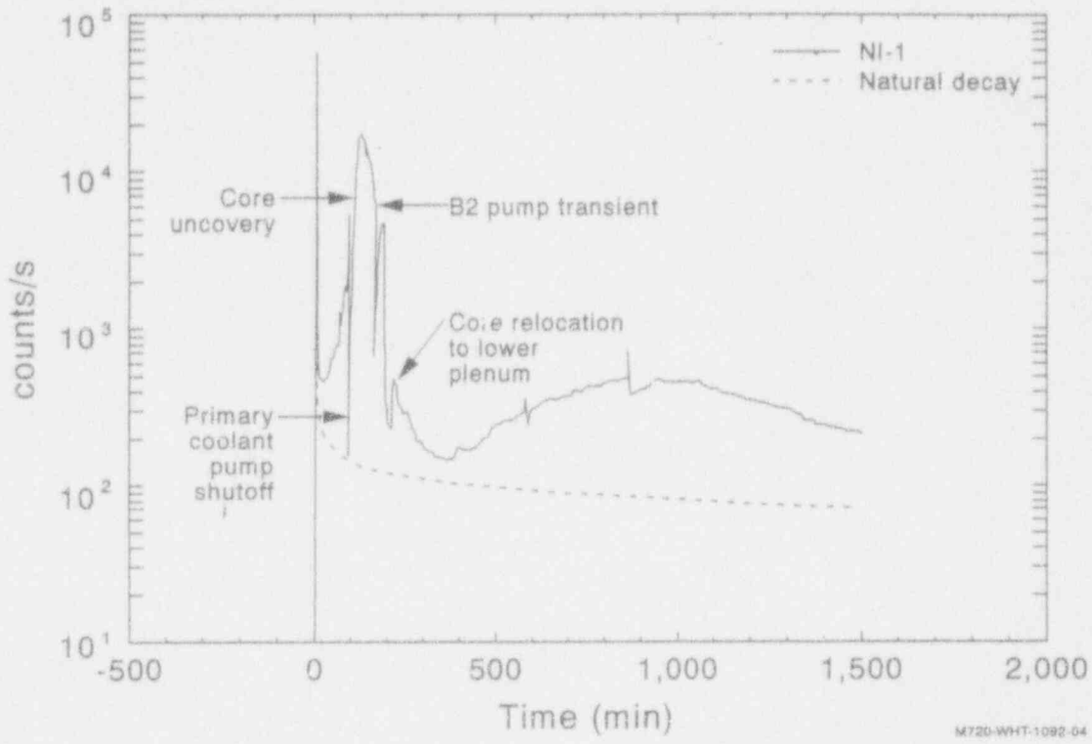

Figure 2-5. SRM count rate.

2.1.3 SPND Data

SPND data provided information relative to core heatup. The sources of SPND data included the alarm system data, which indicated a departure from the normal operating range for any of the 364 SPNDs, and a strip chart recorder monitoring output from 18 SPNDs. Figure 2-6 shows the elevations of SPND levels within the core. Correlation of SPND response with local temperatures by experimental analysis has produced two major conclusions.[3] First, local temperatures can be deduced only when a signal changes polarity. Second, two threshold temperatures, 850 K and 1,350 K, can be identified. In experimental analysis, SPNDs generated negative signals when they reached 850 K and positive signals at 1,350 K. At temperatures around 1,350 K, rapid oxidation of fuel rod cladding would increase the fuel rod temperatures enough to melt the cladding and eventually the UO_2 pellets.

SPND data indicated that temperatures of 850 K were reached within the core at 135 minutes. At 150 minutes, level 6 SPNDs in the upper region of the core indicated temperatures of 1,350 K. At 167 minutes, approximately 33% of the SPNDs at the lower elevations, as low as level 2, alarmed. Along the periphery of the core, SPND measurements indicated temperatures reached 1,350 K by 180 minutes. At 224 minutes, SPNDs at almost all levels at core locations E7, F7, F8, G6, G9, H5, and M9 indicated temperatures of 1,350 K. Simultaneous SPND alarms at all levels in each of the core locations suggest a common damage point to the instrumentation, which may have occurred in the lower plenum. Molten debris

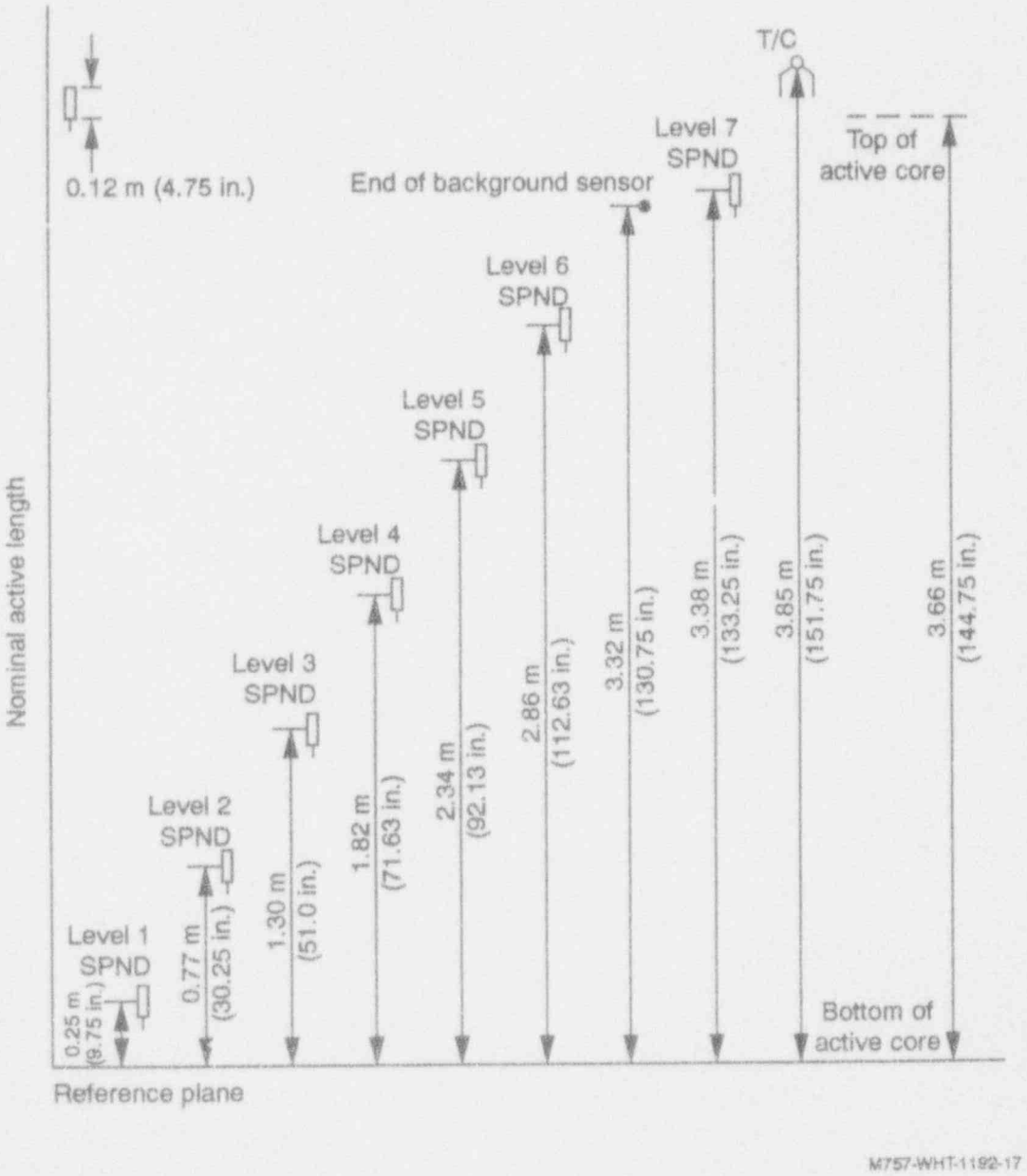

Figure 2-6. Elevations of SPND levels within the core.

flowing across the lower plenum may have heated the SPND leadwires inside the instrument tubes to temperatures high enough to generate thermoelectric currents which would set off the SPND alarms.[3] The timing sequence of level 1 SPND alarms in the vessel between 224 and 226 minutes is mapped in Figure 2-7. The first level 1 alarms occurred at locations P6 and R7 in the southeast quadrant of the vessel. Subsequent alarms moved toward the core center. Level 1 SPND alarms at core locations E9 and H9 alarmed positive between 228 and 232 minutes, along with alarms at higher levels at various core positions. These alarms indicated temperatures of 1,350 K existed either within the core, or in the lower plenum if the leadwires were damaged.

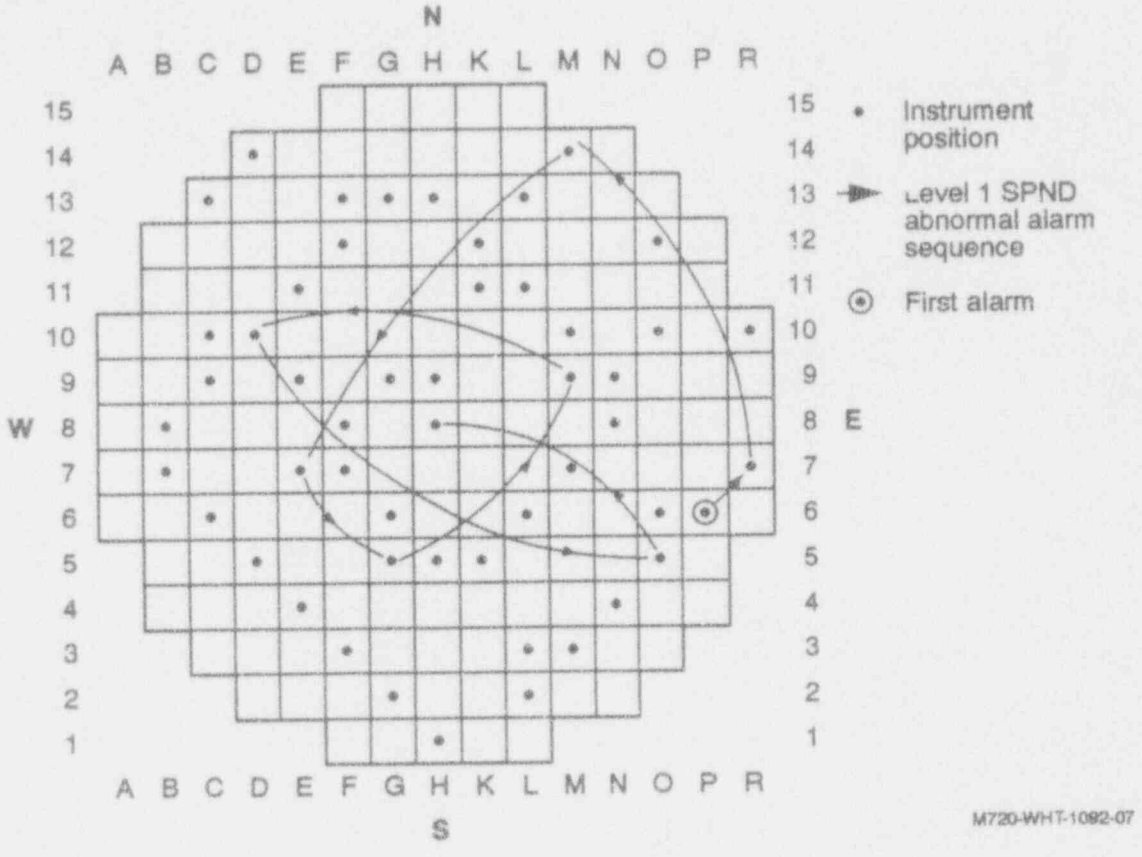

Figure 2-7. SPND level 1 alarm timing.

2.1.4 Core Configuration

The end-state core configuration has been estimated based on the results of core boring operations along with visual inspection of the vessel.[1] Figure 2-8 shows the postulated end-state configuration of the reactor vessel and the core. The end-state configuration was represented by four distinct regions. A void cavity, representing approximately 26% of the original core volume, existed in the upper core region and extended to the core periphery. A loose core debris bed below the void cavity rested on top of a solid crust located at midcore. The upper debris bed was composed of fuel pieces, cladding fragments, and previously molten ceramic and metallic material. The crust encased a region of previously molten core material, part of which surrounded partially intact fuel rods, in the lower half of the core. The fourth region consisted of fuel rod stubs in the bottom of the core, which extended upwards to the previously molten region.

2.1.5 Lower Head Debris

Video inspection and wire probing of the lower head allowed contour maps to be constructed of the debris resting on the lower head.[4] The material on the lower head consisted of a hard layer covered by a bed of loose debris. The distribution of the material on the lower head

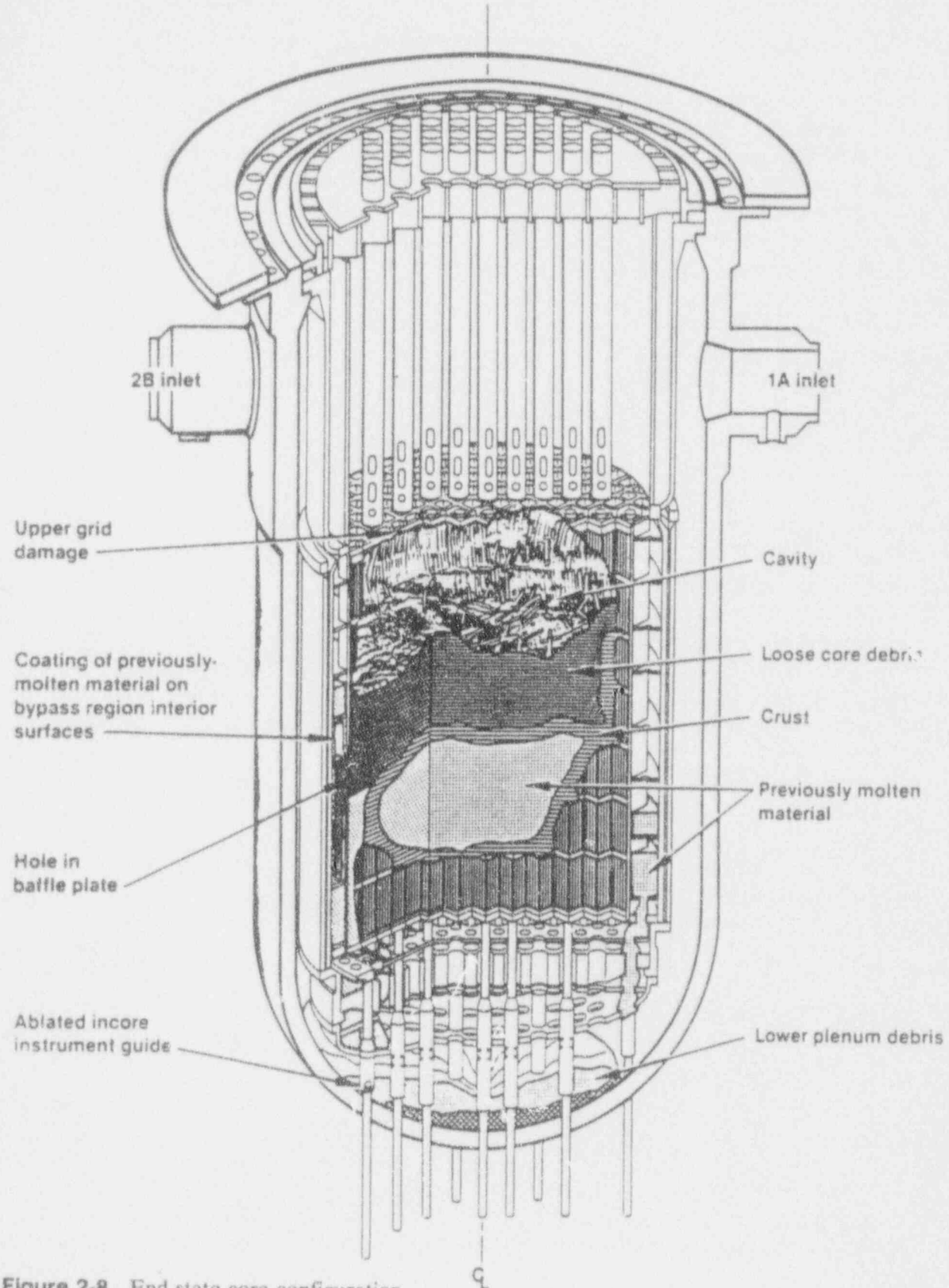

Figure 2-8. End state core configuration.

was neither uniform nor symmetric. The particles composing the loose debris bed varied in size from granules to large rocks. The larger pieces were concentrated toward the periphery, especially in the northeast and southwest quadrants. The granular particles were located towards the center of the core. Results from wire probing examinations were used to obtain the topographical map of the hard layer of debris shown in Figure 2-9. Note that the contour lines shown in Figure 2-9 represent the d· ›th of the hard debris, i.e., the difference between the "hard stop" for the probe tests and the bowl-shaped lower head, rather than the surface contour of the hard layer. As shown in Figure 2-9, the height of the hard layer varied between 0.0 to 0.45 m, and was highest at core locations H8, H9, K8, and K9.[4]

Results from probing 17 of the 52 incore instrumentation tubes indicated that all but one of the tubes were plugged to the extent that a wire would not penetrate into the vessel from the incore seal table. This indicates either the collapse of the probe channel in the instrument string from the pressure gradient, or the presence of melt in the probe channel. Molten debris in the probe channel of the instrument string, see Figure A-43, would not pose a serious safety threat, since it would have to melt through both the instrument string and the instrument tube wall. Penetration into the vessel was achieved at core location L11, and the vessel was gamma-scanned. Results showed increased levels of activity as the probe was retracted from the vessel, suggesting that a layer of fuel-depleted material existed next to the vessel surface. Probes at core locations M7 and G2 came within 0.3 m of penetrating the vessel wall.

Reformed thermocouple junctions embedded in the debris on the lower head indicate that temperatures exceeding 1,000 K existed within the debris bed for three days following the accident.[5] Thermocouple lead wires located in the instrument string of the instrumentation nozzles were melted by the high temperatures of the molten debris, and later reformed new junctions.

2.1.6 TMI-2 Lower Head Video Inspection

Videotaping of the lower head during defueling efforts presented an opportunity to view the damage to the lower head internals, and assisted in postulating relocation scenarios and theories of debris cooling. Ablated nozzles, guide tubes, and the flow distributor plate were videoed. Hard as well as loose debris, ranging from fine silt to large chunks, could be seen. Several surface cracks and crevices were shown, as well as gaps between the nozzles and the debris surrounding the nozzles. With the debris cleared from the lower head, the cladding tear near the nozzle could be seen, as well as the indentations made by the crust impact tool that fractured the layer of hard debris in order to remove it from the vessel.

2.2 TMI-2 VIP Data

2.2.1 Lower Head Temperatures

Hardness and metallurgical examinations were performed on 15 triangular-shaped steel samples, referred to as boat samples, removed from the lower head of the TMI-2 pressure vessel.[6] These examinations identified a hot spot on the lower head of the pressure vessel. Hardness measurements indicate that the material exceeded the ferrite-to-austenite transformation temperature but didn't provide conclusive peak temperature estimates. Eleven of the TMI-2

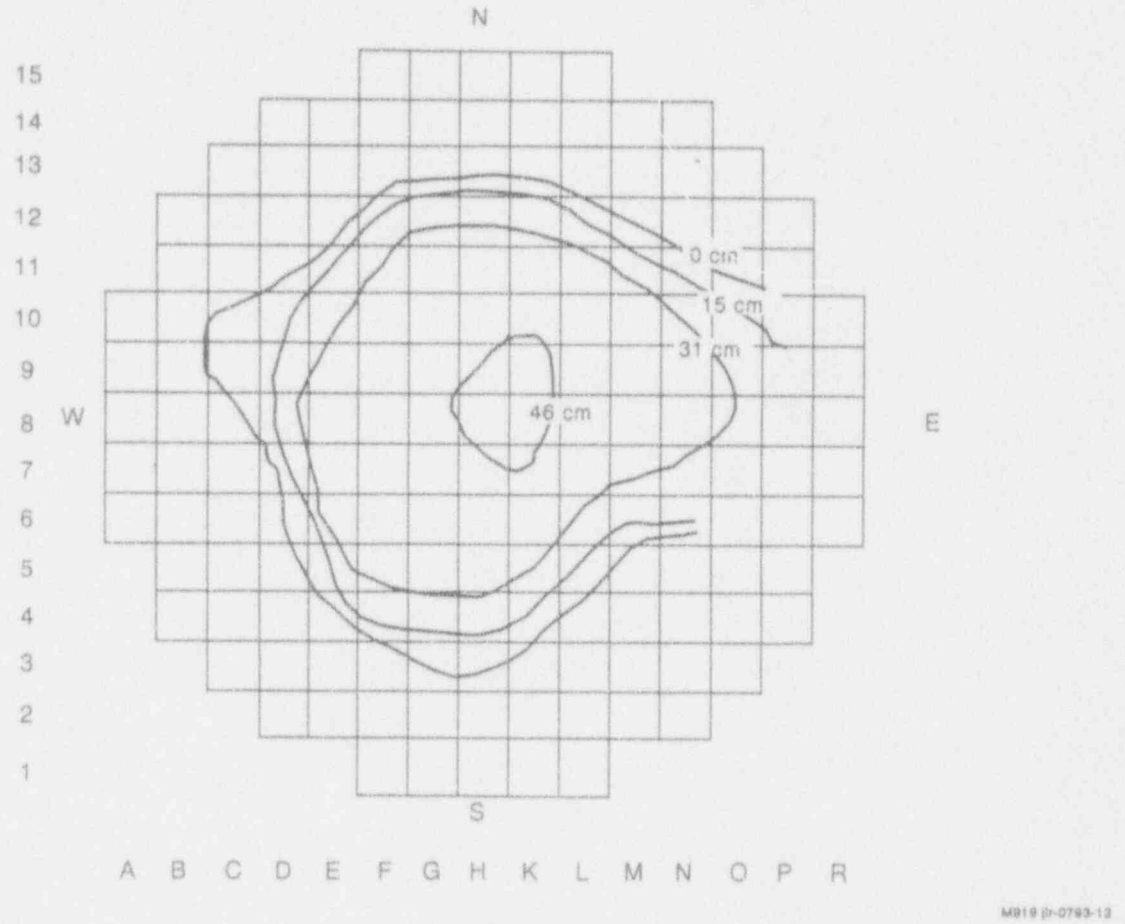

Figure 2-9. Depth of hard layer of solidified debris. (Contour lines designate distance between a "hard stop" from probe tests and the bowl-shaped lower head.)

samples did not exceed 1,000 K during the accident. These samples were removed from core locations D10, E11, F5, H4, H5, H8, K7, K13, L9, M9, and M11. Hardness measurements indicate samples from locations E6, E8, F10, and G8 were exposed to higher temperatures. Bounds on the thermal loading of the four samples were determined through metallurgical comparison with heat-treated archived samples from a similar reactor vessel. Samples from core locations F10 and G8 experienced temperatures in the range of 1,313 to 1,333 K for 30 minutes. Samples at locations E6 and E8 experienced temperatures ranging from 1,348 to 1,373 K for 30 minutes. The temperatures 50 mm inside the vessel surface were estimated to be 100 ± 50 K lower than estimated peak temperatures. Examinations indicate that the vessel material cooled through the transition temperature at rates of 10–100 K/min at times between 15 and 50 minutes after peak hot spot temperatures occurred. Stainless steel cladding showed no signs of melt, even inside the hot spot. Figure 2-10 illustrates the relative position and temperature distribution of the hot spot on the lower head.

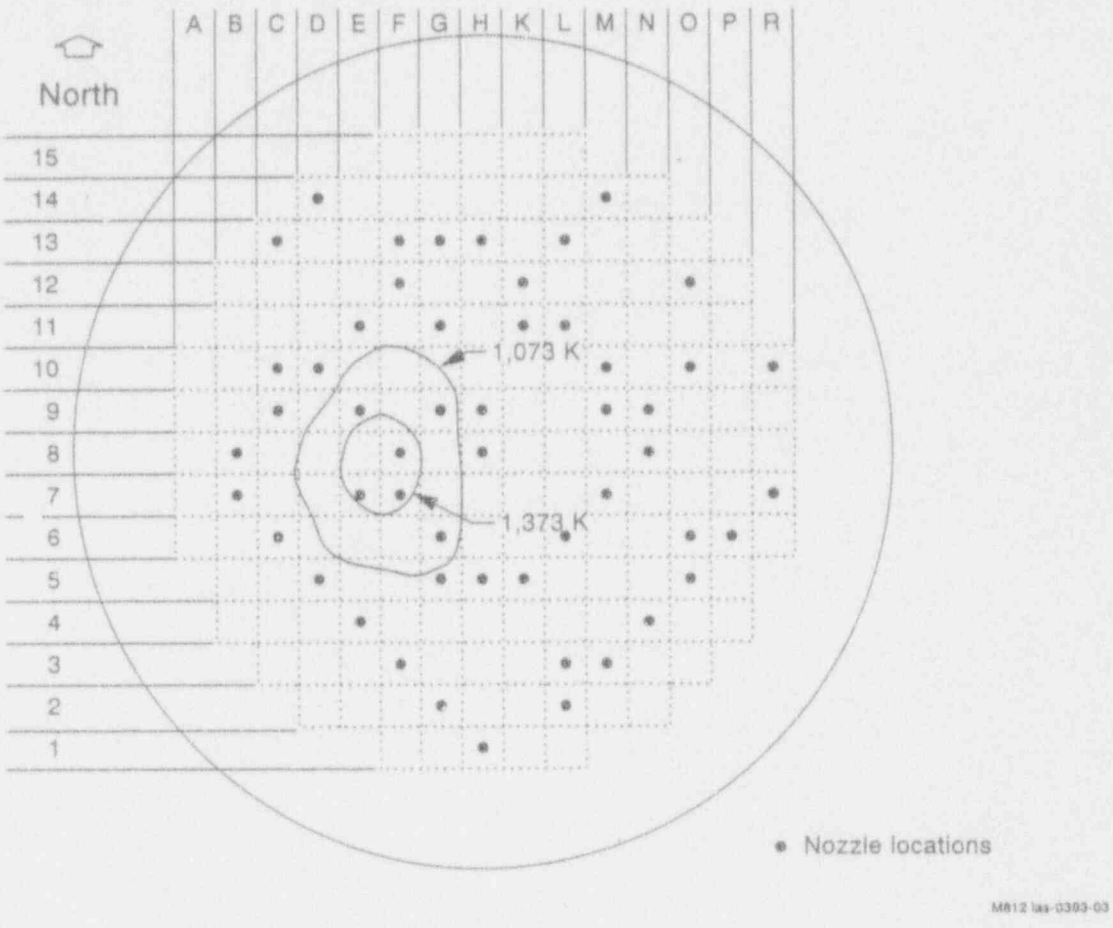

Figure 2-10. Hot spot location on lower head.

2.2.2 Lower Head Debris Properties

The debris on the lower head consisted of a hard layer, from which companion samples were cut, covered by a bed of loose debris. Samples of the solidified melt from the hard layer in contact with the lower head, termed companion samples, were extracted from the vessel in order to assess the properties of the melt.[7] Densities of nine companion samples ranged from 7.45 to 9.40 g/cm^3. Samples with the highest density were extracted from the southeast quadrant of the pressure vessel. Previous examinations[8] indicated that the loose debris varied in density from 6.57 to 8.25 g/cm^3. Differences in density were attributed to variations in the porosity of the melt. Porosities of 16 companion samples ranged from 5 to 41%, averaging 18 ± 11%.

The loose debris and companion samples from the hard layer differed slightly in composition. Loose debris had an average uranium content of 65 wt%, while companion samples contained about 70 wt% uranium. Both had similar amounts of zirconium. The loose debris had slightly higher concentrations of structural materials than the companion samples. The relative composition of the companion samples was determined to be 78 wt% UO_2 and 17 wt% ZrO_2. The remaining 3% represents stainless steel and Inconel constituents that were probably melted during relocation. Metallic melt was found only in samples from the southwest quadrant of the

vessel. Peak temperatures of material within the companion samples, which would have occurred prior to when the molten debris flowed from the core to the lower head, were estimated to have ranged from 2,873 to 3,123 K.

Evidence supports the assumption that metallic material may have existed on the lower head prior to the relocation of the molten $(U,Zr)O_2$. Control assembly material has been found on the surface of nozzle H8 for heights up to 12.0 to 17.0 cm, measured from the base of the nozzle.[9]

2.2.3 Melt Decay Heat

Decay heat calculations were performed to determine the amount of available heat within the bed of molten fuel in the lower head at 224 minutes and at 600 minutes after reactor scram.[7] The decay heat at 224 minutes after scram was found to be 0.18 W/g of uranium and 0.14 W/g of uranium at 600 minutes. Converting the data using the calculated average melt composition of the hard layer (70 wt% U, 13.75 wt% Zr, and 13 wt% O), the decay heat at 224 minutes was 0.13 W/g of melt and at 600 minutes was 0.096 W/g of melt. The accuracy of the reported decay heat values is estimated at ± 20%. Companion sample examinations[7] also indicated the presence of secondary phases of $(Zr,U)O_2$ with Fe and Cr around pores and in the matrix material. The formation of these phases requires a long cooldown period (between 3 and 72 hours), rather than a rapid quench.[7]

2.2.4 Nozzle Ablation

Fourteen nozzles were cut from the lower head of the pressure vessel for examination.[10] These nozzles were at core locations D10, E7, E11, G5, H5, H8, H9, K11, K12, L6, L11, M9, M10, and R7. The initial length of all nozzles was 30.5 cm. Those nozzles removed from the vessel that were not ablated during the accident included E11, H9, K11, K12, L6, L11, and R7. Several of the nozzles, which were within the hot spot, were severely ablated. These nozzles include E9, F7, F8, G6, and G9. The stubs remaining in the vessel at these locations were estimated to be 1.3 to 2.5 cm tall.[a] The ablated heights of the other nozzles removed from the vessel were: H5–14.6 cm, D10–29.2 cm, H8–12.1 cm, M10–10.2 to 12.7 cm, M9–27.9 cm, E7–5.1 cm, and G5–10.2 cm. The height of nozzles that were not cut were not measured. Figure 2-11 shows the relative heights of the nozzles and their positioning within the lower head.

2.2.5 Composition of Melt Attached to Nozzles

Solidified debris in contact with the inside and outside of nozzles D10, E11, H5, H8, L6, and M9 was examined using scanning electron microscopy (SEM) techniques.[9] The results are shown in Table 2-1. The elevations are referenced from the base of each nozzle. Table 2-2 presents results of SEM examinations on debris shards attached to the outside of nozzles E7, G5, M10, and R7.[b] The exact elevations of the measurements are unknown. However, most of the debris shards were removed from the top of each nozzle. No element's percentages were computed.

---

a. Personal communication with Noman Cole, MPR Associates, Inc., Washington, D.C., October 1992.

b. Unpublished research results of Brian K. Schuetz, Idaho National Engineering Laboratory, EG&G Idaho, Inc., Idaho Falls, Idaho.

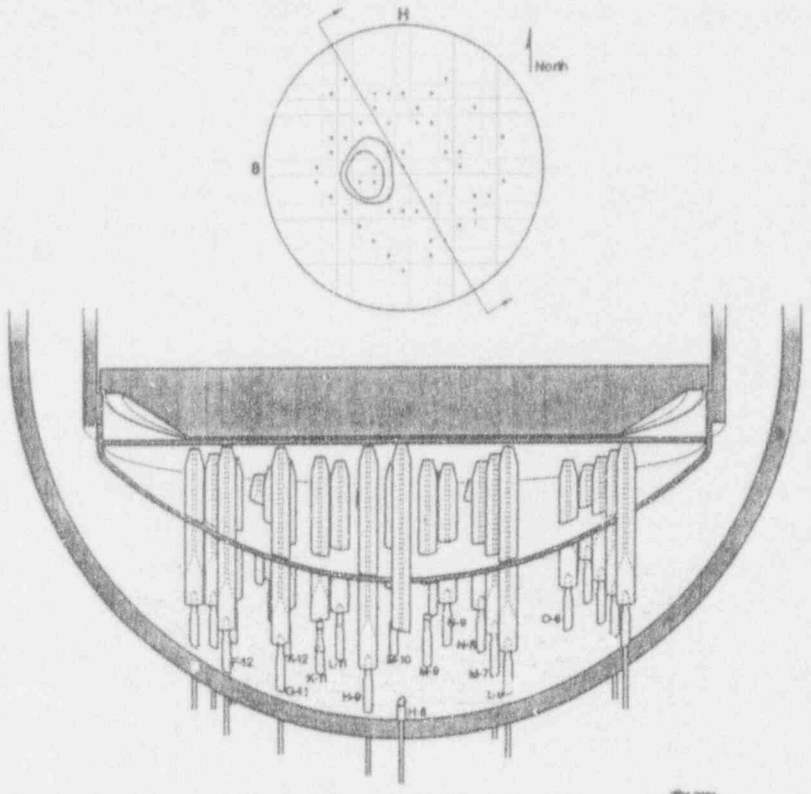

(a) northeast section

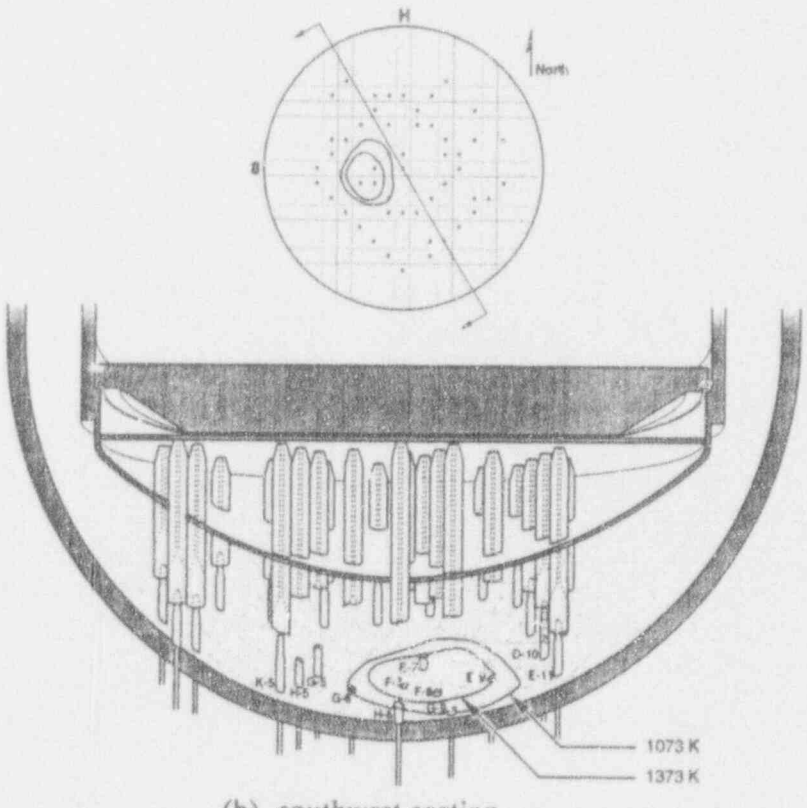

(b) southwest section

Figure 2-11. Three-dimensional figure of nozzle end state in the lower head.

Table 2-1. Composition of debris in contact with nozzles.[a]

Nozzle/Location[c]	Composition, wt%[b] U	Zr	Fe	Ni	Cr	Ag	Cd	Al
M9 @ 279 mm inside								
matrix	29	8	6	5	43	-	-	7
matrix	55	12	5	2	15	-	-	9
particle	58	19	8	11	3	-	-	-
fuel mass	88	9	1	1	1	-	-	-
fuel mass	83	15	1	-	1	-	-	-
fuel mass	55	12	5	15	2	-	-	9
L6 @ 283 mm inside								
shard	100	-	-	-	-	-	-	-
solidified mass	83-87	11-13	2	-	1	-	-	-
grain boundary	41	19	17	-	14	-	-	8
solidified mass	17	54	9	1	11	-	-	9
solidified mass	74	27	-	-	-	-	-	-
H5 @ 140 mm inside								
ceramic area	25-30	13-15	1-3	1	51-57	-	-	-
ceramic area	82	12	1	3	1	-	-	-
ceramic area[d]	(35-40)	(12-16)	-	(40-55)	-	-	-	-
ceramic area	13-30	8-12	7-22	2-10	40-77	-	-	-
ceramic area	28	15	33	11	13	-	-	-
H8 @ 120 mm inside								
particulate area	60	30	4	3	1	-	-	-
D10 @ 280 mm inside								
particle	65	23	4	3	5	-	-	-
particle	63	12	5	15	6	-	-	-
D10 @ 158 mm imbedded in nozzle								
particle	68	23	4	2	2	-	-	-
particle	77	20	1	1	1	-	-	-
particle	91	8	-	1	-	-	-	-

Table 2-1. (continued).

Nozzle/Location[c]	Composition, wt%[b] U	Zr	Fe	Ni	Cr	Ag	Cd	Al
D10 @ 82 mm outside								
particle	14	62	8	6	2	7	-	-
particle	81	16	2	1	-	-	-	-
particle	75	16	6	2	2	-	-	-
particle	10	77	6	5	1	-	-	-
particle	22	78	-	-	-	-	-	-
D10 @ 69 mm outside								
imbedded particle	82	12	1	3	1	-	-	-
E11 @ 280 mm inside								
large shard	83	14	1	-	1	-	-	-
small shard	83	14	2	-	1	-	-	-
matrix	34	53	8	3	3	-	-	-
matrix	47	44	6	2	1	-	-	-
matrix	66	27	4	2	1	-	-	-
matrix	87	10	1	-	1	-	-	-
surface fold outside	74	10	2	6	2	-	-	6
E11 @ 274 mm inside								
inside nozzle	~9	~85	4	2	1	-	-	-
inside nozzle	27	71	1	1	-	-	-	-
agglomerates	62	16	19	3	-	-	-	-
E11 @ 90 mm outside								
outer scale	20	20	57	2	1	-	-	-

a. Normalized to ~100% metal: oxygen not considered.

b. Estimated accuracy is ± 5%.

c. Location from the base of each nozzle.

d. Parentheses identify estimated values for portion of analyzed area.

Table 2-2. Melt constituents on nozzle surfaces.

E7	Zr-U-Ag-Cd-Fe-Cr-Mn
	Zr-Ni-Al-Cr-Nb-Co-Ag-In-Fe-Cr-Mn
	Zr-Fe-Cr-Mn-Ni
	Zr-Nb-Ni-Cr-Fe-Mn-Mg-Al-Ag-Cd
G5	Ni-Al-Si-Co
	Zr-U-Cr-Ag
M10	Fe-Cr-Mn-U-Zr-Nb-Al-Ag-Co-Mg
	Ar-Ni-Fe-Cr-Ag-In
	Zr-Fe-Cr-Mn-Ni-Al
R7	U-Cr-Ni-Al-Nb-In-Te-Sb-Mg-Sn-Zr-Ce-Sr
	U-Zr-Fe-Cr-Mn-Ni-Al-In-Cd

2.2.6 Melt Flow Through Nozzles

The distance molten debris penetrated the nozzles which were removed from the vessel was determined from observation, gamma scanning, and wire probe testing.[9,c] Several nozzles had been severely melted to within 1.3 to 2.5 cm of the vessel.[d] These nozzles included E9, F7, F8, G6, and G9. It is not known if melt was present in the stubs of these nozzles. After cutting the nozzle at core location K11, what appeared to be resolidified fuel was discovered filling the annulus at the top of the stub remaining in the vessel.

The debris penetration elevations from gamma scans for nozzles D10, E11, H5, H8, L6, and M9 are presented in Table 2-3. The penetration elevation was measured from the base of each nozzle. Gamma scans were also performed on nozzles E7, G5, H9, K11, K12, L11, M10, and R7. However, penetration elevations were not estimated for these nozzles because SEM examinations, which would verify the results of the gamma scans, could not be performed due to shutdown of the radiation containment facilities at the Idaho National Engineering Laboratory where the work was to be performed.

Wire probe tests were conducted on eight of the nozzle sections removed from the pressure vessel.[c] The results are presented in Table 2-4. This method identified nozzles with completely blocked coolant passages. Results that indicate no blockage do not imply the absence of melt. Rather, these results indicate that a wire probe was able to penetrate the annulus the length of the nozzle, even though melt may have been present inside the nozzle, and partially blocked the coolant passage.

---

c. Personal communication with Brian K. Schuetz, Idaho National Engineering Laboratory, EG&G Idaho, Inc., Idaho Falls, Idaho, June 29, 1992.

d. Personal communication with Noman Cole, MPA Associates, Inc., Washington, D.C., October 1992.

Table 2-3. Melt penetration elevation[a] (cm).

Nozzle	Gamma scan
D10	5.5 max, 18.4 min
E11	20.4
H5	8.9 max, 11.7 min
H8	< 6.4
L6	7.5
M9	24.1

a. Elevation referenced from the base of each nozzle.

Table 2-4. Wire probe test results.

Nozzle	Probe Results
E7	No blockage
G5	Nozzle completely filled with melt.
H9	No blockage
K11	Complete blockage not encountered, narrowing of the interior noted
K12	No blockages
L11	No blockages
M10	Complete blockage at 5.7 cm from the cut end. (The shape and depth appeared to vary at this location.)
R7	No blockages

2.2.7 Nozzle Temperatures

Microhardness measurements have been completed on selected nozzles.[9] These results, which are only qualitative, indicate temperatures less than 1,223 K existed near the vessel, with the exception of nozzle H8. Table 2-5 presents the results. Low hardness values that were not associated with chromium-depleted areas indicated high temperatures. Analysis of the results show that average temperatures at the base of nozzle D10 remained below 1,223 K. A solidified 304 stainless steel droplet on nozzle D10 indicated a possible temperature of 1,673 K 13.3 cm above the bottom of the vessel. Similar hardness values at the top and bottom of nozzle sample E11 indicated that no significant axial temperature gradients existed in the nozzle. The temperature of nozzle L6 remained below 1,273 K 19.1 cm from the vessel bottom. The surface temperature of nozzle H5 at a position 10.2 cm from the vessel bottom ranged from 1,223 to 1,673 K. Hardness values for nozzle H8 suggested that the average temperature of the nozzle was 1,223 K.

2.3 Relocation Scenario

This section provides a reference for assumptions and initial conditions used in margin-to-failure calculations that require information related to the manner in which material relocated from the core to the lower head. As noted within this section, data were not sufficient to conclusively determine how material relocated to the lower plenum. Hence, several scenarios are postulated. As margin-to-failure calculations were completed, results indicated that certain assumptions made in some of these scenarios were incorrect. In fact, as indicated by results documented in this report, analyses suggest that only Scenarios 2 and 4 (explained below) were not contradicted by margin-to-failure calculation results.

As discussed in Section 2.2, small amounts of control material may have relocated prior to 224 minutes. However, most ceramic material relocated from the core to the lower head 224 to 226 minutes after reactor scram. The relocation was completed in approximately 100 seconds. The relocation was substantiated by a sharp increase in pressure and by the increase in SRM count rate (see Figures 2-1 and 2-5).

The relocation path of molten debris through control support assemblies and peripheral fuel assemblies took place primarily within the southeast quadrant of the vessel. A large quantity of material existed between the grid forging and the flow distributor plate, as well as above the plate, to the north, east, and south of core location N12.[11] Figure 2-12 illustrates the location of these core support structures. Resolidified material that flowed through the distributor plate was observed to the northwest, north, northeast, and east of location N12. Material was also visible between the grid forging and the instrument support plate at the periphery of the core. This did not appear to be a major pathway for relocation, because no debris was observed below the instrument support plate. Debris filled approximately 60–80% of the space between the grid forging and the instrument support plate on the core periphery at core location O7.[11] This was the only location where significant quantities of debris existed between the plates and may have been a major relocation pathway. This fact cannot be verified because no inspection holes exist at this location in the lower head and because no other inspection activities covered the region below the flow distributor plate.

Table 2-5. Microhardness measurements.

Elevation from Vessel (cm)	Nozzle D10	E11	H5	H8	L6	M9
29.0	-	208±29	-	-	-	-
28.3	-	-	-	-	167±7	-
28.0	140±4	-	-	-	-	-
27.4	-	137±4	-	-	-	-
[illegible]	136±3	-	-	-	-	-
[illegible]	-	-	-	-	-	124±5[a]
15.8	124±2	-	-	-	-	-
13.0	-	-	-	105±2[a]	-	-
9.0	-	190±9	-	-	-	-
8.2	161±4	-	-	-	-	-
7.7	-	-	-	-	169±13	-
6.9	168±10	-	-	-	-	-
6.4	-	-	133±4	-	-	-
3.8	-	-	-	-	-	202±28
2.5	-	-	-	198±8	-	-
0.0	-	-	-	217±13[b]	-	-

a. Cr-depleted material.
b. Weldment.

Since there is a lack of conclusive evidence concerning the relocation of debris to the lower head, four scenarios have been postulated to provide background for margin-to-failure calculations.

Scenario 1

Molten debris relocated through lower plenum structures with some amount of jet breakup. As debris flowed through the elliptical flow distributor plate, blockages forced the material toward locations E6, E10, F6, and G10, where the vessel was estimated to have undergone a more severe thermal transient.[6] Debris relocated primarily as a coherent jet from the core distributor plate to the lower head, followed by dispersed particles and molten droplets which fell at a slower rate. The debris formed an insulating crust upon contact with the vessel lower head and/or any metallic material that may have previously relocated to the lower head. Any metallic material was subsumed within the higher temperature molten debris. The increase in RCS pressure was due to steam generated by the heat transferred from the molten debris to the water, which filled the lower head.

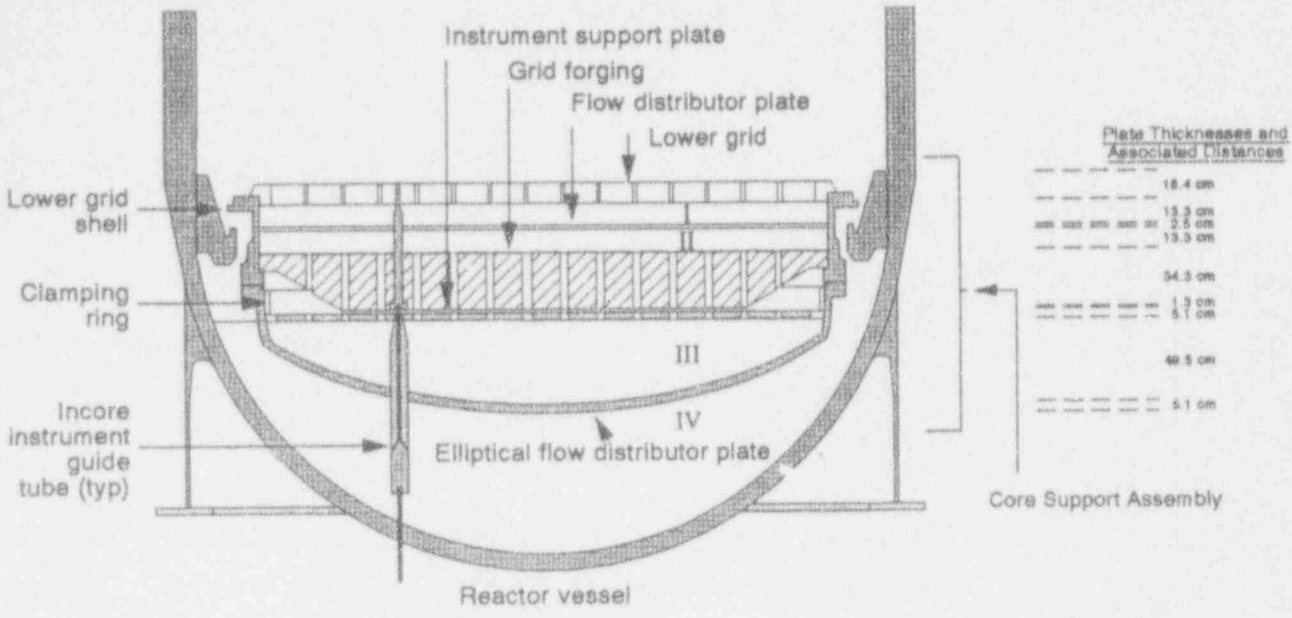

Figure 2-12. Lower head core support assembly.

Scenario 2

Molten debris relocated downward along the periphery of the vessel with little jet breakup. The material was a two-phase "wet sand" (slurry-like) mixture of liquid and solid debris by the time it reached the lower head.[12] The two-phase mixture formed a crust upon contact with the lower head and/or any metallic material that may have previously relocated to the lower head. An upper crust of this material was continuously forming and breaking up as material moved across the surface of the lower head. This action produced the loose debris bed on the upper surface of the debris bed. Any metallic material was subsumed within the higher temperature molten debris near the lower head. In this scenario, it is assumed that the large pressure increase beginning at 224 minutes was not due to fuel/coolant interactions between the jet of molten debris and the coolant in the lower head. Instead, the pressure increase is attributed to fuel/coolant interactions within the core.[13]

Scenario 3

Multiple jets of debris relocated through lower plenum structures and into the coolant in the lower head. Jet breakup resulted in the formation of a rubble bed on top of metallic debris. Voiding occurred in the central region of the loose debris bed, with remelting of debris in central regions following. This newly molten material subsequently flowed downward and subsumed any metallic material near the lower head.

Scenario 4

Molten debris relocated at one point at the periphery of the core and outside through the core barrel and baffle plate. Some jet breakup, steam generation, and melt droplet freezing occurred as the debris relocated through the coolant in the lower head. Crusts were formed by top cooling from RCS coolant and bottom cooling from heat removal by the vessel and any metallic debris on the lower head.

2.4 References

1. J. M. Broughton, P. Kaun, D. A. Petti, E. L. Tolman, "A Scenario of the Three Mile Island Unit 2 Accident," *Nuclear Technology*, *87*, August 1989, p. 34.

2. Nuclear Safety Analysis Center, *Interpretation of TMI-2 Instrument Data*, NSAC/28, Electric Power Research Institute, Palo Alto, CA, May 1982.

3. D. J. N. Taylor, "TMI SPND Interpretation," *Proceedings of the First International Information Meeting on the TMI-2 Accident, Germantown, Maryland, October 1985*, CONF-8510166, October 1985, pp. 65-74.

4. A. P. Kelsey, *Lower Head Debris Topography*, TMI-2 Technical Bulletin TB-89-02, Rev. 0, GPU Nuclear Corporation, Project Planning and Analysis Department, Middletown, PA, February 27, 1989.

5. T. L. Van Witbeck et al., *Three Mile Island Unit 2 Annotated Sequence of Events, March 28, 1979*, GPU-TDR-044, GPU Nuclear, Inc., February 6, 1981.

6. G. E. Korth, *Metallographic and Hardness Examinations of TMI-2 Lower Pressure Vessel Head Samples*, OECD-NEA-TMI-2 VIP TMI V(92)EG01, January 1992.

7. D. W. Akers, S. M. Jensen, B. K. Schuetz, *Companion Sample Examinations*, OECD-NEA-TMI-2 VIP TMI V(92)EG10, July 1992.

8. C. S. Olsen, D. W. Akers, R. K. McCardell, *Examination of Debris from the Lower Head of the TMI-2 Reactor*, GEND-INF-084, January 1988.

9. L. A. Neimark, T. L. Shearer, A. Purohit, and A. G. Hins, *TMI-2 Instrument Nozzle Examinations at Argonne National Laboratory*, OECD-TMI-2 VIP TMI V(93)AL01, February 1993.

10. MPR Associates, Inc., *Removal of Test Specimens from the TMI-2 Reactor Vessel Bottom Head*, MPR-1195, October 1, 1990.

11. G. Worku, *Core Stratification Sampling Program*, TMI-2 Technical Bulletin TB-86-35, Rev. 3, GPU Nuclear Corporation, Project Planning and Analysis Department, Middletown, PA, August 18, 1986.

12. R. V. Strain, L. A. Neimark, and J. E. Sanecki, "Fuel Relocation Mechanisms Based on Microstructures of Debris," *Nuclear Technology*, *87*, No. 1, August 1989, p. 214.

13. M. Epstein, and H. K. Fauske, "The Three Mile Island Unit 2 Core Relocation - Heat Transfer and Mechanism," *Nuclear Technology*, *87*, No. 4, December 1989, p. 1021.

3. SCOPING CALCULATIONS FOR MELT RELOCATION AND THERMAL RESPONSE

As discussed in Section 1, several calculations provided input to the margin-to-failure analyses. This section describes calculations performed to determine the distance melt penetrated through the instrumentation nozzles of the TMI-2 pressure vessel, the potential for a jet of molten debris to fragment as it travels through coolant, and the thermal response of the vessel during and after the relocation of molten debris to the lower head.

Figure 1-1 illustrates how results from calculations in this section are used in subsequent failure analyses. For example, if results from melt penetration calculations indicate that molten fuel will not relocate through a tube to locations below the lower head, the reactor coolant system temperatures would be applied in subsequent tube rupture analyses without performing an ex-vessel tube temperature analysis. If melt penetration calculations indicate molten fuel relocated below the lower head, the ex-vessel tube temperature analysis would be performed, and results from that study would be used as input for the tube rupture analyses. Time-dependent temperature distributions from the vessel thermal analysis were used to evaluate the integrity of the weld holding the lower head penetration tubes to the vessel and the potential for global and localized failures to occur in the vessel.

3.1 Study of Melt Penetration through TMI-2 Instrumentation Nozzles

The objective of this study was to determine the degree of melt ingress into the instrumentation nozzles of the TMI-2 vessel lower head, specifically to determine if melt contacted ex-vessel tube sections. This section provides a description of the instrumentation nozzles extracted from the TMI-2 pressure vessel lower head based on examinations performed at Argonne National Laboratory (ANL) and the Idaho National Engineering Laboratory (INEL), outlines the two analytical models considered for calculating the melt penetration distance, examines the calculational parameters for input to the models, and presents the results of comparisons between model predictions and observed melt depths in the nozzles.

3.1.1 TMI-2 Instrumentation Nozzles

Fourteen in-core instrumentation nozzles were cut from inside the TMI-2 lower head pressure vessel over a period of 4 days in February 1990.[1] The nozzles were designated based on their position in the lower head. The nozzles extracted were D10, E7, E11, G5, H5, H8, H9, K11, K12, L6, L11, M9, M10, and R7. Of the 14 nozzles cut, six of these were shipped to ANL for examination, and the remaining eight were to be examined at the INEL. Figure 3-1 illustrates the position of the nozzles in the lower head.

The eight nozzles received at the INEL were E7, G5, H9, K11, K12, L11, M10, and R7. Each nozzle was visually examined. Radioactivity scans for cobalt-60 and cesium-137 were performed on nozzles H9, K11, K12, L11, M10, and R7.[2] Nozzles G5 and E7 were too short to be scanned. Cutting locations for sectioning each nozzle were identified from the activity profiles. Microphotography was used to view the microstructure and composition of melt attached to the nozzles. However, very few photographs of transverse cuts that might indicate the presence and

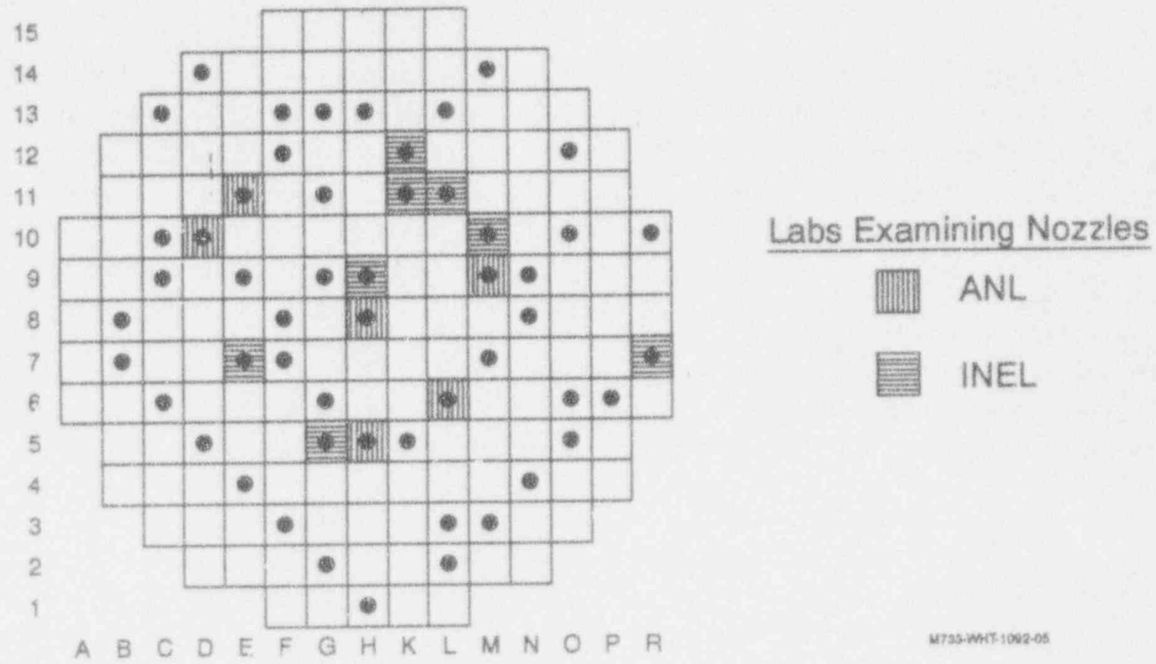

Figure 3-1. TMI-2 instrumentation nozzle map.

cross-sectional area of melt in the nozzle annuli were taken. Wire probe tests were performed on the eight nozzles to determine the extent of blockage by debris within the nozzles (Table 2-4).[a] Further work was discontinued due to a shutdown of the hot cells where the work was to be performed.

The remaining nozzles, D10, E11, H5, H8, L6, and M9, were examined at ANL.[3] The six nozzles underwent visual examinations and activity scans for cobalt-60 and cesium-137. Information derived from the activity scans determined locations for sectioning the nozzles for SEM analysis. Microhardness measurements were also taken at various positions along the length of each nozzle. Microphotography of the six nozzles included transverse cuts along the nozzles, showing the size and position of melt in the annulus between the instrumentation string and nozzle wall. This enabled the melt cross-sectional area along each nozzle to be estimated. Figure 3-2 shows curves of the relative annular area covered by melt as a function of the distance from the base of each nozzle. The area of melt estimates given in Figure 3-2 may include debris such as ablated instrument strings, control assembly material, and ablated nozzle material.

Photographs of transverse cuts through the six nozzles show solidified molten material formed either a kidney shape within the nozzle annulus or a ring around the inside of the nozzle wall. Figure 3-3 illustrates the approximate shapes of the two types of formations found in the nozzles. As shown, the sides of the kidney-shaped melt contact coolant, the other sides contact

a. Personal communication from Brian K. Schuetz, Idaho National Engineering Laboratory, EG&G Idaho, Inc., Idaho Falls, Idaho, June 29, 1992.

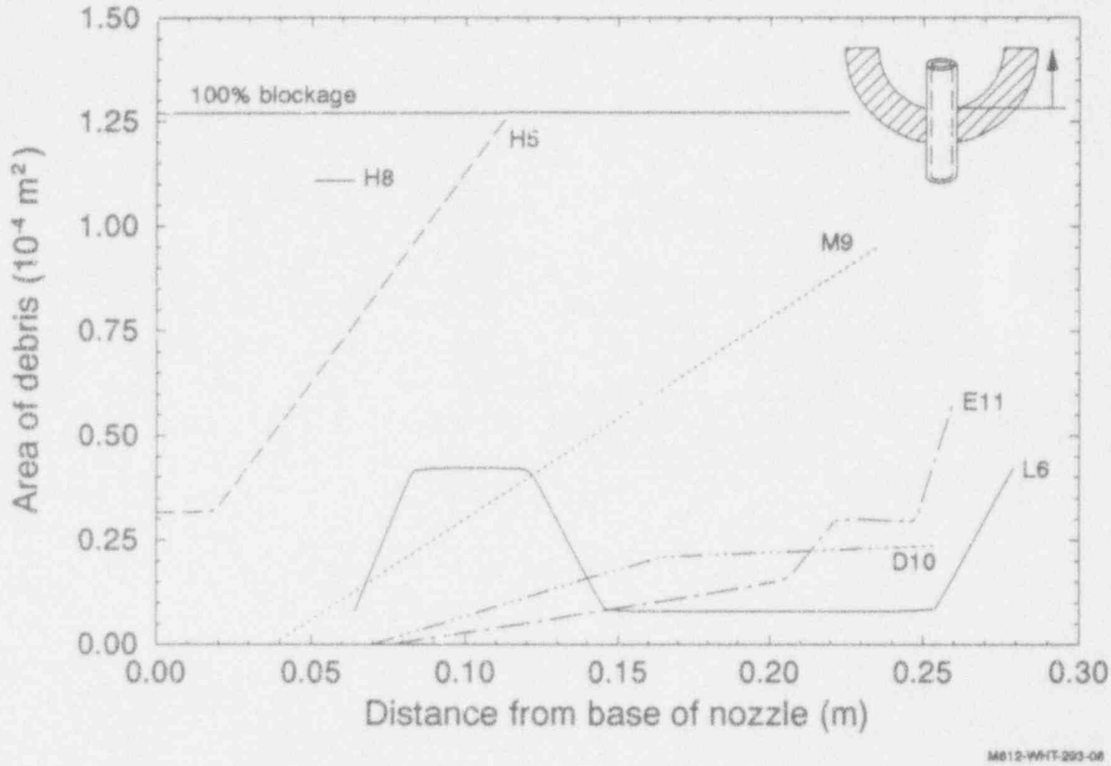

Figure 3-2. Ar··· f debris versus distance from nozzle base for nozzles D10, E11, H5, H8, L6, and M9.

the nozzle wall and/or the instrument string. The circumference of melt in the ring type of formation contacts the nozzle wall on one side and coolant on the other. Five of the six nozzles examined by ANL were determined to hold kidney-shaped melt, and one contained ring-shaped melt.

Nozzle lengths and comments describing each of the 14 nozzles cut from the lower head of the pressure vessel were compiled from various sources[1-4] and are presented in Appendix B. Additional data from nozzle examinations have also been reported previously in Tables 2-1 through 2-5.

3.1.2 Model Selection

Several models have been developed to predict the penetration distance of molten debris through vessel instrumentation nozzles. Reference 5 summarizes previous analytical and experimental studies that have been performed to consider melt transport through failed tubes. Although no validated model is available for predicting melt flow through light water reactor instrument tubes, melt penetration has been experimentally determined to be bounded by distances predicted by the bulk-freezing model first advanced by Ostensen and Jackson[6,7] and a conduction model proposed by Epstein.[8] The selection of the most appropriate model for calculating the distance that the melt flowed through the TMI-2 nozzles is discussed below.

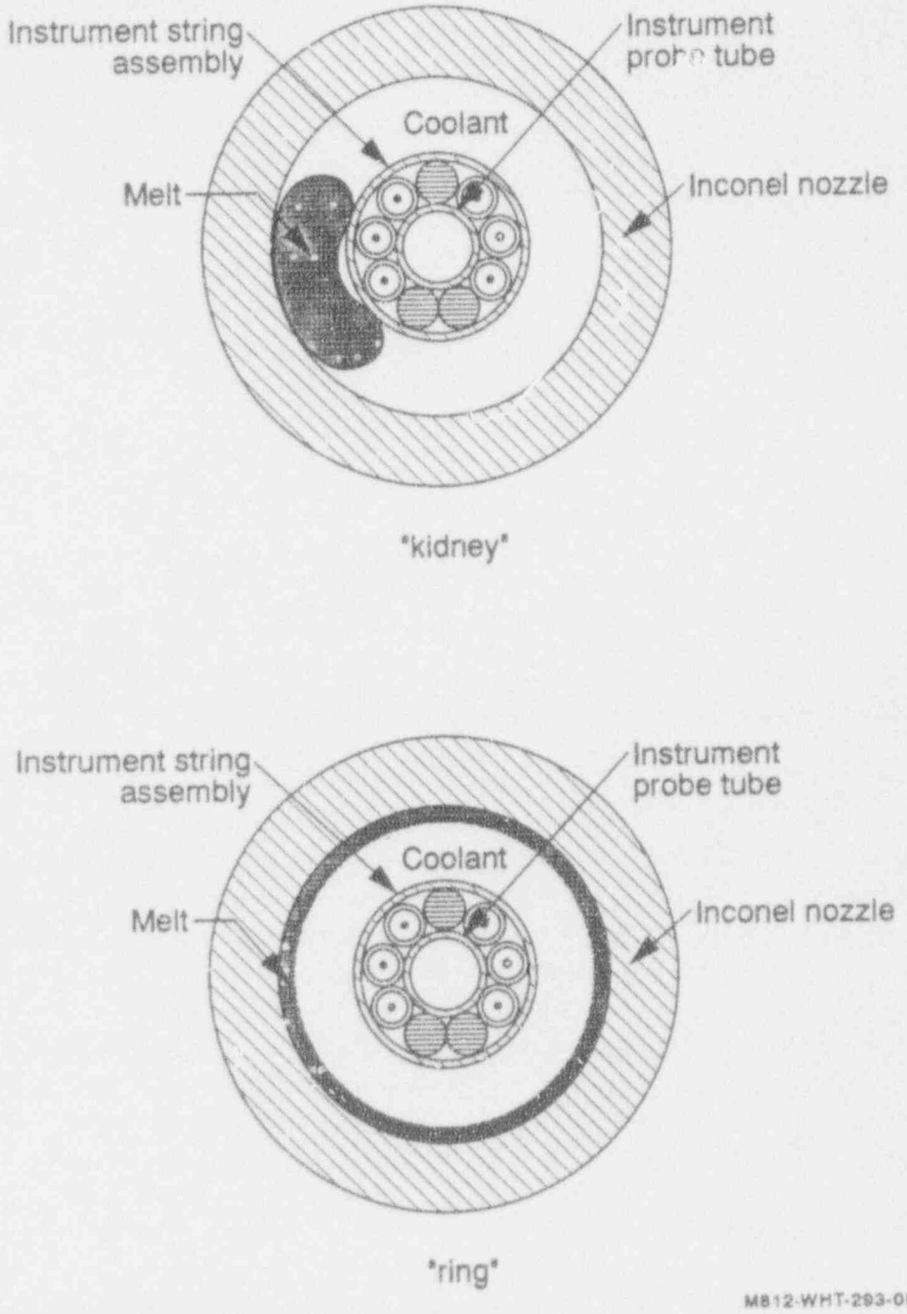

Figure 3-3. Geometry of melt formations.

The conduction layer model assumes that transient freezing is governed by crust buildup at the nozzle wall, where conduction heat transfer governs heat loss from the melt to the nozzle wall. Once the frozen layer closes at the center, flow ceases, and the remaining melt inside the nozzle freezes [see Figure 3-4(a)]. The model ignores heat transfer from the leading edge of the flow and considers only radial heat transfer. The model does not account for the presence of any coolant within the nozzle. The model also assumes a constant melt velocity into a thick-walled channel. Since the molten material is assumed to be at or near its melting point, no convective heat exchange occurs at the melt-crust interface. Crust solidification is assumed to be independent of melt flow dynamics. For all times, t, the crust thickness is zero at the leading edge and maximum at the inlet.

The conduction model predicts a square root dependence for the crust thickness, σ_c, as a function of time, t, in a semi-infinite wall channel[8]

$$\sigma_c(t) = 2\lambda_c\left(\alpha_{id}t\right)^{0.5} \tag{3-1}$$

where

λ_c = solidification constant for the melt in contact with an Inconel or stainless steel nozzle

α_{id} = melt thermal diffusivity.

The solidification constant is found from various approximations of boundary conditions and the number of regions that may experience phase change. The solidification constant for molten ceramic material in contact with either Inconel-600 or stainless steel nozzles is estimated to have a value of ~0.75.[9] Likewise, the solidification constant for molten metallic material in contact with either Inconel-600 or stainless steel nozzles is estimated to have a value of ~0.2.[9]

Substituting the criteria for melt freezing ($\sigma_c = d_e/2$) and the relationship between time and penetration distance, $t = x_p/v_d$, into Equation (3-1), the following relationship was obtained for predicting melt penetration distance:

$$x_p = \frac{d_e Pe}{16\lambda_c^2} \tag{3-2}$$

where

d_e = effective melt diameter

Pe = Peclet number based on the velocity v_d.

The effect of coolant within the nozzles on the melt penetration distance was modeled by assuming a reduction in melt flow area, thus reducing the effective melt diameter as would occur if coolant were present in the nozzle.

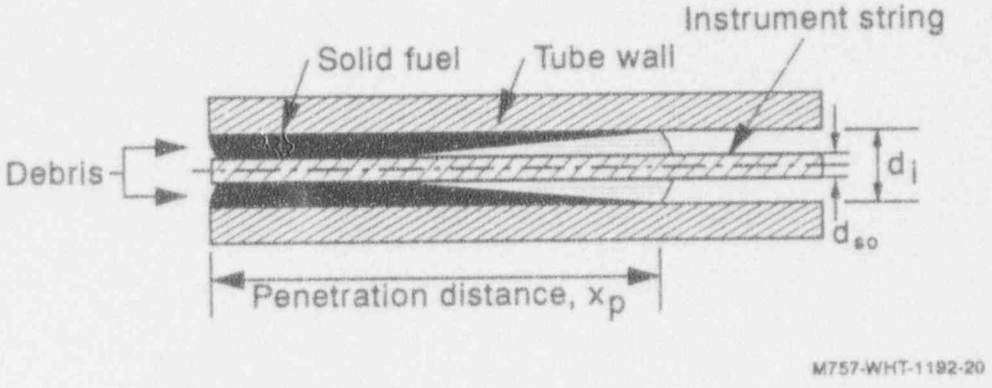

(a) Conduction layer model

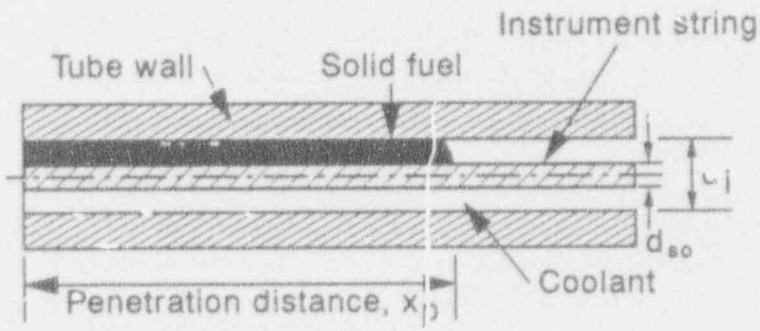

(b) Modified bulk-freezing model showing kidney shaped melt

Figure 3-4 Melt penetration model geometries.

Application of the conduction model for a range of melt areas between 1.6×10^{-5} to 12.7×10^{-5} m^2 predicted penetration distances between 30 and 49,000 cm. The melt area range was based on amounts of melt observed in six of the nozzles removed from the vessel (see Figure 3-2). The distances in the predicted penetration range were much greater than the penetration distances of molten fuel observed in the TMI-2 instrumentation nozzles. Although an attempt to consider the effects of coolant was made by using a reduced effective melt diameter, the penetration distances predicted show that this conduction model is not suitable for modeling the flow of molten fuel through coolant-filled nozzles, as is the case for the TMI-2 instrumentation nozzles.

The bulk-freezing model of Ostensen and Jackson has been modified to account for the presence of coolant in the instrumentation nozzles. The development of the equations for the modified bulk-freezing model are outlined in Appendix B. Figure 3-4(b) illustrates the flow mechanics and assumptions of the modified bulk-freezing model. Preliminary calculations with the modified bulk-freezing model predicted much more reasonable results than the conduction model; therefore, only the penetration distance results of the modified bulk-freezing model are used in comparisons with measured melt penetration distances.

The modified bulk-freezing model assumes that turbulence in the flowing melt prevents a stable crust from forming at the nozzle wall. The melt was modeled as flowing through an annulus with an effective diameter

$$d_e = \sqrt{d_i^2 - d_{so}^2}$$

where

d_i = inner diameter of the nozzle

d_{so} = outer diameter of the instrument string.

Any melt that might be in the instrument string was not considered. Molten debris inside the probe channel of the instrument string would first have to melt through the instrumen: string into the coolant-filled annulus of the nozzle to be considered as a safety threat. The penetration distance was conservatively estimated by assuming the melt stops when the entire amount of molten fuel in the nozzle has solidified. The model uses a heat balance around the molten material to equate the amount of heat given up to solidify the melt, with the convective heat transfer between the melt and the nozzle wall and between the melt and the coolant.

In the derivation of the modified bulk-freezing equation, coolant was allowed to escape from the top of the nozzle. Heat exchange can occur between the melt and the coolant, as well as between the melt and the nozzle wall. Heat transfer from the leading edge of the melt was not considered, along with hydrodynamic effects from melt/coolant interactions. The model does not account for nozzle ablation or for thinning of melt along the nozzle length. However, the model allowed for variations in the melt cross-sectional flow area, which remained constant through the nozzle during the calculation.

In these calculations, it was desired to use a model with a closed-form solution technique so that calculations could be performed to consider a wide range of input parameter uncertainties. Hence, the models used for these calculations do not allow one to consider phenomena such as the dynamic effects of vapor generation, enhanced cooling of the melt's leading edge, and the reduction in melt viscosity during solidification (although sensitivity calculations considering different melt superheats provide some insight into the effects of melt viscosity). However, any vapor generation or enhanced cooling at the melt's leading edge should reduce the potential for melt to travel below the lower head. Thus, a more complex model that includes all these phenomena should predict shorter melt penetration distances.

3.1.3 Model Calculations

Given the uncertainties in several of the input parameters, a matrix of calculational parameters was developed for input to the model to determine the penetration distance. These parameters included the melt composition, the melt flow area, the melt velocity, and coolant conditions. The multiple variations of input parameters resulted in a range of predicted melt penetration distances.

SEM analyses of solidified material in the nozzles examined by ANL indicated compositions ranging from pure uranium to a range of metallics. Compositions varied not only between nozzles and along the length of a nozzle, but also varied for different particles at the same elevation on the nozzles (see Table 2-1). Metallic material within the nozzles resulted primarily from melting of the nozzles. The presence of silver and cadmium in the nozzles indicated that control assembly materials also entered the nozzles, in addition to molten ceramic core material. In order to encompass all possible molten material scenarios, four compositions were examined. These included 100% UO_2, eutectics of 80% UO_2–20% ZrO_2, and 20% UO_2–80% SS-304, and a pure, metallic 100% SS-304 (see Appendix A for properties). These compositions represent bounds for the solidified material found in the nozzles. The 80% UO_2–20% ZrO_2 eutectic is based upon the composition of the companion samples.[10] Although the materials are immiscible, the 20% UO_2–80% SS-304 composition was used to model a metallic material with a high melting temperature.

The melt flow cross-sectional area range used in the model was estimated from the solidified melt pictured in photographs of the nozzles examined by ANL. The photos showed kidney-shaped melt covered between 12.5% to 100% of an annulus, producing a melt flow area range of 1.6×10^{-5} to 12.7×10^{-5} m^2. The kidney shape was approximated in the model by assuming melt completely filled the space between the instrument string and nozzle wall and covered some fraction of the annulus. For this type of formation, the contact area at the coolant-melt interface was independent of the cross-sectional area of melt in the annulus, unless of course the annulus was completely filled with melt. Conservative estimates of the variation in the amount of ring-shaped melt ranged from 1.9×10^{-5} to 7.1×10^{-5} m^2. Figure 3-3 illustrates the two shapes of melt within the nozzles.

The velocity of the melt was required for calculating melt penetration distances. The velocity was evaluated by applying the energy conservation equation for steady, adiabatic flow to the melt in a nozzle. The melt velocity at the point where melt exits the vessel lower head is given by

$$v_d = \sqrt{\frac{2\Delta P/\rho_d + 2gl_t}{4 f_f l_t/d_e + K + 1}} \qquad (3\text{-}3)$$

where

ΔP = pressure differential

f_f = Fanning friction factor

K = entrance loss coefficient

ρ_d = density of the melt

d_e = effective diameter of the nozzle

l_t = distance the melt travels before exiting the lower head.

This velocity was assumed to approximate the average velocity in the nozzle. Note that l_t includes the vessel thickness and the height of the ablated nozzle, which varies depending upon nozzle location. The solution of Equation (3-3) was plotted as a function of dimensionless penetration distance, as shown in Figure 3-5.

The velocity was primarily gravity driven because the annulus where melt was primarily found within these nozzles was at RCS pressure. However, an upper bound was applied, which corresponded to a 2 MPa pressure differential. This pressure differential is approximately equal to the increase in pressure at the time of core relocation (see Figure 2-1). The bounding pressure differential of 0.0 to 2.0 MPa produced a melt velocity range of 2.5 to 10.0 m/s for virtually any value of dimensionless penetration distance, as shown in Figure 3-5.

The coolant conditions in the pressure vessel varied over the accident time frame. The average pressure before core relocation at 224 minutes was 7 MPa.[11] Coolant properties for the analysis of metallic compositions were based on a pressure of 7 MPa because metallic debris was assumed to have entered or existed within the nozzles before the major ceramic core relocation to the lower head. Ceramic melt most likely entered the nozzles soon after core relocation at 224 minutes. For several minutes after relocation, the primary system pressure was 11.5 MPa.[11] Coolant properties for analysis of ceramic melt penetration were based on this higher pressure. The system pressure increased to normal operating pressure around 350 minutes,[12] but solidification of melt within the nozzles had probably occurred prior to that time.

As shown in Figure 2-4, temperatures in the cold legs of both the A and B loops during relocation indicate subcooled to saturated coolant temperatures.[11] Calculations using the modified bulk-freezing model examined melt in contact with either subcooled liquid or saturated liquid. The case of a nozzle void of coolant was also examined to provide a calculational upper bound. In all cases, the nozzle wall temperature was assumed constant and equal to the initial temperature of the coolant.

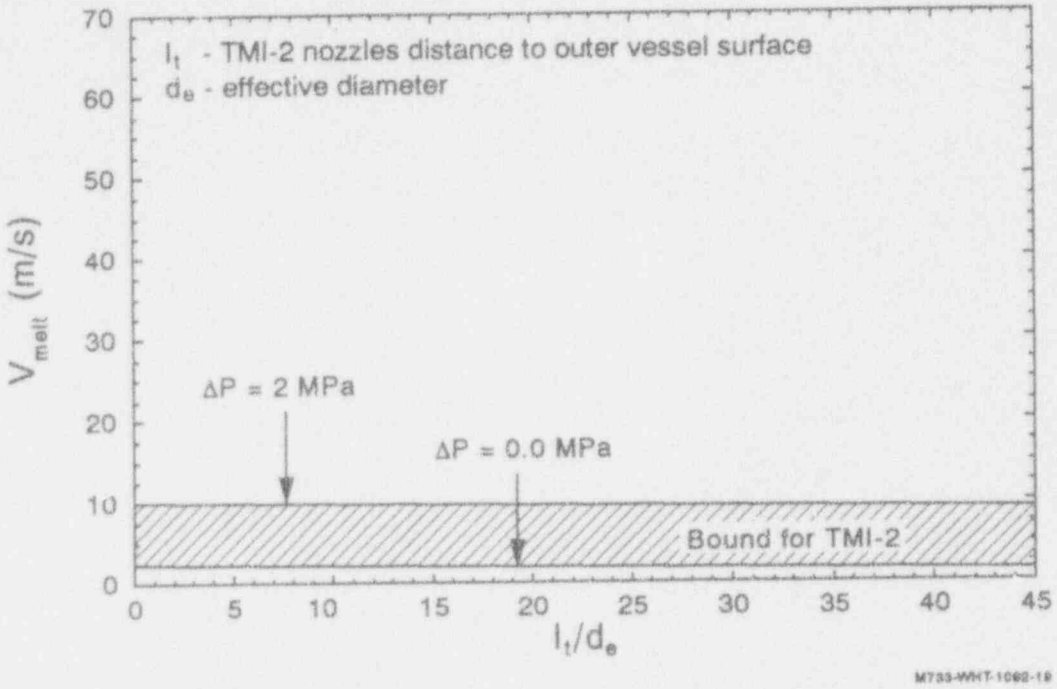

Figure 3-5. Melt velocity plotted as a function of dimensionless penetration distance.

3.1.4 Results

A criterion for the shortest distance that melt must travel to penetrate the lower head was established. The most conservative penetration distance was determined to be 15.0 cm. This distance corresponds to a minimum nozzle stub length of 1.3 cm plus the lower head thickness (13.7 cm). The criterion was developed based on nozzles which had been severely ablated when molten core material relocated to the lower head.

The four representative melt compositions discussed in Section 3.1.3 were initially modeled at their respective solidification temperatures. For each composition, if the distance predicted for melt flow in the absence of coolant at the liquidus temperature was less than the 15.0 cm criterion, superheat temperatures were then modeled.

The melt penetration distances predicted by the modified bulk-freezing model ranged from 0.2 to 26.0 cm for kidney-shaped melt and 0.4 to 21.7 cm for ring-shaped melt. The lower bounds for each melt shape were calculated assuming the smallest melt flow area of gravity-driven ceramic melt, in contact with saturated coolant. The upper bounds were calculated assuming the largest area of 100% SS-304 flowing at 10 m/s. Subranges based on melt composition may be extracted from each of the melt shape ranges given above. The range for ceramic kidney-shaped melt was 0.2 to 14.8 cm, and the range was 0.4 to 11.9 cm for ceramic ring-shaped melt. A range of 3.4 to 26.0 cm was calculated with metallic kidney-shaped melt, and a range of 1.5 to 21.7 cm was calculated for metallic ring-shaped melt.

The calculated penetration distances for both melt formations with a 100% SS-304 composition exceeded the distance criterion of 15.0 cm at the solidification temperature;

therefore, superheat temperatures were not investigated for this composition. Calculated penetration distances were less than the criterion when each of the other three compositions were modeled at their respective solidification temperatures for both kidney and ring shapes. Superheat temperatures of the ceramic compositions were examined, which were slightly higher than the peak temperatures reported in the companion samples.[10] A superheat temperature was also assumed for the eutectic metallic composition. The temperatures existing within the vessel when metallic debris may have entered the nozzles would have been much lower than the core relocation temperature, and the large amounts of melt predicted to cause penetration of the lower head were not seen in the nozzle examinations.[3] Therefore, distances predicted by the model for the SS-304 composition should be considered highly conservative.

The depth of melt penetration within the six nozzles examined at ANL has been measured and reported.[3] Table 3-1 lists the results of the measurements based on gamma scans. Maximum and minimum distances are given for nozzles D10 and H5 because it could not be concluded if the cesium-137 activity was inside or on the surface of the nozzles.[3] The six nozzles are listed in the first column. The shape of solidified material in each nozzle, as seen from photographs, is given in the second column. The third column reports the distances melt traveled through the nozzles, as measured by ANL. Only fuel debris penetrations are reported. The measured depth of fuel in nozzle L6 was attributed to a piece of metallic aluminum which was coated with fuel particles. This debris apparently dropped into the nozzle through the guide tube above and was not from the flow of fuel across the lower head.[3] This type of debris relocation is not predicted with the models used here. Because the debris particle quenches during this type of relocation, it will not impact ex-vessel tube temperatures. To compare with the observed debris penetration distance, the model ranges for the appropriate shape of ceramic melt are listed in the last column. The distances were measured from the top of each sample down into the nozzle [see Figure 3-4(b), distance x_p].

The lower bound of the penetration range for the kidney-shaped ceramic melt was generated with an 80% UO_2–20% ZrO_2 melt composition at a temperature of 3,200 K and velocity of 2.5 m/s, filling one-eighth of the annular cross section and contacting saturated liquid. The kidney-shaped ceramic melt upper bound was based on a nozzle completely filled with 100% UO_2 at a temperature of 3,200 K and velocity of 10.0 m/s. A composition of 80% UO_2–20% ZrO_2 at 3,200 K and 2.5 m/s in contact with saturated coolant for the minimum melt cross-sectional area examined produced the lower limit of the penetration range for the ceramic ring shape. The ceramic ring-shaped upper bound was set by 100% UO_2 at 3,200 K and 10.0 m/s, with the largest amount of melt examined contacting subcooled liquid.

The penetration distance calculated using the modified bulk-freezing model was highly dependent upon the amount of melt flowing through a nozzle. The greater the volume of melt, the farther it would penetrate into a nozzle. The penetration distances were also dependent upon the contact area between the melt and the coolant and between the melt and the nozzle. The penetration distances predicted by the model for the ring-shaped melt were less than those predicted for a kidney formation, given equal volumes of melt in the nozzles, because of the increased surface contact of the ring formation with both the nozzle wall and the coolant. Both surfaces, of course, provide for heat removal from the melt.

Table 3-1. Comparison of measured melt penetration and model predictions.

Nozzle	Melt shape	Measured depth (cm)	Model range ceramic melt (cm)
D10	kidney	10.8 min., 23.7 max.	0.2 - 14.8
H5	kidney	2.9 min., 5.7 max.	0.2 - 14.8
H8	kidney	5.7	0.2 - 14.8
L6	kidney	23.0	0.2 - 14.8
M9	kidney	3.8	0.2 - 14.8
E11	ring	9.8	0.4 - 11.9

Table 3-2 shows the breakdown of maximum penetration distances predicted by the modified bulk-freezing model for each of the four compositions. Data in the fourth column indicate the upper bound on the penetration distance of each melt composition. These upper limits result from modeling a nozzle annulus completely filled with melt. Except for the 100% SS-304 composition, these distances meet the criterion for melt remaining within the vessel lower head (i.e., less than 15 cm). The second column lists the liquidus temperature of each melt composition. Data in column three indicate the degree of superheat above the liquidus temperature on which the calculations were based.

3.1.5 Conclusions

The modified bulk-freezing model was determined to be more applicable than the conduction layer model for the prediction of melt penetration distances through the coolant filled annulus within the TMI-2 instrumentation nozzles. The modified bulk-freezing model accounts for the presence and the state of coolant in contact with melt in the nozzles. The model conservatively predicts the melt penetration distance by not accounting for the energy loss due to nozzle ablation or thinning of the melt flow along the nozzle length. Assuming the melt stops when the entire amount within a nozzle has solidified also produces a conservative distance. Four melt compositions were evaluated over a range of melt flow areas and melt velocities. The model predicts distances that encompass the observed melt penetration in the TMI-2 nozzles. Debris on the outer surface of nozzle D10 and a debris particle falling into nozzle L6 through the overlapping guide tube cause the measured fuel depth in these two nozzles to fall outside the range predicted by the bulk-freezing model. These data points should not be considered when comparing the model with the measured depths.

The model predicts that, in the absence of coolant in the nozzles, only debris with a highly metallic composition may penetrate through the nozzle outside the reactor vessel. The primary source of metallic debris within the nozzles was due to nozzle ablation. Other sources included control assembly materials that possibly quenched and solidified before entering the nozzles. Examinations of the nozzles removed from the vessel indicated neither of these types of metallic debris penetrated the nozzles to a depth of consequence or existed in very large quantities.

Table 3-2. Maximum model predictions of melt penetration distance.

Composition	Liquidus temperature (K)	Superheat (K)	Maximum penetration distance (cm)
100% UO_2	3,113	87	14.8
80% UO_2-20% ZrO_2	2,860	340	10.9
20% UO_2-80% SS-304	2,400	200	13.3
100% SS-304	1,671	0	26.0

Hence, penetration of the lower head by metallic debris was highly unlikely. Model predictions for the 100% UO_2 and 80% UO_2–20% ZrO_2 compositions at 3,200 K indicate ceramic melt would not flow below the lower head, conservatively assuming melt completely filled the annulus of a 1.3-cm stub. The melt temperature assumed was conservatively higher than the reported molten core temperature range of 2,873 K to 3,123 K in a 78% UO_2–17% ZrO_2 composition.[10] These conservative assumptions, along with the likelihood that coolant was present within the nozzles during melt penetration, support the conclusion from results of the melt penetration calculations that molten debris containing fuel did not penetrate beyond the lower head.

As noted in Section 2, wires were inserted into the instrument string probe channel within seventeen instrument tubes (see Figure 3-3). It was found that all but one of the tested tubes were plugged, which indicates that either the probe channel within the string had collapsed or that melt was present within the channel. Hence, wire probes indicating that the instrument string channels are plugged did not conclusively prove that melt was present within these channels below the lower head. In fact, nozzle examination data indicated that the instrument string channels were collapsed at some locations.

The bulk-freezing model predicted ceramic melt flowing through the annulus between the instrument string and the nozzle wall did not breech the lower head. The flow of melt through the instrument string probe channel was not evaluated. Although melt may travel farther through the probe channel because of the pressure difference between the RCS and the probe channel (which is at atmospheric pressure), melt present within the probe channel does not pose a serious safety threat. As discussed in Section 3.1.2, melt present within the probe channel of the instrument string must ablate through the string and the instrument tube wall before an ex-vessel tube rupture can occur.

3.2 Jet Impingement and Thermal Response Calculations

Calculations were performed to investigate melt relocation and the subsequent thermal loading to the vessel during the TMI-2 accident. Specifically, calculations were performed to consider the potential of a debris jet impinging upon the TMI-2 lower head to cause the hot spot temperatures observed in TMI-2 boat sample examinations.[13] Global and localized vessel temperature results were obtained to provide input for subsequent structural analysis calculations to determine the margin to failure in the TMI-2 vessel.

Where possible, input parameters were quantified using data from TMI-2 VIP examinations, data from previous TMI-2 examinations, or other TMI-2 data sources. Parametric studies were performed to investigate the sensitivity of calculational results to input parameter uncertainties. Results from these sensitivity studies are presented and compared with TMI-2 VIP boat sample examination data.

Calculations documented in this section only consider the thermal response of the lower head during and after a substantial amount of ceramic material from the core relocated to the lower plenum. However, scoping calculations were performed to evaluate the impact of previously relocated metallic material on the vessel thermal transient.[b] To maximize the time lag that this layer could have upon vessel heatup, conservative assumptions were applied, such as assuming that metallic material was present on the entire lower head reaching the height observed by Neimark at nozzle H8.[3] Results indicate that the maximum time lag that this layer could have upon vessel heatup is between 10 and 25 minutes.

Finally, calculations were performed to provide insight related to the manner in which material relocated from the core to the lower plenum. As discussed within this section, results from these calculations indicate that some of the relocation scenarios postulated in Section 2 may be eliminated from further consideration.

3.2.1 Melt Relocation

3.2.1.1 Model Description. The potential for a debris jet to quench as it travels through water was analyzed with the TEXAS fuel-coolant interaction model.[16–19] Several computer codes are available for predicting melt/water interactions. However, there is considerable uncertainty in code results because of limited data for validating these computer codes. Hence, several sensitivity studies were performed with the TEXAS code to consider the impact of code uncertainties. TEXAS is a computer model which predicts the behavior of molten fuel interacting with water coolant during the mixing and propagation phases of a molten fuel-coolant interaction (FCI). The model was developed to examine FCI behavior under the assumption that the leading edge of the fuel jet pouring into the coolant is the dominant mixing process; i.e., the process can be considered in a one-dimensional manner.

The model employs a unique Lagrangian-Eulerian formulation in which the fuel is divided into Lagrangian material volumes that are tracked as they pass through an Eulerian mesh containing the water and steam. Each fluid is modeled with a complete set of conservation equations and an equation-of-state to describe the balance of mass, momentum, and energy used for predicting the volume fraction, velocity, and temperature of each fluid, as well as overall pressure.

The unique feature of the TEXAS model is that the Lagrangian fuel particles can dynamically fragment during fuel-coolant mixing and quenching due to relative-velocity-induced fragmentations (Rayleigh-Taylor instabilities). TEXAS follows this process and determines the

---

b. Letter from J. L. Rempe, INEL, to A. Rubin, NRC, "Scoping Calculations Discussed During Recent TMI-2 VIP Meeting," JLR-79-92, November 15, 1992.

fuel mass quenched. TEXAS also considers dynamic fragmentation during an explosion propagation, but this is not relevant to this study, because the high pressure in the TMI-2 reactor pressure vessel suppressed any energetic FCI.

TEXAS only considers leading edge breakup and neglects breakup due to instabilities on the side of the jet, since leading edge breakup is considered to be the dominant effect. In previous analyses,[18] Epstein determined that the rate of jet erosion due to Kelvin-Helmholtz instabilities along the jet column was negligible because of the dampening effects of the vapor film.

A complete description of TEXAS is provided in References 14 through 17. Reference 15 gives an extensive summary of the model with relevant reactor simulations and results.

3.2.1.2 Input Assumptions. Several TEXAS simulations were used to analyze a range of debris jets during their initial mixing phase and to bound possible relocation masses, time periods for relocation, and modeling uncertainties. Total mass flow rates ranging from 300 to 1,000 kg/s were used to model scenarios in which the debris was assumed to relocate through saturated or subcooled water conditions. These values were chosen to maximize the heat transfer rate, although the duration of the jet pour was reduced to keep the total mass that relocated a constant value of 10,000 kg. (Although it is recognized that nearly 19,000 kg of material relocated to the lower head, there is uncertainty related to the amount of material that may have relocated during the 224 to 226 minute time frame. Furthermore, in Section 3.2.2, thermal analyses indicate that the heat load from less than 10,000 kg could result in temperatures that exceeded peak values estimated from metallurgical examinations.) Because melt may have drained from more than one of the holes in the elliptical flow distributor plate, analyses considered one and three jet cases. Table 3-3 lists the five cases considered, with input assumptions related to initial jet velocity, total mass flow rate, jet diameter, and reactor coolant system temperature.

The greatest uncertainty in these simulations involves the initial conditions, which specify the rate of fuel entry into the lower plenum; i.e., the velocity and diameter of the jet, the overall discharge time, and the number of jets impinging upon the lower head. In addition, the amount of coolant subcooling in the vessel was unknown at the time of relocation. Assumptions for these simulations have attempted to bound possible input parameter ranges to discern the effect on quenching behavior.

Melt relocation times up to 1 minute were chosen. Preliminary calculations indicated that relocation times of 1 minute or less maximized the amount of quench that could occur. For all of the cases, the reactor vessel pressure is assumed at 10 MPa during relocation. This is the approximate reactor pressure during the time period (224 to 226 minutes after reactor scram), when most debris relocation is postulated to have occurred. The coolant was assumed to be saturated at a temperature of 584 K for the first four cases. In the final case, a water pool temperature of 100 K below saturation was considered to examine the effect of subcooling on jet breakup and quenching. This value corresponds to an average of the subcooled water temperatures measured in the RCS cold legs and the RCS saturation temperature at the time of relocation (see Figure 2-4).

Assumptions related to the debris were based upon results from companion sample examinations.[10] The debris composition is estimated at 78% UO_2–17% ZrO_2.[10] The remaining

Table 3-3. TEXAS calculational results.

Case	Number of jets	Jet diameter (m)	Initial melt velocity (m/s)	Initial melt mass flow rate (kg/s)	Coolant pressure (MPa)	Coolant temperature (k)	Mass breakup (kg)	Particulate size (mm)
1	1	0.1524	2.4	333 3	10	584	14	15–19
2	3	0.1524	2.4	1000.0	10	584	43	15–19
3	3	0.1524	0.8	333.3	10	584	43	19–24
4	3	0.0762	3.2	333.3	10	584	16	3–24
5	1	0.1524	2.4	333.3	10	484	20	13–18

constituents are primarily stainless steel and Inconel from core structural components. Material properties for this debris composition are found in Appendix A. From a phase diagram for a U-Zr-O compound,[19] a freezing temperature range of 200 K was assumed, with a liquidus temperature of 2,850 K and a solidus temperature of 2,650 K. The debris was initially assumed to have a low superheat of only 50 K above the melt liquidus temperature. This temperature was selected based upon companion sample examination results which indicated that the material arrived at the flow distributor plate and the lower head in a molten state. Although a lower superheat would affect the amount of melt predicted to solidify, it is not felt that the order of magnitude of melt predicted to solidify would change.

Calculations were performed assuming a 0.74-m injection height, which is the height of the elliptical flow distributor plate above the lower head in the center of the pressure vessel lower plenum. The jet flow area was primarily varied by considering single and multiple jet flows through the flow distributor plate. In most cases, jet diameters were assumed to correspond to the diameter of holes in the flow distributor plate. Case 4 was performed to investigate the sensitivity of results to jet diameter, using a jet diameter one-half the size of holes in the flow distributor plate. This smaller jet corresponds to cases where melt had frozen and partially blocked holes of the elliptical flow distributor plate.

3.2.1.3 Results and Discussion. Results from all of the simulations indicate that insignificant amounts of breakup occurred considering the total mass of debris that was assumed to be injected into the lower plenum. Maximum breakup was predicted for cases in which three jets were considered. For the two cases assuming three jets with diameters equal to the diameter of holes in the distributor plate, the total breakup mass was approximately 43 kg. Breakup mass and particle size results are summarized in Table 3-3. Results for the first three cases have a jet length-to-jet diameter ratio (L/D ratio) of less than 5. TEXAS results indicate that only the initial leading edge of the jet (i.e., the first of the Lagrangian material volume parcels) broke up. In Case 4, where there was an L/D ratio of nearly 10, TEXAS predicted that the first three Lagrangian particles of each jet broke up. Based on the model, such a limited L/D is not sufficient for significant breakup of the incoming fuel mass in a saturated water pool.

In summary, the breakup predicted by TEXAS for molten jets of debris draining from the elliptical flow distributor plate is relatively insignificant. Hence, calculation results indicate that the assumption that major amounts of jet breakup occurred during relocation (assumed in Scenario 3 of Section 2) is incorrect. Therefore, subsequent jet impingement and vessel thermal response calculations continued under the assumption that most debris reached the lower plenum in a molten state without significant breakup or quenching. Because calculation results indicate that the "hard" layer by itself could impose a thermal load resulting in temperatures that exceeded peak values estimated from metallurgical examinations (see Section 3.2.2), and because there is uncertainty about when the additional rubble on top of the "hard" layer relocated, no further assessment of the impact of the rubble on vessel thermal response was performed.

3.2.2 Jet Impingement and Vessel Thermal Response

3.2.2.1 Model Description. A simple phenomenological model, TMI, was developed to estimate the heat transfer that occurs during jet impingement and model natural convection from the molten pool of debris to the wall at the bottom of the vessel. The TMI model is essentially a lumped parameter model. However, continuity of heat fluxes at the inner and outer surfaces of the vessel was then applied so that temperature distributions through the vessel wall could be obtained for subsequent vessel structural response calculations. A summary description of phenomena modeled in these calculations is provided below. Governing equations used in the TMI model are found in Appendix C.

The TMI model assumes that there is one jet that impinges at the center of the pressure vessel. Although the location of jet impingement may have been different during the actual TMI-2 scenario, the precise location of the jet is not important in this model because the important heat transfer effects of the jet will still be observed.

The TMI model calculates the temperature history that occurs in the lower head of the pressure vessel during jet impingement and natural convection that occurs in the pool after relocation. The model predicts that a debris crust will form on the pressure vessel when relocated material contacts the vessel wall. This result is based on preliminary calculations, which indicate that the interface temperature is below the melt solidus temperature upon contact. Heat is then transferred through the crust to the vessel. When the molten jet stops draining and surface agitation is reduced, a crust forms on the upper surface of the pool; this upper crust is initially considered to be of uniform thickness as it continues to cool (see Figure 3-6). The model includes the effects of crust porosity on thermal properties using the relationship suggested by Olander.[20] The model also considers the effect of melt solidification upon the viscosity of the molten pool. As discussed in Appendix C, when the temperature of the melt pool drops below the debris liquidus temperature, the solid fraction in the molten pool becomes a factor in the analysis using the relationship proposed by Epstein and Fauske.[21] If the entire pool solidifies, the model is no longer valid and the analysis is terminated.

The pressure vessel is divided into sections, which are best described as a center disk with concentric rings around it. A cross sectional view of this geometry is shown in Figure 3-7. The heat flux from the molten pool travels through the crust and heats up the section of the pressure vessel in contact with the crust. There is no communication between sections in the pressure vessel. Thus, the only portions of the pressure vessel that are directly heated are sections that are

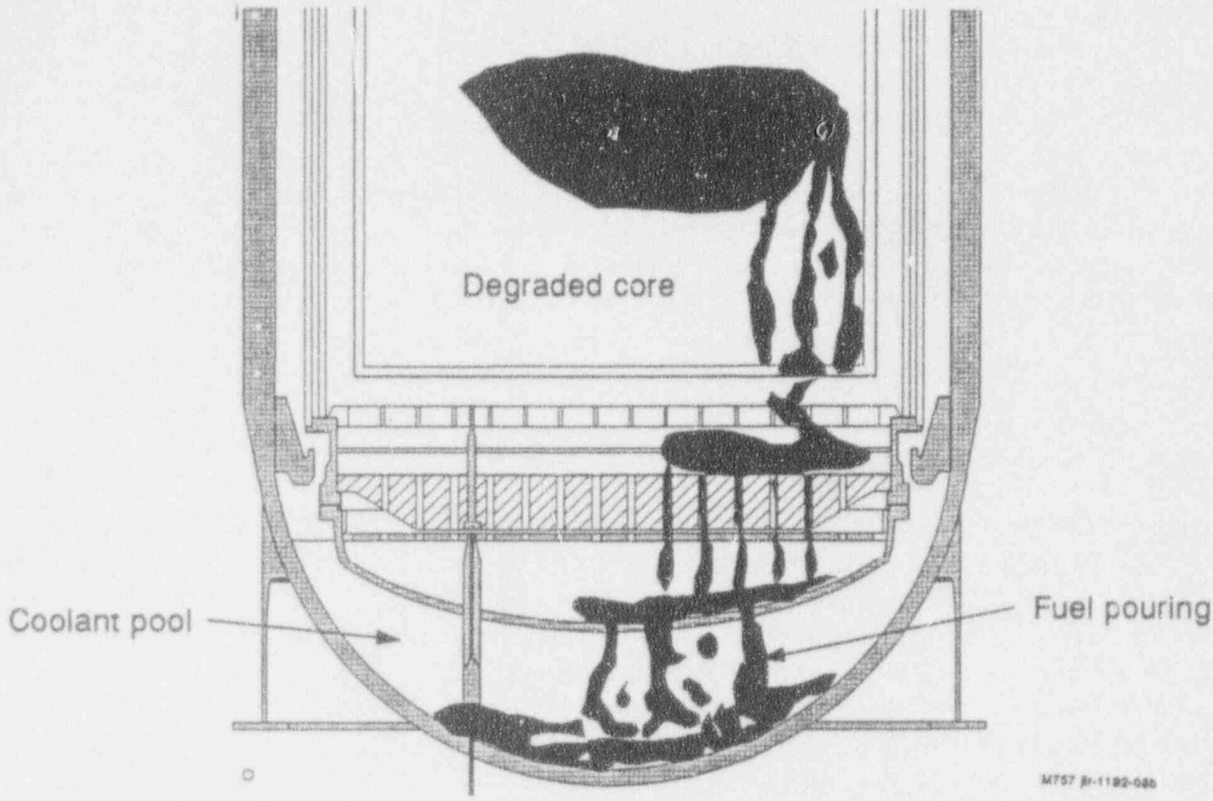

(a) during relocation

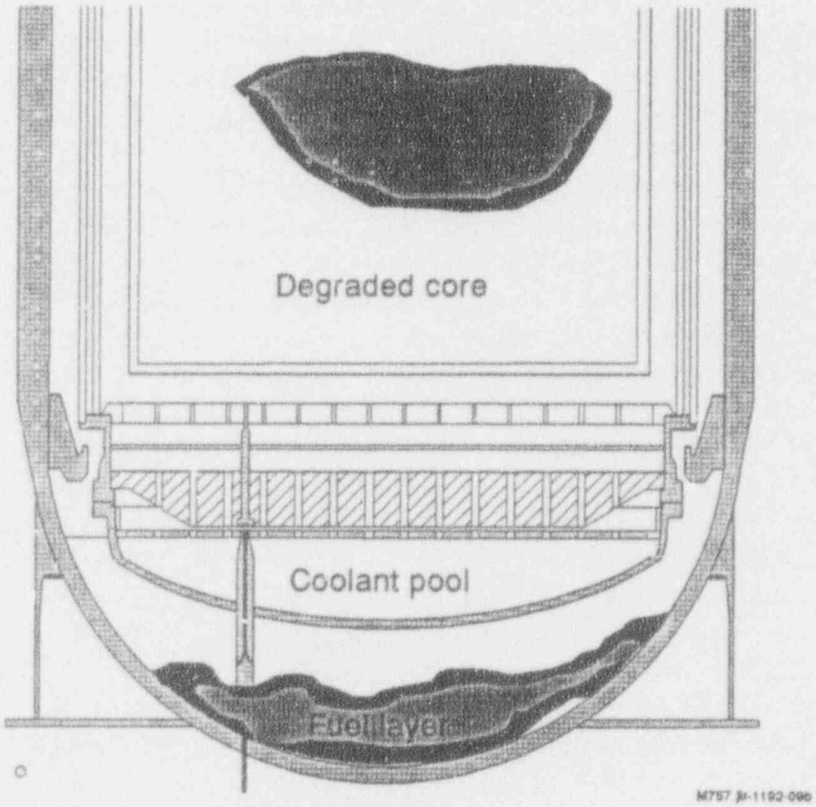

(b) after relocation

Figure 3-6. Thermal loading from jet impingement.

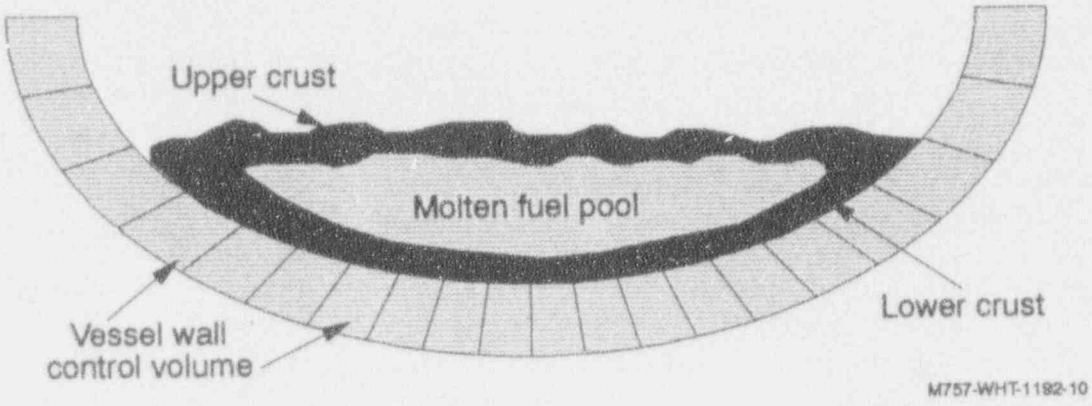

Figure 3-7. Model for TMI-2 thermal analysis.

in direct contact with the crust that has formed on the periphery of the melt pool. The melt pool is considered to be a single control volume at a single temperature, which changes in size due to crust formation. The crusts do not store energy and are considered to be resistances to heat flow that change in size due to the difference between the heat transferred to it (and their decay heat) and the heat transferred through it to the vessel wall.

The transition from jet impingement stagnation heat transfer to the natural convection regime assumes that there is no substantial period over which the debris melt pool would be completely stagnant. This assumption is based upon the assumptions that (a) most of the melt arrives in a molten state and (b) the characteristic time for the onset of natural convection is short compared to the time of interest (several hours). The first assumption is based upon TEXAS calculational results discussed in Section 3.2.1.3. The second assumption is based on results from dimensional analyses, which indicate that the timescale for the onset of natural convection is much less than 1 hour.[22] As discussed in Section 3.2.2.3, calculation results indicate that the time periods of interest in the vessel thermal response are on the order of several hours. Hence, natural convection behavior within the pool is modeled throughout the transient using correlations dependent upon a Rayleigh number based upon internal heat generation within the pool. Decay heat causes some of the pool to remain molten and can cause significant internal natural convection. Heat transfer to the lower crust from the hemispheric molten zone was modeled based upon the work of Jahn and Reineke.[23] The experimental and theoretical work by Jahn and Reineke[23] was also used to predict variations in the heat flux as a function of angle from the bottom of the pool. It should be noted that there is considerable uncertainty in using these data to model large pool behavior during severe accidents. For example, it is estimated that the Rayleigh number for the pools that are formed during a severe accident may be several orders of magnitude higher than the Rayleigh numbers for which the Jahn and Reineke data were obtained. Furthermore, the formation and entrainment of solidified debris in the pool may reduce the heat tranfer predicted by steady-state natural convection correlations.

Heat loss from the melt pool to the coolant in the lower plenum is modeled by initially considering film boiling and radiation heat transfer. This is based upon results from preliminary calculations, which indicate that the fuel/coolant interface temperature is above the critical temperature of water and nucleate boiling could not initially occur. As the upper crust thickens

and the interface temperature decreases, it is expected that film boiling will cease. The model then considers heat loss via nucleate boiling on the upper crust surface. As the interface temperature continues to decrease, the heat transfer due to natural convection is modeled.

A detailed description of the TMI model is found in Reference 22. Governing equations used in the model are summarized in Appendix C.

3.2.2.2 Input Assumptions. To determine the effects of uncertainties in key parameters, various simulations were performed (see Table 3-4). Sensitivity studies were performed to investigate the effect of assumptions related to debris decay heat, debris properties, the interfacial contact resistance between crust on the pool periphery and the vessel, heat removal from the vessel to the containment, the total debris mass that relocated to the lower head, the effective surface area of the upper pool crust that is exposed to reactor vessel coolant, and RCS coolant subcooling.

The decay heat values listed in Table 3-4 are representative values for the TMI-2 core at the time of core relocation. The upper bound decay heat of 1.27 MW/m^3 (Case 1) was obtained from the American Nuclear Society (ANS) Standard 5.1 for the TMI-2 core under the assumption that the noble gases (Xe, Kr), halogens (I,Br), and alkali metals (Cs,Rb) are no longer present in the debris that relocated to the lower head. The nominal value of 1.0 MW/m^3 was used based on estimates by Akers[10] for the ceramic urania/zirconia material examined in the companion samples. A reduced value of 0.95 MW/m^3 is also considered to account for the possibility that the lower head contained a melt with 5% non-fuel material. Decay heat values in Reference 10 are estimated to have an uncertainty of ± 20%. Reference 10 also indicates that companion sample debris underwent a long cooldown period (3–72 hours) because the phase separation between the $(U,Zr)O_2$ and $(Zr,U)O_2$ phases was observed to occur.

As discussed in Section 2.2.2, assumptions related to the debris composition were based upon results from companion sample examinations.[10] Debris which solidifies on the pool lower and upper boundaries is assumed to have an average porosity of about 20%.[10] An interfacial thermal resistance may also be present due to surface roughness between the crust and the vessel. Using the method suggested by Garnier,[24] values for the gap resistance between the vessel and crust were estimated to range between 150 and 10,000 W/m^2K.

Heat losses from the vessel outer surface to the containment were modeled using a heat transfer coefficient that considered losses via natural convection and radiation. As discussed in Reference 5, previous analyses indicate that this heat transfer coefficient may range from 1 to 100 W/m^2K. The value for this coefficient is dependent upon parameters such as vessel temperature and containment temperature, which vary during the transient. A combined convective and radiative heat transfer coefficient between the vessel outer surface and the containment for the TMI-2 accident was estimated to range between 30 and 100 W/m^2K. The manner in which this coefficient was calculated is documented in Appendix C. However, simulations listed in Table 3-4 were performed by selecting relatively high values (70 to 100 W/m^2 K) to maximize heat losses from the vessel because preliminary results indicated that vessel temperatures were exceeding values observed from boat sample examinations. Hence, analyses with a lower heat transfer coefficient would also indicate that vessel temperatures exceeded values estimated from boat sample examinations.

Table 3-4. Vessel thermal response calculation results.

Case	Debris bed mass (kg)	Decay heat power density (MW/m^3)	Debris-to-vessel gap heat transfer coefficient (W/m^2K)	Vessel-to-containment heat transfer coefficient (W/m^2K)	Area ratio[a]	Quasi-steady downward heat flux at 6 hours (kW/m^2)	Peak vessel temperature (K)	Lower crust thickness at 21,600 seconds (cm)	Upper crust thickness at 21,600 seconds (cm)
1	10,000	1.27	10,000	100	1	84	1,525	7.0	5.0
2	10,000	1.00	10,000	100	1	74	1,350	9.0	7.5
3	10,000	1.00	10,000	70	1	63	1,525	8.5	5.0
4	10,000	1.00	10,000	70	3	58	1,425	9.0	20.0
5[b]	7,400	0.95	10,000	100	1	62	1,200	10.0	11.0
6	7,400	0.95	10,000	100	3	60	1,040[c]	7.0[c]	19.0[c]
7[b]	10,000	1.00	1,000	100	1	63	1,220	10.0	11.0
8	10,000	1.00	150	100	1	57	1,137	8.0	7.4
9	10,000	0.95	10,000	100	1	61	1,190	9.5	8.2
10	10,000	0.95	150	100	1	55	1,120	8.4	8.0
11	10,000	1.00	10,000	70	1	65	1,400	9.0	8.0
12[d]	6,800	0.95	10,000	100	1	60	1,180	10.0	11.0
13	6,800	0.95	150	100	1	54	1,105	8.7	10.0
14	6,800	0.75	10,000	100	1	55	1,110	11.0	13.0
15[e]	6,800	0.75	150	100	1	49	1,020	10.5	13.7

a. Ratio between the total surface area and the projected surface area of the upper surface if it was a smooth surface.

b. Same result was obtained for a case with a subcooled water pool of 100 K.

c. Case 6 was truncated at a time of 3,600 s because the molten pool freezes at this time, and the model is not applicable for later times.

d. Input for this case was based upon nominal values for input parameters, such as debris decay heat, vessel-to-debris heat transfer coefficient, and vessel-to-containment heat transfer coefficient.

e. Input for this case was based upon lower bound values for input parameters, such as debris decay heat, vessel-to-debris heat transfer coefficient, and vessel-to-containment heat transfer coefficient.

There is also uncertainty in estimates for the total mass of debris present in the TMI-2 lower head. However, it is estimated that the hard layer of debris in the lower head contained up to 10,000 kg and that additional loose debris was present on top of this hard layer, so that approximately 19,000 kg of material had relocated to the lower head. The calculations documented in this section are concerned with the formation of a molten pool that later became the hard layer in the lower head; therefore, total masses of 6,800 to 10,000 kg were assumed. The value of 6,800 kg represents the hard layer mass estimated using probe test results;[25] the value of 10,000 kg was selected as an upper bound for this mass.

There is the possibility that the surface of the upper crust is not smooth and flat. A rough, cracked, upper crust surface provides more surface area for heat transfer and eventual water ingression and, therefore, better heat transfer to the vessel coolant. The surface area parameter shown in Table 3-4 is a ratio between the total surface and the projected surface area of the upper surface if it were a smooth surface. A maximum value of three was assumed in Cases 4 and 6, based on work by Farmer.[26] This ratio is used as a factor, which bounds the increase in surface area that is exposed to the coolant. It is recognized that this is a crude estimate, and more work is needed to accurately determine the effect, of surface roughness and water ingression into this hard layer.

The coolant was assumed to be saturated at a temperature of 584 K for each of the cases listed in Table 3-4. However, to encompass conditions where there may have been subcooling present in the reactor vessel, Cases 5 and 7 were also analyzed assuming a water pool temperature of 100 K below saturation. This value maximized the subcooling measured in the RCS cold leg temperature following high pressure injection about 15 minutes prior to the time of melt relocation.

3.2.2.3 Results and Discussion. The results for Case 2 are shown and discussed as a base case example. Case 2 was chosen as a convenient example and is not the best estimate for the TMI-2 relocation. Results for the remaining cases are summarized in Table 3-4, and additional details related to calculational results are found in Reference 22. None of these cases are a precise representation of the TMI-2 relocation. The important observation for all these cases is that the qualitative trends are quite similar. The initial and boundary conditions primarily impact quantitative values for parameters, such as peak temperature predictions which are given in Table 3-4.

Initial stages of the thermal transient were found to be characterized by high inner vessel surface temperatures over short time periods on the order of 1 minute. The inner surface vessel temperature at 0 and 30 degrees from the vertical for Case 2 are shown in Figures 3-8 and 3-9. For the short-term behavior depicted in Figure 3-8, it is seen that the temperature of the vessel surface at the jet impingement point (i.e., 0 degrees) peaks at about 1,500 K for times when the debris melt jet is still pouring into the plenum and before significant crust formation occurs. Vessel temperatures are then observed to ramp down before they begin to increase over longer times. This characteristic peak temperature was observed in all of the simulations during the time of jet impingement. Although lower pour rates were observed to decrease the magnitude of the peak temperature, the duration of this initial peak was found to increase for lower pour rates.

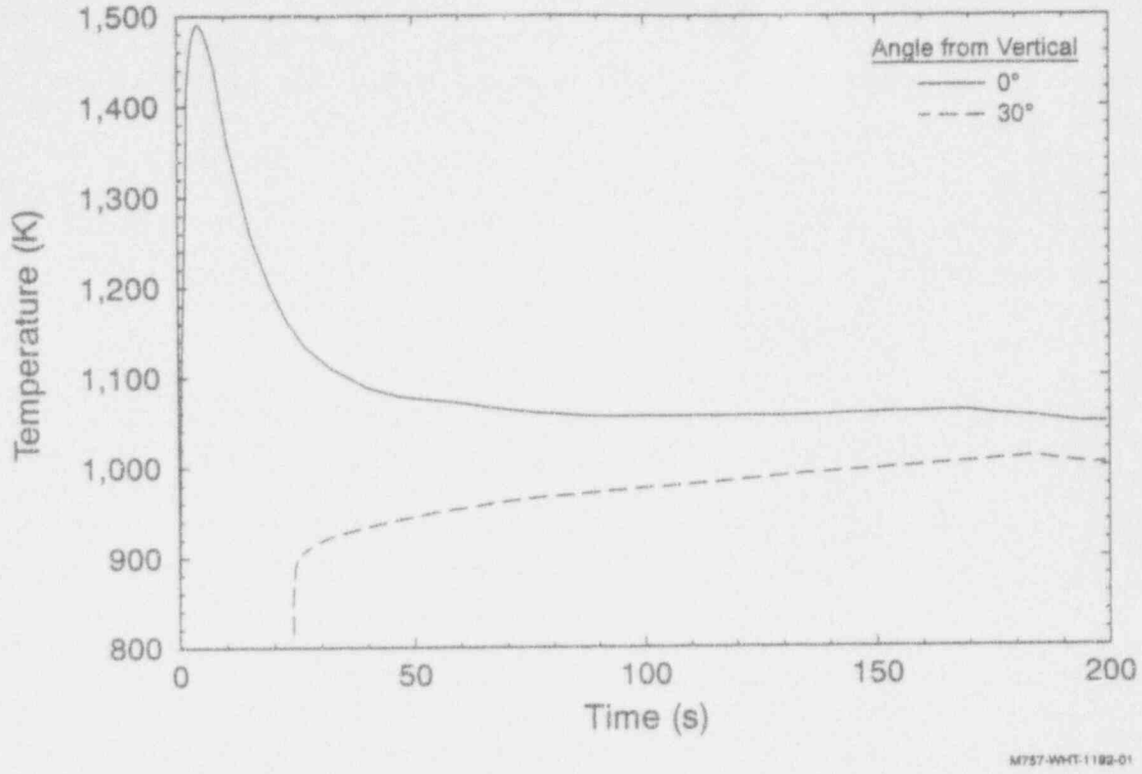

Figure 3-8. Case 2 vessel inner surface temperatures (0 to 200 seconds).

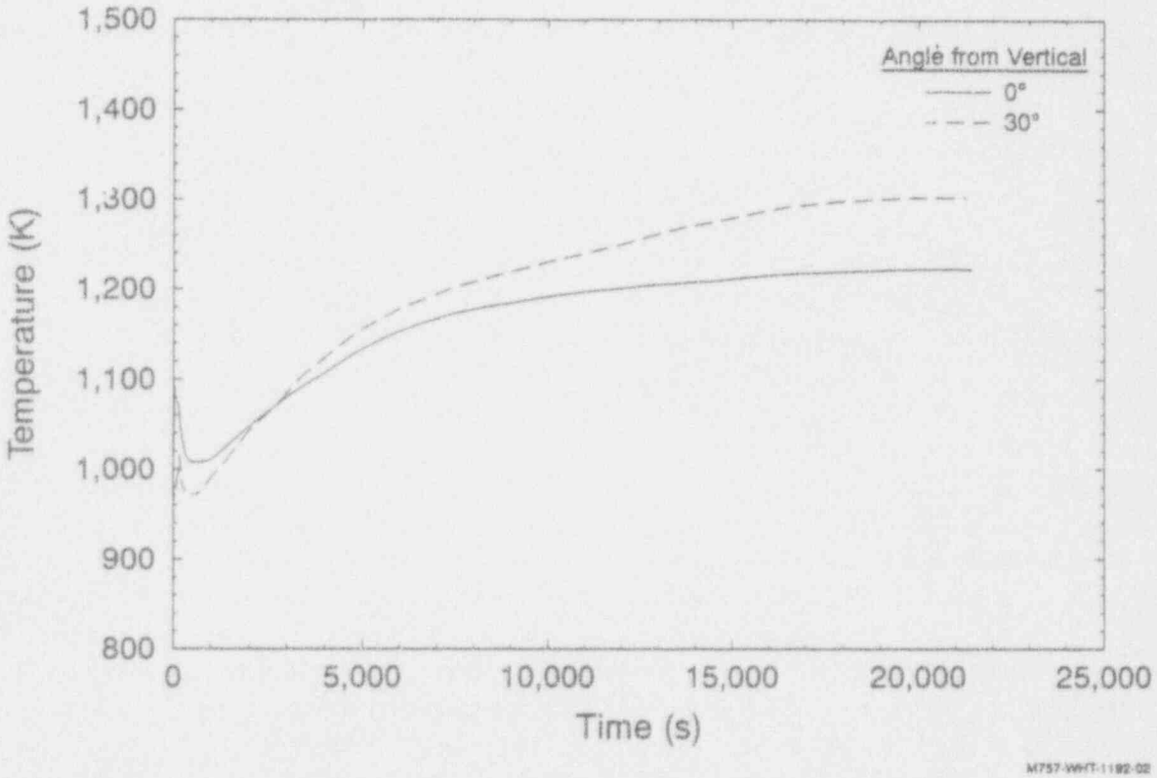

Figure 3-9. Case 2 vessel inner surface temperatures (0 to 21,600 seconds).

The next stage of the thermal transient may be observed in Figure 3-9. As jet impingement ends and the melt pool accumulates, the vessel inner surface temperature decreases and goes through a minimum (in this case, about 1,000 K) and then begins to rise. This occurs because the heat transferred from the melt to the vessel is being transferred to the rest of the vessel wall and diffuses by conduction heat transfer to the outer vessel surface. An additional reason for this phenomena is that additional crust formation occurs in the pool, which reduces the heat transferred to the vessel. Once the conduction thermal wave has reached the outer vessel wall (1,000 to 2,000 seconds), the path for conduction heat transfer has become quasi-steady, and thus the inner surface temperature begins to rise.

The final stage of the thermal transient occurs on the time scale of hours as the inner surface temperature reaches a maximum and then levels off. This phenomenon occurs because the heat loss to the vessel (and then to the containment atmosphere) is now at steady state. Furthermore, the melt pool is cooling and slowly solidifying. Therefore, the driving potential for heating the vessel decreases in this timeframe as a balance is reached between heat gain and heat loss.

These three stages of the transient only occur at locations where jet impingement occurs. At 30 degrees from the bottom, the temperature rise is delayed until the melt pool reaches this elevation and heating begins. The change in slope of the temperature increase at about 6,000 seconds occurs due to a solid-to-solid phase change in the steel. This phase change occurs at ~1,030 K, and the properties of the steel change according to the temperature of the vessel at its centerline. Therefore, the beginning of this effect is not seen when the centerline inner surface temperature reaches 1,030 K, but when the average vessel centerline temperature reaches 1,030 K.

For Case 2, the inner surface temperature reaches a maximum value of 1,300 K at 30 degrees and 1,215 K at 0 degrees (see Figure 3-10). The temperature distribution shown in Figure 3-10 illustrates the effect of the angular dependent heat flux due to internal heat generation. A peak inner surface temperature of 1,340 K is observed to occur at 35 degrees from the vertical. At larger angles from the vertical, the inner surface temperature decreases rapidly, due to upper crust formation over the molten pool. Although this temperature behavior is consistent with deep-pool behavior predicted by the Jahn and Reineke model,[23] it is enhanced because of the one-dimensional model for heat conduction within the pressure vessel and the lack of heat loss through the vessel wall upward into the coolant above the melt; i.e., fin effects are not included. However, when angular heat fluxes predicted with the TMI model are input to a two-dimensional model, heat losses up the vessel wall were typically found to overshadow enhanced convection effects in deeper pools. For example, Case 2 peak vessel surface temperatures shift toward the bottom and center of the lower head. Note that several parameters play a role in the initial importance of convective currents. In addition to pool depth, which is directly correlated to melt mass, the debris decay heat levels are important. In calculations that were performed to evaluate the vessel thermal response to lower debris masses and debris decay heats, such as Case 15, minor variations were predicted in angular heat fluxes.

As shown in Figure 3-11, the thickness of the upper crust and the lower crust at 0 and 30 degrees increases rapidly for initial stages of the transient. However, prior to 5,000 seconds, the crust growth rate levels; and a more modest growth rate occurs. Note that the lower crust

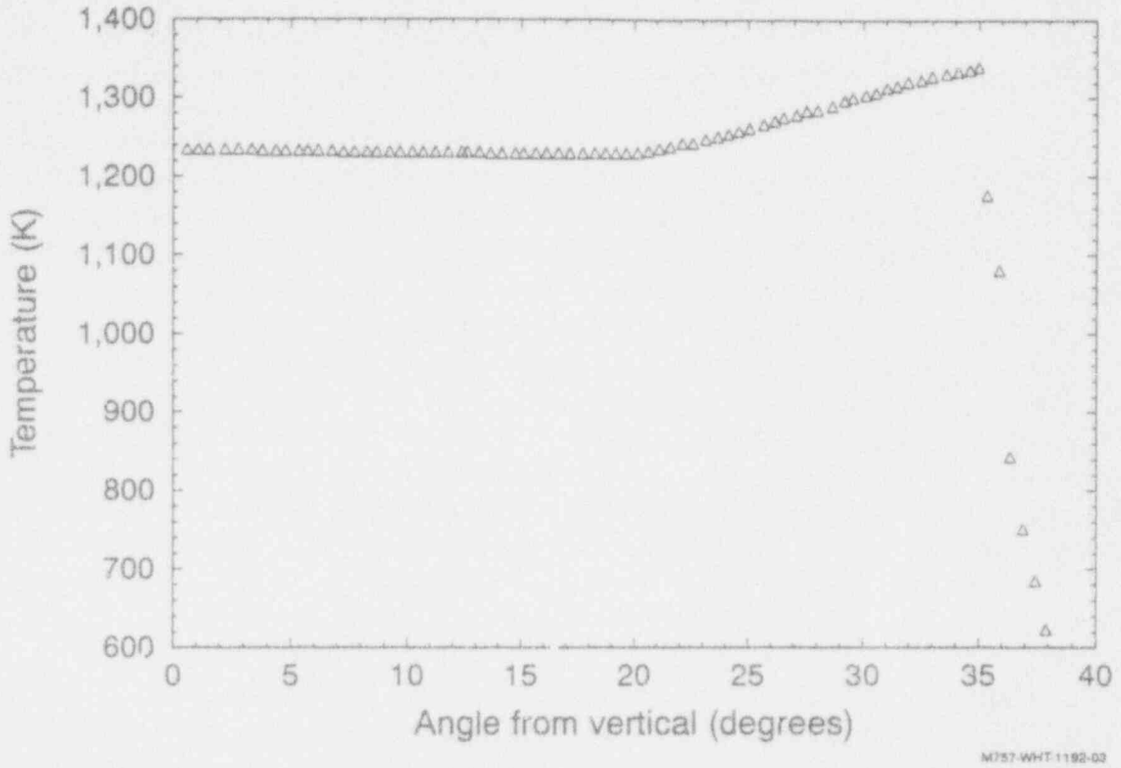

Figure 3-10. Case 2 vessel inner surface temperatures as a function of angle at 21,600 seconds.

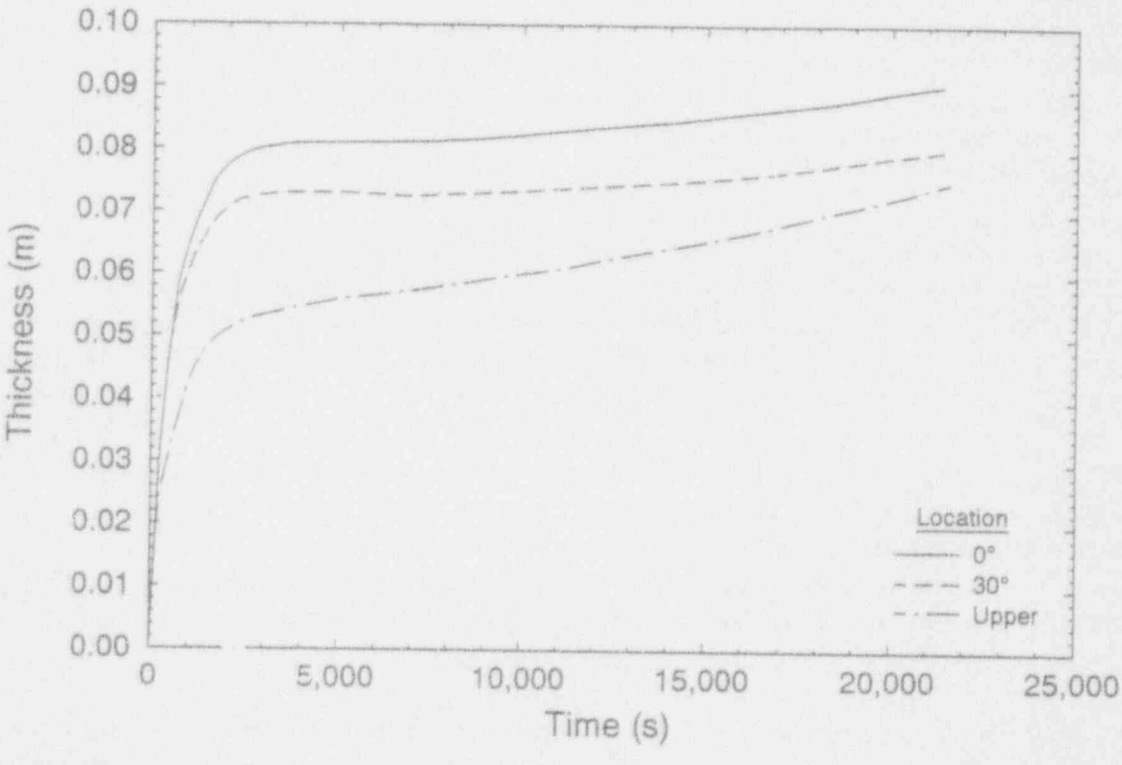

Figure 3-11. Case 2 crust thicknesses.

thickness at 0 degrees is larger than at 30 degrees. This is because higher heat transfer rates to the crust are predicted at 30 degrees.

The total heat transferred to the lower head and to the coolant above the debris is plotted in Figure 3-12. The rapid increase in the heat transferred down at the start of the calculation corresponds to the heat transfer that occurs during the jet impingement stage. The heat transfer upward also has a quick rise at the beginning, since the upper crust does not form until the jet pouring has ceased, which occurs one minute into the Case 2 simulation. The abrupt change in heat transfer to the coolant can be seen more easily in Figure 3-13, where the time-dependent heat fluxes up to the coolant and down to the pressure vessel at the centerline are shown. The rapid decay of heat transfer over short times is due to crust formation on the lower head and degraded jet heat transfer due to the formation of the molten pool. If the surface temperature of the crust above the molten pool falls below the minimum film boiling temperature, then the film boiling regime will collapse and nucleate boiling will exist at the surface. In this case, the heat flux would rise as the crust grows to once again balance the heat flow across the interface. This case indicates that the upward heat flux is about 20% below the downward value. However, this result does change as the initial and boundary conditions are altered.

As noted earlier, results for other cases are summarized in Table 3-4. Results in Table 3-4 are generally for a time of 21,600 seconds, which was a time period past the point where peak temperatures occurred. An exception is Case 6 results, which are for a time of 3,600 seconds. Case 6 results are given at this earlier time because the molten pool freezes at this time and the model is not applicable once the entire pool solidifies. Thus, peak vessel temperatures for Case 6 do not necessarily correspond to the maximum vessel temperature during this transient. This case is only provided to indicate the effects of water ingression and increased upward heat transfer upon the thermal transient. Obviously, the result that the molten debris will solidify within the first hour indicates that increased heat transfer from the debris to the coolant can significantly affect the transient.

The qualitative trends for all the cases are similar; however, the quantitative vessel wall surface peak temperatures differ. The first point to note is that the heating is uniform along the vessel wall, with the only local heating excursion being predicted during the time of jet impingement at the particular location of jet impingement. The model predicts the magnitude of this local hot spot to be on the order of 1,400–1,500 K (see Figure 3-8), and it typically persists for about a minute. This is not in agreement with observations from TMI-2 vessel boat sample material.[13] Hence, the jet impingement process cannot alone explain the localized hot spot temperatures observed in the boat sample examinations, and Scenario 1 from Section 2 was eliminated from further consideration. A much longer duration and more spatially uniform heating is observed to occur at the vessel wall after several hours (~20,000 seconds). Peak vessel inner surface temperatures for this later heating are predicted to be between 1,020-1,525 K, depending upon the initial and boundary conditions selected.

Boat sample examinations indicate that vessel inner surface temperatures for regions outside the hot spot did not reach temperatures above the ferritic-to-austenitic transition. Hence, temperatures predicted for Case 15 (in which lower bound values for inputs were used) are the only results that are consistent with metallurgic examinations. Recognizing that there is considerable uncertainty in model input parameters and in modeling debris/water interactions, it

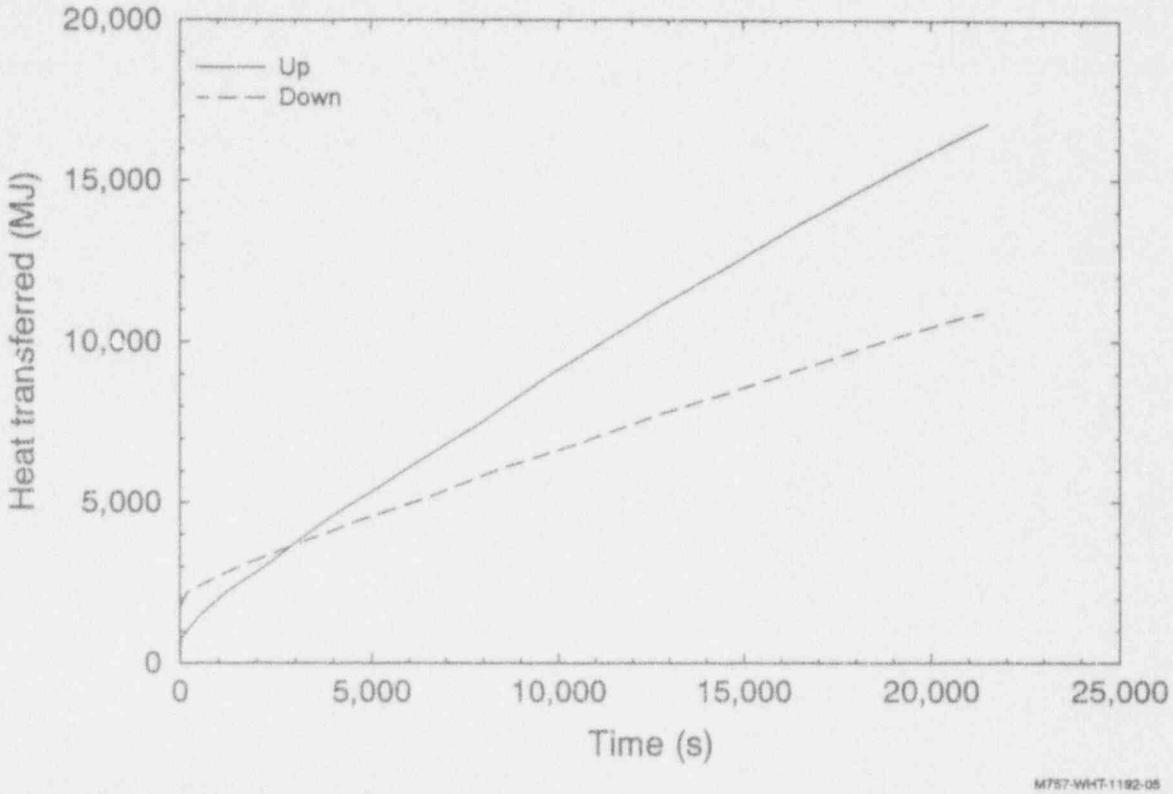

Figure 3-12. Case 2 heat transfer.

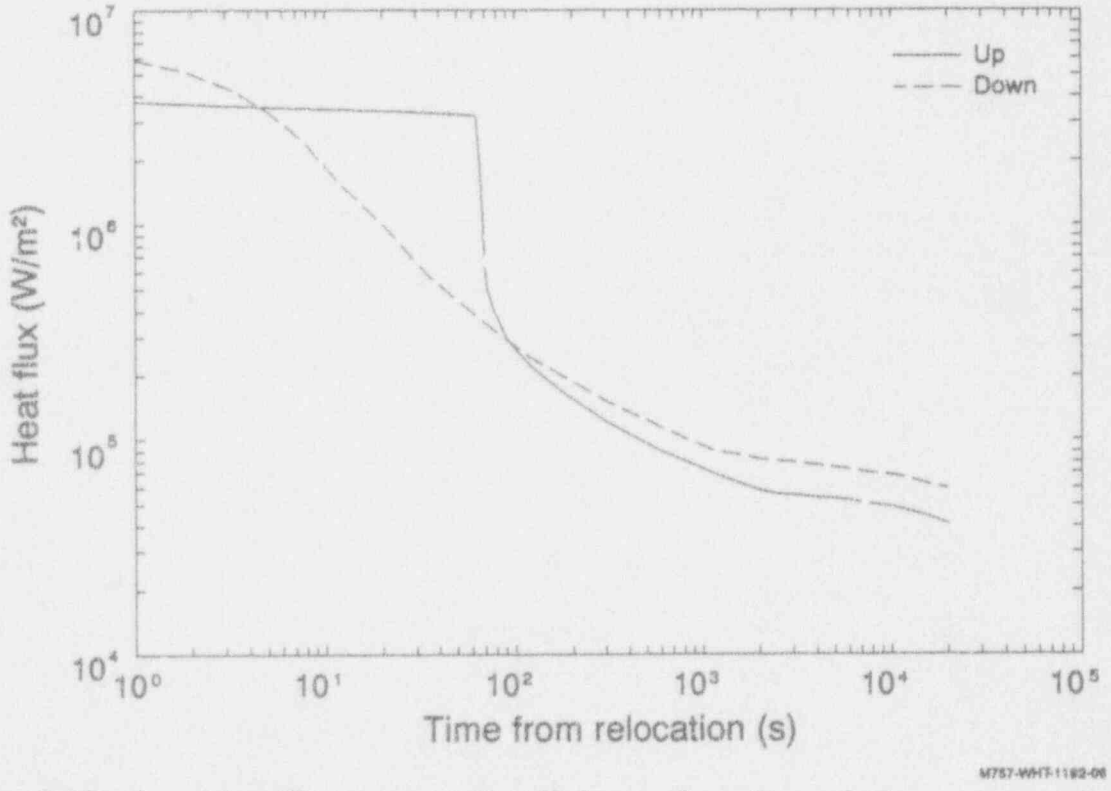

Figure 3-13. Case 2 heat fluxes at centerline (0 degrees from the vertical).

was decided to adopt the following approach for performing calculations to predict global and localized vessel failure:

1. Obtain nominal and lower bound temperature distributions by selecting appropriate values for input parameters.

2. Superimpose a hot spot temperature distribution consistent with results of the vessel steel sample examinations (i.e., a case with heat fluxes close to those used in Case 11, which produces a temperature distribution with peak values between 1,348–1,373 K for about 30 minutes) on temperature distributions where peak values do not exceed the transition temperature.

Time-dependent temperature distributions for the nominal and lower bound cases, Cases 12 and 15 in Table 3-4, respectively, are plotted in Figures 3-14a and 3-15a. Time-dependent heat fluxes for these cases are plotted in Figures 3-14b and 3-15b. The manner in which these temperature distributions were applied in the global and localized vessel failure calculations is discussed in Sections 4.3.1 and 4.4.1.

3.2.3 Summary

Calculations were performed to investigate the potential for the debris jet impinging upon the TMI-2 lower head to cause the hot spot temperatures observed in TMI-2 boat sample examinations. Time-dependent temperature distributions were obtained that can be input to global and localized vessel margin-to-failure calculations.

Calculations provided several useful insights into the TMI-2 accident, which are summarized below.

- Although the quantitative vessel wall surface peak temperature differed, results from several sensitivity studies were qualitatively similar. Namely, the thermal response can be divided into three time periods.

  - An initial localized temperature spike for the time and location of jet impingement (typically, on the order of 1 minute)

  - A transient vessel heatup (typically, on the order of 1 hour)

  - A quasi-steady vessel temperature distribution (typically, lasting for several hours)

  Calculations indicate that the vessel temperature gradient is relatively shallow (150–200 K)

- Rapid crust buildup (5-20 cm) causes the reactor coolant to remove heat from the lower head debris via nucleate boiling. Hence, results were relatively insensitive to coolant subcooling.

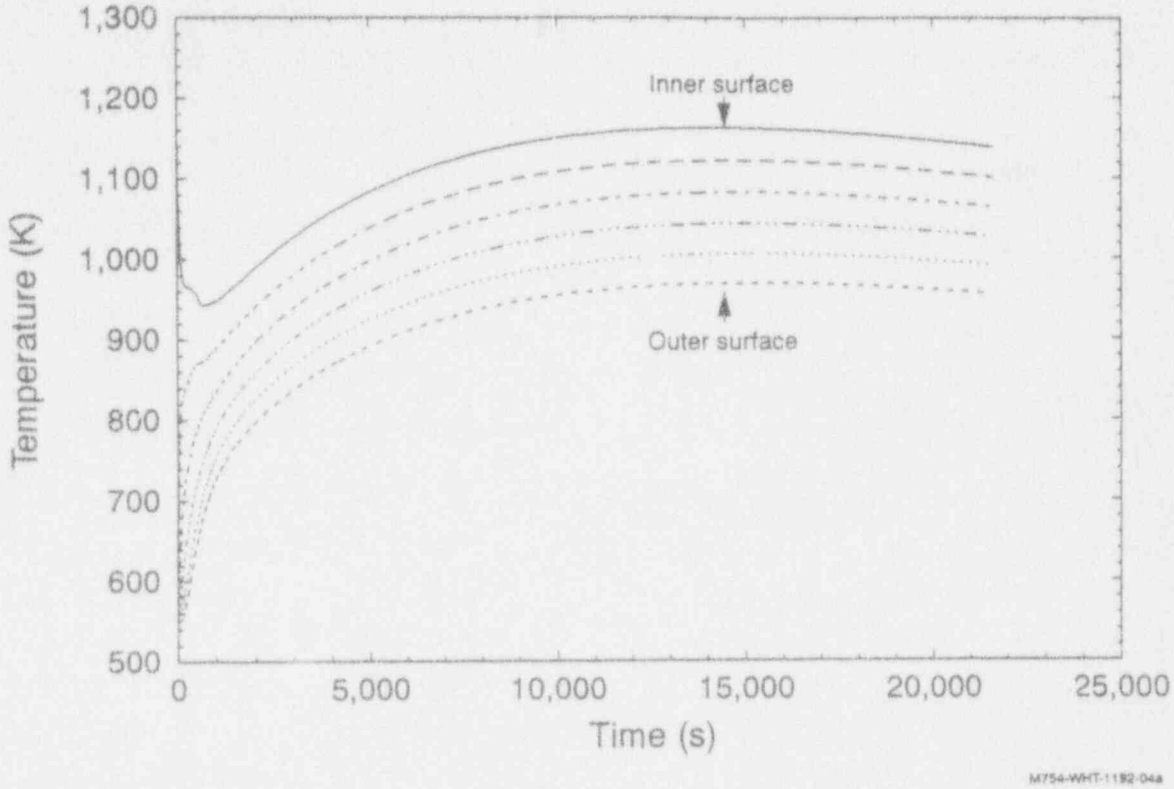

(a) Temperature distribution

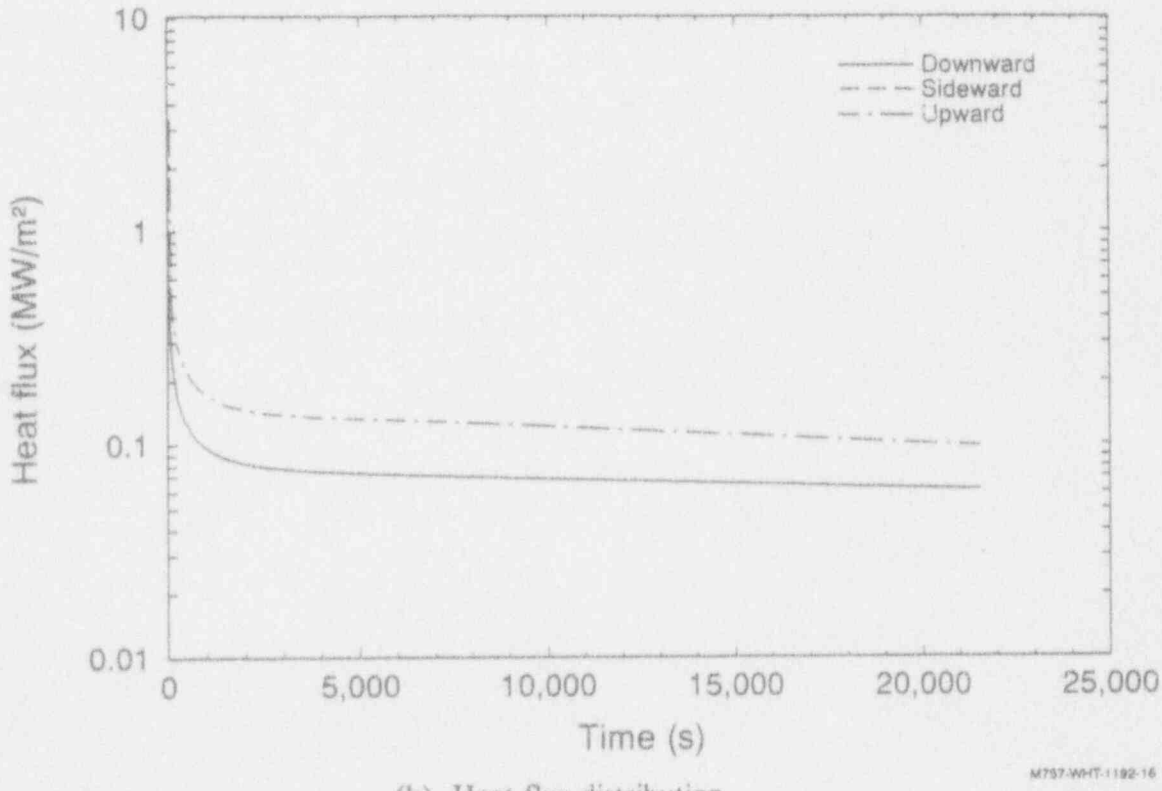

(b) Heat flux distribution

Figure 3-14. Nominal case results.

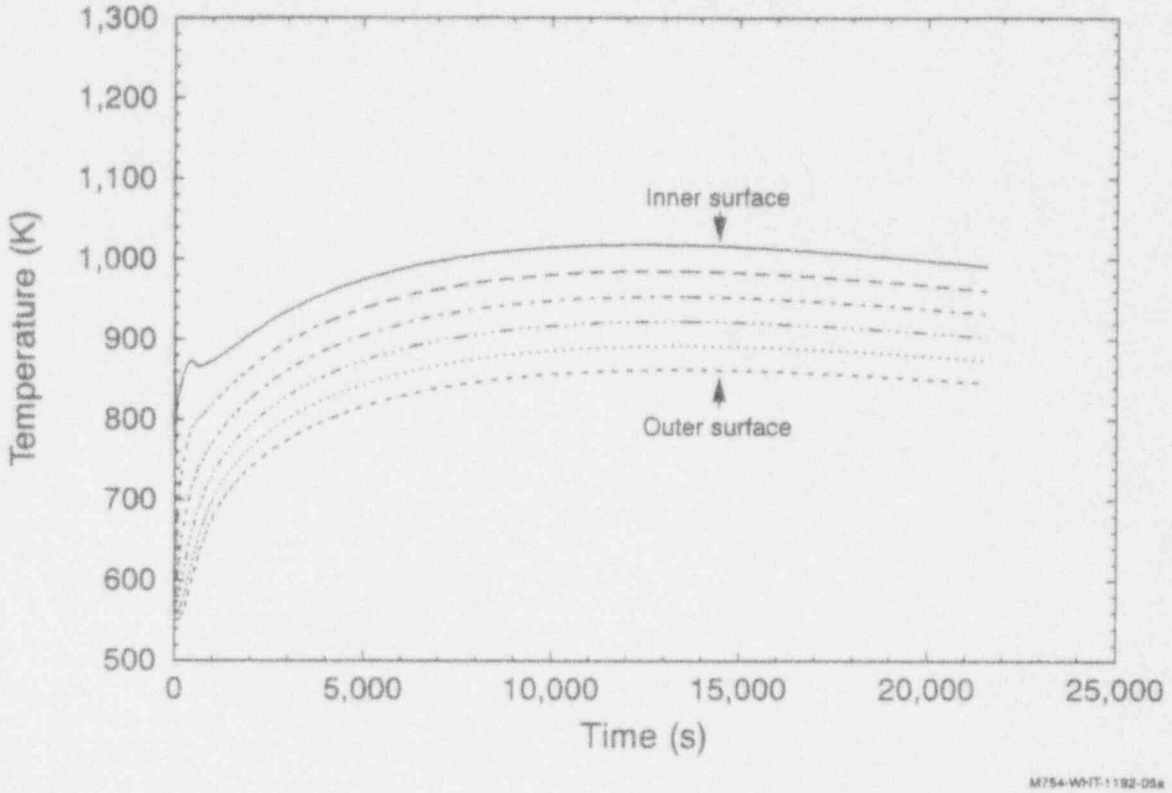

(a) Temperature distribution

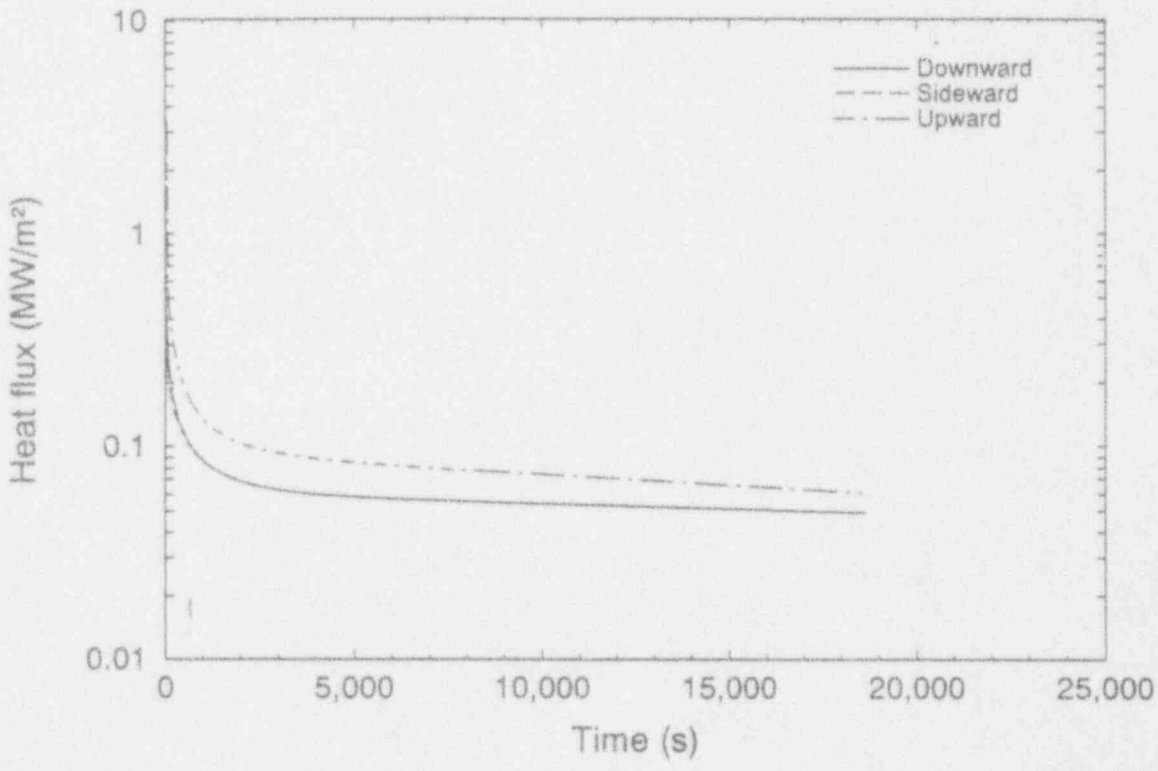

(b) Heat flux distribution

Figure 3-15. Lower bound case results.

- Only a case with lower bound input assumptions was found to result in global peak temperature predictions that do not exceed the ferritic-to-austenitic steel transition temperature range.

- The magnitude and duration of hot spot temperatures estimated in TMI-2 vessel examinations could not have been caused by an impinging jet. Rather, hot spot temperatures must have occurred later in the scenario from a sustained heat load due to molten debris upon the lower head. Hence, calculation results indicate that the assumption that hot spot temperatures were caused by a coherent jet impinging upon the vessel (assumed in Scenario 1 of Section 2.3) is incorrect.

- The limited area estimated in TMI-2 vessel examinations to have experienced hot spot temperatures suggests that this region was subjected to a localized heat source, such as might occur with a non-homogeneous debris bed or a localized region with enhanced debris-to-vessel contact.

3.3 Summary for Melt Relocation and Thermal Response Calculations

Prior to performing failure analyses, scoping calculations were performed to provide boundary conditions for the subsequent tube and vessel failure analyses. Calculations included in this section consider the potential for molten debris to travel through instrumentation nozzles of the TMI-2 pressure vessel, the potential for a jet of molten debris to fragment as it travels through coolant, and the thermal response of the vessel during and after relocation of molten debris. Input to these calculations was based upon data from companion sample debris examinations, nozzle examinations, and other available sources of TMI-2 data, such as plant instrumentation data. Where possible, data from vessel "boat sample" metallurgical examinations, such as peak vessel temperatures, were used as a check on thermal analysis results.

Major insights from these calculations are summarized below:

- Ceramic melt is not predicted to travel through TMI-2 instrument nozzles to locations below the vessel. Hence, ex-vessel tube temperatures are not predicted to experience higher temperatures than the reactor coolant system temperatures, and tube failure calculations should be performed using RCS temperatures.

- The amount of breakup occurring as melt relocated to the lower plenum is insignificant. Hence, calculation results indicate that the assumption that significant jet breakup occurred during relocation (assumed in Scenario 3 of Section 2.3) is incorrect.

- The magnitude and duration of hot spot temperatures estimated in TMI-2 vessel examinations were not caused by an impinging jet. Ratner, hot spot temperatures must have occurred later in the scenario from a sustained heat load from molten debris upon the lower head. The limited area estimated to have experienced hot spot temperatures suggests that this region was subjected to a localized heat source, such as might occur with a nonhomogeneous debris bed or a localized region with enhanced debris-to-vessel

contact. Hence, calculation results indicate that the assumption that hot spot temperatures were caused by a coherent jet impinging upon the vessel (assumed in Scenario 1 of Section 2.3) is incorrect.

- Only a case with lower bound input assumptions was found to result in global peak temperature predictions that do not contradict the results from boat sample examination data, namely that global vessel temperatures remain below values where the vessel material undergoes a transition from ferritic-to-austenitic steel. It should be noted that the cooling rates observed in metallurgical examinations of vessel specimens in the hot spot region were not predicted in any of the cases analyzed in this section.

3.4 References

1. MPR Associates, Inc., *Removal of Test Specimens from the TMI-2 Reactor Vessel Bottom Head*, MPR-1195, October 1, 1990.

2. D. W. Akers, "INEL Nozzle and Guide Tube Examinations," *Eighth OECD TMI-2 VIP Program Review Meeting, Idaho Falls, Idaho, May 12-13, 1992*, Presentation OECD-NEA-TMI-2 VIP TMI V(92)EG05.

3. L. A. Neimark, T. L. Shearer, A. Purohit, and A. G. Hins, *TMI-2 Instrument Nozzle Examinations at Argonne National Laboratory*, OECD-NEA-TMI-2 VIP TMI V(93)AL01, February 1993.

4. R. K. McCardell et al., *TMI-2 Reactor Vessel Lower Head Integrity Program Plan*, OECD-NEA-TMI-2 VIP TMI V(89)21, June 1989.

5. J. L. Rempe, et. al., *Light Water Reactor Lower Head Failure Analysis*, NUREG/CR-5642, EGG-2618, October 1993.

6. R. W. Ostensen and J. F. Jackson, *Extended Fuel Motion Study*, ANL-RDP-18, July 1973, pp. 7.4–7.7.

7. R. W. Ostensen et al., "Fuel Flow and Freezing in the Upper Subassembly Structure Following an LMFBR Disassembly," *Transactions of the American Nuclear Society, 18*, 1974, p. 214.

8. M. Epstein et al., "Transient Freezing of Flowing Ceramic Fuel in a Steel Channel," *Nuclear Science and Engineering*, 61, 1976, pp. 310-323.

9. M. Epstein, "Heat Conduction in the UO_2-Cladding Composite Body with Simultaneous Solidification and Melting," *Nuclear Science and Engineering, 51*, 1973, pp. 84-87.

10. D. W. Akers, S. M. Jensen, B. K. Schuetz, *Companion Sample Examinations*, OECD-NEA-TMI-2 VIP, TMI V(92)EG10, July 1992.

11. E. L. Tolman et al., *TMI-2 Accident Scenario Update*, EGG-TMI-7489, December 1986.

12. P. Kuan and E. L. Tolman, *Electromatic Relief Valve Flow and Primary System Hydrogen Storage during the TMI-2 Accident*, EGG-TMI-7703, May 1987.

13. G. E. Korth, *Metallographic and Hardness Examinations of TMI-2 Lower Pressure Vessel Head Samples*, OECD-NEA-TMI-2 VIP TMI V(92)EG01, January 1992.

14. C. C. Chu, M. L. Corradini, "A Transient Model for Fuel-Coolant Interactions," *Proceedings of the Thermal Reactor Safety Meeting, San Diego, California, February 2-6, 1986*, Vol 1, pp. II.2-1 through II.2-10.

15. C. C. Chu, *One-Dimensional Transient Fluid Model for Fuel-Coolant Interaction Analysis*, Ph.D dissertation, University of Wisconsin-Madison, Madison, WI, May 1986.

16. C. C. Chu, M. L. Corradini, "One-Dimensional Fuel-Coolant Interaction," *Journal of Nuclear Science and Engineering, 101*, No. 1, January 1989, p. 48-71.

17. C. C. Chu, M. L. Corradini, J. Murphy, J. Tang, *A Code Manual for TEXAS-II: One Dimensional Transient Fluid Model for Fuel-Coolant Interaction Analysis,* University of Wisconsin Report, UWRSR-39, July 1992.

18. M. Epstein, et al., "Simultaneous Melting and Freezing in the Impingement Region of a Liquid Jet," *AICHE Journal*, 26, September 1980, p. 743.

19. Sandia National Laboratory, *Core-Meltdown Experimental Review*, SAND74-0382, August 1975.

20. D. R. Olander, *Fundamental Aspects of Nuclear Reactor Fuel Elements,* University of California-Berkeley, TID-26711-P1, published by the Energy Research and Development Administration, November 1977.

21. M. Epstein, H. K. Fauske, "Steam Film Instability and the Mixing of Core Melt Jets and Water," *Proceedings of the 1985 ANS/ASME/AIChE National Heat Transfer Conference, Denver, Colorado,* August 1985.

22. J. A. Kos, *Model of Fuel-Melt Quenching in the Lower Plenum of the RPV,* Masters of Science thesis, University of Wisconsin, Madison, WI, August 1992.

23. M. Jahn, H. H. Reineke, "Free Convection Heat Transfer with Internal Heat Sources Calculations and Measurements", *Proceedings of the Fifth International Heat Transfer Conference, Tokyo, Japan*, 3, 1974, p. 74.

24. J. Garnier, *Ex-Reactor Determination of Thermal and Contact Conductance*, NUREG/CR-0330, April 1979.

25. Kelsey, A. P., *Lower Head Debris Topography*, TMI-2 Technical Bulletin TB-89-02, Rev. 0., GPU Nuclear Corporation, Project Planning and Analysis Department, Middletown, PA, February 27, 1989.

26. M. T. Farmer, et al., "CORQUENCH: A Model for Gas Sparging–Enhanced, Melt-Water, Film Boiling Heat Transfer," Presented at the *ANS Winter Meeting, CONF-901101--31, Washington, D.C., November 11-15, 1990.*

4. SCOPING CALCULATIONS FOR STRUCTURAL RESPONSE AND MARGIN-TO-FAILURE ESTIMATES

As discussed in Section 1, margin-to-failure calculations were performed to evaluate the potential for the TMI-2 vessel to fail via mechanisms such as tube ejection (which must be preceded by weld failure), tube rupture, global vessel failure, and localized vessel failure.

Figure 1-1 illustrates how calculations within this section are coordinated. Thermal analyses, documented in Section 3, provide input for these calculations. For each failure mechanism considered, estimates are provided for a margin to failure to provide insight into which mechanisms had smaller failure margins during the TMI-2 accident.

4.1 Margin-to-Failure Background

Margin to failure, as defined by exceeding ultimate strength or by creep failure, is evaluated for each failure mechanism. The ultimate-strength margin to failure is straight forward, calculated as a function of the ratio of the maximum effective stress to the ultimate strength. Creep margin to failure is more ambiguous to define. Unlike ultimate strength, creep failure is time dependent. Given enough time at high temperatures with some stress, a creep failure will be predicted even when the ultimate-strength-based margin to failure is significant.

As a basis of comparison between failure mechanisms, a margin to failure for creep failure using a stress-based damage failure criterion was defined by the consensus of the Structural Mechanics Peer Review Group.[1] The procedure includes converting the multi-dimensional stress state to an effective stress, interpolating the time to failure for constant temperature and stress using the Larson-Miller parameter (LMP), and predicting time to failure for the actual stress and temperature history using a time damage model. The entire procedure has not been verified experimentally for cases such as the TMI-2 vessel, where temperature and pressure are changing and a temperature gradient exists through the thickness. However, the individual steps (calculation of effective stress, interpolation of time to failure with the LMP and use of the time damage model) have been verified experimentally.[2-6] Additionally, this procedure has been used in previous creep analysis of a case with a geometry very similar to the TMI-2 vessel and penetrations: thick-wall furnace tubes, under internal pressure with a temperature gradient through the thickness.[7]

Currently, there is not a single method or procedure that is universally accepted for defining margin to failure. Using a stress-based criterion, other methods are available for each of the steps outlined above. For example, past discussions have centered on the use of Mises effective or maximum tensile stress. The proper stress depends on whether crack initiation or propagation dominates the creep behavior.[8] Other parameters can be used to interpolate time to failure for constant stress and temperature. Finally, several damage models have been proposed in lieu of the stress-based time damage model.

Some of the damage models proposed in the published literature include a strain damage model,[9] combined strain and time damage models,[10,11] and a combined strain and temperature damage model.[12] Experimental studies comparing time damage and strain damage models for

high-alloy steels have shown that in some cases the time damage models are more conservative; in other cases, the strain damage model is more conservative; and in many cases, a combined criterion appears to give the best results.[10,11] It is difficult to assess the applicability of the time and temperature damage model to SA533B, since it was developed for zircaloy, which is not a ferrous material.

No single creep failure criterion, which likely is material dependent, has been proven to be superior. It is beyond the scope of this project to determine which failure criterion is best for SA533B under accident conditions. Given the limited data for SA533B at very high temperatures and the scatter in creep data, a simple procedure that has been used in prior published analyses was initially recommended by the Structural Mechanics Peer Review Group for the margin-to-failure calculations. However, results from initial calculations using this stress-based damage failure criterion predicted failure at times when strains were quite small (less than 10%). Members of the Structural Mechanics Peer Review Group noted that these results suggest that the stress-based damage failure criterion used in initial calculations was too conservative. Hence, a second set of calculations (reported in Section 5.2) were performed in which failure was defined as the point where mechanical instability occurs rather than invoking a stress-based damage failure criterion.

4.2 Scoping Analysis for TMI Penetration Tube Weld Failure

A penetration ejection model was developed in the NRC-sponsored lower head program[13] to predict penetration ejection, assuming that the penetration weld failed. Prior to using the tube ejection model, it is necessary to establish that weld failure occurs. Metallurgical evidence from the VIP examinations indicates that the Inconel penetration welds did not melt. Stainless steel cladding, which has approximately the same melt temperature as Inconel, showed no signs of melt, even inside the hot spot.[14] Actual examination of a penetration weld slightly outside the hot spot revealed no melting of the weld (including the buildup above the vessel surface).[15] From this evidence, it was concluded that penetration welds did not melt.

This analysis examines the mechanical behavior of the weld for penetrations inside the hot spot, subject to the maximum predicted temperatures and maximum recorded pressures during the accident. Its purpose is to evaluate the possibility of weld failure by exceeding ultimate strength or by creep. If weld integrity is assured, further penetration ejection analysis is not needed (weld integrity precludes ejection).

4.2.1 Model Description

This analysis used a mechanics of materials approach, comparing weld stresses to ultimate strength data and weld creep rupture strength data. Applied stresses, from system pressure and tube dead weight, were assumed to be carried by the weld in pure shear. A margin to failure, based on ultimate capacity, was calculated. The time to fail by creep, at the accident temperatures and the assumed pressure, was calculated using the LMP.

4.2.2 Input Assumptions

Input assumptions for the best-estimate analysis are described below. Uncertainties in the assumptions are provided in the next section.

Geometry

It was assumed that the critical region for penetration weld failure was in the hot spot of the vessel, located approximately 0.5 m from the centerline of the vessel. Schematics of a centerline instrument tube and penetration weld are shown in Figures 4-1 and 4-2.[16,17] Although Figure 4-1 shows the tube intersecting the vessel at 90 degrees, tubes in the hot spot intersect the vessel obliquely because the hot spot is not located at the bottom of the vessel. This did not affect the analysis, due to conservative assumptions in the weld shear area described below. The length of the instrument tube, 5.47 m, from the vessel to the first unistrut support was used to calculate the dead weight of the tube, as shown in Figures 4-2 and 4-3. The unistrut support is located, as shown, at the horizontal end of the pipe bend.[a]

The weld shear area was taken as the area of intersection between the tube and the weld. As a conservative measure, the weld area associated with the weld buildup above the cladding was ignored.

Material Properties

An INCO82T weld joins the Inconel-600 tube and the SA533B vessel material. High temperature Inconel-600 tensile and creep properties[13] were used for this analysis, because high temperature INCO82T properties were not available. In general, this will produce conservative results, since weld materials have higher strength properties than their base material counterparts. Inconel-600 ultimate strength as a function of temperature and the LMP fit for creep data are included in Appendix A.

Loads and Temperatures

This analysis assumed that the pressure load and instrument tube dead weight were carried in pure shear, solely by the penetration weld, as shown in Figure 4-3. The maximum recorded system pressure for over 10 hours after relocation (see Figure 2-2), 15 MPa, was used. The dead weight was calculated from the length of tubing from the lower head to the first unistrut support. The unistrut support was not allowed to bear any of the load. The peak weld temperature was assumed to be 1,361 K for 0.5 hours. This is the mid-point for the peak temperature range (1,348–1,373 K) estimated from metallurgical examination.[14]

4.2.3 Uncertainties

Primary sources of uncertainty in this analysis were the peak temperature estimates from TMI-2 boat sample examinations[14] and the creep data fit to the LMP. The range for temperature

---

a. Personal communication with Babcock and Wilcox personnel, Lynchberg, Virginia, September, 1992.

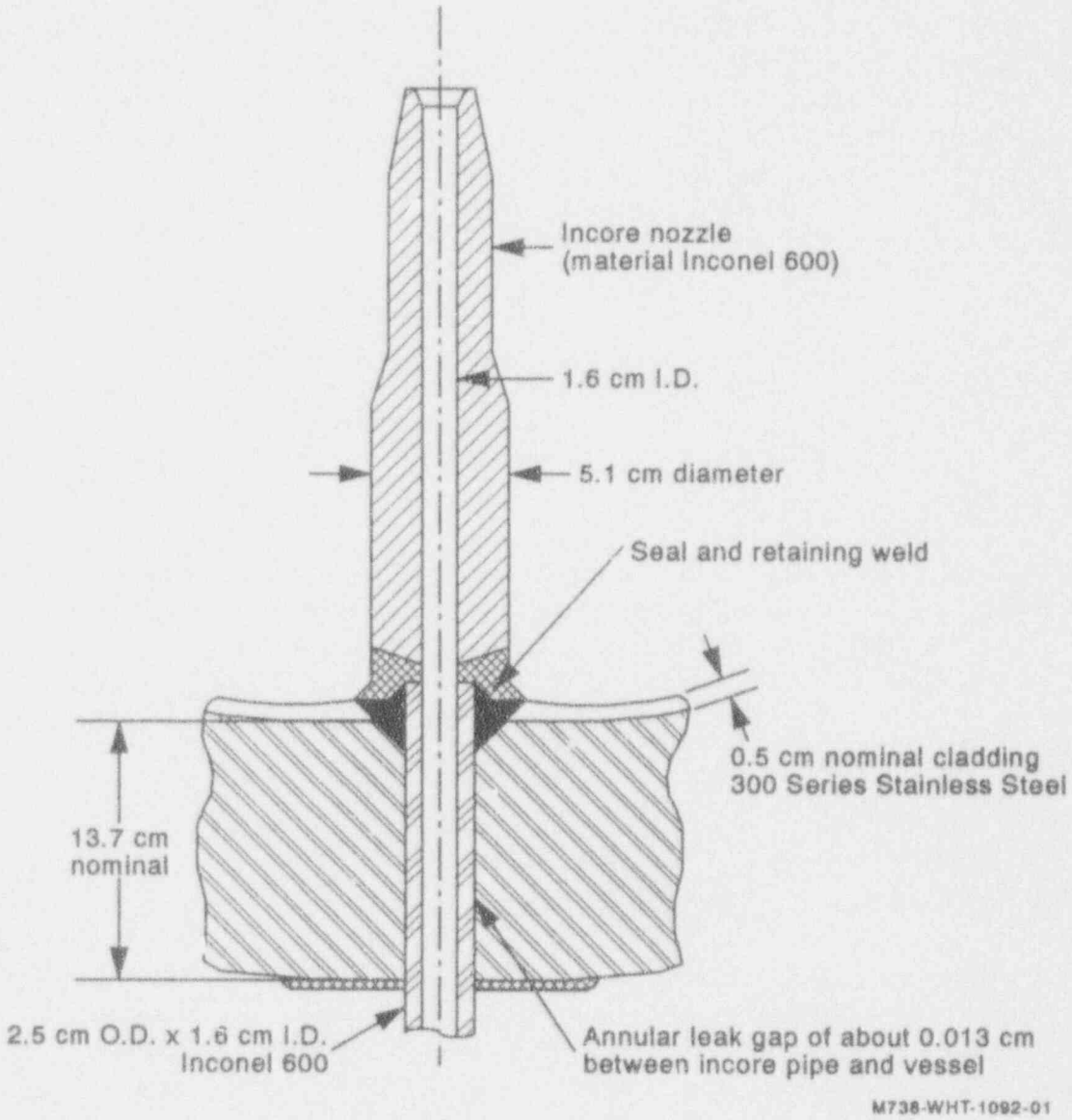

Figure 4-1. Schematic of instrument tube penetration.

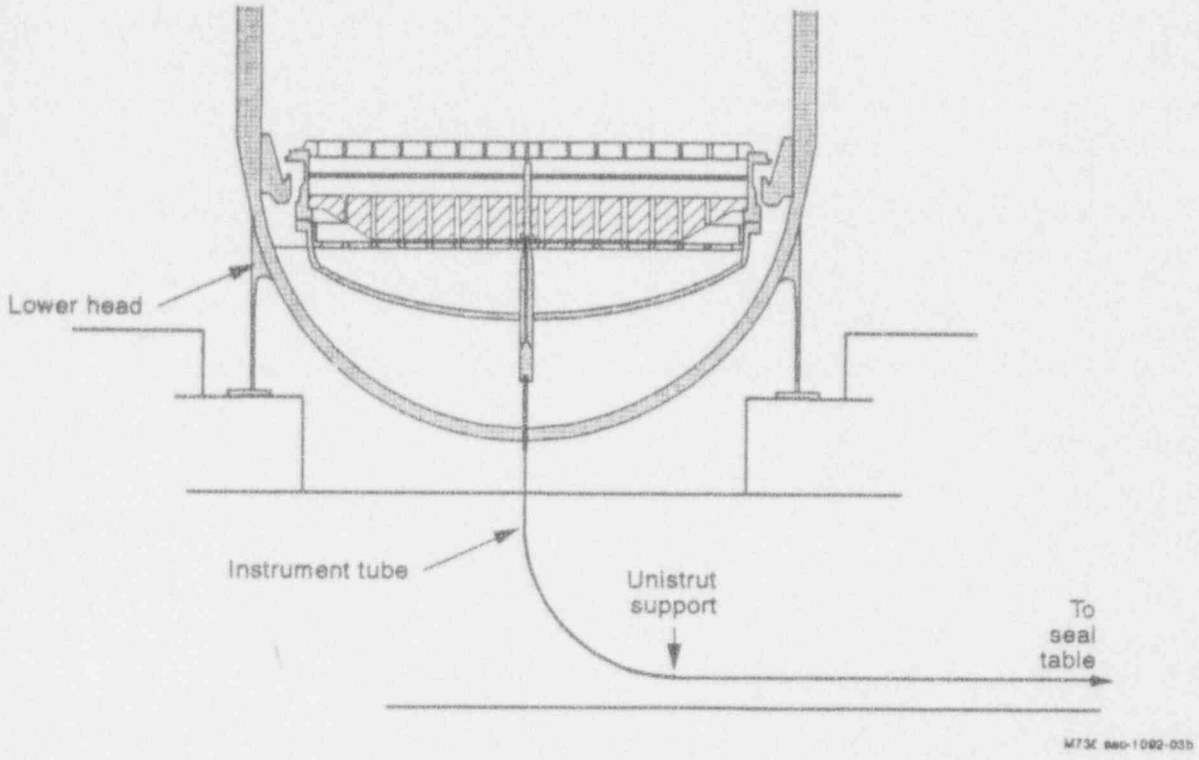

Figure 4-2. Schematic of instrument tube and vessel showing location of unistrut support.

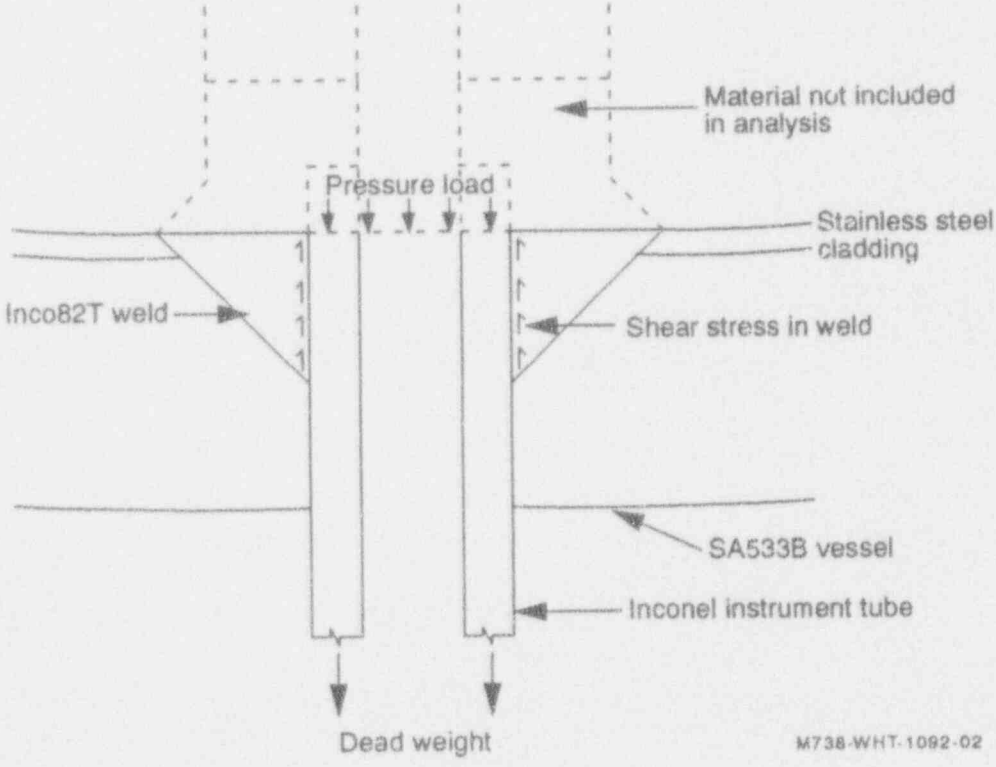

Figure 4-3. Schematic of instrument tube penetration showing applied loads, shear stress and weld buildup material.

uncertainties (1,348–1,373 K) was taken from metallurgical studies.[14] Upper and lower bounds for the LMP data were statistically fit[18] to 95% confidence limits, as shown in Appendix A, Figure A-33. The minimum ablation height was also uncertain; therefore, the most reasonable, conservative estimate was used.

The upper limit of the margin to failure and creep failure time were calculated using the lower peak temperature, 1,348 K, and the upper limit of the LMP fit to stress. For the lower limit of margin to failure and creep failure time, the upper peak temperature, 1,373 K, and lower limit of the LMP were used. Upper and lower limit fits for the LMP are listed in Appendix D. Calculations are similar to the best-estimate calculations shown in Appendix D.

4.2.4 Results

Results from calculations, detailed in Appendix D, indicate that the dead load is less than 2% of the total load. The effective stress due to applied loads, 12.32 MPa, is low relative to the ultimate strength, 30.78 MPa, for Inconel-600 at 1,361 K. The Mises effective stress was used because it was found to be more conservative than the Huddleston effective stress[2] with a pure shear stress state. Ultimate-strength margin to failure was defined for this analysis as

Margin to Failure = (1 − effective stress/ultimate strength)100%.

This makes the best-estimate, ultimate-strength margin to failure equal to 60% (see Table 4-1).

If the peak temperature (1,361 K) and maximum system pressure (15 MPa) were held constant, the time to rupture is 7.2 hours (see Table 4-2). Estimated time at peak temperature was 0.5 hours. Naturally, the material spent time at some elevated temperature after peaking, but the fact that the weld could carry the most severe conditions for 6.7 hours longer than they were actually imposed assures that the TMI-2 accident would not have caused weld failure.

Table 4-1. Ultimate strength margin to failure for instrument tube weld failure.

Upper limit (1,348 K)	65%
Best estimate (1,361 K)	60%
Lower limit (1,373 K)	54%

Table 4-2. Time to creep failure for instrument tube weld failure.

Upper limit (1,348 K, upper LMP)	16.9 h
Best estimate (1,361 K, best LMP)	7.2 h
Lower limit (1,373 K, lower LMP)	4.2 h

4.2.5 Discussion

This analysis showed that the ultimate-strength margin to failure for the penetration weld during the TMI-2 accident was at least 54%. If the peak temperature and a 15 MPa system pressure were both maintained constant, the minimum time to creep failure was 4.2 hours. These results, convincing in the large, ultimate-strength margin to failure and the long estimated time to creep failure, are conservative for the following reasons:

- The weld buildup material was ignored, reducing the load bearing weld area (shear area).
- The minimum weld depth into the vessel was used to calculate load bearing weld area (shear area).
- The analysis assumed a pressure of 15 MPa. The maximum temperature may have occurred with a lower pressure.
- Calculations for the time to creep failure held the peak temperature constant, when in fact, the peak temperature was estimated for only 0.5 hours.
- The load was carried solely by the weld. None of the load was distributed to the unistrut support.

Ultimate strength failure was not predicted because the applied stress on the weld was very low. Although the assumed temperature for the weld was relatively high (1,348–1,373 K), the low applied stress (12.32 MPa, 1.786 ksi) presented little challenge to the ultimate strength of the weld, as indicated by the 60% best estimate for margin to failure. Again, because stresses were low, best-estimate creep failure was not predicted before 7.2 hours. Since penetration weld integrity during the TMI-2 accident was assured, penetration ejection was ruled out as a possible failure mode.

4.3 Ex-Vessel Instrument Tube Failure

Another possible failure mode of the primary system containment associated with the instrument tube was that of the tube bursting under accident conditions in a location outside the vessel lower head. This failure would reduce the pressure in the tube, increase the pressure differential across any melt entering the tube from the debris bed above, and allow additional melt penetration through the vessel wall and out of the primary pressure containment. An approach based on force equilibrium, similar to that of the instrument weld margin to failure was used to evaluate tube failure. Margins to failure based on creep time to failure and ultimate strength were calculated.

4.3.1 Calculations

As discussed in Section 3, the melt penetration analysis of the instrument tube indicated that melt would not penetrate beyond the vessel thickness. Hence, the temperature conditions for this analysis were limited to those of the reactor coolant system during the accident (see Figure 1-1).

An upper bound on the coolant temperature (600 K) was taken to be the saturation temperature corresponding to the peak system pressure during the first 12 hours after relocation. The lower-bound temperature (400 K) was based on the minimum value measured in the cold leg during the transient. Since these conditions were expected to result in high margins to failure, a constant upper-bound system pressure of 15 MPa was assumed for the loading. This simplified the analysis and produced a conservative result.

The TMI-2 penetration tube is made of Inconel-600 material. Plots of ultimate strength as a function of temperature and the LMP fit for the creep test data for this material are included in Appendix A, Figures A-28 and A-33.

As Figure 4-4 indicates, the operating system pressure is the primary load on the instrument tube. Because the instrument tube configuration below the lower head (see Figure 4-2) makes a large bend and is subsequently routed horizontally, the ex-vessel pressure load results in an axial stress component, as well as a hoop stress component, in the wall of the tube. Huddleston's criteria[2] for multi-axial conditions was applied to calculate the effective stress (Appendix A-2.3.1).

This effective stress, $\bar{\sigma}$ was compared to the ultimate strength, S_u, of the material at 600 K and 400 K to determine an ultimate-strength margin to failure as shown in

$$MF = \left(1 - \frac{\bar{\sigma}}{S_u}\right) 100\% \ . \qquad (4\text{-}1)$$

The creep time to failure was calculated using the applied stress resulting from a constant 15 MPa system pressure, the bounding temperatures, and the Larson-Miller curve for Inconel-600.

4.3.2 Results

Results of these calculations indicate that the ultimate strength margin to failure is 96.0 % at a temperature of 400 K and 95.8% at 600 K. The small variation in margin to failure is a result of the minor variation in the ultimate strength for Inconel-600 in this temperature range. Times to creep rupture at these temperatures are of the order of 10^{15} and 10^{29} hours. Hence, both measures of margin to failure calculated here are very high.

4.4 Global Vessel Rupture

A calculation of margin to failure for global vessel rupture requires that the lower head be considered for a structural collapse mechanism under the primary loading of the vessel's internal pressure. Thermal stresses complicate the analysis by causing stress redistribution, some plastic response, and, at higher temperatures and stresses, creep relaxation, resulting in further stress redistribution. These stresses tend not to cause ultimate collapse of a structure unless the primary load-carrying capacity is affected by the thermal plasticity and creep damage.

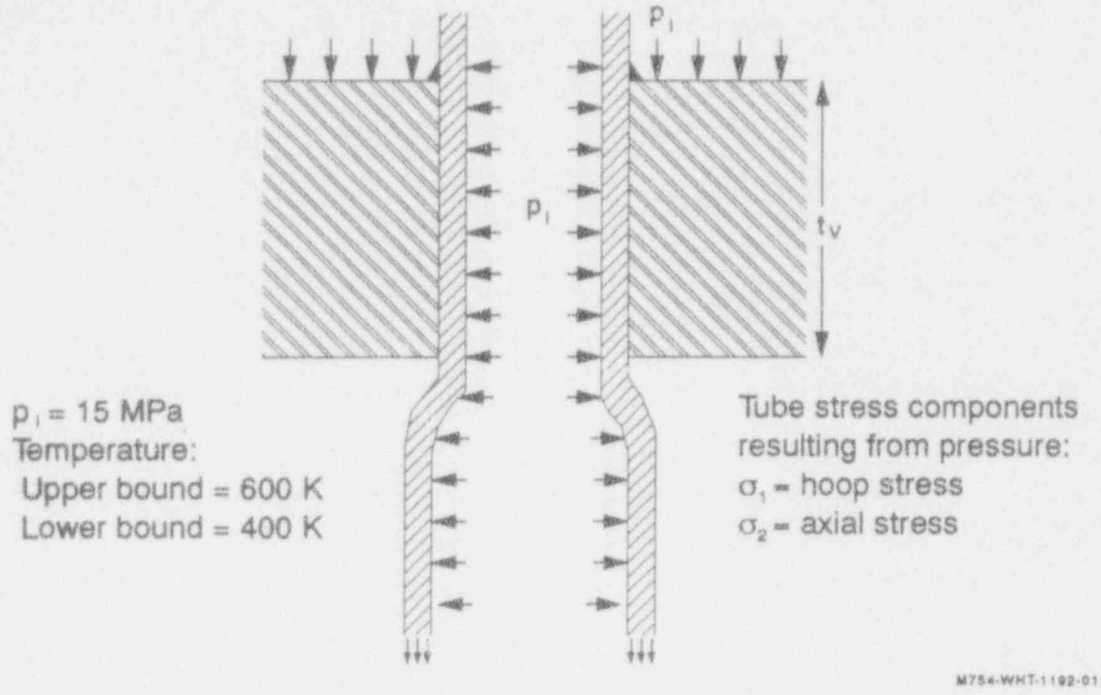

Figure 4-4. Schematic of configuration used to evaluate ex-vessel tube rupture.

Structural evaluations of margin to failure for global rupture of the vessel could range from relatively simple to rather complex calculations. In these analyses, only two-dimensional axisymmetric cases were considered. Three-dimensional effects may influence the vessel behavior, but given the uncertainties in the thermal input and mechanical properties, a two-dimensional analysis was considered appropriate for this study. In a more straightforward fashion, force equilibrium of the system pressure and the ultimate collapse load of the vessel could be computed. In more complex calculations, based on structural finite element analysis of the vessel wall, stress redistribution from thermal stress and creep relaxation could be performed. However, it was desired to perform several parameter studies in the margin-to-failure calculations. Hence, the scoping calculations for global vessel rupture were based on the simpler, force equilibrium method.

4.4.1 Input Data

Data for this analysis have come from several sources. Vessel material properties, which are found in Appendix A, were based primarily on creep and tensile tests that were performed as part of the TMI-2 VIP. The time-dependent vessel temperature distributions were based on the nominal and lower-bound global temperature results discussed in Section 3.2. The primary mechanical load on the vessel wall during the accident resulted from the operating system pressure, which was measured during the accident. TMI-2 vessel lower head dimensions, which are also listed in Appendix A, formed the basis for the analysis geometry.

As discussed in Appendix A, TMI-2 VIP creep tests were performed for temperatures ranging from 873 to 1,373 K in 100-degree increments, and a Larson-Miller curve (see Figure A-40) was obtained from these data. Tensile tests were performed at room temperature

and the same temperature range for which creep tests were performed. Because no tests were performed in the TMI-2 VIP for temperatures between 300 and 873 K, ultimate strength data reported in the ASTM Data Series Publication DS47[19] were used to augment the strength curve. Ultimate strength data from these two programs are compared in Figure A-36 of Appendix A.

As discussed in Section 3.2, time-dependent vessel wall temperature distributions were estimated based on uncertainties in several sources of input, including the debris decay heat levels from companion sample examinations. Two time-dependent temperature distributions [see Figures 3-14(a) and 3-15(a)] were used in the vessel structural response calculations: (a) the nominal case and (b) the lower-bound case.

4.4.2 Model Description

This model evaluates the margin to failure of the vessel lower head ultimate capacity, or collapse load, against the applied load of the operating system pressure. The model accommodates time-dependent, through-thickness temperature gradients and time-dependent applied pressures. The ultimate capacity calculated is based on the membrane-load-carrying capacity of the vessel head wall segments, which have not reached a time-accumulated, total-creep-damaged state.

Major parameters for evaluating force equilibrium in the reactor vessel lower head are illustrated in Figure 4-5. The applied load, L_i, on the vessel is given by

$$L_i = p_i \pi r_m^2 \tag{4-2}$$

and is a result of the system pressure, p_i, acting upon the area inscribed by the hemisphere of the lower head. For thin-walled vessels, the mean radius, r_m, of the vessel wall may be used. This applied load, L_i, is resisted by membrane stresses, σ_φ, in the vessel wall of thickness t_v. These membrane stresses may be calculated by the force equilibrium equation, which is determined by summing forces along the axis of symmetry:

$$p_i \pi r_m^2 - 2\pi r_m \sigma_\varphi t_v = 0 \ . \tag{4-3}$$

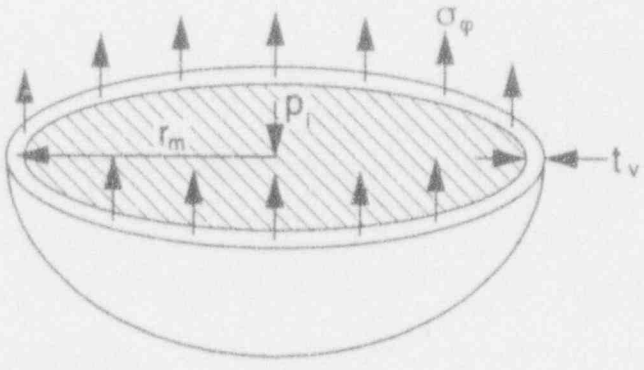

Figure 4-5. Force equilibrium for vessel internal pressure.

The ultimate capacity, C_i, of the wall results when the membrane stress reaches the material's ultimate strength:

$$C_i = 2\pi r_m S_u t_v \ . \tag{4-4}$$

Hence, failure is predicted when the applied load is greater than or equal to the ultimate capacity and the margin to failure is zero.

Creep damage is considered in this model by applying the time-damage rule, in conjunction with the LMP, to each segment at every time increment. Briefly, the stresses are related to the LMP, from which a predicted time to fail is calculated for each segment, given the segment temperatures. The damage for each segment, at each time increment, is calculated from a ratio of the time increment and the time to fail. Damage is then summed over all the time increments. Total damage is achieved when the accumulated damage reaches a value of 1. At that point, the segment is assumed not to have any load carrying capability. This procedure for calculating damage, given a stress and temperature history, is presented, in more detail, in Appendix A-2.3. Using these concepts of damage and capacity, a model for determining vessel head load capacity under creep damaged conditions was developed. In Figure 4-6, the lower head is depicted with an internal time-varying pressure and a through-wall, time-varying temperature distribution. Calculating vessel wall stresses resulting from the current pressure at 20 segments through the wall, damage was assessed at each of the 20 locations for the segments' current temperature. Once the totally damaged segments had been determined, the capacity of the remainder of the vessel wall was calculated by first determining the ultimate capacity of each segment for which damage had not been total. This was simply the ultimate strength of the vessel material at the

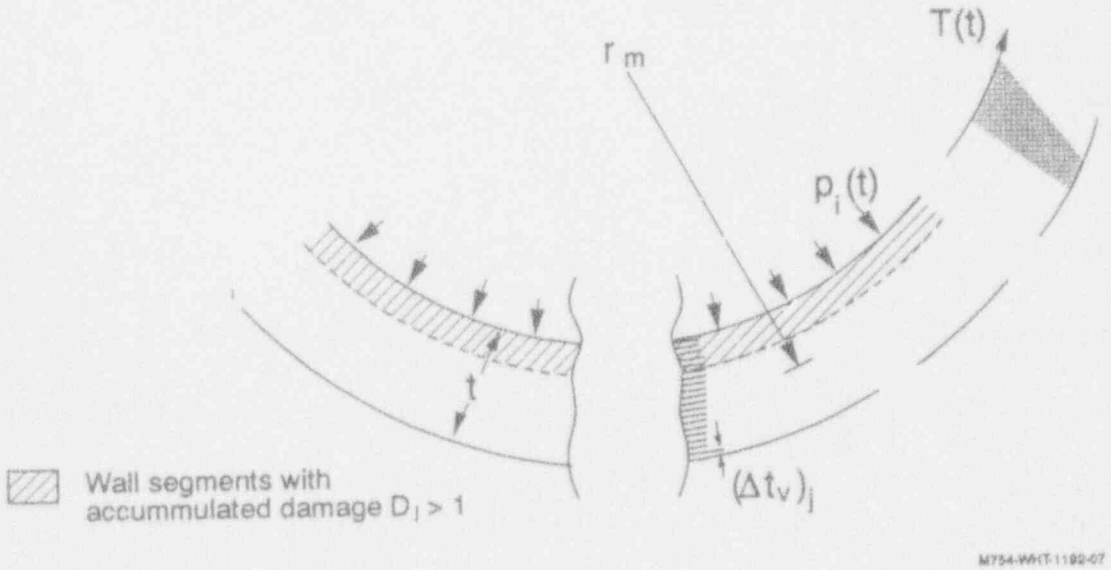

Figure 4-6. Creep damaged vessel capacity.

segment's current temperature, $S_{u_{ij}}$, multiplied by the segment area. Finally, each segment capacity was summed, and a total wall capacity, C_i, was determined by

$$C_i = 2\pi \sum_{j=1}^{20} r_j \, S_{u_{ij}} \, (\Delta t_v)_j \; . \tag{4-5}$$

This total capacity was then compared to the current pressure load, Equation (4-2), and an ultimate-strength margin to failure at the current time in the analysis calculated by:

$$MF_i = \left(1 - \frac{L_i}{C_i}\right) 100\% \; . \tag{4-6}$$

To this point, the calculation of stress in the vessel wall was simply expressed as the stress induced in a thin-walled, spherical shell from an internal pressure. It can be shown that, for this case, the formula for stress derived from equilibrium in Equation (4-3) is also the Mises stress. Huddleston[2] has shown that multi-axial stress states in some materials undergoing strength tests result in strength values below those of uniaxial strength tests. In Reference 2, Huddleston discusses a method for determining a correction factor to be applied to the Mises wall stress so that appropriate strength levels are used in a structural analysis. This method utilizes stress invariants. Because of the use of stress invariants, it was decided that all three components of stress should be calculated in the vessel wall. Thus, using the more general, thick-walled assumptions for stress in a spherical shell, calculations for hoop, σ_θ, meridional, σ_φ, and radial stress, σ_r, were made. Roark[20] expresses these stresses as a function of radial distance, r, from the center of curvature of the shell:

$$\begin{aligned} \sigma_\varphi = \sigma_\theta &= \frac{p_i \, r_i^3}{2r^3} \cdot \frac{r_o^3 + 2r^3}{r_o^3 - r_i^3} \\ \sigma_r &= -\frac{p_i r_i^3}{r^3} \cdot \frac{r_o^3 - r^3}{r_o^3 - r_i^3} \end{aligned} \tag{4-7}$$

Applying the Huddleston criteria to the calculated stresses throughout the wall thickness resulted in a factor of 1.0[illegible]6 being applied to the Mises stress calculated at the outer surface and 1.068 at the inner surface of the vessel wall. Thus, with the thick-walled stress calculations and the Huddleston criteria, there was some variation of stress through the wall. However, the variation of stress was small since the geometry of the head readily meets the thin-walled shell definition.

Now that the critical elements of the model have been defined, a general description of the calculation procedure is needed to tie all the concepts together into a calculational model. The general flow of the program follows that of the diagram in Figure 4-7. In the diagram, the subscript i indicates the current time step in the analysis, while j refers to the particular vessel wall segment at which calculations are being made. The remaining terms in the diagram have been

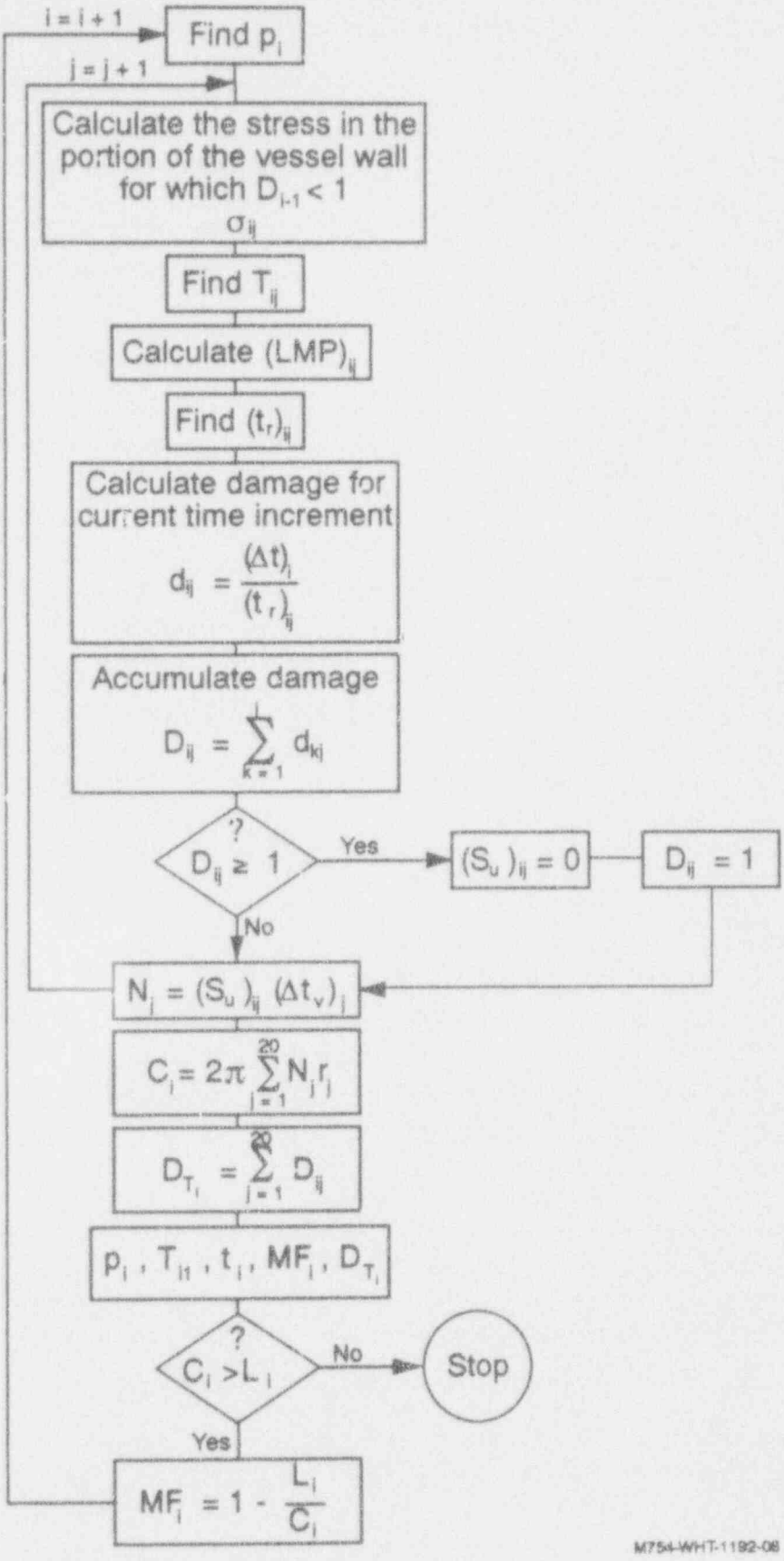

Figure 4-7. Global creep rupture model flow diagram.

discussed previously. Note that in the calculation of stresses at each time step, the vessel wall inner radius is extended radially outward to the furthest extent of total damage in the wall segments so that the stress is distributed only among the remaining wall segments. The program first calculates the damage levels in the wall segments under the current conditions in the analysis. Then, the vessel wall ultimate capacity at the current step is determined; subsequently, the margin to failure is calculated using the current pressure load. Current parameters in the analysis are printed, and, finally, the load is compared to the capacity to determine whether further time iterations are necessary or failure has occurred and the solution can stop.

4.4.3 Global Rupture Analysis Results

Results of the global rupture analyses for the nominal temperature distribution and accompanying system pressure case indicate vessel failure would have occurred 1.7 hours after the start of the major core relocation in the accident. Figure 4-8 summarizes the results for the nominal case and illustrates the phasing of vessel wall temperature, system pressure, progression of calculated vessel wall damage, and the calculated failure margin history during the accident. The inner-most wall segment temperature history is plotted in Figure 4-8(a), with the time-dependent margin to failure calculated as described in Section 4.4.2. The history of total wall segment damage is shown in Figure 4-8(b) concurrently with the operating system pressure. Significant damage began accumulating after 1.1 hours and quickly accelerated to failure after 1.5 hours. At 1.1 hours, the inner vessel wall segment experienced temperatures of 1,040 K with system pressure near 9 MPa. At 1.6 hours in this history, the system began to repressurize because the pressurizer block valve was closed. Beyond this point, the damage rate accelerated to final ultimate failure of the vessel at 1.7 hours. Time-dependent margins to failure ranged from over 80% at the beginning of core relocation to 45% at 1.5 hours and then dropped sharply to zero at 1.7 hours.

The model calculated failure to occur for the lower-bound temperature case after 2.3 hours. These results are summarized in the plots of Figure 4-9. For this scenario, the temperature rise was slower, and the vessel lasted until normal system operating pressure levels were restored and the inner wall temperature reached 1,000 K. Major wall damage began after 2.0 hours and very rapidly accelerated to failure at 2.3 hours. Failure margins again started at 80% and reduced to about 45% at the 2-hour mark and quickly dropped to zero afterwards.

Upper and lower bounds for 95% confidence on the LMP, as shown in Appendix A, Figure A-40, were used to determine the time to rupture with the current model. This resulted in variations in time to rupture of approximately 10 minutes. As discussed in Appendix A-2.3.2, a more accurate fit to Larson-Miller data was found subsequent to this analysis; however, results are not expected to change significantly because failure prediction is apparently due to the increase in system pressure while the vessel was above its transition temperature (1,000 K).

Because vessel failure did not actually occur in the TMI-2 accident, it was obvious that some aspect of the accident was not adequately reflected in the analytical models. In an effort to offer some indication of the lower bounds of vessel wall temperatures that would result in failure according to this structural model, a parameter study was subsequently performed.

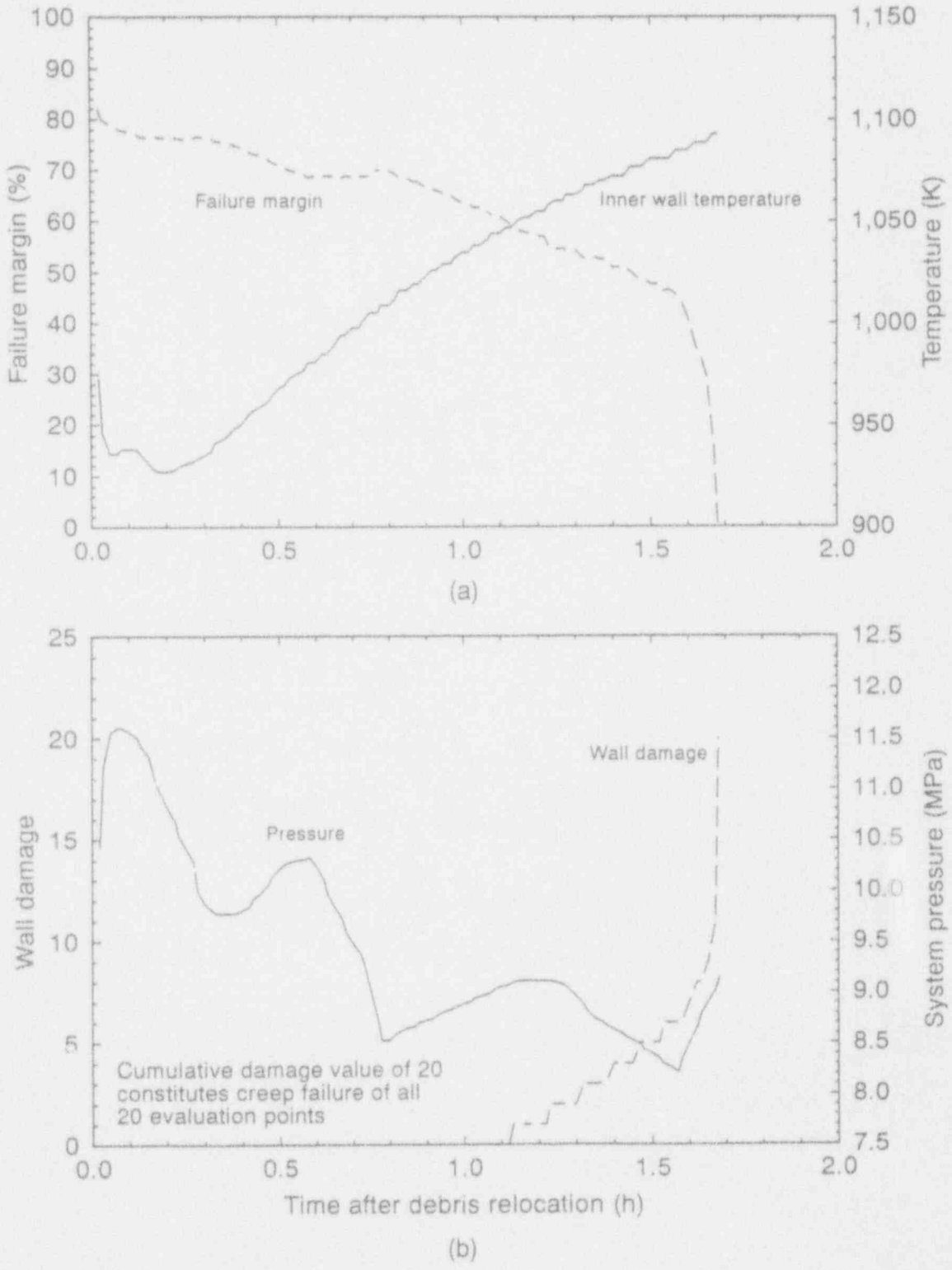

Figure 4-8. Nominal case results.

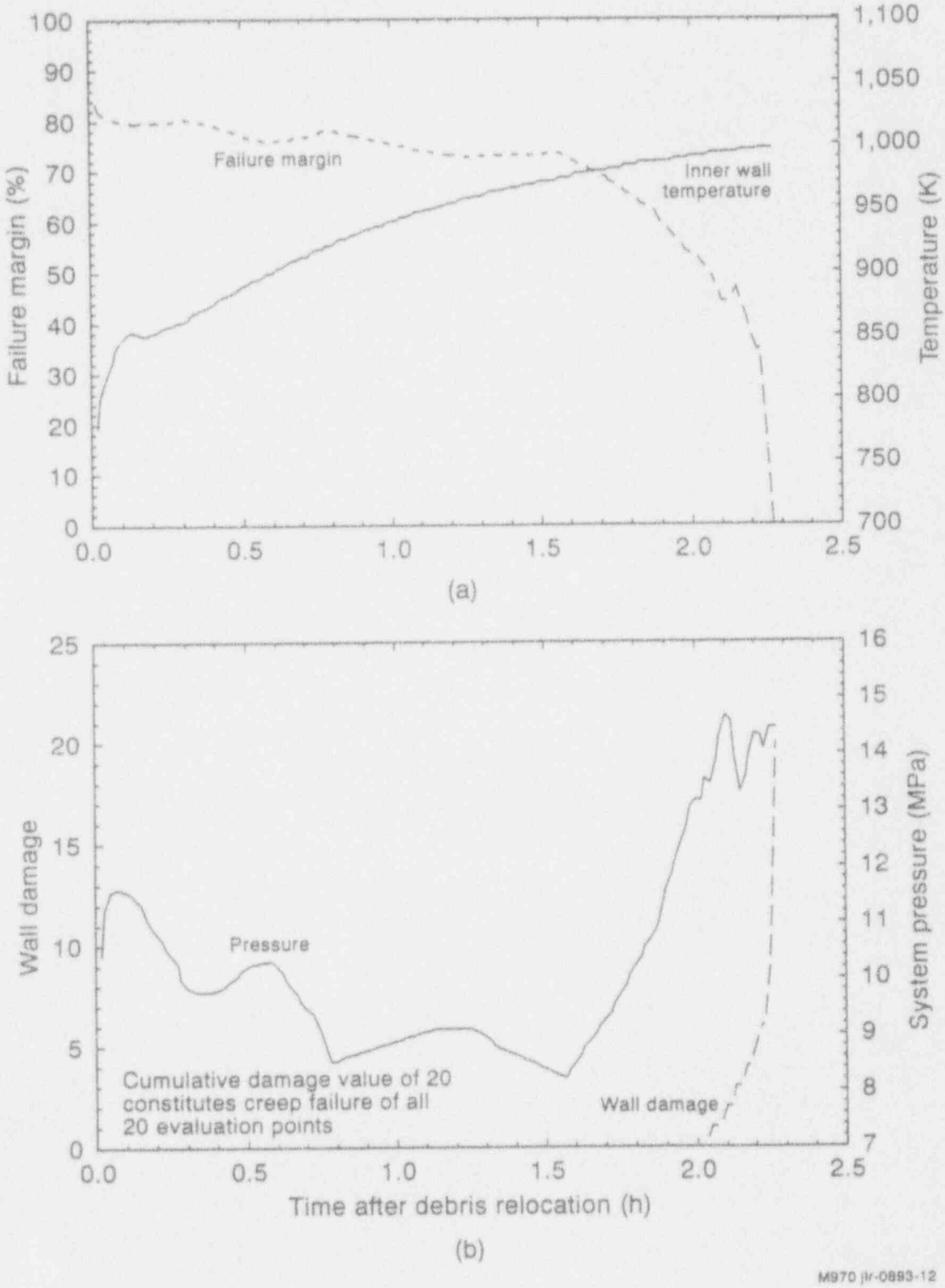

Figure 4-9. Lower bound case results.

For the parameter study, a constant internal pressure of 14.4 MPa was applied to the model concurrently with constant linear temperature distributions in the vessel wall. A number of different cases were run, and their times to failure were recorded. Figure 4-10 plots the inner and outer wall temperatures of each analysis and the resulting calculated times to vessel failure. For inner wall temperatures of 1,000 K, failure times of 1 hour or less were calculated. Inner wall temperatures of 900 K resulted in failure times between 1 and 30 hours. Finally, for inner wall temperatures of 800 K, failures occurred after 40 to 250 hours.

As shown in Figure 2-2, the vessel maintained a system pressure of approximately 14.4 MPa for nearly 3 hours. Hence, Figure 4-10 indicates that failure would be predicted if inside wall temperatures were in the 800 to 900 K range while the vessel was held at 14.4 MPa.

4.4.4 Conclusions from the Global Rupture Analysis

As discussed previously, temperature distributions used in these analyses reflect models with relatively slow cooling rates in order to correspond with companion sample examination results. These temperature scenarios result in calculations predicting vessel failure, with the nominal temperature case failing at 1.7 hours and the lower-bound case failing at 2.3 hours after core relocation. In addition, subsequent parameter studies indicate that vessel failure would occur for temperatures above the 800 to 900 K level for the time periods that the vessel was kept at 14.4 MPa. Obviously, vessel failure did not occur during the TMI-2 accident. Hence, these calculations indicate that the global vessel temperatures decreased more rapidly in the accident, probably within 1.5 to 2 hours after core relocation, which would have been before the system was repressurized to above 14.4 MPa. In addition, results suggest that a stress-based damage failure criterion may be too conservative.

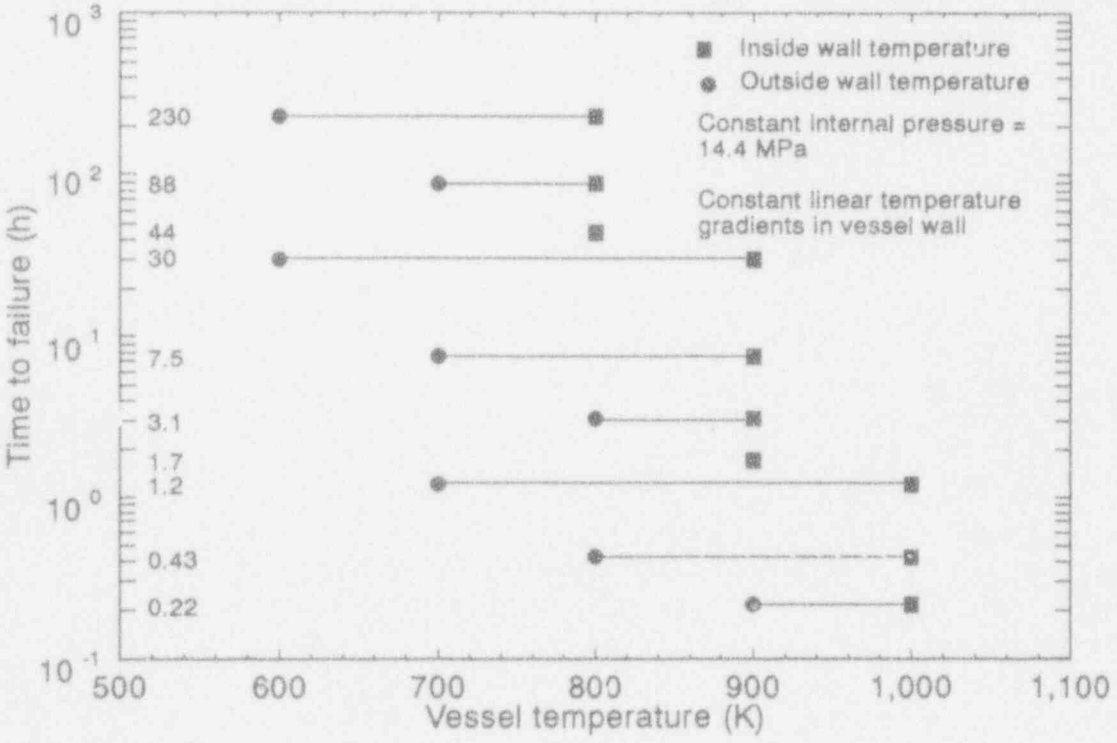

Figure 4-10. Global failure times predicted for constant pressure and temperatures. M754 gR-1192-02

4.5 Localized Vessel Failure

This section discusses the failure associated with the application of an elevated heat flux over a localized region, resulting in temperatures and temperature gradients consistent with metallurgical observations of the TMI-2 boat samples. This section addresses the analytical tools and input assumptions associated with the thermal model, the features and input assumptions of the structural model, and the results from both aspects of the analysis and the implications for the TMI-2 transient.

4.5.1 Thermal Model

The features of the interaction of the debris with the vessel have been discussed in Section 3.2. These models, while focusing on the physics of the interactions, are only one-dimensional in nature because they lack coupling between adjacent angular segments of the vessel. Because the localized effects analysis necessitates use of temperature distributions with gradients along (as well as through) the shell surface, a two-dimensional continuum axisymmetric finite element model was made of the lower head. The commercial finite element code PAFEC[21] was used to obtain the transient, two-dimensional temperature profiles. A mesh of the two-dimensional model is shown in Figure 4-11. Important points of the model that merit further discussion include the choice of mesh size in relation to both the physical problem and coupling with the structural model described in Section 4.5.2, boundary and initial conditions and time step selection, and material properties.

The mesh along the meridian is uniform and spaced in half-degree increments between the bottom of the shell and the junction with the cylindrical part of the vessel. The radial mesh is nonuniform, with the finest divisions near the inner surface where the sudden application of a heat flux requires many nodes to capture the resulting thermal spike. The PAFEC Users' manual[21] recommends that initial time steps and mesh sizes be selected so that the Fourier number at the interface,

$$Fo = \frac{\alpha_{ho}\Delta t}{\Delta x^2} \tag{4-8}$$

is on the order of unity. The thermal diffusivity of the SA533B is approximately 10^{-5} m^2/s, and the initial time step is 0.2 seconds, so Δx is selected to be approximately 10^{-3} m near the interface. Fifteen nodes are used through-thickness at each half-degree location to define 14 four-node quadrilateral temperature elements. Ten of the 15 through-thickness nodes correspond to Gauss points used in the structural analysis described in Section 4.5.2. Time steps are initially very short, 0.2 seconds, but become progressively larger as the rate of temperature change diminishes. Table 4-3 shows the time step used in various time intervals.

The transient temperature distribution is obtained with PAFEC using a 48-hour simulation period. Time-dependent heat fluxes are available from the debris/vessel thermal interaction analysis in Section 3.2 for a 6-hour period; heat fluxes on the vessel inner surface in the interval between 6 and 48 hours are obtained by defining a decay constant from the time rate of change

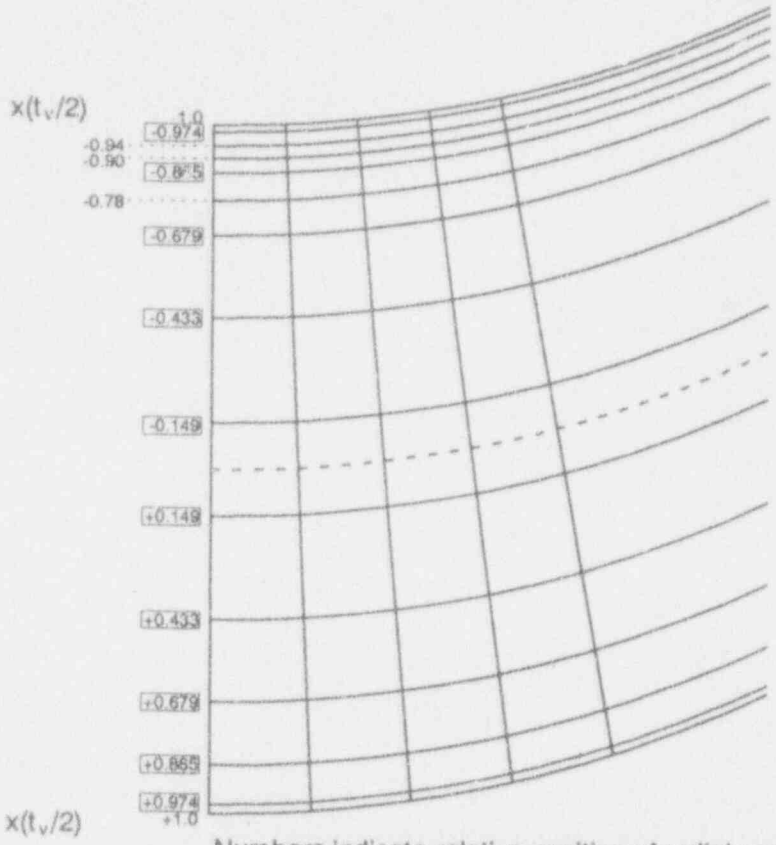

Figure 4-11. Mesh of two-dimensional continuum axisymmetric finite element model for determining time-dependent temperature distributions in the reactor vessel wall.

of the available heat fluxes in the 5-to-6-hour period and then assuming the heat fluxes decay exponentially from their values at 6 hours as:

$$q''(t > 6\ hours) = q''(t = 6\ hours)\exp[-\lambda(t-6)] \quad . \tag{4-9}$$

Using this approach, it is found that 48 hours into the simulation, the heat fluxes fall to a level resulting in a temperature distribution nearly equal to the initial temperature profile. The initial temperature distribution is assumed to vary linearly through the thickness and to have no variations along the meridian.

The initial temperature of the vessel inner surface is selected to correspond approximately to the saturation temperature of water at RCS pressure. Saturation temperature varies from 530 K to 620 K between 5 and 15 MPa. An inner surface temperature of 600 K was selected as a representative saturation temperature. The outer surface temperature is selected so that the

Table 4-3. Time step selection in thermal analysis versus time interval.

Interval (s)	Time step (s)
$0 < t < 1$	0.2
$1 < t < 10$	0.5
$10 < t < 30$	1.0
$30 < t < 60$	2.0
$60 < t < 200$	10.0
$200 < t < 1{,}000$	20.0
$1{,}000 < t < 2{,}000$	50.0
$2{,}000 < t < 5{,}000$	100.0
$5{,}000 < t < 22{,}800$	200.0
$22{,}800 < t < 72{,}800$	1,000.0
$72{,}800 < t < 172{,}800$	5,000.0

transient analysis may begin from an initial temperature distribution that is also a steady-state distribution. The outer surface temperature is selected so that the heat flux evaluated from conduction through the shell matches the heat flux evaluated from the heat transfer coefficient and the difference between the outer surface shell temperature and the ambient temperature (see Figure 4-12). The heat transfer coefficient on the outer surface is assumed to be 100 $W/m^2 \cdot K$. As discussed in Section 3.2.2.2, this value represents an upper bound that considers both radiative and convective heat transfer from the vessel. This upper bound is selected to maximize the temperature gradient through the vessel thickness. Smaller values of h produce more uniform temperatures through thickness and generally result in shorter times to failure. The ambient air temperature is assumed to be 400 K. The actual ambient air temperature would be time dependent, increasing from an initial value of approximately 300 K to the value of 400 K as the containment atmosphere is heated during the accident. Heat transfer through the outer surface would be larger if the actual ambient temperature history were modelled. Neither the ambient temperature nor the outer heat transfer coefficient is varied over the course of the simulation. The thermal conductivity of the vessel is a temperature-dependent function, varying from 50 $W/m \cdot K$ at 300 K to 30 $W/m \cdot K$ at 1,000 K. A value of 40 $W/m \cdot K$ was assumed as representative. Using this thermal conductivity, and values of heat transfer coefficient and ambient air temperature as described, the outer surface temperature of the vessel becomes 550 K. Temperatures at the junction of the shell with the cylindrical part of the vessel are fixed at the representative saturation temperature of 600 K over the entire transient. Boundary conditions on the inner surface take the form of either applied heat fluxes from the lumped capacitance debris/vessel thermal analysis described in Section 3.2 or a heat transfer coefficient between the vessel inner surface and the water pool consistent with nucleate boiling.

Section 3.2.2.3 describes variations in applied heat flux over the inner surface with maximum heat fluxes away from the bottom of the pool. These maximum values arise from natural convection currents that develop in the molten material. The duration and magnitude depend strongly on the depth of the molten pool. If the pool is quite deep, the temperature near the junction of the pool with the colder part of the vessel may be tens of degrees Kelvin higher than

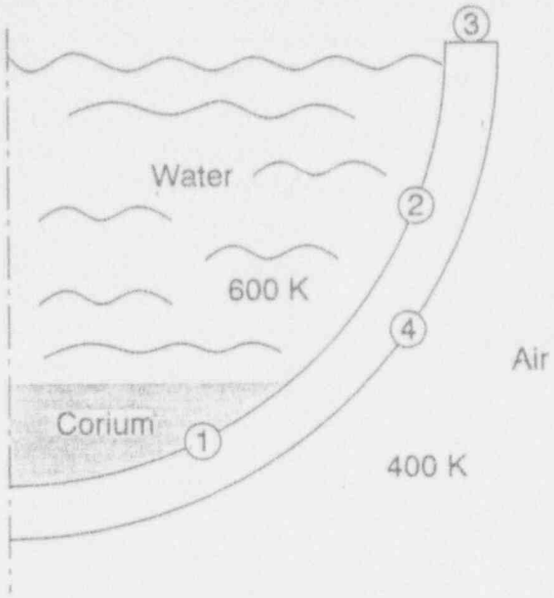

① Shell inner surface, adjacent to molten mass; time-dependent heat fluxes applied from corium/vessel thermal interaction analysis

② Shell inner surface adjacent to water; heat transfer coefficient representative of nucleate boiling

③ Nodes at junction with cylindrical pressure vessel; temperature fixed at 600 K

④ Shell outer surface, heat transfer coefficient to ambient air at 400 K

M939-WHT-893-31

Figure 4-12. Two-dimensional thermal analysis boundary conditions.

the temperature at the vessel bottom. This temperature gradient may persist throughout the entire transient. If the pool is of moderate depth, the temperature gradient may be less dramatic and exist only through the early part of the transient. If the pool is shallow, the peak temperature will exist at the bottom of the shell. In the latter two cases, there is sufficient heat transfer from the vessel wall just underneath the molten pool region to the cooler part of the vessel wall (through a fin effect) to prevent establishing a peak temperature in the highest heat flux region. Because the existence of peak temperatures away from the vessel bottom requires deep pools, and the magnitude of these peak temperatures is at most tens of degrees Kelvin hotter than temperatures at the shell bottom, and because the focus of the localized failure analysis is on hot spots several hundred degrees Kelvin hotter than a background temperature distribution, it was not deemed necessary to include spatial variations in the background heat flux. As discussed in Section 3.2.2.3, a uniform spatial heat flux is used to obtain a background temperature distribution (nominal and lower-bound case heat fluxes are plotted in Figures 3-14b

and 3-15b, respectively). A higher uniform heat flux is used in the hot spot region, so that the heat flux distribution consists of a step change between two uniform distributions.

At higher elevations on the inner surface, a heat transfer coefficient of 3×10^5 W/m^2 K is assumed to exist between the vessel inner surface and 600 K water. The coefficient is large enough to effectively fix the vessel inner surface temperature at 600 K, so that the vessel remains very stiff outside the region of applied heat fluxes. Although PAFEC has nonlinear material capability, the rapid changes in the SA533B heat capacity with temperature through the phase transition made it difficult to run the problem to completion using this nonlinear capability. In particular, it was not possible to converge in the first few time steps, where the thermal load results in material straddling the phase transition within the first few millimeters of the inner surface. Accordingly, analyses were performed with constant, but representative, values of material properties: the density was taken as 7,800 kg/m^3, the heat capacity as 700 J/kg K, and the thermal conductivity as 40 W/m K.

4.5.2 Structural Model

The structural model is a variation of a finite deformation shell theory described in Reference 22. Details of the adopted form of the method are described in Reference 13, and calculations performed to verify the model are described in Appendix E. The shell theory allows or thermal, plastic, and creep strains but is not as general as an axisymmetric continuum model in that (a) the radial stress is taken as zero, whereas the radial stress in the actual problem varies from a compressive value having a magnitude equal to the pressure on the shell inner surface and falling to zero on the shell outer surface, (b) the shear strain is assumed to have a parabolic variation through thickness, and (c) total (elastic + plastic + thermal + creep) normal strains are assumed to vary linearly through thickness. The degrees of freedom in the shell theory are defined at the shell middle surface and consist of meridian hoop strain equal to the radial displacement divided by the radial distance to the point of interest, u/r, a rotation of the shell relative to its original configuration, β, and a material shear, γ, describing rotation of material relative to the normal to the deformed middle surface. The advantages of the shell theory relative to a finite element continuum model are: (a) the algorithm provides a natural way of nesting nodes in the vicinity of the hot spot while minimizing the total number of degrees of freedom; and (b) the band width of the matrix is narrow (11 elements), permitting rapid solution ($<<$ 1 workstation CPU - second per iteration) of the linearized system of equations. This latter point is not trivial as simulations of TMI-2-like transients, from capturing the response to the thermal load through the asymptotic cooling of the vessel, require thousands of time steps (load increments) with five to ten iterations/increment. It is therefore not unusual for tens of thousands of solutions to a linearized system of equations to be required in a single simulation. Aspects of the model that merit further discussion here include time step selection and coupling of TMI-2 conditions to the structural model; means of evaluating thermal, plastic and creep components of strain; and methods of evaluating damage and clipping ligaments.

Time step selection is driven principally by the severity of stress and temperature distributions in the shell. Associated with each node on the middle surface, where degrees of freedom are defined, are ten Gauss points distributed through-thickness, the most extreme of which are $\pm$ 0.974 $\times$ half-thickness away from the middle surface. Stresses and strains are defined at each of these points and determine the evolution of the shell deformation. At every Gauss

point, time steps are evaluated that advance the creep strain a fixed increment, say $\Delta\varepsilon_{cr} = 0.0001$, based on the local temperature and stress. The creep time step (Δt_{creep}) selected is the minimum of this set of time steps. Since some of the nodes in the thermal model are defined at through-thickness locations corresponding to these ten Gauss points, only a linear interpolation along the meridian is required to determine the temperature at a particular Gauss point from the thermal model. In the TMI-2 transient, both the pressure and temperature histories are taken as piecewise linear functions of time, the temperature history is taken from the finite element analysis, and the pressure history is taken from the trace shown in Figure 2-2. At any time during the transient, there will be three characteristic time steps:

Δt_{creep} = time step selected on basis of creep strain rates

Δt_{press} = time step to next time at which a pressure state is defined

Δt_{temp} = time step to next time at which a temperature distribution is defined.

The time step selected is the minimum of these three values.

Thermal, plastic, and creep components of strain are evaluated from the properties of the SA533B steel (Appendix A-2.2). The mean thermal coefficient is plotted in Appendix A, Figure A-38. At each time step, the thermal strain is updated by integrating the thermal expansion coefficient over the updated temperature history. The resulting expansion and contraction of the vessel are responsible for many of the features of the observed stress states.

Plastic strains develop whenever the equivalent stress at a point exceeds the yield strength for that temperature. The yield strength is plotted as a function of temperature in Appendix A, Figure A-35, and can be seen to drop rapidly as the steel moves through its transition temperature above 1,000 K. At temperatures between those for which values are provided, the yield strength is obtained by linear interpolation. Values of Young's modulus are similarly plotted in Figure A-34 of Appendix A and are obtained at each point by linearly interpolating between given values. Although specific values of stress versus plastic strain are available, the behavior of the steel, particularly at elevated temperatures, is close to elastic/perfectly plastic. For this reason, the stress/strain relations above yield are obtained from a power law hardening relation

$$\frac{\bar{\sigma}}{S_y(T)} = \left(\frac{\bar{\varepsilon}}{\varepsilon_y(T)}\right)^{1/n} \tag{4-10}$$

where

$\bar{\sigma}$ = effective stress

$\bar{\varepsilon}$ = effective strain (less thermal and creep components)

$S_y(T)$ = yield stresses

$\varepsilon_y(T)$ = yield strains

An exponent of $n = 10$ is used for the SA533B steel. Whereas the creep strains are evaluated from the stress and temperature states and drive the vessel deformation, the plastic strains are calculated as a reaction to the deformation. The plastic strains are calculated in the following manner:

1. New total strains are evaluated from the creep strain increment.

2. A trial stress state is evaluated at each point by adding an elastic stress increment to the previous stress state.

3. If the new resultant stress state is below the yield stress, the stress increment is elastic and there is no additional plastic strain. If the new resultant exceeds yield, the individual stress components are scaled down by the ratio of yield stress/trial resultant, new elastic strain components are evaluated from the revised stress state, and plastic strain increments are evaluated as the difference between total and the sum of thermal, elastic, and creep strains.

The principal driving force of vessel deformation is creep under stress and temperature. Creep strains for low (≤922 K) and high (≥1,000 K) temperature are evaluated slightly differently. At low temperature, creep strain rates are evaluated on the basis of an algorithm suggested by Reddy and Ayres,[23] based on their experimental lower temperature (<922 K) data. The high temperature (and alternative low temperature) relations are provided from the NRC-sponsored lower head failure program[13] and have been fit to a power law form. Power law constants were fit from primary and secondary creep data only; tertiary creep was omitted to simplify the analysis. Because tertiary creep was not modeled, the strains at the predicted failure time are artificially low. However, it should be noted that the failure criterion used in this analysis is stress-based and independent of strain. The assumption here is that the difference in stress distribution caused by tertiary behavior does not significantly affect the predicted time to failure. Structural property data for SA533B vessel steel are given in Appendix A-2.2.

The TMI-2 Structural Mechanics Peer Review Group[1] agreed to define failure by a cumulative time damage rule used in conjunction with the stress-based LMP. Details of the procedure are outlined in Appendix A-2.3. An average damage is obtained by a simple uniformly-weighted average of all damages at the individual Gauss points in the vessel. The rate of change of this average damage plays an important role in defining the margin to failure.

When the damage at a Gauss point exceeds 1, the yield locus at that point is shrunk to zero, removing the load-carrying capacity at that point and forcing redistribution of load to the remaining intact points. This is referred to as ligament-clipping in the discussion of the results below. Because the creep strain rates are driven by stress and temperature, creep strain increments evaluated as described previously will also go to zero at the clipped ligaments, which has the inadvertent effect of restraining material flow at points that have been clipped. To avoid

this unphysical restraint, creep strain increments at fully damaged points are set by the most adjacent intact points. The purpose of ligament-clipping is to model accelerated failure as portions of the structure become fully damaged. Failure is defined to have occurred when all through-thickness ligaments have been clipped at a particular node.

The effective stress used in the LMP is a measure suggested by Huddleston[4-2] which has been shown to correspond more closely than the Mises or Tresca theories to experimental data for biaxial creep tests of steel (see Appendix A-2.3). The significant aspect of this stress measure is that damage in compressive states does not accumulate as rapidly as in the tensile stress states. This feature is apparent in the damage accumulation rates of some of the simulations discussed below.

4.5.3 Results of Thermal and Structural Response

In order to understand the relative roles of the background and hot spot temperature distribution, three cases were considered: (a) the effect of the lower-bound global temperature distribution, without the hot spot, (b) the effect of the hot spot temperatures imposed on a shell with cool background temperatures (600 K inner surface, 550 K outer surface), and (c) the effect of the hot spot temperatures imposed on top of the lower-bound background temperature.

The lower-bound temperature distribution corresponds to case 15 in Table 3-4. Contour plots of the temperature fields at 1,000 seconds, 1 hour, and 2 hours are shown in Figures 4-13(a), (b), and (c). At 2 hours, the inner surface temperatures approach the peak value of 1,020 K cited in Table 3-4. As an aside, excellent agreement is obtained between the finite element analysis and the simpler energy balance of the debris/vessel interaction with respect to peak inner surface temperature when the heat fluxes are applied to a large segment of the lower head, i.e., when the behavior at the bottom of the shell is essentially one-dimensional.

The structural response to this lower-bound background is illustrated in Figures 4-14 and 4-15, which shows the evolution of shell deformation and the ligaments clipped as the transient proceeds, and in Figure 4-16, which illustrates damage rate and accumulated damage as a function of time. In Figure 4-14, the vessel is shown at six times during the transient, the dashed lines represent the vessel shape before load application, and the solid lines represent the shape of the deformed shell. An "x" is plotted at each Gauss point where damage has reached 100%. It is interesting to note that the most heavily damaged states are not at the bottom of the shell, but about midway between the bottom and the edge of the molten mass. A comparison of meridian and hoop stresses at the bottom of the shell (node 1) and at the most heavily damaged region (node 120) at 1.44 hours is shown in Table 4-4. Given the heat fluxes characterizing the lower-bound condition, Figures 4-13(b) and (c) illustrate that a 150–200 K temperature gradient exists through thickness, placing the outer surface temperatures in the 800–850 K range between 1 and 2 hours into the transient. Once the material passes through its transition temperature, it is incapable of supporting normal stresses above tens of MPa. This forces the cooler material on the outer surface to support the majority of the tensile stress required to react the applied loads, and damage tends to accumulate most rapidly at the outer surface. Figure 4-14 indicates that the first ligaments to reach 100% damage occur on the shell's outer surface, and that damage rapidly propagates from the outside to the interior. As will be seen later, it is not always the case that maximum damage rates occur on the outer ligaments; instead, maximum damage occurs wherever

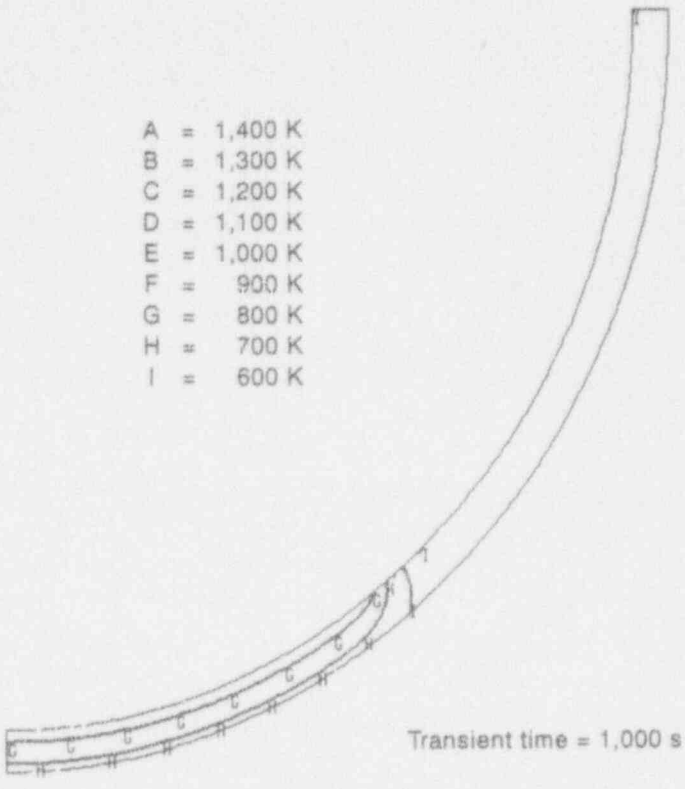

(a) 1,000 seconds after debris relocation

M970 jlr-0893-01

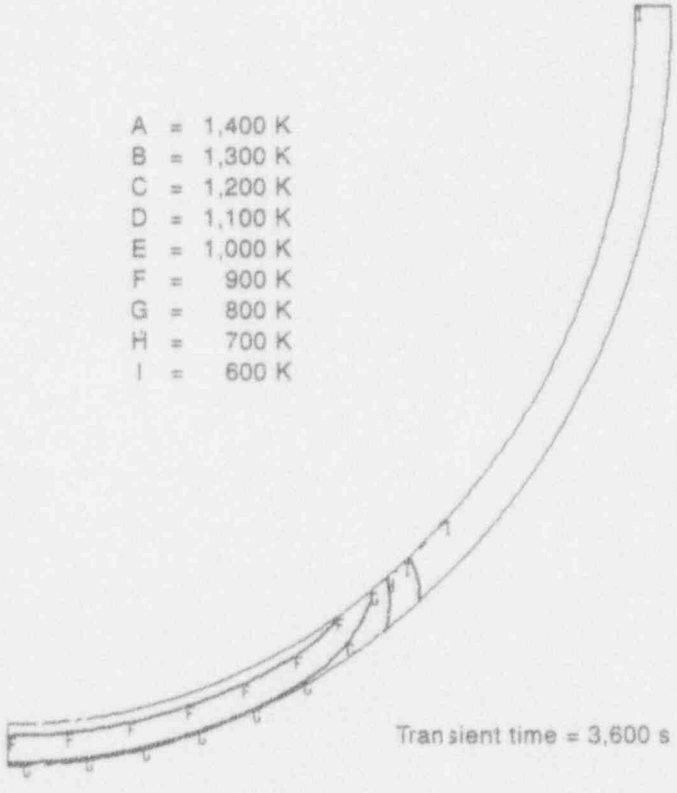

(b) 1 hour after debris relocation

M970 jlr-0893-02

Figure 4-13. Temperature distribution associated with lower bound background heat fluxes.

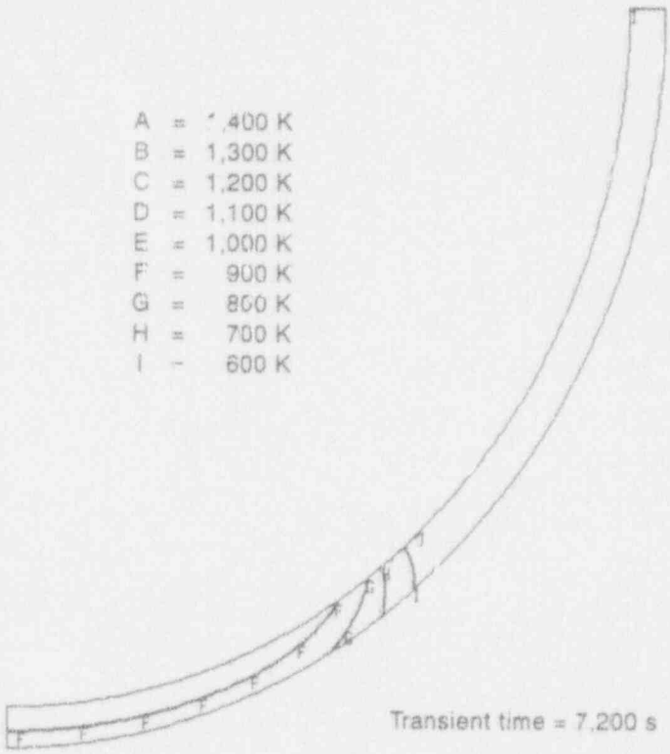

(c) 2 hours after debris relocation

M970 jlr-0893-03

(c) 2 hours after debris relocation

Figure 4-13. (continued).

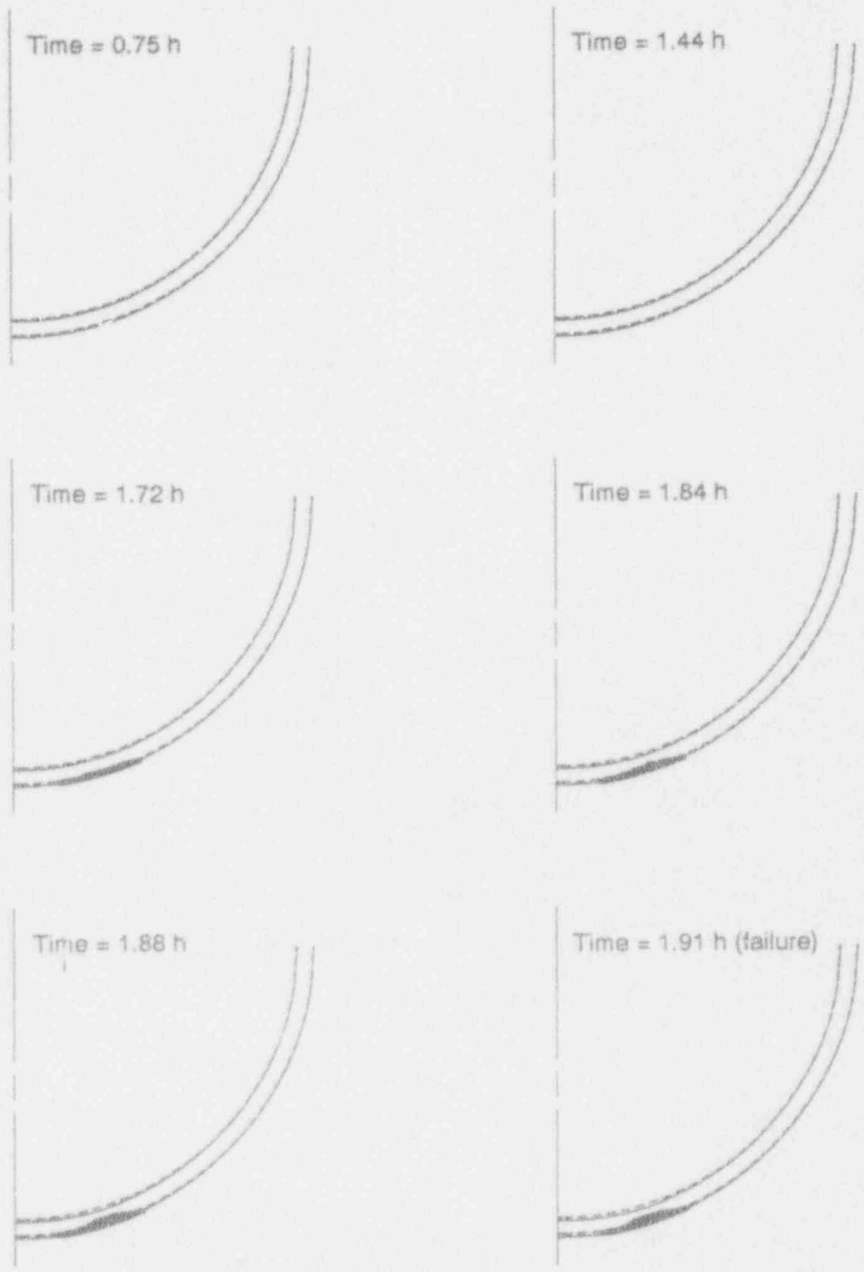

Figure 4-14. Distributions of 100% damaged ligaments at various times after debris relocation in the lower bound background temperature problem.

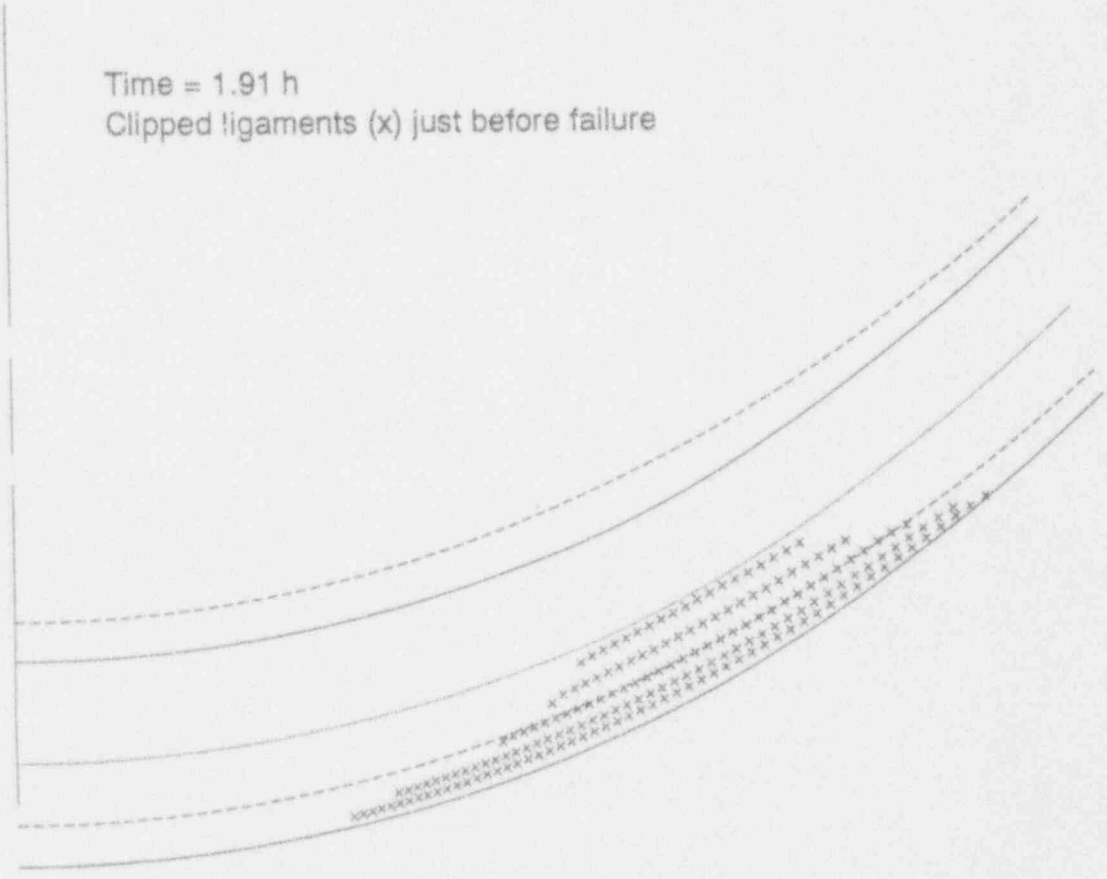

Figure 4-15. Distribution of 100% damaged ligaments just prior to failure (1.91 hours after debris relocation) in the lower bound background temperature problem. Note: displacements shown may be low due to omission of tertiary creep.

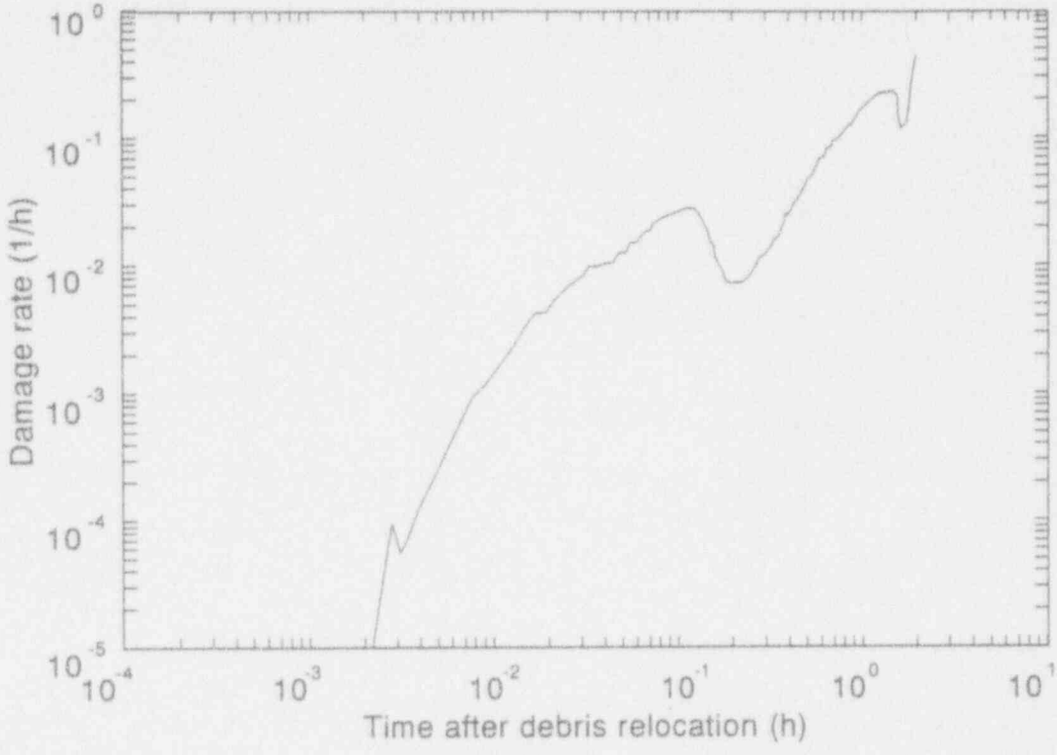

M919 jli-0793-03

(a) Damage rate versus time

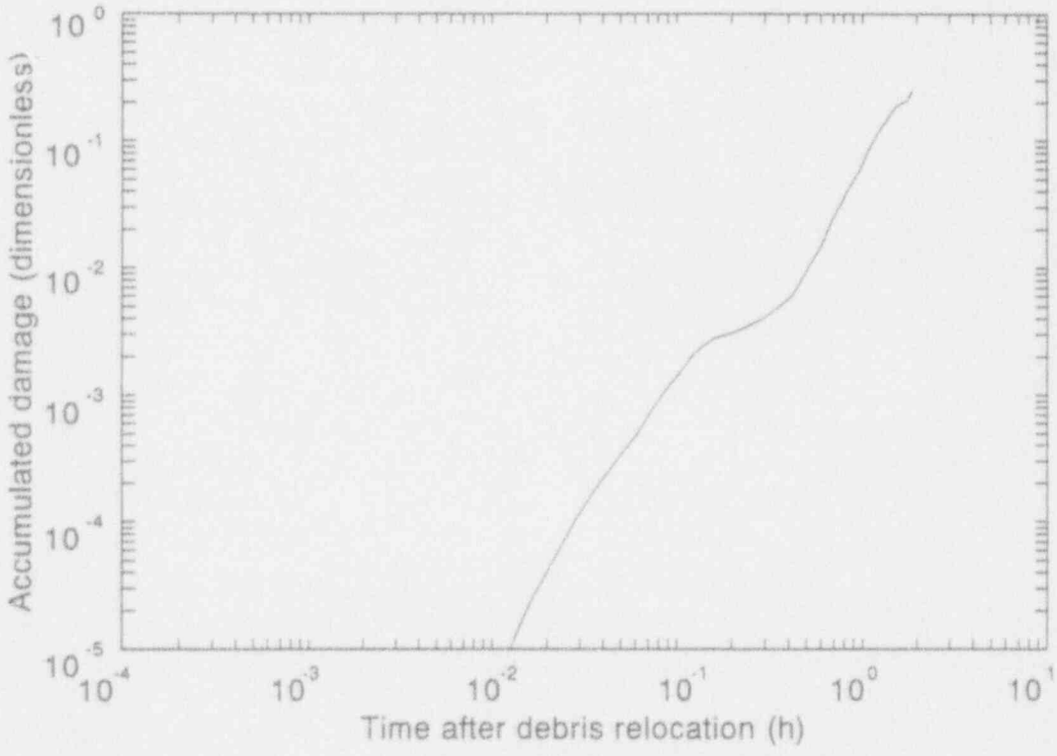

M919 jli-0793-04

(b) Accumulated damage versus time

Figure 4-16. Lower bound background temperature problem results.

Table 4-4. Comparison of stress status at shell bottom (node 1) and most heavily damaged region (node 120) at 1.44 hours into lower-bound transient.

node 1

Position	σ_φ (MPa)	σ_θ (MPa)	Temperature (K)	Damage
-0.974	4.40	4.40	972	0.020
-0.865	5.04	5.04	962	0.010
-0.679	-1.28	-1.28	946	0.0016
-0.433	-8.57	-8.57	924	4.0E-6
-0.149	51.2	51.2	901	0.0012
+0.149	93.6	93.6	877	0.046
+0.433	138.0	138.0	856	0.166
+0.679	181.3	181.3	839	0.423
+0.865	215.5	215.5	826	0.660
+0.974	240.3	240.3	818	0.668

node 120

Position	σ_φ (MPa)	σ_θ (MPa)	Temperature (K)	Damage
0.974	-6.14	-6.61	970	0.027
-0.865	-7.02	-7.57	960	0.018
-0.679	10.9	-11.7	944	0.0063
-0.433	-59.0	-60.8	922	0.0020
-0.149	-26.6	-52.1	899	2.6E-5
+0.149	79.1	41.9	876	0.015
+0.433	147.4	99.7	854	0.194
+0.679	217.8	154.4	837	0.732
+0.865	273.7	193.0	824	0.866
+0.974	282.2	197.2	817	0.803

the highest tensile stresses are sustained, and this can occur on the inner surface of the shell following cooldown from elevated temperatures.

The additional stress of node 120 relative to node 1 arises because there is a degree of restraint at the bottom of the shell due to symmetry (no rotation) and at the junction with the cool material (large, but finite, resistance to rotation and displacement). The material at node 120 experiences the greatest displacement from its original position and the maximum component of bending stress, while experiencing nearly the same temperature as the material at node 1.

Under these conditions, the highest damage rates are in this middle region and the first ligaments clipped are located there. Clipping ligaments forces redistribution of load and places remaining intact Gauss points under more severe stress. Only about 15 minutes elapsed between the first point to be clipped and the state shown in the lower right hand corner of Figure 4-14, where failure is imminent. An expanded view of this state is shown in Figure 4-15, and the hoop and meridian stresses and damage states of the intact points at node 120 are shown in Table 4-5. The simulation is only able to run another few increments at time steps $<10^{-4}$ hours before it is unable to converge on a solution, and so this state has been taken as the point of failure. Finally, the damage rate and accumulated damage are shown in Figure 4-16 (a) and (b). With the exception of a couple of small depressions, the damage rate is a monotonically increasing function of time. The sharp rise in damage rate at 1.6 hours is associated with the beginning of repressurization from 8.3 MPa to 13–14 MPa.

After predicting failure in 2 hours for a background distribution based on lower-bound input assumptions, the effect of a hot spot was evaluated for a shell with a benign background temperature to confirm that the hot spot temperatures alone would not result in a localized failure. Since metallographic examinations of vessel specimens outside the hot spot only indicate that they did not reach the ferritic-to-austenitic transition temperature (approximately 1,000 K), global vessel temperatures could have been considerably lower than this transition temperature. (Note that peak values predicted in the lower-bound temperature distribution were approximately equal to the transition temperature.) To bound possible temperatures in this cooler case, the initial temperature distribution from the lower-bound case was used; that is, a linear distribution of temperature through the thickness with a 600-K inner surface temperature and a 550-K outer surface temperature. Elevated heat fluxes were applied to a 10-degree sector of the lower head measured from the vertical; this corresponds to a hot spot diameter of 0.76 m. On the basis of metallurgical observations of TMI-2 boat samples, it is known that some inner surface material in the hot spot region reached temperatures in excess of 1,320 K but lower than 1,370 K for a period of about half an hour. Selecting heat fluxes that produce these results over the small region of the hot spot is not trivial, because the hot spot radius is now of comparable size to the vessel thickness and hence the problem is two-dimensional in nature. To obtain hot spot temperatures, heat fluxes with sufficient magnitude to induce temperatures of 1,400 K in the one-dimensional model, such as Case 11 in Table 3-4, produced lower temperatures in the two-dimensional model. As discussed previously, a slightly higher heat transfer coefficient was imposed upon the finite element simulation in order to obtain the desired initial temperatures. The fin effect provides an additional heat sink from the hotter to the cooler parts of the vessel. The combined effect from these two factors requires substantially higher heat fluxes to produce the same temperature. Because heat fluxes in the hot spot region are applied uniformly over a given area, temperatures on the inner surface in the hot spot region vary from a maximum value at the bottom of the shell to much lower values near the edge of the applied heat flux. Inspection of the TMI-2 boat samples indicated that the most severe material conditions corresponded to temperatures in excess of 1,320 K for a period no greater than 30 minutes to 1 hour. Table 4-6 lists the position of each node on the inner surface measured from the bottom of the shell, its peak temperature during the transient and when, if applicable, that temperature rises and falls above/below 1,320 K. It can be seen from this table that the inner surface node labeled 61 corresponds approximately to the conditions observed in the TMI-2 boat samples.

Table 4-5. Stress states in most heavily damaged region (node 120) at 1.91 hours into lower-bound transient.

Position	σ_ϕ (MPa)	σ_θ (MPa)	Temperature (K)	Damage
-0.974	112.2	54.5	989	0.060
-0.865	116.9	60.4	980	0.045
-0.679	160.0	96.0	964	0.058
-0.433	163.4	107.9	943	0.075
0.149	216.0	156.9	920	0.526
+0.149	—	—	896	1+
+0.433	—	—	875	1+
+0.679	—	—	857	1+
+0.865	—	—	843	1+
+0.974	—	—	836	1+

Table 4-6. Peak temperatures of inner surface nodes in high heat flux region.

Node	Angle w/vertical	r (cm)	T_{peak} (K)	Δt >1320 K (hours)
1	0	0	1342	1.70
16	0.5	1.92	1340	1.64
31	1.0	3.84	1337	1.50
46	1.5	5.76	1331	1.28
61	2.0	7.68	1324	0.75
76	2.5	9.60	1314	NA
91	3.0	11.5	1302	NA
106	3.5	13.4	1287	NA
121	4.0	15.4	1270	NA
136	4.5	17.4	1251	NA
151	5.0	19.2	1228	NA
166	5.5	21.1	1203	NA
181	6.0	23.0	1175	NA
196	6.5	24.9	1142	NA
211	7.0	26.8	1106	NA
226	7.5	28.7	1065	NA
241	8.0	30.6	1019	NA
256	8.5	32.5	964	NA
271	9.0	34.4	895	NA
286	9.5	36.3	818	NA
301	10.0	38.2	603	NA

Material closer to the shell bottom is above 1,320 K for a longer period of time. Conditions used to achieve this transient are therefore consistent with the TMI-2 VIP metallurgical observations.

The finite element simulation is run over a 48-hour period, even though the heat fluxes from the debris/vessel interaction analysis are only applied over 6 hours. The heat fluxes after 6 hours were assumed to decay exponentially with a characteristic time constant computed from the behavior in the 5-to-6-hour period; after about 48 hours, these heat fluxes reach the values consistent with the 50 K through-thickness gradient of the initial temperature distribution, and the structure has nearly returned to its initial state. At times beyond 48 hours, the vessel is held at the 48-hour state. Contour plots of temperatures in the hot spot region are shown in Figure 4-17 for the following times: (a) 1,000 seconds, (b) 1 hour, (c) 2 hours, (d) 3 hours, (e) 6 hours, (f) 12 hours and (g) 24 hours. The structural response to these conditions was run to 1,000 hours, and the vessel survived. One of the most enlightening aspects of the response is shown in Figure 4-18 (a) and (b), which shows both damage rate and accumulated damage versus time. There are four distinct peaks in the damage rate. The first, between 3 and 30 seconds, is associated with the thermal load; the nodes on the inner surface experience a relatively severe damage rate as they reach temperatures in excess of 1,300 K and yield in compression as they expand against the cooler shell. This severe damage rate is diminished as the temperature front moves into the interior of the vessel.

The second damage rate peak occurs just over 1,000 seconds into the transient and corresponds to the largest rate (0.1 $hour^{-1}$) at any time during the transient. This state occurs when the temperature front has elevated the outer surface temperatures to levels of 800 to 850 K; the outer surface material is supporting large tensile stress (~250 MPa) and at this temperature experiences both a high damage rate and creep rate. This damage rate is dissipated when the temperature front completely penetrates the shell, pushing the outer surface temperature above 1,000 K, reducing the temperature gradient and associated stresses.

At 1.6 hours after debris relocates onto the lower head, the system is repressurized, and the damage rate experiences a third peak, although of substantially lesser size than the transient heatup peak. The fluctuations in the repressurization peak mirror the fluctuations in the TMI-2 pressure history associated with relief valve opening and reseating. Although the pressure history for the transient indicates that these fluctuations continued until 260 minutes after relocation, the pressure history for these calculations assumed a constant pressure for time periods greater than 180 minutes after relocation and the fluctuations disappear from the damage rate plot after this time.[b] Repressurization to 14.5 MPa at 2.1 hours also corresponds to the attainment of maximum temperatures in the shell, so the damage rate decreases shortly after repressurization as the shell cools.

---

b. Although failure time predictions would vary if the actual TMI-2 pressure history were used, it is not felt that these variations would be significant since the RCS was repressurized to values over 15 MPa at 11 hours after relocation and failure calculations were performed for up to 1,000 hours after relocation.

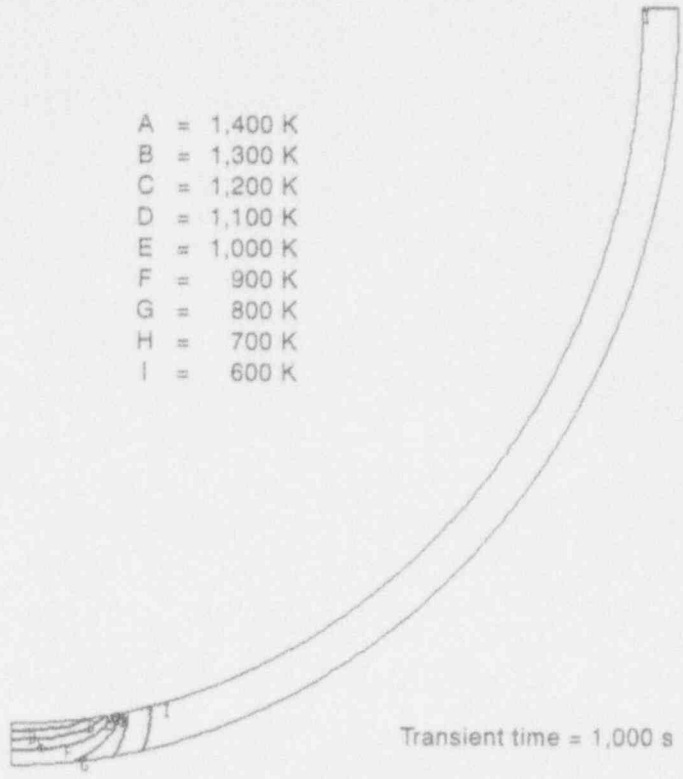

(a) 1,000 seconds after debris relocation

M970 jlr-0893-04

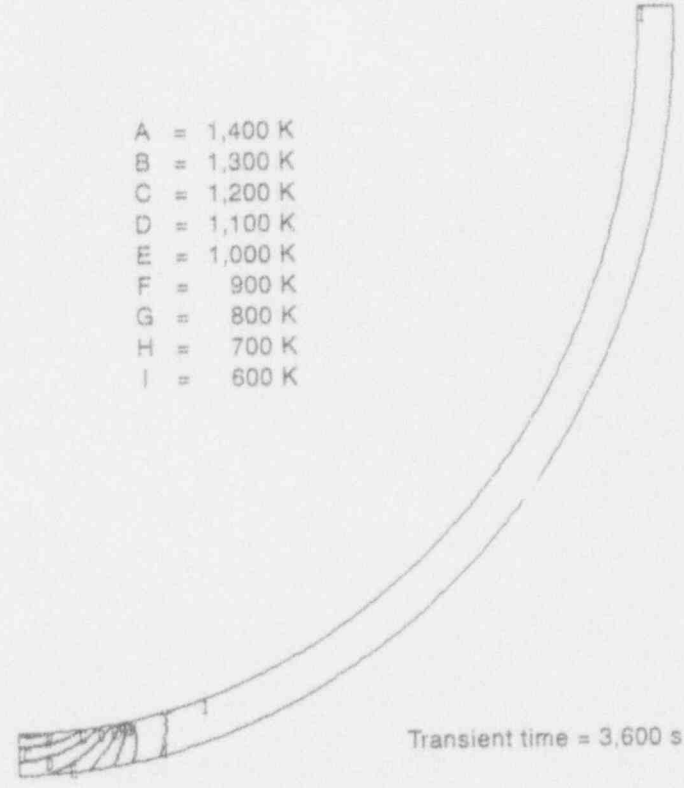

(b) 1 hour after debris relocation

Figure 4-17. Temperature distribution associated with hot spot on cool (600 K) background.

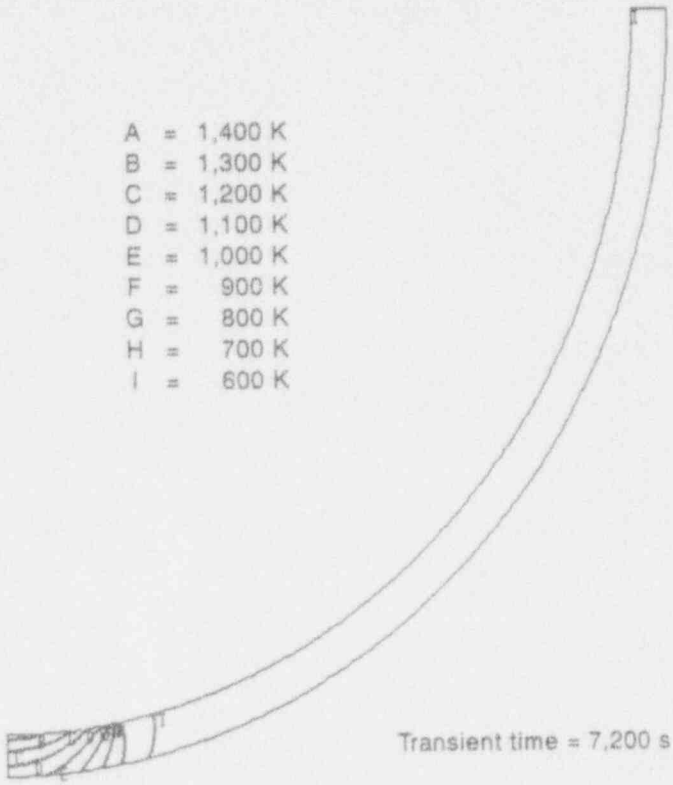

(c) 2 hours after debris relocation

M970 jr-0893-06

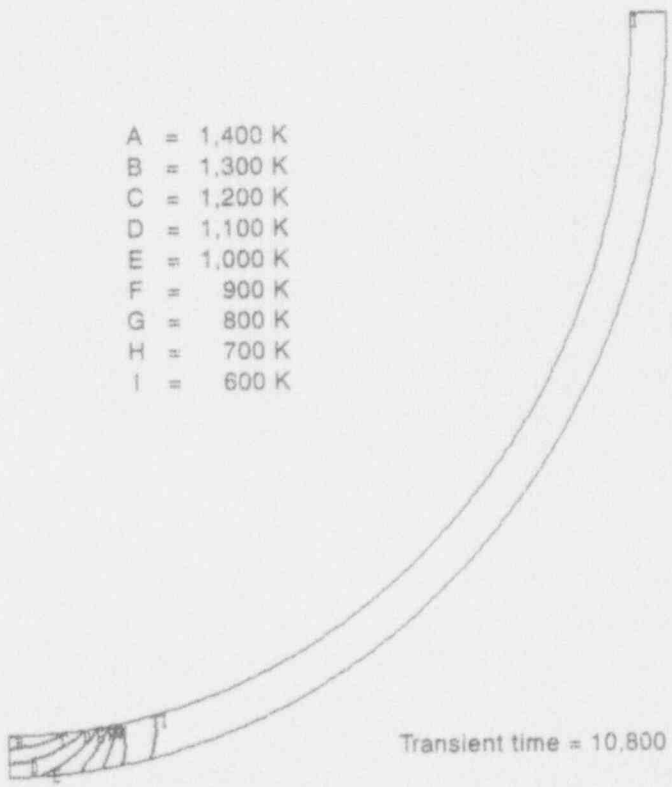

(d) 3 hours after debris relocation

M970 jr-0893-07

Figure 4-17. (continued).

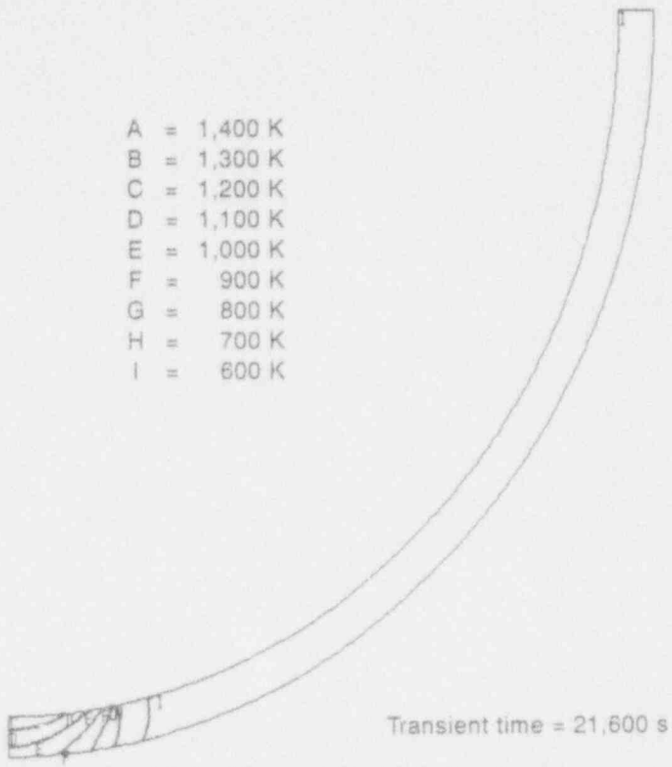

(e) 6 hours after debris relocation

M970 IV-0893-08

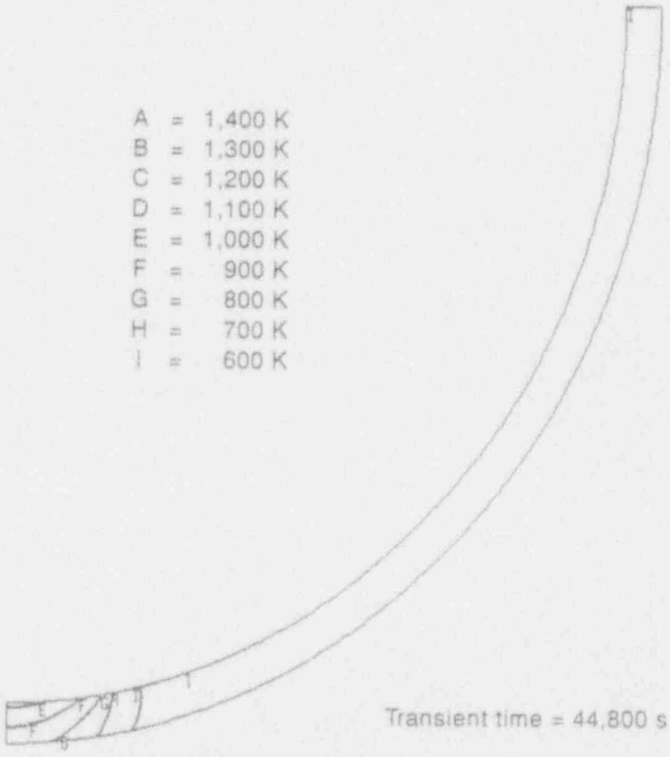

(f) 12 hours after debris relocation

M970 IV-0893-09

Figure 4-17. (continued).

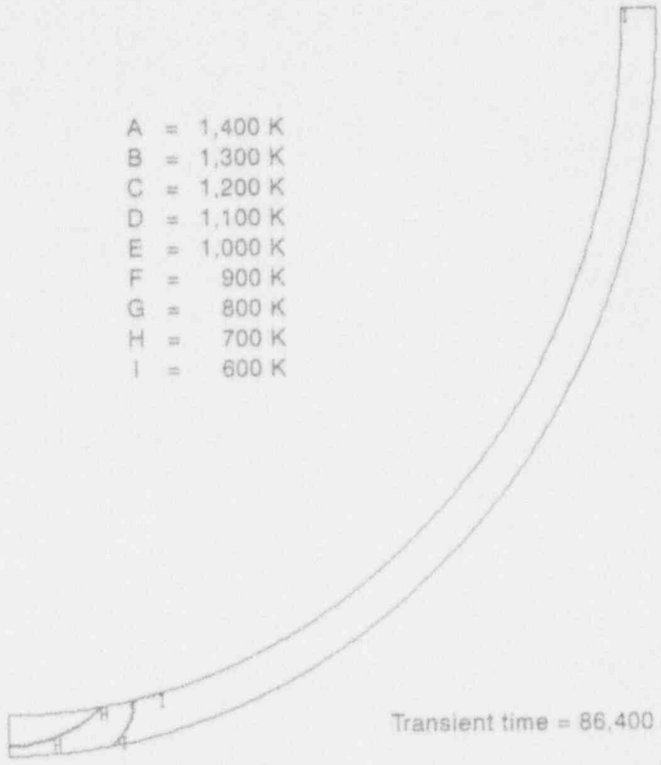

(g) 24 hours after debris relocation

M970 jlr-0893-10

Figure 4-17. (continued).

The final and most interesting damage rate peak occurs about 24 hours after the transient and is associated with cooldown. During the heatup and high temperature periods, material near the inner surface of the shell at the shell bottom experiences compressive stress and undergoes negative creep strain under compressive load. Initially high compressive stresses relax to the modest values shown in the top third of Table 4-7 which lists the stress distribution at the shell bottom 2.7 hours into the transient. As the shell cools, this material then contracts and experiences tension; the second third of Table 4-7 shows the stress distribution at the shell bottom 12.1 hours into the transient. As this material drops another few hundred degrees Kelvin during the cooldown period, tensile stresses on the bottom inner surface reach the +100 MPa range, causing rapid damage accumulation and the damage rate peak, shown in Figure 4-18 (a) and (b), at 24 hours. Only a few ligaments fail during the heatup and maximum temperature period. Interestingly, unlike the first case (global temperature distribution without a hot spot) where outside ligaments fail first, here, the first ligaments to fail are on the inside surface, where analysis shows that a cusp would begin to form due to bulging of the hot spot. In both cases, high tensile stresses drive the failures. During the cooldown period, for this case, a substantial number of ligaments fail, producing the stress distribution at 640 hours shown in the final third of Table 4-7. The clipped ligament distribution for this case at 1,000 hours is shown in Figure 4-19. It should be emphasized that the asymptotic condition used in the thermal analysis was implemented to make a smooth transition from the high heat fluxes back to the initial state, and that physical

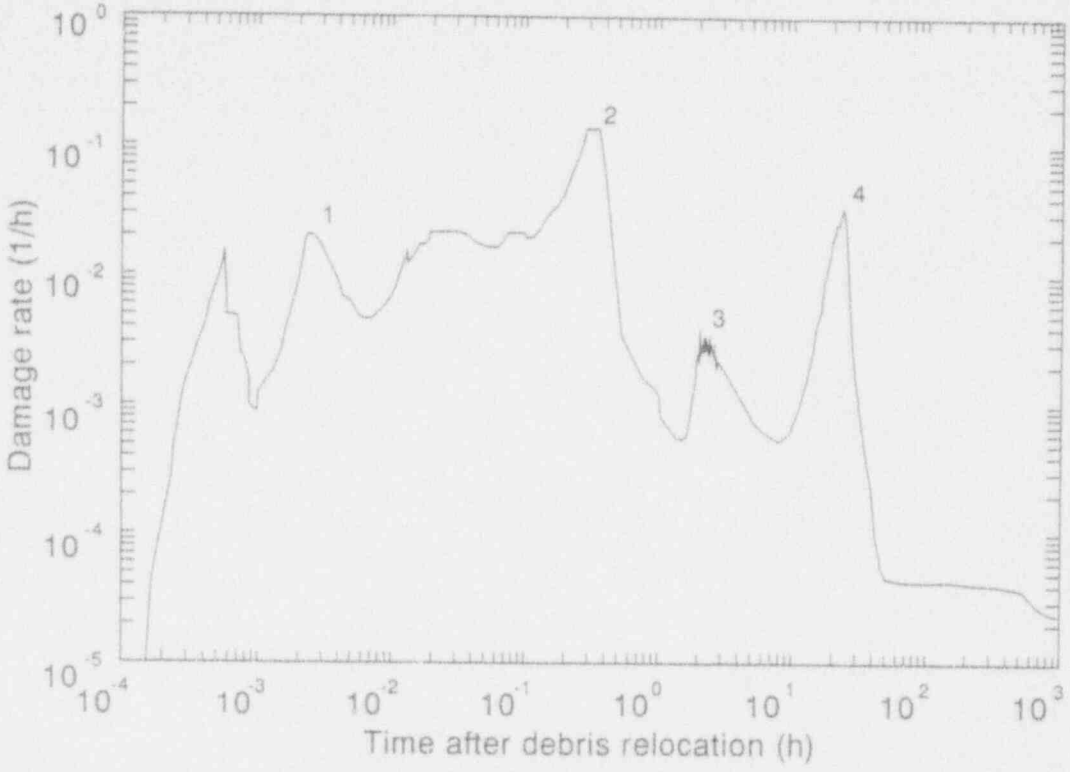

M919 jr-0793-05

(a) Damage rate versus time

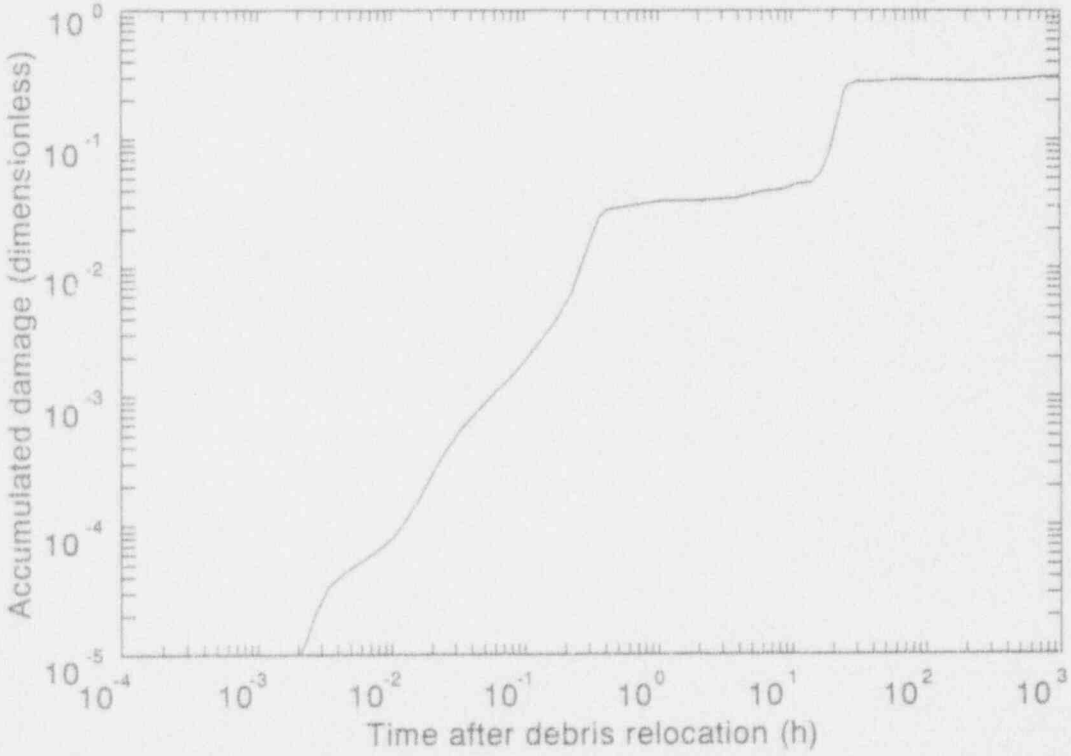

M919 jr-0793-06

(b) Accumulated damage versus time

Figure 4-18. Hot spot on cool (600 K) background problem results.

Table 4-7. Stress distributions at bottom of shell at various times during transient (hot spot on cool background).

t = 2.7 hours

Position	σ_φ (MPa)	σ_θ (MPa)	Temperature (K)	Damage
-0.974	-4.60	-4.60	1,313	0.0042
-0.865	-4.82	-4.82	1,292	0.0067
-0.679	-5.92	-5.92	1,258	0.023
-0.433	-8.98	-8.98	1,216	0.035
-0.149	-9.44	-9.44	1,171	0.041
+0.149	-3.50	-3.50	1,127	0.034
+0.433	14.2	14.2	1,091	0.014
+0.679	19.4	19.4	1,061	0.016
+0.865	23.4	23.4	1,041	0.174
+0.974	23.5	23.5	1,030	0.481

t = 12.1 hours

Position	σ_φ (MPa)	σ_θ (MPa)	Temperature (K)	Damage
-0.974	12.9	12.9	1,020	0.0073
-0.865	10.1	10.1	1,007	0.0093
-0.679	9.14	9.14	985	0.025
-0.433	11.0	11.0	957	0.036
-0.149	20.4	20.4	928	0.042
+0.149	54.4	54.4	899	0.037
+0.433	43.6	43.6	875	0.018
+0.679	6.15	6.15	855	0.020
+0.865	-18.9	-18.9	842	0.177
+0.974	-28.8	-28.8	834	0.487

t = 643 hours

Position	σ_φ (MPa)	σ_θ (MPa)	Temperature (K)	Damage
-0.974	—	—	599	1+
-0.865	—	—	596	1+
-0.679	—	—	591	1+
-0.433	—	—	585	1+
-0.149	—	—	577	1+
+0.149	—	—	570	1+
+0.433	364.3	364.3	563	0.398
+0.679	334.1	334.1	557	0.084
+0.865	50.4	50.4	553	0.177
+0.974	-141.2	-141.2	550	0.488

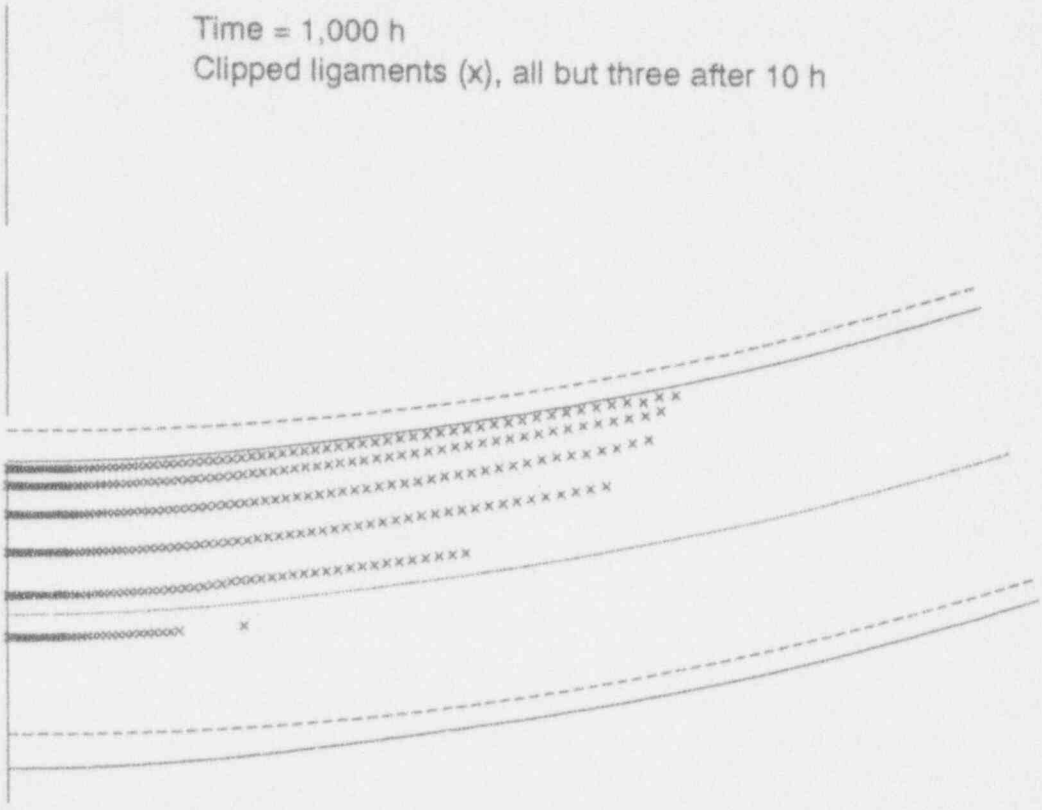

Figure 4-19. Distribution of 100% damaged ligaments at 1,000 hours after debris relocation into hot spot on cool (600 K) background transient. Note: displacements shown may be low due to omission of tertiary creep.

evidence exists suggesting the cooling rate was as high as 50 K/minute.[14] Under these circumstances, the accumulated damage may well have been far below that required to fail individual ligaments, and the severe damage distribution in Figure 4-18 (b) may not therefore be representative of the residual damage state of the TMI-2 lower head. Despite the severe stress distribution at the bottom of Table 4-7, the simulation continued to run out to 1,000 hours without vessel failure.

Having defined a hot spot problem that survives the transient, it is desirable to determine the margin to failure for this case. As discussed in Section 4.1, margin to failure was initially defined by the consensus of the Structural Mechanics Peer Review Group[1] to be the time the vessel can sustain the temperature and pressure conditions present at the point of maximum damage rate. Since inspection of Figure 4-18 (a) indicates several peaks exist in the damage rate during the transient, a unique definition of margin to failure is not possible. In the analysis that follows, margin to failure is evaluated on the basis of fixed conditions at peaks 2, 3, and 4 in Figure 4-18 (a). The peak associated with the initial thermal load (peak 1) is not relevant to the margin-to-failure analysis, since only the material on the inner surface experiences elevated temperature during the first 3 to 30 seconds into the transient. Margin to failure is then defined as the minimum of all margin-to-failure calculations evaluated from peaks in the damage rate.

When conditions are fixed at peak 2, 0.305 hours into the transient, the subsequent evolution of damage is as shown in Figure 4-20 (a) and (b). In this figure, the damage rate for the original transient is shown as a dashed line to accentuate the differences in damage rate once the pressure and temperature are fixed. The pressure at 0.305 hours is 9.8 MPa, and the temperatures on the outside of the shell are still modest. Under these conditions, the stress distribution in the hot spot region creeps out, damage falls monotonically with time, and the vessel survives out to 1,000 hours. It is interesting to note that the damage state at 1,000 hours under these conditions, shown in Figure 4-21, is significantly more benign than that associated with the actual transient (see Figure 4-19), because the shell never experiences the complete heatup and cooldown, producing the highly damaging tensile states described previously. The margin to failure for these conditions is therefore undefined, but it appears from Figures 4-20 and 4-21 that it greatly exceeds 1,000 hours and may be infinite.

A similar result is not obtained, however, when margin to failure is defined on the basis of peak 3 in Figure 4-18 (a). In this case, repressurization has pushed the pressure to 14.6 MPa, and the inner surface temperature has exceeded the SA533B threshold hot spot temperature, peaking at 1,340 K. Under these conditions, the hot spot has become a soft plug of material and is gradually punched out of the vessel at elevated pressure. The damage rate now evolves as shown in Figure 4-22 (a) and (b). For a few hours after fixing the pressure and temperature states, the damage rate is nearly constant, but as the plug is pushed out of the vessel, damage accumulation is accelerated and the vessel fails 10 hours into the transient. Margin to failure in this instance is 8 hours. The vessel geometry and damage distribution just before failure are now shown in Figure 4-23. The cusp or bulge associated with expulsion of the soft plug is clearly visible, and the 100% damaged states indicate the plug is being sheared off from the remainder of the vessel.

Finally, margin to failure was evaluated by fixing conditions at 23 hours into the transient, where damage rate reaches a peak during cooldown. Under these conditions, pressure is fixed at 14.6 MPa, and the inner and outer surface temperatures underneath the hot spot have dropped to 790 and 675 K respectively. This is still hot enough to result in damage accumulation, as shown in Figure 4-24, and failure occurs at 82 hours into the transient, providing a margin to failure of just under 60 hours. The damage distribution just before failure is shown in Figure 4-25, indicating a failure mode driven by tensile stresses formed from partial cooling. Of the three margin-to-failure calculations, that associated with maximum pressure and temperature conditions imposes the most severe limitations (peak 3), and margin to failure is calculated as 8 hours.

To examine differences in failure time and behavior, calculations of thermal and structural response were undertaken for the case of a hot spot imposed on the lower-bound background heat flux. A representative temperature contour plot is shown in Figure 4-26, again 2 hours into the transient. It comes as no surprise that this loading results in failure before the 1.9 hours determined from the lower-bound background loading only. It is interesting to see, however, that the presence of the hot spot has dramatically changed the failure geometry and the damage distribution at failure. Figure 4-27 shows the deformed vessel geometry and damage distribution just prior to failure 1.5 hours into the transient. The presence of the hot spot has facilitated vessel sag, and 100% damaged ligaments extend all the way to the bottom of the shell.

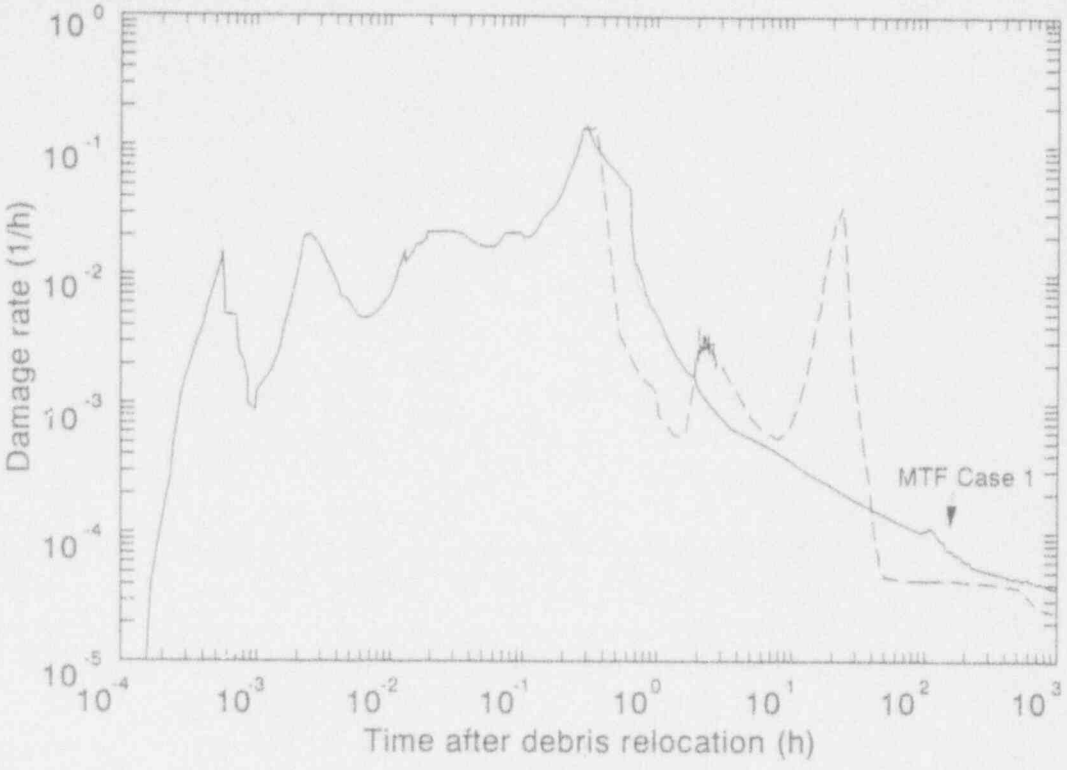

(a) Damage rate versus time

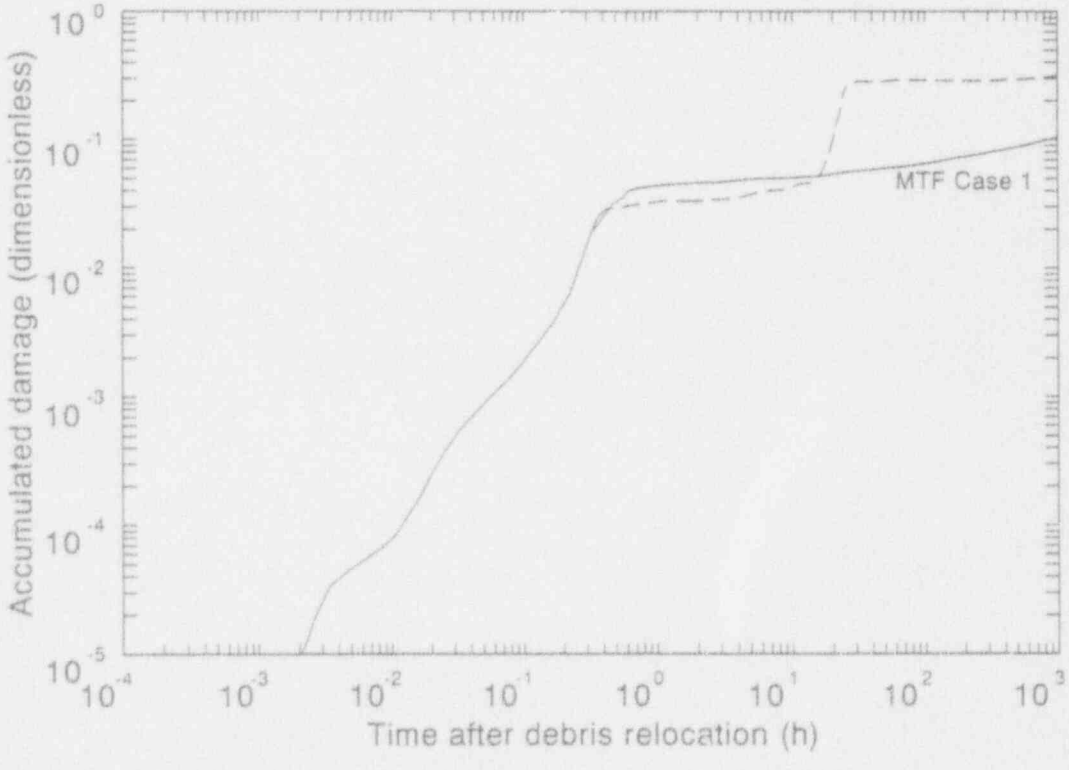

(b) Accumulated damage versus time

Figure 4-20. MF-1 calculation for hot spot on cool background problem results.

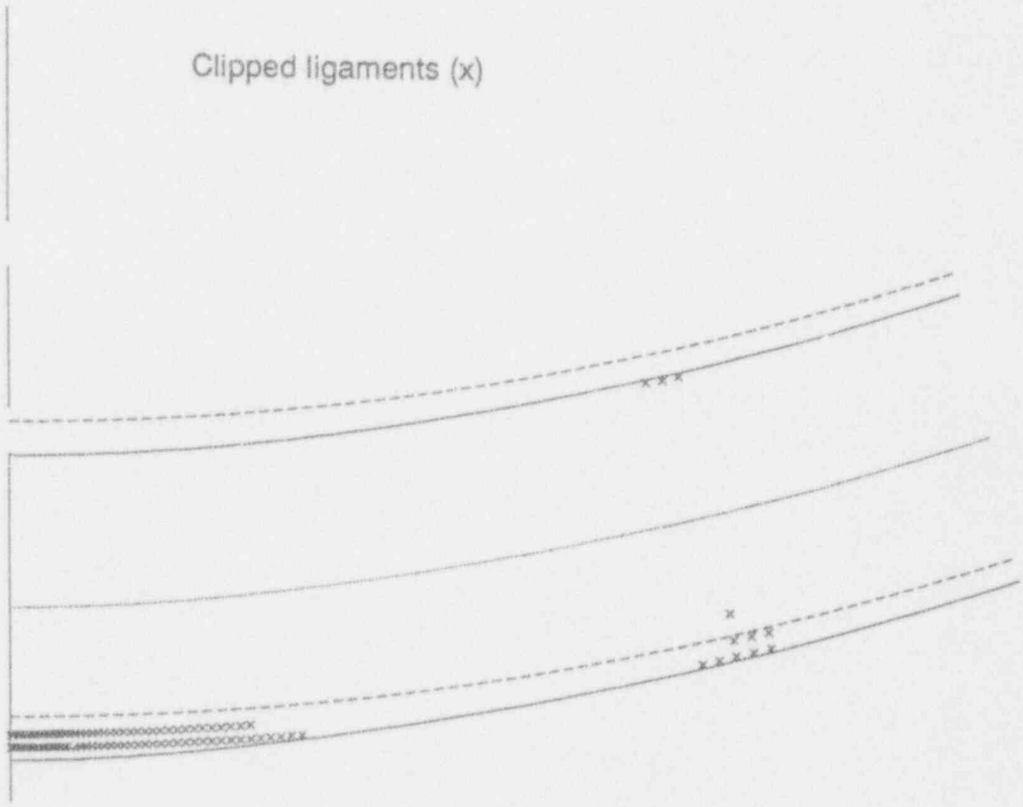

Figure 4-21. Distribution of 100% damaged ligaments at 1,000 hours after debris relocation into MF-1 calculation for hot spot on cool background.

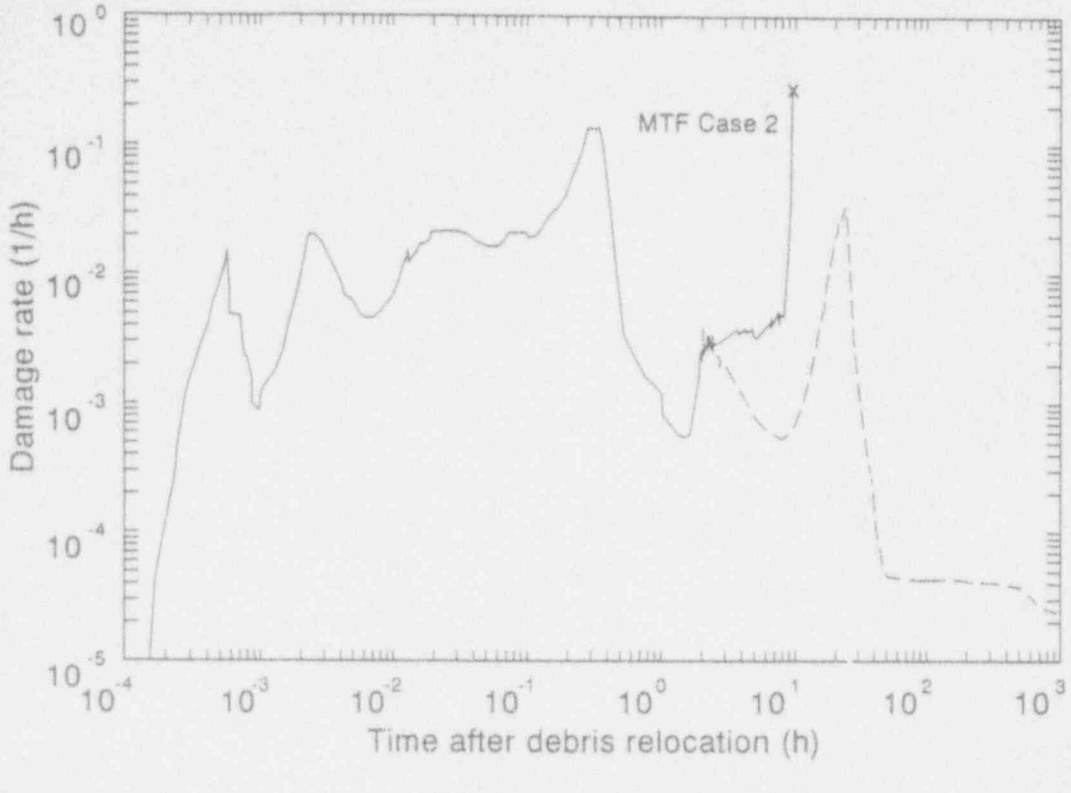

(a) Damage rate versus time

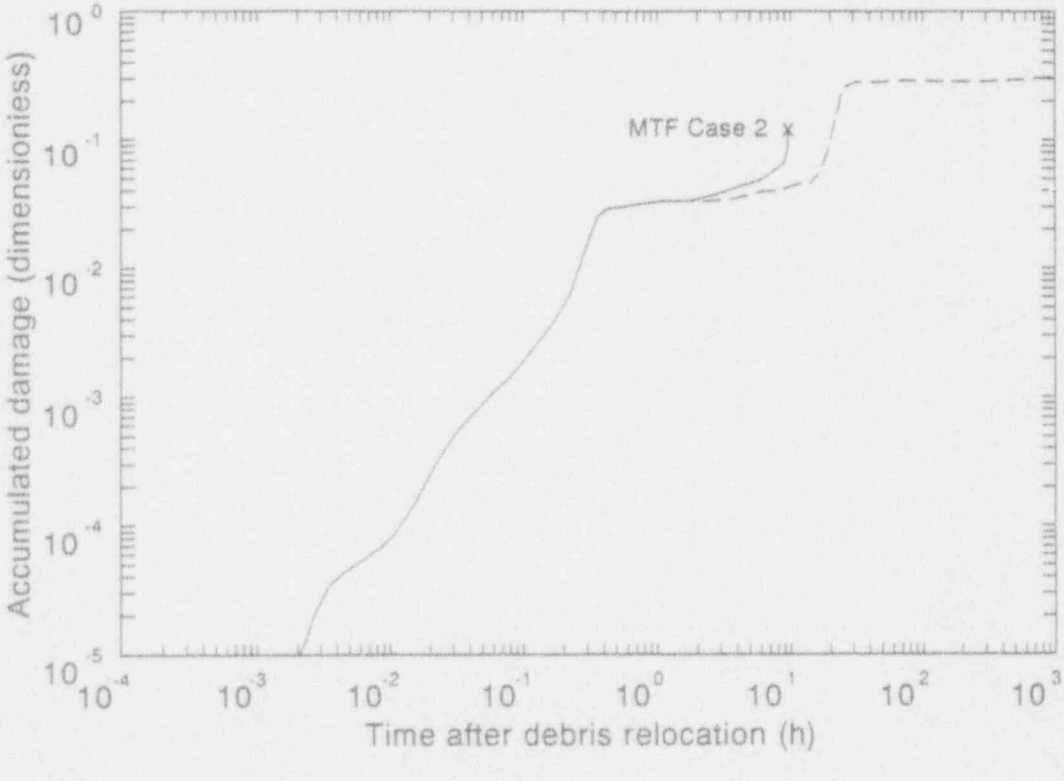

(b) Accumulated damage versus time

Figure 4-22. MF-2 calculation for hot spot on cool background problem results.

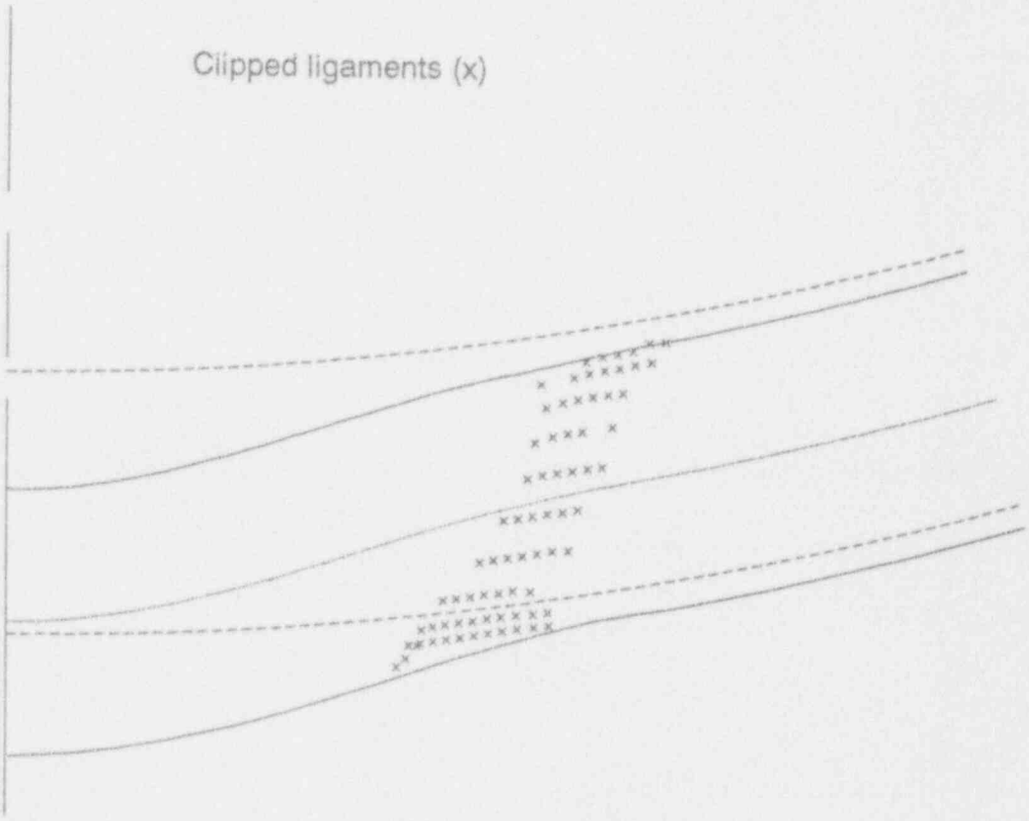

Figure 4-23. Distribution of 100% damaged ligaments just prior to failure (10 hours after debris relocation) in MF-2 calculation for hot spot on cool (600 K) background.

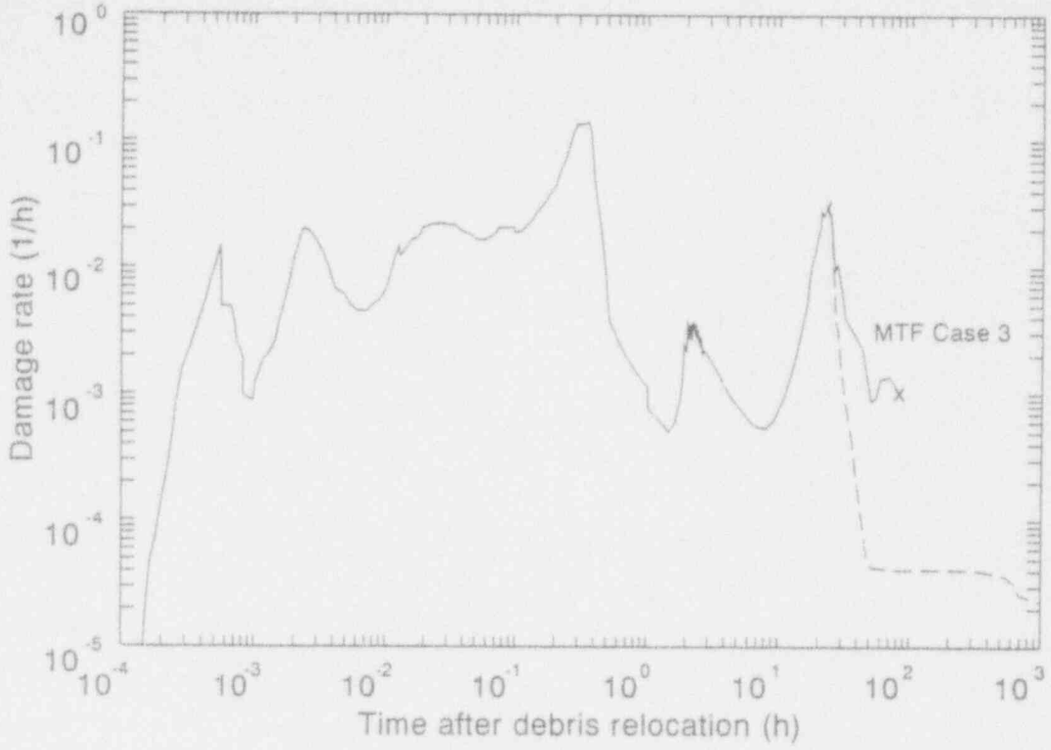

(a) Damage rate versus time

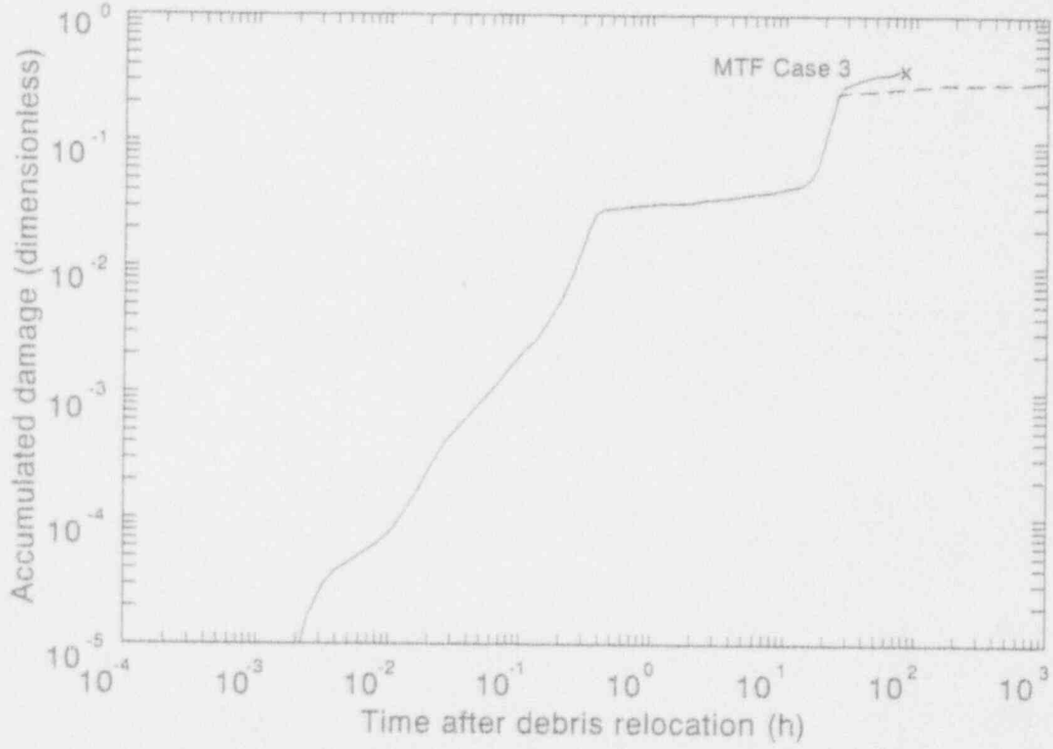

(b) Accumulated damage versus time

Figure 4-24. MF-3 calculation for hot spot on cool background problem results.

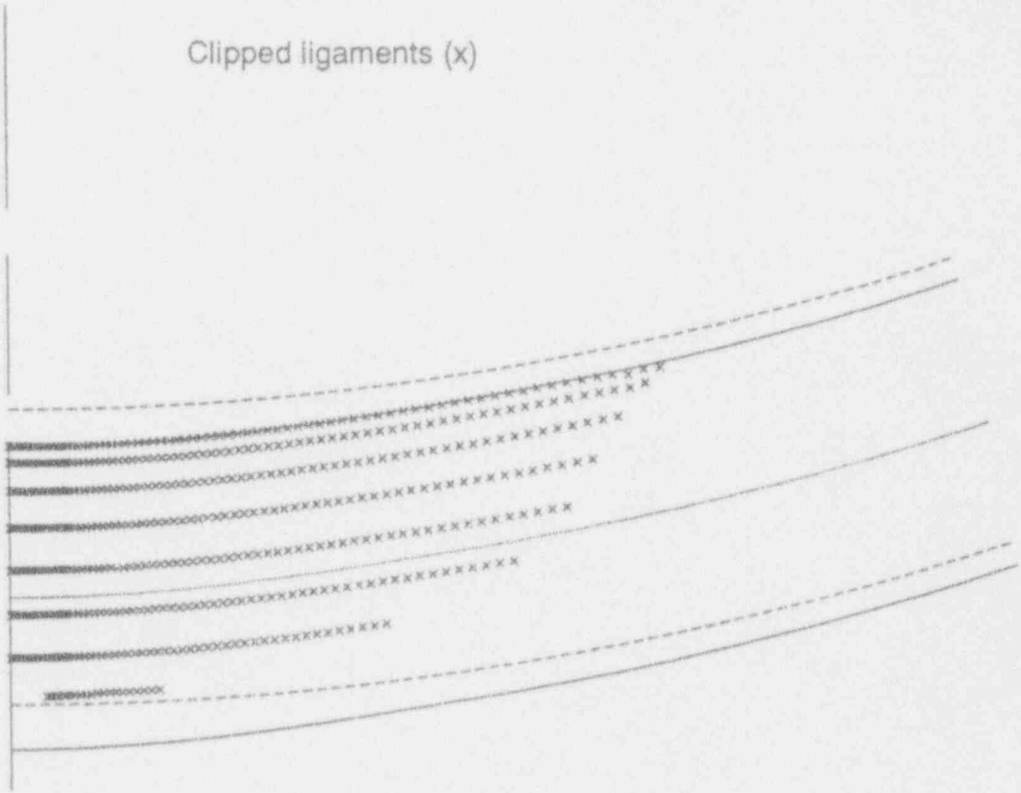

Figure 4-25. Distribution of 100% damaged ligaments just prior to failure (82 hours after debris relocation) in MF-3 calculation for hot spot on cool (600 K) background.

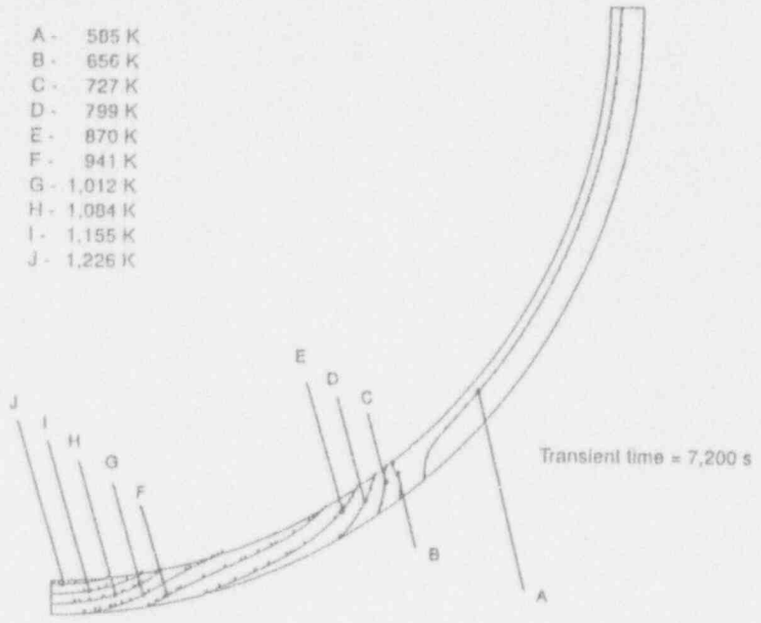

Figure 4-26. Temperature distribution associated with hot spot on lower bound background at 2 hours after debris relocation into transient.

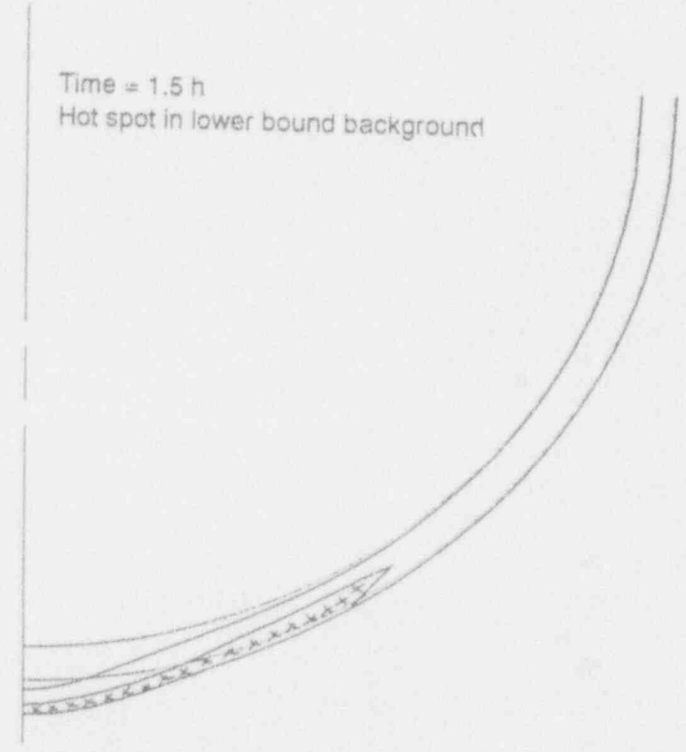

Figure 4-27. Distribution of 100% damaged ligaments just prior to failure (1.5 hours after debris relocation) in hot spot on lower bound background problem.

4.5.4 Conclusions and Comments

The three cases examined in this investigation indicate that background heat flux plays a pivotal role in determining whether or not the vessel survives. The vessel fails readily without any hot spot if heat fluxes characteristic of the lower-bound analysis (Case 15 of Table 3-4) are applied over a large angular segment of the lower head. The vessel is capable of surviving local hot spots in the temperature range and of the duration inferred from TMI-2 VIP metallurgical examinations, but the balance of the shell must remain cool.

The present work also identified areas where the margin to failure, as defined by the Structural Mechanics Peer Review Group,[1] may need refinement. When the vessel survives, several peaks in the damage rate versus time plot are apparent. If margin to failure is defined on the basis of the maximum damage rate sustained during vessel heatup in Figure 4-18 (a), margin to failure is essentially infinite. Of the three peaks in damage rate, the lowest margin to failure is associated with the smallest peak, providing a margin to failure of 8 hours. Finally, these analyses have illustrated that the failure mode, vessel deformation, and damage distribution at failure depend strongly on the thermal and pressure history.

4.6 Conclusions from Margin-to-Failure Calculations

Scoping calculations were performed to evaluate the failure margin that existed in the reactor vessel during the TMI-2 accident. Tube and vessel failure mechanisms were investigated. Where possible, margin-to-failure parameters were obtained to characterize the potential for a particular mechanism to occur.

As noted in Figure 1-1, prior to performing a tube ejection analysis, it must be established that the weld holding the nozzle to the vessel has failed. Since it is not known if the hot spot temperatures occurred at the same time that the RCS was repressurized to 15 MPa, weld failure calculations were conservatively performed assuming that peak temperatures and pressures occurred simultaneously. Results indicate that even for these very conservative assumptions, there was considerable margin in the weld's integrity. Hence, the need for any tube ejection analysis was eliminated.

As discussed in Section 3.1, melt penetration calculations indicate that ceramic melt would not penetrate below the vessel head. Hence, ex-vessel tube rupture calculations were performed assuming tube temperatures consistent with the vessel coolant temperatures. Since such temperatures were expected to result in very high margins to failure, a constant upper system pressure of 15 MPa was also applied in the tube failure calculations. Results indicate that the margin to failure for this mechanism was also very high. Hence, the potential for tube failure via ejection and rupture were eliminated.

The potential for the vessel to experience a global failure was evaluated for nominal and lower-bound temperature distributions from Section 3.2. Note that both of these temperature distributions were obtained by assuming that the molten debris experienced relatively slow cooling rates in order to be consistent with companion sample examination data. Global failure was predicted to occur at 1.7 hours after relocation for the nominal case and 2.3 hours after relocation for the lower-bound case. In fact, parametric studies indicate that failure is predicted for inner

surface temperatures of the vessel above 800 to 900 K in less than 3 hours, if the reactor vessel is maintained at pressures near the operating pressure. Obviously, vessel failure did not occur during the TMI-2 accident. Hence, analyses indicate that debris cooling must have occurred within the first 2 hours to prevent global vessel failure. In addition, results suggest that a stress-based damage failure criterion may be too conservative for predicting failure.

The potential for the vessel to experience a localized failure was evaluated by imposing hot spot temperatures on two background distributions, the Section 3.2 lower-bound case temperatures and a benign case with temperatures remaining at the initial conditions for the lower-bound case. These two temperature distributions bounded possible background distributions predicted by metallographic examinations, since boat sample data indicate that temperatures outside the hot spot remained below the ferritic-to-austenitic transition temperature and it is known that vessel temperatures were at least at operating conditions. Lower-bound case results indicate that the presence of a hot spot reduces predicted failure times from 1.9 to 1.5 hours. Furthermore, the geometry of the vessel and the damage distribution in the vessel just prior to failure differs because of the hot spot. However, results from the benign case indicate that the vessel is capable of surviving local hot spots in the temperature range and of the duration inferred from the metallurgical examinations if the balance of the shell remains relatively cool.

In summary, results from these failure analyses indicate that the margin to failure for tube failures was very large, effectively eliminating tube failures as potential failure mechanisms during the TMI-2 event. Global and localized failure analyses suggest that debris cooling occurred within the first 2 hours after debris relocation (although there are insufficient data from companion sample examinations to quantify the timing and rate of this cooling). In addition, analyses results suggest that a stress-based damage failure criterion may be too conservative for predicting failure. Localized vessel failure calculations illustrate that it is possible for the vessel to withstand the hot spot temperatures and durations inferred from the vessel metallurgical examinations if the balance of the vessel remains relatively cool. Therefore, calculational results suggest that the background temperature behavior of the vessel, which is dependent upon the heat load from molten debris relocating to the lower head, is key to obtaining estimates for vessel failure margin.

4.7 References

1. J. Strosnider, "Summary Record of the TMI-VIP Structural Mechanics Peer Review Group Meeting," *OECD TMI Vessel Investigation Project, Idaho Falls, Idaho, May 11, 1992,* NEA.TMIV/MAN(92)09, July 20, 1992.

2. R. Huddleston, "An Improved Multiaxial Creep-Rupture Strength Criterion," *Journal of Pressure Vessel Technology, 107,* November, 1985, pp. 421–429.

3. F. R. Larson and J. Miller, "A Time-Temperature Relationship for Rupture and Creep Stresses," *Transactions of the ASME, 78,* July 1952, pp. 765–775.

4. R. M. Goldoff, "Comparison of Parameter Methods for Extrapolating High-Temperature Data," *Journal of Basic Engineering, 81,* Series D, No. 4, December 1959, pp. 629–643.

5. E. L. Robinson, "Effect of Temperature Variation on the Creep Strength of Steels," *Transactions of the ASME, 60*, 1938, pp. 253–259.

6. P. N. Randall, "Cumulative Creep Damage in Creep Rupture Tests of a Carbon Steel," *Journal of Basic Engineering, 84*, 2, June 1962, pp. 239–242.

7. I. Finnie and M. Patel, "Life-Prediction for Furnace Tubes Operating in the Creep-Rupture Range," *Mechanical Behavior of Materials: Proceeding of the 1974 Symposium on Mechanical Behavior of Materials, August 21-24, Kyoto, Japan, 1974*, Volume 2, Published by Society of Materials Science, Japan, pp. 215-225.

8. M. M. Abo El Ata and I. Finnie, "On the Prediction of Creep-Rupture Life of Components Under Multiaxial Stress," *Second International Union of Theoretical and Applied Mechanics Symposium on Creep in Structures, August 1970,* published by Springer Verlag, Berlin, Germany, 1972, pp. 80-95.

9. L. Y. Liberman, "Relaxation Tensile Strength and Failure of EI612 and 20Kh1M1F-L Steels," *Metalloved. i Term. Obrabotka Metal., 4*, 1962, pp. 6–13.

10. H. R. Voorhees and J. W. Freeman, *Notch Sensitivity of Aircraft Structural and Engine Alloys, Part II. Further Studies with A-286 Alloy*, Wright Air Development Center, Technical Report, 50-470, January 1959, p. 23.

11. M. M. Abo El Ata and I. Finnie, "A Study of Creep Damage Rules," *Journal of Basic Engineering, 94*, September 1972, pp. 533–543.

12. Y. R. Rashid, "Transient Failure of Zircaloy Cladding," *Nuclear Engineering and Design, 101*, 1987, pp. 305–313.

13. J. L. Rempe et al., *Light Water Reactor Lower Head Failure Analysis*, NUREG/CR-5642, October 1993.

14. G. E. Korth, *Metallographic and Hardness Examinations of TMI-2 Lower Pressure Vessel Head Samples*, OECD TMI-2 VIP, TMI V(92) EG01, January 1992.

15. J. R. Wolf et al., *Integration Report*, OECD-NEA-TMI-2 VIP TMI V(93)EG02, September 1993.

16. MPR Associates, *Phase 4 Status Report, Removal of Test Specimens from the TMI-2 Reactor Vessel Bottom Head, Project Summary*, MPR-1195, October 1, 1990, Drawing No. F-80-107-89 July 22, 1988.

17. MPR Associates, *Phase 4 Status Report, Removal of Test Specimens from the TMI-2 Reactor Vessel Bottom Head, Project Summary*, MPR-1195, October 1, 1990, Drawing No. F-80-328, July 24, 1990.

18. N. R. Draper and H. Smith, *Applied Regression Analysis*, second edition, New York: John Wiley & Sons, Inc., 1981, pp. 20–29.

19. G. V. Smith, *Evaluations of the Elevated Temperature Tensile and Creep Rupture Properties of C-Mo, Mn.-Mo, and Mn-Mo-Ni Steels*, Philadelphia: American Society for Testing Materials, 1971.

20. W. C. Young, *Roark's Formulas for Stress and Strain*, sixth edition, New York: McGraw-Hill, Inc., 1989.

21. [illegible] Version 6.1, Nottingham, England: PAFEC Ltd., 1984.

22. S. Lin, T. Lin, and B. Mazelsky, "Large Deflection of Axisymmetric Shell with Creep Strain," *ASCE Journal of Engineering Mechanics, 100*, 1974, pp. 79–94.

23. G. B. Reddy and D. J. Ayres, *High Temperature Elastic-Plastic Creep Properties for SA533 Grade B Class 1 [illegible]508 Materials*, EPRI-NP-2763, December 1982.

5. SCOPING CALCULATIONS TO INVESTIGATE DEBRIS COOLING AND FAILURE CRITERION

As discussed in Sections 3 and 4, the initial scoping margin-to-failure calculational results are inconsistent with several observations from VIP metallurgical examinations:[1]

- Nominal case thermal analysis results indicate that the vessel temperatures outside the hot spot exceeded 1,000 K, which is inconsistent with metallurgical examination data.
- Thermal analyses results indicate that hot spot temperatures occurred for longer than the 30 minutes indicated by metallurgical examinations.
- Nominal case thermal analysis results indicate that the vessel temperatures did not cool at the 10 to 100 K/minute rates through the SA533B steel transition temperature as indicated by metallurgical examinations.
- Structural analysis results for the nominal and lower-bound cases indicate that the vessel would fail prior to the time when it was repressurized to 15 MPa.

As noted in Section 3.2, thermal analyses were performed based upon debris properties (e.g., decay heat levels, slow cooling rate) from the companion sample examinations. However, thermal and structural calculational results combined with metallurgical examination results clearly indicate that the analysis needs to model some form of cooling that was not evident in the TMI-2 companion sample examinations. In addition, analysis results suggest that a stress-based damage failure criterion may be too conservative for predicting failure. This section describes analyses performed to investigate the effects of debris cooling and failure criterion on calculational results.

5.1 Slow and Rapid Cooling Analyses

Although there are insufficient data to determine the exact mechanisms that caused the debris to cool within the first two hours after relocation, two possible forms of cooling are investigated in this section that have the potential to produce this additional cooling:

Slow Cooling—In this mode, it is assumed that channels or cracks in the debris allowed for infusion of water that cooled the debris near the channels but left the interior portions hot. As noted in Section 2.1.6, some cracks were observed on the upper surface of the hard layer of debris on the lower head in TMI-2 videos.

Rapid Cooling—In this mode, it is assumed that gaps or channels between the debris crust and the lower head allowed relatively high flow rates of coolant between the debris and the vessel. As noted in Section 2.1.6, the limited video shots of the interface between the vessel and the debris are inconclusive about the presence of such a gap, although gaps between the debris and nozzles were seen.

The simultaneous presence of gaps between the debris and the vessel surface and cracks within the debris provides multiple pathways for steam release (e.g., water may travel down along the gap and boil up through cracks).

Using the two-dimensional finite element thermal analysis code and the finite-difference model applied in Section 4.5, calculations were performed to determine cooling rates due to each type of cooling mechanism so that the vessel response would be consistent with data from the metallurgical examinations. Then, scoping calculations were performed to determine if coolant flowing through a reasonable number of channels within the debris and/or gaps between the debris and the vessel could support the estimated cooling rates. Finally, scoping calculations were performed to determine if the hypothesis of debris cooling after relocation could be substantiated by evaluating the mass and internal energy within the vessel using measured plant data or parameters that were inferred from measured plant data.

5.1.1 Slow Cooling Analysis

It was shown in Section 4.5 that the vessel is capable of surviving hot spots if the balance of the vessel remains relatively cool. In this subsection, attempts are made to quantify the cooling needed to achieve a relatively cooler temperature in the vessel region outside the hot spot that will prevent vessel failure. The results presented in this section assume that after the vessel reaches its peak temperature within the hot spot, it returns asymptotically to its initial, cool temperature profile. The rate at which the vessel returns to its initial temperature distribution is assumed to be governed by the decay heat. This is identical to the procedure used for the "hot spot on cool background" problem described in Section 4.5. Results are presented here for hot spots superimposed on 50%, 25% and 33% of nominal background heat flux. For these three cases, it is predicted that the vessel fails in 2.8 hours, survives, and fails in 6.5 hours, respectively. Therefore, under slow cooling assumptions, the vessel is predicted to survive a hot spot in the presence of a background heat flux somewhere between 25% and 33% the nominal value.

There are two minor differences between input used for calculations in this section and Section 4.5. The first is the use of a less conservative Larson-Miller Parameter at temperatures below 850 K. Comparisons between the new VIP data and existing data[2,3] indicate that the use of a single Larson-Miller Parameter over the entire temperature range of interest imposes a somewhat conservative damage rate on the material at low temperatures. Hence, the calculations described in this section were performed using a revised Larson-Miller Parameter that includes additional low temperature data. In examining results in this section, it can be seen that the damage peaks during cooldown are somewhat smaller than the cooldown damage peaks in Section 4.5. Thus, residual damage states and margins to failure reported in Section 4.5 may be somewhat conservative. Second, the drop in the pressure history between 4 and 11 hours after relocation was not included in the Section 4.5 simulations. This omission did not impact most of the calculations in Section 4.5 because vessel failure was predicted to occur prior to 4 hours after debris relocation. Although these two updates were included in these calculations, it is not felt that these updates significantly impact calculation results.

The time dependent temperature distributions in the vessel are similar to those presented in Section 4.5 for the "hot spot on cool background" problem. A single contour plot is included here to illustrate the differences. Figure 5-1 shows temperature contours for a hot spot on 50% of

nominal case background heat fluxes at 2 hours after relocation. There is now a more gradual transition between the hot spot and the coolest part of the vessel. Note in particular the subdomain of the vessel defined by the contours at 800 and 900 K. Failure occurs as this region shears off from the remainder of the vessel. The vessel is predicted to fail 2.8 hours after relocation when the hot spot is superimposed on 50% of nominal background heat fluxes. Figure 5-2 shows the damage rate and accumulated damage for this simulation, and Figure 5-3 shows the evolution of vessel deformation and damage distribution. The shear failure mode is evident in Figure 5-3. Note that only the outermost ligaments directly underneath the hot spot have experienced 100% damage throughout the layer.

Figures 5-4 through 5-8 present similar information for the case of a hot spot on 25% of nominal background heat fluxes. Figure 5-4 indicates that the 800–900 K contours are now nested more closely to the hot spot. Figures 5-5 and 5-6 show the corresponding damage rate, accumulated damage and vessel deformation and damage distribution. Inspection of Figure 5-6 indicates the beginning of a shear failure, but the remainder of the vessel provides sufficient constraint to prevent failure. An interesting feature of Figure 5-5 is the pronounced drop in damage rate between 4 and 11 hours after relocation. This corresponds to the drop in the pressure history. The minimum pressure during this drop is about 3 MPa; Figure 5-5 indicates that a drop in the pressure from 15 to 3 MPa results in a drop in accumulated damage by two orders of magnitude. Repressurization to 16 MPa at 11 hours pushes the damage rate back up to 0.01 hour^{-1}, but subsequent cooling results in a rapidly diminishing damage rate. To understand the sensitivity of the results to the presence or absence of this pressure drop, an additional simulation was performed without the drop. Figure 5-7 illustrates the resulting change in damage

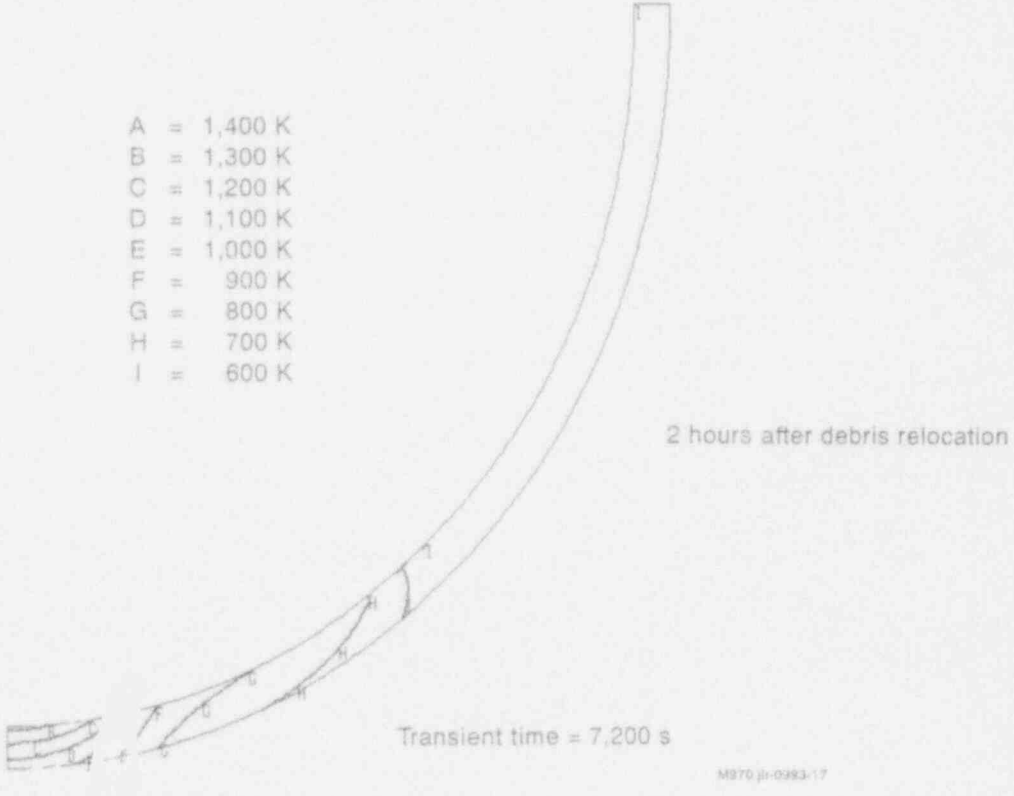

Figure 5-1. Temperature distribution of hot spot on 50% of nominal background heat fluxes.

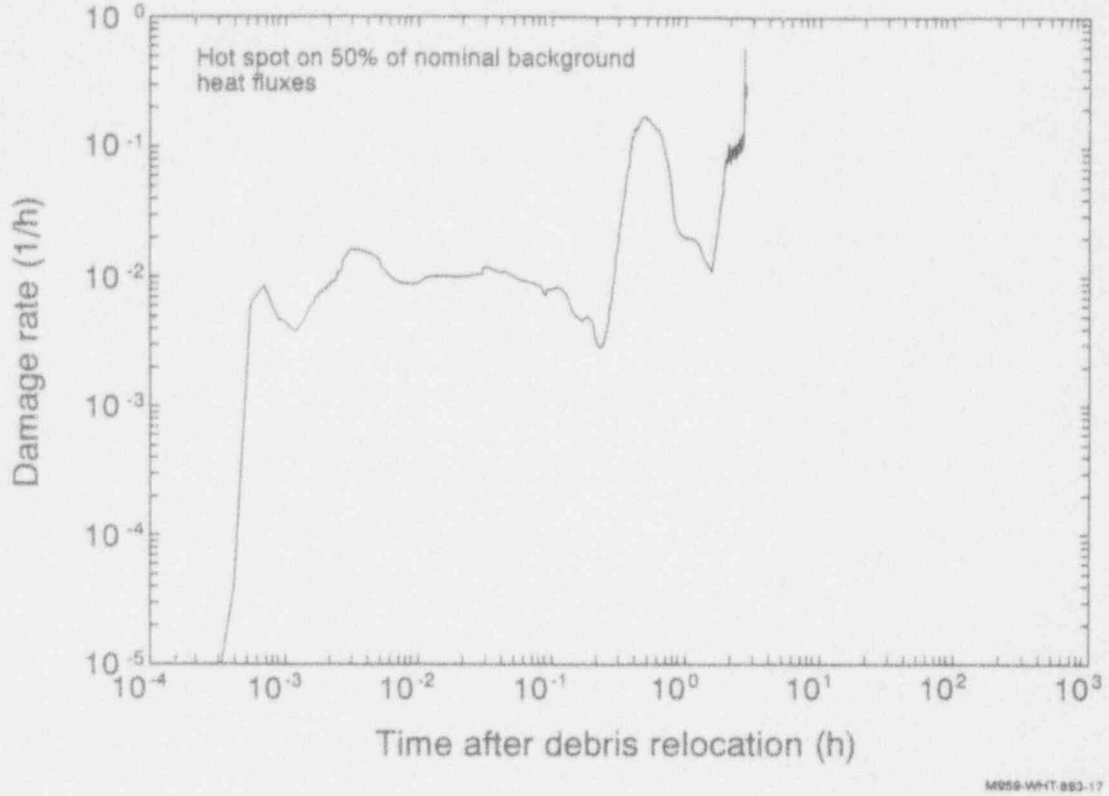

(a) Damage rate

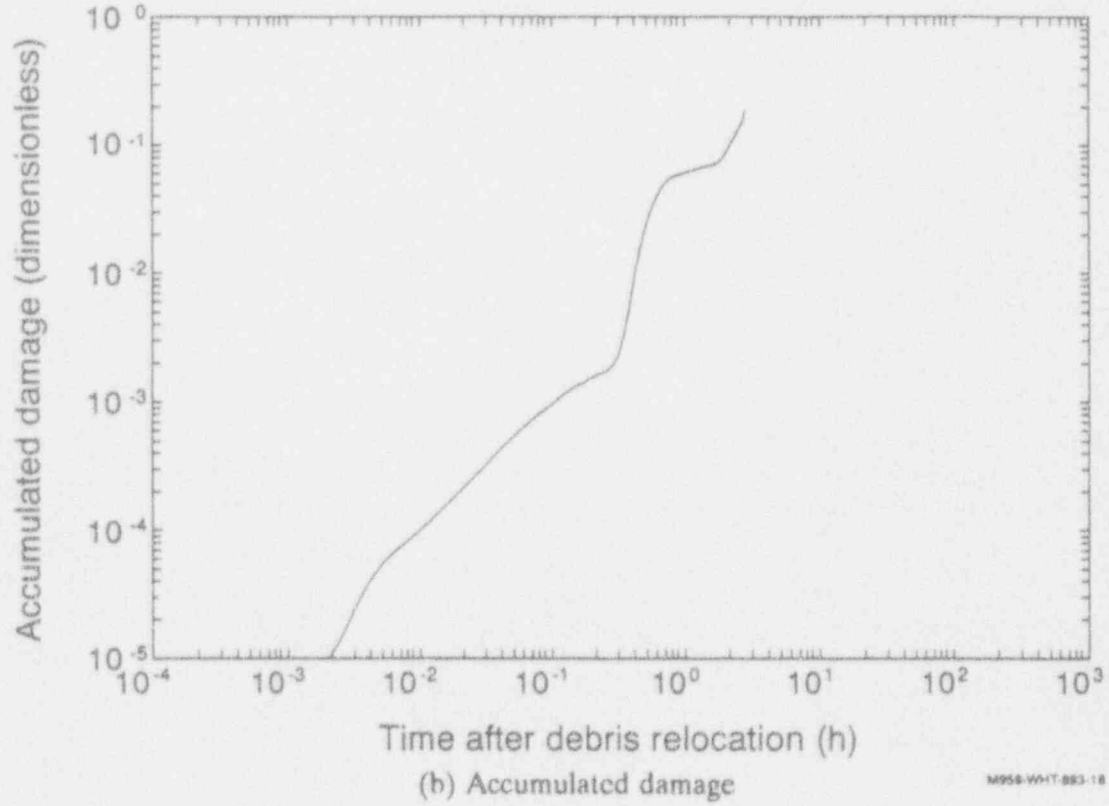

(b) Accumulated damage

Figure 5-2. Results for case with hot spot on 50% of nominal background heat fluxes.

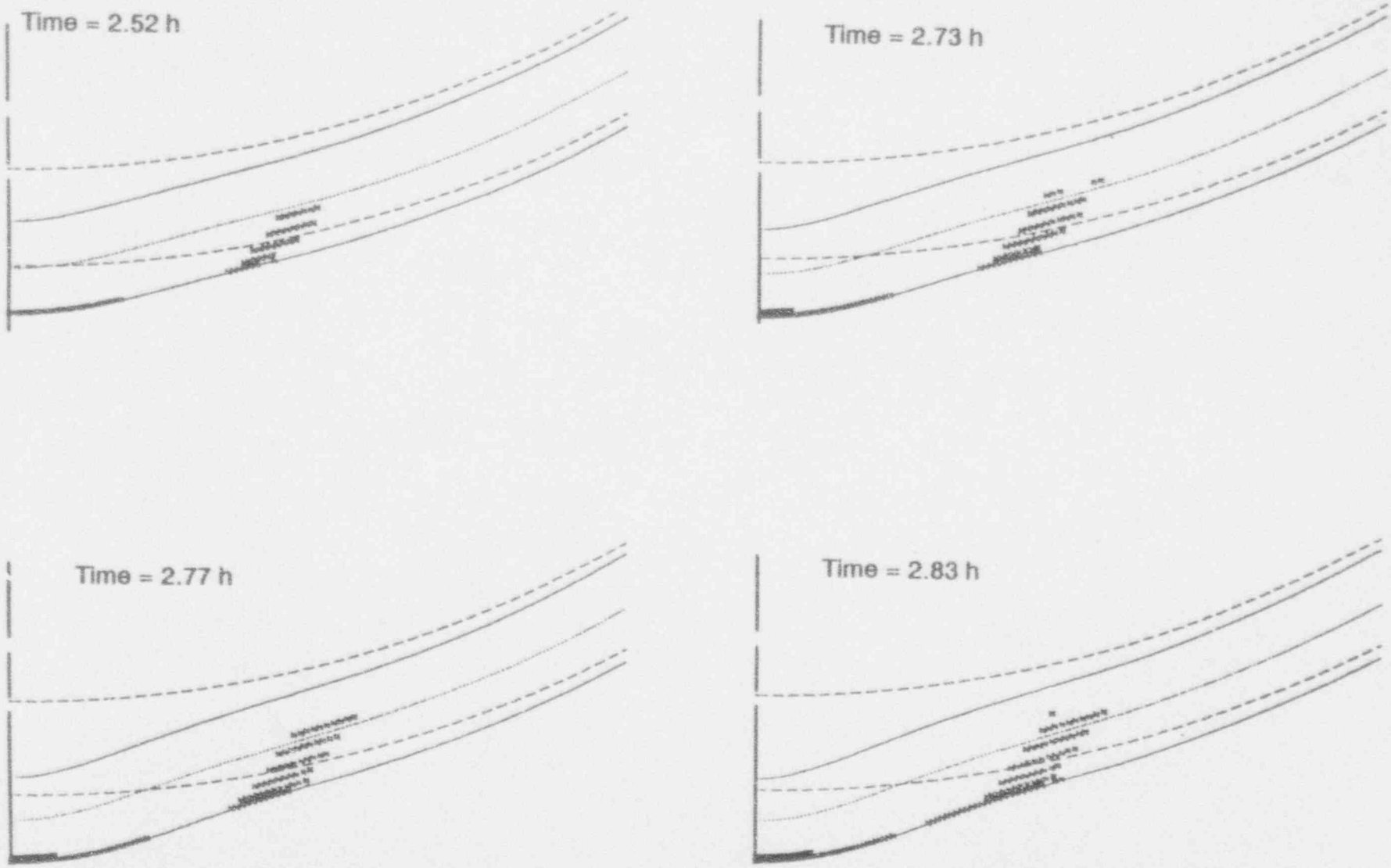

Figure 5-3. Distribution of 100% damaged ligaments at various times for the hot spot on 50% of nominal background heat fluxes.

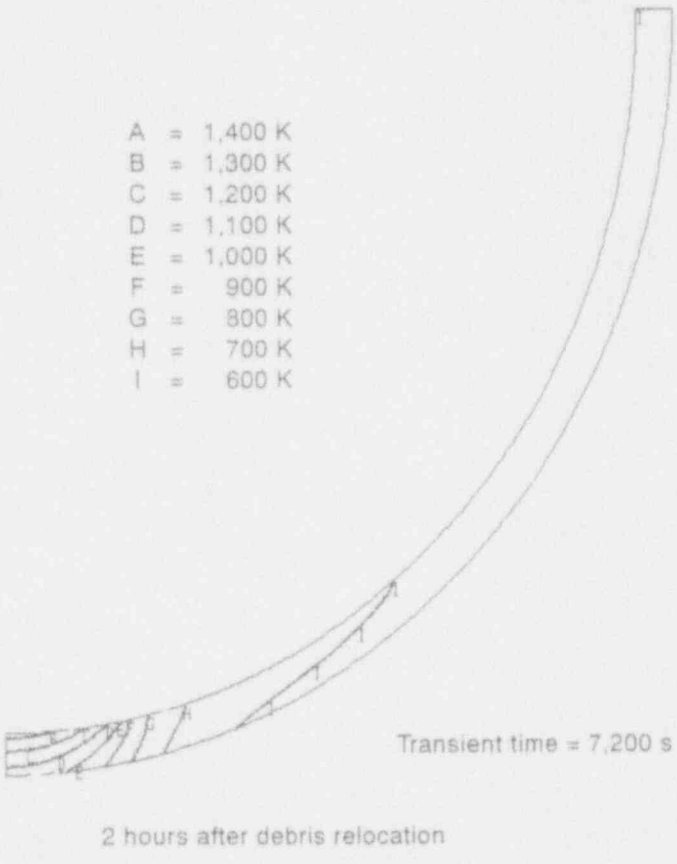

Figure 5-4. Temperature distribution of hot spot on 25% of nominal background heat fluxes.

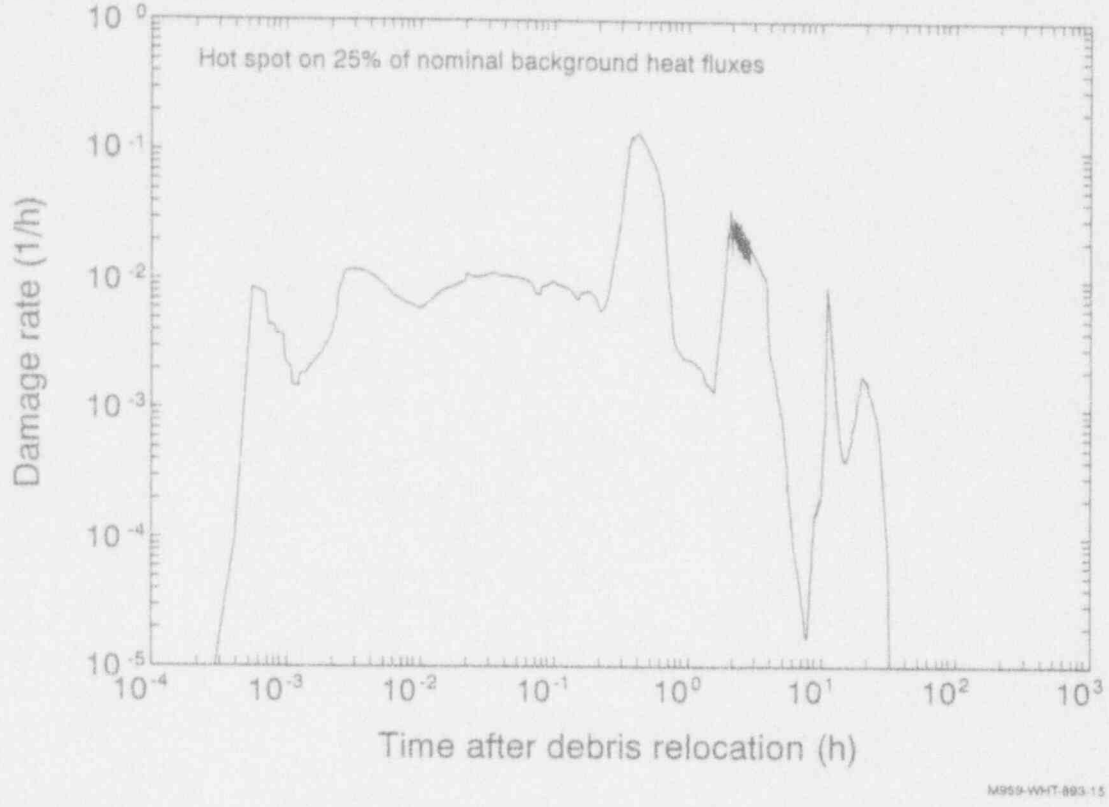

(a) Damage rate

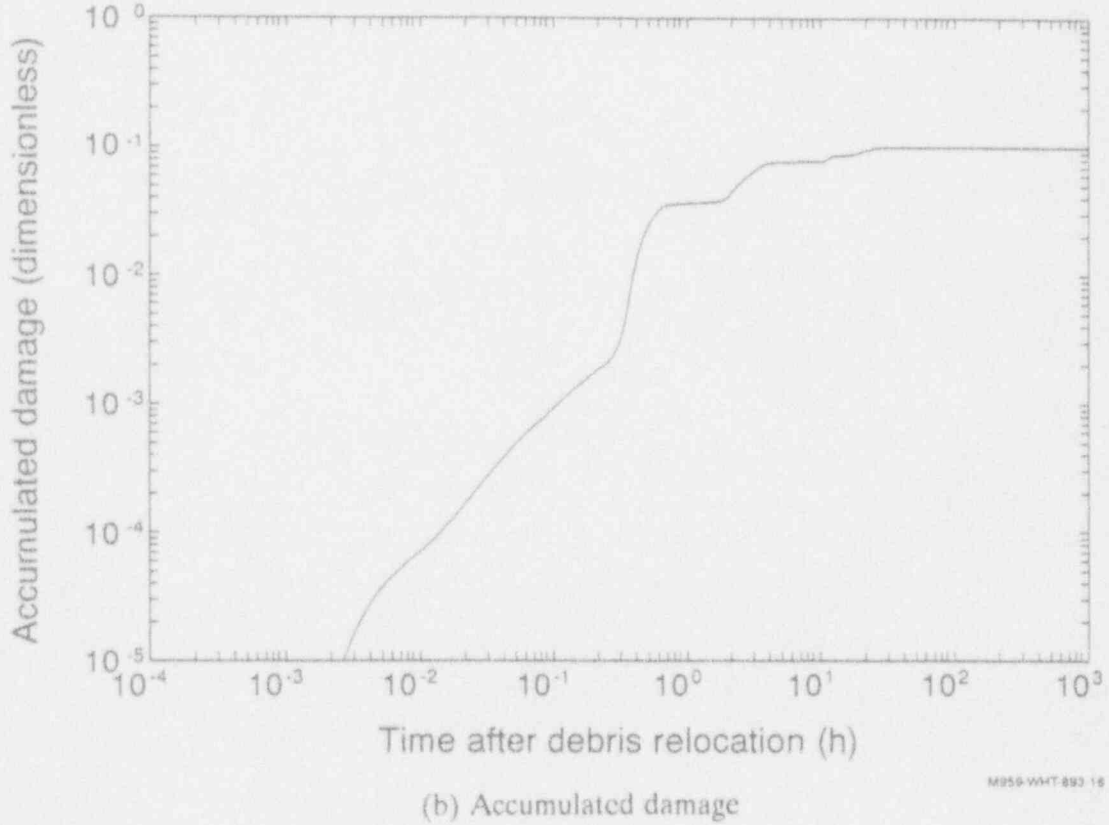

(b) Accumulated damage

Figure 5-5. Results for case with hot spot on 25% of nominal background heat fluxes.

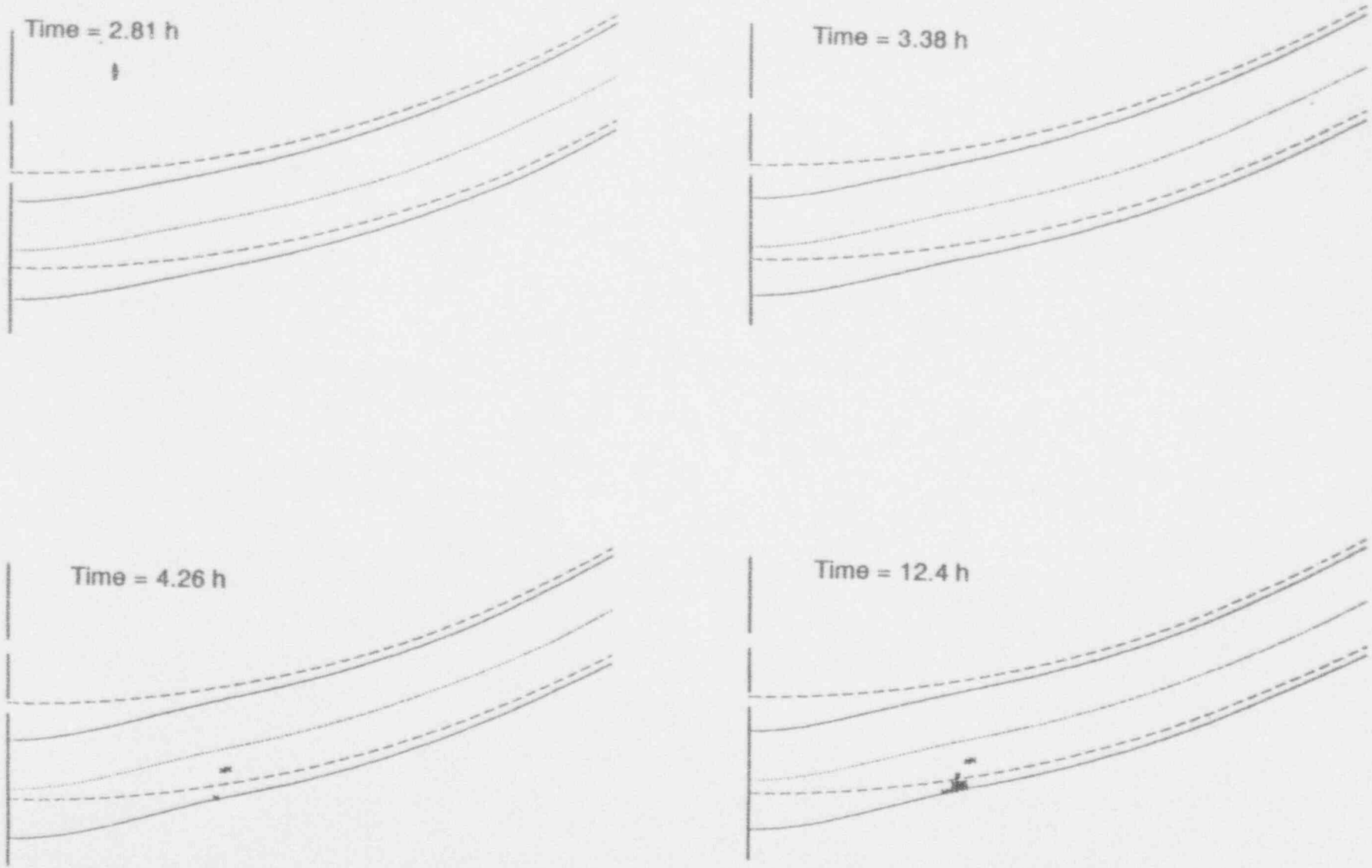

Figure 5-6. Distribution of 100% damaged ligaments at various times for the hot spot on 25% of nominal background heat fluxes.

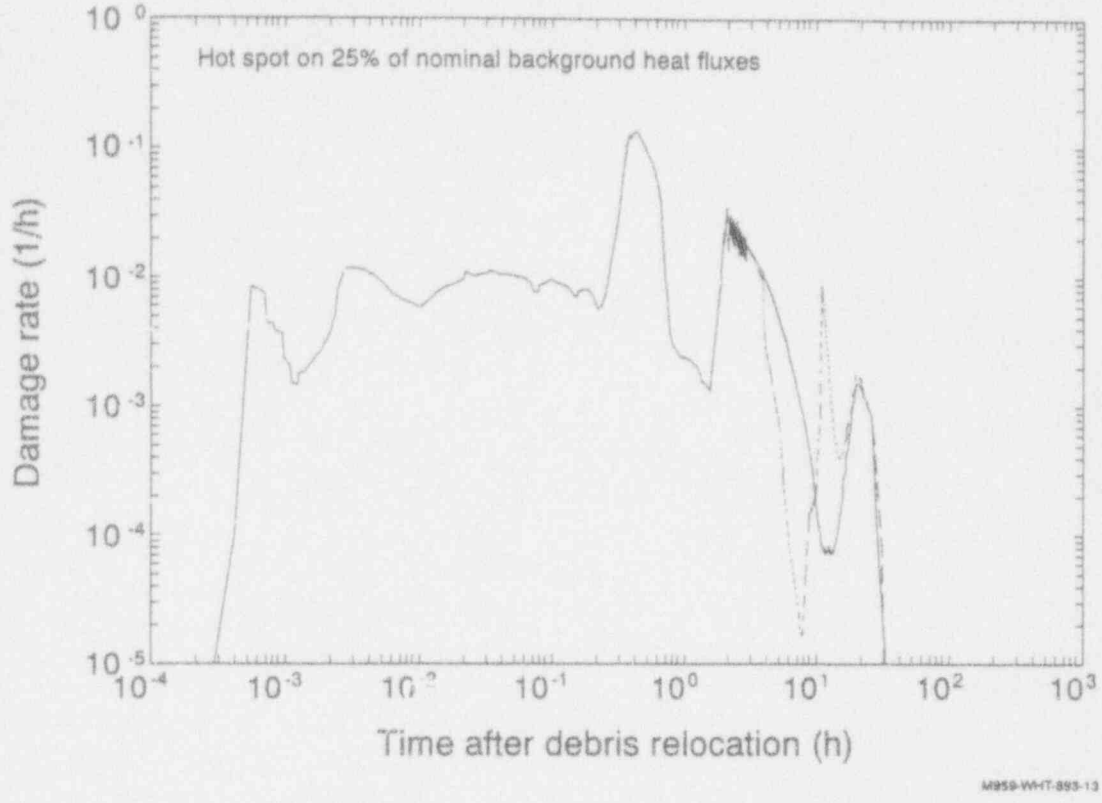

a) Damage rate

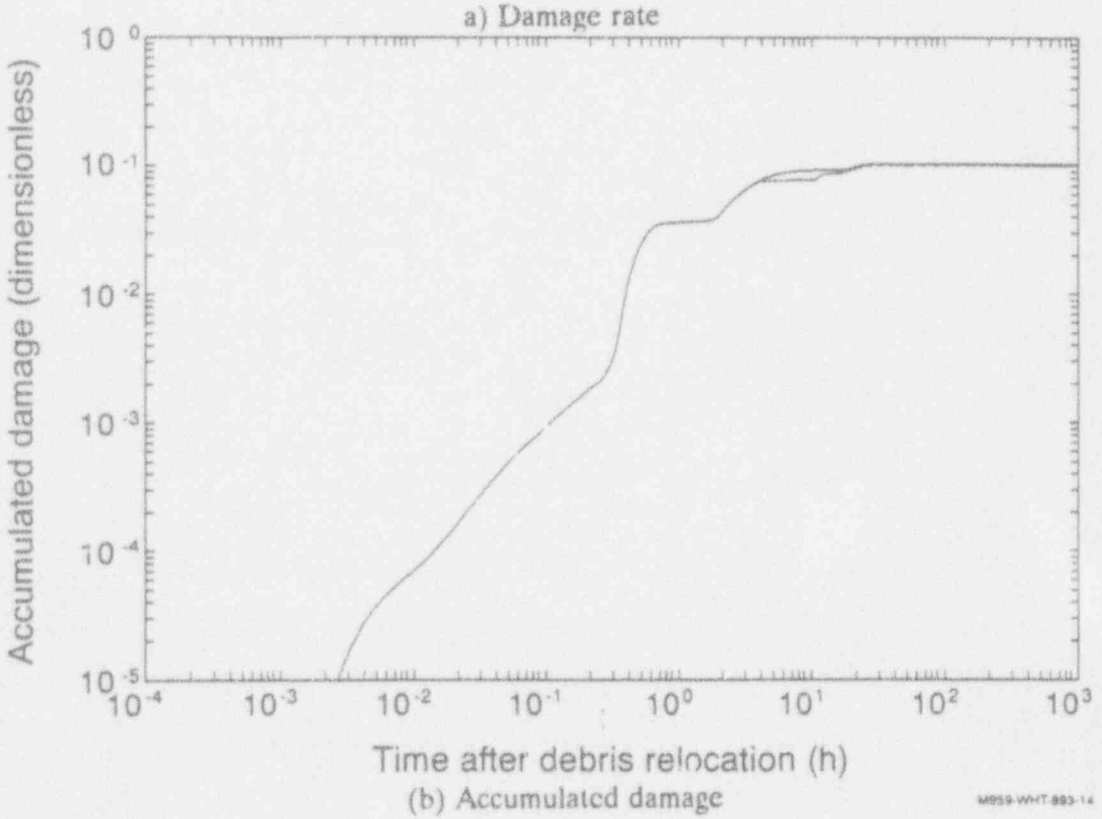

(b) Accumulated damage

Figure 5-7. Results for case with hot spot on 25% of nominal background heat fluxes when pressure depression is absent.

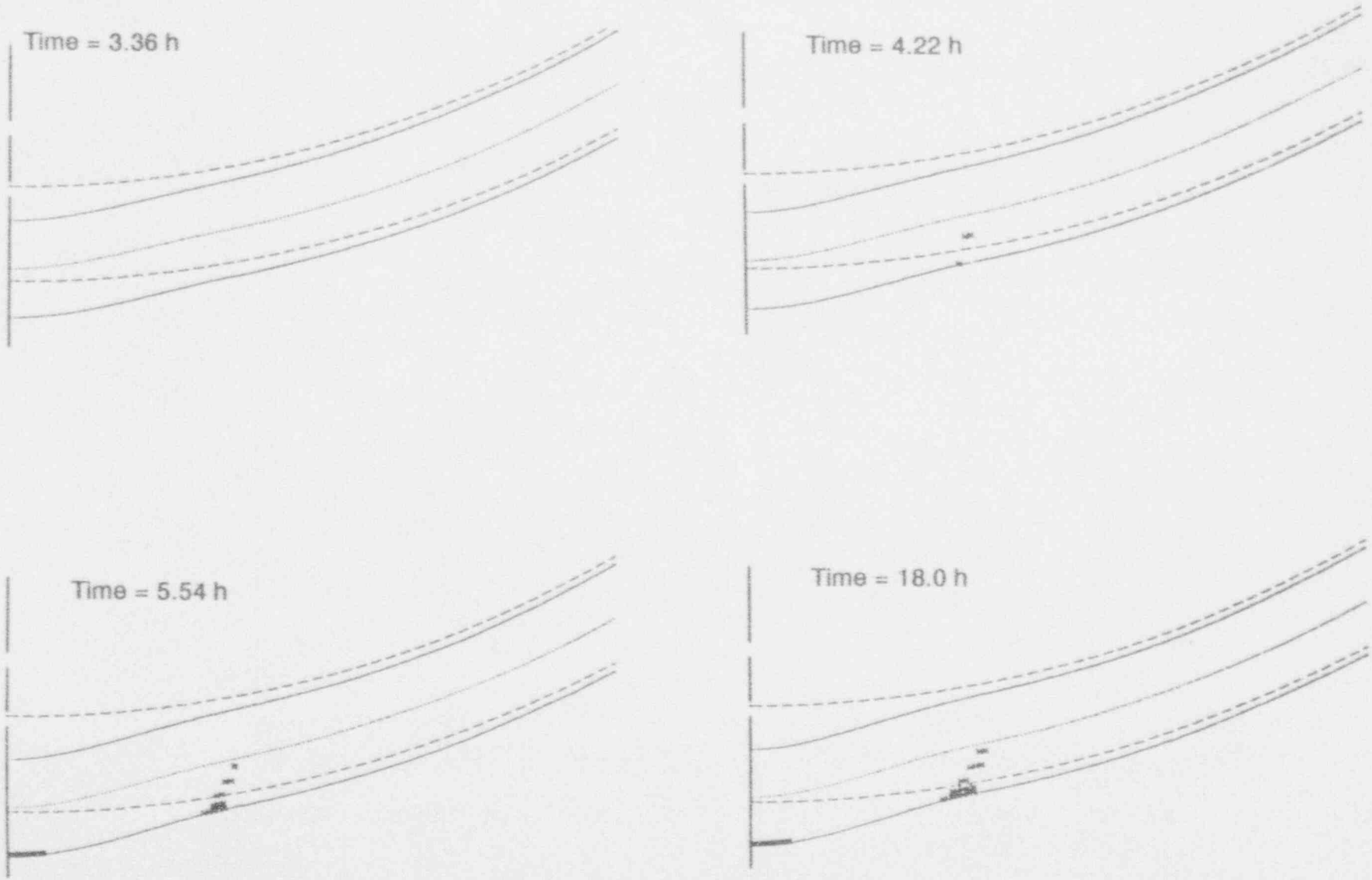

Figure 5-8. Change in damage distribution when pressure depression is absent.

rate. The dashed line in the plot represents the case with the pressure drop. Damage falls more gradually when the pressure is held constant, but there is also no peak following the dip because of the absence of repressurization. The two damage rates become nearly identical again during the later stages of cooling. The net result is a negligible difference in accumulated damage at the end of the transient. Figure 5-8 indicates that the shear failure mechanism propagates further into the interior of the vessel when the pressure is fixed. However, the vessel is still predicted to survive.

The drop in the pressure history is more significant for the case of a hot spot on 33% of nominal background heat fluxes because the vessel is close to failure 4 hours after the relocation when the drop occurs. Figures 5-9 through 5-11 provide a representative temperature contour plot, damage rate and vessel deformation and damage distribution to complement Figures 5-1 through 5-3 for the 50% of nominal case and Figures 5-4 through 5-6 for the 25% of nominal case. The plot in Figure 5-10 is enlightening in that the damage rate appears to be increasing during the half hour prior to the pressure drop. This ordinarily suggests the vessel is approaching failure. The drop in pressure permits the vessel to last about another 2 hours before failure occurs. The damage distribution in Figure 5-11 indicates that the shear failure mode has successfully penetrated most of the shell by 5.2 hours after relocation, and only the low pressure level allows the vessel to survive another hour. On the basis of these simulations, the vessel is predicted to be capable of surviving a hot spot when the background heat flux is below a threshold level between 25% and 33% of its nominal value.

5.1.2 Rapid Cooling Analysis

Metallurgical evidence suggests the hot spot may have experienced rapid cooling after reaching temperatures in excess of 1,320 K.[1] Cooling rates cited are in the range of 10–100 K/min in the temperature interval 1,000–1,100 K at times between 15-50 minutes after the hot spot reached 1,320 K. Under these conditions, the vessel would be capable of surviving a hot spot on a higher background heat flux than the maximum heat fluxes calculated for cases only experiencing slow cooling. The purpose of this subsection is to quantify the level of background heat flux, as a percentage of nominal, the vessel could sustain without failing and compare it with maximum allowable heat fluxes calculated for slow cooling cases. Although there are uncertainties in both the timing and the rate of cooling, it was decided to fix the timing so that rapid cooling is initiated 30 minutes after the vessel reaches 1,320 K. In the results presented below, this corresponds to about 2.17 hours after the relocation. Two different rapid cooling rates, 10 K/min and 50 K/min, were selected to investigate the sensitivity of the response to the cooling rate.

A major difference between rapid and slow cooling calculations lies in the thermal boundary conditions applied to the shell to achieve the desired cooling rates. The simplest boundary condition to implement is a step change in time, in the hot spot region, from the hot spot heat flux to the background heat flux. Results from one such analysis are discussed below, but this boundary condition was found to be unacceptable because it did not produce high enough cooling rates in the temperature range of interest. It is important to keep in mind that the vessel temperature must fall 220 K from its peak value before it enters the transition temperature range (the range in which the inferred cooling rates were observed). When the heat flux is suddenly lowered from peak to background values in the hot spot region, the cooling rate is initially very

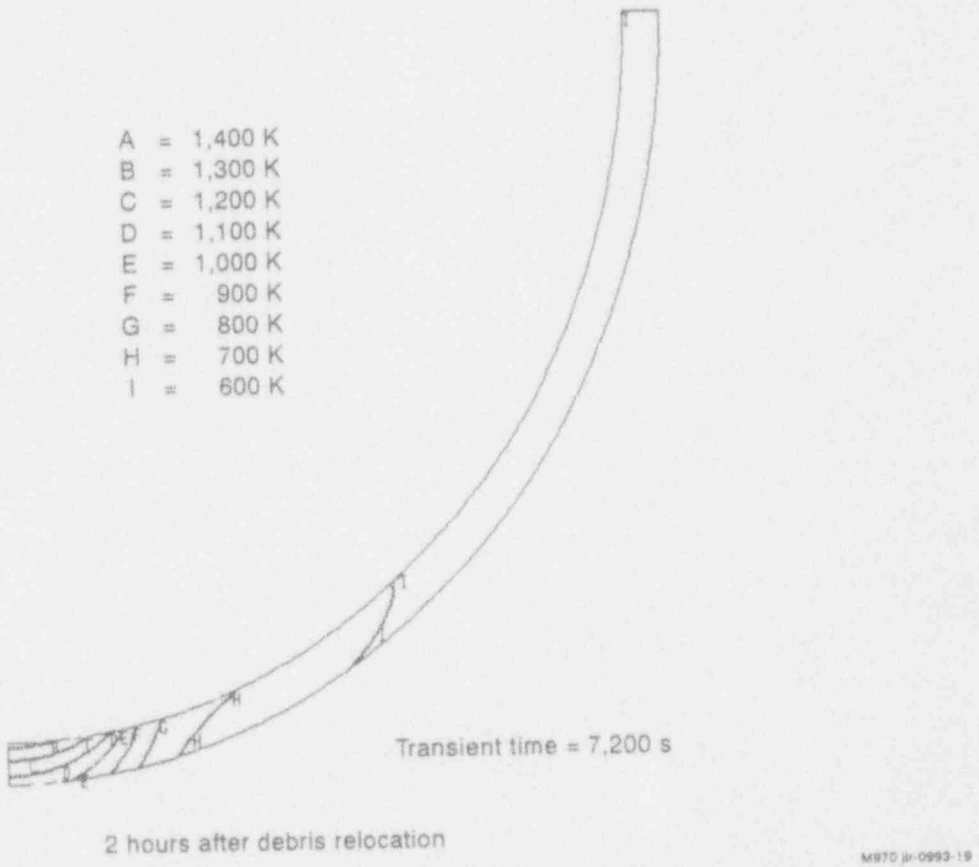

Figure 5-9. Temperature distribution of hot spot on 33% of nominal background heat fluxes.

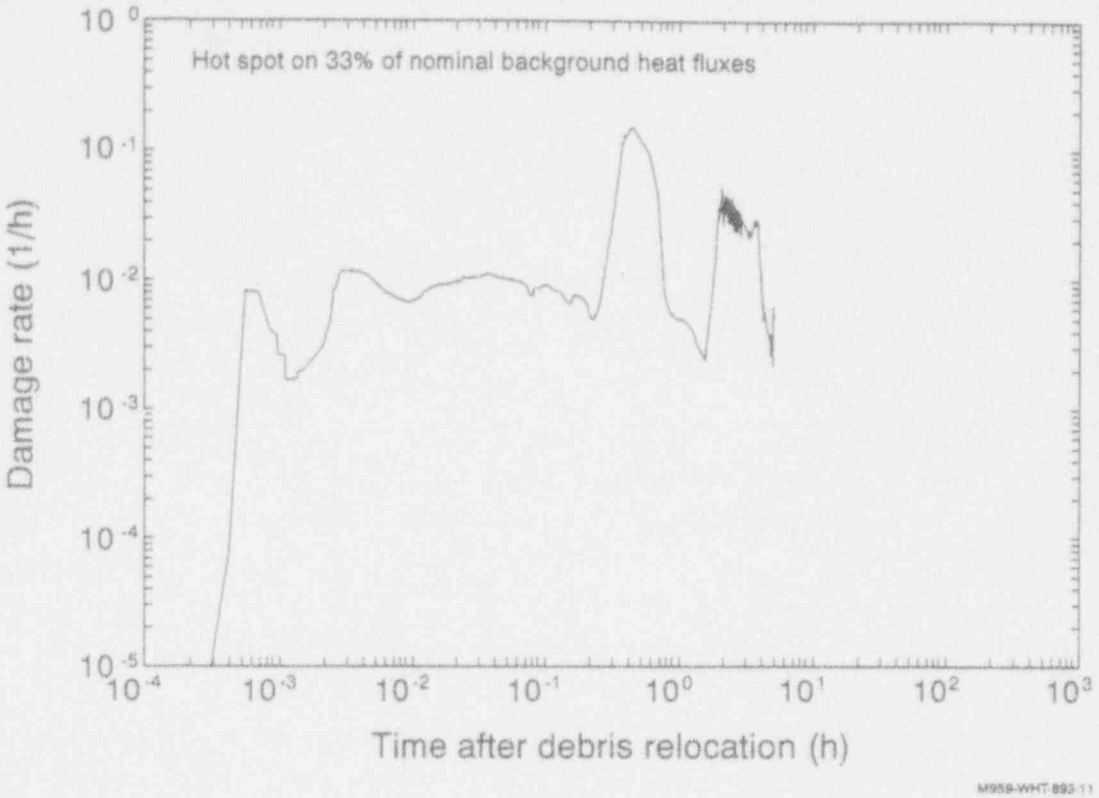

a) Damage rate

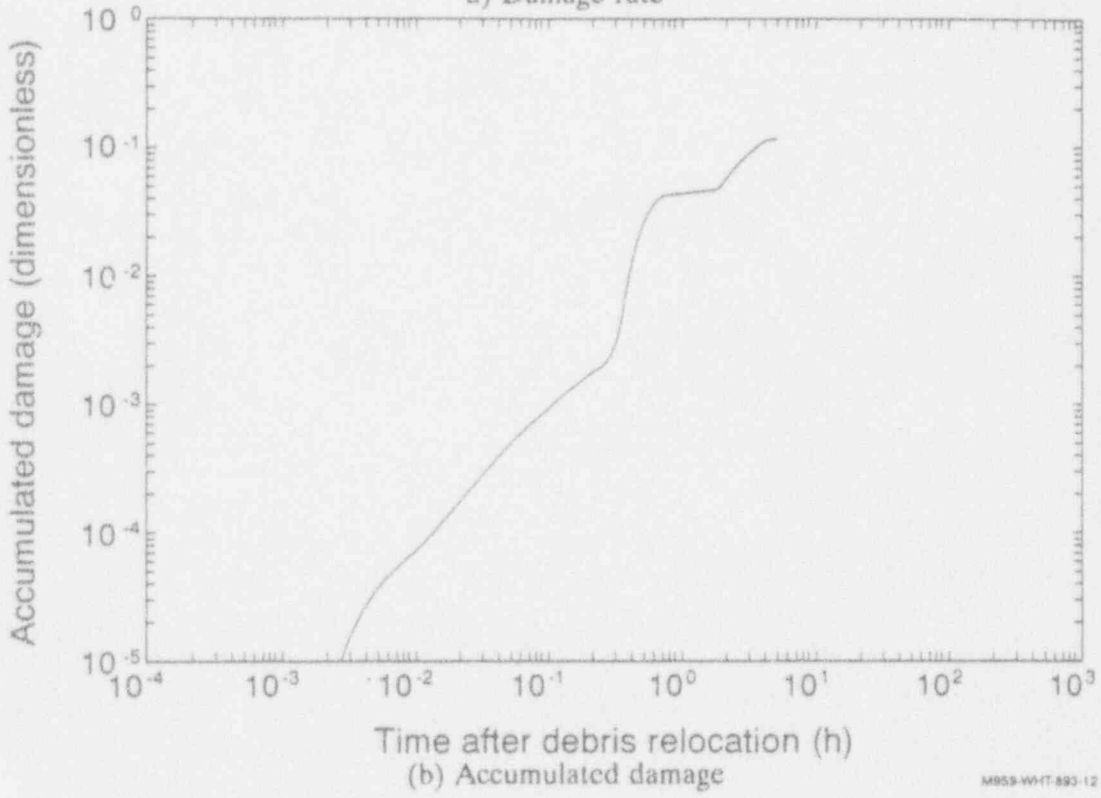

(b) Accumulated damage

Figure 5-10. Results for case with hot spot on 33% of nominal background heat fluxes.

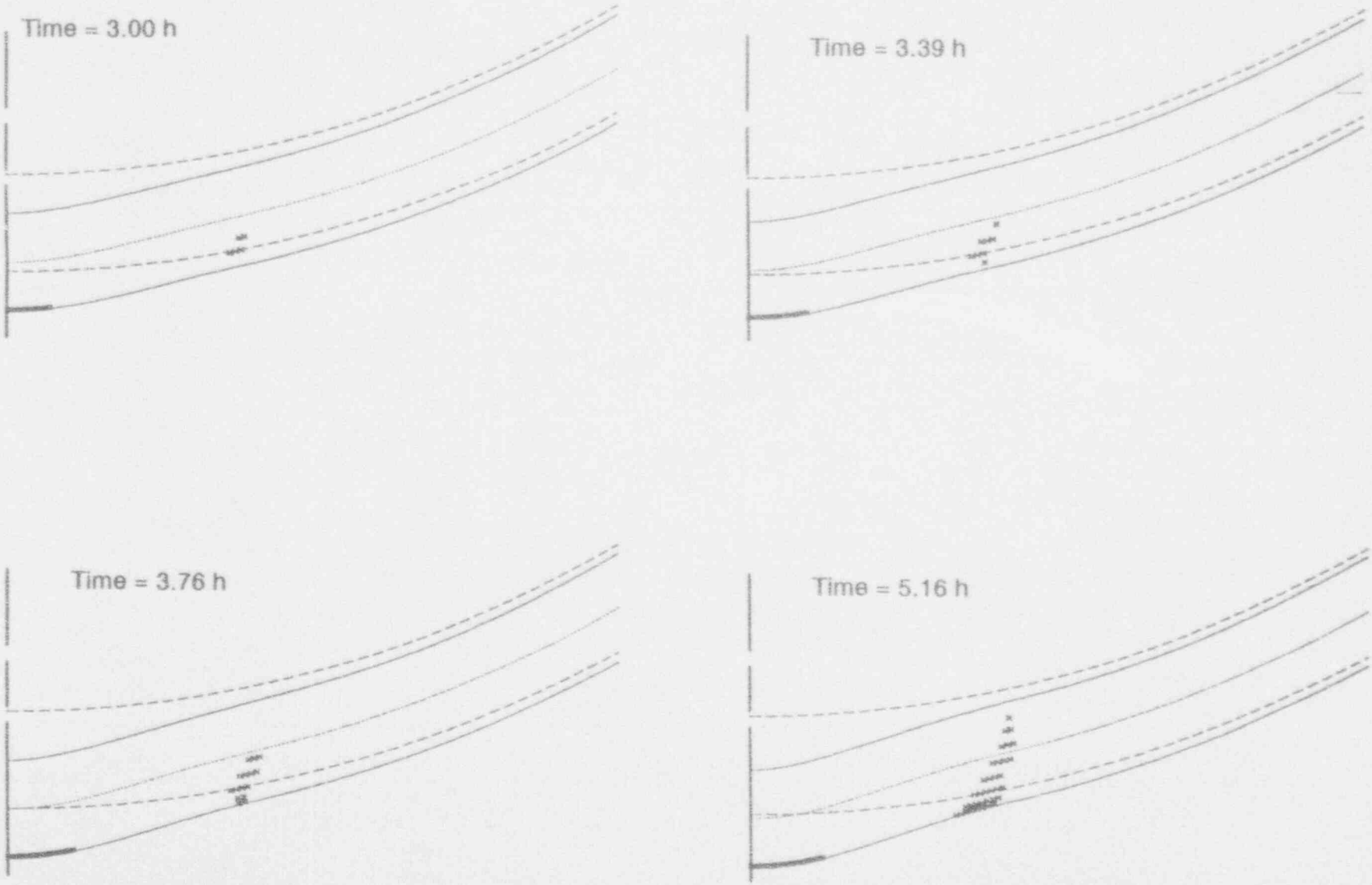

Figure 5-11. Distribution of 100% damaged ligaments at various times for the hot spot on 33% of nominal background heat fluxes.

rapid, but by the time the temperature reaches 1,100 K, the cooling rate is only 6–7 K/min. Several sets of boundary conditions were attempted to obtain the observed cooling rates. No variations of the step change boundary condition successfully achieved the minimum value. Results indicate that, in order to reach the inferred cooling rates, heat must flow from the vessel to some combination of water and debris on the inner surface. The inner surface heat flux in the hot spot region must therefore change sign during the transient, eventually returning to modest positive values as the temperature difference between the steel and the water/debris on the inner surface diminishes. Physically, this type of cooling implies that the vessel and debris rapidly cool during the time period that the heat flux is negative because heat is being transferred to water as it penetrates through gaps between the vessel inner surface and the debris. At later times, the vessel temperature is slightly cooler than the debris because the debris contains some decay heat. Hence, the heat flux is again positive because some heat is transferred to the vessel.

The heat flux history used in the hot spot region is illustrated in Figure 5-12. At approximately 2.17 hours after the relocation, the hot spot has been above 1,320 K for 30 minutes. The heat flux is then decreased linearly (quenched) to a negative value over a period of 500 seconds, the magnitude of the negative value depending on the cooling rate desired. The choice of a 500 second time interval is arbitrary; it was selected to avoid the need for extremely small time steps during the change. The negative heat flux is applied until the inner surface falls below 1,000 K. Shortly thereafter, usually when the inner surface temperature has fallen to 800–900 K, the negative heat flux is returned to the positive background level over another 500-second interval, and the transient is allowed to proceed as the background level decays until temperatures reach benign values. Figure 5-13 shows the temperature history of the inner surface following "quench" from a hot spot on 33% of nominal background. The solid line represents a case with a 10°C/min cooling rate, and the dashed line represents a case with a 100°C/min cooling rate. An inadvertent consequence of the simplistic heat flux history in Figure 5-12 is the temperature rise following the transition back to positive background values. This is not likely to occur, but it seems to be of no consequence in the structural analysis. Contour plots of the temperature distribution in the lower head are shown in Figures 5-14 (a) through 5-14 (h) corresponding to 0, 200, 400, 600, 800, 1,000, 1,500, and 2,000 seconds after initiation of rapid quench for the 50 K/min cooling case initiated from 33% of nominal background. The plots illustrate that heat flows from the vessel to both the ambient atmosphere on the outer surface and the water/debris on the inner surface.

Structural implications of rapid cooling are presented for four cases corresponding to cooling rates of 10 and 50 K/min initiated from hot spots on 33% and 50% of nominal background heat flux. The negative values of heat flux in the hot spot required to obtain these rates were 25 and 125 kW/m^2, respectively. Figure 5-15 shows damage rates and accumulated damage for three cooling histories from the 33% nominal case. The solid line represents damage following asymptotic cooling associated with the step change. The dotted and dashed lines represent the 10 and 50 K/min cooling rates, respectively. The plots show that more damage is accumulated earlier for the more rapid cooling rates. This follows from the higher tensile states that evolve during the more rapid cooling transients; there is less time for the tensile states to relax (creep) in the more rapid cooling cases, so that tensile states are sustained at higher levels. Given the larger damage that occurs in tension using the Huddleston stress measure, the damage rates are higher. Results from this case in which rapid cooling is imposed on the hot spot with 33% of nominal heat fluxes did not differ significantly, however, because there are no ligament failures anywhere

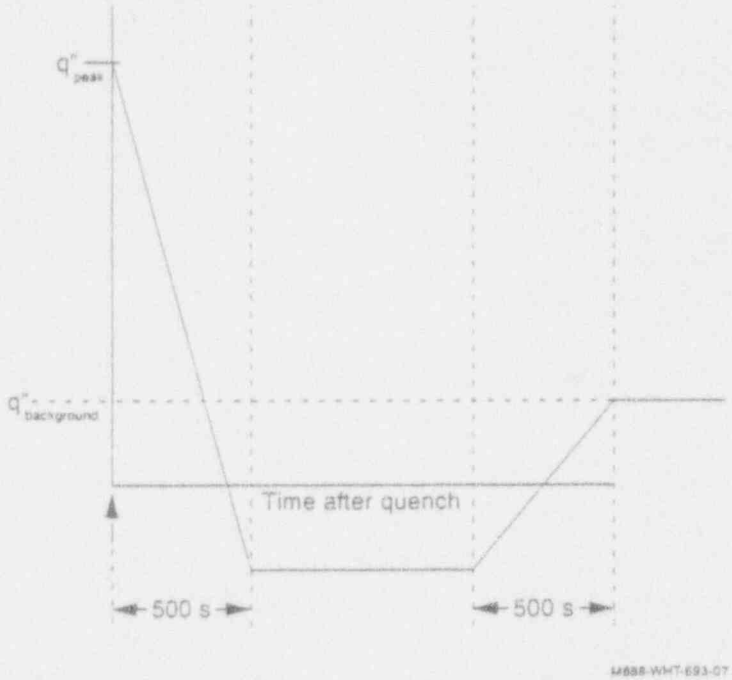

Figure 5-12. Heat flux history in hot spot region for rapid cooling cases.

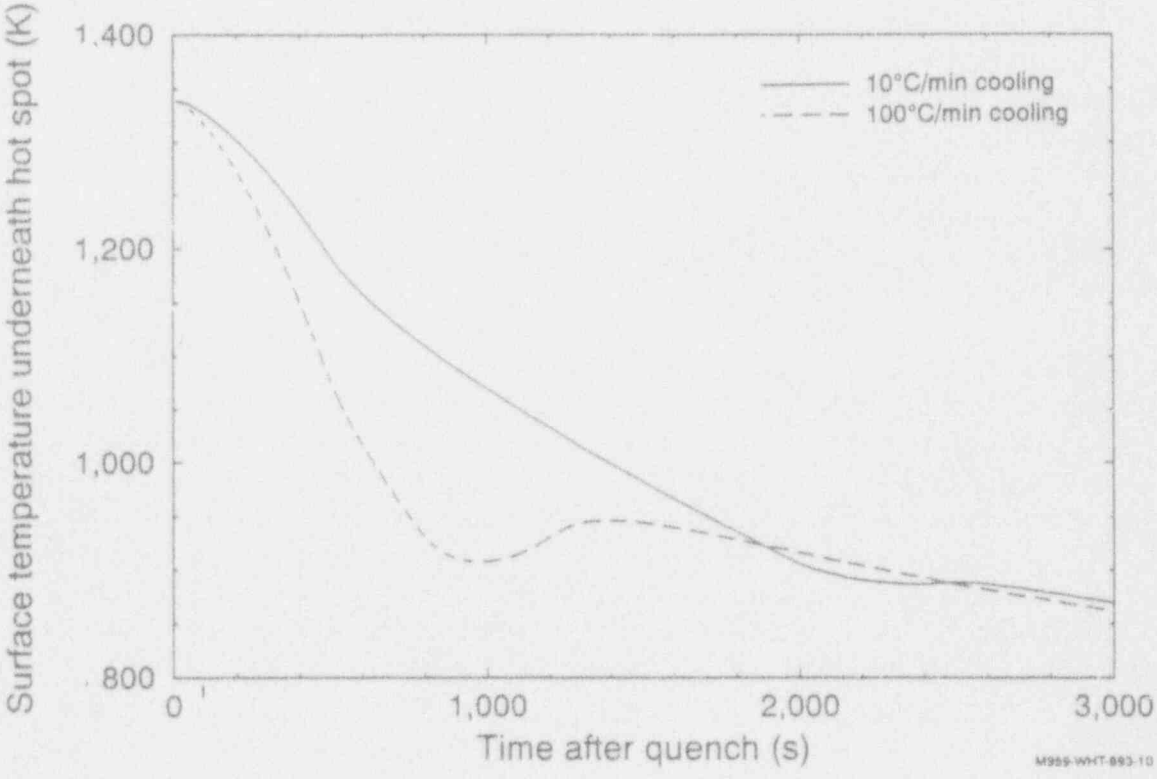

Figure 5-13. Surface temperature underneath hot spot following initiation of rapid cooling.

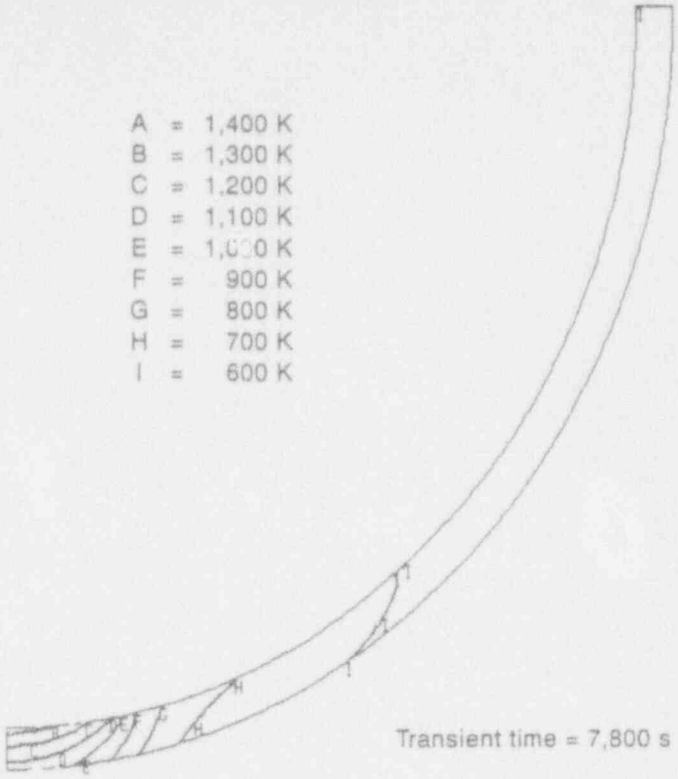

(a)

M970 jlr-0993-20

(a) 7,800 seconds into the transient

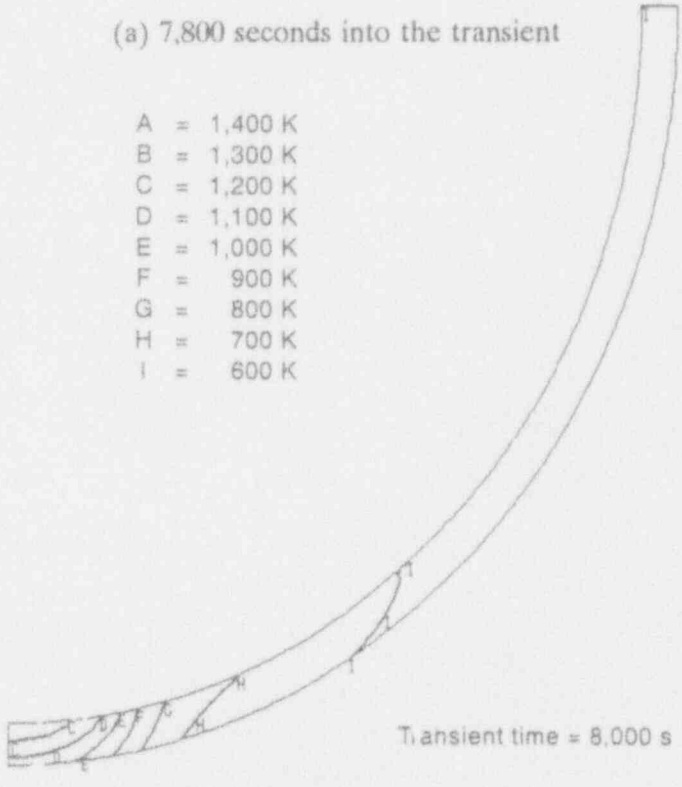

(b)

M970 jlr-0993-21

(b) 8,000 seconds into the transient

Figure 5-14. Evolution of temperature profile in vessel following initiation of rapid cooling.

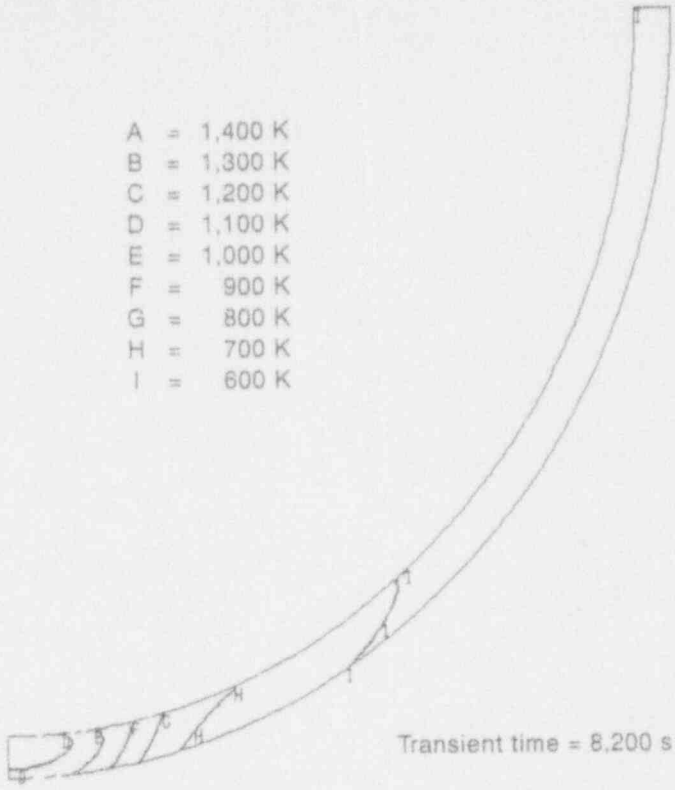

(c)

M970 jlr-0993-22

(c) 8,200 seconds into the transient

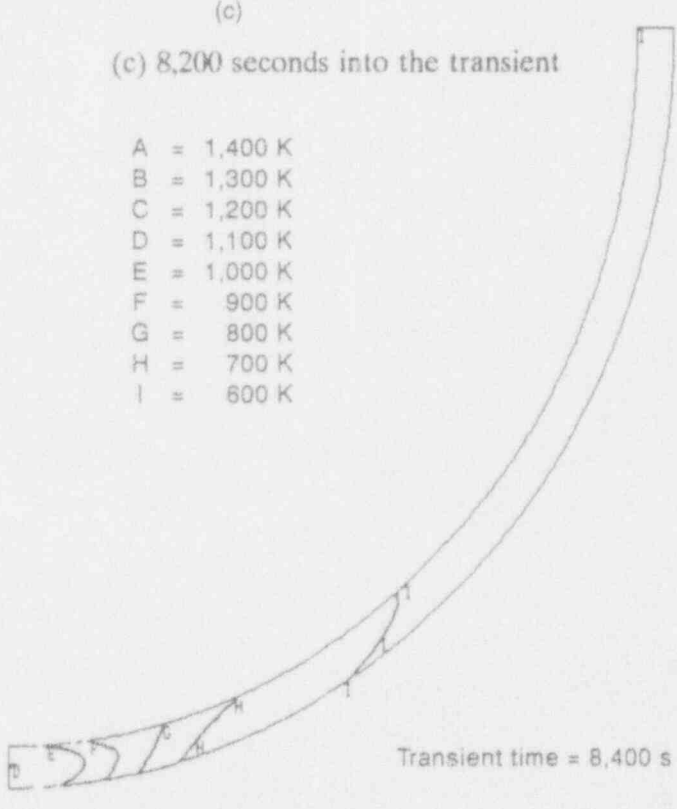

(d)

M970 jlr-0993-23

(d) 8,400 seconds into the transient

Figure 5-14. (continued).

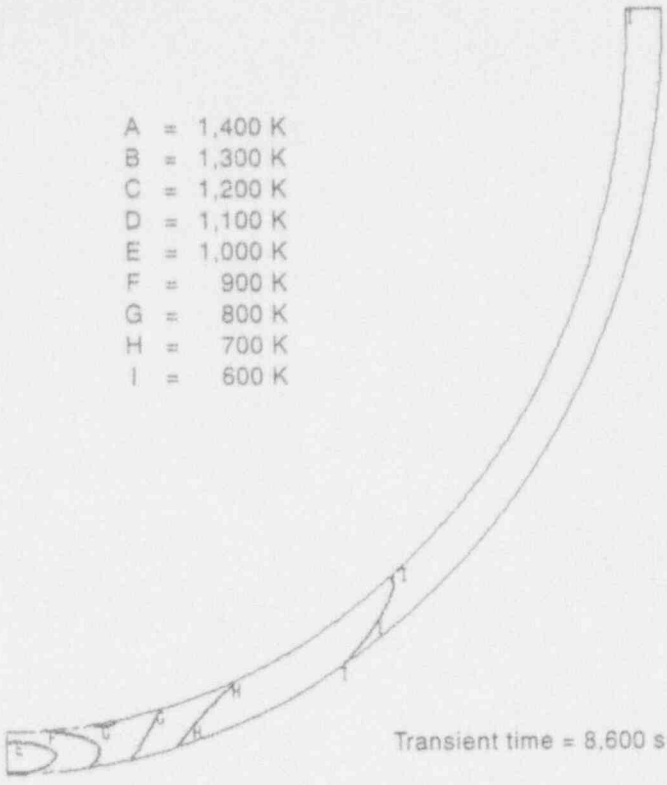

(e)

M970 jlr-0993-24

(e) 8,600 seconds into the transient

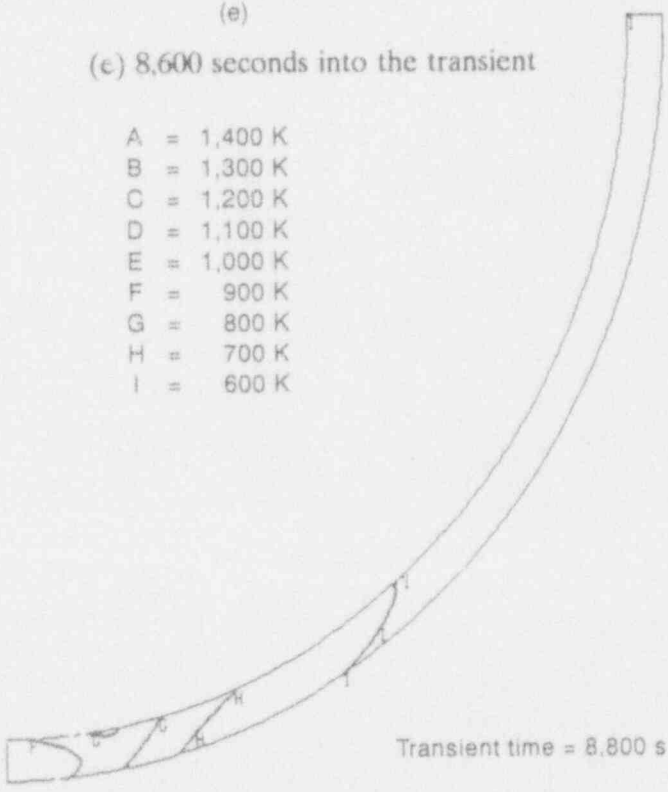

(f)

M970 jlr-0993-25

(f) 8,800 seconds into the transient

Figure 5-14. (continued).

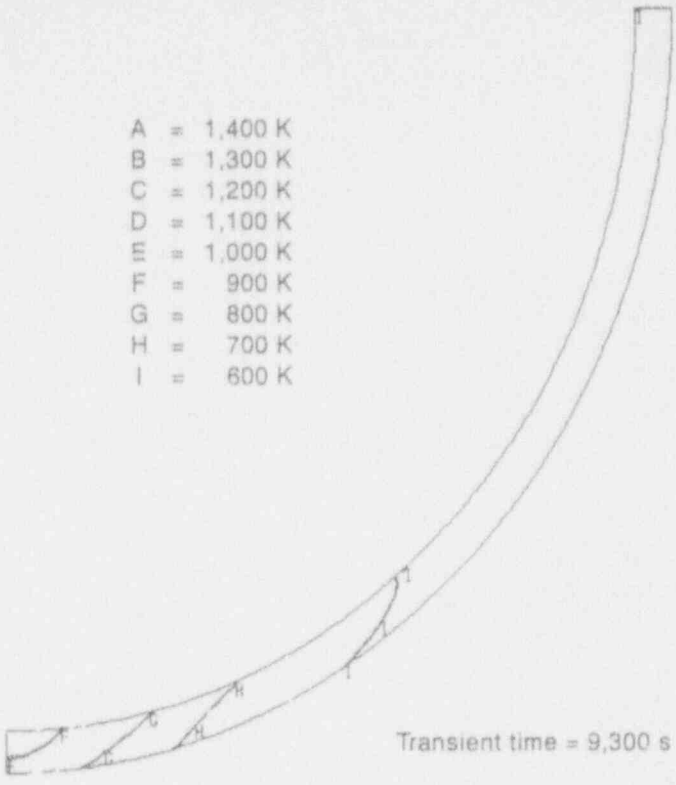

(g)

M970 jlr-0993-26

(g) 9,300 seconds into the transient

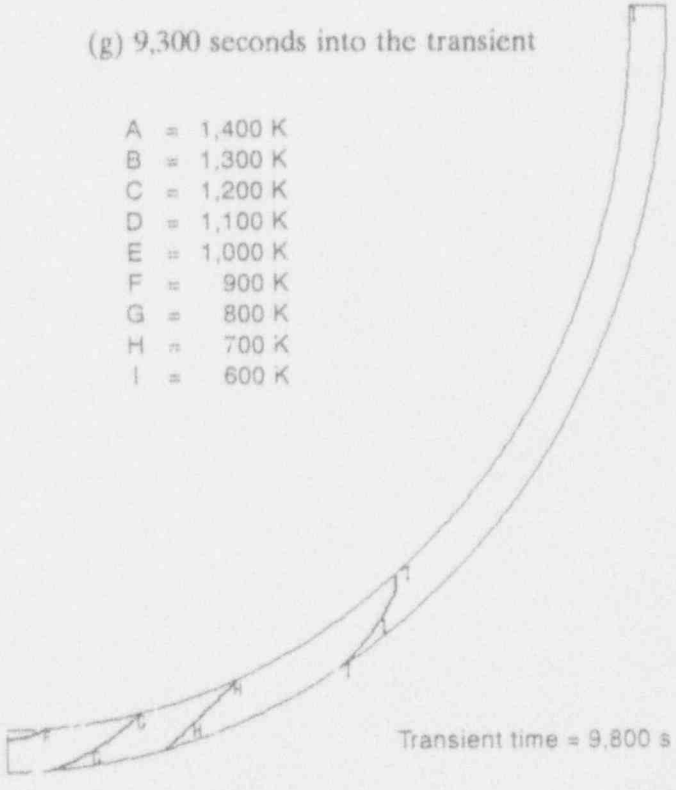

(h)

M970 jlr-0993-27

(h) 9,800 seconds into the transient

Figure 5-14. (continued).

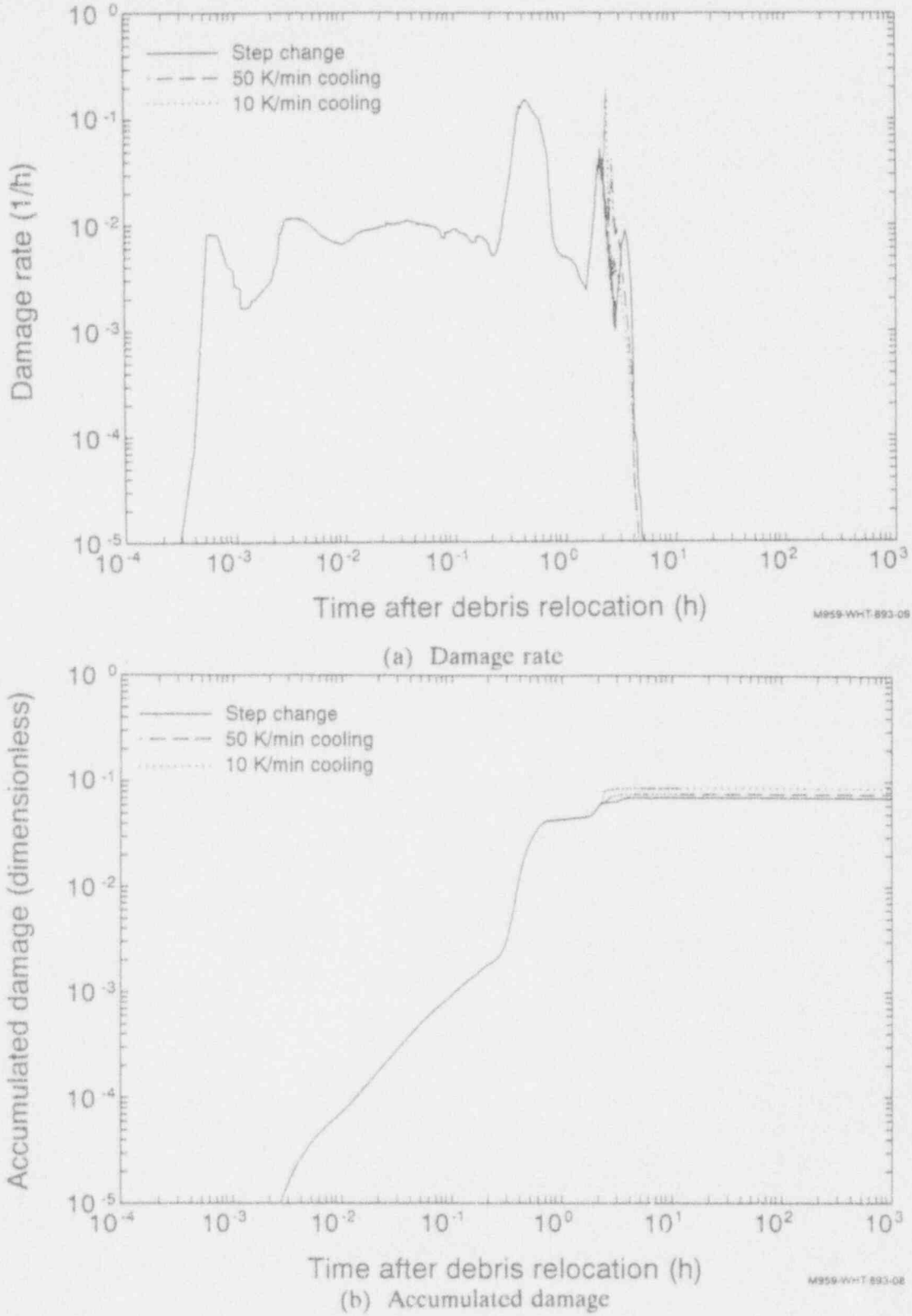

Figure 5-15. Results for case with rapid cooling of hot spot on 33% of nominal background heat fluxes.

in the vessel in either case. Figure 5-16 shows damage rate and accumulated damage for 10 K/min (solid) and 50 K/min (dashed) cooling from a hot spot on 50% of nominal. The damage rates are above those in Figure 5-15, and the vessel experiences some ligament damage before and after cooling, as shown in Figure 5-17; but the vessel again survives. There is little difference between ligament failure distributions in the two different cooling rate cases, suggesting that the magnitude of the cooling does not significantly impact structural results. It appears that the vessel would have to be very close to failure before rapid cooling is initiated in order for the cooling rate to prevent vessel failure.

Simulations were also run for a hot spot on 75% of the nominal heat flux, but these simulations predict vessel failure in a little over 2 hours. The vessel does not survive the required 2.17 hours preceding initiation of rapid cooling. Thus, it appears that the vessel is capable of surviving a hot spot on 60–65% of the nominal background heat flux when rapid cooling is initiated. As discussed above, the precise value of the percentage of the nominal heat flux is sensitive to the timing at which cooling is initiated, as the majority of the damage accumulates just before rapid cooling occurs. As a rough measure, however, it appears the vessel is capable of sustaining a hot spot with twice the background heat flux in the presence of rapid cooling compared with the same conditions with slow cooling.

5.1.3 Debris Configurations to Obtain Required Cooling Rates

Results in Section 5.1.1 indicate that the vessel thermal and structural response would be consistent with metallurgical examinations if both rapid and slow cooling mechanisms were present in the debris. Although results are dependent on the time at which rapid cooling is initiated, calculations indicate that the heat load from the debris must be reduced to somewhere between 50 and 75% of the nominal case values to simulate the required amount of slow cooling and that cooling heat fluxes between 25 and 125 kW/m^2 are needed to simulate the required amount of rapid cooling. Although there are insufficient data to quantitavely determine the exact mechanisms that caused this amount of cooling, this section documents results from scoping calculations that were performed to investigate some possible mechanisms that could provide this cooling.

5.1.3.1 Methodology. Estimating the number and size of debris cracks and the size of a debris-to-vessel gap requires many assumptions related to debris properties and heat transfer parameters. The large uncertainty in debris parameters was treated by estimating upper and lower bounds for each parameter. Results were then obtained by propagating upper and lower-bound estimates. Results in Section 5.1.1 and 5.1.2 indicate that both rapid and slow cooling mechanisms were needed in order to be consistent with metallurgical examination data. Therefore, it is assumed that the simultaneous presence of gaps between the vessel and the debris and the presence of cracks within the debris provides multiple pathways for steam release (e.g., water may travel down along the gap and boil up through the cracks). Hence, these calculations do not consider steam blockage due to countercurrent flow.

There is little, if any, basis for many of the heat transfer parameters. Therefore, calculations were initially performed assuming that the coolant remains in a liquid state. Because single phase heat transfer from a liquid is lower than subcooled or saturated boiling heat transfer, these initial calculations provide estimates for debris configurations required with minimal heat transfer. As

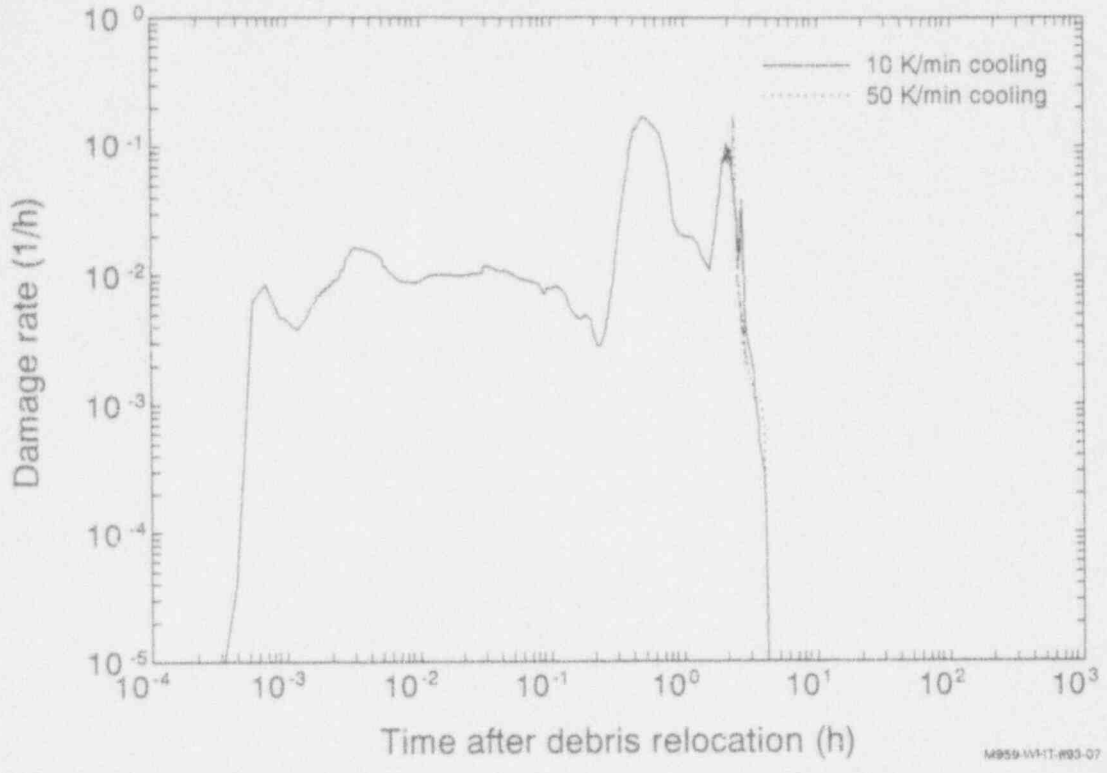

(a) Damage rate

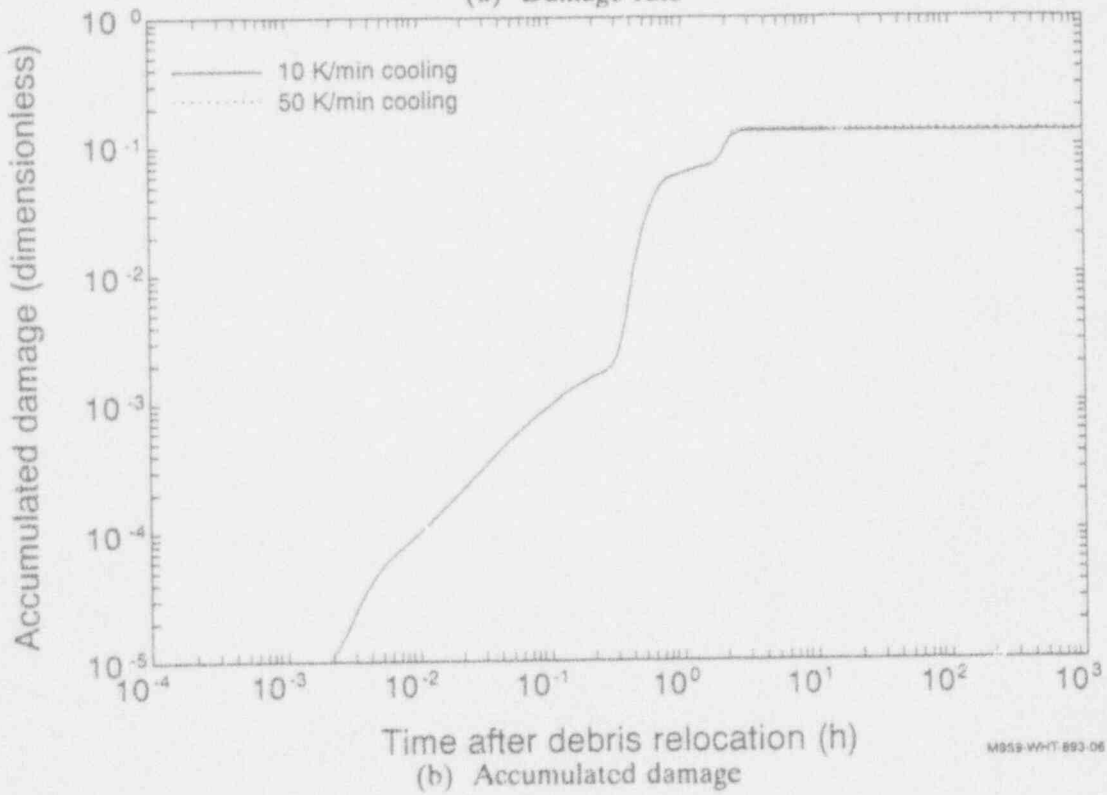

(b) Accumulated damage

Figure 5-16. Results for case with rapid cooling of hot spot on 50% of nominal background heat fluxes.

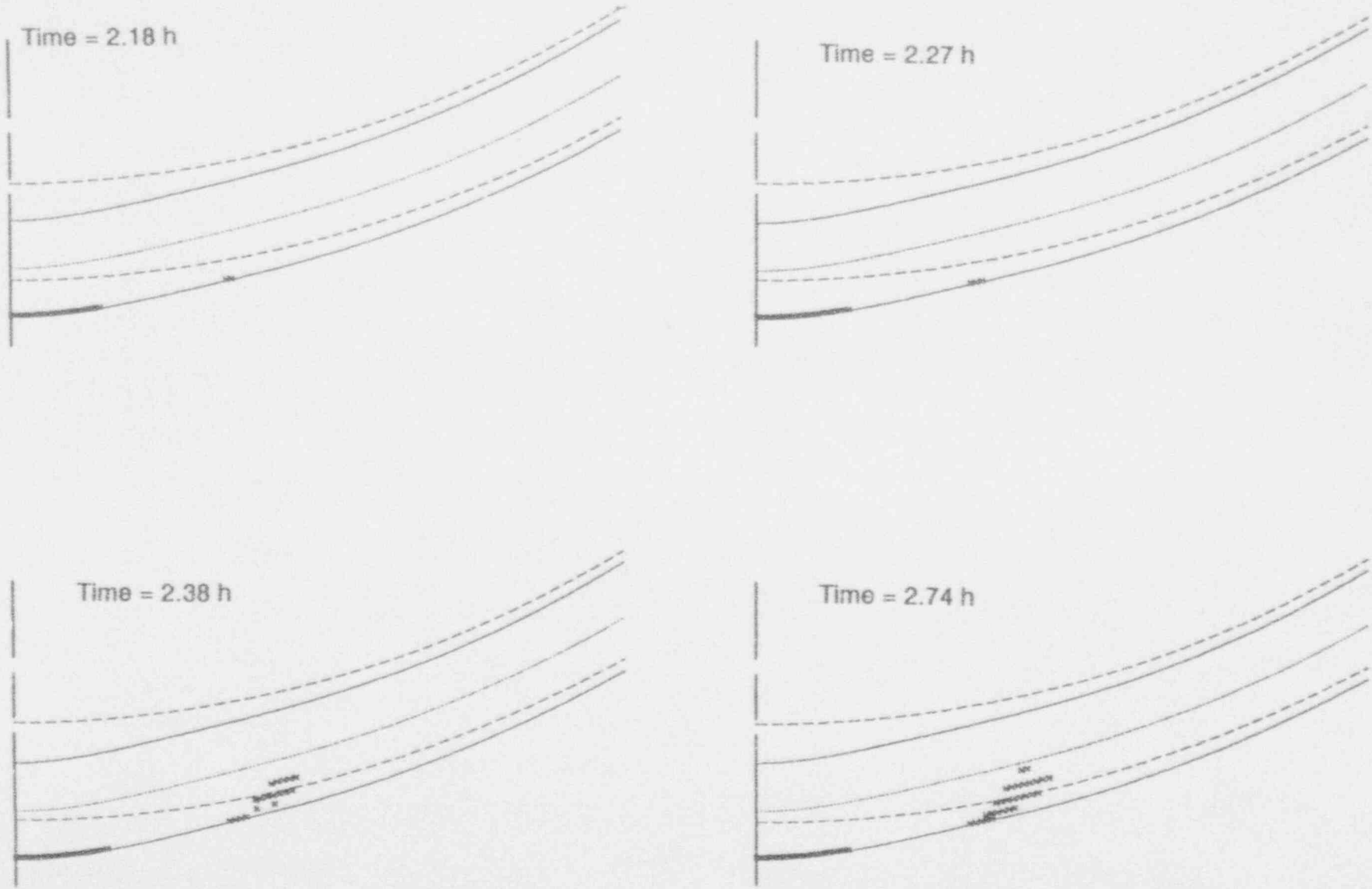

Figure 5-17. Distribution of 100% damaged ligaments at various times for rapid cooling of hot spot on 50% of nominal background heat fluxes.

will be shown in Section 5.1.3.2, results based upon this conservative heat transfer assumption indicate that debris configurations required for either of these mechanisms are reasonable. Hence, additional types of heat transfer, in which cooling is more efficient, were not investigated. Major assumptions used in both of these calculations are discussed below. Table 5-1 summarizes calculational input values.

Debris Mass and Geometry

Only the hard layer of debris was considered in these calculations because there is uncertainty about when the additional rubble on top of the hard layer relocated. As discussed in Section 3.2, the mass of this hard layer is estimated to be between 6,800 and 10,000 kg. Using properties for the 78% UO_2–17% ZrO_2 debris composition in Appendix A and assuming that the debris relocates to form a level pool in the hemispherical lower head (see Figure 5-18), the values listed in Table 5-1 for the height of the debris, z_{debris}, the radius of the debris on the upper surface, a, and the surface area of the debris facing the vessel, A_{down}, were estimated.

Debris Heat Flux to the Vessel

Results from Section 3.2 indicate that the average value of the heat flux from the debris downward to the vessel for the nominal case, q''_{nom}, is 70 kW/m^2. It is assumed that the upward heat flux to the coolant is not impacted by the addition of cracks in the debris or the presence of coolant in a gap between the vessel and the debris. Although it is recognized that the upward heat flux would also be impacted by these cooling mechanisms, there are insufficient data available to quantify this impact and it is not felt that this impact will affect the order-of-magnitude estimates being obtained from these calculations.

Initial and Final Coolant State

Because single phase heat transfer from a liquid is much lower than subcooled or saturated boiling heat transfer, initial calculations were performed by assuming that the coolant remains liquid as it is heated in a crack or in the debris-to-vessel gap. Cold leg temperature measurements indicate that the coolant temperatures varied from 400 to 520 K during the transient (see Figure 2-4). Hence, the coolant was subcooled when it entered the crack or gap (the temperature of 520 K occurred when the vessel pressure was above 10 MPa; hence the coolant was below the 10 MPa saturation temperature of 584 K). The coolant exit temperature was assumed to equal the saturation temperature at the reactor coolant system pressure (calculations considered pressures from 3 to 15 MPa, which is the range of pressures measured within the TMI-2 vessel during the accident).

Initial Debris Temperature

Companion sample examinations[4] indicate that the debris must have been at least 2,870 K in the core prior to relocation. Although it is recognized that the debris may have been significantly cooler when it arrived at the lower head, this value was used as an upper bound in these calculations. A lower-bound debris temperature of 1,000 K was selected. This value is consistent with readings from reformed thermocouple junctions embedded in the debris for up to three days after the accident (see Section 2.1.5).

Table 5-1. Summary of input assumptions for enhanced cooling calculations.

Parameter	Symbol	Lower bound	Upper bound
Debris mass in hard layer, kg	M_d	6,800	10,000
Debris height in hard layer, m	z_{debris}	0.34	0.42
Radius of debris on upper surface of hard layer, m	a	1.2	1.3
Surface area of debris facing vessel, m^2	A_{down}	4.8	5.8
Crack effective diameter, m	D_e	0.005	NA[a]
Crack length, m	z_{crack}	z_{debris}[b]	NA
Debris-to-vessel gap thickness, m	t_{gap}	0.001	NA
Coolant inlet temperature, K	T_{in}	400	520
Coolant exit temperature, K	T_{out}	T_{sat}[c]	T_{sat}
RCS pressure, MPa	P_{RCS}	3.0	15.0
Initial debris temperature, K	T_{debris}	1,000	2,870

a. Only lower-bound estimates for crack and gap geometries were considered in calculations.

b. A lower bound for a "through crack" length corresponds to the debris height.

c. The coolant exit temperature was set equal to the saturation temperature for the pressure assumed.

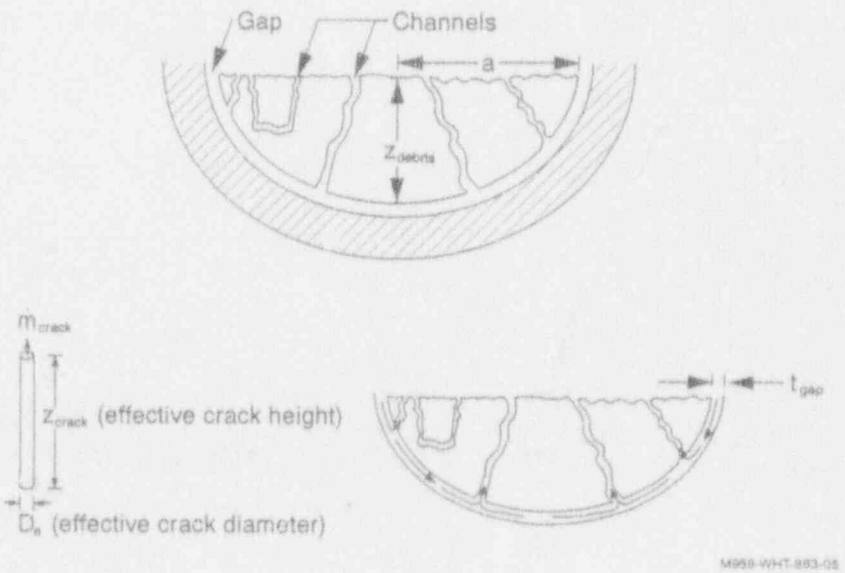

Figure 5-18. Debris geometry for estimating crack and gap cooling.

Heat Transfer Conditions

Initial calculations were performed assuming that heat is only transferred via convection to a single phase coolant. Although it is expected that buoyancy effects would dominate convection, correlations for natural and forced convection of laminar and turbulent flow were considered.

Natural convection correlations are typically dependent upon parameters such as the Grashof number, *Gr*, and the Prandtl number, *Pr*, or their product, the Rayleigh number, *Ra*. These parameters are defined in Equations (5-1) through (5-3):

$$Gr = \frac{\rho_f^2 \, g \, \beta_f \left(T_{debris} - T_{bulk}\right) L_{char}^3}{\mu_f^2} \tag{5-1}$$

$$Pr = \frac{c_{pf} \mu_f}{k_f} \tag{5-2}$$

$$Ra = Gr \, Pr = \frac{\rho_f^2 \, c_{pf} \, g \, \beta_f \left(T_{debris} - T_{bulk}\right) L_{char}^3}{\mu_f \, k_f} \tag{5-3}$$

where

ρ = density (kg/m^3)

g = gravitational acceleration constant 9.8 (m/s^2)

β = thermal expansion coefficient (K^{-1})

T_{debris} = debris temperature (K)

T_{bulk} = bulk coolant temperature = $\frac{1}{2}\left(T_{in} + T_{sat}\right)$, K

L_{char} = characteristic length (m)

μ = viscosity (N-s/m^2)

c_p = specific heat capacity (J/kg-k)

k = thermal conductivity (W/m-k)

and the subscript, *f*, indicates that coolant properties are to be evaluated at the bulk coolant temperature.

Forced convection correlations are typically dependent upon the Prandtl number, which was defined above, and the Reynolds number, *Re*, which is given by

$$Re = \frac{\dot{m}\, L_{char}}{A_{flow}\, \mu_f} \tag{5-4}$$

where

A_{flow} = cross sectional flow area (m^2)

$\dot{m}$ = mass flow rate (kg/s).

In addition to the above assumptions, several additional assumptions were required that were specific to each calculation. These additional assumptions, along with the governing equations used in each calculation, are found in Sections 5.1.3.1.1 and 5.1.3.1.2.

5.1.3.1.1 Assumptions and Governing Equations for Estimating the Number of Cracks in the Debris—This section describes the method used to determine if coolant flowing through cracks within the debris could remove sufficient heat to prevent vessel failure. Calculations were initially performed assuming the presence of "through cracks" in the debris in conjunction with a gap between the debris and the vessel. Therefore, coolant is able to flow through the crack without any countercurrent flow considerations. Although it is expected that cracks would probably be rectangular and characterized by a depth, width, and height, these calculations modeled the cracks by considering an effective diameter, D_e, and a height, z_{crack} (see Figure 5-18).

Lower-bound crack dimensions were used in order to maximize the number of cracks needed to cool the debris. The effective diameter was initially assumed as 0.5 cm, which corresponds to a 0.2 cm by 1.0 cm rectangular shape. A minimum height for a "through crack" within the debris was estimated to be approximately twice the average height of the debris bed, which corresponds to the maximum debris bed height.

The number of cracks required to remove heat from the debris was estimated by applying the equation for conservation of energy in conjunction with appropriate equations for estimating the convective heat transfer coefficient from the debris to the coolant. As noted above, calculations were initially performed assuming that the coolant entered in a subcooled state and exited as saturated liquid. Although a smaller number of cracks could remove the required heat if the coolant is assumed to boil, the small number of cracks required to remove heat with this minimal heat transfer assumption indicates that no additional investigation is needed.

The governing equations used to estimate the number of cracks are summarized below. First, conservation of energy was applied:

$$q_{sink} = n\ h\ A_{crack}\left(T_{debris} - T_{bulk}\right) \tag{5-5}$$

where

n = number of cracks

h = convective heat transfer coefficient

A_{crack} = surface area in each crack with diameter, D_e, and length, z_{crack} (m^2)

= $\pi\ D_e\ z_{crack}$

and the total amount of heat removed by coolant flowing through the cracks, q_{sink}, is estimated based upon results in Section 5.1.1 using

$$q_{sink} \le 0.75\ q''_{nom}\ A_{down}\ . \tag{5-6}$$

The convective heat transfer coefficient, h, is dependent upon the mass and heat transfer conditions. Although it is expected that natural convection will dominate heat transfer, correlations for both natural and forced convection were considered. In forced convection cases, a Reynolds number was obtained based upon the mass flow rate of coolant through all the cracks, $\dot{m}_{tot}$:

$$\dot{m}_{tot} = \frac{q_{sink}}{(h_{sat} - h_{in})} = n\,\dot{m}_{crack} \tag{5-7}$$

where

h_{in} = coolant inlet enthalpy (J/kg)

h_{sat} = saturated liquid enthalpy (J/kg).

For coolant flowing though isothermal channels in which natural convection dominates, Rohsenow[5] presents several correlations for various geometries that are valid for $Ra < 10^4$. For a cylindrical channel, Rohsenow[5] suggests that the following correlation based upon experimental data measurement and analyses[6,7] be applied:

$$h = \frac{2k_f}{D_e}\left[\left(\frac{Ra}{16}\right)^{-1.03} + \left(0.6\ Ra^{0.25}\right)^{-1.03}\right]^{-\frac{1}{1.03}} \tag{5-8}$$

For a rectangular channel with a 4-to-1 side ratio, Rohsenow[5] suggests

$$h = \frac{2k_f}{D_e}\left[\left(\frac{Ra}{18.7}\right)^{-1.5} + \left(0.6\ Ra^{0.25}\right)^{-1.5}\right]^{-\frac{1}{1.5}} \tag{5-9}$$

where the characteristic length parameter, L^3_{char}, used to evaluate the Rayleigh number in both of the above correlations is given by

$$L^3_{char} = \left(\frac{D_e}{2}\right)^3\left(\frac{D_e}{2\ z_{crack}}\right) \quad . \tag{5-10}$$

For laminar flow, a variety of theoretical relationships are available to model heat transfer under forced convection depending on the boundary conditions (constant surface heat flux or surface temperatures, developing velocity profile or fully developed flow, etc.). A list of correlations for laminar flow with fully developed velocity and temperature profiles through various cross sectional shapes with a constant heat flux is given in Todreas and Kazimi.[8] From this list, bounding geometries of a circular channel and a rectangular channel with an 8-to-1 side-length ratio were considered:

$$\begin{aligned} h &= 4.364\ \frac{k_f}{D_e} \quad \text{(for flow through a circular channel)} \\ h &= 6.60\ \frac{k_f}{D_e} \quad \text{(for flow through a rectangular channel with an 8-to-1 side ratio)} \ . \end{aligned} \tag{5-11}$$

The following empirical equation based on experimental data takes into account the effect of varying physical properties across a laminar flow stream and the influence of free convection[9]

$$h = 0.17\frac{k_f}{D_e}\left[Re_f\right]^{0.33}\left[Pr_f\right]^{0.43}\left[\frac{Pr_f}{Pr_w}\right]^{0.25}\left[Gr^*_f\right]^{0.1} \tag{5-12}$$

where the modified Grashof number, Gr^*, is evaluated by replacing the coolant density in Equation 5-1 with

$$\rho^*_f = \rho_f\left(1 - \beta_f\left(T_{debris} - T_{bulk}\right)\right) \quad . \tag{5-13}$$

The characteristic length for evaluating the Reynolds and modified Grashof numbers in Equation (5-12) is the crack effective diameter, D_e, and the subscript, w, on the Prandtl number

designates that the coolant should be evaluated at the debris surface temperature. This relationship is considered valid for $z_{crack}/D_e > 50$ and $Re < 2{,}000$.

For turbulent flow, the Dittus-Boelter[10] correlation was applied to consider forced convective heat transfer

$$h = \frac{k_f}{D_e} 0.023 \left[Re_f\right]^{0.8} \left[Pr_f\right]^{0.3} \tag{5-14}$$

where the characteristic length for evaluating the Reynolds number is the crack effective diameter, D_e.

Each of the heat transfer correlations was combined with the energy conservation equation to solve for the number of cracks required to remove the required heat from the debris to prevent vessel failure. Results are discussed in Section 5.1.3.2.

5.1.3.1.2 Assumptions and Governing Equations for Estimating the Gap Width between the Debris and the Vessel—This section describes the method used to determine if coolant flowing through a gap between the debris and the vessel could result in coolant rates consistent with metallurgical examinations. Calculations were performed assuming that coolant is able to travel in a direct path through a gap of thickness, t_{gap}, without any countercurrent flow considerations (see Figure 5-18). A lower-bound gap thickness of 0.1 cm was selected in order to minimize heat losses from the debris.

In Section 5.1.2, it is estimated that cooling heat fluxes less than 125 kW/m^2 are needed to obtain cooling rates consistent with metallurgical exams. Hence, the total amount of heat that needs to be removed by coolant flow between the vessel and the debris can be estimated using

$$q_{remove} \geq \left(125{,}000\ W/m^2 \right) \left(A_{down} \right) \ . \tag{5-15}$$

The heat removed by the coolant can also be estimated by applying

$$q_{remove} = h\ A_{down} \left(T_{debris} - T_{bulk} \right) \ . \tag{5-16}$$

Hence, rapid cooling is possible for cases where the convective heat transfer coefficient satisfies the following relationship:

$$h \geq \frac{125{,}000\ W/m^2}{T_{debris} - T_{bulk}} \ . \tag{5-17}$$

To determine if heat transfer coefficients from the debris to the coolant satisfy the above relationship, single phase liquid heat transfer correlations were first considered because they provide a lower limit on the heat transfer from the debris to the coolant. Although a large

number of correlations for predicting heat transfer to a liquid are available, no correlations could be found that were directly applicable to the geometry in question. Hence, several single phase liquid heat transfer correlations for various geometries were compared to obtain an order-of-magnitude estimate for the heat transfer coefficient.

Heat transfer coefficient correlations for flow between parallel plates in which natural convection dominates heat transfer were considered most appropriate for these calculations. However, forced and natural convection correlations were considered for flow between parallel plates as well as for flow over a sphere and flow over vertical and horizontal surfaces. Correlations applied in these calculations are described below.

For flow between vertical parallel plates under natural convection, Rohsenow[5] suggests

$$h = \frac{k_f}{t_{gap}} \left[\left(\frac{Ra}{24} \right)^{-1.9} + \left(0.6\ Ra^{0.25} \right)^{-1.9} \right]^{-\frac{1}{1.9}} \tag{5-18}$$

for cases in which $Ra < 10^5$. The characteristic length parameter, L^3_{char}, used to evaluate the Rayleigh number in the above correlation is given by

$$L^3_{char} = a^3 \left(\frac{t_{gap}}{a} \right) \quad . \tag{5-19}$$

For forced convection between horizontal plates, both laminar and turbulent flow correlations were considered. For laminar flow, Todreas and Kazimi[8] suggest

$$h = 8.235\ \frac{k_f}{4t_{gap}} \quad , \tag{5-20}$$

For turbulent flow between horizontal parallel plates under forced convection, the Dittus-Boelter equation[10] was applied as suggested by Welty:[11]

$$h = \frac{k_f}{4t_{gap}}\ 0.023 \left[Re_f \right]^{0.8} \left[Pr_f \right]^{0.3} \tag{5-21}$$

where the characteristic length, L_{char}, for evaluating the Reynold's number is four times the gap thickness ($L_{char} = 4t_{gap}$).

For fluids with $10 < Ra < 10^9$ flowing over an isothermal sphere, Raithby and Hollands[12,13] recommend that heat transfer under natural convection be modeled using

$$h = \frac{k_f}{2a}\left[(2.0 + 0.52\,Ra^{0.25})^6 + \left(0.1\,Ra^{\frac{1}{3}}\right)^6\right]^{\frac{1}{6}} \quad . \tag{5-22}$$

For a liquid with $10^4 < Ra < 10^9$ flowing over a sphere, Welty[11] suggests that heat transfer under natural convection be estimated using

$$h = \frac{k_f}{2a} 0.53\,(Ra)^{\frac{1}{4}} \quad . \tag{5-23}$$

The characteristic length, L_{char}, for estimating the Rayleigh number in both of the above correlations is the debris upper surface diameter, $2a$.

For a vertical plate, the following equations are recommended for the ranges indicated:[14]

$$h = \frac{k_f}{a}\,0.55\,(Ra)^{0.25} \quad (\text{for } Ra < 10^9) \tag{5-24}$$

$$h = \frac{k_f}{a}\,0.021\,(Ra)^{0.4} \quad (\text{for } Ra > 10^9) \tag{5-25}$$

where the characteristic length, L_{char}, for evaluating the Rayleigh number is the upper surface of the debris bed, a.

For a heated horizontal surface facing downward, the following equation is recommended for $3 \times 10^5 < Ra < 10^{10}$ (Reference 14):

$$h = \frac{k_f}{a}\,0.27\,(Ra)^{0.25} \tag{5-26}$$

where the characteristic length, L_{char}, for evaluating the Rayleigh number is the radius of the upper surface of the debris bed, a.

The above correlations were evaluated for the range of parameters considered. Results are tabulated and discussed in Section 5.1.3.2.

5.1.3.2 Results. Equations presented in Section 5.1.3.1 were applied to determine if coolant flowing through cracks within the debris bed and/or a gap between the debris and the vessel could prevent vessel failure and cause the vessel to cool at rates consistent with metallurgical examinations. Results for each type of cooling mode are discussed below.

5.1.3.2.1 Number and Geometry of Cracks for Slow Cooling—Equations in Section 5.1.3.1.1 were combined to solve for the number of cracks required to reduce the downward heat flux to the vessel sufficiently to prevent vessel failure. Calculations considered the upper and lower estimates in Table 5-1 for debris and coolant properties (calculations considered uncertainty due to debris mass, RCS pressure, etc.). Because a large temperature range for the surface temperature of cracks within the debris is considered in Table 5-1 (1,000 to 2,870 K), calculational results are also presented for cases in which it is assumed that the surface of the cracks within the debris are at a mid-range temperature of 1,700 K.

Although it is felt that buoyancy effects would dominate heat transfer, conditions for coolant within the cracks are unknown. Hence, calculations considered both correlations for natural and forced convection. Both turbulent and laminar flow correlations were applied for forced flow conditions. Rayleigh numbers for natural convection correlations and Reynolds numbers for forced convection correlations were calculated to check that correlations were appropriate.

Natural convection correlations considered both circular and rectangular channels for flow with Rayleigh numbers less than approximately 10^4. Results (shown in Table 5-2) for these correlations indicate that between 7 and 174 cracks are needed within the hard layer of debris to remove the required heat. If the debris temperature is assumed to be 1,700 K (rather than the entire 1,000 to 2,879 K range considered above), only 16 to 52 cracks are required. Rayleigh numbers for these calculations varied from 6,500 to 47,000, which is fairly consistent with the range suggested for these correlations.

Several correlations were evaluated in which heat transfer was assumed to be dominated by laminar flow under forced convection. Results indicate that less than 218 cracks are needed for debris temperatures between 1,000 and 2,870 K, and less than 83 cracks are needed for a debris temperature of 1,700 K. However, the Reynolds number for most of the cases considered was well above 2,300. Hence, results indicate that turbulent flow correlations are more appropriate. Results from calculations with the Dittus-Boelter correlation[10] for turbulent flow under forced convection indicate that between one and three cracks are needed to remove the required heat, with less than one crack needed if the cracked surface of the debris is at 1,700 K.

In summary, results indicate that less than 218 cracks within the hard layer of debris in the TMI-2 vessel could prevent vessel failure. Using this upper-bound number, the volume of cracks would be less than 8×10^{-6} m^3. The volume of the hard layer of debris within the lower head is estimated as between 0.8 and 1.0 m^3. Hence, it is estimated that a relatively insignificant volume of cracks within the TMI-2 debris bed could have removed a sufficient amount of heat to prevent vessel failure even with the conservative assumption that heat transfer is limited to single phase liquid heat transfer.

5.1.3.2.2 Gap Geometry for Rapid Cooling—Based upon the upper and lower values of debris and coolant properties in Table 5-1, it is estimated that the heat transfer coefficient between the debris and the coolant within the debris to vessel gap must be greater than 180 W/m^2K. Heat transfer correlations in Section 5.1.3.1.2 were evaluated for the range of values in Table 5-1. Results, which are tabulated in Table 5-3, indicate that the heat transfer coefficient for coolant traveling through this gap could range from 330 to 9,800 W/m^2K.

Table 5-2. Results for estimating the number of cracks to cool TMI-2 debris.

Correlation	Basis	Assumptions	Range	Number of cracks required (range of values)	
				T_{debris} 1,000–2,870 K	T_{debris} 1,700 K
Elenbass & Dyer	Experimental and theoretical	Natural convection through an isothermal cylinder	$Ra < 10^4$	16-174	38-52
Rohsenow	Experimental and theoretical	Natural convection through an isothermal channel	$Ra < 10^4$ 4:1 side ratio	7-74	16-22
Todreas & Kazimi	Theoretical	Fully developed laminar flow under forced convection through a cylinder with a constant heat flux	$Re < 2{,}300$	32-218	63-83
Todreas & Kazimi	Theoretical	Fully developed laminar flow under forced convection through a rectangular channel with a constant heat flux	$Re < 2{,}300$ 8:1 side ratio	21-144	41-55
Collier	Experimental	Laminar flow under forced convection modified to include natural convection effects	$Re < 2{,}000$ $z_{crack}/D_e > 50$	3-77	7-21
Dittus-Boelter	Experimental	Turbulent flow under forced convection	$Re > 2{,}300$	1-3	< 1

Table 5-3. Results for estimating heat transfer coefficient through a debris-to-vessel gap.

Correlation	Basis	Assumption	Range	Heat transfer coefficient (W/m^2K)
Rohsenow	Experimental and theoretical	Natural convection through heated vertical parallel plates	$Ra < 10^5$	330-450
Kazimi and Todreas	Theoretical	Laminar flow under forced convection between heated horizontal parallel plates	$Re < 2{,}300$	1,150-1,380
Dittus-Boelter	Experimental and theoretical	Turbulent flow under forced convection between heated horizontal plates	$Re > 2{,}300$	2,240-5,380
Raithby and Hollands	Experimental and theoretical	Natural convection over an isothermal sphere	$10 \leq Ra \leq 10^9$	4,200-4,750
Welty	Experimental	Natural convection over a spherical surface	$10^4 < Ra < 10^9$	2,000-2,350
Eckert and Jackson	Experimental and theoretical	Natural convection over a heated vertical wall	$Ra < 10^9$	4,900-6,000
Eckert and Jackson	Experimental	Natural convection over a heated vertical wall	$Ra > 10^9$	8,800-9,800
McAdams	Experimental	Natural convection over a downward facing, heated, horizontal heated plate	$3 \times 10^5 < Ra < 10^{10}$	640-750

Natural convection correlations indicate that heat transfer coefficients would range from 330 to 9,800 W/m^2K. Although the Rayleigh number varied considerably with the type of characteristic length selected, values for cases assuming flow between parallel plates ranged between 17 and 235, which is well below the 10^5 upper limited cited in Rohsenow.[5] Although these cases also resulted in lower estimates for the heat transfer coefficient, it is estimated that sufficient heat could be removed if heat transfer is dominated by natural convection.

Forced convection correlations indicate that heat transfer coefficients would range from 1,150 to 5,380 W/m^2K. The Reynolds number was estimated to be between above 3,340 for all of the cases considered. Hence, the correlation for turbulent forced convection is more appropriate. However, the large values predicted for forced convection for either laminar or turbulent flow conditions indicate that the vessel could be cooled if a gap were present.

In summary, it appears that the presence of a gap could result in the cooling rates estimated in metallurgical examinations. Although heat transfer was conservatively assumed to be limited to a single phase liquid, results indicate that more than the required heat could be removed.

5.1.4 Changes in Lower Head Debris Internal Energy after Relocation

The potential for debris cooling to have occurred prior to the time that the vessel was repressurized was investigated by applying volume, mass, and energy balances on debris and coolant in the vessel. Measured plant data, such as the RCS pressure and coolant cold leg temperatures, and parameters, such as coolant flow rates entering and exiting the vessel that were inferred from measured plant data, were used to quantify input for this analysis. Governing equations and input parameters for these calculations are discussed in Section 5.1.4.1. As discussed in Section 5.1.4.1, conservative assumptions, which maximized the internal energy within the debris at the time that the vessel was repressurized, were applied to simplify this analysis. Because of these simplifying assumptions, results from these scoping calculations, which are presented in Section 5.1.4.2, should be viewed as order-of-magnitude estimates that indicate the relationship between the debris internal energy at the time of relocation and at the time before the vessel was repressurized.

5.1.4.1 Method for Predicting Changes in Lower Head Debris Internal Energy. Initial scoping calculations in Section 3 and 4 indicate that some form of debris cooling must have occurred in the vessel after the time when a major relocation occurred (~220 minutes) and prior to the time that the vessel was repressurized (~320 minutes). By applying some simplifying assumptions related to heat transfer in the vessel, an order-of-magnitude estimate of the change in debris internal energy after debris relocation can be obtained using thermal-hydraulic parameters that were either directly measured during the accident or inferred from plant data measured during the accident.

Volume, mass, and energy conservation equations were applied to debris and coolant in the TMI-2 vessel to determine the change in debris internal energy during the time interval of interest (between 220 and 320 minutes after reactor trip). Figure 5-19 illustrates the control volume assumed for applying these conservation equations.

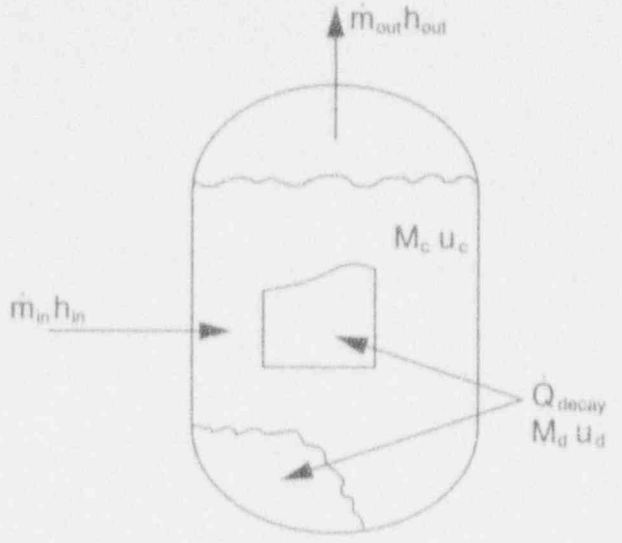

Figure 5-19. Control volume for internal energy calculations.

First, conservation of volume in the vessel at the beginning and end states (designated by the subscripts, 1 and 2, respectively) yields

$$V_{coolant} = M_{c1}\left[\left(1 - x_1\right)v_{l1} + x_1 v_{g1}\right] \tag{5-27}$$

$$V_{coolant} = M_{c2}\left[\left(1 - x_2\right)v_{l2} + x_2 v_{g2}\right] \tag{5-28}$$

where

$V_{coolant}$ = Reactor coolant system volume (m^3)

M_c = Coolant mass in the RCS (kg)

x = RCS quality

v_l = Saturated liquid specific volume (m^3/kg)

v_g = Saturated vapor specific volume (m^3/kg).

Second, conservation of mass in the vessel was applied:

$$M_{c1} + \int_1^2 \sum \dot{m}_{in}dt = M_{c2} + \int_1^2 \sum \dot{m}_{out}dt \tag{5-29}$$

where

$\dot{m}_{in}$ = mass flowrate of coolant entering the vessel (kg/s)

$\dot{m}_{out}$ = mass flowrate of coolant exiting the vessel (kg/s).

Sources of coolant entering the vessel during this time period include normal RCS makeup and high pressure injection from the emergency core cooling system. Sources of coolant exiting the vessel during this time period include normal RCS letdown and coolant flowing out the open PORV.

Finally, conservation of energy in the vessel was applied:

$$\int_1^2 \dot{m}_{in} h_{in} dt + M_{c1}\left[(1 - x_1)u_{l1} + x_1 u_{g1}\right] + \int_1^2 \dot{Q}_{decay} dt + M_{dtot} u_{d1} = M_{c2}\left[(1 - x_2)u_{l2} + x_2 u_{g2}\right] + \int_1^2 \dot{m}_{out} h_{out} dt + M_{dtot} u_{d2} \quad (5\text{-}30)$$

where

$\dot{Q}_{decay}$ = debris decay heat (W)

M_{dtot} = total debris mass in the vessel (kg)

h_{in} = enthalpy of coolant entering the vessel (J/kg)

h_{out} = enthalpy of coolant exiting the vessel (J/kg)

u_d = debris internal energy (J/kg)

u_l = coolant internal energy (J/kg).

Because the above energy equation is applied during the time period after relocation, energy from zircaloy oxidation is neglected since most oxidation is predicted to occur during earlier stages of the transient. Because the main RCS pumps did not run during this time period, the primary source of heat loss from the system is associated with mass exiting the system. Although additional heat may be transferred to upper plenum structures in the vessel via natural circulation, these losses were conservatively neglected to maximize estimates for debris internal energy at the time that the vessel was repressurized (state 2).

The above equations were solved to obtain a relationship between the change in debris internal energy, $M_{dtot}(u_{d2}-u_{d1})$, as a function of other parameters in the system. Although many of these system parameters are not known precisely, an extensive effort was made under previous

TMI-2 research programs to estimate their values and associated uncertainty using measured plant data.[16-20]

Data needed to evaluate the change in internal energy in the above relationship are discussed below. Where possible, uncertainties in data are quantified.

Coolant Entering the Vessel

During the time period of interest (220 to 320 minutes), coolant entered the RCS via the high pressure injection (HPI) and the makeup system. Makeup coolant is provided to the RCS through the reactor coolant pump seals and via the normal makeup line. During an accident in which the RCS pressure drops below 11.4 MPa or the reactor building pressure exceeds 0.2 MPa, high pressure water is injected from the borated water storage tank into the RCS via the HPI pumps. Although makeup and HPI flow rates were not recorded during the accident, Anderson[18] estimated these flow rates based upon knowledge of the HPI system and analysis of the known accident progression.[18] Recommended makeup and HPI flow rates are plotted in Figure 5-20. Anderson acknowledges that there is considerable uncertainty in makeup and HPI flow rate estimates. Several possible variations to the values plotted in Figure 5-20, which typically vary by ±25%, are suggested by Anderson.

Coolant Exiting the Vessel

During the time period of interest, coolant exited the system via the normal coolant letdown system and via the pilot operated relief valve (PORV), which failed in a stuck-open position. Although neither of these flow rates was measured during the transient, data for other plant parameters have been used to estimate these flow rates.

RCS pump seal flow entering the RCS necessitates a continuous letdown flow of reactor coolant to maintain the desired coolant inventory balance. Letdown flow is also required for removal of impurities and boric acid from the reactor coolant. The letdown mass flow rate was estimated by performing an energy balance on the letdown coolers using the measured A-loop cold leg temperature as the primary side inlet temperature.[16] The resulting flow rate is plotted in Figure 5-21. Sensitivity studies indicate that the uncertainty in the letdown flow is ± 1.2 kg/s.

The pressurizer PORV in TMI-2 opened at its setpoint of 15.6 MPa a few seconds after the initiation of the accident and failed in the stuck-open position. After the PORV opened, flow through the PORV depended on the status of the block valve situated upstream of the PORV. Although the flow rate out the PORV was not measured, it has been estimated based on knowledge of measured plant parameters, such as the RCS pressure history; the status of the block valve, which is situated upstream of the PORV; and the pressurizer liquid level.

Kuan and Tolman[19] calculated the discharge flow out the PORV based on an approximation that the flow rate is proportional to the square root of the primary system pressure. For the time period of interest for the present analysis (between 220 and 318 minutes after reactor scram), they assumed that the system was filled with saturated liquid.

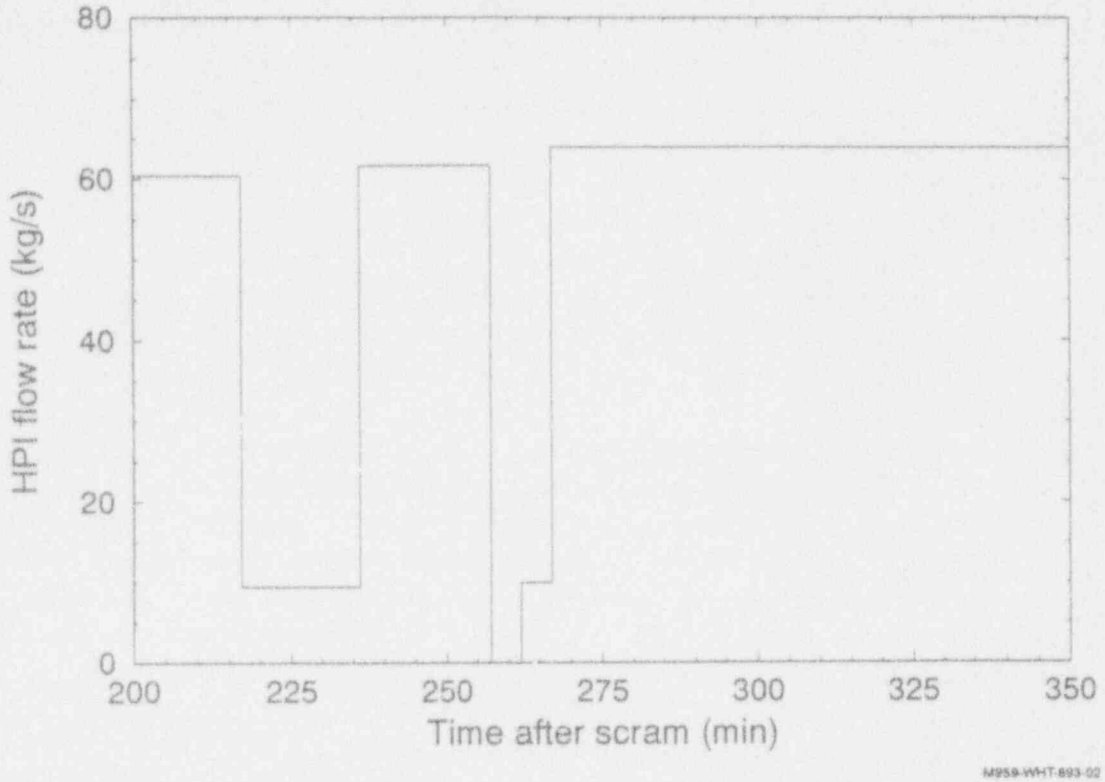

Figure 5-20. Combined high pressure injection and makeup flow into the RCS.

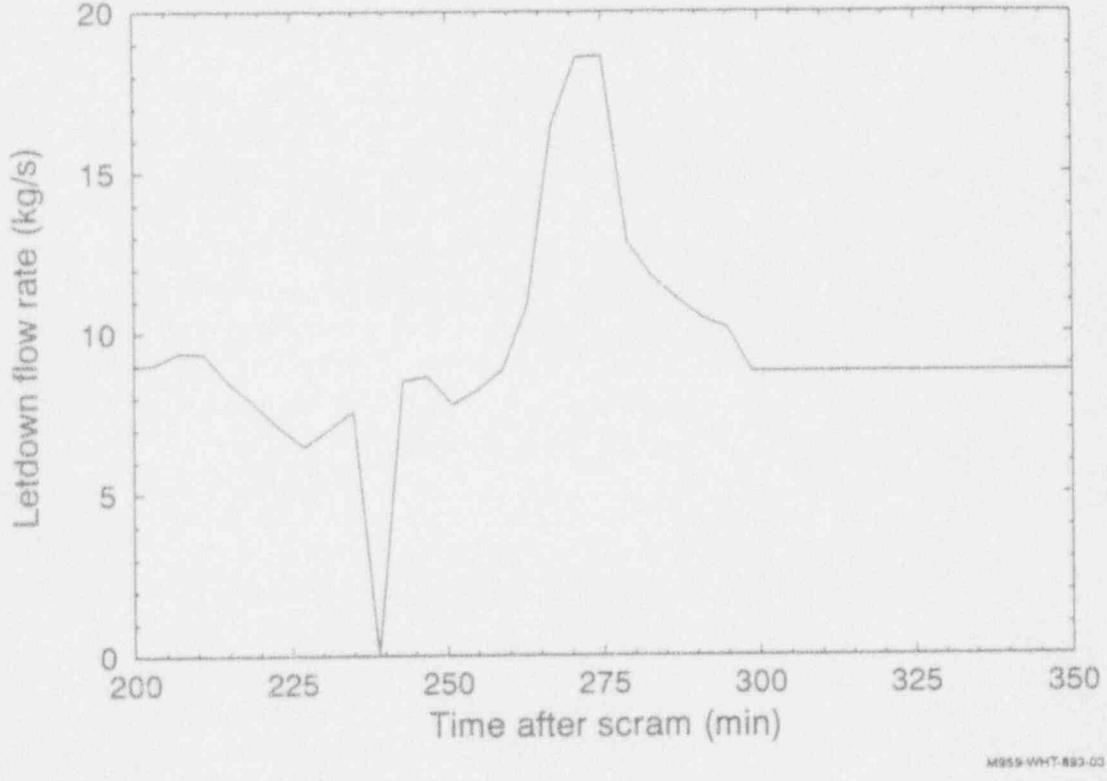

Figure 5-21. Letdown flow rate of coolant.

Nomura[20] estimated the PORV flow rate using the homogenous equilibrium critical flow model for higher qualities (i.e, $0.02 < x \leq 1$), the Henry-Fauske model [21] for saturated liquid (i.e., $x = 0$), and a curve fit between the two models at low quality ($0 < x < 0.02$). The quality at the PORV orifice was based on the measured pressurizer liquid level and the Wilson bubble rise model.[22]

An approximate version based upon the detailed flow rates estimated by Nomura[20] is compared with values predicted by Kuan[19] in Figure 5-22. As indicated in the figure, flow rates between 220 and 320 minutes are within about 10% of each other. Both Kuan and Nomura estimate that their calculated PORV flow rates have an uncertainty of ±20%.

RCS Thermal Properties

RCS thermal properties, such as internal energy, were obtained from Keenen[23] based on the system pressure and coolant temperature measurements for the time periods of interest. The system pressure history, shown in Figure 2-2, is a composite pressure curve that was based upon several sources of plant data. The maximum calculated uncertainty for points on this composite pressure curve is estimated to be ±0.2 MPa.[16] No plant data conclusively indicate the quality of the coolant in the system at either 220 or 320 minutes. Therefore, the debris internal energy at the endstate was maximized by assuming that the coolant was subcooled at a temperature consistent with the cold leg temperature data in Figure 2-3. In addition, sensitivity studies were performed to consider a large range of possible initial and final coolant quality conditions.

Debris Decay Heat

The decay power in the debris is related to the amount of fission products retained in the core material. During the TMI-2 accident, significant release of volatile fission products occurred. For example, in the lower plenum, it is estimated that only 3% of the iodine and 13% of the cesium were retained.[24] The reductions in total core decay power as a result of volatile fission product release for the TMI-2 fuel inventory were estimated by Schnitzler.[25] For the time periods of interest, results indicate that the decay power can be reduced by as much 40%. Using a decay power curve,[26] the power of the TMI-2 core at 224 minutes was estimated as approximately 25 MWt. However, if the reduction resulting from volatile fission product release is included, this number can be as low as 18 MWt. Sensitivity studies were performed in the present study to determine the impact of debris decay heat on debris internal energy change.

RCS Coolant Volume

The volume of coolant in the RCS, including the pressurizer volume, was estimated by several sources[17,27] to be between 327 and 334 m^3.

5.1.4.2 Results. The equations presented in Section 5.1.4.1 were combined to obtain a relationship between the change in debris internal energy, $M_d(u_{d2}-u_{d1})$, as a function of input parameters quantified in Section 5.1.4.1 and the quality in the system. Uncertainties in the input parameters, which were discussed above, were considered by evaluating upper and lower bounds for these parameters.

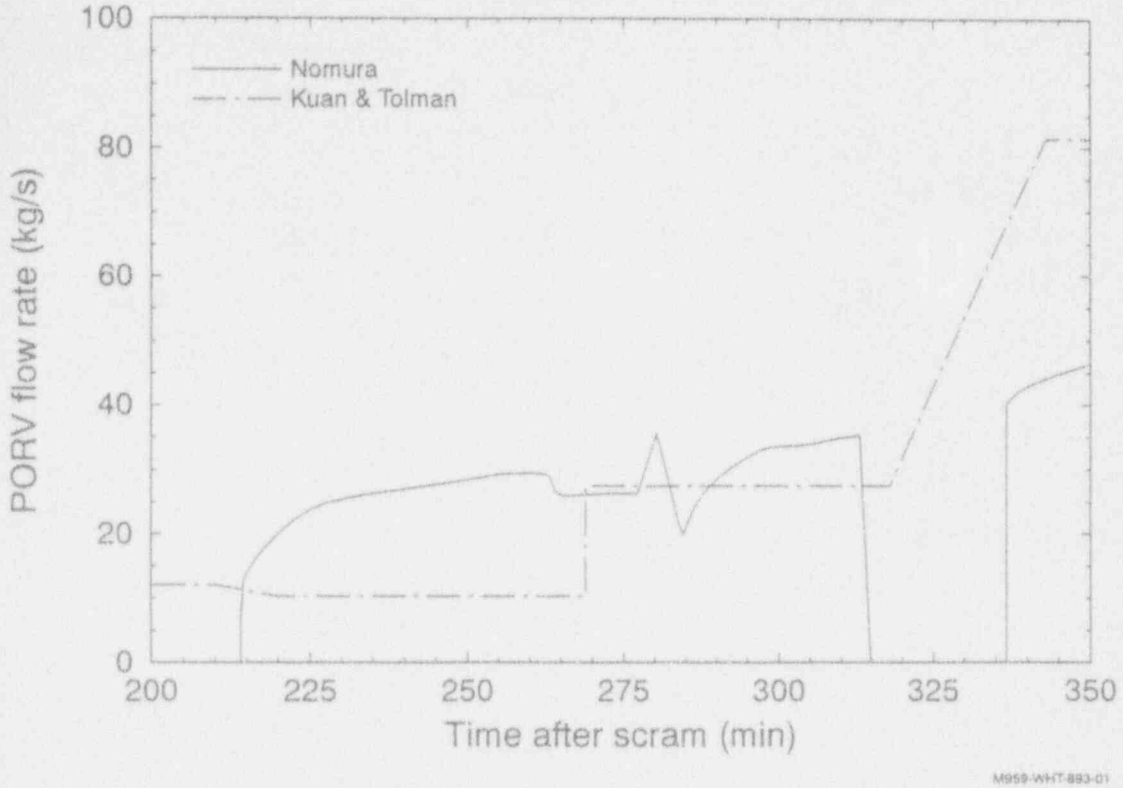

Figure 5-22. Pilot-operated relief valve flow rate.

Table 5-4 summarizes results for the cases considered. Because of simplifying assumptions used in this scoping calculation, values in this table should be viewed only as order-of-magnitude estimates that provide insight into the change in debris energy. For example, any heat losses to the vessel or upper plenum structures were neglected in this analysis in order to maximize Table 5-4 estimates for the quantity, $M_d(u_{d2}-u_{d1})$. However, Table 5-4 results indicate that the debris did cool in the time interval between debris relocation and vessel repressurization because all estimates for $M_{dtot}(u_{d2}-u_{d1})$ are negative. Although there is considerable uncertainty associated with Table 5-4 values for the changes in debris internal energy, it is useful to compare these values with the amount of energy needed to solidify and cool the debris. For example, if the decreases in internal energy values cited in Table 5-4 are assigned to all of the 20,000 metric tonnes of material that relocated to the lower head, there is sufficient cooling for the $(U,Zr)0_2$ composition cited in companion sample examinations[4] to have solidified and experience a decrease in temperature ranging from 420 to 2,250 K.

Values for cases based upon best estimate input values in Table 5-4 indicate that the endstate quality in the vessel remains relatively low for a large range of possible initial qualities. The low endstate quality values reflect data indicating that large quantities of cool liquid were pumped into the vessel prior to this time. Values for $M_{dtot}(u_{d2}-u_{d1})$ are plotted versus initial coolant quality for best estimate flow rate cases in Figure 5-23. As indicated by the curve in this figure, the magnitude of the decrease in internal energy increases if there is more liquid initially present to cool the debris.

Table 5-4. Results for estimating change in debris internal energy.

Case	Final quality	Initial quality	Change in internal energy (MJ)	Percent different from best estimate with x_2=0.00[a]
Best estimate flow rates, coolant volume (V_{cool} = 330 m^3), and decay heat (Q_{decay} = 20 MW)	100 K subcooled	0.04	-10,400.	-58.00
	0.00	0.10	-24,600.	0.00
	0.01	0.17	-24,200.	1.63
	0.03	0.42	-23,700.	-3.82
	0.04	0.69	-23,400.	-4.85
	0.05	0.94	-23,400.	-5.24
25% increase in entering coolant	0.00	0.51	-34,200.	38.90
25% decrease in entering coolant	0.00	0.02	-15,100.	-39.10
20% increase in exiting coolant	0.00	0.05	-24,700.	-0.35
20% decrease in exiting coolant	0.00	0.19	-24,600.	0.35
Upper-bound decay heat (Q_{decay} = 25 MW)	0.00	0.10	-21,600.	-12.17
Lower-bound decay heat (Q_{decay} = 18 MW)	0.00	0.10	-25,800.	-12.17
Upper-coolant volume (V_{cool} = 334 m^3)	0.00	0.10	-24,600.	-0.06
Lower-coolant volume (V_{cool} = 327 m^3)	0.00	0.10	-24,700.	0.04

a. Defined by the following equation

$$\frac{M_{dtot}\left(u_{d2} - u_{d1}\right)\big|_{sens.\ case} - M_{dtot}\left(u_{d2} - u_{d1}\right)\big|_{best\ est.\ case}}{M_{dtot}\left(u_{d2} - u_{d1}\right)\big|_{best\ est.\ case}} \times 100\ \% \quad .$$

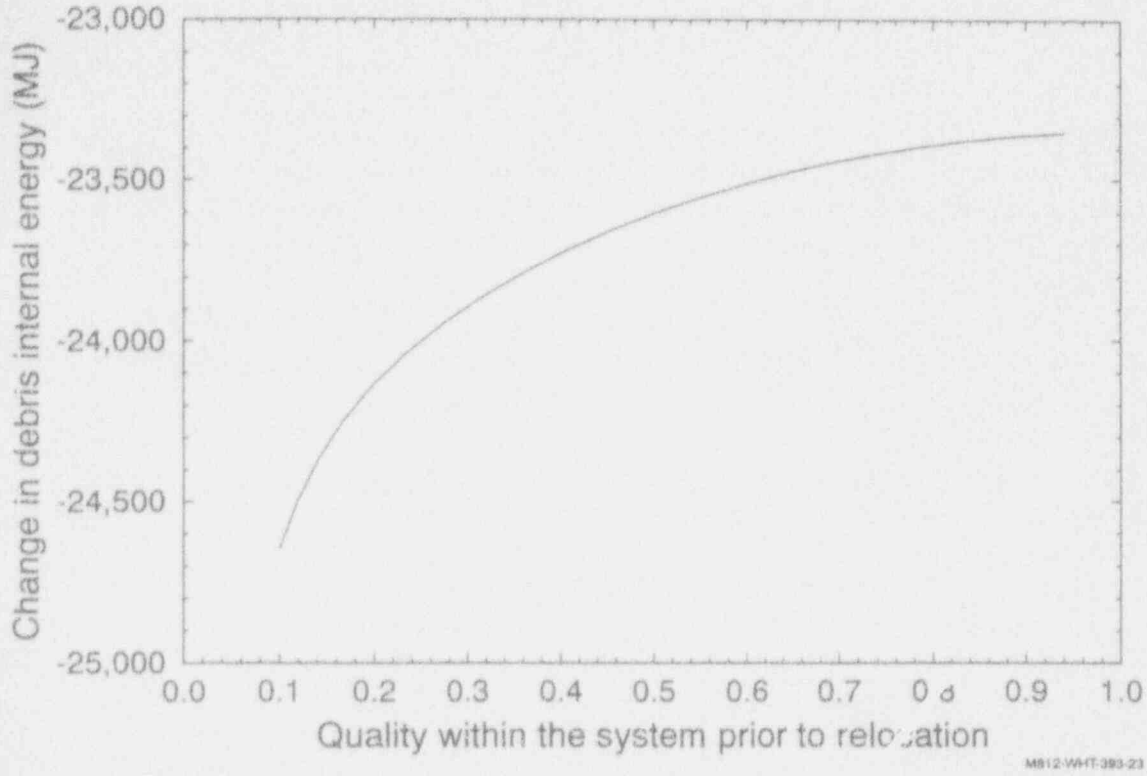

Figure 5-23. Change in debris internal energy versus coolant quality.

Results in Table 5-4 also are useful for understanding the relative impact of changes in input parameters on the amount of heat loss from the debris. Table 5-4 indicates that the smallest decrease in internal energy will occur if the coolant is subcooled at the time the vessel is repressurized because less energy would have been transferred from the debris to the coolant. Table 5-4 indicates that the change in internal energy is also sensitive to inlet flow rate assumptions. Values in this table indicate that values for $M_{diot}(u_{d2}-u_{d1})$ are decreased by nearly 40% if lower-bound inlet coolant flow rates are assumed because there is less coolant available to remove heat from the debris.

In summary, measured data and parameters based on data measured during the TMI-2 accident have been used to estimate the change in debris internal energy between the time that the debris relocated to the lower plenum and the time that the vessel repressurized as a result of the block valve closing. Although several simplifying assumptions were used to estimate the change in debris energy, these assumptions tended to maximize the internal energy at the time of repressurization. Results indicate that the debris was cooling after it relocated to the lower plenum.

Although companion sample examinations did not substantiate that portions of the debris experienced significant cooling within the first 2 hours after melt relocation, it should be noted that the mass of the companion samples was small compared to the mass that relocated (only 6.7 kg of the 19,000 kg that relocated were examined)[4] and that results in Sections 5.1.3 indicate that a minimal volume of cooling channels within the debris and a minimal size gap between the debris and the vessel could supply the cooling indicated by vessel metallurgical examinations.

5.2 Mechanical Instability Failure Criterion Analyses

Inspection of plots of vessel deformation and damage distribution in the previous sections illustrates that, in many cases, predicted failure strains are quite small (less than 10%). As discussed in Reference 28, members of the Structural Mechanics Peer Review Group have noted that these results suggest the stress-based failure criterion used is too conservative. It is therefore desirable to perform a similar set of calculations with a less conservative failure criterion to see how the required reduction in nominal loading is changed when the criterion is modified. Results in the previous sections were also performed with constitutive relations based solely on secondary creep. It has also been suggested that one of the reasons for the low predicted failure strains is the lack of tertiary data in the constitutive relations.[28] For these reasons, another set of structural simulations was performed. The failure criterion used in the simulations described in this section is one of mechanical instability. Damage is not used, and no ligaments are clipped. As the structure approaches failure, it advances a fixed increment of deformation in progressively shorter time intervals. When characteristic deflections and rotations are plotted versus time, a distinct knee appears in the curve which marks the onset of mechanical instability. This defines the point of failure.

Tertiary constitutive relations used in these calculations are discussed in Appendix A. It is apparent that very strong nonlinearities exist in both stress and time. For these reasons, it was not uncommon for simulations to require in excess of ten thousand load increments to reach the failure point. Three characteristic quantities were used to define the point of failure: the vertical deflection at the bottom of the shell, directly underneath the hot spot; the maximum hoop strain, also directly underneath the hot spot; and the maximum rotation of the shell meridian, located somewhere in the cusped region. As the simulation proceeds towards the failure point, it becomes increasingly difficult for the shell to reach an equilibrium configuration. Early in the simulation, only a few iterations are required within a load increment to reach convergence. As the vessel nears failure, the number of iterations required to reach convergence first reaches ten, then tens of, then finally a hundred iterations to reach convergence. Failure is defined at that load increment where the simulation can not find an equilibrium position after a thousand iterations.

Three types of calculations were performed to investigate the influence of failure criterion and the inclusion of tertiary creep. First, calculations were performed using the nominal heat fluxes without a hot spot. Second, calculations were performed to quantify the amount of slow cooling needed to preclude vessel failure, similar to the calculations described in Section 5.1.1, using the new failure criterion. Finally, calculations were performed to determine the amount of rapid cooling needed to obtain cooling rates consistent with the cooling indicated by vessel metallurgical examinations, similar to the calculations described in Section 5. 2.

5.2.1 Effects of Including Tertiary Creep

To see the influence of the tertiary strains, a calculation was first performed for the case of nominal heat flux applied to a sector of the lower head without the hot spot. In one simulation, the constitutive relations included only the secondary creep regime, while in the other, both secondary and tertiary relations were used. Results comparing maximum deflections and rotations are shown in Figure 5-24, and the vessel deformation and distribution of tertiary ligaments is

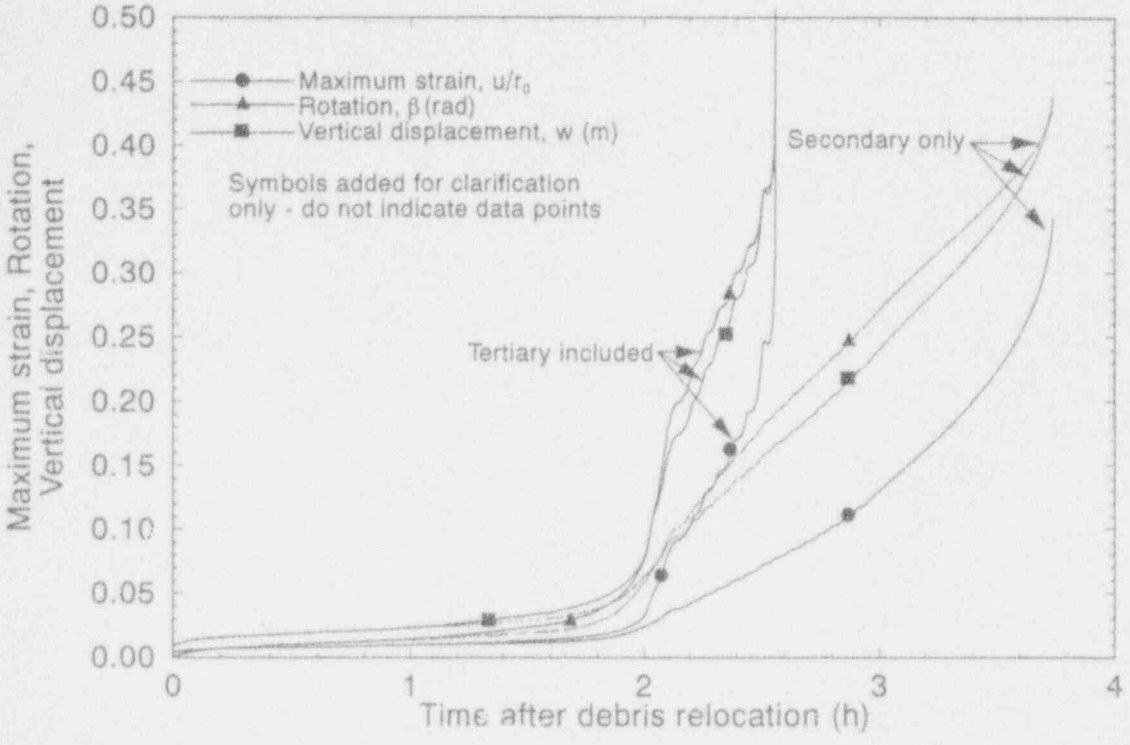

M971 jlr-0893-05a

Figure 5-24. Comparison of results obtained with and without tertiary creep for the nominal case without a hot spot.

shown in Figure 5-25. The simulation including only the secondary regime failed in just under 3.75 hours. The simulation based on the tertiary regime achieved the deflections illustrated in Figures 5-24 and 5-25. Results indicate that failure occurs at 2.56 hours.

There are two striking features in Figure 5-24. The first is that deflections and rotations begin to grow rapidly with the onset of repressurization in the 1.6 to 2.0 hour time interval. The second is the impact of pressure fluctuations during the period of valve opening and reseating in the 2.1 to 3.0 hour interval. Using constitutive relations in the secondary regime, these pressure fluctuations are of no particular consequence; they introduce only a modest oscillation about the mean values of displacement and rotation. Once the tertiary regime is included, however, each pressure fluctuation ratchets up the deformation by a substantial increment. The tertiary regime propagates from the bottom of the shell up the meridian and from the outside towards the inside. The tertiary regime has propagated all the way through the thickness of the bottom of the shell by 2.33 hours into the transient.

5.2.2 Effects of Failure Criterion on Slow Cooling Analysis Results

Simulations involving the hot spot on various background heat flux distributions were performed, and results are presented in Figures 5-26 through 5-37. Figure 5-26 summarizes results involving the hot spot on 100%, 75% and 50% of the nominal background heat flux distribution. Failures times are well defined for the cases of hot spots on 100% and 75% of

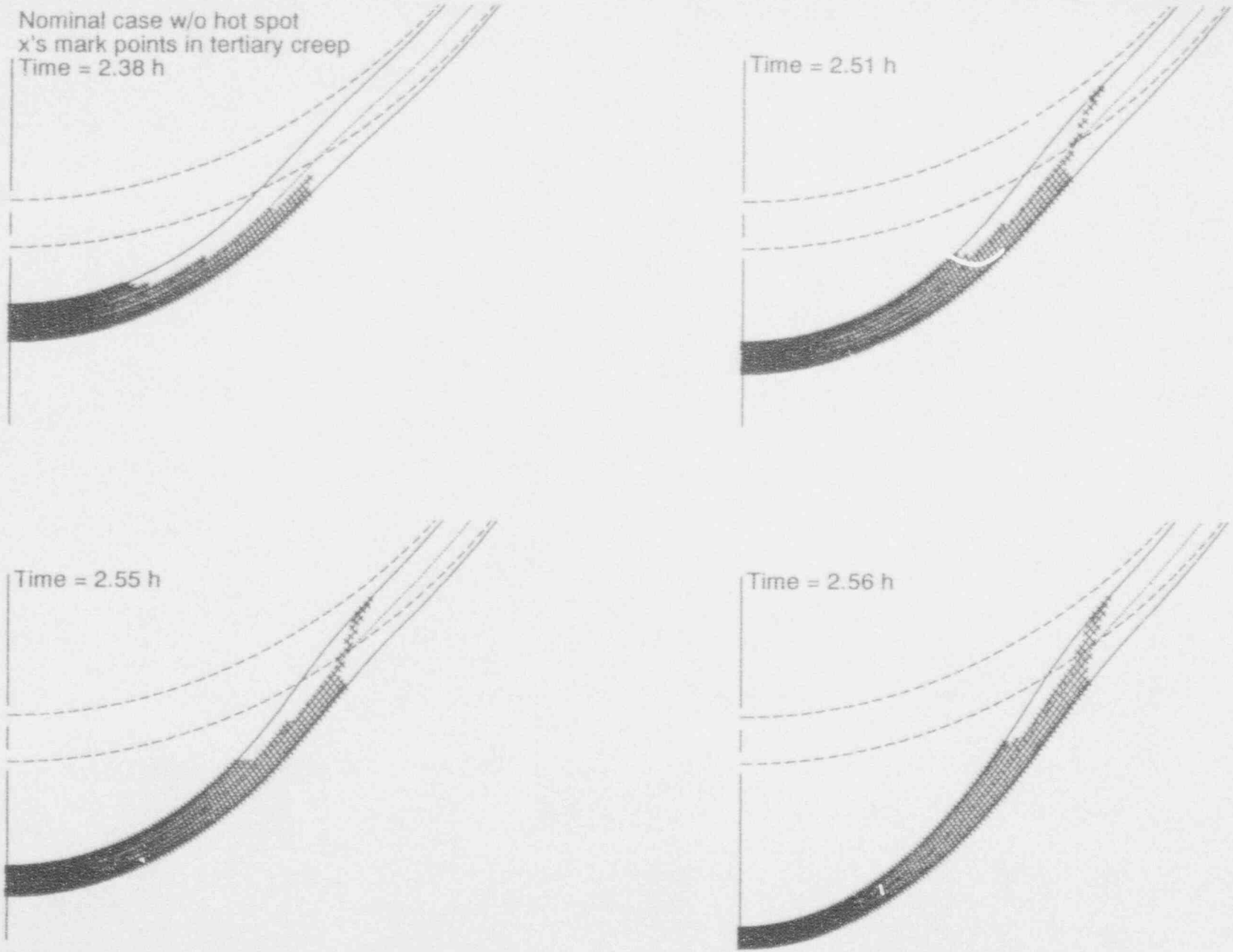

Figure 5-25. Distribution of ligaments experiencing tertiary creep at various times for the nominal case without a hot spot.

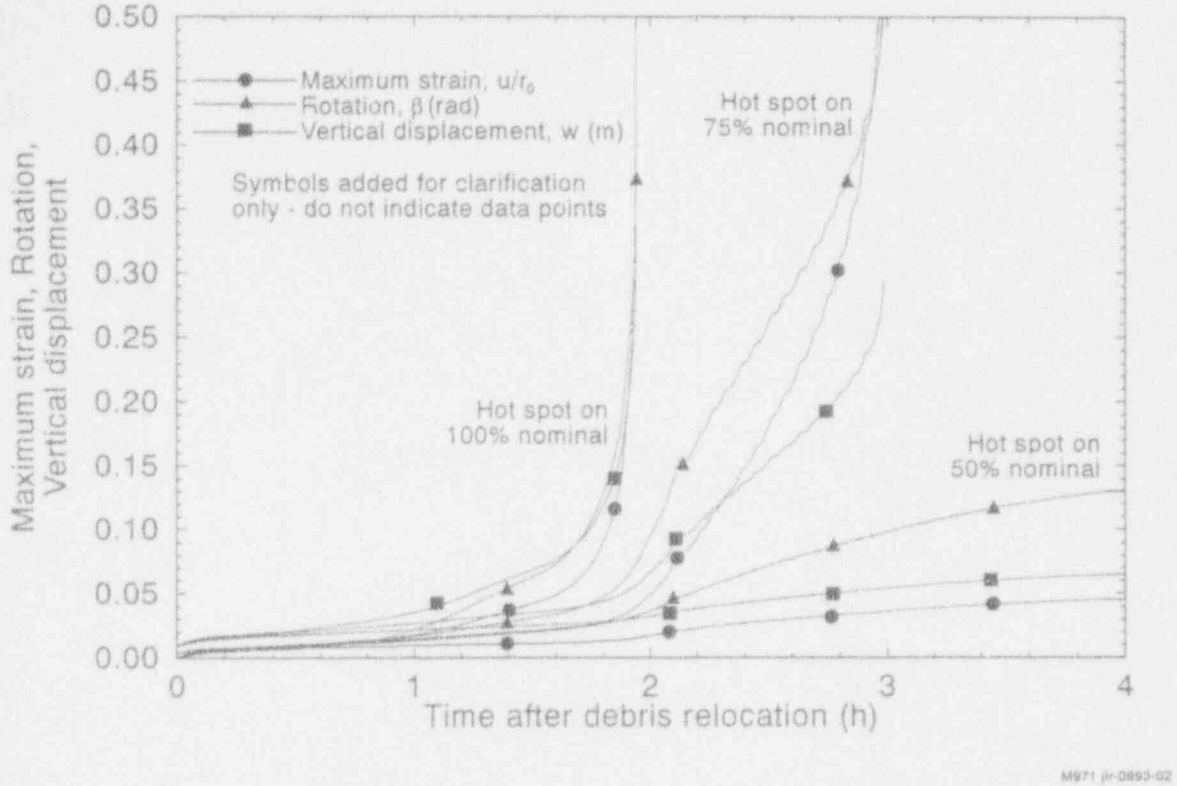

Figure 5-26. Comparison of results for cases with a hot spot on various nominal heat fluxes.

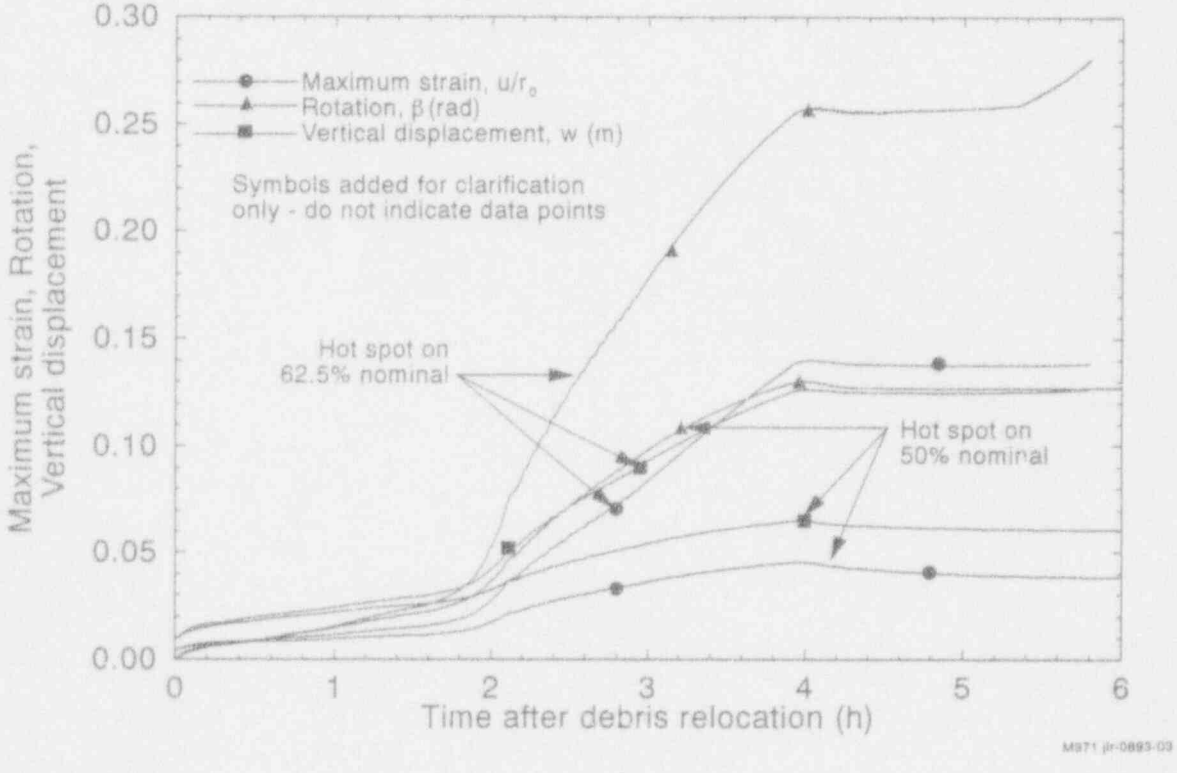

Figure 5-27. Comparison of results for cases with a hot spot on 50% and 62.5% nominal heat fluxes.

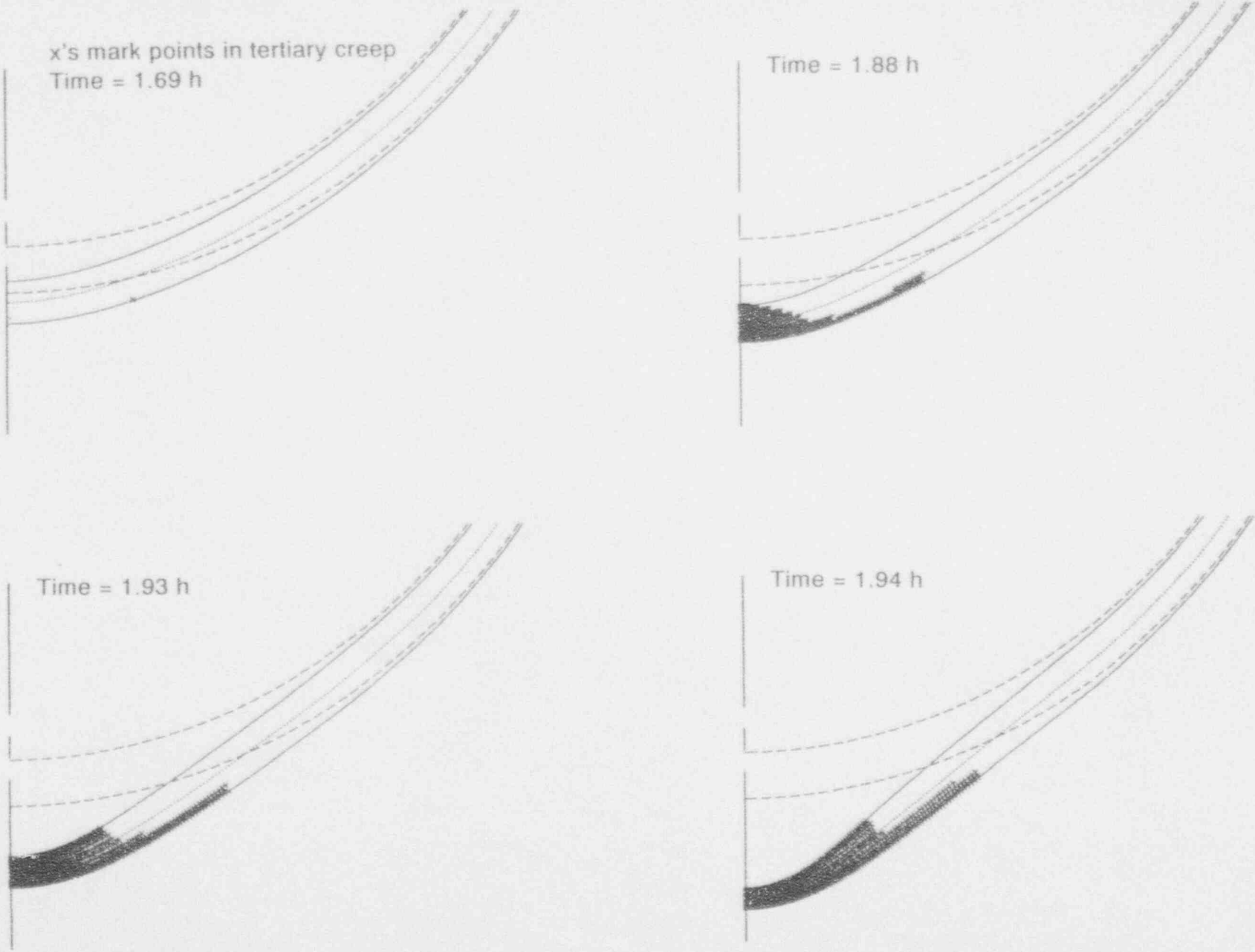

Figure 5-28. Distribution of ligaments experiencing tertiary creep at various times for the 100% nominal case with a hot spot.

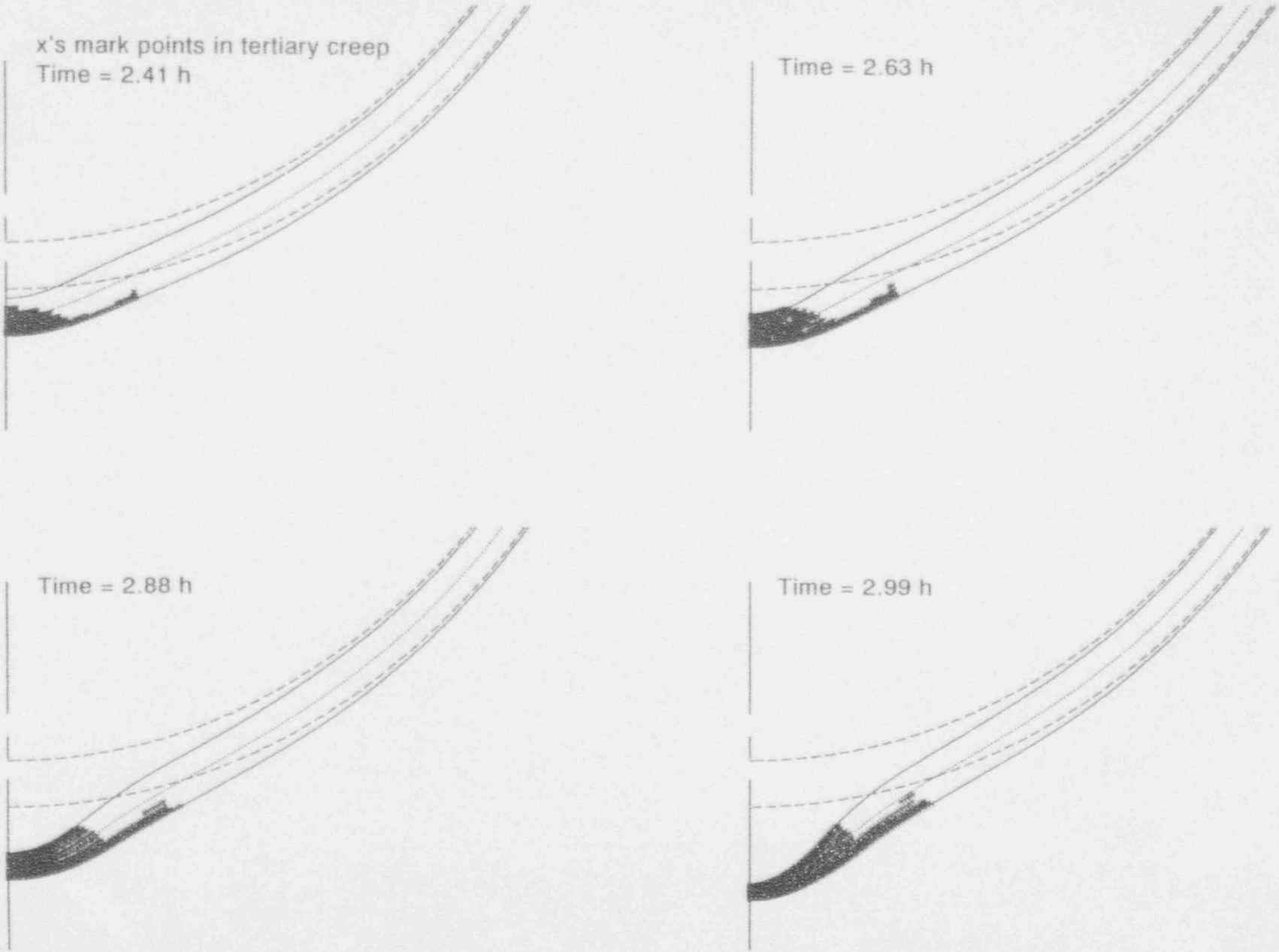

Figure 5-29. Distribution of ligaments experiencing tertiary creep at various times for the 75% nominal case with a hot spot.

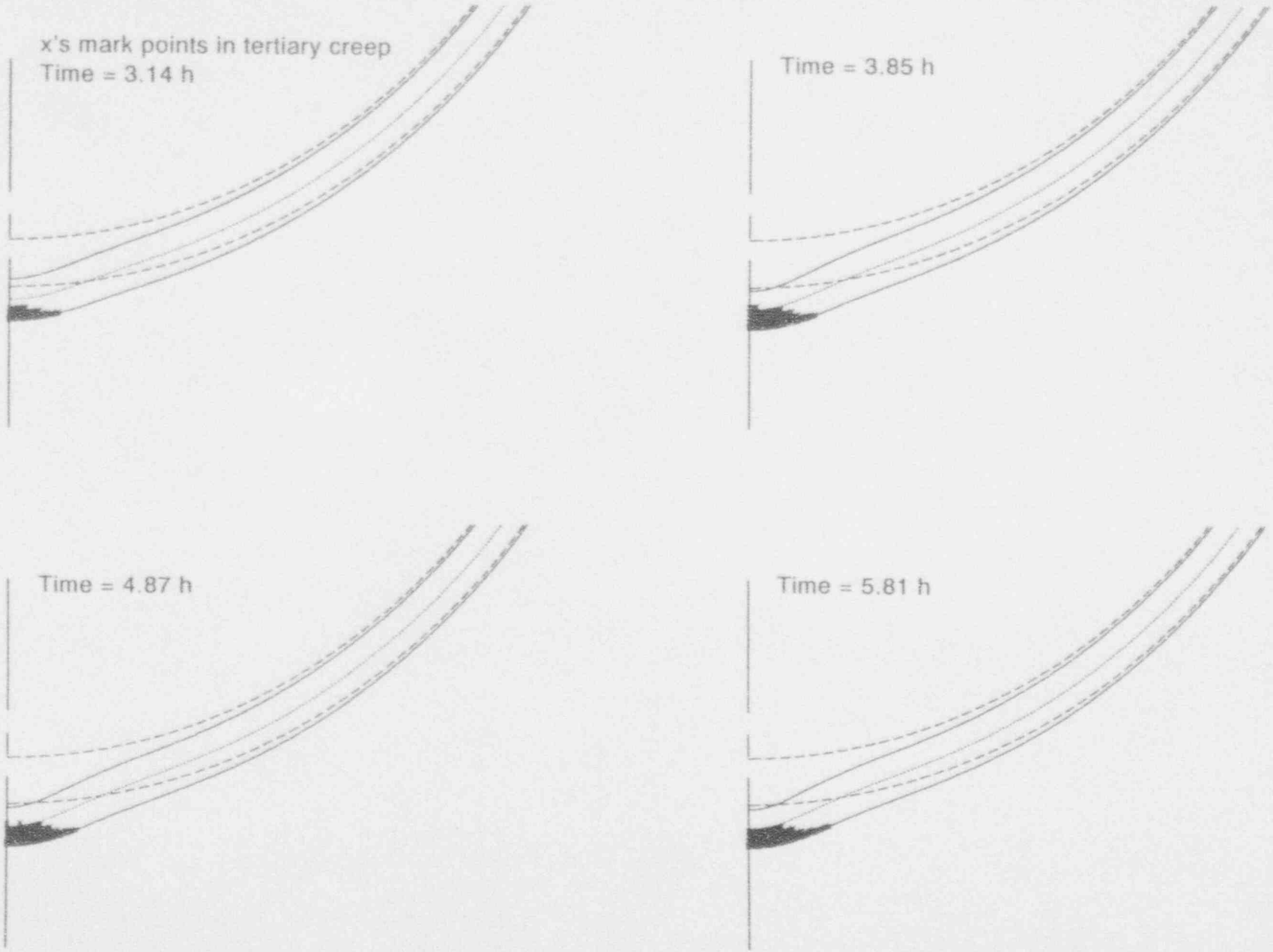

Figure 5-30. Distribution of ligaments experiencing tertiary creep at various times for the 62.5% nominal case with a hot spot.

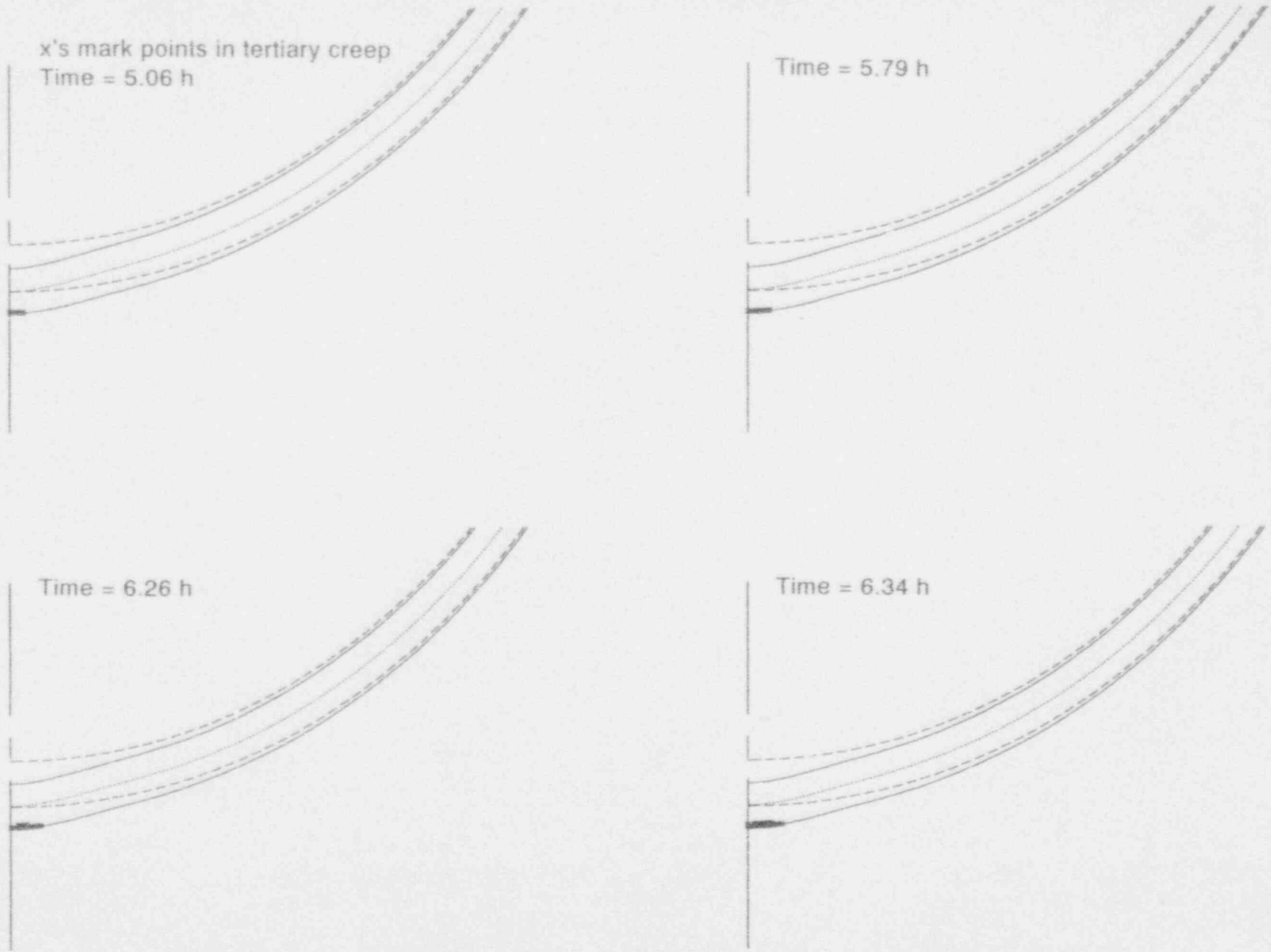

Figure 5-31. Distribution of ligaments experiencing tertiary creep at various times for the 50% nominal case with a hot spot.

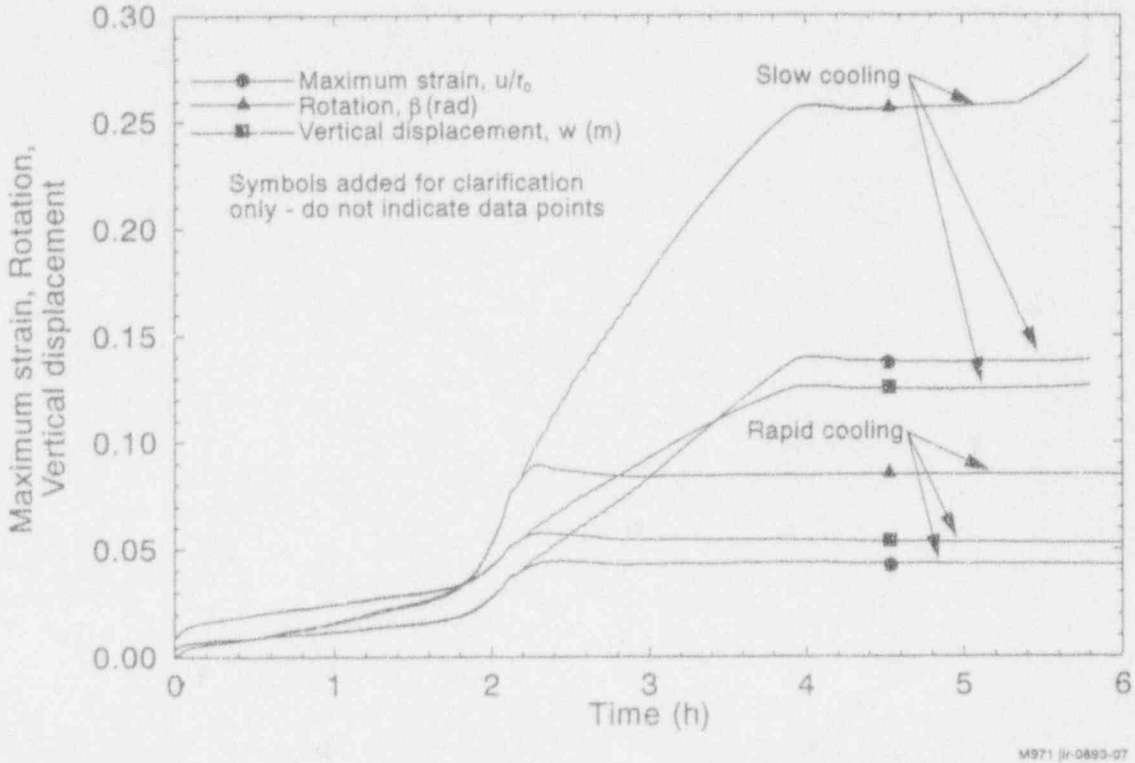

Figure 5-32. Comparison of results with and without rapid cooling for a 62.5% nominal case with a hot spot.

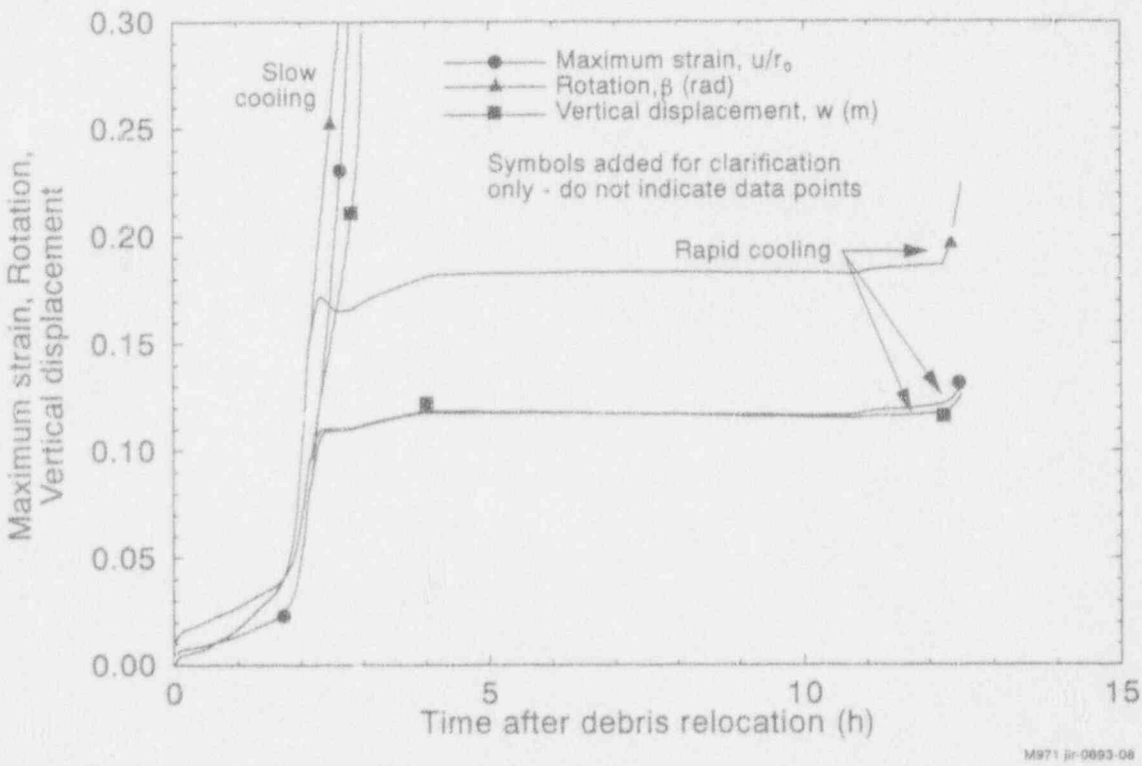

Figure 5-33. Comparison of results with and without rapid cooling for a 75% nominal case with a hot spot.

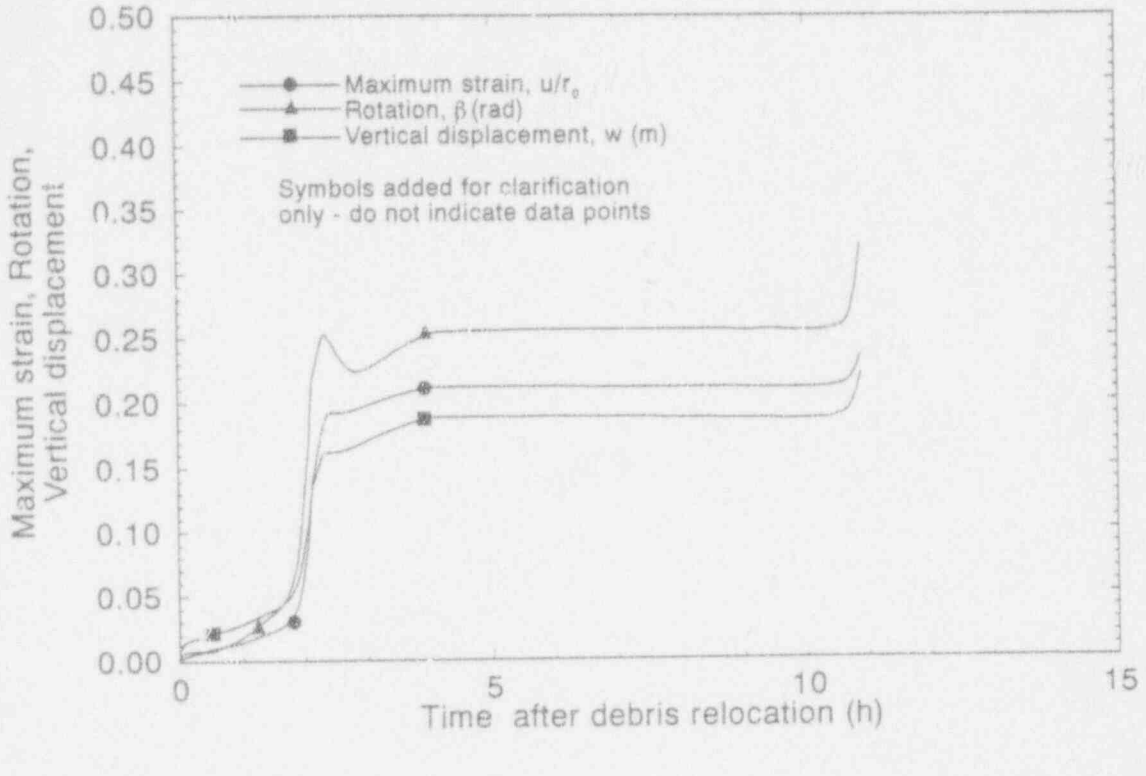

M971 jlr-0893-05

Figure 5-34. Results for a 80% nominal case with a hot spot and rapid cooling.

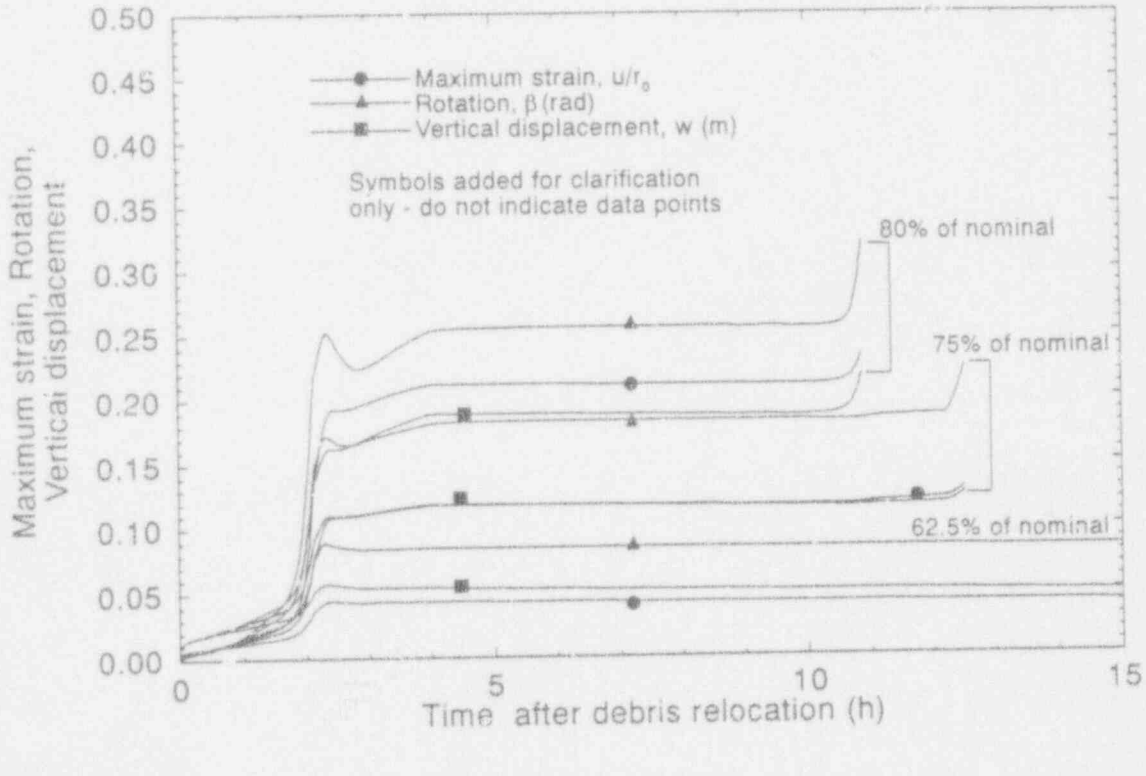

M971 jlr-0893-06

Figure 5-35. Comparison of results for rapid cooling on various nominal heat fluxes with a hot spot.

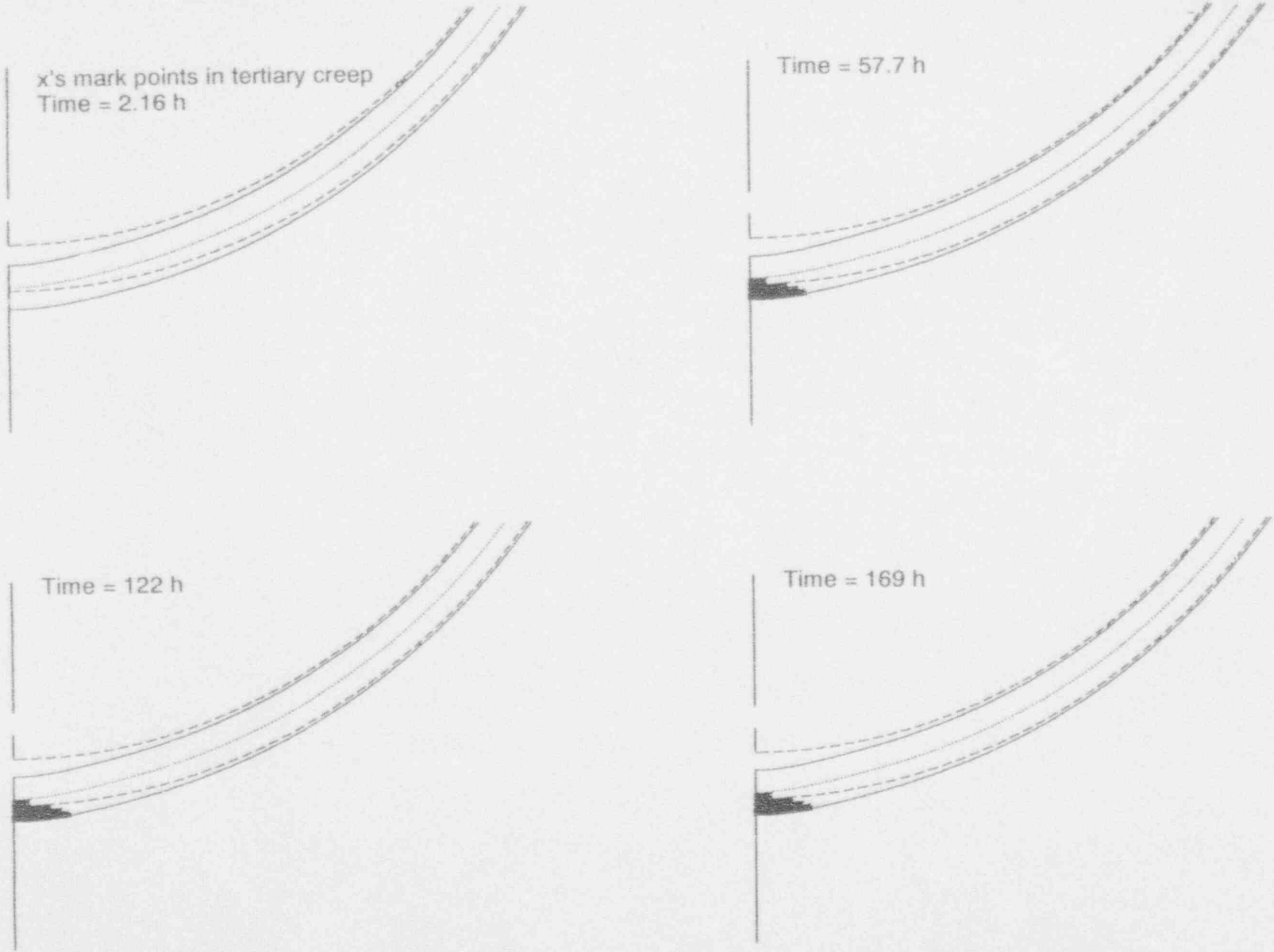

Figure 5-36. Distribution of ligaments experiencing tertiary creep at various times for the 62.5% nominal case with a hot spot and rapid cooling.

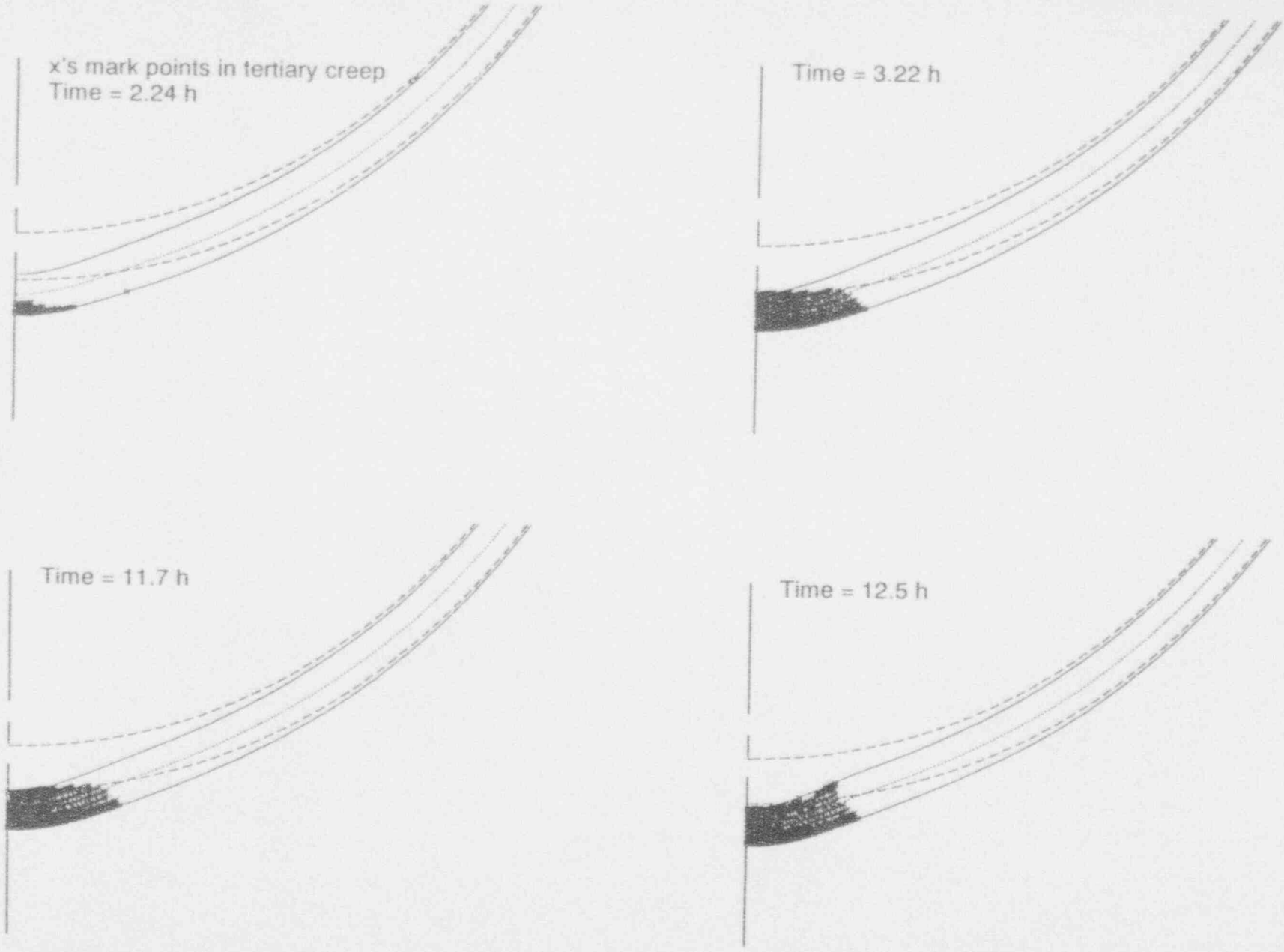

Figure 5-37. Distribution of ligaments experiencing tertiary creep at various times for the 75% nominal case with a hot spot and rapid cooling.

nominal, with failures occurring just under two and three hours respectively. A very different response is seen for the case involving the hot spot on 50% of nominal background. Here the rate of change of deformations appears to become more modest with time after a few hours.

To further define the fraction of nominal heat flux resulting in failure, a case was run corresponding to 62.5% of nominal. A comparison of this case with the case involving 50% nominal is shown in Figure 5-27. Note that both the vertical and horizontal scales differ from Figure 5-26. At approximately four hours into the transient, the pressure history contains a substantial depression, resulting in pressures as low as 3 MPa before ascending back to 16 MPa at 11 hours. The rate of change of deformations drops dramatically once this depression is encountered. In the case of a hot spot on 50% nominal, the hot region is still quite restrained before depressurization, with very small tensile normal stress components in the hot spot region. When the system depressurizes, the vessel unloads elastically, and most of the hot spot experiences compression following depressurization. Only the outer two ligaments experience tension at this time. The structure creeps down for a period of time, so that the hoop strain actually decreases during depressurization. There is less of this effect for the case of 62.5% of nominal, and, after the depressurization is complete (approximately 5.25 hours), values for these deformation parameters begin to rise again. The increase in meridian rotation at this time is the most obvious of the three. Unfortunately, the combination of depressurization with the partial propagation of tertiary creep through the vessel results in a few severe stress states which slow the simulation down dramatically. Ligaments were allowed to and did return to the secondary regime, but this did not relieve all points from the tertiary regime. As a result, it was not possible to get the simulation to advance past six hours with the actual pressure history. Figure 5-27 illustrates that the case involving 62.5% of the nominal heat flux advanced to substantially greater deformations than the case involving 50% nominal heat flux before the depressurization, and the deformations appear to recover and continue to climb after depressurization. Results involving rapid cooling, discussed below, suggest that a vessel experiencing these deflections and subject to repressurization to 16 MPa will again experience rapid rates of increasing deformation. The simulations suggest that the vessel is not able to survive slow cooling of a hot spot on a background heat flux 62.5% of the nominal level.

Figures 5-28 through 5-31 illustrate the distribution of tertiary ligaments for the cases of hot spots on 100%, 75%, 62.5% and 50% of nominal background heat fluxes under the actual pressure history. It is clear from the figures that the tertiary regime occupies a decreasing fraction of the lower head as the nominal background heat flux is reduced, until, at 62.5% of nominal, it is unable to propagate all the way through thickness before the depressurization. Also note that once the depressurization occurs, the through thickness propagation recedes in the case of 62.5% nominal. The results of these slow cooling analyses are that the vessel is capable of surviving a hot spot on a background heat flux between 50% and 62.5% of nominal; this is to be compared with the results from the stress-based damage failure criterion results, which suggest that survival is possible on a background between 25% and 33% of the nominal case heat flux (see Section 5.1.1).

5.2.3 Effects of Failure Criterion on Rapid Cooling Case Results

Rapid cooling simulations were performed for hot spots on background heat fluxes equal to 62.5%, 75% and 80% of the nominal level. Maximum values of deformation parameters are

plotted in Figures 5-32 through 5-35, and distributions of tertiary ligaments and vessel deformations are shown in Figures 5-36 through 5-38. Rapid cooling in all cases was initiated at 2.16 hours into the transient, at which time the hot spot had been above 1320 K for a sufficient period of time to be consistent with observations from TMI-2 metallurgical examinations. At the time rapid cooling is initiated for the case of 62.5% of the nominal heat flux, the vessel has experienced only modest deflections, and the hot spot is still well restrained. Initiation of rapid cooling results in a small decrease in all freedoms and the vessel asymptotically reaches a benign state. The vessel easily survives the case of rapid cooling for 62.5% of the nominal heat flux. In the cases of rapid cooling for 75% and 80% of the nominal heat flux, the vessel has experienced considerably greater deformation before rapid cooling is initiated. The characteristic response of the freedoms is quite different from the case of 62.5% of the nominal heat flux. During the cooling period itself, there is little change in either the peak strain or vertical deflection, but the maximum meridian rotation decreases. Once the cooldown is completed, all freedoms continue to increase, but at a slower pace than experienced before the initiation of rapid cooling. At four hours into the transient, the system depressurizes, and virtually no change in any of the freedoms occurs during this period. Once the system begins to repressurize at 11 hours, however, all freedoms begin to rapidly increase again. Although these latter two cases were not run all the way to failure, it appears from the plots that failure occurs in about 13 and 11 hours, respectively, for the cases of rapid cooling of a hot spot from 75% and 80% of the nominal background heat flux. Figure 5-35 shows a comparison of the three cases with rapid cooling.

Plots of vessel deformation and the distribution of tertiary ligaments are shown in Figures 5-36 through 5-38. A word about the secondary to tertiary transition criterion is in order to permit comparisons of Figures 5-28 through 5-31 with Figures 5-36 through 5-38. The transition criterion is based on strain, and the transition strain is a function of both temperature and stress as described in Appendix A. The creep data indicate the transition occurs at relatively low strains (few percent) at low temperatures (873 K), but that the transition strain increases dramatically (as high as 20%) at intermediate temperatures (1,073 K), before falling again to 10-12% at high temperatures (1,273 K). In examining the distributions of tertiary ligaments in Figures 5-28 through 5-31, it should be kept in mind that these are slow cooling cases with the hot spot near its peak temperature, and substantial strains are required to reach the tertiary transition through thickness. Once rapid cooling is initiated, the temperatures fall dramatically, and the vessel can experience the tertiary state at more modest strains. In examining Figure 5-36, for instance, corresponding to rapid cooling of a hot spot on 62.5% of nominal background, it can be seen that at 2.16 hours, just about the time rapid cooling is initiated, there are no tertiary ligaments in the vessel. The vessel is still at elevated temperature, and the lack of tertiary ligaments is consistent with the first frames in Figures 5-28 through 5-31, which show only a few tertiary ligaments at comparable strains. Once rapid cooling is initiated, however, the transition from secondary to tertiary occurs at more modest strains, so that the outer half of the vessel underneath the hot spot enters the tertiary regime. The stress levels in the tertiary regions of Figure 5-36 are nearly zero, with the entire load being taken by the inner portion of the vessel. Figures 5-37 and 5-38 both indicate that the vessel has experienced some propagation of the tertiary regime through thickness prior to rapid cooling, and the onset of cooling is sufficient to push the entire hot spot region into the tertiary regime through thickness. This would be largely responsible for the rapid rates of increase of freedoms following repressurization at 11 hours.

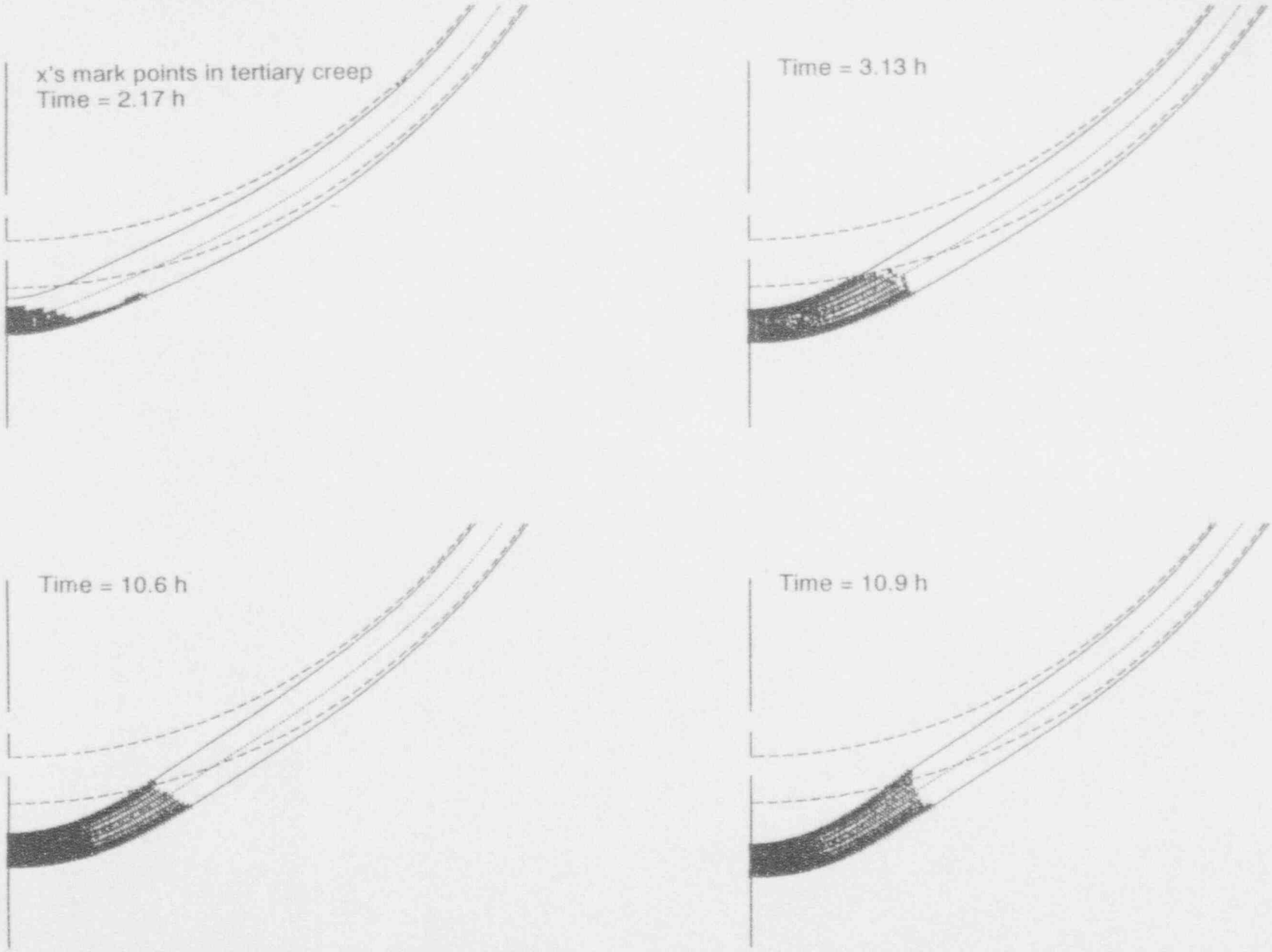

Figure 5-38. Distribution of ligaments experiencing tertiary creep at various times for the 80% nominal case with a hot spot and rapid cooling.

It should also be noted that the tertiary data in Appendix A are provided at and above 873 K. Below this temperature, the relationships at 873 K were used. Twelve hours into the transient following rapid cooling, temperatures in the hot spot region were only 50–100 K below this value, so the use of these relationships at these temperatures is conservative but not unwarranted. At some point, however, there needs to be a criterion for deciding at what temperature the transition from tertiary back to secondary is permitted. The final states in Figure 5-36, for instance, are at 573 K, where creep is not likely to occur at all, and the notion of some states being in the tertiary regime is meaningless. In this particular simulation, however, the final tertiary states are entirely benign and of no consequence to the vessel's survival.

In summary, it has been found that vessel survival based on a mechanical instability failure criterion is possible for a hot spot on 50% to 62.5% of nominal case background heat flux under slow cooling conditions, and between 62.5% and 75% of nominal case heat fluxes in the presence of rapid cooling. Levels of survivable heat flux are substantially larger than in the slow cooling case analyzed using the stress-based damage failure criterion, but the distinction between slow and rapid cooling survivability is not nearly as great.

5.3 Conclusions

Additional calculations were completed to investigate two areas of uncertainty identified by the initial scoping calculations in Section 4. Specifically, the amount of cooling that occurred within the debris after relocation and the criterion used for predicting vessel failure were investigated with additional sensitivity studies.

Although data are not sufficient to determine the exact mechanism that caused the debris to cool within the first two hours after relocation, two possible forms of cooling were investigated that have the potential to produce this additional cooling:

- A slow cooling mode in which it is assumed that water slowly removes heat as it travels through cracks in the debris

- A rapid cooling mode in which it is assumed that coolant rapidly removes heat as it travels through gaps or channels between the vessel and debris.

Three types of calculations were performed to investigate debris cooling. Using a stress-based damage failure criterion, calculations were first performed to quantify the magnitude of cooling needed to prevent vessel failure and obtain vessel temperature responses consistent with VIP metallurgical examination data. Then, analyses were performed to evaluate the type of debris configuration (i.e., the number and size of cracks and the gap size) needed to obtain the estimated cooling rates. Finally, the hypothesis of debris cooling was evaluated using an energy balance based on parameters measured directly during the accident or inferred from data measured during the accident.

Slow cooling analysis results indicate that the vessel will survive a hot spot in the presence of a background heat flux that is between 25% and 33% of the nominal, best estimate, heat flux assumptions in Section 3. Rapid cooling analysis results indicate that negative heat fluxes

between 25 and 125 kW/m^2 are needed to obtain cooling rates consistent with metallurgical examination data of vessel steel in the hot spot region.

Although higher percentages of the nominal heat flux in the region outside the hot spot may occur if rapid cooling is present, analyses indicate that a combination of both cooling mechanisms must occur in order for results to be consistent with metallurgical examination data. For example, if only a slow cooling mechanism were present, the vessel temperatures would not experience the rapid cooling rates observed in the metallurgical examinations. Furthermore, a rapid cooling analysis for a case in which a 75% nominal background heat flux is imposed on the vessel indicates that the vessel would fail before the hot spot temperatures could be sustained for the 30 minute time period estimated in metallurgical examinations. Therefore, these cooling analyses not only provided an estimate for the magnitude of cooling that must occur, but also indicated that analyses considering both cooling mechanisms were needed in order to be consistent with results of the TMI-2 VIP examinations.

Scoping thermal analyses were performed to postulate the types of cracks or gaps that are needed in the debris to obtain the estimated cooling rates. Conservative heat transfer assumptions were used in these analyses to obtain lower estimates on the amount of heat that would be removed by coolant traveling through debris cracks or a debris-to-vessel coolant gap. Results indicate that the nominal background heat flux could be reduced by 25% if less than 220 "through cracks" with a 0.5-cm effective diameter existed in the hard layer of debris on the lower head. This number of cracks represents an insignificant volume fraction of the hard layer of debris in the lower head. Calculations also indicate that coolant traveling through a 0.1-cm gap between the debris and the vessel could result in the rapid vessel cooling rates estimated by metallurgical examination data. Note that both of these calculations conservatively assumed that the coolant remained liquid as it removed heat from the debris. If the coolant traveling within the debris channels was assumed to boil, heat transfer would be much more efficient (thus reducing the number and/or size of channels).

An energy balance considering coolant mass flows entering and leaving the vessel indicates that the debris must have cooled after relocation. Calculations were conservatively performed by neglecting heat losses to the vessel and internal structures. Input parameters, such as debris decay heat, coolant injection rates, and relief valve flow rates, were quantified based on data measured during the accident or inferred from data measured during the accident. For all cases evaluated, which included upper-bound and lower-bound estimates on debris decay heat and mass flow rates, the debris was predicted to cool in the time period between debris relocation and vessel repressurization.

Calculations were also performed to assess the influence of failure criterion and the inclusion of tertiary creep on failure predictions. Specifically, analyses were performed including the effects of tertiary creep with failure defined as the point where mechanical instability occurs rather than invoking a stress-based damage failure criterion. Results from these calculations indicate that the vessel would survive if exposed to a hot spot on 50 to 62.5% of the nominal case heat fluxes under slow cooling and between 62.5 and 75% of the nominal heat fluxes in the presence of rapid cooling. The percentages of nominal case heat fluxes for which the vessel is predicted to survive for the slow cooling cases are nearly a factor of two larger than percentages predicted using a stress-based damage failure criterion. However, the percentages of nominal case

heat flux for which the vessel is predicted to survive for the rapid cooling cases is similar to levels predicted with the stress-based damage failure criterion.

In summary, scoping calculations led to the hypothesis that the debris cooled within the first two hours after relocation although there are insufficient data to determine the exact mechanisms that caused the debris to cool. Although the magnitude of cooling required was lower when a mechanical instability failure criterion was used instead of a stress-based damage failure criterion, analyses using either failure criterion indicated that the debris cooled within the first two hours after relocation. This cooling is substantiated by calculations based upon RCS coolant injection and relief rates. Several plausible mechanisms for achieving this cooling were investigated. Calculations indicate that the debris cooling rates needed to prevent vessel failure could be achieved if a minimal volume of cracks were present in the debris. Furthermore, it is predicted that coolant traveling through a minimal size of gap between the debris and the vessel could cool the vessel at rates consistent with the results of metallurgical examinations of the vessel steel samples.

5.4 References

1. D. R. Dierks and L. A. Neimark, *Results of Mechanical Tests and Supplementary Metallographic Examinations of the TMI-2 Lower Head Samples*, OECD-NEA-TMI-2 VIP TMI (93) AL02, June 1993.

2. G. V. Smith, *Evaluations of the Elevated Temperature Tensile and Creep-Rupture Properties of C-Mo, Mn-Mo, and Mn-Mo-Ni Steels*, Metal Properties Council, American Society for Testing and Materials, ASTM Data Series Publication DS47, November 1971.

3. National Research Institute for Metals, NRIM Creep Data Sheet 18B, *Elevated Temperature Properties of 1.3Mn-0.5Mo-0.5Ni Steel Plates for Boilers and Other Pressure Vessels (SBV 2)*, Tokyo, Japan, 1987.

4. D. W. Akers et al., *Companion Sample Examinations*, OECD-NEA-TMI-2 VIP TMI V(92)EG10, July 1992.

5. W. M. Rohsenow, J. P. Hartnett, and E. N. Ganić, *Handbook of Heat Transfer Fundamentals*, Second Edition, New York: McGraw-Hill Book Company, 1985.

6. W. Elenbass, "The Dissipation of Heat by Free Convection: The Inner Surface of Vertical Tubes of Different Shapes of Cross-Section," *Physical, IX*, No. 8, 1942, pp. 865-874.

7. J. R. Dyer, "Natural Convective Flow Through a Vertical Duct With Restricted Entry," *International Journal of Heat and Mass Transfer, 211*, 1978, pp. 1341-1354.

8. N. E. Todreas, and M. S. Kazimi, *Nuclear Systems I, Thermal Hydraulic Fundamentals*, New York: Hemisphere Publishing Corporation, 1990.

9. J. G. Collier, *Convective Boiling and Condensation*, Second Edition, New York: McGraw-Hill International Book Company, 1972.

10. F. W. Dittus, and L. M. K. Boelter, "Heat Transfer in Automobile Radiators of the Tubular Type," *University of California Publications in Engineering 2, No. 3*, 1930, pp. 443–461.

11. J. R. Welty, C. E. Wicks, and R. E. Wilson, *Fundamentals of Momentum, Heat, and Mass Transfer,* Second Edition, New York: John Wiley & Sons, 1976.

12. G. D. Raithby, and K. G. T. Hollands, "A General Method for Obtaining Approximate Solutions to Laminar and Turbulent Free Convection Problems," in *Advances in Heat Transfer, 11*, edited by T. F. Irvine and J. P. Hartnett, pp. 266–315, New York: Academic, 1975.

13. G. D. Raithby, et al., "Free Convection Heat Transfer from Spheroids," *Journal of Heat Transfer, 98*, 1976, pp. 452-458.

14. E. R. G. Eckert, and T. W. Jackson, *Analytical Investigation of Flow and Heat Transfer in Coolant Passages of Free Convection Liquid Cooled Turbines, NACA RM, E50D25*, July 1950.

15. W. H. McAdams, *Heat Transmission,* Third Edition, New York: McGraw-Hill, 1954.

16. R. D. McCormick, *TMI-2 Data Summary Report,* EGG-TMI-7843, September 1987.

17. Nuclear Safety Analysis Center, *Analysis of Three Mile Island—Unit 2 Accident*, NSAC-80-1, March 1980.

18. J. L. Anderson, *Recommended HPI Rates for the TMI-2 Analysis Exercise (0-300 Minutes)*, EGG-TMI-7833, September 1987.

19. P. Kuan, and E. L. Tolman, *Electromatic Relief Valve Flow and Primary System Hydrogen Storage during the TMI-2 Accident,* EGG-TMI-7703, May 1987.

20. Y. Nomura, *PORV Discharge Flow during the TMI-2 Accident*, EGG-TMI-7825, July 1987.

21. R. E. Henry and H. F. Fauske, "The Two-Phase Critical Flow of One-Component Mixtures in Nozzles, Orifices, and Short Tubes," *Journal of Heat Transfer*, May 1971, pp. 179-187.

22. K. H. Sun et al., "The Prediction of Two-Phase Mixture Level and Hydrodynamically-Controlled Dryout under Low Flow Conditions," *International Journal of Multiphase Flow, 7*, No. 5, 1981, pp. 521-543.

23. J. H. Keenan, et al., *Steam Tables—Thermodynamic Properties of Water Including Vapor, Liquid, and Solid Phases,* New York: John Wiley & Sons, 1978.

24. R. R. Hobbins, et al., "Fission Product Release as a Function of Chemistry and Fuel Morphology," *Fission Product Transport Processes in Reactor Accidents*, New York: Hemisphere, 1990, pp. 215–224.

25. B. G. Schnitzler, *Fission Product Decay Heat Modeling for Disrupted Fuel Regions (FDECAY)*, EGG-PHYS-5698, December 1981.

26. J. R. Larson, *System Analysis Handbook*, NUREG/CR-4041, EGG-2534, December 1984.

27. J. L. Rempe, et al., *Light Water Reactor Lower Head Failure Analysis*, NUREG/CR-5642, October 1993.

28. Y. R. Rashid, "Summary of Comments on the Margin-to-Failure Report," *Presentation at the 11th Programme Review Meeting of the OECD NEA Vessel Investigation Project*, TMI V(93)MAN, May 17, 1993.

6. SUMMARY AND CONCLUSIONS

As part of the TMI-2 VIP, margin-to-failure calculations were performed to increase understanding about events that occurred during the TMI-2 accident. Because there is considerable uncertainty in input parameters for these calculations, analyses relied upon methods with closed-form or simplified numerical solution techniques. With this approach, a large number of cases could be evaluated rapidly and efficiently.

Calculations were performed to consider the four failure mechanisms identified in Figure 6-1:

- Tube rupture
- Tube ejection
- Global vessel failure
- Localized vessel failure.

Unshaded shapes in Figure 6-1 indicate which analyses were performed in this study. Note that several analyses for evaluating certain phenomena—such as jet impingement, melt penetration distance, vessel thermal response, and weld failure—provided input to the failure analyses. As indicated by the shaded boxes, results from some of these preliminary analyses eliminated the need for subsequent analyses. For example, results from melt penetration calculations indicate that molten fuel will not relocate to locations below the lower head. Therefore, reactor coolant system temperatures were applied in subsequent tube rupture analyses, rather than performing an ex-vessel tube heatup analysis with debris in the tube.

As indicated in Figure 6-1, these calculations employed three major sources of VIP examination data:

- Nozzle examination data for characterizing melt composition and penetration distances within nozzles
- Companion sample examination data for characterizing debris properties, such as decay heat and material composition
- Vessel steel boat sample examination data for characterizing peak vessel temperatures, duration of peak temperatures, and vessel cooling rate.

Some of the data were used to quantify input to the calculations and some were used to verify output from the calculations. As illustrated by results within this report, some of the companion sample data—namely that the debris underwent slow cooling—were inconsistent with the vessel steel cooling rate inferred from examinations of the boat samples. When results based upon companion sample data indicated that vessel failure would occur, it was postulated that additional cooling, not indicated by companion sample data, needed to be considered in the analysis. Hence, calculations were performed to quantify the magnitude of this cooling and the hypothesized debris

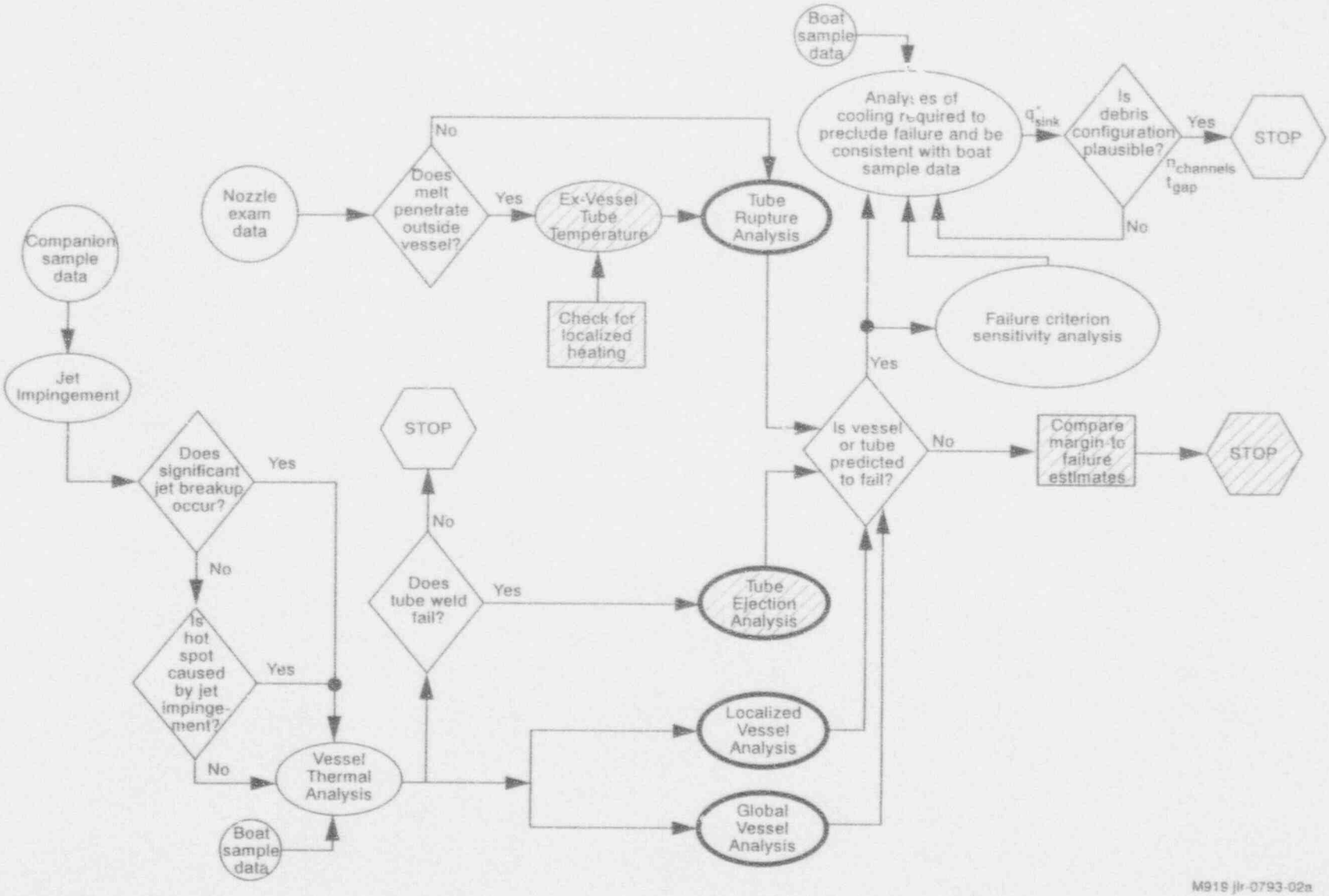

Figure 6-1. Flow diagram illustrating margin-to-failure calculations performed in this study.

configuration required to support this cooling. An energy balance was also performed to verify the existence of this cooling based upon plant thermal hydrsulic parameters.

Results from calculations documented in this report are summarized in this section. These calculations not only provide insights into the potential for vessel failure, they also provided insights into the manner in which debris relocated into the lower plenum and the potential for debris cooling after relocation. Insights gained from these calculations may have implications for severe accident analyses in general.

6.1 Summary of Results

Results from scoping calculations are presented in this section according to the order shown in the flow diagram (Figure 6-1). Starting at the upper left hand corner ("nozzle exam data"), melt penetration calculations (reported in Section 3) indicate that molten debris would not penetrate below the vessel head with sufficient heat capacity to raise ex-vessel penetration tube temperatures. Hence, ex-vessel tube rupture calculations were performed assuming tube temperatures consistent with the vessel coolant temperatures. Since such temperatures were expected to result in very high margins to failure, a constant upper system pressure of 15 MPa was also applied in the tube failure calculations. Results indicate that the margin to failure for this mechanism was very high.

Jet impingement calculations (left side of Figure 6-1) indicate that the amount of breakup that occurred as melt relocated to the lower plenum was insignificant. Hence, calculation results indicate that the postulated scenario with major amounts of jet breakup occurring during relocation (Scenario 3 of Section 2.3) is incorrect. Jet impingement calculations also indicate that the magnitude and duration of the hot spot temperatures estimated in TMI-2 vessel examinations could not have been caused by an impinging jet. Rather, hot spot temperatures are predicted to occur later in the scenario due to a sustained heat load from molten debris on the lower head. The limited area estimated to have experienced hot spot temperatures suggests that this region was subjected to a localized heat source, such as might occur with a non-homogeneous debris bed or a localized region with enhanced debris-to-vessel contact. Hence, calculation results indicate that the scenario with hot spot temperatures caused by a coherent jet impinging upon the vessel (assumed in Scenario 1 of Section 2.3) is incorrect.

Although the quantitative value predicted for the vessel wall surface peak temperature differed in each case, results from several sensitivity studies were qualitatively similar. Namely, the thermal response can be divided into the following three time periods:

- An initial localized temperature spike for the time and location of jet impingement (typically lasts for about 1 minute)
- A transient vessel heatup (typically lasts for about 1 hour)
- A quasi-steady vessel temperature distribution (typically lasts for several hours).

Only a case with lower bound input assumptions (discussed in Section 3.2) resulted in global vessel temperature predictions that are consistent with the boat sample examination data; namely

that vessel temperatures remain below values where the material undergoes a transition from ferritic to austenitic steel.

As noted in Figure 6-1, prior to performing a tube ejection analysis, it must be established that the weld holding the nozzle to the vessel has failed. Since it is not known if the hot spot temperatures occurred at the same time that the RCS was repressurized to 15 MPa, weld failure calculations were conservatively performed assuming that peak temperatures and pressures occurred simultaneously. Results indicate that even for these very conservative assumptions, there was considerable margin in the weld's integrity. Therefore, there was no need for a tube ejection analysis.

The potential for the vessel to experience a global failure was evaluated for vessel temperature distributions based upon nominal and lower bound input assumptions (see Section 3.2). Note that both of these temperature distributions were obtained by assuming that the molten debris experienced relatively slow cooling rates, in order to be consistent with companion sample examination data. Global failure was predicted to occur at 1.7 hours after relocation for the nominal case and 2.3 hours after relocation for the lower bound case. In fact, parametric studies indicate that failure is predicted in less than 3 hours for temperatures above 800 to 900 K, if the reactor vessel is maintained at pressures near the operating pressure. Thus, results indicate that enhanced debris cooling occurred within the first 2 hours to prevent global vessel failure.

The potential for the vessel to experience a localized failure was evaluated by imposing hot spot temperatures on two background distributions, the lower bound case temperatures and a benign case with cool background temperatures. These two temperature distributions bounded possible background distributions. Boat sample examinations indicate that temperatures outside the hot spot remained below the ferritic to austenitic transition temperature, and the minimum vessel temperature was the normal operating condition temperature. Results for the lower bound case indicate that the presence of a hot spot reduces failure time predictions by about 0.4 hours. Furthermore, the presence of the hot spot affected predictions of the geometry of the vessel and the damage distribution in the vessel at the time of failure. However, results from the benign case indicate that the vessel is capable of surviving local hot spots in the temperature range and of the duration inferred from the metallurgical examinations if the balance of the shell remains relatively cool.

Results from thermal and structural calculations based upon debris decay heats from companion sample examinations combined with the relatively rapid vessel cooling indicated by metallurgical examinations indicate that some form of debris cooling occurred that was not evident in the TMI-2 companion samples. In addition, analysis results suggest that a stress-based damage failure criterion may be too conservative for predicting failure. Therefore, additional analyses were performed to investigate the effects of debris cooling and failure criterion on calculation results. An energy balance considering coolant mass flows entering and leaving the vessel indicate that the debris cooled in the time period between relocation and vessel repressurization (between 220 and 320 minutes). Although there are insufficient TMI-2 data to determine the exact mechanisms that caused the debris to cool, scoping calculations were performed to investigate two forms of cooling that have the potential to produce additional cooling:

- A slow cooling mode in which it is assumed that water slowly removes heat as it travels through channels or "cracks" within the debris

- A rapid cooling mode in which it is assumed that coolant rapidly removes heat as it travels through channels or "gaps" between the vessel and the debris.

Slow cooling analysis results indicate that coolant traveling through a relatively insignificant volume of cracks within the debris (i.e. less than 1% of debris volume) will remove sufficient heat to prevent vessel failure. Rapid cooling analysis results indicate that coolant traveling through a gap of minimal thickness (i.e. as small as 1 mm) will remove sufficient heat to allow the vessel to experience cooling rates consistent with the results of metallurgical examinations of the vessel steel samples. In order for either of the above forms of cooling to occur, coolant must be present within the lower head. Hence, the presence of coolant within the lower head during the TMI-2 accident was instrumental in providing these postulated forms of cooling.

Although the magnitude of cooling required was decreased when the stress-based damage failure criterion was replaced with a mechanical instability failure criterion, calculational results indicate that a combination of both cooling mechanisms is needed in order for results to be consistent with metallurgical examination data. For example, if only a slow cooling mechanism was present, the vessel temperatures would not be predicted to experience the rapid cooling rates observed in the metallurgical examinations. Furthermore, analyses indicate that a vessel subjected to peak hot spot temperatures on nominal case background heat fluxes could not survive the 30-minute time period estimated in metallurgical examinations. Thus, analyses indicate that both mechanisms need to be considered in order to obtain results consistent with TMI-2 VIP examinations.

6.2 Insights from Calculations and Severe Accident Implications

Major insights from the failure analyses include:

- The large margin-to-failure estimates for tube failure mechanisms essentially preclude the potential for tube failure to occur during the TMI-2 event.

- It is possible for the vessel to withstand the hot spot temperatures and durations determined from the vessel metallurgical examinations if the balance of the vessel outside the hot spot remains relatively cool. Localized and global vessel failure calculations indicate that the background temperature behavior of the vessel (i.e., outside the hot spot), which is highly dependent upon the heat load from relocated debris in the lower head, is key to predicting failure from either of these mechanisms.

- Debris cooling may have occurred within the first two hours after relocation to the lower head. Although companion sample examination data are insufficient to quantify the timing and rate of debris cooling, additional scoping calculations indicate that the debris cooled in the time interval after relocation and before vessel repressurization.

- Debris cooling may have occurred via coolant traveling in channels within the debris and in channels between the debris and the vessel. Although there are insufficient

TMI-2 data to determine the exact mechanisms that caused the debris to cool, scoping calculations indicate that the presence of a relatively insignificant volume of flow channels within the debris or a relatively thin channel between the debris and the vessel would have significantly enhanced debris cooling during this time period.

Several results and insights from these calculations may have considerable impact upon severe accident safety analyses. Some of these implications are the following:

- The background, or global, temperature behavior is key to predicting PWR vessel failure at high pressure conditions. Although vessel failure times may be shortened if a localized region of the vessel is exposed to higher temperatures, cool background temperatures have the potential to prevent such failures.

- If relocating debris solidifies containing channels or with channels between it and the vessel, debris coolability may be enhanced. Hence, TMI-2 analyses may provide additional insight about phenomena not currently modeled in severe accident analyses that could provide additional safety margins for such analyses.

Hence, the importance of these calculations is not only limited to increasing understanding of the TMI-2 accident. Calculation results may also provide another step toward answering broader severe accident questions.

Appendix A

Modeling Input

Appendix A

Modeling Input

A.1 Thermal Material Property Data

This section summarizes the material data used for the thermal calculations in the TMI-2 margin to failure analyses. Temperature-dependent properties, such as thermal conductivity, density, enthalpy, specific heat, and viscosity of the debris and vessel material are included.

A.1.1 UO_2 Data

This section contains data for properties of UO_2. Properties, such as thermal conductivity, theoretical density, enthalpy, specific heat capacity, and viscosity are summarized in Figures A-1 through A-5. As indicated in the figures, these data are based upon information in Reference A-1. Reference A-1 also indicates that the solidus and liquidus temperature for UO_2 is 3,113 K.

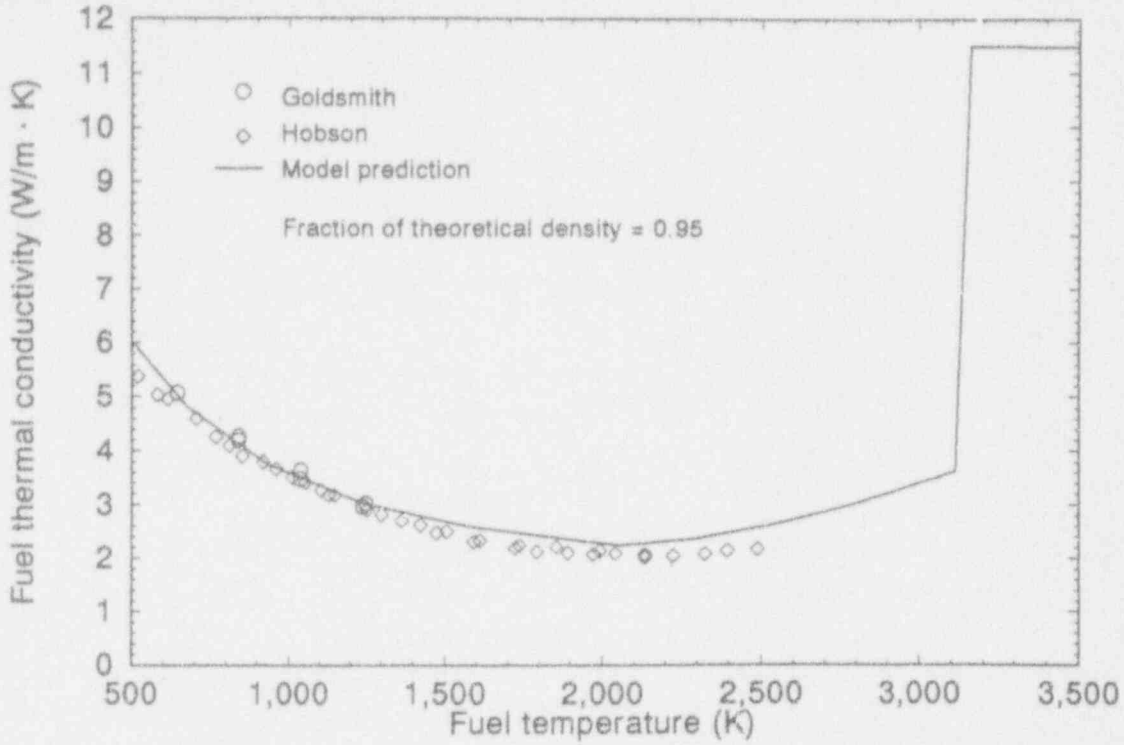

M619 jlr-0692-07

Figure A-1. Model prediction for thermal conduction of 0.95 TD UO_2 compared with data from specimens with densities in the range of 0.945 to 0.955 TD.[A-1]

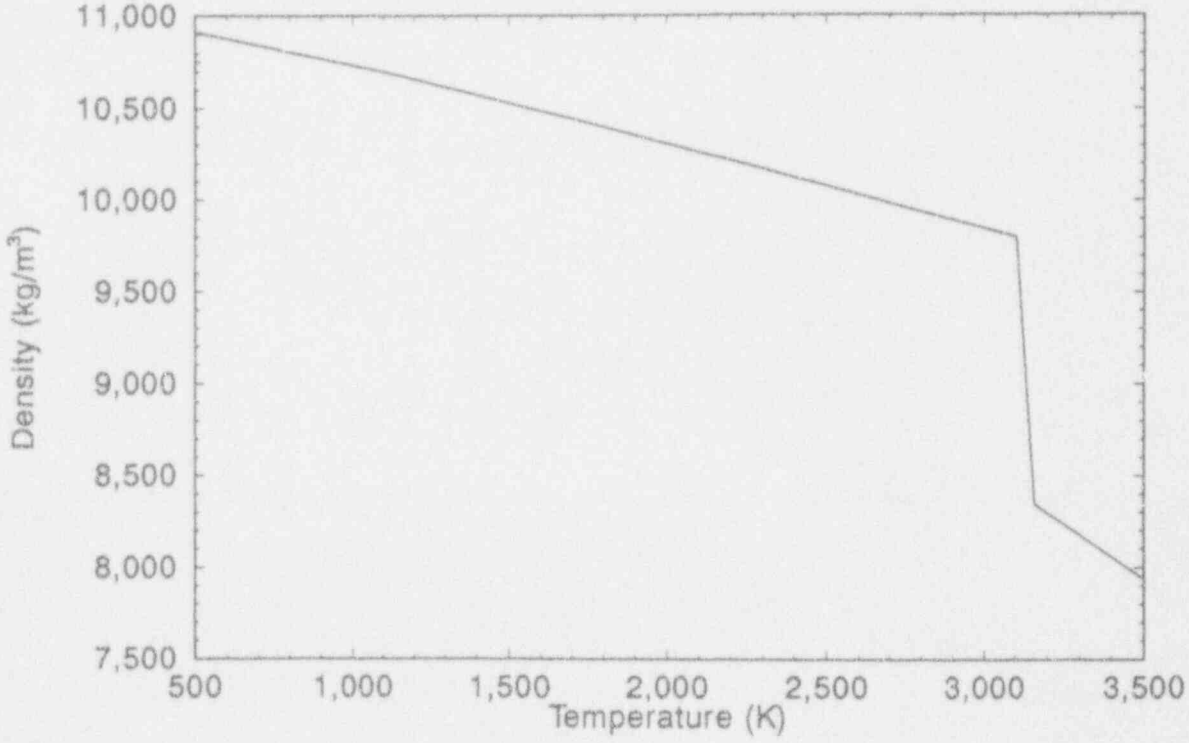

Figure A-2. Theoretical density of UO_2.[A-1]

M619 jlr-0692-08

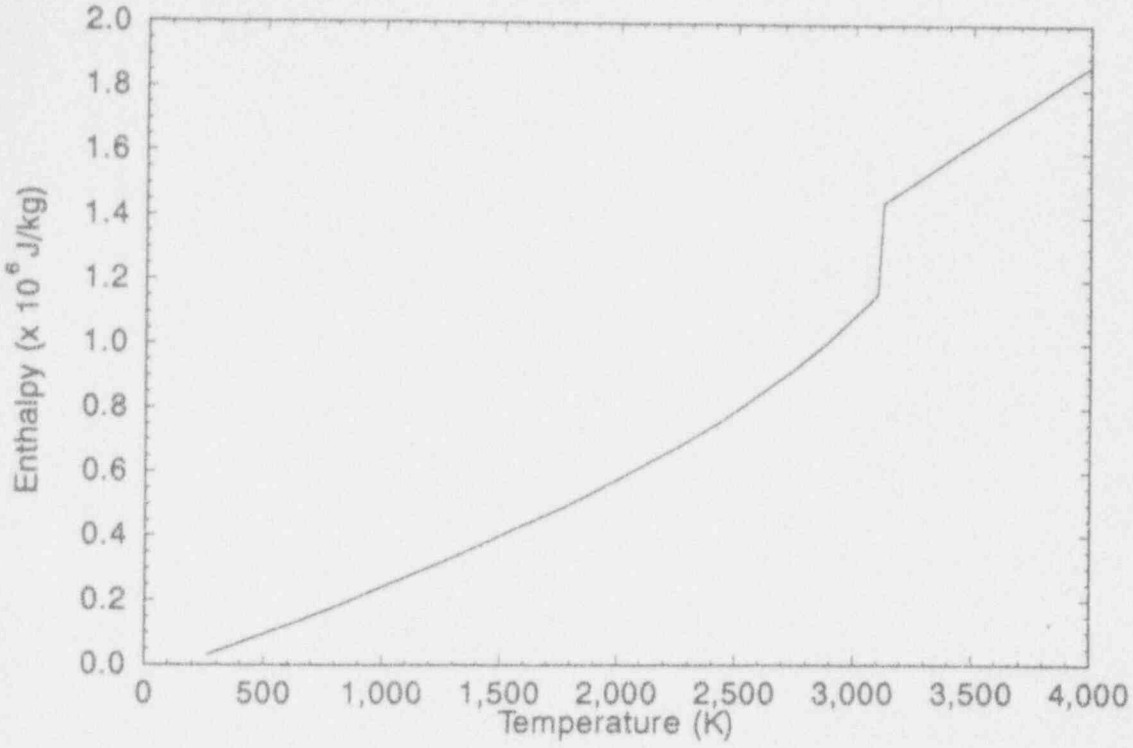

Figure A-3. Enthalpy of UO_2 as a function of temperature to 4,000 K.[A-1]

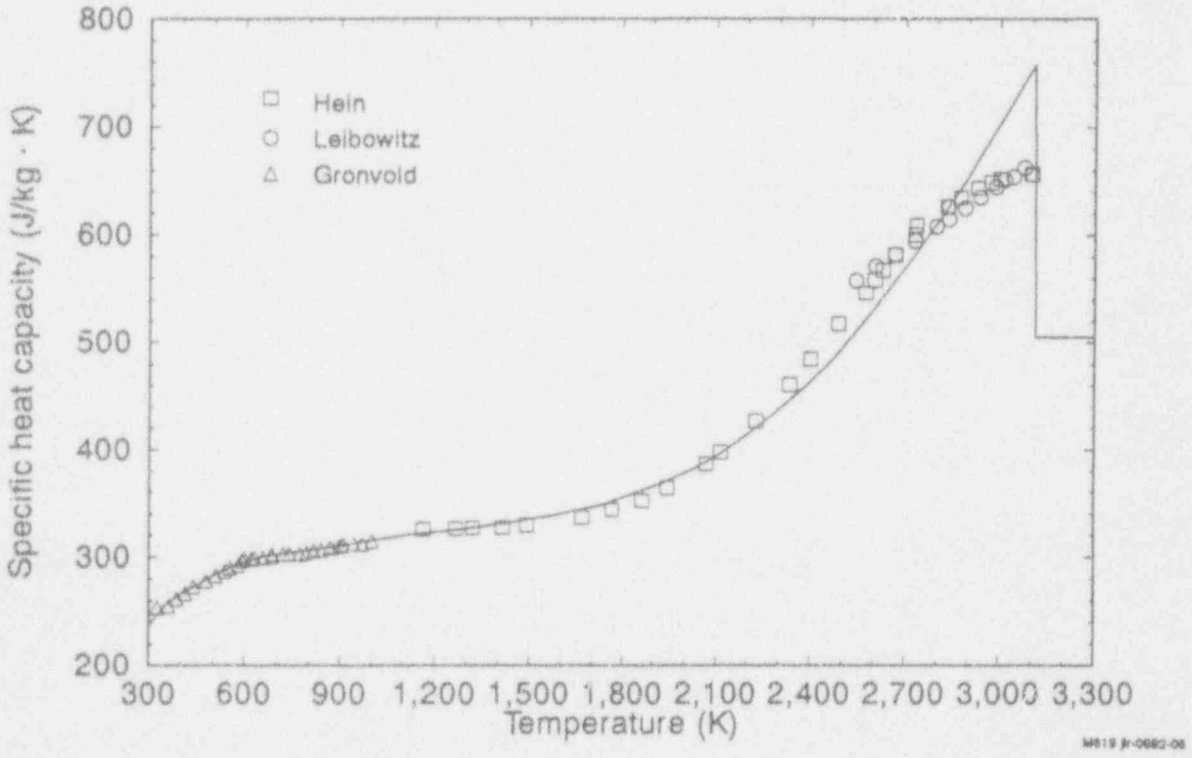

Figure A-4. UO_2 specific heat capacity data from three experimenters compared with UO_2 specific heat capacity correlation (solid line).[A-1]

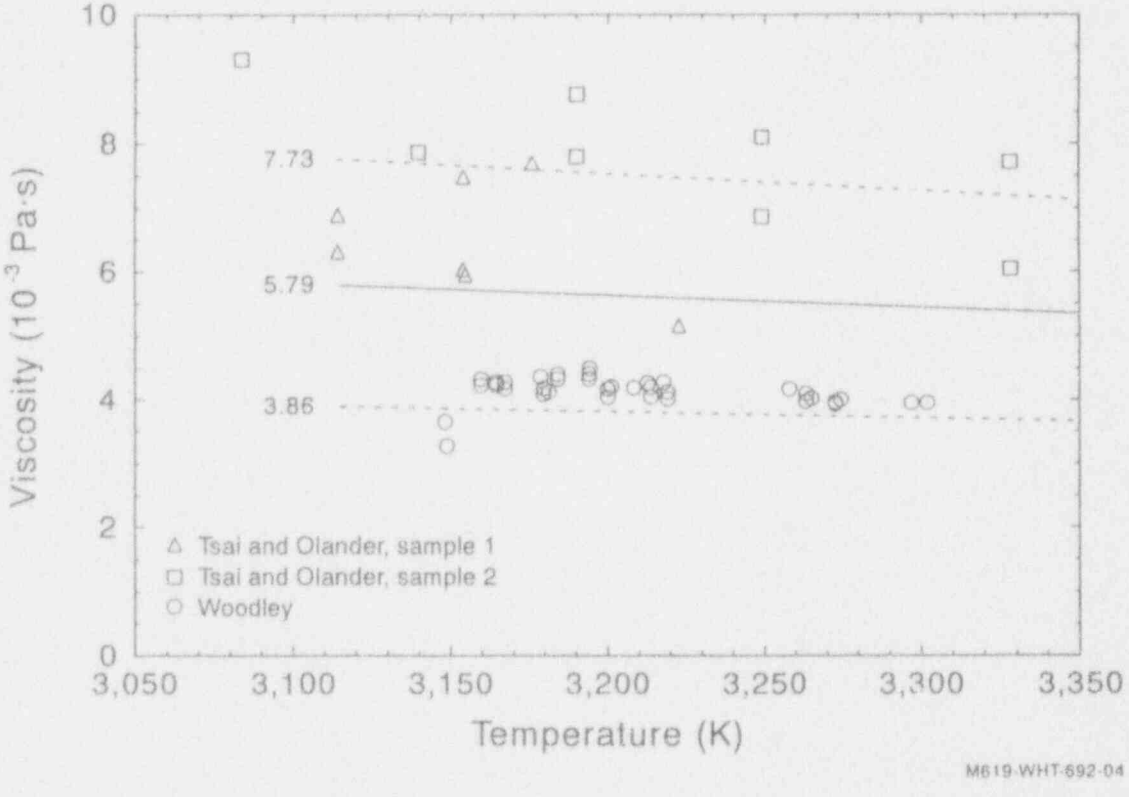

Figure A-5. Estimated UO_2 viscosity (solid line) with upper and lower uncertainty estimates (dashed lines) compared with data.[A-1]

A.1.2 ZrO_2 Data

This section contains data for properties of ZrO_2. Properties, such as thermal conductivity, theoretical density, enthalpy, and specific heat capacity are summarized in Figures A-6 through A-9. As indicated in the figures, this data is based upon information in Reference A-1. Reference A-1 also states that the solidus and liquidus temperature for ZrO_2 is 2,960 K, assuming that the oxygen-to-metal ratio is 2.0.

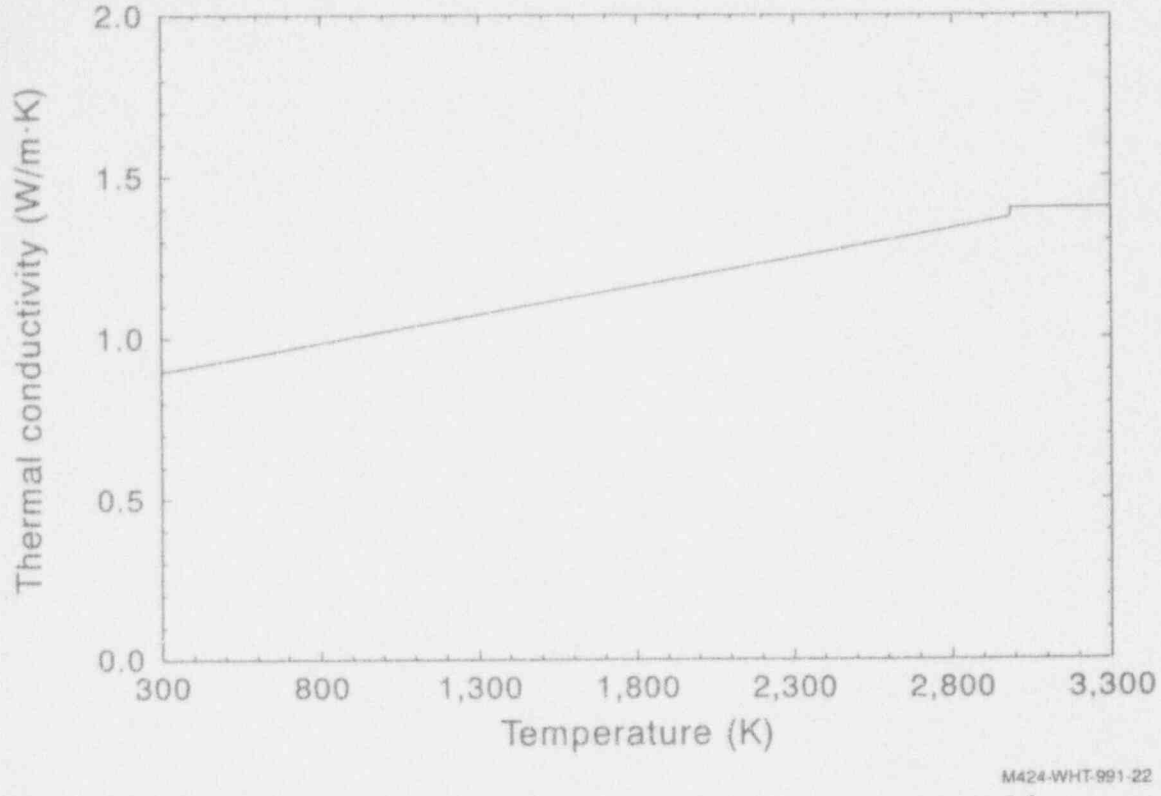

Figure A-6. Zircaloy oxide thermal conductivity as a function of temperature.[A-1]

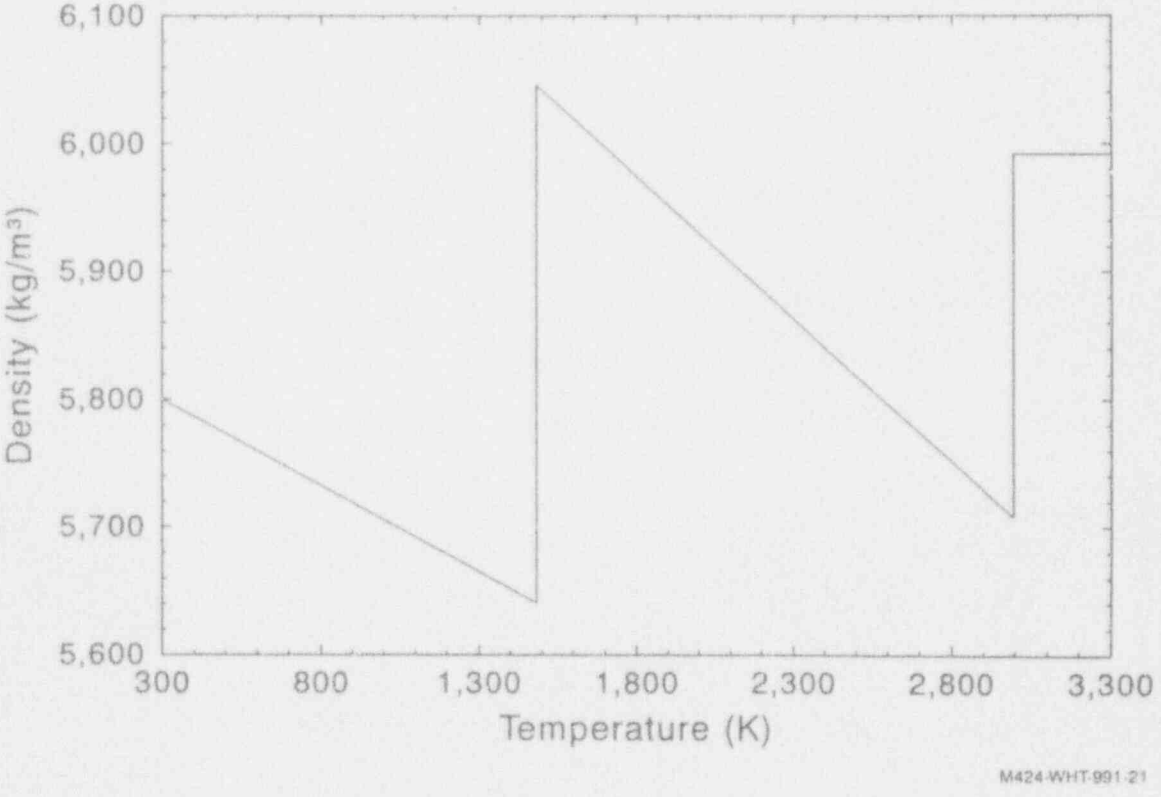

Figure A-7. Zircaloy oxide density as a function of temperature.[A-1]

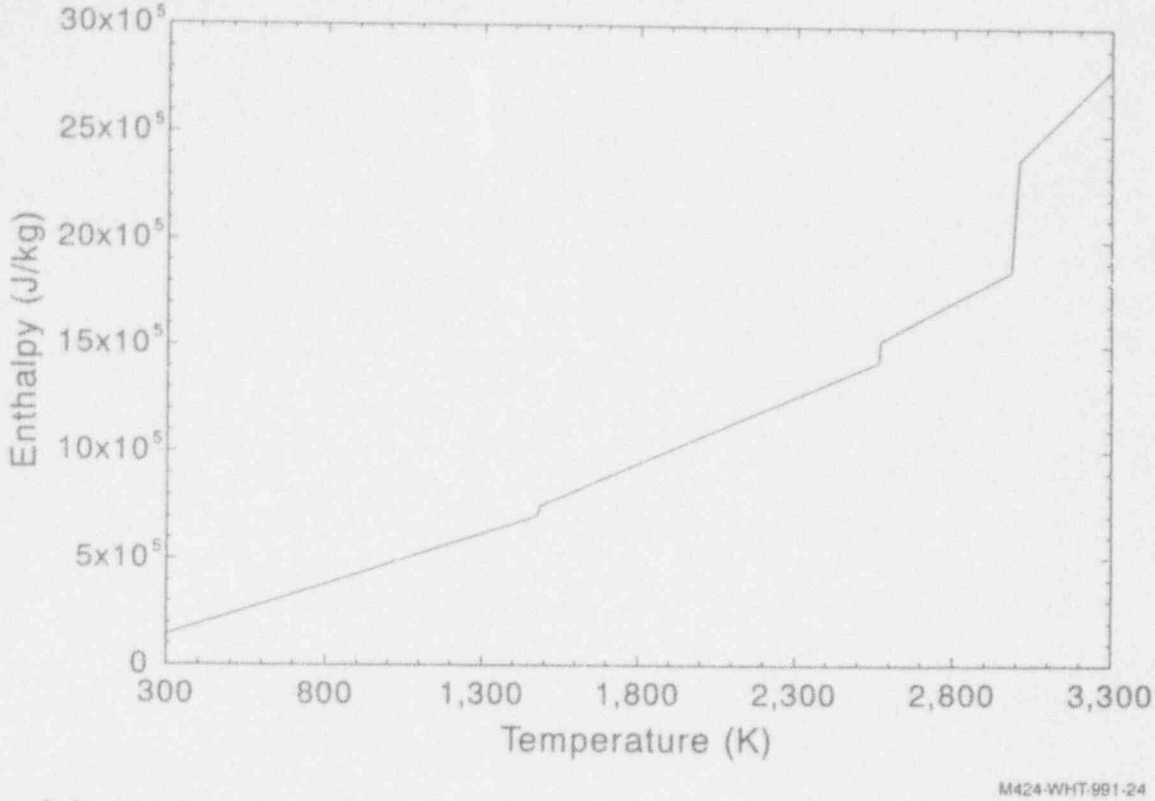

Figure A-8. Zircaloy oxide enthalpy as a function of temperature.[A-1]

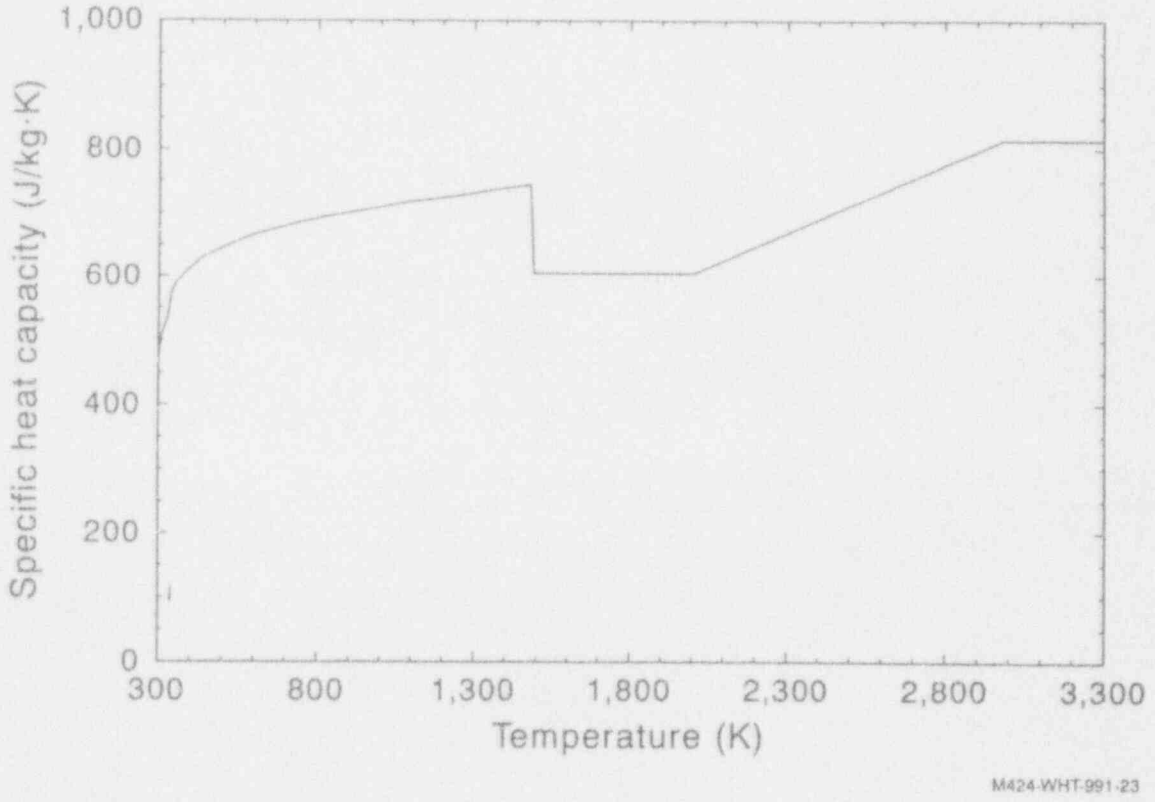

Figure A-9. Zircaloy oxide specific heat capacity as a function of temperature.[A-1]

A.1.3 $(U,Zr)O_2$ Compound Data

This section contains data for properties of a 78% UO_2–17% ZrO_2 weight fraction compound, which is the composition estimated for debris companion samples.[A-2] Properties, such as thermal conductivity, theoretical density, enthalpy, specific heat capacity are summarized in Figures A-10 through A-13. As indicated in the figures, this data was calculated using information in Reference A-1. Based on the phase diagram for U-Zr-O in Reference A-3, it is estimated that the solidus temperature for this compound is 2,650 K and that the liquidus temperature for this compound is approximately 2,850 K.

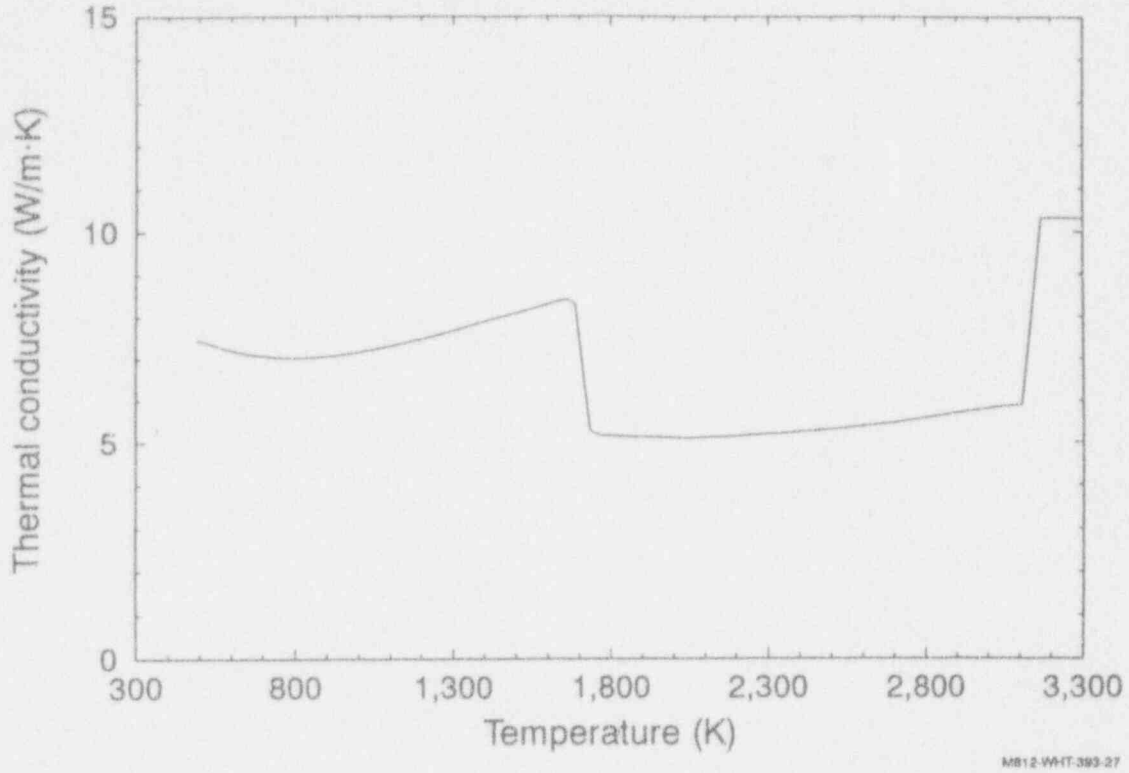

Figure A-10. Thermal conductivity for a 78% UO_2—17% ZrO_2 weight fraction compound.[A-1]

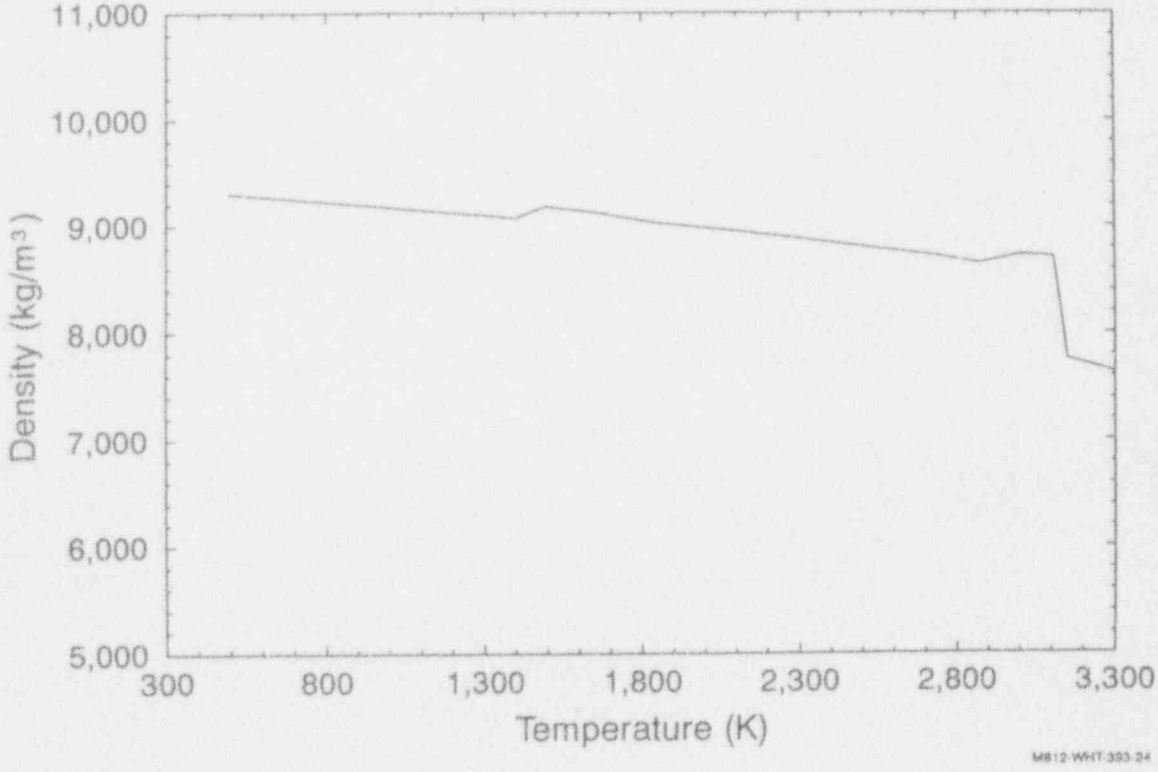

Figure A-11. Density for a 78% UO_2—17% ZrO_2 weight fraction compound.[A-1]

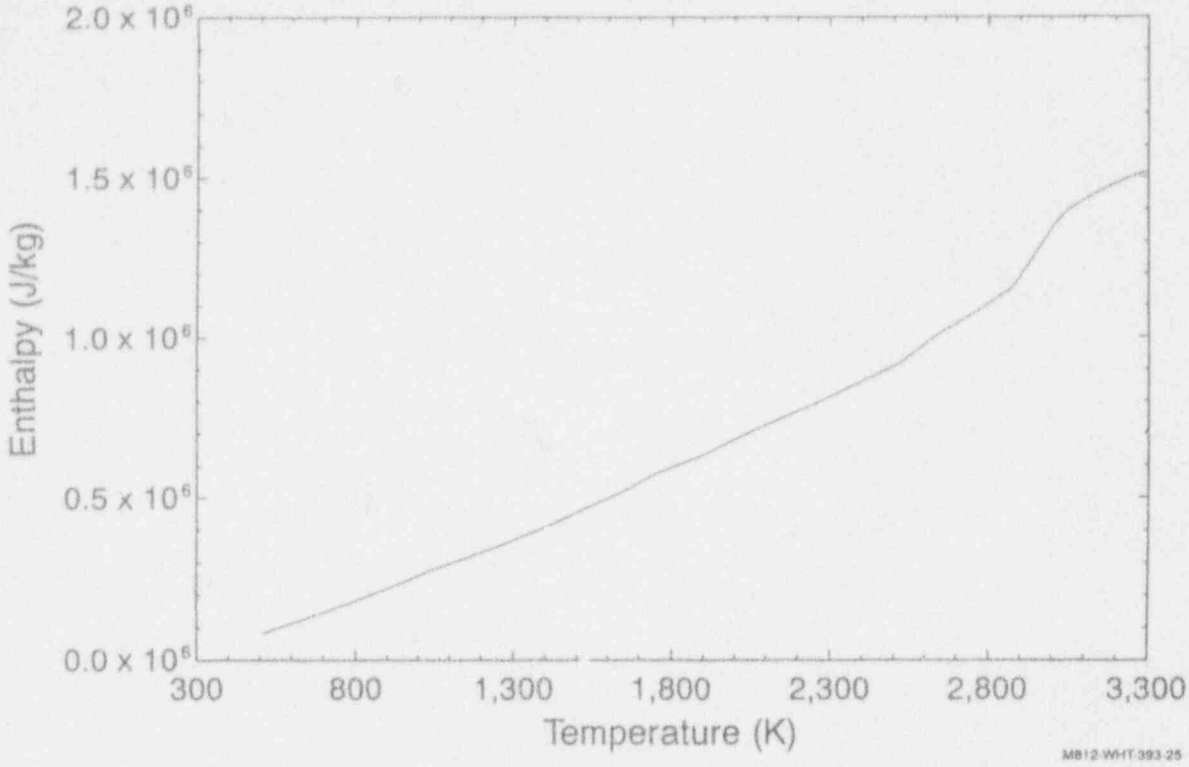

Figure A-12. Enthalpy for a 78% UO_2–17% ZrO_2 weight fraction compound.[A-1]

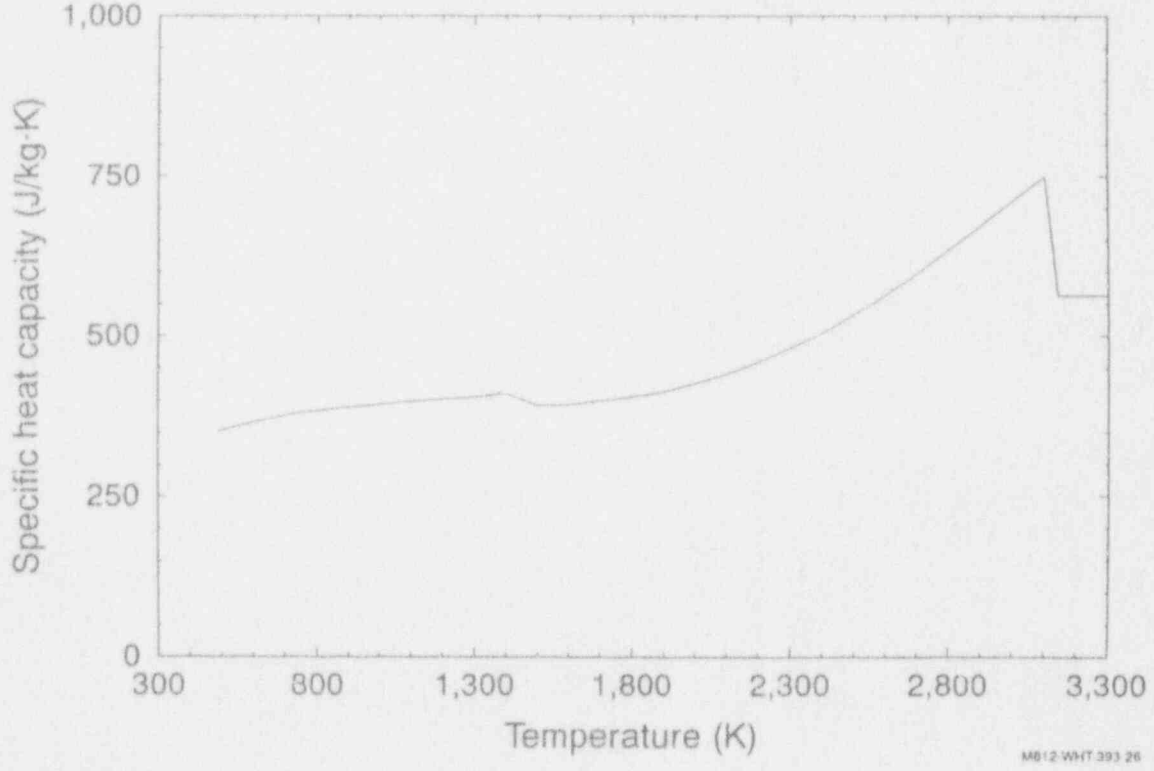

Figure A-13. Specific heat capacity for a 78% UO_2–17% ZrO_2 weight fraction compound.[A-1]

A.1.4 Inconel-600 Data

This section contains data for properties of Inconel-600, which is the material used in the TMI-2 instrument tube nozzles. Properties, such as thermal conductivity, theoretical density, and specific heat capacity are summarized in Figures A-14 through A-16. As indicated in these figures, the data are extrapolated for temperatures above 1,100 K. This data is based upon information in References A-4 and A-5. Reference A-4 indicates that the solidus and liquidus temperatures for Inconel-600 are 1,644 and 1,700 K, respectively.

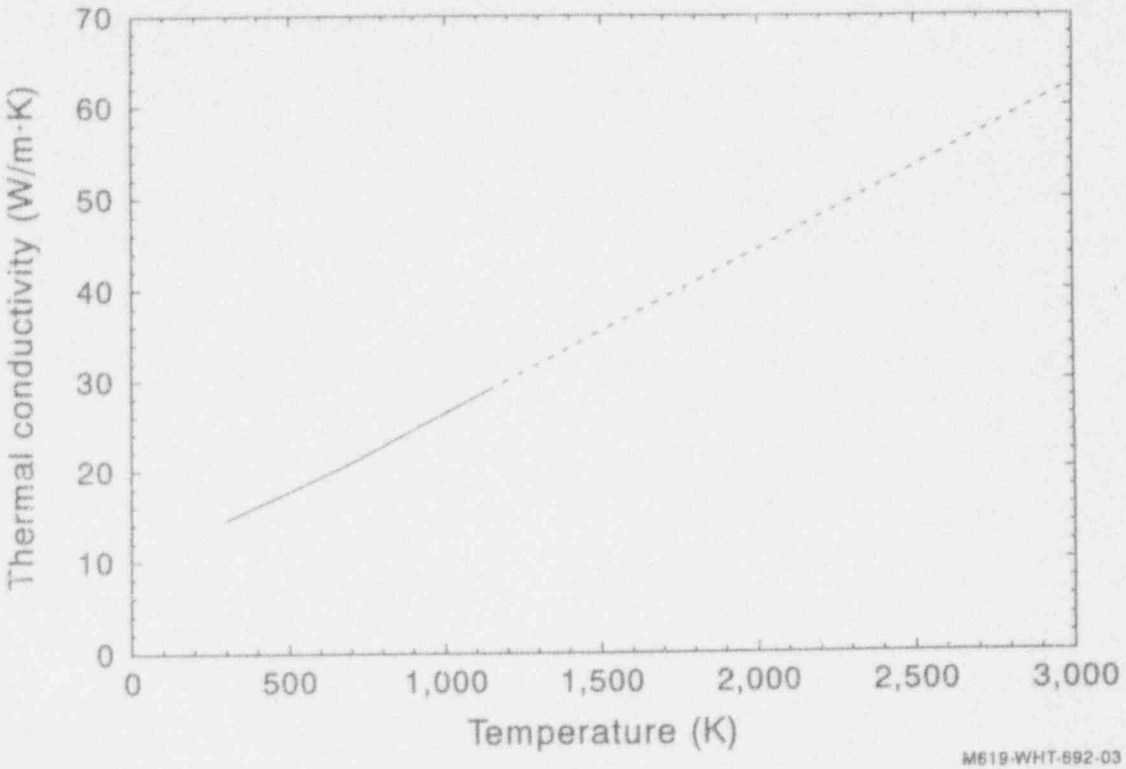

Figure A-14. Inconel-600 thermal conductivity as a function of temperature.[A-5]

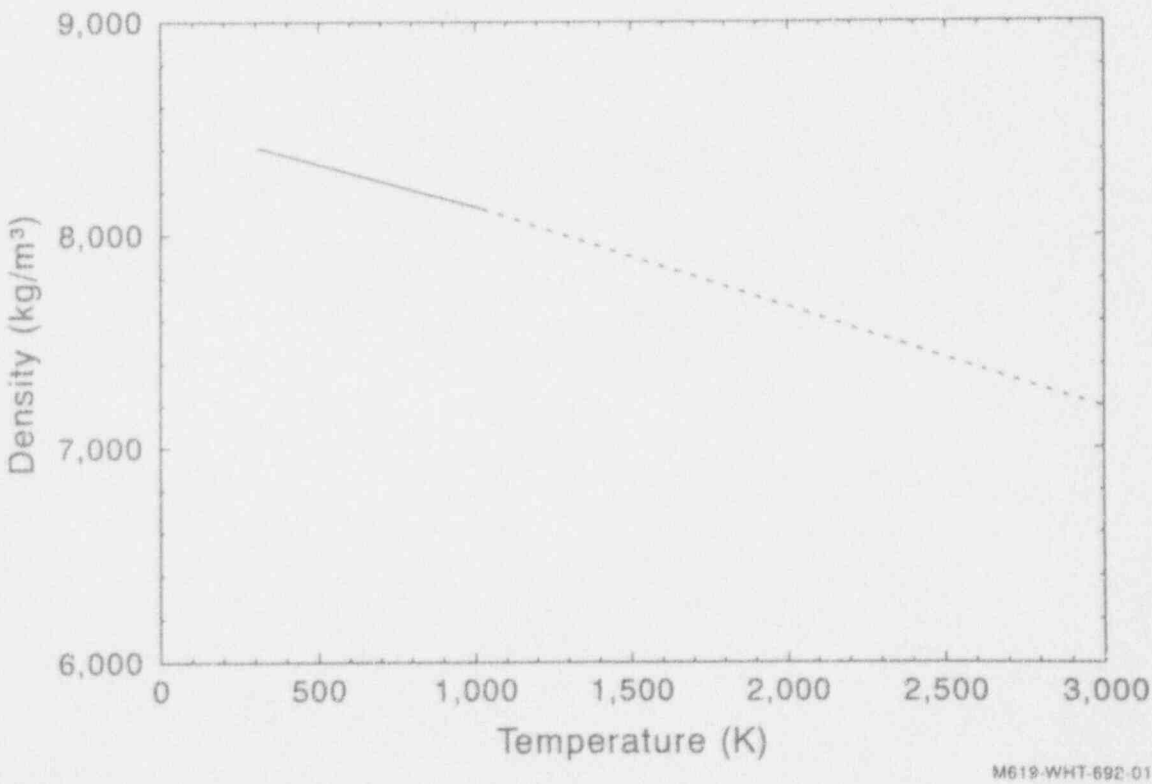

Figure A-15. Inconel-600 density as a function of temperature.[A-4]

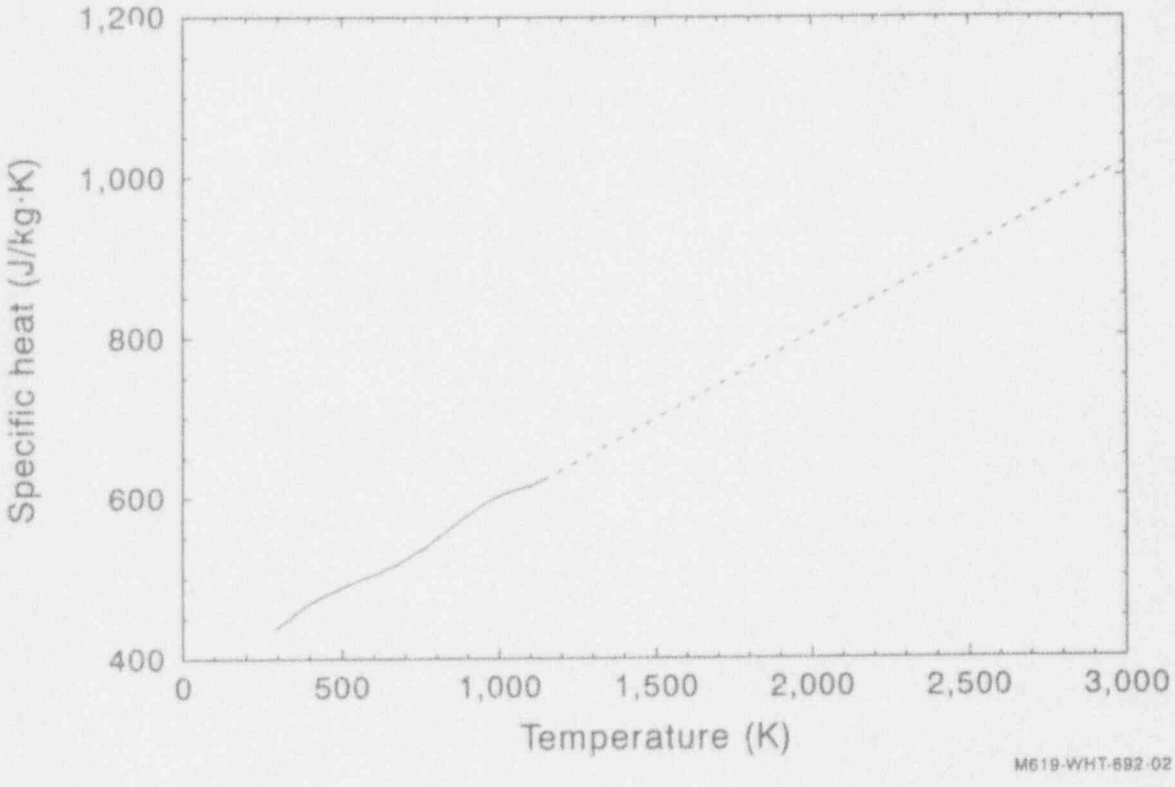

Figure A-16. Inconel-600 specific heat as a function of temperature.[A-5]

A.1.5 SA533B1 Carbon Steel Data

This section contains data for properties of SA533 Grade B Class 1 (SA533B1) carbon steel, which is the material used in the TMI-2 vessel. Properties, such as thermal conductivity, density, specific heat capacity, and thermal diffusivity are summarized in Figures A-17 through A-20. References for the data are indicated in each figure. Information in Reference A-6 indicates that the solidus and liquidus temperature for SA533B1 carbon steel is 1,789 K.

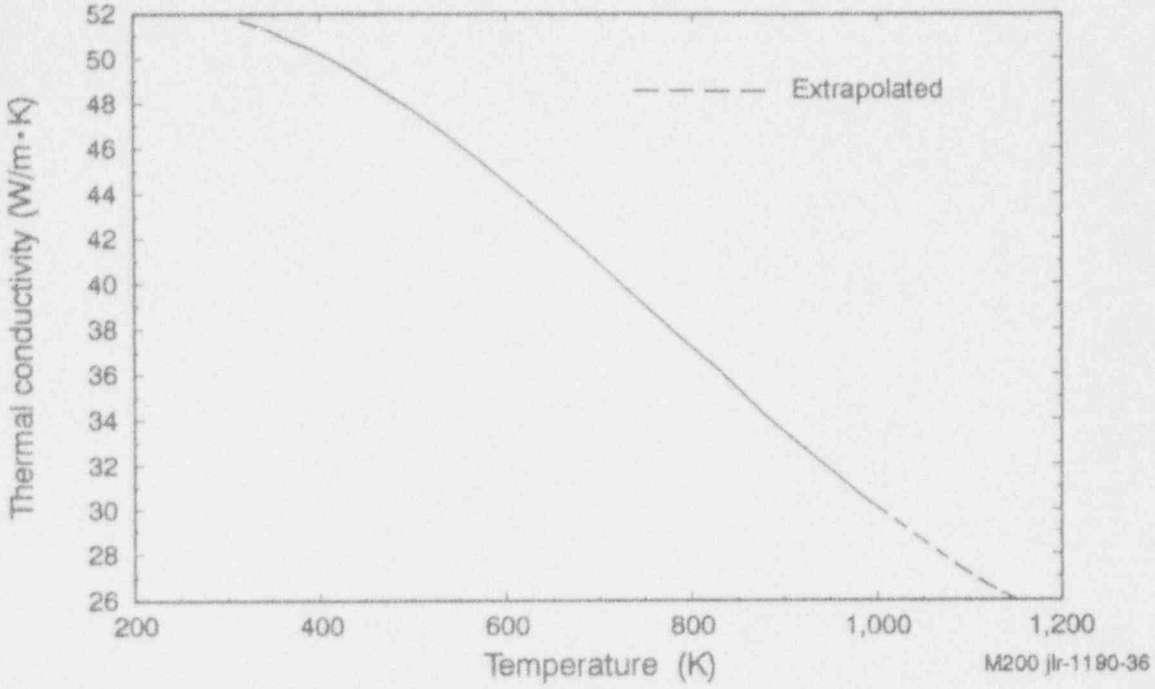

Figure A-17. Thermal conductivity of carbon steel (SA533B1).[A-7,A-8]

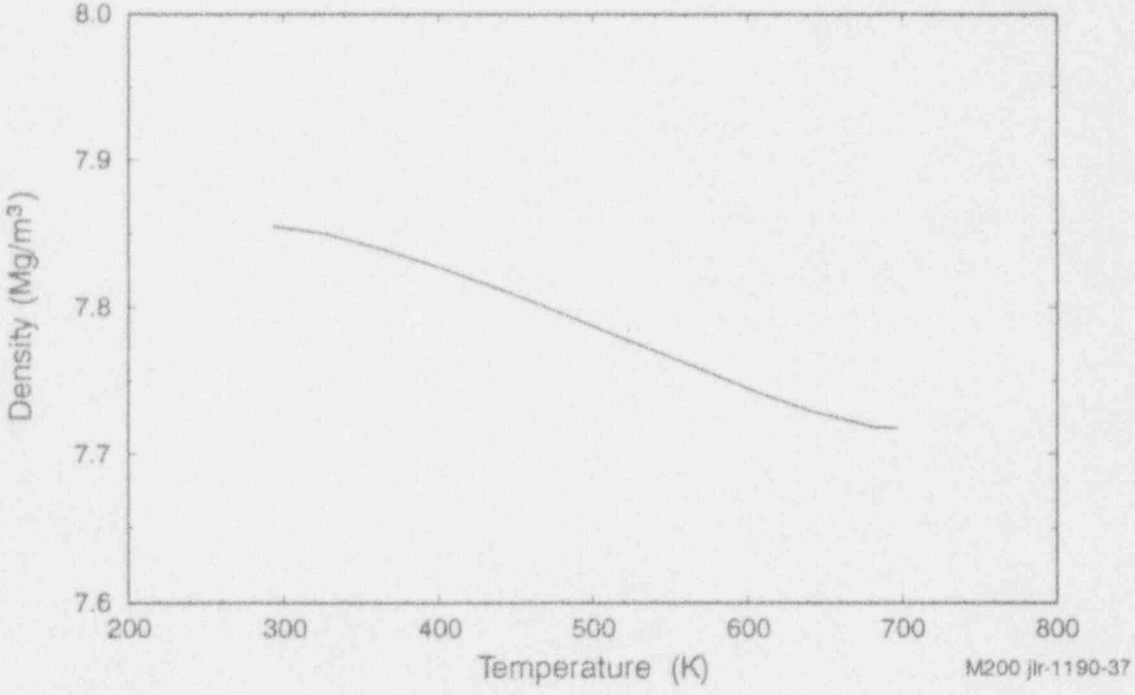

Figure A-18. Density of carbon steel (SA533B1).[A-9]

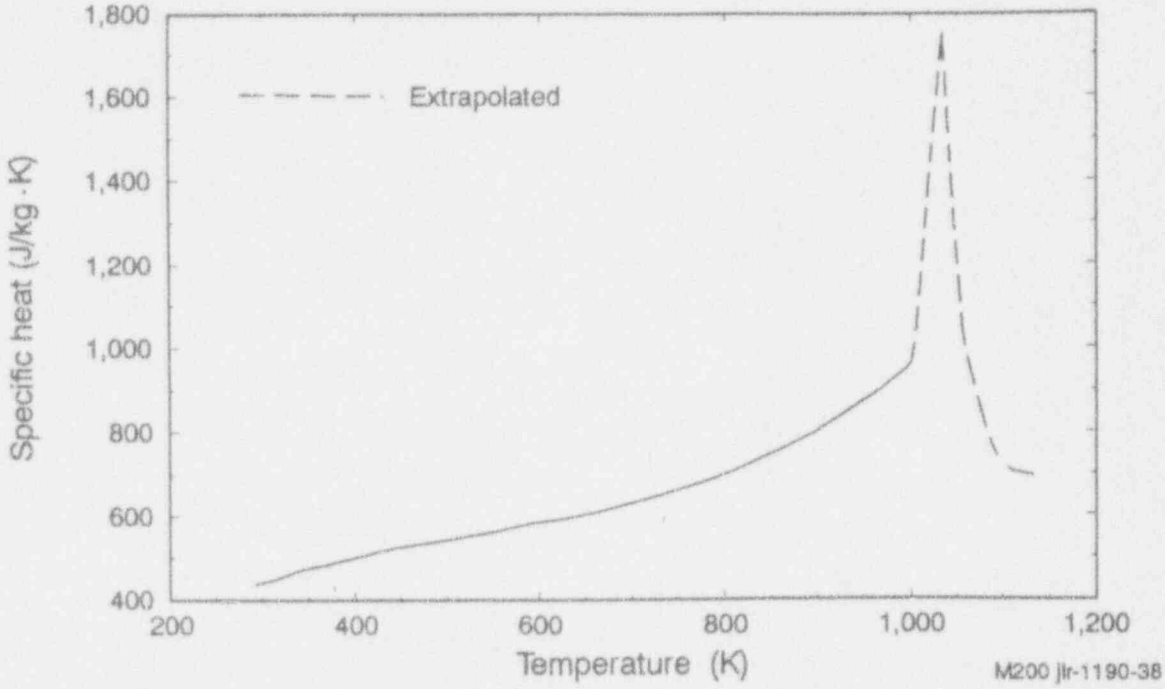

Figure A-19. Specific heat of carbon steel (SA533B1).[A-10,A-11,A-12,A-13]

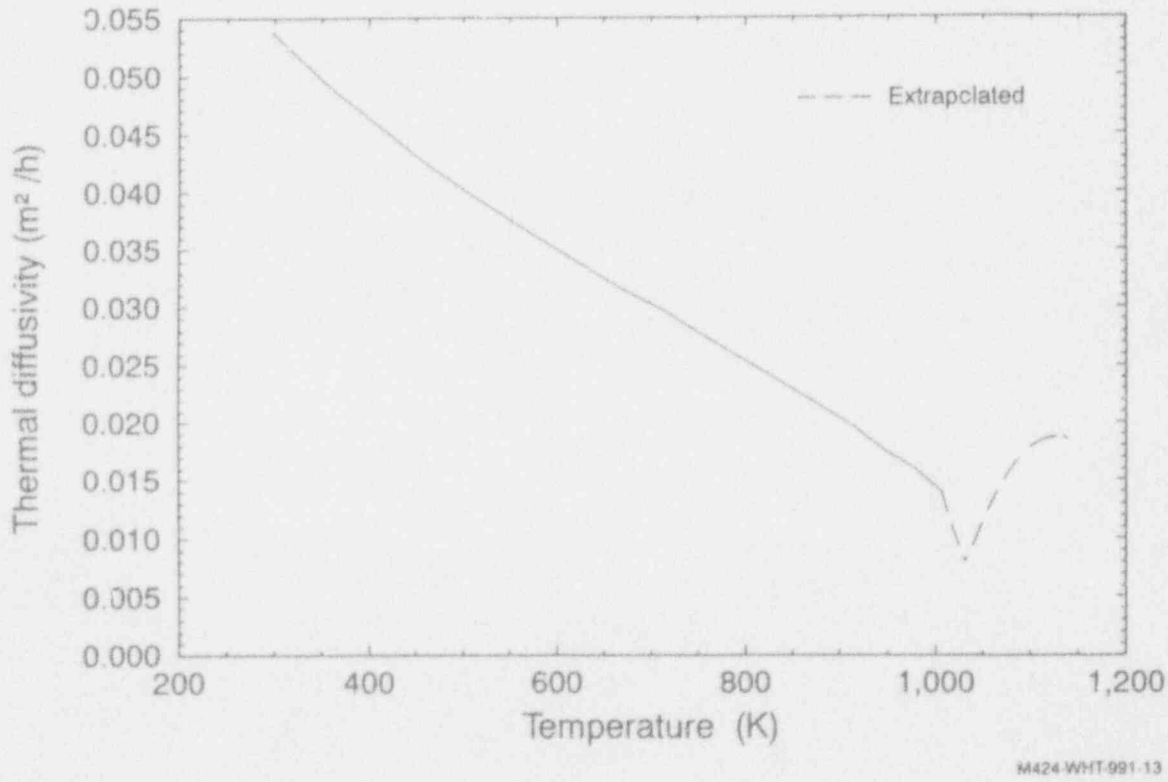

Figure A-20. Thermal diffusivity of carbon steel (SA533B1).[A-9,A-14]

A.1.6 Stainless Steel Data

This section contains data for the following properties of stainless steel: thermal conductivity, density, enthalpy, and specific heat capacity. These data are summarized in Figures A-21 through A-24.

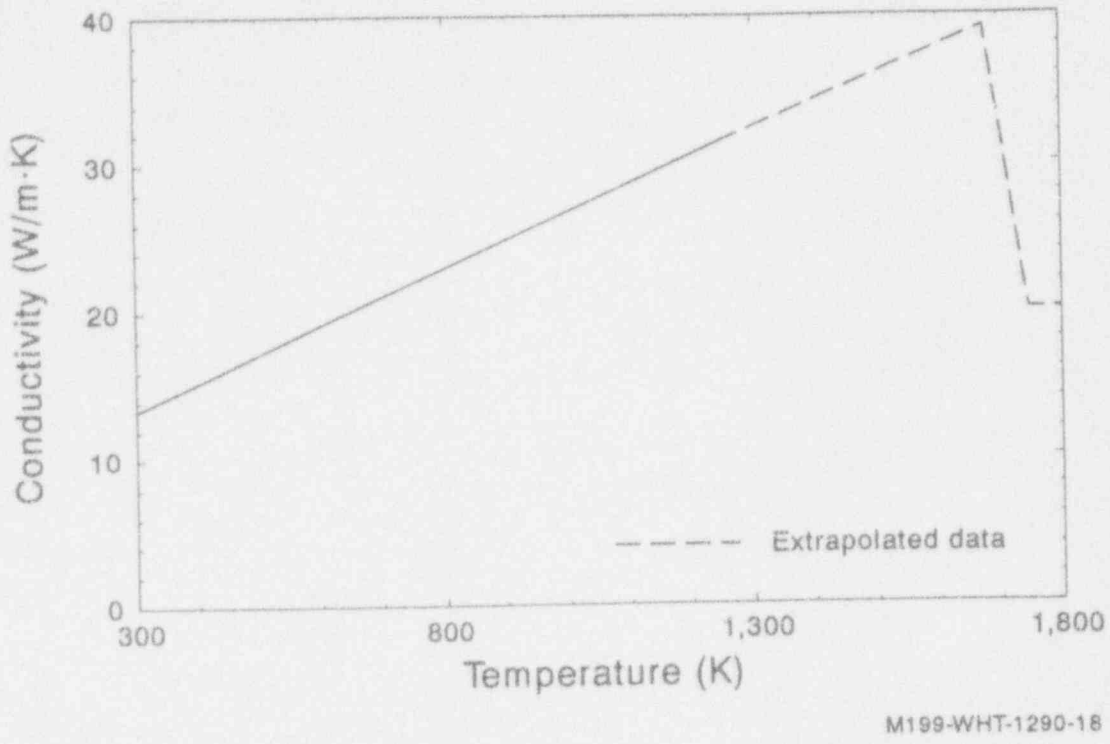

Figure A-21. Stainless steel thermal conductivity.[A-1]

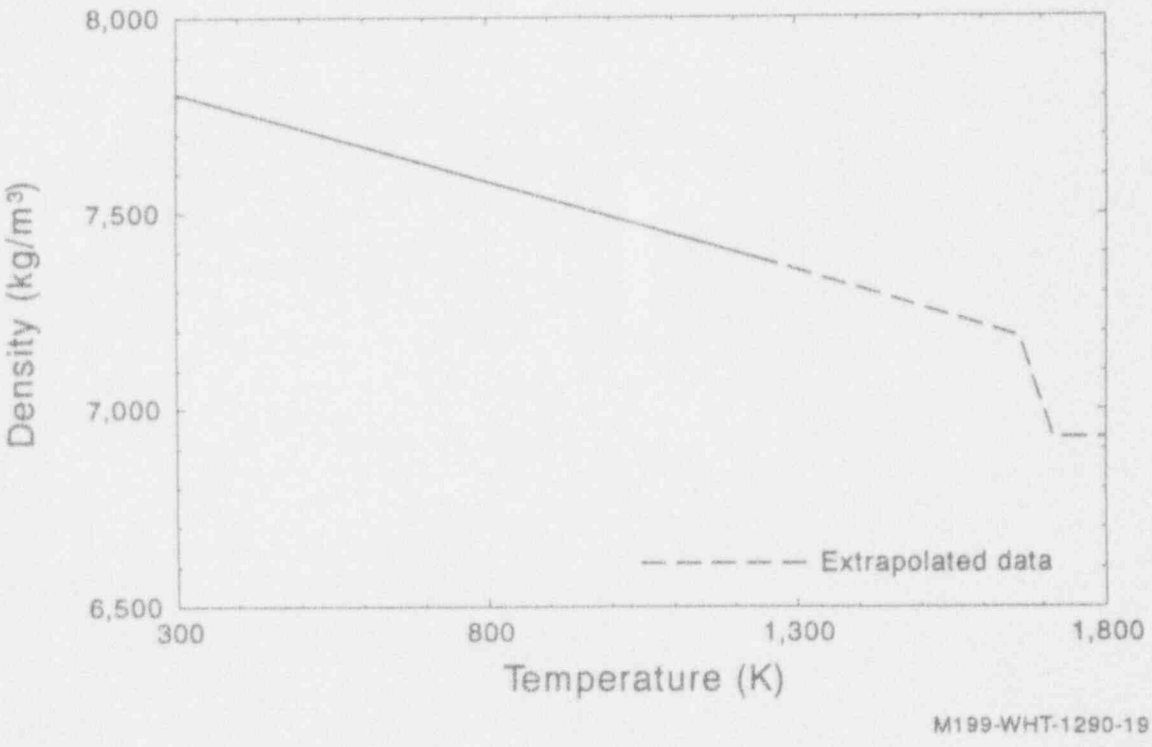

Figure A-22. Stainless steel density.[A-1]

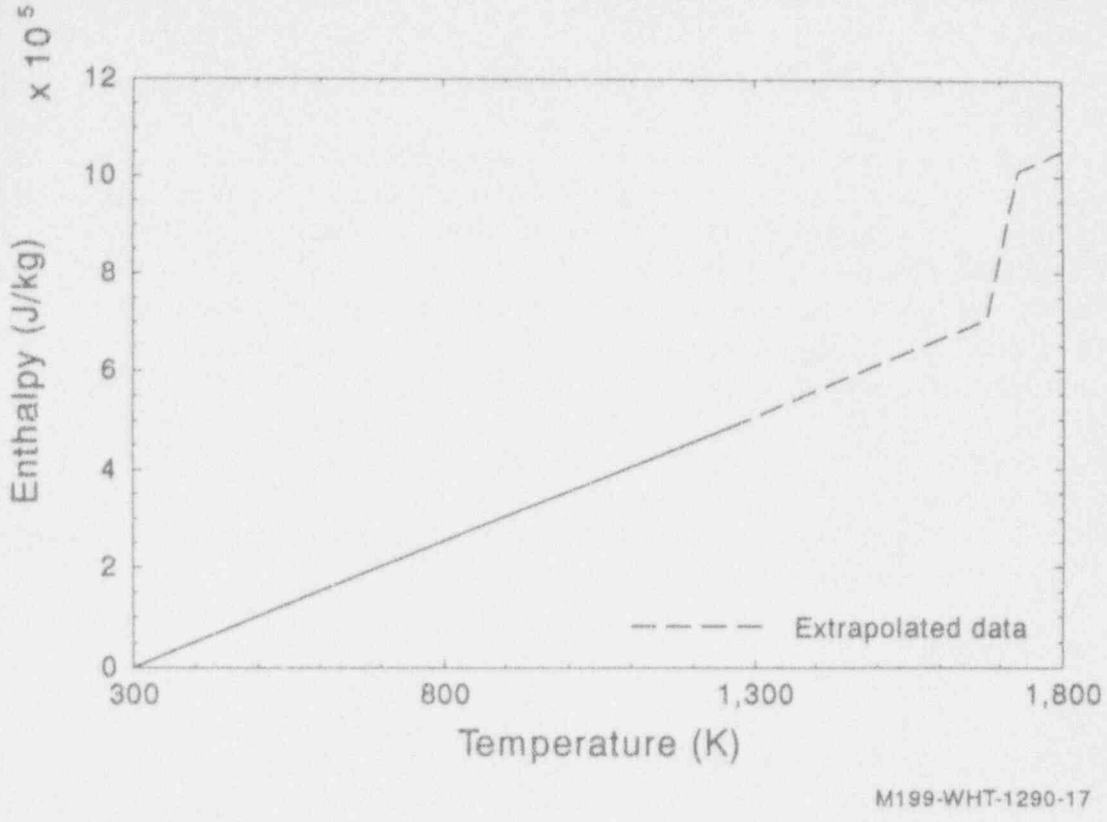

Figure A-23. Stainless steel enthalpy.[A-1]

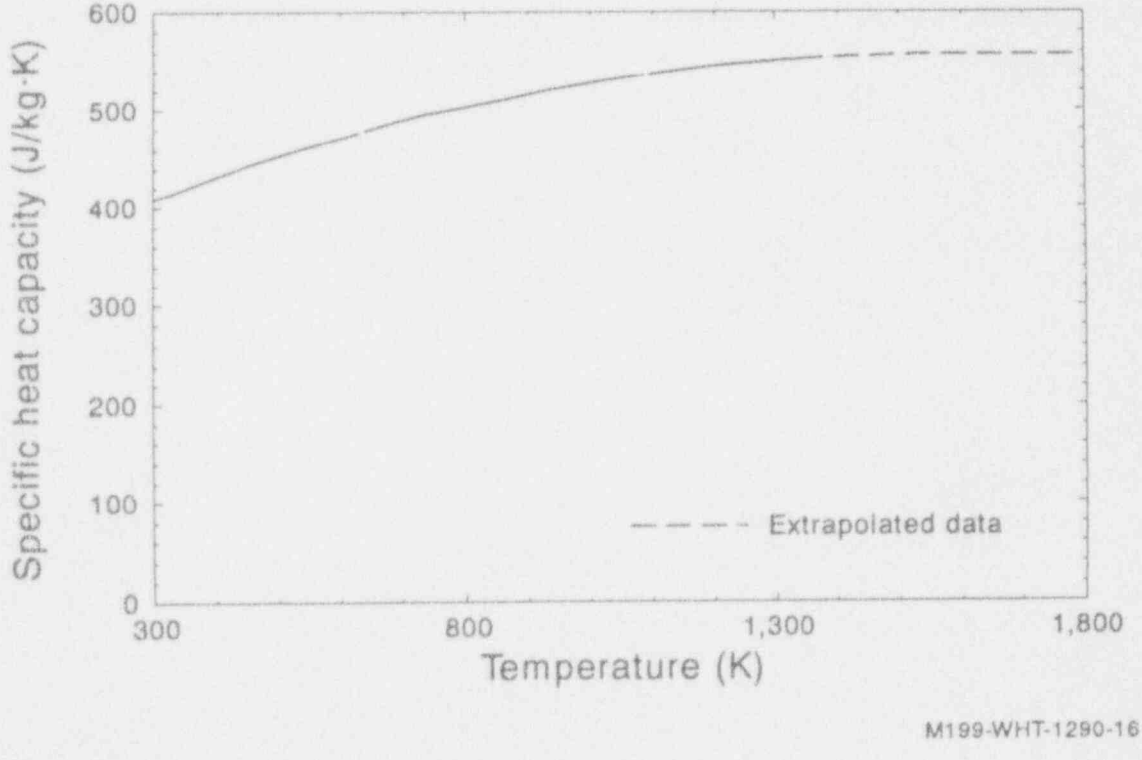

Figure A-24. Stainless steel heat capacity at constant pressure.[A-1]

A.2 Structural Material Property Data

Structural calculations for the TMI margin-to-failure analysis used the material data for Inconel-600 and SA533B steel summarized in this appendix. Included are temperature-dependent structural properties such as elastic modulus, Poisson's ratio, yield strength, ultimate strength and thermal coefficient of expansion. The elastic portions of the stress-strain curves were derived from published values of temperature-dependent elastic moduli, plastic portions were taken from test data. Creep failure times are plotted for corresponding stresses at various temperatures and the Larson-Miller parameter is plotted as a function of log(stress).

Some of the data listed in the tables (e.g., % total elongation) and in the figures (e.g., Inconel-600 Poisson's ratio) were not actually used in the analysis, but are included for completeness. For penetration ejection analysis, weld material was assumed to have the same material properties as its base Inconel-600 material.

A.2.1 Inconel Data

This section contains data for structural properties of Inconel-600, annealed for 1 hour at 1,143 K and force air cooled. Temperature-dependent properties include elastic modulus, Poisson's ratio, yield strength, ultimate strength and thermal coefficient of expansion. In Figures A-25 through A-33 stress-strain curves are plotted for various temperatures, creep rupture times are plotted for corresponding stresses at various temperatures, and the Larson-Miller parameter is plotted against log(stress). Tables A-1 and A-2 contain listings of tensile and creep data. Not all temperature-dependent properties were used in the penetration tube rupture or penetration weld analyses, but are included here for completeness. Much of the high temperature property data was obtained as part of the NRC-sponsored Lower Head Failure Program.[A-15]

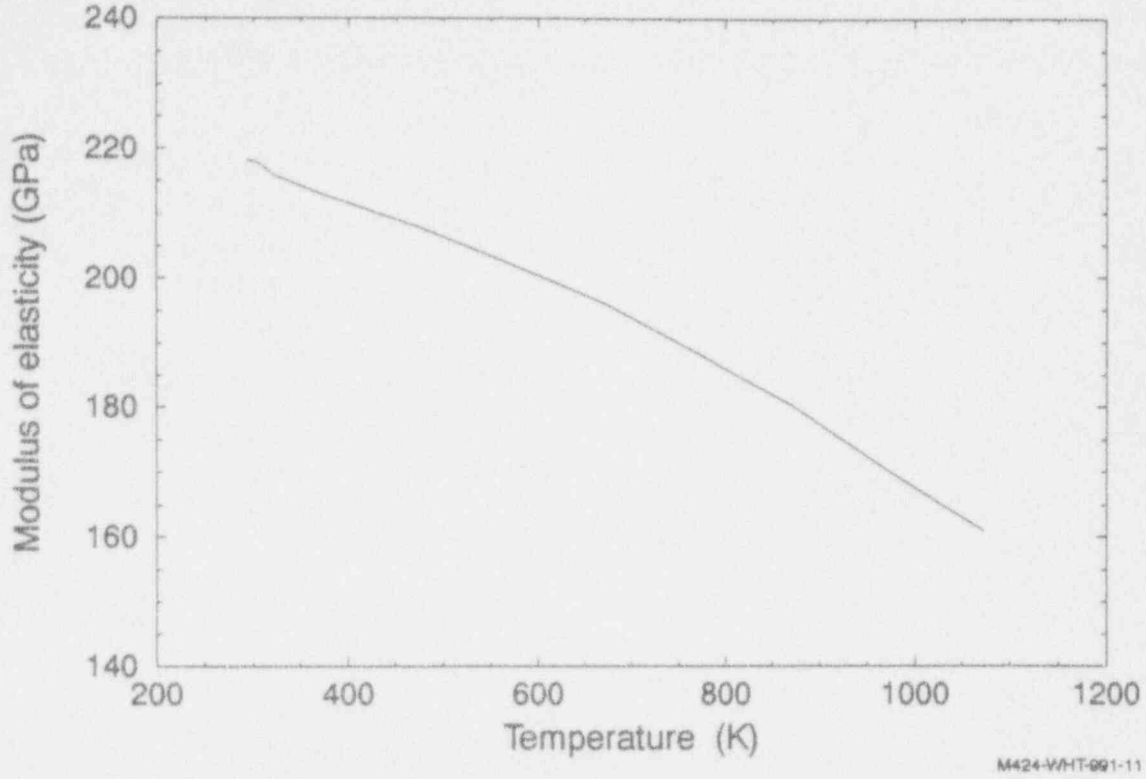

Figure A-25. Inconel-600 elastic modulus as a function of temperature.[A-5]

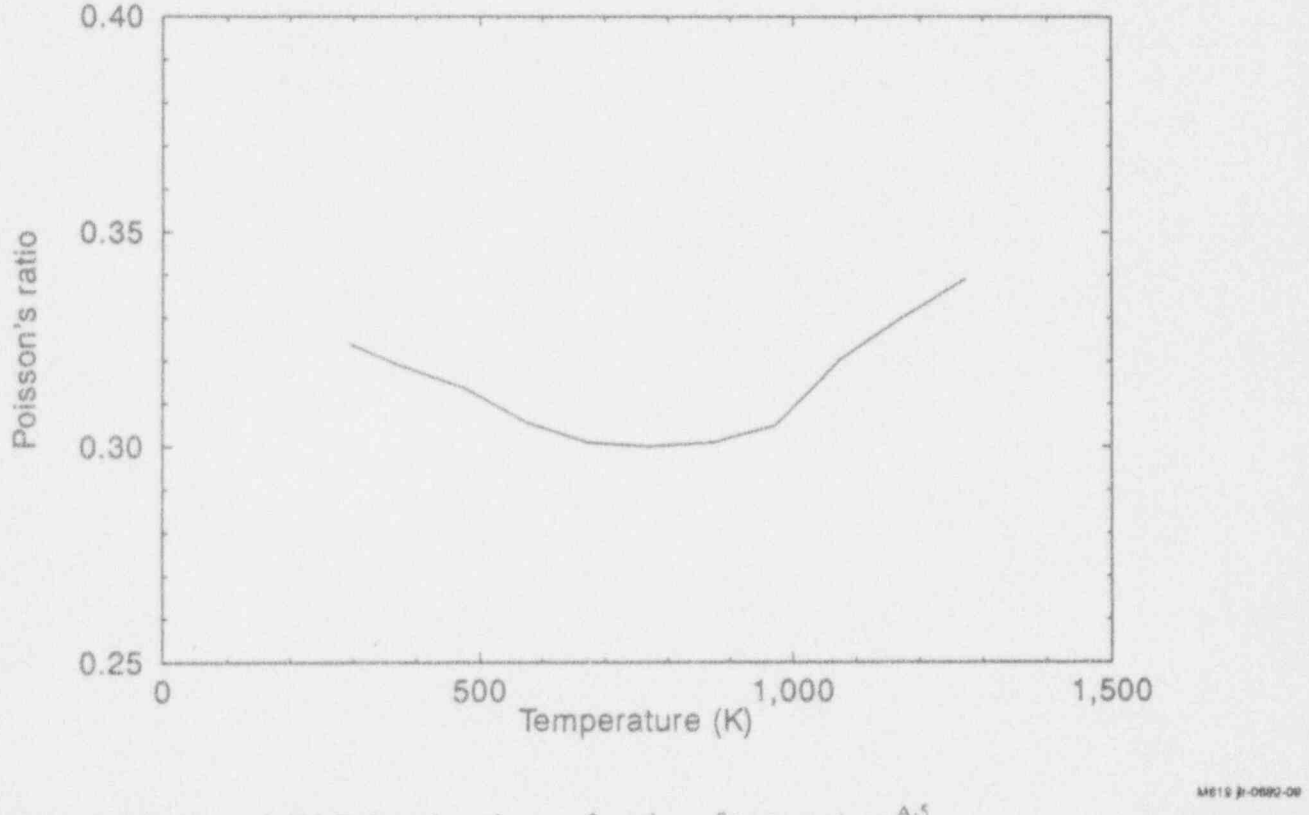

Figure A-26. Inconel-600 Poisson's ratio as a function of temperature.[A-5]

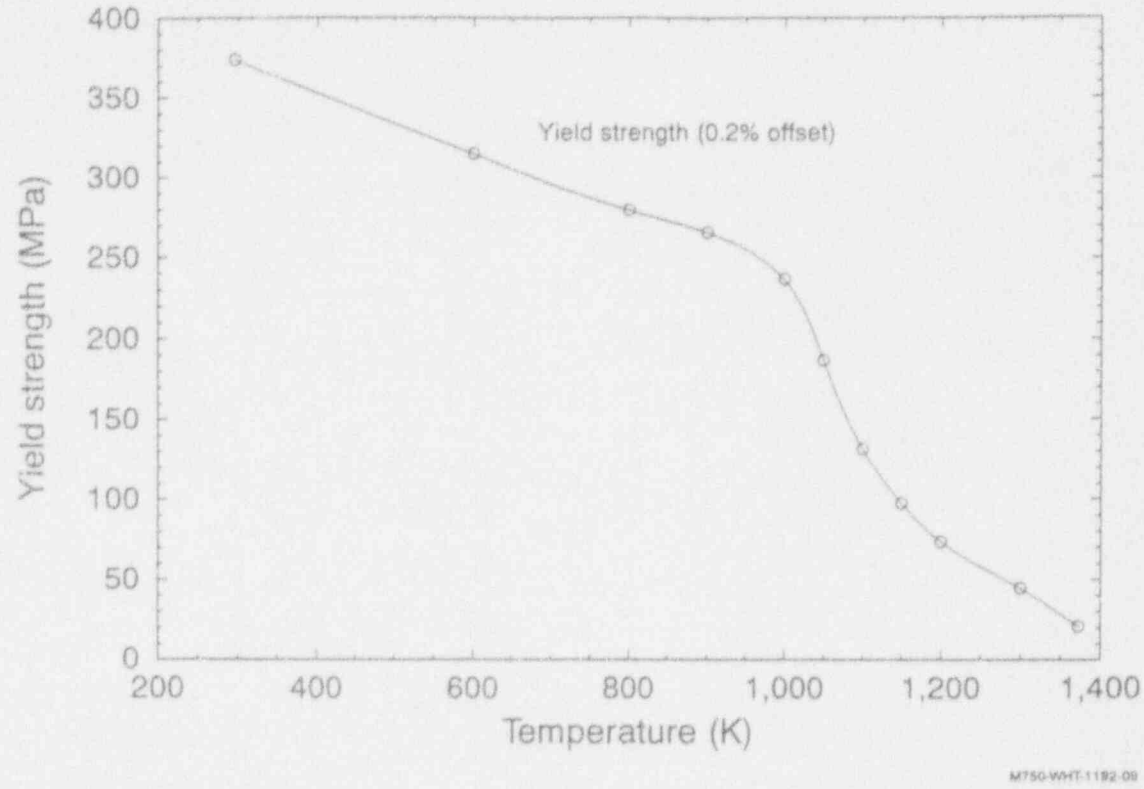

Figure A-27. Inconel-600 yield strength as a function of temperature.[A-15]

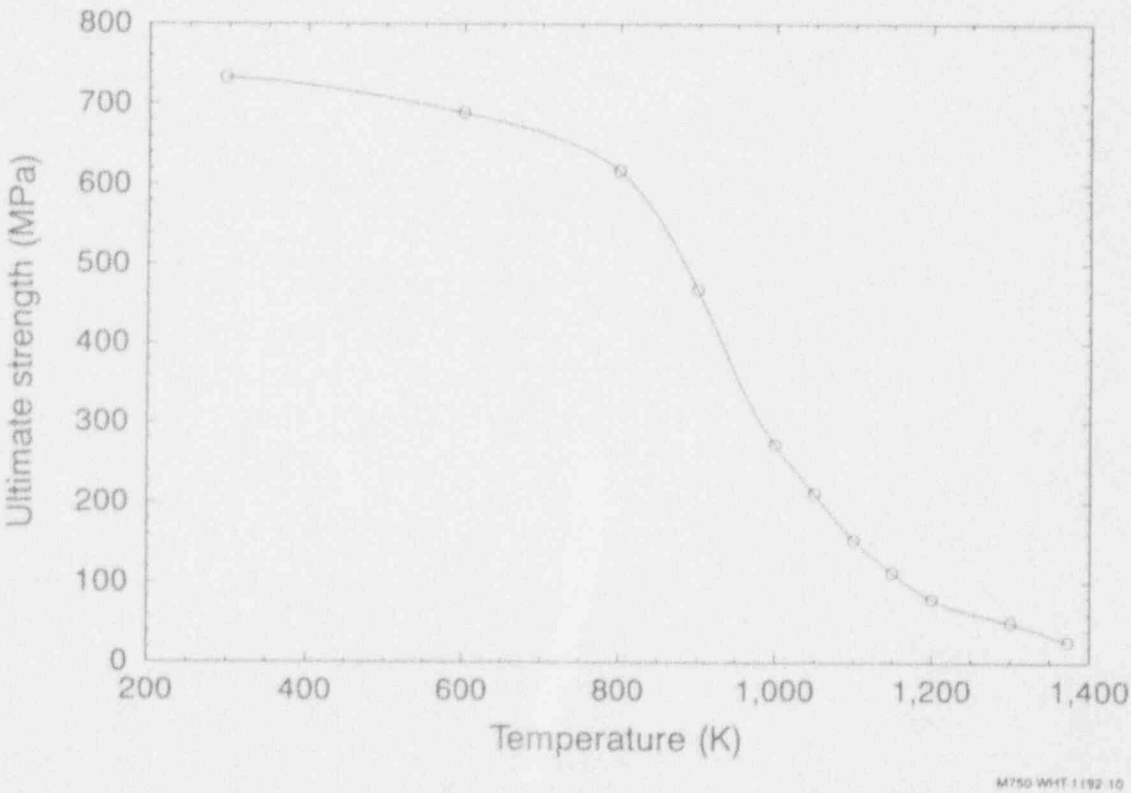

Figure A-28. Inconel-600 ultimate strength as a function of temperature.[A-15]

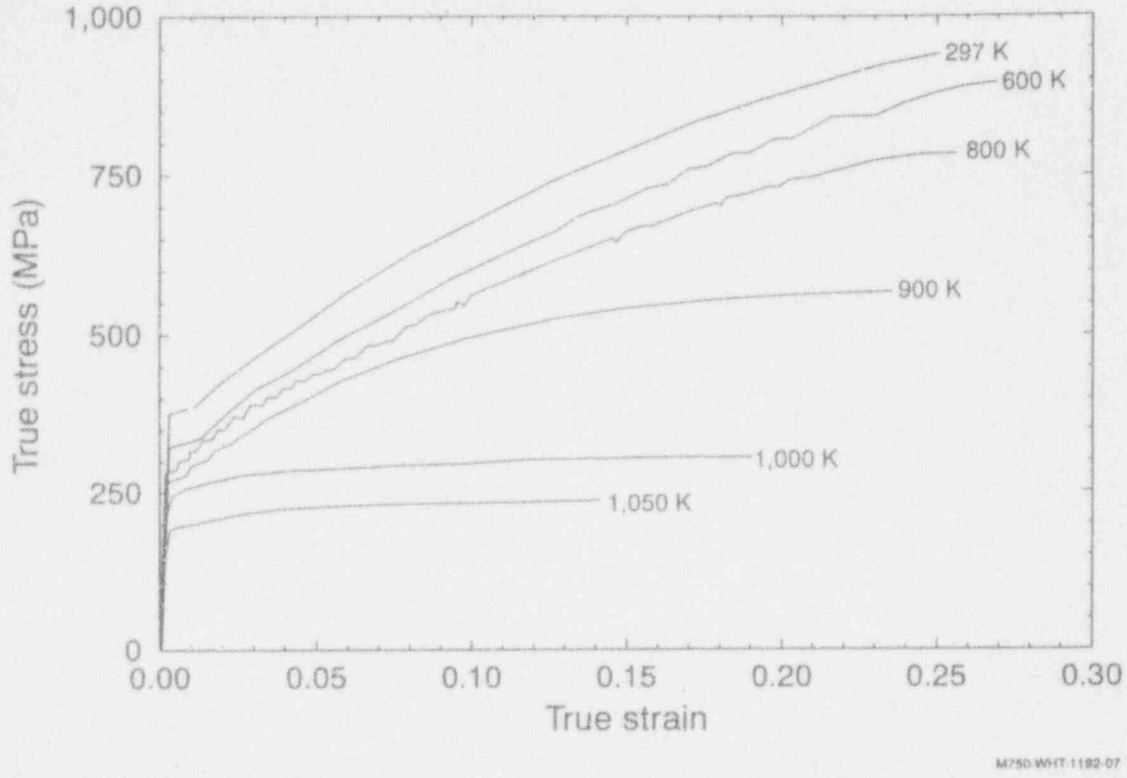

Figure A-29. Inconel-600 stress-strain curves for 297 to 1,050 K.[A-15]

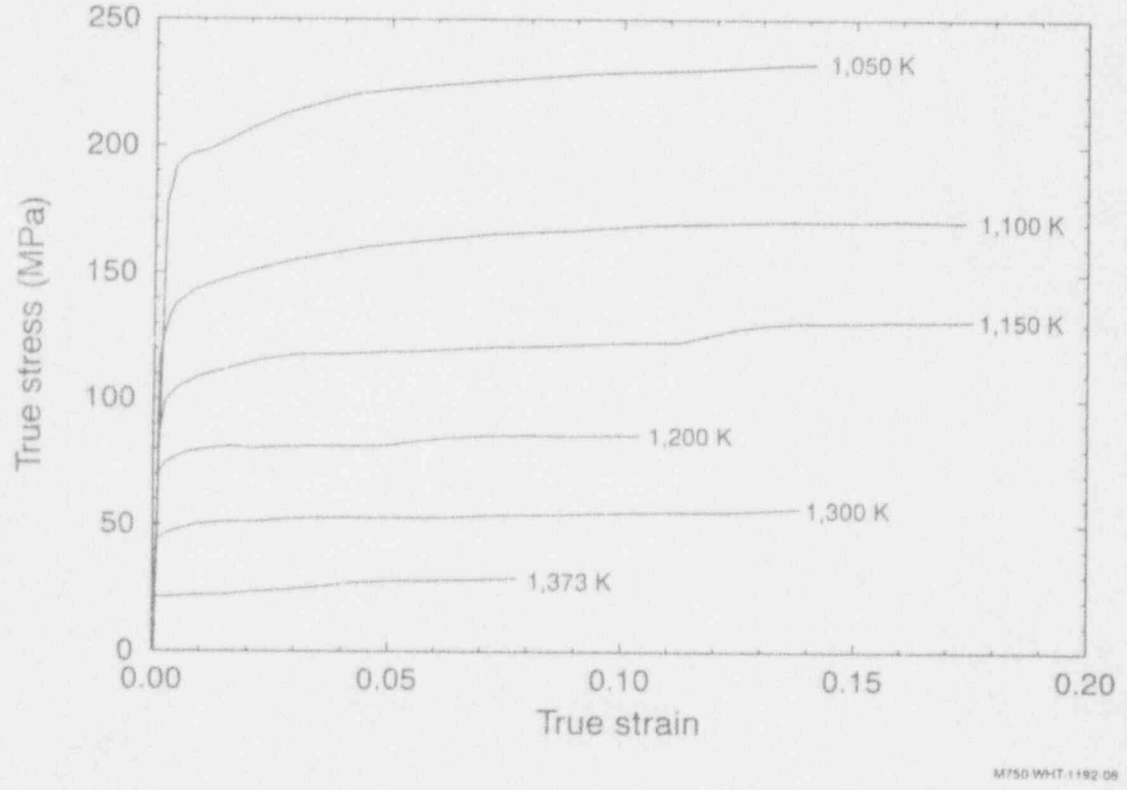

Figure A-30. Inconel-600 stress-strain curves for 1,050 to 1,373 K.[A-15]

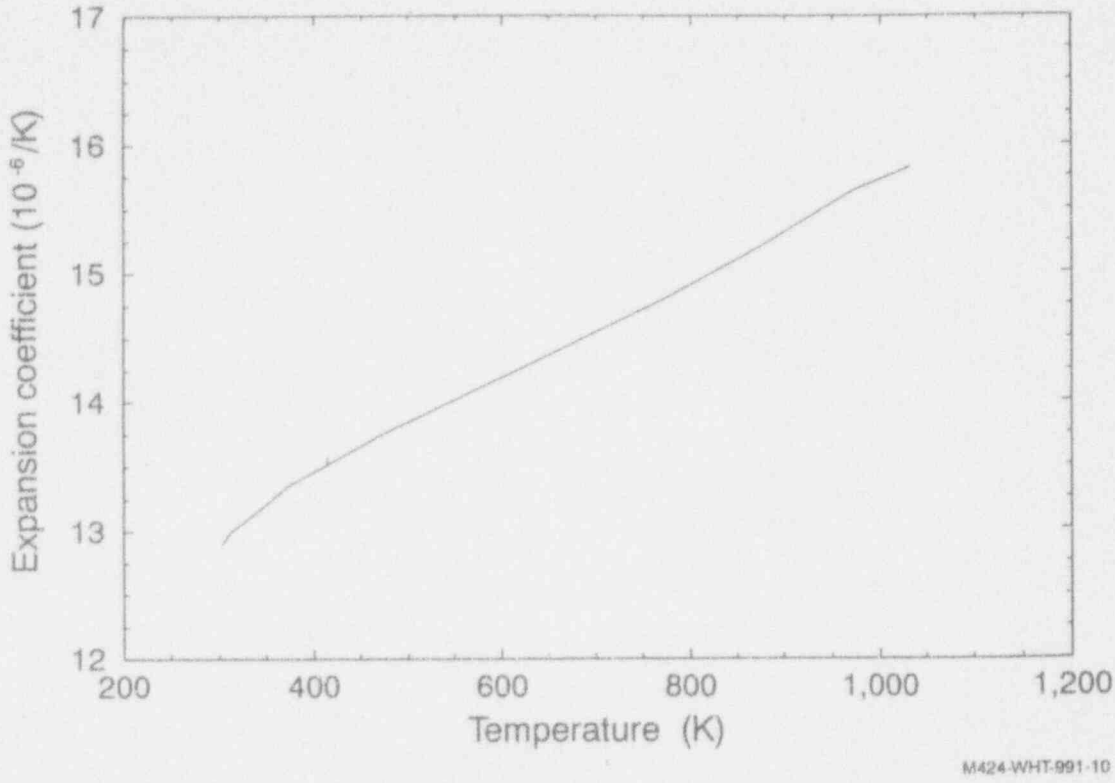

Figure A-31. Inconel-600 mean linear thermal coefficient of expansion as a function of temperature.[A-5]

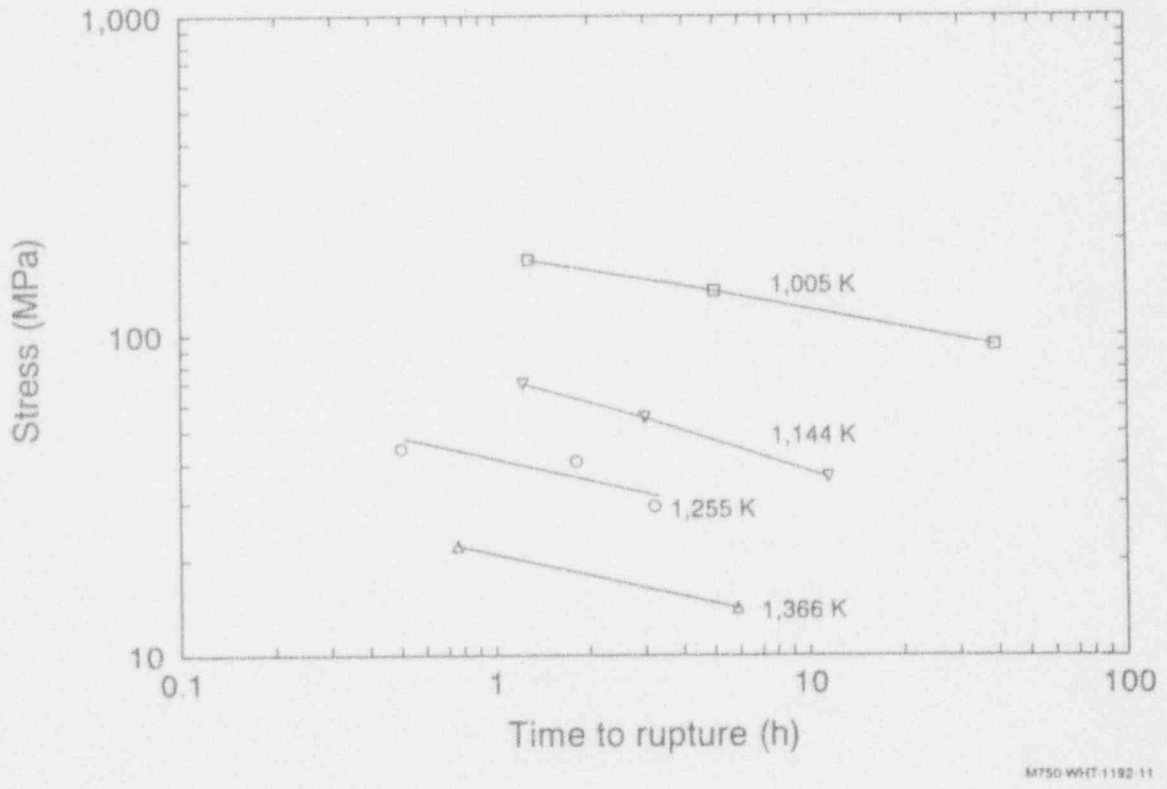

Figure A-32. Inconel-600 creep time to rupture as a function of stress and temperature.[A-15]

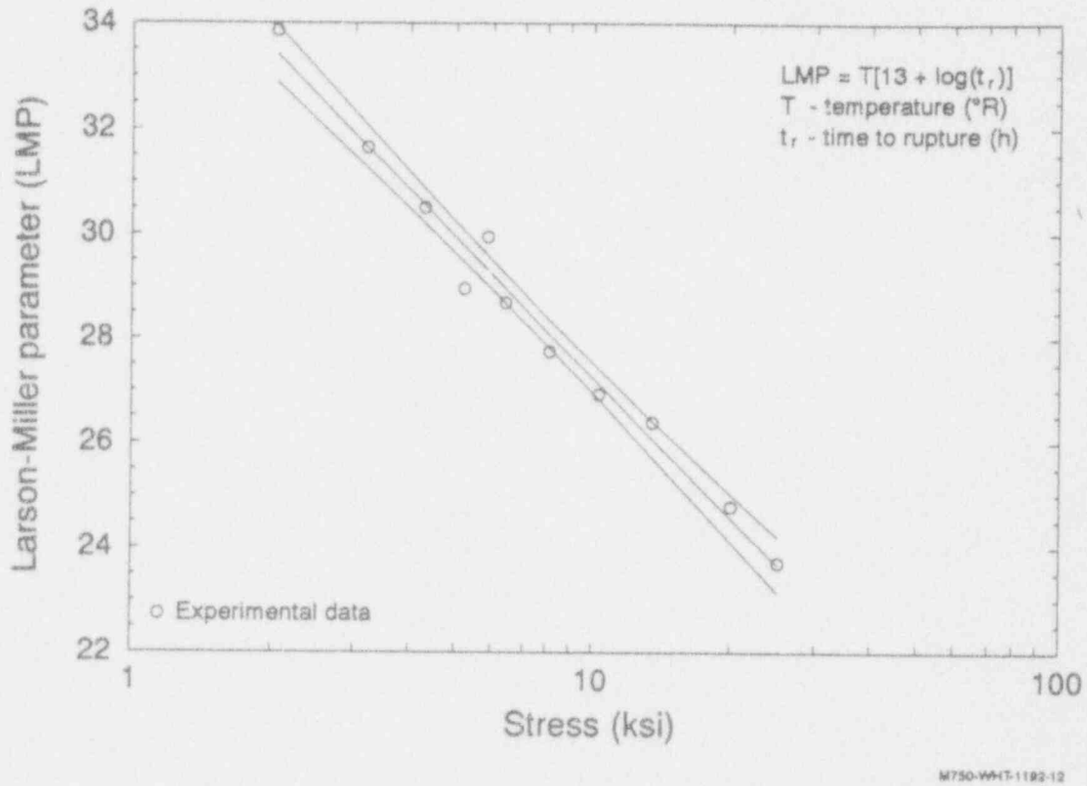

Figure A-33. Inconel-600 Larson-Miller parameter versus log (stress) with 95% confidence limits for tests between 873 and 1,473 K.[A-15]

Table A-1. Inconel-600 tensile test results.

Temperature (K)	Yield strength (MPa)	Ultimate strength (MPa)	Uniform elongation (%)	Total elongation (%)	Reduction of area (%)
297.0	374.00	733.00	30	43	68
600.0	315.00	689.00	30	39	61
800.0	280.00	617.00	26	39	65
900.0	266.00	468.00	16	45	73
1,000.0	237.00	273.00	4	76	94
1,050.0	187.00	212.00	6	76	95
1,100.0	132.00	154.00	6	76	93
1,150.0	98.00	113.00	5	88	91
1,200.0	74.00	79.00	7	62	83
1,300.0	45.00	50.00	3	66	91
1,373.0	21.00	27.00	7	55	97

Table A-2. Inconel-600 creep test results.

Temperature (K)	Stress (MPa)	Time to rupture (h)
1,005.0	173.2	1.30
1,005.0	137.8	5.00
1,005.0	93.6	38.50
1,144.0	71.1	1.20
1,144.0	55.6	3.00
1,144.0	36.1	11.50
1,255.0	44.4	0.50
1,255.0	40.6	1.80
1,255.0	29.5	3.20
1,366.0	22.2	0.75
1,366.0	14.1	5.90

A.2.2 SA533B Data

This section contains data for structural properties of SA533B. Temperature-dependent properties include elastic modulus, yield strength, ultimate strength, and thermal coefficient of expansion. A Poisson's ratio of 0.3 was assumed in the localized vessel failure model. Stress-strain curves and creep test results from high temperature, TMI-2 VIP testing of TMI-2 vessel material are shown in Figures A-34 through A-40 and Tables A-3 and A-4. Tensile data includes previously published data, as well as the TMI-2 VIP data. The elastic portions of the stress-strain curves were derived from published values of temperature-dependent elastic moduli. TMI-2 VIP strain measurements were designed for relatively large deformations and were not sensitive enough to accurately measure elastic moduli. For this reason, published values of a chemically similar material (STBA12) were used to develop the elastic portions of the stress-strain curves. The plastic portion of the stress-strain curve at each test temperature was taken from a representative TMI-2 VIP test specimen.

The creep properties include deformation behavior (power law relations for strain versus time curves at given temperatures and pressures) and failure behavior (Larson-Miller parameter). The scoping global vessel analyses in Section 4.4 only required the failure behavior, whereas the localized vessel analyses required both failure and deformation behavior.

The Larson-Miller parameter is used in creep problems to predict failure (time to rupture), given a stress and temperature. Results from TMI-2 VIP test data are shown in Figure A-40. The creep data for tests conducted at temperatures below the transition temperature (1,000 K) only include specimens which did not reach 1,000 K during the accident. Specimens subjected to accident temperatures above 1,000 K during the accident were considered atypical because they exhibited unusually high yield and ultimate strength when tested at temperatures below 1,000 K. Because the lowest TMI-2 VIP test temperature was 873 K, data from other published sources[A-16, A-17] were used to predict creep failures for lower temperatures, rather than extrapolating the TMI-2 data beyond its range (Figure A-41).

Data for strain versus time data used in the localized vessel analyses were taken from several different sources. At low temperatures, creep strain rates were evaluated on the basis of an algorithm suggested be Reddy and Ayres[A-18], based on their experimental lower temperature (<922 K) data. Creep strain rates are evaluated from the relation

$$\dot{\bar{\varepsilon}}_{cr} = (1+\mu)^{1/1+\mu} \left(\frac{\bar{\sigma}}{\sigma_m}\right)^{m/1+\mu} \left(\frac{t}{\tau}\right)^{1/1+\mu} \qquad \text{(A-1)}$$

where τ is a characteristic time (10^7 hours), t is time (hours), $^{1}/_{1+\mu}$ and $^{m}/_{1+\mu}$ are temperature-dependent expressions, $\bar{\sigma}$ is an effective stress (Huddleston's effective stress[A-21] is used in the localized effects model; see Section A.2.3.1) and σ_m is a stress and temperature dependent constant. The only difficulty with this relationship is that some combinations of stress and elevated temperature produce negative values of σ_m, which is evidently intended to be a positive quantity. For this reason, the procedure at temperatures below 922 K is to use these relations as long as $\bar{\sigma}/\sigma_m$ in Equation (A-1) exceeds one. If the ratio falls below unity, alternative relations are used.

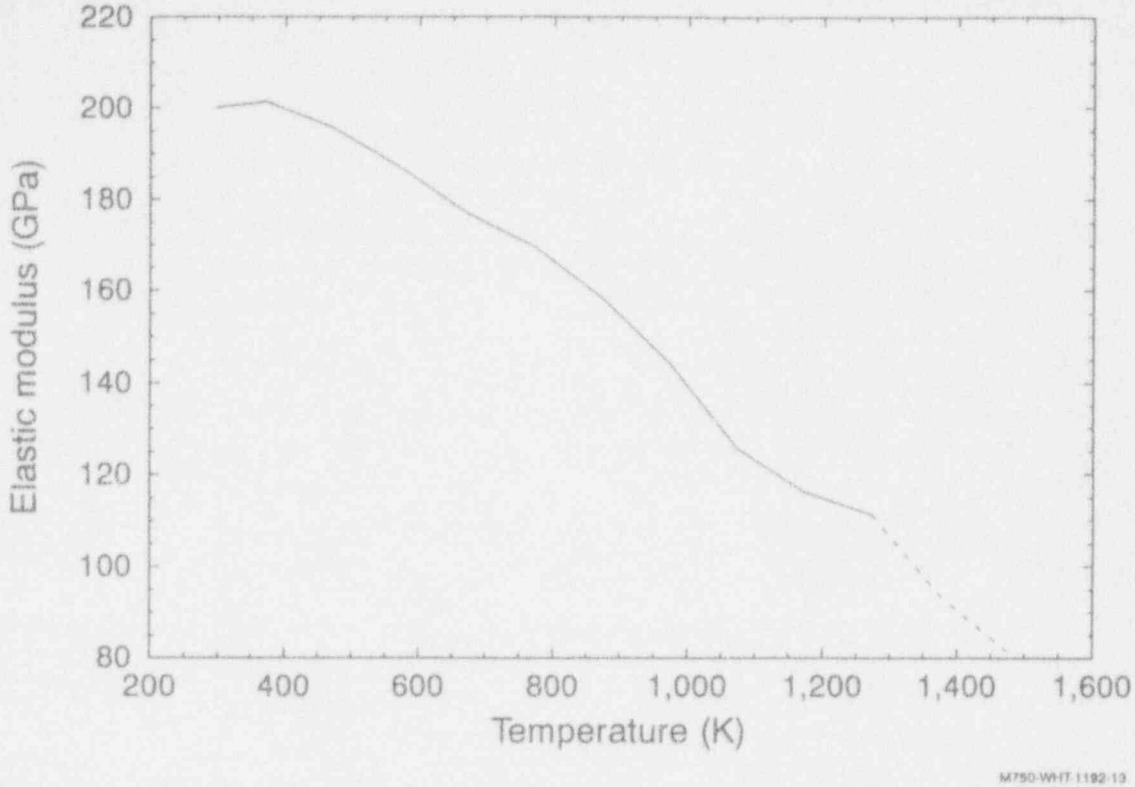

Figure A-34. STBA12 (chemically similar to SA533B) modulus as a function of temperature.[A-19]

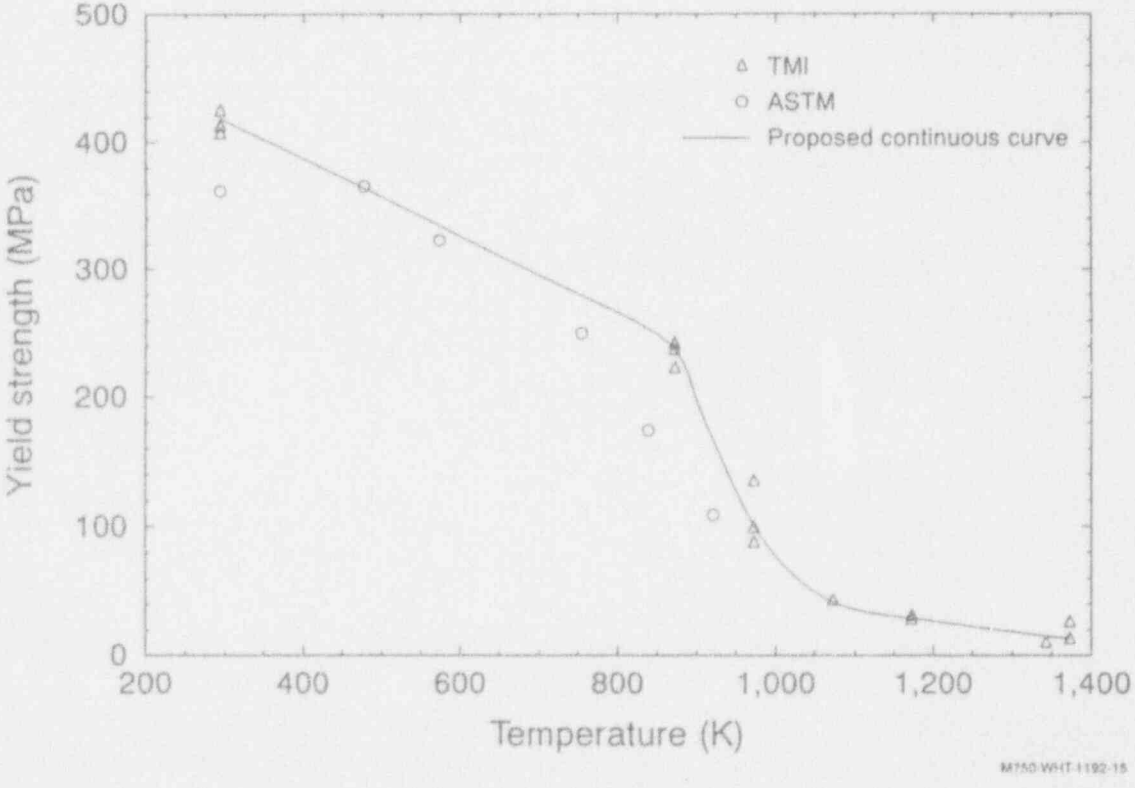

Figure A-35. SA533B 0.2% offset yield strength as a function of temperature, based on TMI-2 VIP and ASTM data.[A-16]

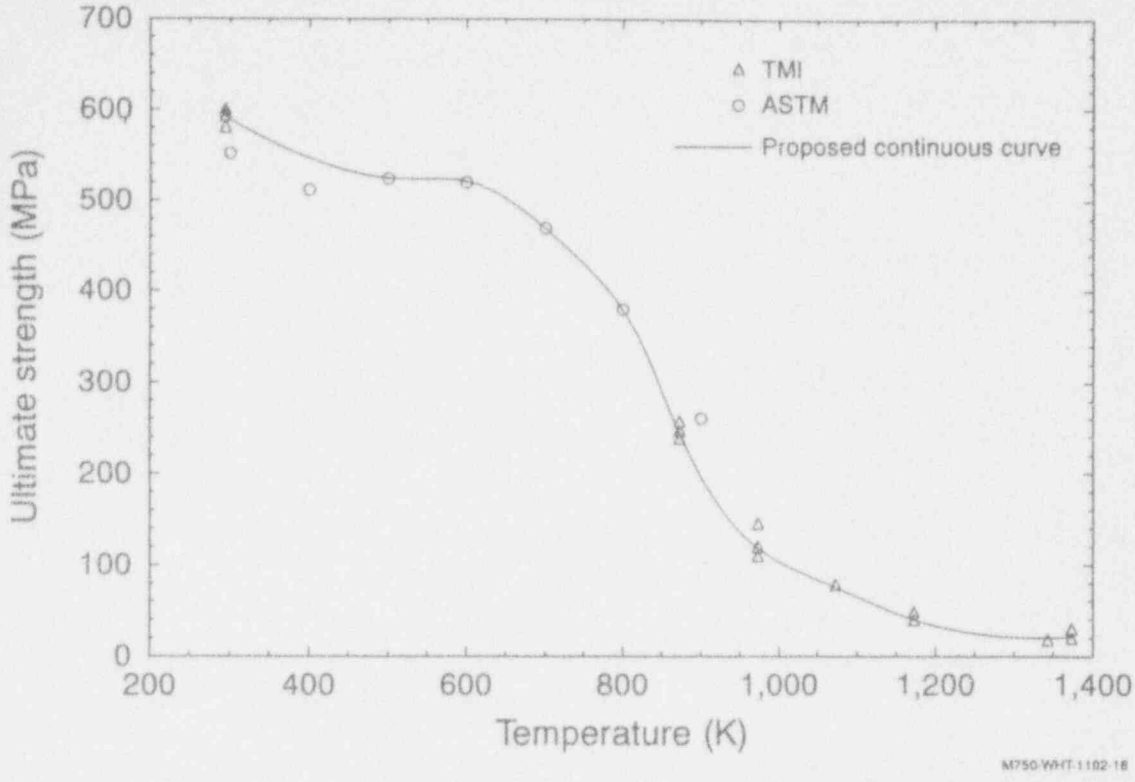

Figure A-36. SA533B ultimate strength as a function of temperature, based on TMI-2 VIP data.

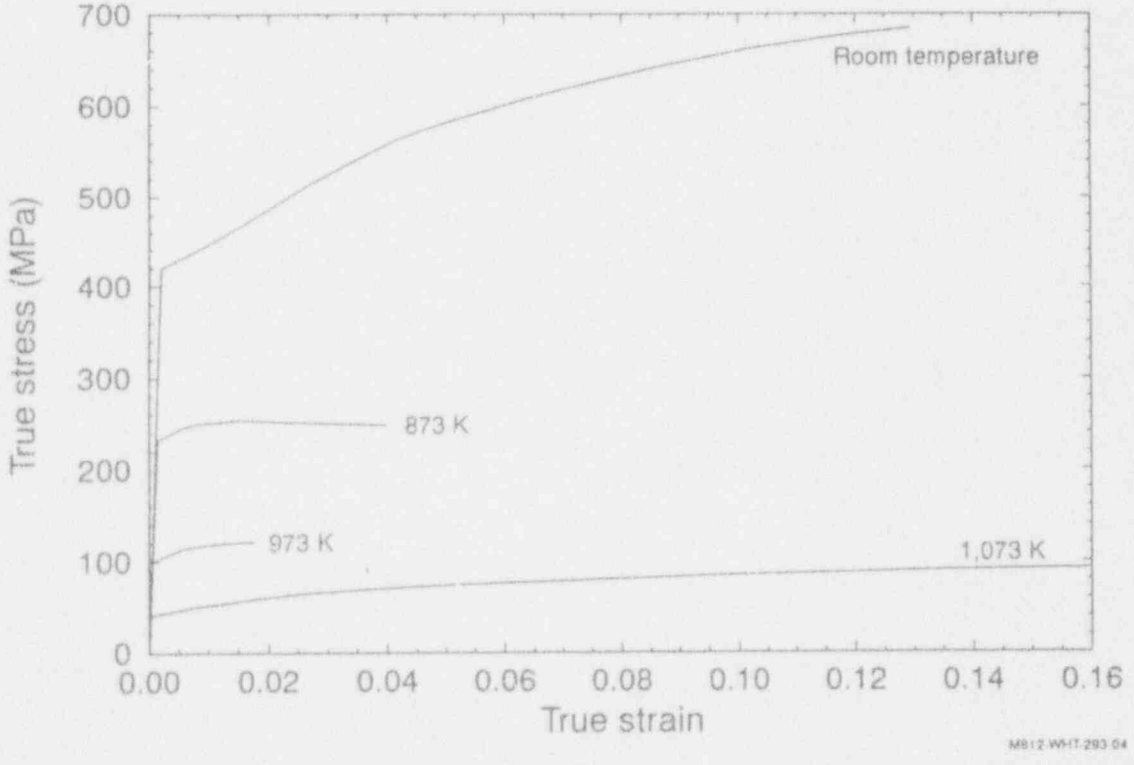

Figure A-37 (a). SA533B stress-strain curves for 297 K and 873 to 1,073 K, based on TMI-2 VIP data.

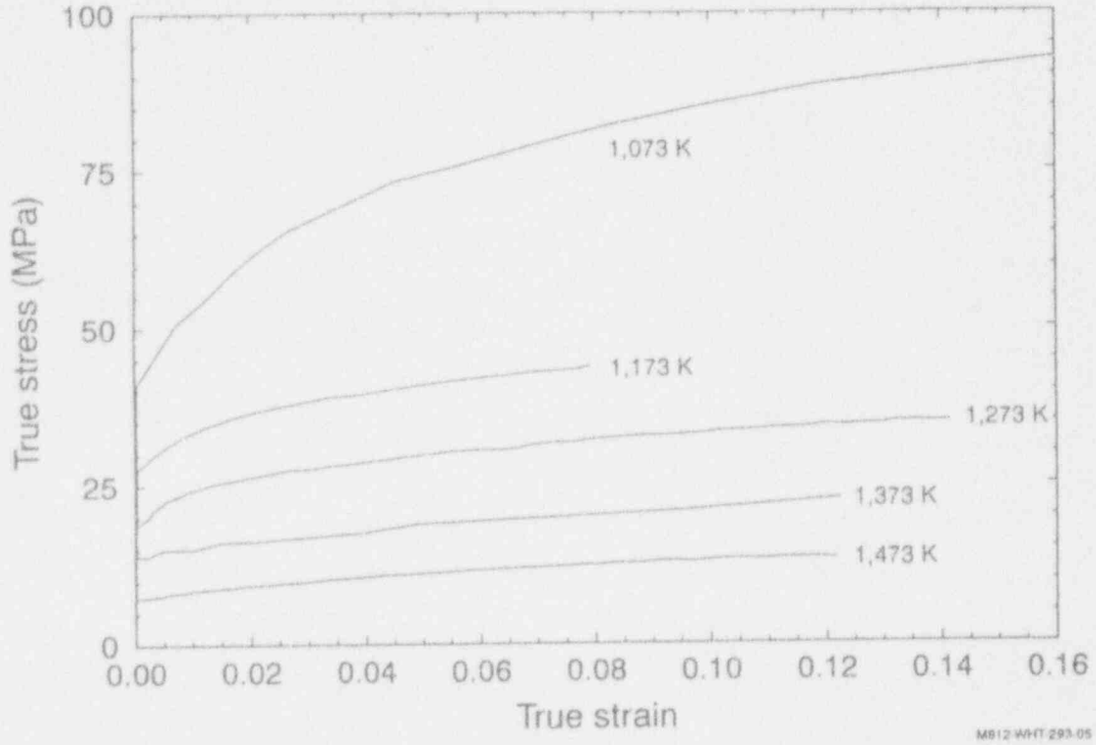

Figure A-37 (b). SA533B stress-strain curves for 1,073 to 1,473 K, based on TMI-2 VIP data.

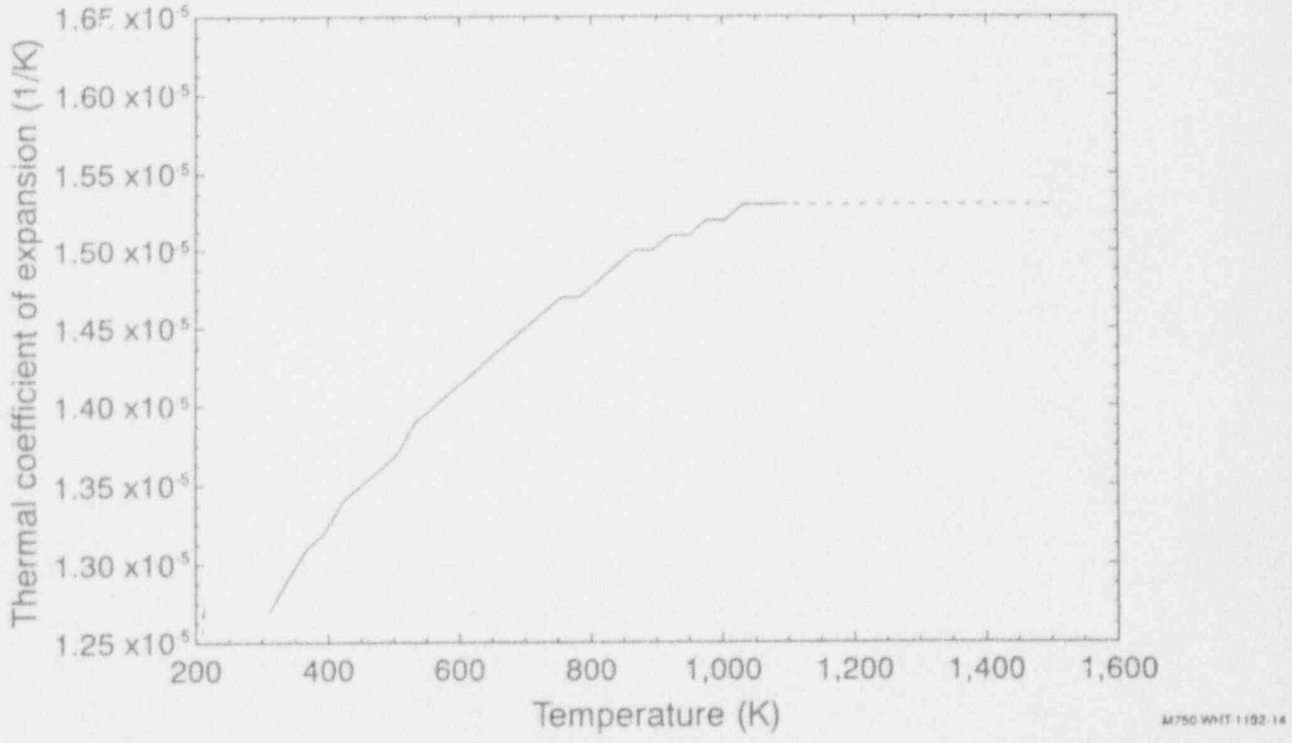

Figure A-38. SA533B mean linear coefficient of thermal expansion as a function of temperature.[A-20]

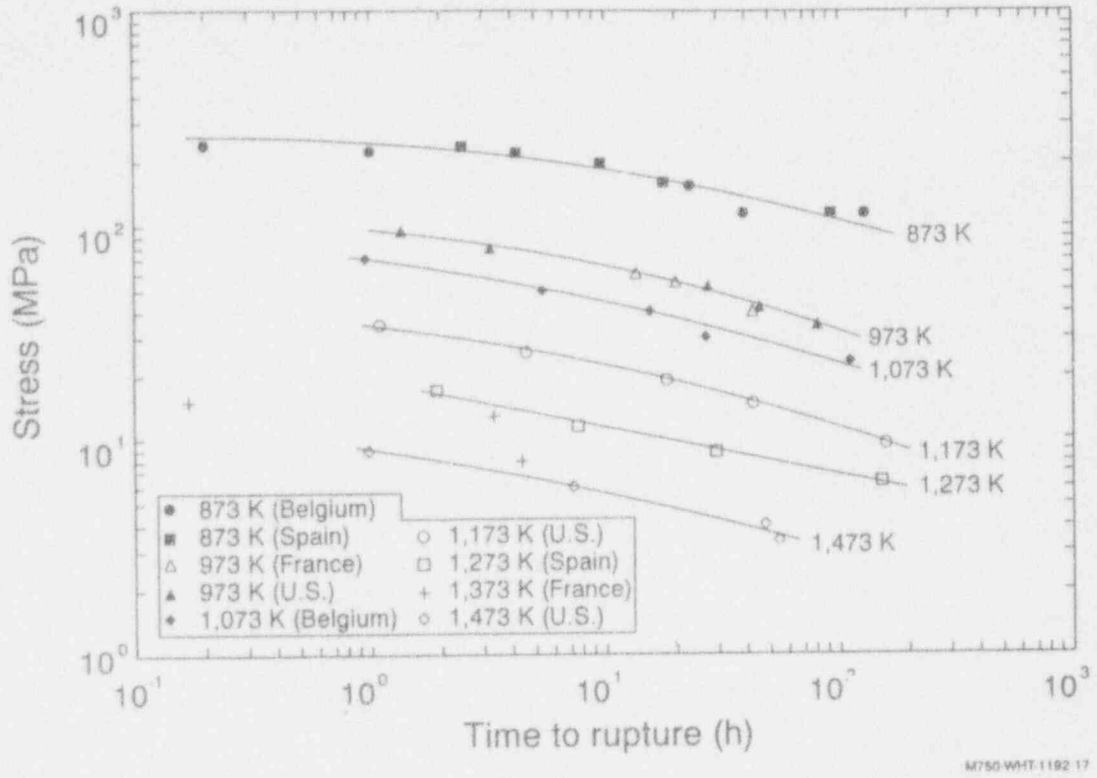

Figure A-39. SA533B creep time to rupture as a function of stress and temperature, based on TMI-2 VIP data.

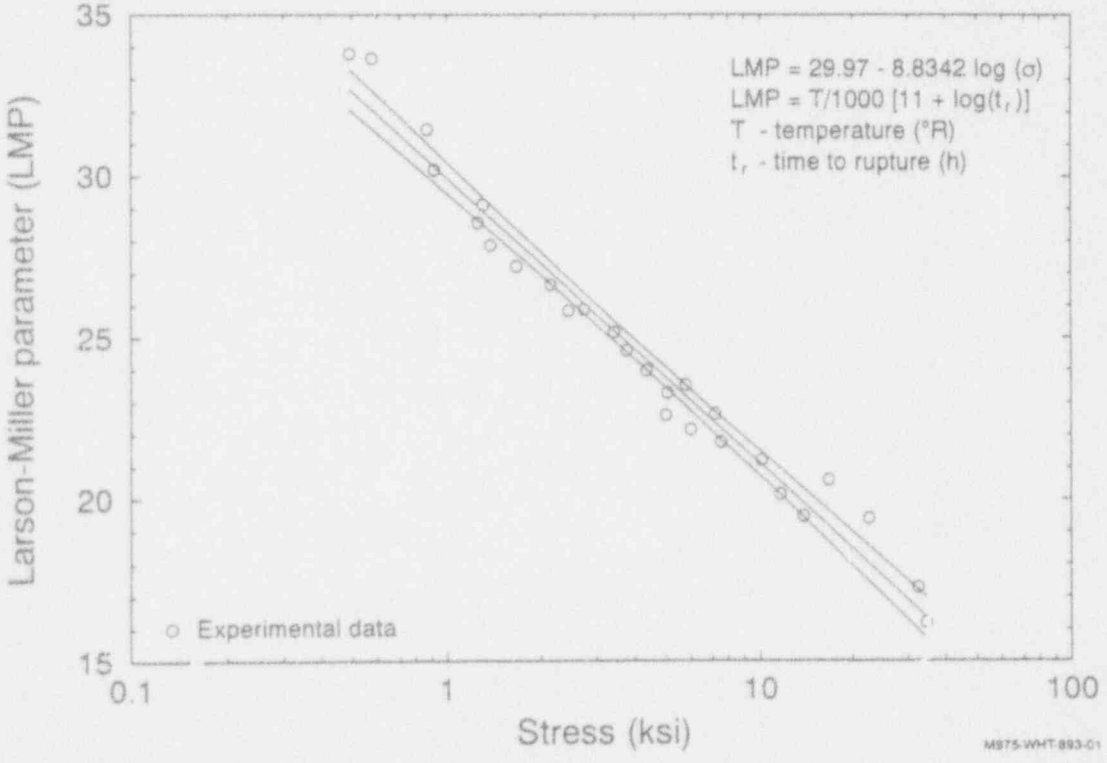

Figure A-40. SA533B Larson-Miller parameter versus log (stress) with 95% confidence limits for tests between 873 K and 1,473 K, based on TMI-2 VIP data.

Table A-3. SA533B TMI-2 VIP tensile test results.

Country/ specimen	Temperature (K)	Yield strength (MPa)	Ultimate strength (MPa)	Uniform elongation (%)	Total elongation (%)	Reduction of area (%)
Spain/ K-7	294.0	426.00	600.00	13.0	29	63
France/ M-11	294.0	408.00	581.00	11.0	22	65
Belgium/ K-13	294.0	414.00	594.00	11.0	24	72
U.S.A./ L-9	294.0	423.00	592.00	9.0	16	62
Spain/ K-7	873.0	238.00	247.00	3.2	48	81
France/ M-11	873.0	224.00	239.00	1.2	33	75
Belgium/ K-13	873.0	243.00	257.00	0.8	25	72
U.S.A./ L-9	873.0	231.00	256.00	1.6	44	91
Spain/ K-7	973.0	89.00	110.00	4.8	83	87
France/ M-11	973.0	136.00	146.00	1.6	42	66
Belgium/ K-13	973.0	100.00	120.00	1.7	77	90
U.S.A./ H-8	973.0	126.00	137.00	2.8	50	86
France/ L-9	1,073.0	44.00	79.00	18.0	64	43
U.S.A./ G-8	1,073.0	52.00	77.00	15.0	80	65
Spain/ L-9	1,173.0	29.00	40.00	13./	36	27
Belgium/ F-3	1,173.0	32.00	49.00	13.0	43	31
U.S.A./ H-8	1,273.0	20.00	30.00	14.0	42	35
Spain/ L-9	1,343.0	11.00	19.00	13.0	(110)	(Not received)
Belgium/ F5-T7	1,373.0	14.00	20.00	13.0	124	97
U.S.A./ H-8	1,473.0	7.60	12.00	12.0	93	99

Table A-4. SA533B TMI-2 VIP creep test results.

Country/specimen	Temperature (K)	Stress (MPa)	Time to rupture (h)
Belgium/K-13	873.0	240.01	0.20
Belgium/K-13	873.0	225.00	1.00
Belgium/K-13	873.0	155.00	23.10
Belgium/K-13	873.0	115.00	128.00
U.S.A./H-8	973.0	95.10	1.34
U.S.A./H-8	973.0	80.00	3.27
U.S.A./H-8	973.0	52.10	27.60
U.S.A./H-8	973.0	41.60	46.00
U.S.A./H-8	973.0	34.50	81.60
Belgium/F-5	1,073.0	70.00	0.95
Belgium/F-5	1,073.0	50.00	5.40
Belgium/F-5	1,073.0	40.00	15.50
Belgium/F-5	1,073.0	30.00	27.00
Belgium/F-5	1,073.0	23.70	1,1.00
U.S.A./H-5	1,173.0	35.00	1.09
U.S.A./H-5	1,173.0	26.00	4.55
U.S.A./H-5	1,173.0	19.00	18.10
U.S.A./H-5	1,173.0	14.80	42.30
U.S.A./H-5	1,173.0	9.51	159.50
Spain/K-7	1,273.0	16.90	1.90
Spain/K-7	1,273.0	11.50	7.54
Spain/K-7	1,273.0	8.70	29.64
Spain/K-7	1,273.0	6.30	152.80
U.S.A./M-8	1,473.0	9.00	0.98
U.S.A./M-8	1,473.0	6.00	7.26
U.S.A./M-8	1,473.0	4.00	48.20
U.S.A./M-8	1,473.0	3.40	55.10

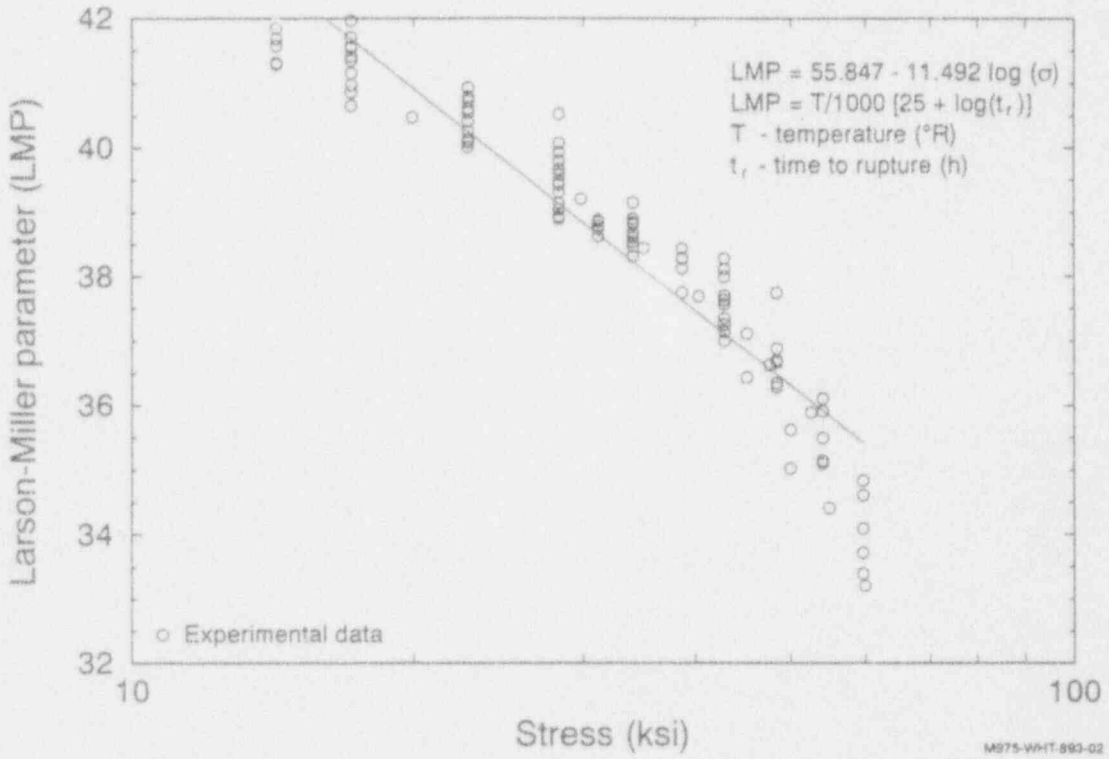

Figure A-41. SA533B Larson-Miller parameter versus log (stress) for tests between 723 K and 823 K, based on published data.[A-16, A-17]

Table A-5. Power law coefficients used in creep strain relations.

Temperature (K)	A	m	n
672	5.2913E-15	4.2406	0.3324
755	9.7568E-12	3.1412	0.4440
839	2.8923E-10	3.0288	0.5137
922	4.0310E-7	2.0050	0.5252
1,000	2.7564E-5	1.7627	1.0000
1,050	1.5003E-8	4.1983	1.0000
1,150	3.5934E-7	3.5747	1.0000
1,250	3.3895E-8	5.7124	1.0000
1,373	1.4911E-6	6.2967	1.0000

The high temperature creep strain behavior for the scoping calculations in Secton 4.5.2 used data provided from the USNRC-sponsored lower head failure program. TMI-2 VIP data was not available at the time that these calculations were performed. The data was fit to the following power law (or Bailey-Norton) form:

$$\bar{\varepsilon}_{cr} = A(T)\bar{\sigma}^{n(T)}t^{n(T)} \quad . \tag{A-2}$$

Table A-5 lists the values of the coefficients A, m, and n as functions of temperature. The first four entries are fits to the relations of Reddy and Ayres and are used as a backup for obtaining creep strain rates when combinations of stress and temperature render unacceptable ratios of $\bar{\sigma}/\sigma_m$.

The Bailey-Norton constants for primary and secondary creep listed in Table A-6 are from testing of the TMI-2 vessel material and were used in Section 5.1 calculations to investigate enhanced cooling. As with the data used to derive Larson-Miller parameters, creep data for tests conducted at temperatures below the transition temperature (1,000 K) only include specimens which did not reach 1,000 K during the accident. Some of the data listed in the tables (e.g., % total elongation in Table A-3) were not actually used in the analysis, but are included for completeness.

Table A-7 contains equation fits for primary and secondary creep, as well as tertiary creep, used in Section 5.2 comparisons of stress-based versus strain-based failure criteria. The primary/secondary fits were used until the tertiary point (also listed in Table A-7) was reached, at which point the tertiary fits were used. Primary/secondary fits for Tables A-6 and A-7 are not identical because the fits in Table A-6 attempted to use as much of the curves as possible, whereas the fits for Table A-7 do not include data beyond the tertiary point. In addition, a more accurate least squares fit was used to obtain the constants in Table A-7.

Table A-6. SA533B TMI-2 VIP creep test results, Bailey Norton constants used in Section 5.1 slow and rapid cooling analysis.

Temperature (K)	A	m	n
873.0	7.8163E-14	5.0287	0.98760
973.0	4.9614E-10	4.1548	1.16840
1,073.0	6.2661E-08	3.5945	0.79562
1,173.0	5.6481E-08	4.4051	1.04690
1,273.0	1.8897E-06	3.9414	0.93976
1,473.0	1.0505E-04	3.4700	0.91029

a. Constants are used in Equation A-2.

A.2.3 Structural Failure Criterion

A stress-based failure criterion was defined by consensus of the Structural Mechanics Peer Review Group.[A-22] The procedure includes converting a multi-dimensional stress state to an effective stress, interpolating the time to failure for constant stress and temperature using the Larson-Miller parameter and predicting time to failure for the actual stress and temperature history using a time damage model. The Huddleston criterion for calculating effective stress is described below, followed by a brief discussion of the Larson-Miller parameter and the time damage rule.

A.2.3.1 Huddleston Criterion for Effective Stress. The effective (or equivalent) stress used in the Larson-Miller parameter is a measure suggested by Reference A-21 and based on biaxial creep tests of steel. The stress measure for ferritic steels may be written using

$$\tilde{\sigma} = \sigma_{vm} \exp[0.2(J_1/S_s - 1)] \qquad \text{(A-3)}$$

where

$\tilde{\sigma}$ = the effective stress.

Table A-7. SA533B TMI-2 VIP creep test results, Bailey-Norton constants used to compare Section 5.2 creep failure criteria.[a]

Primary and secondary curves

Temperature (K)	A	m	n	Notes
873	1.6672E-12	4.47023	0.71308	
973	1.3925E-12	5.4352	1.21024	34.5 MPa omitted[b]
1,073	2.5619E-08	3.81621	0.79783	
1,173	1.4268E-08	4.71562	1.08466	
1,273	1.1152E-06	4.15893	0.97798	2 unphysical data points removed from 6.3 MPa
1,473	8.9176E-05	3.5891	0.70114	3.4 MPa omitted[c]

Tertiary curves

Temperature (K)	A	m	n	Notes
873	8.3387E-12	4.47023	3.946	225 MPa only[d]
973	3.5818E-28	13.4311	2.53973	80.0 and 95.1 MPa only[e]
1,073	4.2601E-08	3.81621	2.4084	70 MPa only[f]
1,173				use I&II fit[g]
1,273				use I&II fit[g]
1,473	5.7553E-08	7.25974	1.5341	6.0 and 9.0 MPa only[h]

Tertiary points

Temperature (K)	$\bar{\sigma}$ (MPa)	t (h)	$\bar{\epsilon}_{cr}$ (%)
873	225	0.66	5.30
873	155	15.0	7.49
973	95.1	0.674	4.88
973	80	1.907	6.71
973	52.1	15.0	7.31
1,073	70	0.729	21.9
1,073	50	4.58	23.3
1,173	no tert. curves		
1,273	no tert. curves		
1,473	9.0	0.4215	12.94
1,473	6.0	2.51664	10.57
1,473	4.0	35.3	26.41

Table A-7. (continued).

a. Constants are used in Equation A-2.

b. Removing the curve at 34.5 MPa results in much better fits for the remaining curves. The remaining curves are at 41.6 MPa, 52.1 MPa, 80 MPa, and 95.1 MPa.

c. Removing the curve at 3.4 MPa results in much better fits for the remaining curves. The remaining curves are at 4.0 MPa, 6.0 MPa and 9.0 MPa.

d. Only the 225 MPa curve was fit for tertiary. The remaining curves did not exhibit tertiary within 15 hours.

e. Only the 80 MPa and 95.1 curves were fit for tertiary. The remaining curves did not exhibit tertiary behavior within 15 hours.

f. Only the 70 MPa curve was fit for tertiary. The remaining curves did not exhibit tertiary within 15 hours (23.7 and 30 MPa) or had a reasonably good fit to the primary and secondary curves throughout their history (40 and 50 MPa).

g. The constants listed for primary and secondary behavior fit the entire history reasonably well. A tertiary fit was attempted with 11.5 MPa and 16.9 MPa, but the fit was not good.

h. Only the 6.0 MPa and 9.0 MPa curves were fit for tertiary. The remaining curve at 4.0 MPa did not exhibit tertiary behavior within 15 hours.

σ_{vm} = the von Mises stress

J_1 = the first stress invariant

S_s = a modulus of principal stresses.

$$J_1 = \sigma_1 + \sigma_2 + \sigma_3 \qquad \text{(A-4)}$$

$$S_s = \sigma_1^2 + \sigma_2^2 + \sigma_3^2 \ . \qquad \text{(A-5)}$$

A.2.3.2 Time Damage Rule and the Larson-Miller Parameter. At each Gauss point (for localized vessel failure model) or vessel wall segment (for vessel global rupture model), the damage was evaluated by calculating an equivalent, or effective, stress $(\bar{\sigma})$ and finding the Larson-Miller parameter (LMP) for SA533B vessel steel from

$$LMP = 29.97 - 8.8342 \log(\bar{\sigma}) \quad \text{(A-6)}$$

where $\bar{\sigma}$ is in ksi, (see Figure A-36). Time to rupture (t_r), for SA533B vessel steel, was obtained at that stress and a known temperature (T) from

$$t_r = 10^{[LMP(1000)/T - 11]} \quad \text{(A-7)}$$

where t_r is in hours and T is in Rankine.

Equations (A-6) and (A-7) were fit from TMI-2 VIP data where testing temperatures were above 873 K. Implemented in the simple global vessel calculations, they were found to give very conservative results when extrapolated to lower temperatures. Supplementing the TMI-2 VIP data with lower temperature data from other sources,[A-16,A-17] the following relationships were found to apply. These were used in the localized vessel failure calculations. (Note: Using these equations in the simple global vessel calculations would not change the conclusions of that analysis).

For $723 < T < 850$ K,

$$LMP = 55.847 - 11.492 \log(\sigma) \quad \text{(A-8)}$$

$$t_r = 10^{[LMP(1,000)/T - 25]} \quad \text{(A-9)}$$

For $850 \leq T < 1{,}473$ K,

$$LMP = 30.014 - 12.127 \log(\sigma) + 5.1831 [\log(\sigma)]^2 - 1.8394[\log(\sigma)]^3 \quad \text{(A-10)}$$

$$t_r = 10^{[LMP(1,000)/T - 11]} \quad \text{(A-11)}$$

The damage within a time step Δt is $\Delta t/t_r$ and the accumulated damage at a Gauss point or wall segment from all time steps i is

$$D = \Sigma (\Delta t_i/t_r) \quad \text{(A-12)}$$

This procedure is also discussed in Reference A-23.

A.3 Geometrical Data

This section contains dimensions used in the TMI-2 margin-to-failure analyses. Dimensioned diagrams of the vessel, instrument nozzle, cavity configuration, and reactor vessel insulation placement are included in Figures A-42 through A-45.

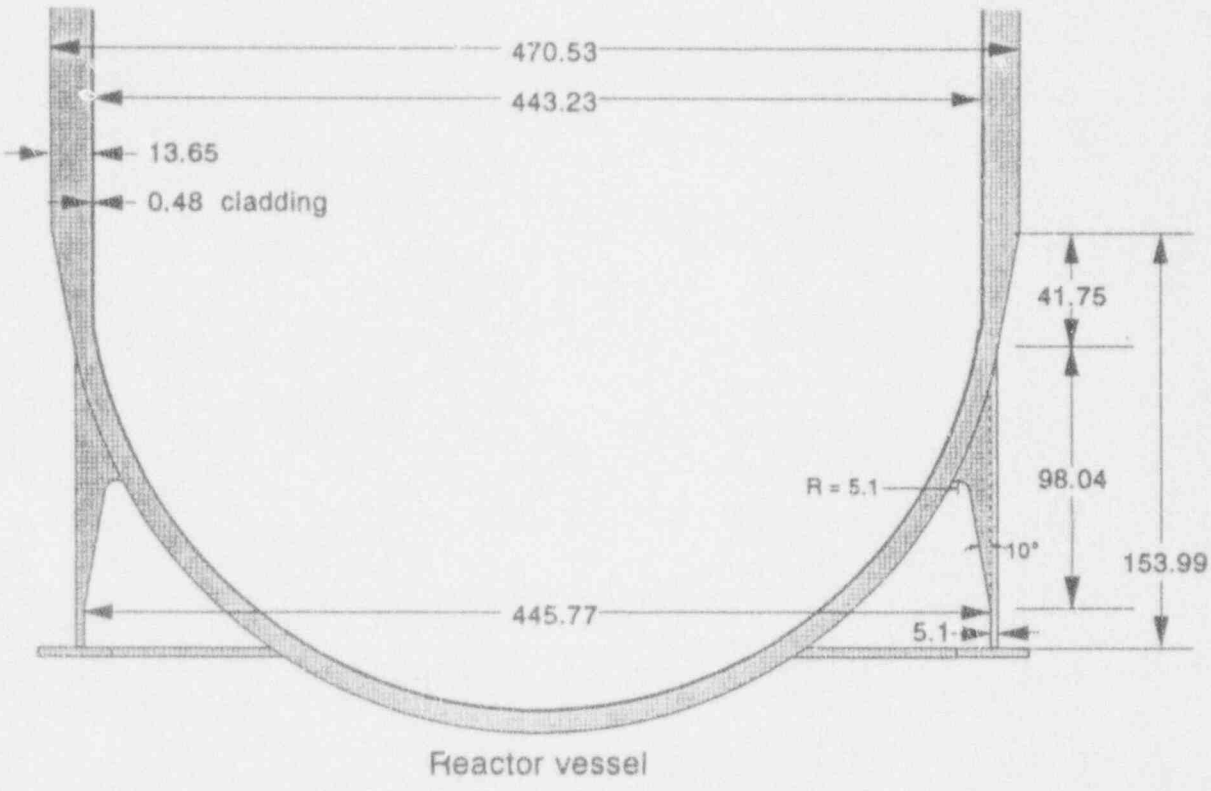

Figure A-42. Dimensioned drawing of TMI-2 lower head (see Table A-8 for references for dimensions).

Table A-8. References for TMI-2 lower head dimensions shown in Figure A-42.

Vessel		
Material	SA533B1	
Thickness—reference	13.65 cm	B&W Drawing 126970, Rev. 4 "Vessel Head and Suppt Assy & Details," 1/20/75.
Thickness—minimum	12.7 cm	B&W Drawing 126971 E, Rev. 6 " Inst. Nozzle Det. & Assy.," 12/6/74.
Inner diameter (to base metal)	443.23 cm	B&W Drawing 126970, Rev. 4 "Vessel Head and Suppt Assy & Details," 1/20/75.
Outer diameter	470.53 cm	B&W Drawing 126970, Rev. 4 "Vessel Head and Suppt Assy & Details," 1/20/75.
Cladding		
Material	SS304	
Thickness—nominal	0.48 cm	B&W Drawing 126970, Rev. 4 "Vessel Head and Suppt Assy & Details," 1/20/75.
Thickness—minimum	0.32 cm	B&W Drawing 126970, Rev. 4 "Vessel Head and Suppt Assy & Details," 1/20/75.
Skirt		
Material		
Inner diameter	445.77 cm	B&W Drawing 126970, Rev. 4 "Vessel Head and Suppt Assy & Details," 1/20/75.
Thickness	5.1 cm	B&W Drawing 126963 E, Rev. 11 "Arrgt. Reactor Vessel Long. Sec.," 6/18/75.
Point of attachment (distance from hemisphere to point where skirt attaches to outer surface)	41.75 cm	B&W Drawing 126970, Rev. 4 "Vessel Head and Suppt Assy & Details," 1/20/75.
Length (from hemisphere to end of skirt)	153.99 cm	
Radius for junction between skirt and vessel	5.1 cm	B&W Drawing 126970, Rev. 4 "Vessel Head and Suppt Assy & Details," 1/20/75.
Distance between hemisphere and point where skirt angles in at 10 degrees	98.04	B&W Drawing 126970, Rev. 4 "Vessel Head and Suppt Assy & Details," 1/20/75.

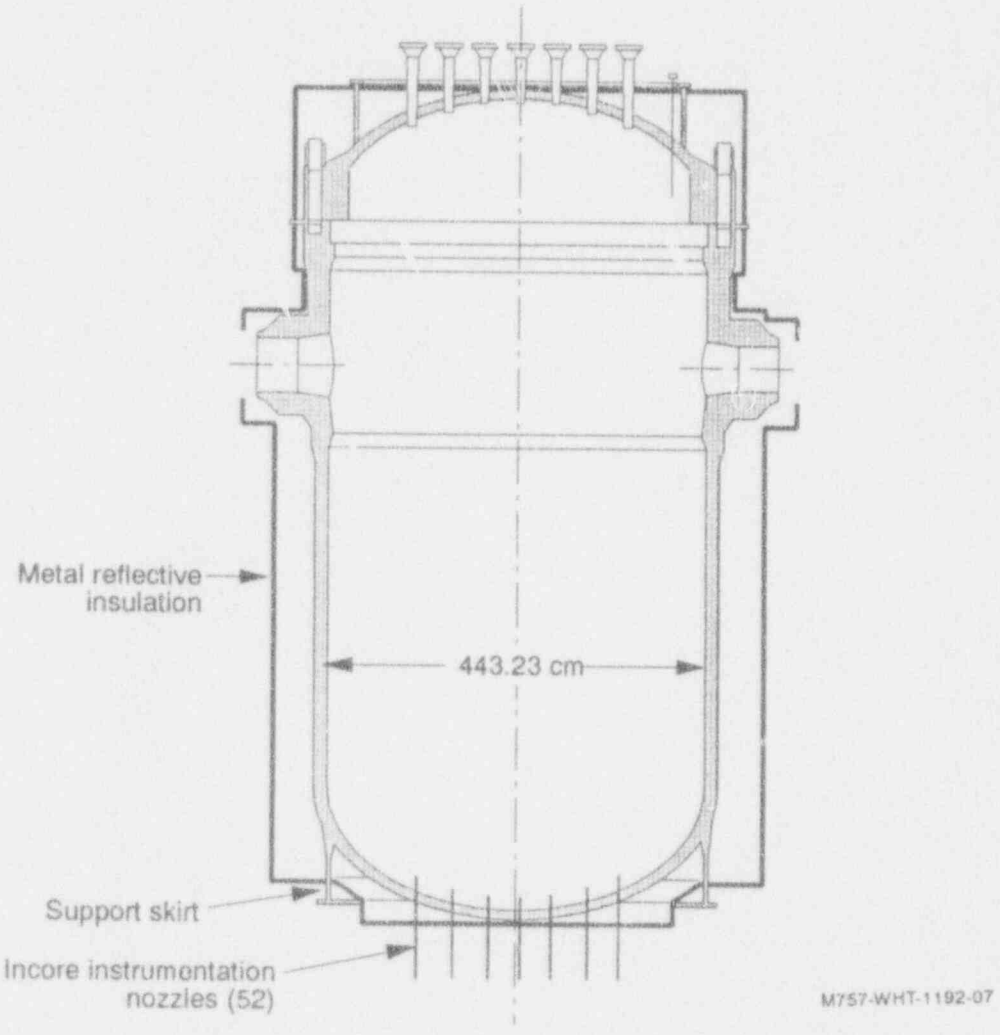

Figure A-43. Drawing illustrating insulation placement around TMI-2 reactor vessel.[A-24]

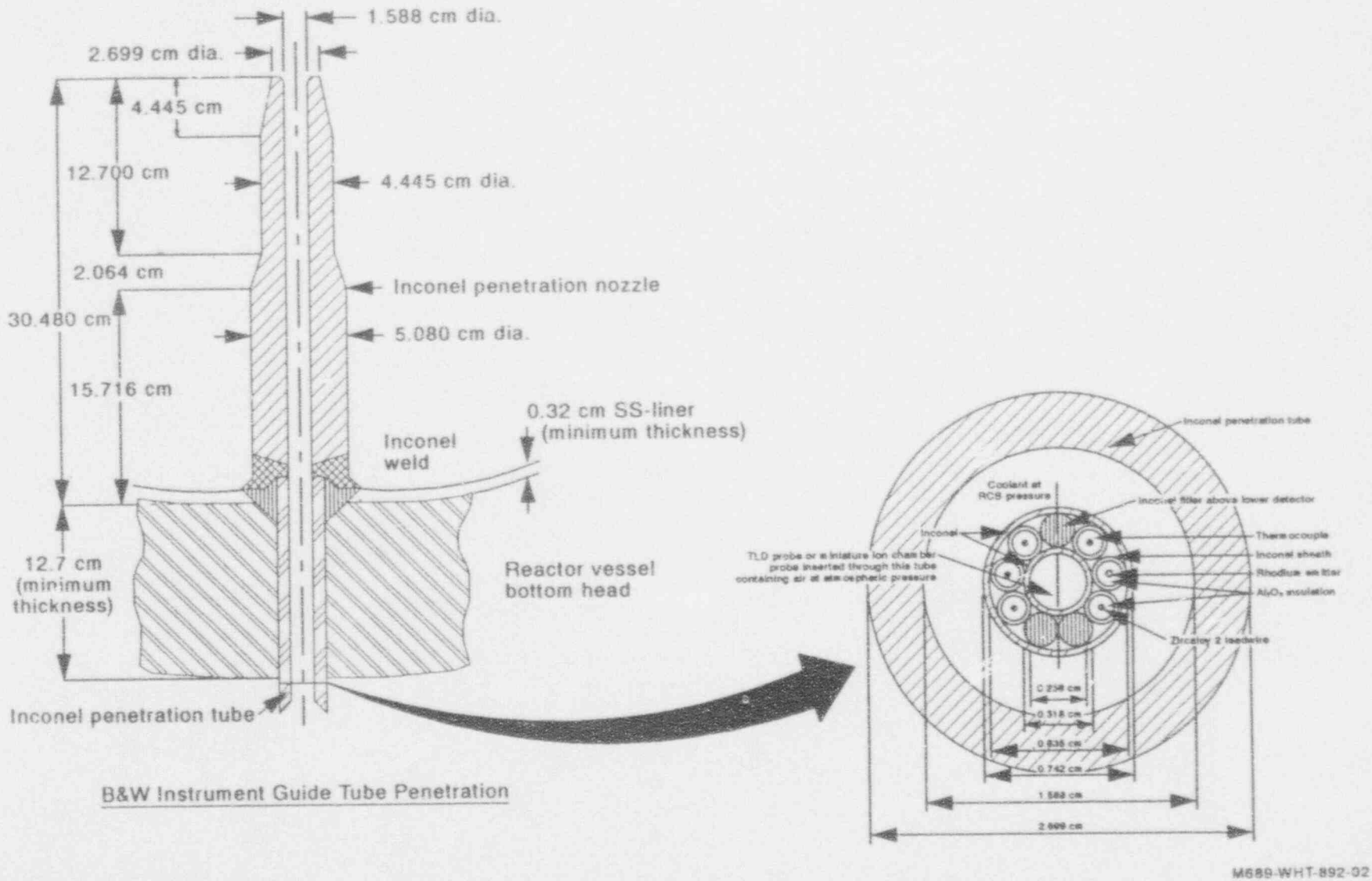

B&W Instrument Guide Tube Penetration

Figure A-44. Dimensioned drawing of TMI-2 instrument nozzle.[A-25]

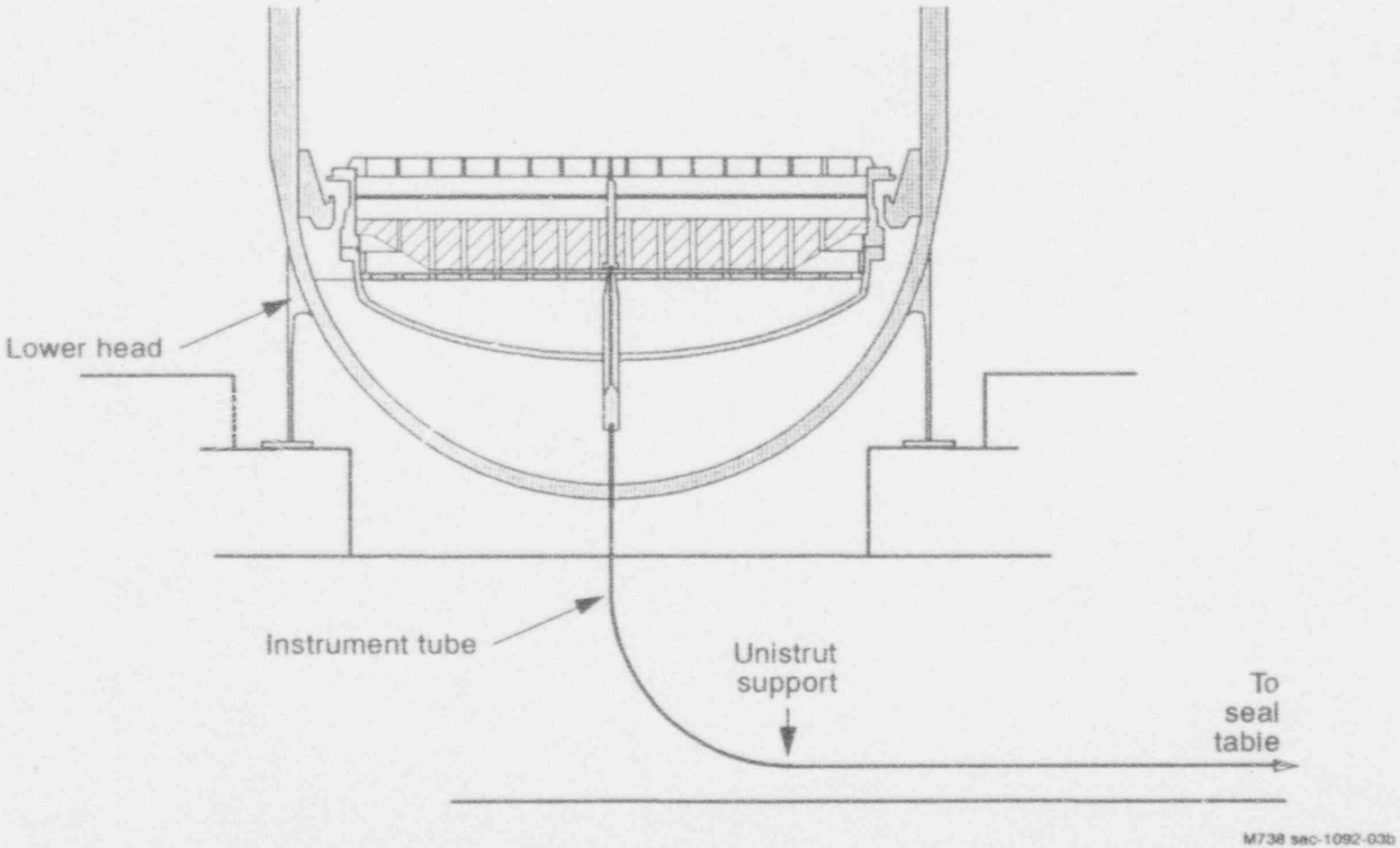

Figure A-45. Drawing illustrating instrument tube arrangement below TMI-2 reactor vessel.[A-25,a]

a. Personal communication with B&W personnel, September 1992.

A.4 References

A-1. J. K. Hohorst, *SCDAP/RELAP5/MOD2 Code Manual, Volume 4: MATPRO - A Library of Materials Properties for Light-Water-Reactor Accident Analysis,* NUREG/CR-5273, EGG-2555, February 1990.

A-2. D. W. Akers, et al., *Companion Sample Examinations,* OECD-NEA-TMI-2 VIP TMIV(92)EG10, July 1992.

A-3. Sandia Laboratories, *Core Meltdown Experimental Review*, SAND74-0382, August, 1992.

A-4. Air Force Materials Laboratory, *Aerospace Structural Metals Handbook,* 1990 Edition, Revised 1989, Air Force Materials Laboratory.

A-5. Huntington Alloy, *Inconel-600,* Technical Bulletin of the International Nickel Company, Inc., now Inco Alloys International, Inc., Huntington Alloy Products Division, Seventh edition, Huntington, West Virginia, 1987.

A-6. R. F. Bolz and G. L. Tuve, (eds.), *CRC Handbook of Tables for Applied Engineering Science*, Second Edition, Boca Raton, Florida: The Chemical Rubber Company Press, 1976.

A-7. D. L. Timrot, *Determination of Thermal Conductivity and Heat Capacity of Steels,* Zhurnal Tekhinicheskoi Fizinki, 5, 1935, pp. 1011-1036.

A-8. R. W. Powell, and M. J. Hickman, "Thermal Conductivity and Electrical Resistivity of a Series of Steels," *Journal of the Iron Steel Institute*, Special Report No. 24, Part 3, London, 1939, pp. 242-251.

A-9. B. E. Neimark, and V. E. Lynsternik, "Effect of Chilling on the Thermal Diffusivity of Carbon Steels," *Teploenergetika, 7*, pp. 16-18, 1960.

A-10. J. H. Awbery, A. R. Calloner, P. R. Pallister, and R. W. Powell, "The Physical Properties of a Series of Steels - Part II," *Journal of the Iron Steel Institute*, 154(2), London, 1946, pp. 83-111.

A-11. P. R. Pallister, "Specific Heat and Resistivity of Mild Steel," *Journal of the Iron Steel Institute*, 185(4), London, 1957, pp. 474-482.

A-12. British Iron and Steel Research Association, *Physical Constants of Some Commercial Steels at Elevated Temperatures,* London: Butterworth's Scientific Publication, Ltd., 1957, p. 38.

A-13. E. Griffiths, R. W. Powell, and M. J., Hickman, "The Physical Properties of a Series of Steels-I," *Journal of the Iron Steel Institute*, Special Report No., 24, London, pp. 215-251.

A-14. E. G. Shuidkovskii, "Measurement of the Thermal Conductivity of Metals by the Method of Angstrom," *Journal Tech. Phys., 8*, USSR, 1938, pp. 935-947.

A-15. J. L. Rempe, et al., *Light Water Reactor Lower Head Failure Analysis*, NUREG/CR-5642, EGG-2618, October 1993, Appendix B.

A-16. G. V. Smith, *Evaluations of the Elevated Temperature Tensile and Creep Rupture Properties of C-Mo, Mn-Mo and Mn-Mo-Ni Steels*, Metal Properties Council, American Society for Testing and Materials, ASTM Data Series Publication DS47, 1971.

A-17. National Research Institute for Metals, *Data Sheets on the Elevated-Temperature Properties of 1.3 Mn-0.5 Mo-0.5 Ni Steel Plates for Boilers and Other pressure Vessels (SBV 2)*, NRIM Creep Data Sheet No. 18B, Japan, December 1987.

A-18. G. B. Reddy and D. J. Ayres, *High Temperature Elastic-Plastic Creep Properties for SA533 Grade B Class 1 and SA508 Materials*, EPRI-NP-2763, December 1982.

A-19. Y. Takeuti, et al., "Thermal-Stress Problems in Industry. 3: Temperature Dependency of Elastic Moduli for Several Metals at Temperatures from 196°C to 1000°C," *Journal of Thermal Stresses, 2*: 1979, pp. 233-250.

A-20. R. A. Moen, *Thermophysical Properties of Ferrous Structural Alloys*, HEDL-TME-78-47, April 1978.

A-21. R. L. Huddleston, "An Improved Multiaxial Creep-Rupture Strength Criterion," American Society of Mechanical Engineers, *Journal of Pressure Vessel Technology*, 107, 1985, pp. 421-429.

A-22. J. Strosnider, "Summary Record of the TMI-VIP Structural Mechanics Peer Review Group Meeting," *OECD TMI Vessel Investigation Project, Idaho Falls, Idaho, May 11, 1992, NEA.TMIV/MAN(92)09*, July 20, 1992.

A-23. H. Kraus, *Creep Analysis*, New York, New York: John Wiley and Sons, 1980, pp. 98-106.

A-24. Sacramento Municipal Utility District, *Rancho Seco Final Safety Analysis Report*, Docket No. 50-312, Sacramento Municipal Utility District, 1971.

A-25. MPR Associates, *Phase 4 Status Report, Removal of Test Specimens from the TMI-2 Reactor Vessel Bottom Head, Project Summary, MPR-1195,* October 1, 1990, Drawing no. F-80-107-89, July 1990.

Appendix B

Supporting Information for Melt Penetration Calculations

Appendix B

Supporting Information for Melt Penetration Calculations

B.1 Compilation of Instrumentation Nozzle Data

In the information below, cut elevations and ablation elevations reported by MPR Associates[B-1] should be considered as nominal distances. Elevations are given from the nadir of the lower head inside the pressure vessel. Figure B-1 illustrates the relative positions of the various elevations given in the information below for several of the nozzles. A discrepancy of 1.27 cm in the total length of nozzles D10 and E11 exists. The missing length might be attributed to uneven cutting. In the dimensions presented below the missing length was assumed to exist between the nozzle cut and the sample and was added into the fuel penetration elevation and nozzle ablation elevation. Fuel penetration measurements were based on gamma scans.

Nozzle **D10**
Examining Lab: ANL
Length: 23.5 cm
Elevation of nozzle at cut: 28.8 cm
Fuel penetration elevation in nozzle: 42.8 cm min., 29.9 cm max.
Debris penetration elevation in instrument probe tube: 28.8 cm
Debris composition in instrument probe tube: ceramic
Nozzle ablation elevation: 53.6 cm
Comments: A gamma scan for fuel depth indicated a small amount of fuel at the nozzle tip and fuel throughout the nozzle, with the highest concentration at an elevation of 21.6 cm. The instrument probe tube in the center of the instrument string had collapsed. (Surface temperatures of 1,673 K were estimated at the 21.6 cm elevation.)

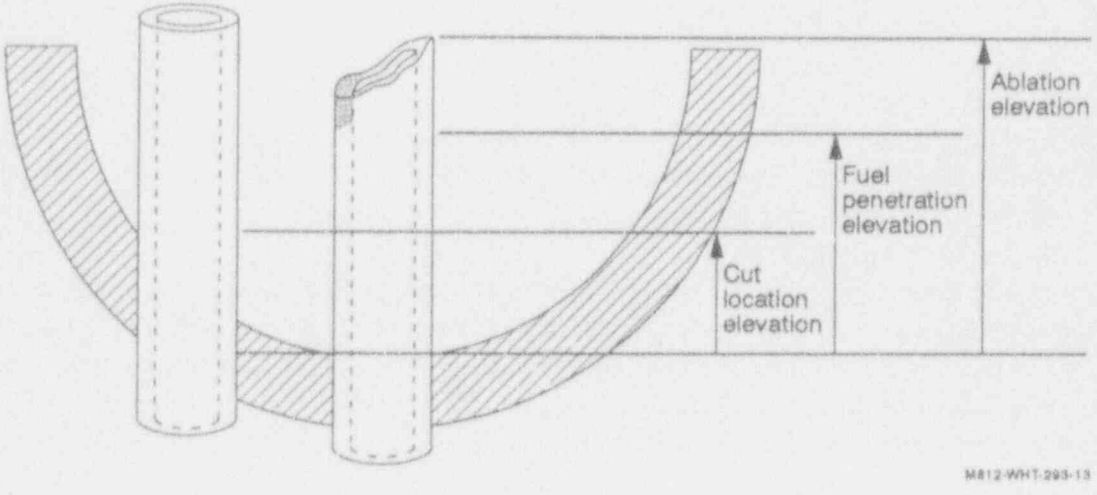

Figure B-1. Relative positioning of elevational data.

Nozzle E7
Examining Lab: INEL
Length: 1.3-1.6 cm
Comments: Nozzle was severely damaged. A crack extends through one wall of the nozzle. Due to the short length, a gamma scan was not performed. The instrument string was removed from the sample. No blockages were encountered with a wire probe test.

Nozzle E11
Examining Lab: ANL
Length: 22.5 cm
Elevation of nozzle at cut: 28.4 cm
Fuel penetration elevation in nozzle: 42.5 cm
Debris penetration elevation in instrument probe tube: 28.4 cm
Debris composition in instrument probe tube: ceramic and metallic
Nozzle ablation elevation: 52.3 cm
Comments: Undamaged nozzle was cut to allow access to vessel sample. Gamma scan for fuel depth showed a large concentration of fuel at the nozzle tip and a smaller amount inside the nozzle approximately 7.6 cm from the tip. The instrument string was loose but intact and was pulled out. The outer surface of the nozzle tip appeared thermally ablated by aluminum. Debris in the center of the nozzle consisted of fuel shards and oxidized instrument lead conduit. (Surface deposits appear non-adherent below the 27.2 cm elevation, indicating temperatures less than 1,273 K.)

Nozzle G5
Examining Lab: INEL
Length: 4.4 cm
Comments: The nozzle was heavily damaged and too short to be gamma scanned. A wire probe test indicated the nozzle was completely plugged with melt. There are insufficient data to determine if melt penetration ends above or below the cut.

Nozzle H5
Examining Lab: ANL
Length: 14.6 cm
Elevation of nozzle at cut: 10.7 cm
Fuel penetration elevation in nozzle: 22.4 cm min., 19.6 cm max.
Debris penetration elevation in instrument probe tube: 10.7 cm
Debris composition in instrument probe tube: ceramic and metallic
Nozzle ablation elevation: 25.3 cm
Comments: The nozzle was cut off flush with the vessel. About 15.9 cm was ablated from the top of the nozzle. A gamma scan for fuel depth was performed. Debris appeared to cover the outside tip of the nozzle. A slug of Inconel was present in the annulus, extending to the bottom of the nozzle. (Temperatures varied from 1,673 K at 36.6 cm elevation to less than 1,033 K at the bottom of the nozzle, 29.0 cm elevation).

Nozzle **H8**
Examining Lab: ANL
Length: 7.0 cm
Elevation of nozzle at cut: 5.1 cm
Fuel penetration elevation in nozzle: <6.4 cm
Debris penetration elevation in instrument probe tube: 5.1 cm
Debris composition in instrument probe tube: ceramic and metallic
Nozzle ablation elevation: 12.1 cm
Comments: Nozzle was approximately 15.2 cm long postaccident. About 5.1 cm was broken off during lower head defueling. After cutting the nozzle, the length was 7.0 cm. A gamma scan for fuel depth indicated fuel throughout the nozzle, with the highest concentration at the nozzle tip. Molten Inconel was found inside the nozzle within 1.3 cm of the bottom of the nozzle. The temperature of the Inconel was estimated to be approximately 1,223 K.

Nozzle **H9**
Examining Lab: INEL
Length: 24.1 cm
Comments: Nozzle sustained very little visual damage. The instrument string was still intact. Gamma scans show high fuel concentrations at two positions in the nozzle, 5.1 cm and 14.0 cm from the point where the nozzle was cut. Probe testing revealed no blockage.

Nozzle **K11**
Examining Lab: INEL
Length: 23.5 cm
Comments: Nozzle was badly damaged 7.6 to 20.3 cm above the vessel surface, with one-half the wall thickness melted away. This was the only nozzle where melt ablated the outside of the nozzle wall. The top 15.2 cm was leaning at an angle of 10-20 degrees. Gamma scans showed fuel over the entire length of the nozzle, but complete blockage was not encountered by a wire probe. MPR Associates reported that melt filled the cross sectional area of the remaining 5.1 cm nozzle stub in the vessel.[B-2]

Nozzle **K12**
Examining Lab: INEL
Length: 25.7 cm with instrument string, 24.4 cm without instrument string
Comments: This was a relatively undamaged nozzle, but gamma scans showed a high, steady concentration of fuel throughout the entire nozzle. No blockages were detected from a wire probe test.

Nozzle **L6**
Examining Lab: ANL
Length: 24.1 cm
Elevation of nozzle at cut: 15.7 cm
Fuel penetration elevation in nozzle: 16.9 cm
Debris penetration elevation in instrument probe tube: 15.7 cm
Debris composition in instrument probe tube: ceramic and metallic
Nozzle ablation elevation: 39.9 cm

Comments: The nozzle had minor damage to the upper 0.5 cm wall section. A gamma scan for fuel depth was performed. Control materials entered the nozzle prior to fuel. No significant axial temperature gradient was present in the nozzle.

Nozzle **L11**
Examining Lab: INEL
Length: 22.9 cm
Comments: This was a relatively undamaged nozzle except for a 5.1 cm region at the shoulder of the nozzle, extending 5.1 to 10.2 cm from the bottom end. A gamma scan showed high fuel activity present 7.6 cm from the base. No blockage of the nozzle was found from a probe test.

Nozzle **M9**
Examining Lab: ANL
Length: 25.4 cm
Elevation of nozzle at cut: 14.5 cm
Fuel penetration elevation in nozzle: 36.0 cm
Debris penetration elevation in instrument probe tube: 33.0 cm
Debris composition in instrument probe tube: ceramic and metallic
Nozzle ablation elevation: 39.9 cm
Comments: There was minor damage to the top of nozzle, believed to be caused by molten fuel as opposed to a solid crust of fuel. A gamma scan for fuel depth showed fuel only in the top 5.1 cm of nozzle.

Nozzle **M10**
Examining Lab: INEL
Length: 16.2 cm
Comments: There was severe melt damage to the top 6.4 cm of the nozzle. The upper portion of the nozzle appears to have been melted. A gamma scan showed higher concentration of fuel near the base end of the nozzle than at the tip. Wire probe tests indicated melt plugged the nozzle to within 5.7 cm of the bottom end.

Nozzle **R7**
Examining Lab: INEL
Length: 23.2 cm
Comments: Fuel adhered to the top of the nozzle and protruded approximately 2.5 cm above the nozzle. The instrument string was partially molten at the top end. A gamma scan showed high fuel concentration at the tip of the nozzle, with a smaller concentration halfway down the nozzle. No blockages were determined from a wire probe test.

B.2 Derivation of Modified Bulk-Freezing Model Equations

The derivation begins with a heat balance on the debris,

$$m_d c_{pd}(T_d - T_{mp}) + m_d L_d = h_{id} A_{id}(T_d - T_i) t_{sol} + h_{wd} A_{wd}(T_d - T_c) t_{sol} \quad . \tag{B-1}$$

The heat transfer coefficient between the debris and the coolant can be replaced by terms accounting for the energy change of the coolant, derived from a separate heat balance around the coolant in azimuthal contact with the debris. The heat balance is dependent upon the coolant state. For example, assume the coolant is saturated liquid at the time the debris solidifies, then

$$h_{wd} A_{wd}(T_d - T_c) t_{sol} = m_{sat_l} c_{p_l}(T_{sat} - T_i) \quad . \tag{B-2}$$

Substituting this expression into Equation (B-1),

$$m_d \left\{ c_{pd}(T_d - T_{mp}) + L_d \right\} = h_{id} A_{id}(T_d - T_i) t_{sol} + m_{sat_l} c_{p_l}(T_{sat} - T_i) \quad . \tag{B-3}$$

In the above equations, t_{sol} is the time required for debris of length x_p to solidify while traveling at a constant velocity v_d, such that $t_{sol} = x_p / v_d$. The mass of debris and coolant are given as

$$m_d = \rho_d x \frac{\pi}{4} d_e^2 x_p \tag{B-4}$$

$$m_{sat_l} = \rho_{sat_l}(1 - x) \frac{\pi}{4} d_e^2 x_p \tag{B-5}$$

where x is the fraction of the effective cross-sectional area covered by debris. The A_{id} in the heat transfer coefficient term is the circumferential contact area between the debris and the nozzle wall,

$$A_{id} = x \pi (d_i + d_{so}) x_p \quad . \tag{B-6}$$

Substituting Equations (B-4) through (B-6), the heat balance, Equation (B-3), becomes

$$\rho_d x \frac{\pi}{4} d_e^2 x_p \left\{ c_{pd}(T_d - T_{mp}) + L_d \right\} = h_{id} x \pi (d_i + d_{so}) x_p (T_d - T_i) \frac{x_p}{v_d} + \rho_{sat_l}(1 - x) \frac{\pi}{4} d_e^2 x_p c_{pl}(T_{sat} - T_i) \quad . \tag{B-7}$$

After simplification and rearrangement, the dimensionless penetration distance is

$$\frac{x_p}{(d_i - d_{so})} = \frac{.25\nu_d}{h_{id}(T_d - T_i)}\left[\rho_d\left\{c_{pd}(T_d - T_{mp}) + L_d\right\} - \left(\frac{1}{x} - 1\right)\rho_{sat_l}c_{pl}(T_{sat} - T_i)\right] \quad . \tag{B-8}$$

The definition of the effective diameter, $d_e^2 = d_i^2 - d_{so}^2$, was used in the simplification. The heat transfer coefficient may be replaced by a Nusselt number correlation. A Nusselt number correlation for liquid metals in concentric annuli[B-2] was used. The correlation is

$$Nu = 5.25 + 0.0188\ Pe^{0.8}\left(\frac{d_i}{d_{so}}\right)^{0.3} \quad . \tag{B-9}$$

The Peclet number in Equation (B-9) is defined as

$$Pe = \frac{d_e \nu_d \rho_d c_{pd}}{k_d} \quad . \tag{B-10}$$

Inserting Equation (B-9), the dimensionless distance for debris in contact with saturated coolant becomes

$$\frac{x_p}{(d_i - d_{so})} = .25Pe\ \frac{\left[\rho_d\left\{c_{pd}(T_d - T_{mp}) + L_d\right\} - \left(\frac{1}{x} - 1\right)\left\{\rho_{sat_l}c_{pl}(T_{sat} - T_i)\right\}\right]}{\rho_d c_{pd}(T_d - T_i)\left(5.25 + 0.0188\ Pe^{0.8}\left(\frac{d_i}{d_{so}}\right)^{0.3}\right)} \quad . \tag{B-11}$$

As observed from Equation (B-11), several variations of the modified bulk-freezing equation are possible. The form of the equation depends upon the Nusselt number correlation and the final coolant conditions. Equations incorporating Nusselt numbers for annular nozzles will be presented. Two cases of coolant state are implemented. At the time of solidification, the coolant in radial contact with the debris is modeled as either subcooled liquid or saturated liquid. If the coolant remains subcooled, but at a temperature above the initial temperature, the penetration distance is

$$x_p = 0.25Pe(d_i - d_{so})\frac{\left[\rho_d\left\{c_{pd}(T_d - T_{mp}) + L_d\right\} - \left(\frac{1}{x} - 1\right)\rho_{sub}c_{pl}(T_{sub} - T_i)\right]}{\rho_d c_{pd}(T_d - T_i)\left(5.25 + 0.0188\ Pe^{0.8}\left(\frac{d_i}{d_{so}}\right)^{0.3}\right)} \tag{B-12}$$

For the case in which the coolant in contact with the debris becomes saturated liquid, the relation is

$$x_p = 0.25\ Pe(d_i - d_{so})\frac{\left[\rho_d\left\{c_{pd}(T_d - T_{mp}) + L_d\right\} - \left(\frac{1}{x} - 1\right)\left\{\rho_{satf}c_{pf}(T_{sat} - T_i)\right\}\right]}{\rho_d f_{pd}(T_d - T_i)\left(5.25 + 0.0188\ Pe^{0.8}\left(\frac{d_i}{d_{so}}\right)^{0.3}\right)} \quad \text{(B-13)}$$

For the case in which no coolant is present and the debris fills the nozzle, a heat balance yields

$$x_p = 0.25\ Pe(d_i - d_{so})\frac{\left[(T_d - T_{mp}) + L_d/c_{pd}\right]}{(T_d - T_i)\left(5.25 + 0.0188\ Pe^{0.8}\left(\frac{d_i}{d_{so}}\right)^{0.3}\right)} \quad \text{(B-14)}$$

One of the six nozzles examined at ANL was found to contain debris in a ring formation around the inside of the nozzle wall. The above equations were modified for this variation in shape and are presented below for the specific case of saturated coolant. The equation for the case of subcooled liquid can be discerned from the equation above. For this debris shape, a more general equation may be written where any thickness of the debris can be input:

$$x_p = \frac{0.25\ Pe}{\rho_d f_{pd} d_i(T_d - T_i)\left(5.25 + 0.0188\ Pe^{0.8}\left(\frac{d_i}{d_{so}}\right)^{0.3}\right)} \cdot \frac{}{\left[\rho_d(d_i^2 - d_d^2)\left\{c_{pd}(T_d - T_{mp}) + L_d\right\} - (d_d^2 - d_{so}^2)(1/x - 1)\left\{\rho_{satf}c_{pf}(T_{sat} - T_i)\right\}\right]} \quad \text{(B-15)}$$

B.3 References

B-1. MPR Associates, Inc., *Removal of Test Specimens from the TMI-2 Reactor Vessel Bottom Head*, MPR-1195, October 1, 1990.

B-2. N.E. Todreas and M.S. Kazimi, *Nuclear Systems I: Thermal Hydraulic Fundamentals*, New York: Hemisphere Publishing Corp, 1990.

Appendix C

TMI Model Description

Appendix C

TMI Model Description

C.1 TMI Model Description

Heat transfer to the pressure vessel is modelled using an overall heat transfer coefficient, which is obtained by assuming that the energy transferred through the crust equals the energy transferred to the pressure vessel. The heat transfer coefficient through the crust, h_{crust} is given by a value which represents steady state conduction through the crust thickness, δ_{crust}.[a]

$$h_{crust} = \frac{k_{crust}}{\delta_{crust}} \quad . \tag{C-1}$$

The pressure vessel heat transfer coefficient, h_{pv}, is given by the maximum of the following two values.

$$h_{pv} = MAX \left[\frac{k_v}{\sqrt{\pi \alpha_v t}} \; or \; \frac{k_v}{t_v / 2.0} \right] \quad . \tag{C-2}$$

An overall heat transfer coefficient, U_{down} which represents heat transfer to the pressure vessel is therefore given by

$$\frac{1}{U_{down}} = \frac{1}{h_{crust}} + \frac{1}{h_{pv}} + \frac{1}{h_{int}} \quad . \tag{C-3}$$

Note that an interfacial heat transfer coefficient, h_{int}, is included in the overall heat transfer coefficient to account for the interfacial thermal resistance that may be present due to surface roughness between the crust and the vessel. Using the method suggested by Garnier,[C-1] values for the gap resistance between the vessel and crust were estimated to range from 150 to 10,000W/m^{2}K.

The heat fluxes to the fuel crust surface next to the pressure vessel at short times (~1 minute) are dominated by the impinging jet, while at long times the heat fluxes are controlled by natural convection due to internal heat generation in the melt pool. Heat transfer coefficients due to the jet, h_{din}, for the impingement region and the laminar boundary layer region around it are exponentially reduced to the coefficients resulting from internal natural convection over a

---

a. A complete list of variables is found in the Nomenclature

time period that is longer than the time it takes the jet to drain, t_{drain}. This relationship is shown below.

Stagnation Region:

$$h_{din} = h_{dc} + \exp\left[\frac{-t}{t_{drain} / 8}\right]\left[\frac{Nu_{stag}k_{jet}}{D_{jet}} - h_{dc}\right] \quad . \tag{C-4}$$

Laminar Boundary Layer Region:

$$h_{din} = h_{dc} + \exp\left[\frac{-t}{t_{drain} / 8}\right]\left[\frac{Nu(r)k_{jet}}{D_{jet}} - h_{dc}\right] \quad . \tag{C-5}$$

The Nusselt number for the jet stagnation region and for the laminar boundary layer region were modeled based on simulated experiments[C-2] and analysis[C-3] of the impingement of liquid jets on a wall with possible simultaneous melting and freezing. The complete formulations are provided in Reference C-4.

The transition from jet impingement stagnation heat transfer to the natural convection regime assumes that there is no substantial period over which the melt pool would be completely stagnant. This assumption is based upon the assumptions: (a) that most of the melt arrives in a molten state, and (b) that the characteristic time for the onset of natural convection is short compared to the time of interest (several hours). The first assumption is based upon TEXAS calculational results discussed in Section 3.2. The second assumption is based on results from dimensional analyses, which indicate that the timescale for the onset of natural convection is much less than one hour.[C-4]

Internal heat generation resulting from fission products causes some of the pool to remain molten and can cause significant internal natural convection. The only appropriate correlation for the heat transfer coefficient to the lower crust, h_{dc}, for a hemispheric molten zone with internal heat generation, Q_{hg}, was found from the work of Jahn and Reineke:[C-5]

$$h_{dc} = f(\varphi)0.54Ra^{0.18}\frac{k_p}{R_m} \tag{C-6}$$

where

$$Ra = \frac{g\beta_p Q_{hg} R_m^5}{\alpha_{tp}\nu_p k_p} \tag{C-7}$$

while

$$R_m = \frac{R_{crust} + h}{2} \tag{C-8}$$

and

$$\begin{aligned} f(\varphi) &= 0.2 && \text{if } \varphi < 20 \text{ degrees} \\ f(\varphi) &= 0.2 + 1.8\frac{\varphi - 20}{55} && \text{if } 20 < \varphi < 75 \text{ degrees} \\ f(\varphi) &= 2.0 && \text{if } \varphi > 75 \text{ degrees} \end{aligned} \tag{C-9}$$

The variation of the heat flux as a function of the angle, φ, is given by the experimental and theoretical work done by Jahn and Reineke.[C-5] (See Figure C-1 for the definitions of φ, R_{crust}, and h.)

The overall heat transfer coefficient for heat transferred from the pressure vessel to its surroundings is represented by a heat transfer coefficient through the outer half of the pressure vessel thickness, h_{cond}, and a heat transfer coefficient on the outside of the pressure vessel, h_{pvo}. The heat transfer coefficient through the half thickness of the pressure vessel is represented by

$$h_{cond} = \frac{k_{pv}}{t_v / 2.0} \tag{C-10}$$

and the overall heat transfer coefficient representing heat transfer to the surroundings is given by

$$\frac{1}{U_{out}} = \frac{1}{h_{cond}} + \frac{1}{h_{pvo}} \quad . \tag{C-11}$$

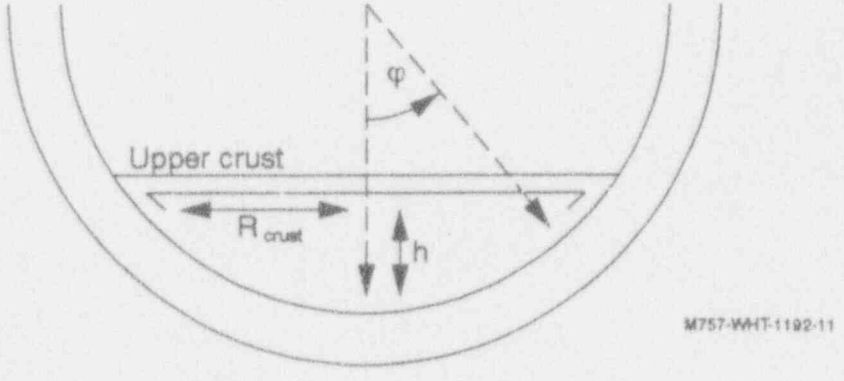

Figure C-1. Definition of geometrical parameters for estimating convective heat transfer from a molten pool.[C-5]

Now that the heat transfer aspects surrounding the lower crust are defined, an energy balance can be written which determines the growth of the crust:

$$\rho_{crust} L_{crust} A_{dcrust} \frac{d\delta_{dcrust}}{dt} = U_{down} A_{pvi} \left(T_{mp,p} - T_{wall} \right) - h_{dirt} A_{dcrust} \left(T_p - T_{mp,p} \right) - q''' V_{dcrust} \quad . \tag{C-12}$$

This balance is done for each control volume section of the pressure vessel, therefore allowing for variable lower crust thickness. A major assumption in this energy balance for the crust is that the change in sensible heat of the crust during its growth is small compared to the latent heat released during its growth; i.e., $L_{crust} >> c_{pd}$, where L_{crust} is the latent heat of fusion, and $c_p \Delta T$ is the change in the average crust thermal energy over the time period of interest. For calculations in Section 3.2, this inequality holds, and the assumption is reasonable.

For the upper energy loss, the heat transferred from the upper surface of the melt pool to the saturated water (584 K, 10 MPa) is now examined. Film boiling and radiation are the initial heat transfer modes expected. This is based on the fact that the interface temperature is above the critical temperature of water and nucleate boiling would not occur in such a circumstance. Total heat flux up from the pool is determined by an overall energy balance based on two-phase flow [C-6, C-7, C-8] and is given by

$$q''_{fbf} = q''_{fb,sub} + 0.75 q''_{r} \quad . \tag{C-13}$$

The film boiling heat transfer from the upper surface of the melt pool while the jet is still draining is given by the correlation[C-8]

$$q''_{fb} = 0.425 \left[\frac{g(\rho_f - \rho_g)\rho_g k_g^3 h_{fg}}{\mu_g \left[\frac{\sigma_f}{g(\rho_f - \rho_g)} \right]^{0.5}} \right]^{0.25} \left(T_p - T_{sat} \right)^{0.75} \tag{C-14a}$$

$$q''_{fb,sub} = q''_{fb} \left[1.0 + 0.98 \frac{\left(T_{sat} - T_{bulk} \right)^4}{\left(T_p - T_{sat} \right)^4} \right]^{0.25} \quad . \tag{C-14b}$$

The heat transfer to the water due to radiation is given by

$$q''_{r} = \sigma_{sb} \varepsilon_{crust} \left[T_p^4 - T_{bulk}^4 \right] \quad . \tag{C-15}$$

An emissivity of 0.8 was assumed for the debris crust based on known properties. These correlations are used directly for the heat transfer from the melt pool until the jet stops draining, at which time it is assumed that a stable crust can form on the surface of the melt pool. Once the crust forms, an overall heat transfer coefficient representing the heat transfer to the water

must be obtained. Again, the overall heat transfer coefficient can be used because it is assumed that the heat transfer through the crust is equal to the heat transferred into the coolant. Noting from Equation C-1 that the heat transfer coefficient through the crust is given by

$$h_{crust} = \frac{k_{crust}}{\delta_{crust}} \tag{C-16}$$

while the heat transfer coefficient for film boiling and radiation from the crust to the water is given by

$$h_{fb,r} = \frac{q''_{fb,r}}{T_{int} - T_{sat}} \tag{C-17}$$

where $q''_{fb,r}$ is calculated using Equation C-13 with T_p replaced by T_{int}, the interface temperature at the upper surface of the crust. The overall heat transfer coefficient from the pool to the water is a combination of the heat transfer through the crust and the heat transfer coefficient from the crust to the water:

$$\frac{1}{U_{up}} = \frac{1}{h_{crust}} = \frac{1}{h_{fb,r}} \quad . \tag{C-18}$$

As the upper crust thickens and the interface temperature decreases, it is expected that film boiling will cease. Experience indicates that the minimum film boiling point would occur at this critical temperature (647 K), and eventually nucleate boiling will occur on the upper crust surface. In order to be consistent (i.e., keep the heat flux through the crust equal to that removed from the crust), the interface temperature was calculated by equating the heat flux through the crust and the heat flux given by nucleate boiling, q''_{NB}

$$q''_{NB} = \frac{\mu_f h_{fg}}{0.014^{3.03}} \frac{1.0}{\sqrt{\frac{\sigma_f}{g(\rho_f - \rho_g)}}} \left[\frac{c_{pf}(T_p - T_{sat})}{h_{fg} Pr_f^{1.7}} \right]^{3.03} \tag{C-19}$$

with T_p replaced by the interface temperature. This modeling approach results in the instantaneous removal of energy from the upper crust resulting in a steeper temperature gradient in the crust. The heat flux increases correspondingly to the representative heat flux given by the nucleate boiling correlation. As the interface temperature continues to decrease, the heat transfer due to natural convection becomes important. Therefore, the heat flux is now given by

$$q''_{t} = q''_{NB} + q''_{NC} - q''_{ONB} \tag{C-20}$$

where q''_{ONB} is the heat flux at the onset of nucleate boiling (negligible) and the heat flux due to natural convection q''_{NC} is given by Collier:[C-6]

$$q''_{NC} = \left[\frac{g\rho_f^3 c_{pf}\beta}{\mu k_f}\right]^{0.33} 0.14 k_f \left[T_{int} - T_{sat}\right]^{4/3} \quad . \tag{C-21}$$

The heat transfer to the upper crust from the molten pool due to convection from internal heat generation is given by[C-5]

$$h_{uc} = 0.36 Ra^{0.23} \frac{k_p}{R_m} \tag{C-22}$$

where the above variables were defined during the discussion of the heat transfer to the lower crust.

The energy balance to determine the growth of the upper crust is very similar to that of the lower crust:

$$\rho_{ucrust} L_{ucrust} A_{ucrust} \frac{d\delta_{ucrust}}{dt} = U_{up} A_{top}\left(T_{mp,p} - T_{bulk}\right) - h_{uc} A_{ucrust}\left(T_p - T_{mp,p}\right) - q''' V_{ucrust} \quad . \tag{C-23}$$

As noted above in the discussion about the energy balance for the lower curst [Equation (C-12)], these energy balances assume that the change in sensible heat of the crust during its growth is small compared to the latent heat released during its growth.

In order to put the model together, an energy balance centered around the heat in and out of the melt pool is used. Two different balances are needed, the following energy balance is applied while the jet is still draining,

$$\Delta T_p M_p c_p = \dot{m} c_{jet}\left(T_{jet} - T_p\right)\Delta t + q''' \frac{M_p}{\rho_p}\Delta t - h_{dirt} A_{dcrust}\left(T_p - T_{mp,p}\right)\Delta t - h_{uc} A_{ucrust}\left(T_p - T_{mp,p}\right)\Delta t \tag{C-24}$$

while this balance is applied after the jet has ended:

$$\Delta T_p M_p c_p = q''' \frac{M_p}{\rho_p} \Delta t - h_{dir} A_{dcrust} \left(T_p - T_{mp,p}\right) \Delta t - h_{uc} A_{ucrust} \left(T_p - T_{mp,p}\right) \Delta t \quad . \tag{C-25}$$

The temperatures in the pressure vessel are incremented appropriately according to the equation

$$\Delta T_v M_v c_{pv} = U_{down} A_{pvi} \left(T_{mp,p} - T_{wall}\right) \Delta t - U_{out} A_{pvo} \left(T_{wall} - T_{bulk}\right) \Delta t \quad . \tag{C-26}$$

One should remember that this energy balance follows the average temperature of the vessel wall, T_v, as it changes with time due to heat flow in from the melt pool and heat flow out to the ambient. The continuity of heat fluxes at the inner and outer vessel surfaces were then used to determine the through-wall vessel temperatures, such as shown in Figures 3-14(a) and 3-15(a).

Other aspects of the TMI model that should be mentioned are the effect of the freezing temperature range on the solid fraction and, consequently, its effect on the viscosity of the molten pool and the effect of the porosity on the thermal conductivity of the crust. When the temperature of the melt pool falls below the liquidus temperature of the debris (2,850 K), the solid fraction in the molten pool will become a factor in the analysis. The solid fraction to temperature relationship in the freezing range has been taken to be linear. That is, at 2,850 K, the solid fraction of the melt pool is equal to zero; at 2,750 K, the solid fraction is equal to 0.5; and at 2,650 K (i.e., the solidus temperature), the solid fraction is equal to 1.0. The viscosity change due to the increase in solid fraction is important, as it plays a role when calculating the Ra number for the heat fluxes due to internal heat generation. The relationship between solid fraction, X_s, viscosity of the pool, μ_p, and viscosity of the jet, μ_{jet}, is shown below:[C-9]

$$\mu_p = \mu_{jet} 1.5 \left[\frac{1 - 1/3\left(1 - X_s\right)}{\left(1 - X_s\right)^4} \right] \quad . \tag{C-27}$$

The porosity in the crust will decrease the thermal conductivity. The relationship between porosity, P_{crust}, and thermal conductivity of a solid with and without porosity, k_{por}, and k_s, respectively, was obtained from Olander[C-10]

$$\frac{k_{por}}{k_s} = \frac{1 - P_{crust}}{1 + \left(\alpha_{sf} - 1\right) P_{crust}} \tag{C-28}$$

where α_{sf} is the shape factor equal to 1.5 for equal size spherical pores.

Heat transfer from the vessel at temperature, T_v, to the containment at temperature, T_a, is modeled using a heat transfer coefficient, h_{pvo}, that considers losses via natural convection and radiation (i.e., $h_{pvo} = h_{conv} + h_{rad}$). The convective component of this coefficient, h_{conv}, was estimated to range from 6 to 30 W/m^{2}K, based upon typical values cited in Reference C-11 for

natural convection. The radiative component, h_{rad}, was calculated to range from 20 to 65 W/m^{2}K using the following equation:[C-12]

$$h_{rad} = \frac{\sigma_{sb}\, \varepsilon_{ves} \left(T_v^4 - T_a^4\right)}{T_v - T_a} \quad . \tag{C-29}$$

Hence, the heat transfer coefficient on the outer surface of the vessel is estimated to range from 30 to 100 W/m^{2}K.

C.2 References

C-1. J. Garnier, *Ex-Reactor Determination of Thermal and Contact Conductance*, NUREG/CR-0330, April 1979.

C-2. M. Epstein et. al., "Simultaneous Melting and Freezing in the Impingement Region of a Liquid Jet," *AIChE Journal, 26*, September 1980, p. 743.

C-3. X. Liu, J. H. Lienhard, and J. S. Lombara, "Convective Heat Transfer for Impingement of Circular Liquid Jets," *Journal of Heat Transfer, 113*, 1991, p. 571.

C-4. J. A. Kos, *Model of Fuel-Melt Quenching in the Lower Plenum of the RPV,* Master of Science thesis, University of Wisconsin, Madison, Wisconsin, August 1992.

C-5. M. Jahn, and H. H. Reineke, "Free Convection Heat Transfer with Internal Heat Sources Calculations and Measurements," *Proceedings of the Fifth International Heat Transfer Conference, Tokyo, Japan, 3*, Paper NC2.8, 1974, pp. 74-78.

C-6. J. G. Collier, *Convective Boiling Condensation,* New York: McGraw-Hill, 1972.

C-7. V. J. Dhir, and G. P. Purohit, "Subcooled Film-Boiling Heat Transfer from Sphere," *Nuclear Engineering and Design, 47*, 1978, p. 49.

C-8. J. G. Collier, *Convective Boiling Condensation,* Chapter 4, New York: McGraw-Hill, 1972.

C-9. M. Epstein, and H. K. Fauske, "Steam Film Instability and the Mixing of Core Melt Jets and Water," *American Nuclear Society Proceedings of the National Heat Transfer Conference, Denver, Colorado, August 4-7, 1985* p. 277.

C-10. D. R. Olander, *Fundamental Aspects of Nuclear Reactor Fuel Elements,* University of California-Berkeley, published by the Technical Information Center Energy Research and Development Administration, (TID-26711-P1), November 1977.

C-11. Todreas, N. E. and M. S. Kazimi, *Nuclear Systems I--Thermal Hydraulic Fundamentals,* New York: Hemisphere Publishing, 1990.

C-12. Welty, J. R., C. E. Wicks, and R. E. Wilson, *Fundamentals of Momentum, Heat and Mass Transfer,* New York: Y. Wiley & Sons, 1976.

Appendix D

Best Estimate Calculations for Tube Weld Failure

Appendix D

Best Estimate Calculations for Tube Weld Failure

LOADS

Pressure loads, F_p

$OD = 0.0254\ m\ (1.0\ in)$ [D-1]
$P = 15E6\ Pa$ [D-2]

where OD is the outer diameter of the instrument tube and P is the system pressure.

$F_p = (15E6\ Pa)(\pi/4)(0.0254m)^2 = 7601\ N$

Deadweight loads, F_d

$ID = 0.01554\ m$ [D-1]
$OD = 0.0254\ m$ [D-1]
$L_t = 5.47\ m$ [D-3,a]
$\rho = 8400\ kg/m^3$

where ID is the inner diameter, OD is the outer diameter, L is the length of the instrument tube to the nearest unistrut support, and ρ is the density of Inconel-600.

$F_d = (5.47\ m)(p/4)[(0.0254\ m)^2 - (0.01554\ m)^2](8400\ kg/m^3)(9.8\ m/s^2)$
$F_d = 143\ N$

Total force on weld, F_{total}

$F_{total} = F_p + F_d = 7744\ N$

SHEAR AREA OF THE WELD, A_S

$OD = 0.0254\ m$
$L_w = 0.01365\ m$ [b]

where OD is the outer diameter of the instrument tube and L_w is the length of the weld below the vessel cladding.

$A_s = \pi(0.0254\ m)(0.01365\ m) = 1.089E\text{-}3\ m^2$

---

a. Personal communication with Babcock & Wilcox personnel, September 1992.

b. Babcock & Wilcox drawing # 126971E6, October 1991.

APPLIED SHEAR STRESS τ AND EFFECTIVE STRESS, σ_{vm}

$\tau = F_{total}/A_s = (7744\ N)/(1.089E\text{-}3\ m^2) = 7.11E6\ Pa$

$\sigma_{vm} = 1.732\tau = 12.32E6\ Pa\ (1.786\ ksi)$

ULTIMATE STRENGTH MARGIN TO FAILURE, MF

$MF = 1 - \sigma_{vm}/S_u = 1 - 12.32E6/30.78E6 = 0.60 = 60\%$

where σ_{vm} is the von Mises effective stress, and S_u is the ultimate strength (30.78 MPa) of Inconel-600 at 1,348 K (2,450°R) obtained from high temperature tensile tests.[D-4]

Note: At 1,348 K, S_u is 35 MPa; at 1,373 K, S_u is 27 MPa.

TIME TO CREEP FAILURE USING LARSON-MILLER PARAMETER, t_r

$LMP = 36.196 - 8.9433[\log(\sigma_{vm})]$
$\log(t_r) = (LMP)(1000)/T - 13$

where LMP is the Larson-Miller parameter, σ_{vm} is the effective stress (in ksi), and T is the temperature (°R). These equations are fit from high temperature creep rupture experiments.[D-4]

$LMP = 36.196 - 8.9433[\log(1.786\ ksi)] = 33.943$
$\log(t_r) = (33.943)(1000)/(2450°R) - 13$
$t_r = 7.2\ h$

95% CERTAINTY LIMITS FOR LARSON-MILLER PARAMETER

$LMP(95\%) = LMP \pm 2.069SD$

$SD = 0.42691\ [0.90909 + \{\log(\sigma_{vm}) - 0.86372\}^2/1.09944]^{0.5}$

where σ_{vm} is the Mises effective stress (in ksi).[D-4,D-5]

D.1 References

D-1. MPR Associates, Inc., *Removal of Test Specimens from the TMI-2 Reactor Vessel Bottom Head,* MPR-1195, October 1, 1990, Drawing No. F-73-30-328, July 24, 1990.

D-2. G. L. Thinnes, *TMI-2 Lower Head Creep Rupture Analysis*, EGG-TMI-8133, August, 1988, p. 10.

D-3. MPR Associates, Inc., *Removal of Test Specimens from the TMI-2 Reactor Vessel Bottom Head,* MPR-1195, October 1, 1990, Drawing No. F-80-107-89 July 22, 1988.

D-4. J. L. Rempe, et al., *Light Water Reactor Lower Head Failure Analysis* NUREG/CR-5642, EGG-2618, October 1993.

D-5. N. R. Draper and H. Smith, *Applied Regression Analysis*, second edition, New York: John Wiley & Sons, Inc., 1981, pp. 20-29.

Appendix E

Results from Verification Calculations for Localized Effects Model

Appendix E

Results from Verification Calculations for Localized Effects Model

E.1 Summary

The verification of the shell model (TSM) used to evaluate the potential for localized vessel failure has provided several insights into the applicability of this program for use in lower head severe accident structural response calculations. First of all, it must be remembered that the purpose for developing this program was to provide a fast-running solution to predict the collapse of a localized portion of the vessel wall, resulting from hot spots in a debris bed resting on the lower head. Thus, the program would be appropriate for scoping parameter studies in various accident scenarios. Results of the benchmark problems used in this verification effort indicate that TSM performs well for its intended purpose.

TSM was benchmarked against an ABAQUS[E-1] axisymmetric solid finite element model using two hot spot load cases. One load case consisted of a moderate thermal gradient in the hot spot region and an internal pressure of 45 MPa, and the second case represented a more severe temperature gradient in the hot spot region and an applied pressure of 55 MPa. These pressures were selected to enhance plastic deformation through the thickness of the wall and are several times greater than the 15.5 MPa expected in reactor operations. The choice of these pressures did help to identify a portion of the disagreement between ABAQUS and TSM.

In the cooler boundary areas of the hot spot and the cooler portion of the vessel wall under the hot spot, which was basically that portion outside the vessel midsurface, hoop and meridional stresses were within 4% of the ABAQUS model results. TSM generally underpredicted the strains in both of these benchmark hot spot cases. Because TSM is based on shell model assumptions, which neglect radial stresses through the vessel wall, it underpredicted stresses and strains in the hoop and meridional components in the very hottest areas of the model. This was because the vessel material was relatively soft in these areas at the load case temperatures and the radial stresses, as calculated in the ABAQUS model, were of the same order as the hoop and meridional stresses. Thus, the Poisson effect from the radial stresses would significantly affect the hoop and meridional components. TSM underpredicted hoop and meridional stresses by as much as 60% in these hottest areas, where the stresses were typically two orders of magnitude lower than the peak values on the shell outer surface. Total strain comparisons ranged from underpredictions of 24% on the inside surface to 11% on the outside surface in the hot spot region for the severe thermal gradient load case. In the cooler boundary areas strain comparisons ranged from underpredictions of 13% on the inner surface to 7% on the outer surface. Examinations of the plastic strains indicated that plasticity of the wall had propagated from the outside inward one Gauss point further in the ABAQUS model than in the TSM model for the two hot spot load cases.

It should be noted, however, that the cooler outer portions of the vessel wall carry the majority of the pressure load in these cases and that vessel wall material yielding eventually begins at the

outer surface and propagates inward to final failure. Hoop and meridian stress levels are typically 35 times higher in the outer portions than the inner regions of the vessel wall. Thus, model accuracy in these high stress areas is most crucial to accurate predictions of vessel failure margins.

The benchmark thermal load cases included a maximum internal pressure of 45 to 55 MPa, while an accident condition would result in maximum pressures no greater than around 15 MPa. Therefore, additional cases were examined where the thermal loadings of both hot spot load cases were applied to TSM and ABAQUS models with an internal pressure load of 15 MPa. For the moderate thermal load case, TSM calculated stresses in the inside third of the wall 13% lower than those of ABAQUS, while the remaining portion of the wall was within 3%. The severe thermal load case stresses were an average of 4% lower than the ABAQUS model results throughout the wall. Total meridian and hoop strains ranged from underpredictions of 16% on the inside to 2% on the outside portions of the vessel wall in the hot spot region and within 5% in areas away from the hot spot. This represents a substantially better agreement than the same thermal conditions at elevated pressures and indicates TSM assumption of negligible radial stress is acceptable for loading histories representative of accident conditions.

E.2 Introduction

Verification calculations were undertaken to compare results from the localized creep rupture model, described in Section 4.2.2 and Appendix D of Reference E-2, and a finite element model developed with the ABAQUS code.[E-1] As described in Reference E-2, Section 4.2.2 and Appendix D, the localized creep rupture model, which was developed at the University of Wisconsin, Madison, is a finite difference shell theory model. Several benchmark problems have been performed to compare results from TSM (see Figure E-1) and the ABAQUS finite element code, which used an axisymmetric continuum model (see Figure E-2). The remainder of this appendix is divided up as follows: Section E-3 details the four benchmark problems, Section E-4 describes TSM and ABAQUS models, Section E-5 discusses the results from the first two (spherically symmetric) benchmark problems, Section E-6 includes the results from the remaining two (localized thermal loading) benchmark problems, and Section E-7 gives conclusions. Variables used in this section are defined in the Nomenclature.

E.3 Description of Benchmark Problems and Material Properties

Four benchmark problems were suggested[a] as verification calculations for TSM. The suggested problems were refined during the analysis to reach required final states; specifically, the relative contributions of thermal and pressure loadings were modified to achieve plasticity one-quarter of the way through the thickness at some location along the shell. The purpose of the problems was to determine the ability of TSM to accurately resolve the spatial variation of displacement, stress, and strain fields in the vicinity of a localized thermal loading (hot spot). None of the problems included creep in the material response; creep introduces complexities in the material model and

a. Professor R. H. Dodds, member of the TMI-2 Structural Mechanics Peer Review Group, University of Illinois at Champaign-Urbana, letter to S. A. Chávez, INEL, regarding benchmarking calculations of model for predicting localized rupture (Consulting Agreement 94-160236-HRS-284-92), July 20, 1992.

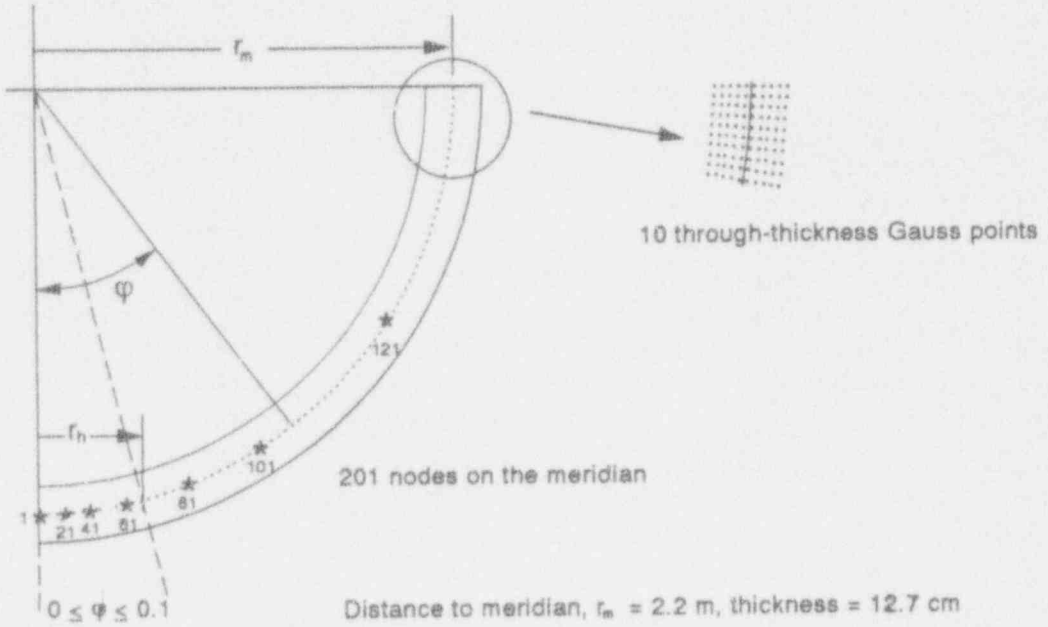

Figure E-1. The shell model (TSM).

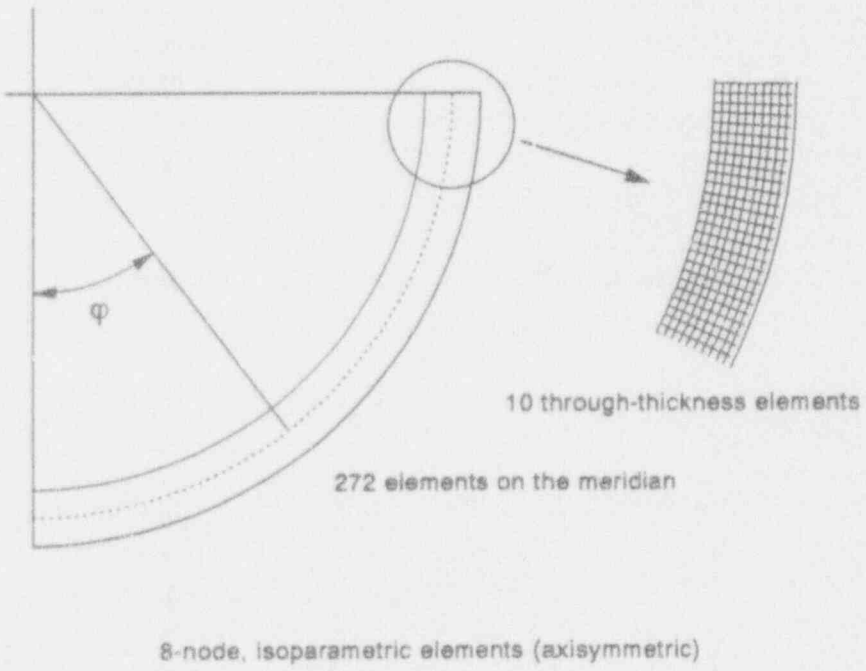

Figure E-2. ABAQUS model.

global solution algorithms but not in the ability to represent the spatial variation of the computed fields. The four problems considered were:

1. **Internal Pressure Only**: This problem tested the elastic response of TSM by ramping an internal pressure load to 10 MPa while employing material properties at 300 K. The problem was essentially one-dimensional with no variation along the meridian. This problem is shown as Case I in Figure E-3.

2. **Internal Pressure, Background Temperature**: This problem tested the elastic-plastic response by employing an internal pressure and a background temperature profile. The response was one-dimensional. The desired final state must show plasticity penetrating one-quarter of the wall. The problem was run by taking the initial state as 0 MPa internal pressure, and inside and outside surface temperatures (T_{in}, T_{out}) at 300 K. The subsequent state of 10 MPa, T_{in} at 900 K and T_{out} at 700 K (and a linear temperature gradient through-thickness) was reached by linearly ramping both pressure and temperature. This second state corresponded to the background state for Problems 3 and 4. At this point, yielding initiated at the outer surface of the shell in TSM. Continued ramping of both temperatures and pressure to reach the desired final state was found to be unacceptable because of the progressive softening of the shell at elevated temperatures (above 1,000 K). The desired final state was reached by ramping the pressure to 35 MPa while holding T_{in} and T_{out} at 900 and 700 K, respectively. This problem is shown as Case II in Figure E-3.

3. **Internal Pressure, Moderate Localized Thermal Loading**: This problem tested the elastic-plastic response by employing a moderate localized thermal loading onto a background internal pressure and temperature profile, producing a two-dimensional loading with modest gradients along the meridian directly underneath the hot spot. The desired final state must show plasticity penetrating one-quarter of the wall. The problem first established the spherically symmetric state described in Problem 2 (10 MPa pressure, temperature field of T_{in} at 900 K and T_{out} at 700 K, linear through-thickness temperature gradient). At this point, a moderate localized thermal loading was applied. This loading consisted of ramping the temperature at the bottom inner surface to 1,400 K (at $\varphi = 0$), with a linear gradient to the outside surface and to the background profile at $\varphi = 0.1$ (see Figure E-1). Then the internal pressure was increased to 45 MPa to reach the final state. This problem is shown as Case III in Figure E-3.

4. **Internal Pressure, Severe Localized Thermal Loading**: This problem tested the elastic-plastic response by employing a severe localized thermal loading onto a background internal pressure and temperature profile, representing a two-dimensional problem with pronounced gradients along the meridian. The desired final state must show plasticity penetrating one-quarter of the wall directly underneath the hot spot. The problem first established the spherically symmetric state described in Problem 2 (10 MPa internal pressure, temperature field of T_{in} at 900 K and T_{out} at 700 K, linear through-thickness temperature gradient). At this point, a Type 2 (hot lump defined by Equation 4-54, Ref. E-2) temperature distribution was applied over $0 < \varphi < 0.1$, with a peak temperature of 1,400 K. This temperature profile was more severe than that of Problem 3 due to the nonlinearity of the distribution. Then the internal pressure was increased to 55 MPa to reach the final state. This problem is shown as Case IV in Figure E-3.

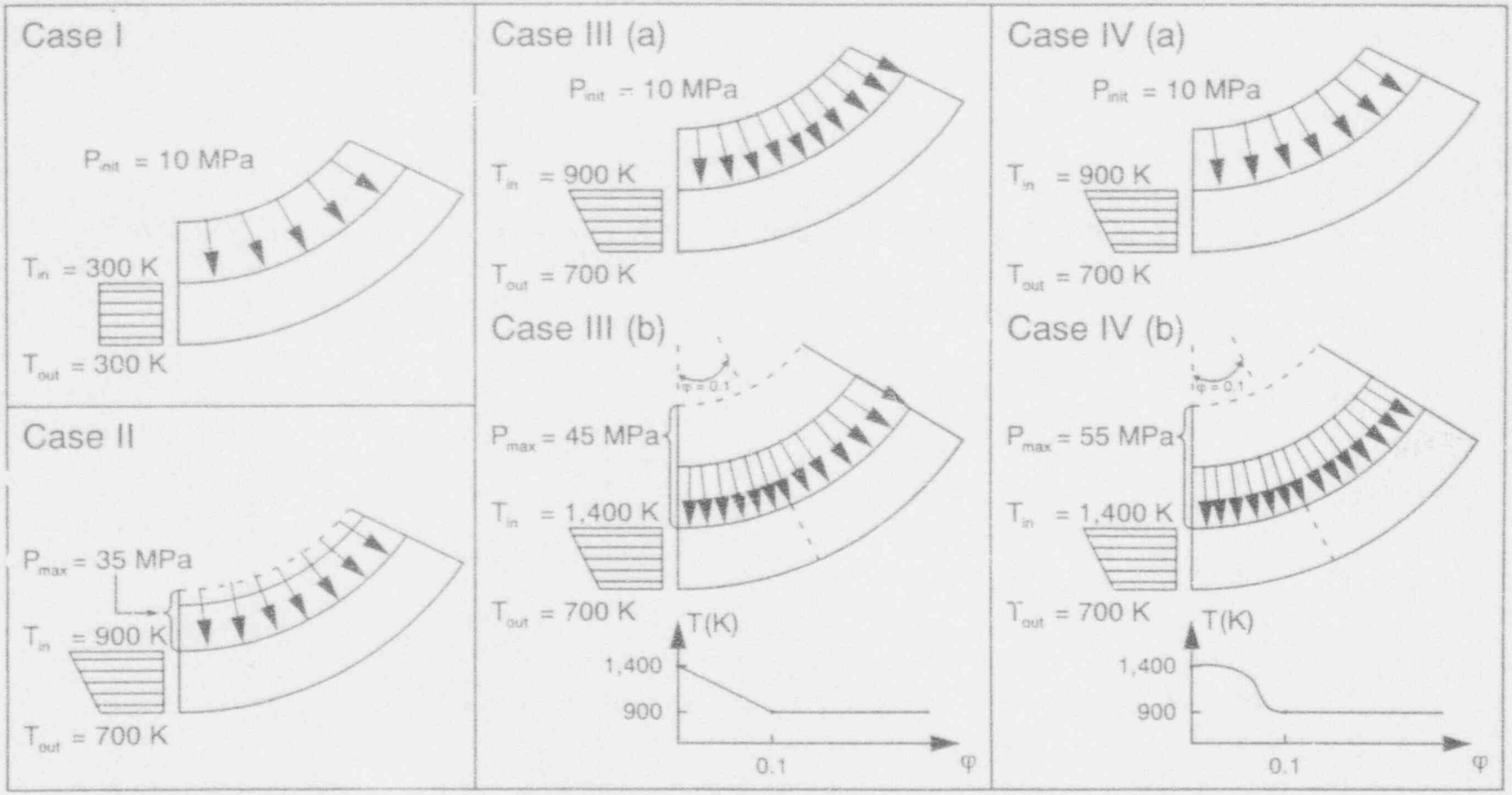

M757-WHT-1192-14

Figure E-3. Benchmark problem loadings.

The material properties required for these analyses included Young's modulus as a function of temperature, mean thermal expansion coefficient as a function of temperature, and yield strength and plastic deformation characteristics as independent of temperature. The material properties used were taken from Reference E-2 (Appendices B and E) and Reference E-3. Poisson's ratio was taken as independent of temperature as $\nu = 0.29$.

E.4 TSM and ABAQUS Models

The spatial model for TSM calculations was made using the axisymmetric representation $r_h/r_m = \xi^2$ with 201 nodes, where r_h is the horizontal distance from the vertical axis and r_m is the initial radius of the vessel middle surface (see Figure E-1). The model represented a spherical head with a mean radius, r_m, of 2.2 m and a uniform thickness of 12.7 cm.

The ABAQUS model consisted of a quarter sphere that utilized axisymmetric solid (8-node, isoparametric with reduced integration) elements. The model was meshed with 10 elements through the thickness and 272 along the meridian (uniformly spaced), giving approximately square elements. The free ends of the quarter sphere were restrained for symmetry, the loading conditions and geometry being symmetric about the two global axes. A second ABAQUS model was prepared with 15 elements through the thickness and 408 along the meridian. Both ABAQUS models were evaluated using ABAQUS, a multi-purpose finite element solution package, for all four benchmark problems. The output data (stress, strain and displacement) for the two ABAQUS models were compared, and the results showed that the data were within less than 1%. This indicated that the mesh refinement of the first ABAQUS model was sufficient to accurately describe the response for the benchmark problems. Only the results of the first ABAQUS model were compared to those of TSM in the following sections. Figure E-2 outlines the ABAQUS model.

Note that the ABAQUS model was developed so that nodes in both TSM and ABAQUS models overlapped at ξ = 0, 0.1, 0.2, 0.3, 0.4, 0.5 and 0.6, corresponding to TSM node numbers 1 (shell bottom), 21, 41, 61, 81, 101 and 121 (see Figure E-1). The through-thickness location of information differed in the two models, with TSM providing information at ten Gauss points through the thickness, while ABAQUS calculated information at element integration points, then interpolated (and averaged) that information at the nodes. This latter difference required interpolation of results from the ABAQUS nodes to TSM Gauss points in order for the comparison of results to be made. All comparisons using average data weighted each data point equally, unless specified differently in the discussion. In the spherically symmetric problems (Benchmark Problems 1 and 2 only) the results were identical on all radial lines and only one set of output information was given.

E.5 Results of Benchmark Problems 1 and 2

Benchmark Problems 1 and 2 were spherically symmetric problems. A separate means of evaluating TSM exists in that closed-form solutions are available for infinitesimal deformation, constant elastic property problems with arbitrary temperature distributions through thickness. Since some insight into the shortcomings of TSM can be gained by obtaining closed-form

solutions, the results are summarized below. In a spherically symmetric problem, the meridian and hoop strains and stresses become identical and the radial equilibrium equation is:

$$\frac{d\sigma_r}{dr} + \frac{2\left(\sigma_r - \sigma_\varphi\right)}{r} = 0 \quad . \tag{E-1}$$

The Hooke's Law relationships are

$$\sigma_r = \frac{E\left(\varepsilon_r - \varepsilon_T\right)}{1+\nu} + \frac{\left[\nu E\left(\varepsilon_r - \varepsilon_T + 2\left(\varepsilon_r - \varepsilon_T\right)\right)\right]}{\left(1+\nu\right)\left(1-2\nu\right)} \tag{E-2}$$

$$\sigma_\varphi = \frac{E\left(\varepsilon_\varphi - \varepsilon_T\right)}{1+\nu} + \frac{\left[\nu E\left(\varepsilon_r - \varepsilon_T + 2\left(\varepsilon_r - \varepsilon_T\right)\right)\right]}{\left(1+\nu\right)\left(1-2\nu\right)} \quad . \tag{E-3}$$

Using the strain/displacement relationships:

$$\varepsilon_r = \frac{du}{dr} \quad \text{and} \quad \varepsilon_\varphi = \frac{u}{r} \tag{E-4}$$

the Hooke's Law form of the stress/displacement relationship may be substituted into the equilibrium equation to obtain a second-order equation for u:

$$\frac{d^2u}{dr^2} + \frac{2}{r}\left[\frac{du}{dr} - \frac{u}{r}\right] = \frac{1+\nu}{1-\nu}\frac{d\varepsilon_T}{dr} \quad . \tag{E-5}$$

The complete solution of which is

$$u\left(r\right) = C_1 r - \frac{C_2}{r^2} + \frac{1+\nu}{r^2\left(1-\nu\right)}\int_a^b \varepsilon_T r'^2 dr' \tag{E-6}$$

subject to the resolution of constants C_1 and C_2. If the requirements are that $\sigma_r = -p$ at $r = a$ and $\sigma_r = 0$ at $r = b$, then the strains can be shown to be

$$\varepsilon_\varphi = \frac{1-2\nu}{1-\left(a/b\right)^3}\frac{p}{E}\left[\left(a/b\right)^3 + \frac{\left(1+\nu\right)\left(a/r\right)^3}{2\left(1-2\nu\right)}\right] + \frac{2\left(1-2\nu\right)\varepsilon_{Tav}}{3\left(1-\nu\right)}\left[1 + \frac{\left(1+\nu\right)\left(a/r\right)^3}{2\left(1-2\nu\right)}\right] \tag{E-7}$$

$$+ \frac{1 + \nu}{(1 - \nu)r^2} \int_a^b \varepsilon_T r'^2 \, dr'$$

$$\varepsilon_r = \frac{1 - 2\nu}{1 - (a/b)^3} \frac{p}{E} \left[(a/b)^3 - \frac{(1 + \nu)(a/r)^3}{2(1 - 2\nu)} \right] + \frac{2(1 - 2\nu)\varepsilon_{Tav}}{3(1 - \nu)} \left[1 - \frac{(1 + \nu)(a/r)^3}{2(1 - 2\nu)} \right] \tag{E-8}$$

$$+ \frac{(1 + \nu)\varepsilon_T}{(1 - \nu)} - \frac{2(1 + \nu)}{(1 - \nu)r^2} \int_a^b \varepsilon_T r'^2 dr' \, .$$

where ε_{Tav} is the average thermal strain, defined as

$$\varepsilon_{Tav} = \frac{3}{b^3 - a^3} \int_a^b \varepsilon_T r^2 \, dr \, . \tag{E-9}$$

In Benchmark Problem 1 (see Figure E-3), a purely elastic response showed that stresses and strains varied through the thickness for the exact solution (from closed form equations) and ABAQUS. The stress and strain results of the exact and ABAQUS solutions were within 1%. TSM stress and strain results were constant throughout the thickness at the calculated average for the shell.

For an internal pressure of 10 MPa with the inner surface temperature brought to 900 K and the outer surface temperature brought to 700 K (from initially 300 K), a purely elastic analysis produced TSM stresses that varied throughout the thickness. Those stresses were within 2% of the values for the exact solution. However, TSM strains were constant throughout the thickness at the calculated average for the shell. The most obvious shortcoming of TSM is in the isothermal problem. With the strains formulated as, for instance,

$$\varepsilon_\varphi = \varepsilon_{\varphi n} \left(1 + \xi / R_\varphi \right) + \xi \left[1/R_\varphi - 1/R_{\varphi o} + \left(\gamma' / \alpha_o \right) \sec^2 \gamma \right] \tag{E-10}$$

and the deformed radius of curvature related to the initial radius of curvature through

$$R_\varphi = \frac{R_{\varphi o} \left(1 + \varepsilon_{\varphi n} \right)}{\left(1 + \beta' / \varphi_o' \right)} \tag{E-11}$$

then in spherically symmetric problems ($\beta = \varphi = 0$), substitution of $R_\varphi = R_{\varphi o} (1 + \varepsilon_{\varphi n})$ into the strain measure [see Equation (E-10)] yields

$$\varepsilon_\varphi = \varepsilon_{\varphi n} \tag{E-12}$$

i.e., no through-thickness dependence. The exact result shows the strain measure has a constant component and a component that scales inversely to distance cubed. The shortcoming is of less consequence in the problem with a temperature gradient through the thickness because the gradient in thermal strain provides a much larger bending component of stress than is obtained from the finite thickness of the shell.

In Benchmark Problem 2 (see Figure E-3), yielding occurred approximately 1/4 way through the thickness after ramping the internal pressure to 35 MPa. The ABAQUS data was interpolated to coincide with TSM Gauss point data. Since TSM results varied somewhat from ABAQUS, a comparison of the difference was in order. The comparison used the ABAQUS results as the baseline. TSM values for meridional stress were on the average 1.0% below ABAQUS in the outer two-thirds of the wall. In the inner one-third of the wall the meridional stress levels predicted by TSM were an average of 50% below those given by ABAQUS. That underprediction was due to the radial stresses in the area, whose magnitudes were on the same order as those of the meridional stresses. TSM assumes that the radial component of stress was negligible throughout the model. That assumption was not true in the inner third of the wall, and TSM meridional stress levels reflected that error. Benchmark Problems 3 and 4 discuss that assumption in detail.

TSM values for total meridional strain averaged 1% below ABAQUS. The ABAQUS plastic strains began one Gauss point location closer to the inside surface than those of TSM. However, TSM meridional plastic strains were an average of 1% above those of ABAQUS.

E.6 Results of Benchmark Problems 3 and 4

A far greater amount of output information was associated with Benchmark Problems 3 and 4 because the hoop and meridian stresses and strains were not generally identical and those states varied along the shell meridian. In Problem 3, the inner surface temperature was raised to 1,400 K (over the defined local area), then the pressure was raised to 45 MPa to get yielding 1/4 way through the thickness in the vicinity of $\varphi = 0$. Yielding occurred to a greater extent under these conditions at positions away from the bottom (edge of shell at $\varphi = 0$) of the shell. In Problem 4, the inner surface temperature was raised to 1,400 K (over the defined local area), then the pressure was raised to 55 MPa to get yielding 1/4 way through the thickness at the shell bottom. Again, yielding was more severe away from $\varphi = 0$ in this case.

E.6.1 Problem 3 Results

The moderate localized thermal loading applied in this problem is shown in Figure E-3. The pressure was raised to 45 MPa to get yielding 1/4 way through the thickness in the vicinity of $\varphi = 0$. It is of interest that yielding occurred to a greater extent under these conditions at positions away from the bottom (edge of shell at $\varphi = 0$) of the shell. Due to the volume of data and locations available in the models, the evaluation was limited to 7 specific meridional points and their 10 associated through-thickness Gauss point locations. Four of the meridional points were within the hot spot, one on the inside edge (near $\varphi = 0$), two in the middle, and one near the outside edge. The fifth through seventh points were outside of the hot spot, the fifth being near the outside edge of the spot, the sixth and seventh being well away from it (see Figure E-1).

A graphical representation of the comparison between TSM and ABAQUS meridian and hoop stresses is given in Figures E-4 through E-10. Note that TSM meridian and hoop stresses inside the midplane in the hot spot underpredicted those calculated by ABAQUS. This portion of the wall was very soft because of the temperature profile and the material definition. A small percentage of the total load was carried by this half of the wall. It is noted that because of the softness of the wall the radial component of stress up to the midplane maintained a magnitude higher than that of the hoop and meridian stresses. The underprediction of hoop and meridian stresses by TSM was largely due to the absence of a radial stress component in TSM model. This was confirmed by comparing the ABAQUS and TSM results at the same thermal conditions at a lower pressure (discussed below). As discussed in Reference E-2, Section 4.2.2 and Appendix D, TSM solution scheme assumed that radial stresses were negligible. This was true beyond the midplane in the hot spot since the radial stresses quickly decreased to zero at the outside surface while the hoop and meridian stresses increased by a factor of 50 to 100. TSM meridian and hoop stresses in this area underpredicted those calculated by ABAQUS by about 2%. This portion of the wall carried the majority of the load, and shell yielding propagated from the outer surface inward. Near the outside edge of the hot spot (point 61) and far-field (points 81 through 121), meridian and hoop stresses were about 18% lower in the inner 30% of the wall than predicted by ABAQUS, while the stresses over the outer 70% of the wall were within 3%.

TSM solution scheme and model were prepared for the purpose of predicting a particular failure mechanism (a bulging/shear-through type due to a local hot spot) in a reactor vessel lower head during an accident scenario. It is important to note that Benchmark Problem 3 included a maximum internal pressure of 45 MPa where an accident condition would specify maximum pressures closer to 15 MPa. Therefore, the moderate localized thermal loading of Problem 3 was applied to TSM and ABAQUS models with a maximum internal pressure load of 15 MPa. Figure E-11 shows the comparison of the hoop and meridian stresses of the two models for node point 41 (located in the middle of the hot spot). TSM stresses in the inside third of the wall were 13% (or less) lower than those of ABAQUS while the remaining portion of the wall was within 3%. These levels of agreement are representative of all points examined along the meridian (1, 21,..121) and indicate that the discrepancies in Figures E-4 through E-10 are rooted largely in the absence of a radial stress in TSM and not the severity of the temperature gradient.

TSM total meridian and hoop strain results for Benchmark Problem 3 underpredicted the values calculated by ABAQUS on an average of 3.6%. Figure E-12 gives the comparison of total hoop and meridian strains for node 41, which is typical of all node locations.

TSM Benchmark Problem 3 results at the middle of the hot spot (nodes 21 and 41) showed that plastic strains (meridian and hoop) began at the seventh Gauss point location (of 10 total) from the inside surface and increased to the outer surface. ABAQUS results identified plastic strains beginning at the sixth location and increasing to the outside surface. The difference was 100% for the seventh location (where plastic strains were smallest), then decreased for each successive location to an average of 8% at the outside surface (where plastic strains reached a maximum). Outside of the hot spot (nodes 81 through 121), the plastic strain in both models began one Gauss point location closer to the inside surface. The difference in plastic strains was 100% for the fourth location (where plasticity began in the ABAQUS model) but averaged 9% or less for the entire outer half of the wall.

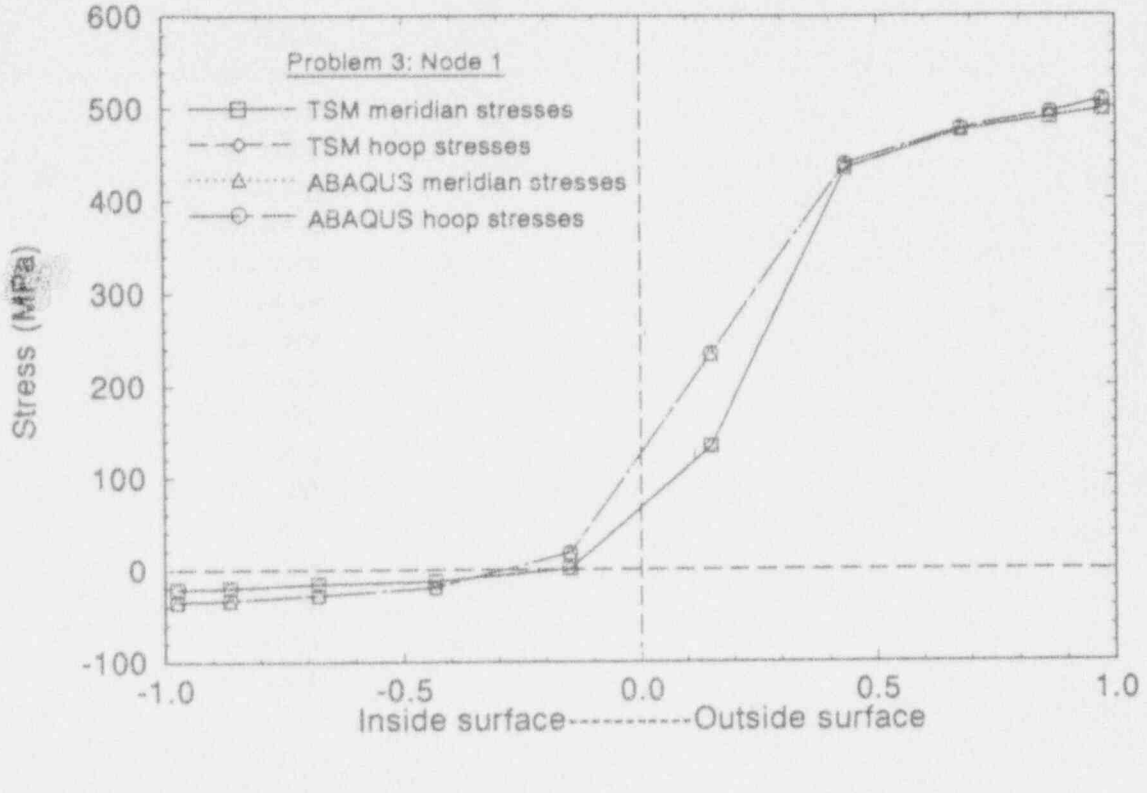

Figure E-4. Problem 3: node 1 stresses.

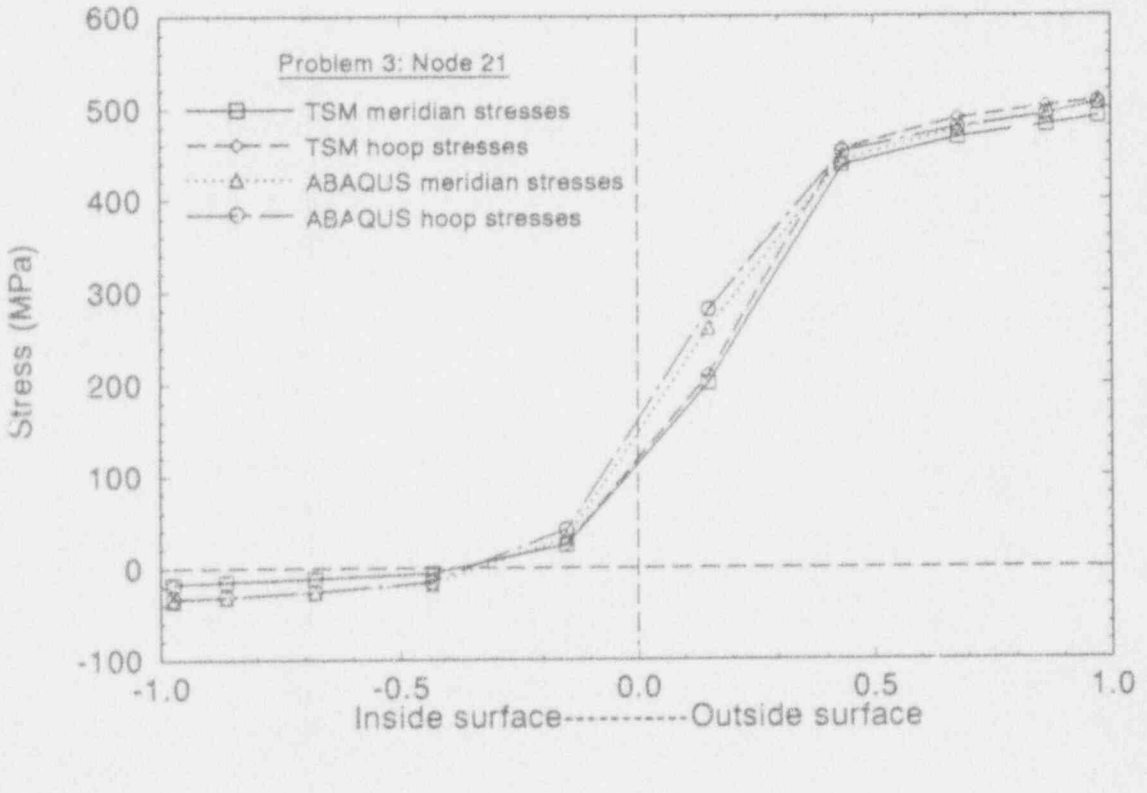

Figure E-5. Problem 3: node 21 stresses.

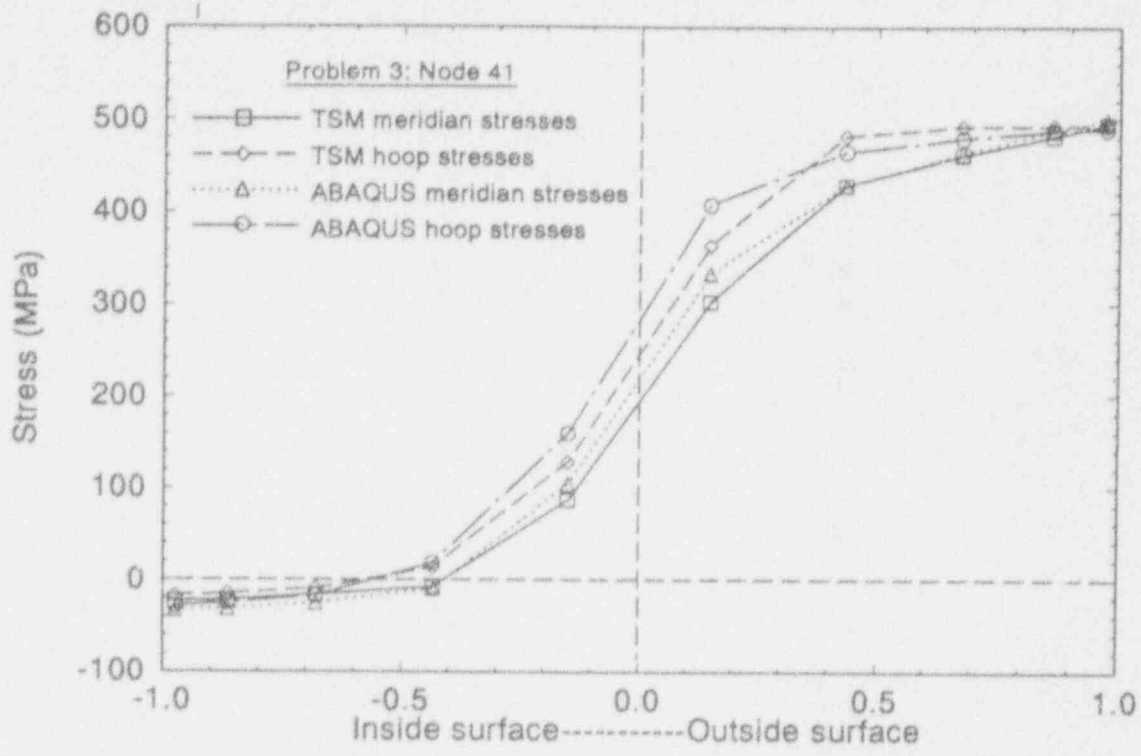

M756 ss-1192-03

Figure E-6. Problem 3: node 41 stresses.

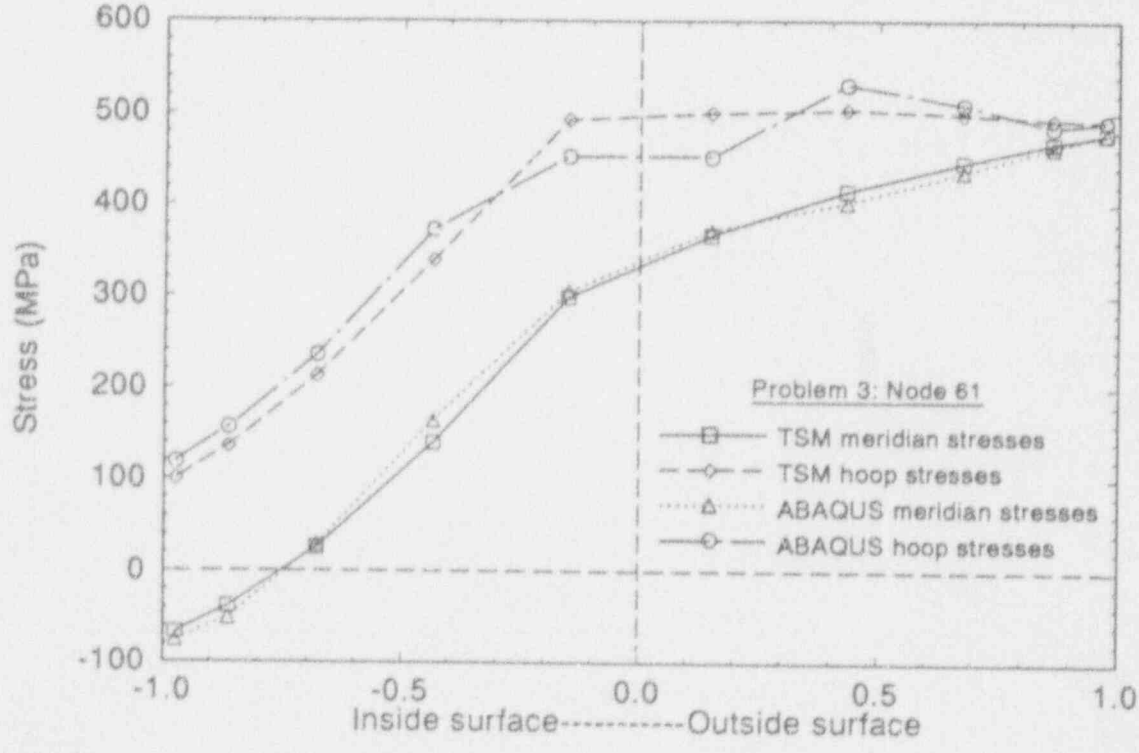

M756 ss-1192-04

Figure E-7. Problem 3: node 61 stresses.

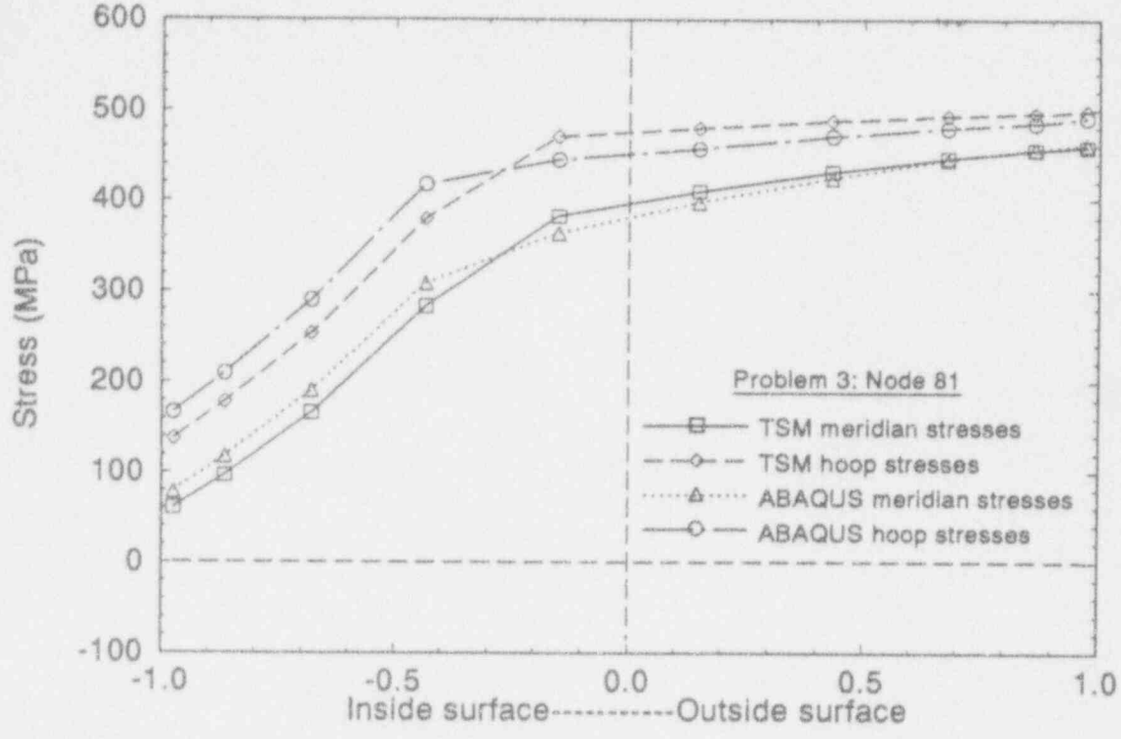

Figure E-8. Problem 3: node 81 stresses.

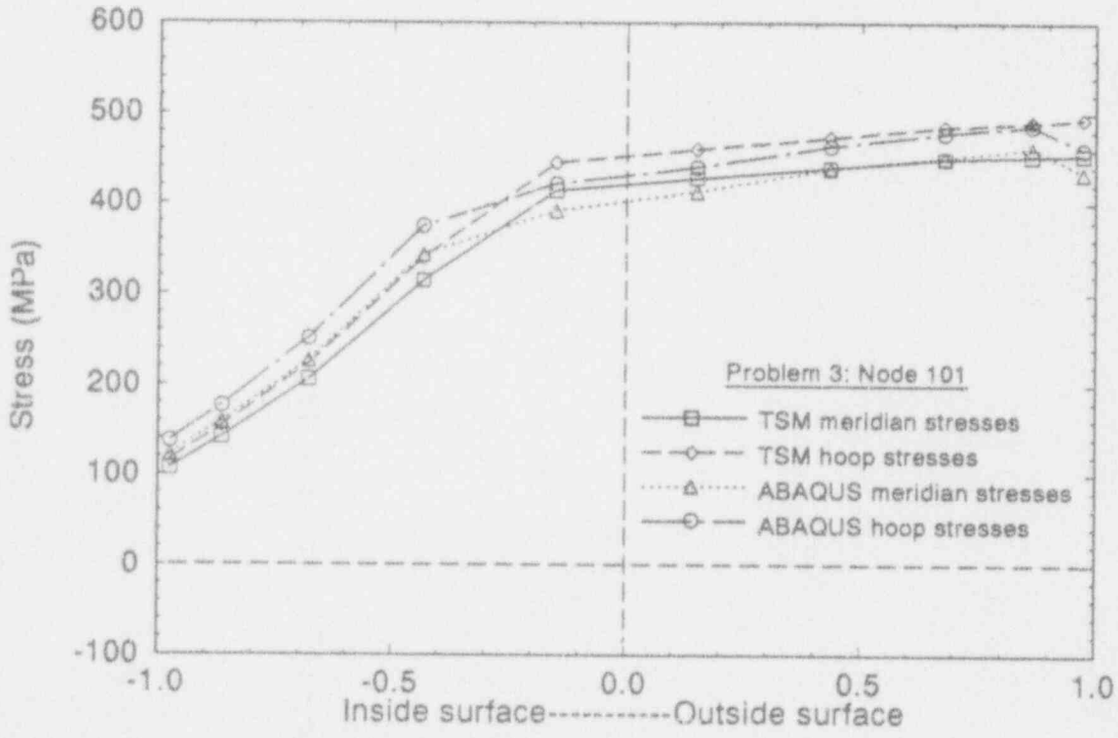

Figure E-9. Problem 3: node 101 stresses.

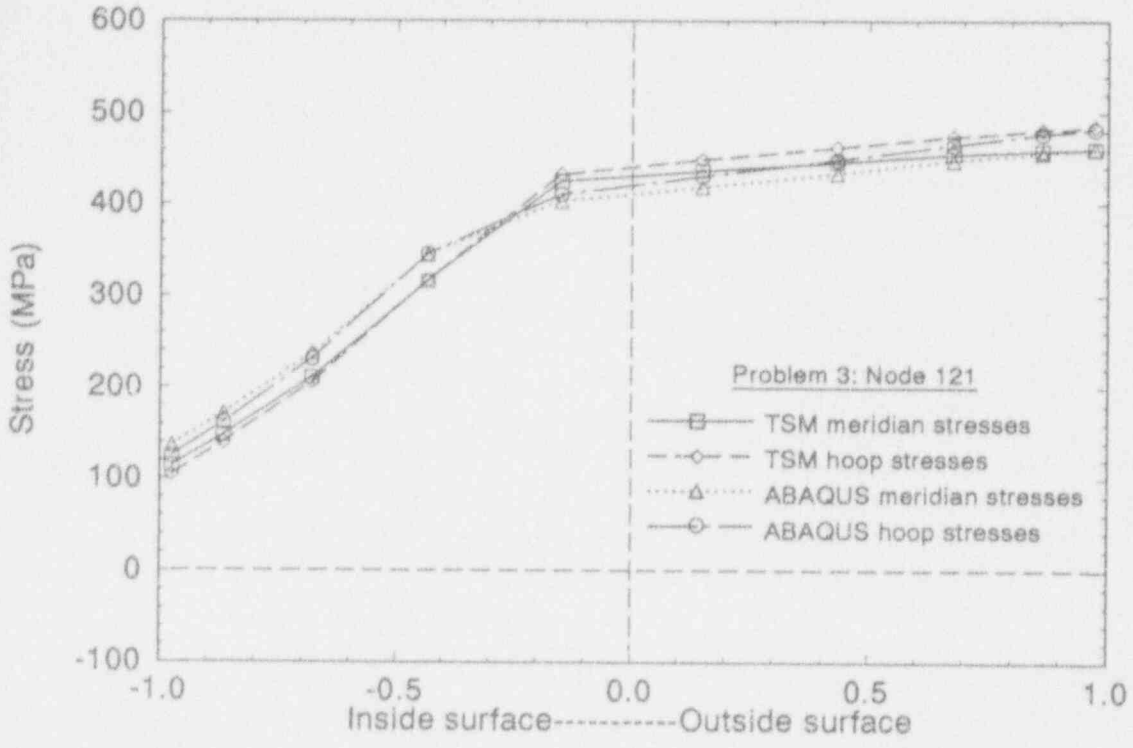

M756 ss-1192-07

Figure E-10. Problem 3: node 121 stresses.

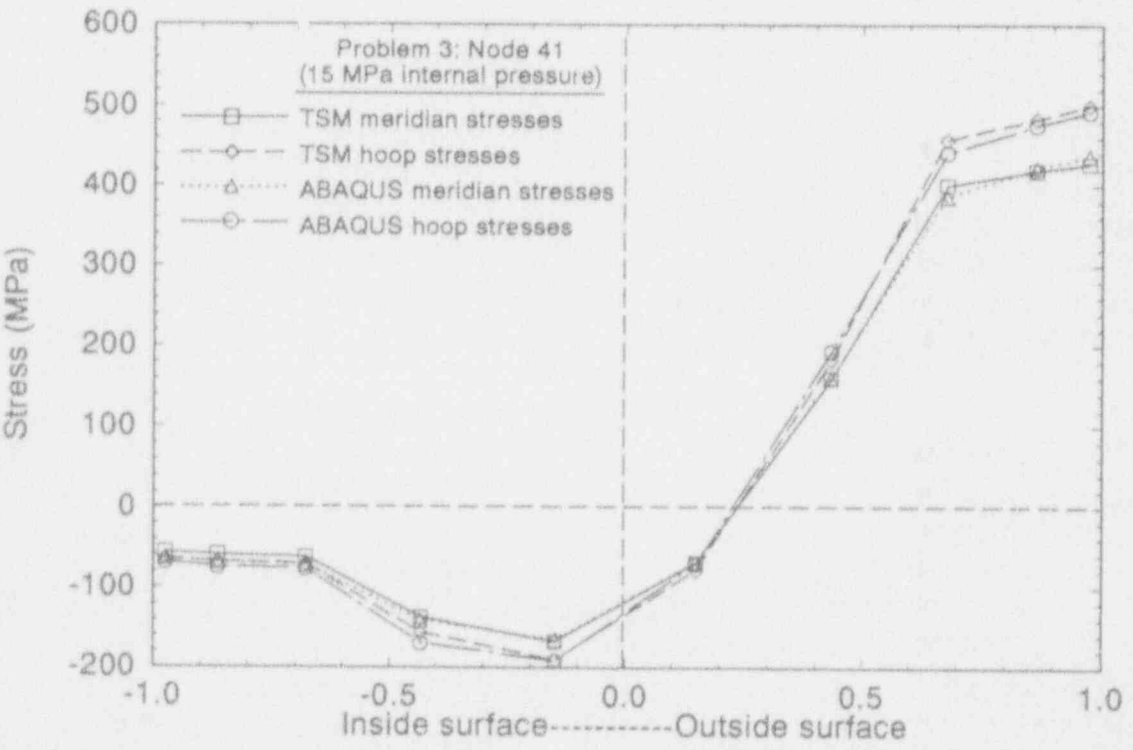

M756 ss-1192-18

Figure E-11. Problem 3 thermal loading with only 15 MPa internal pressure: node 41 stresses.

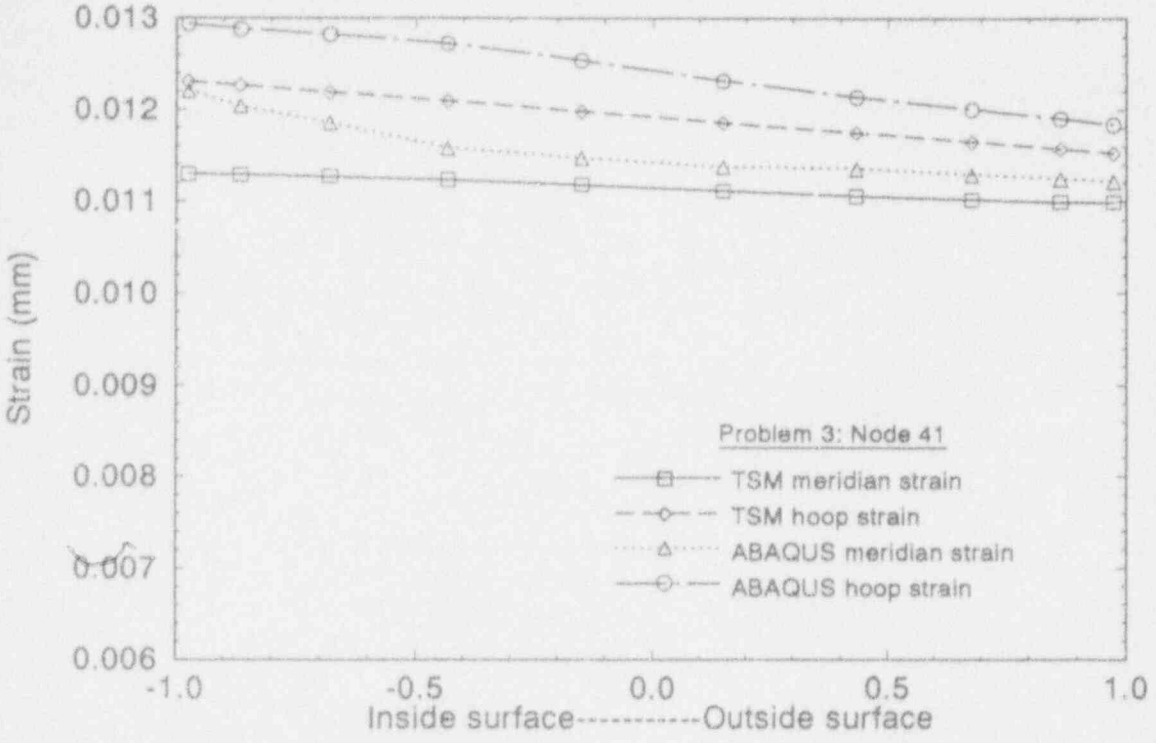

M756 ss-1192-15

Figure E-12. Problem 3: node 41 strains.

E.6.2 Problem 4 Results

The severe localized thermal loading for this problem involved a nonlinear temperature distribution (see Figure E-3). The pressure was raised to 55 MPa to get yielding 1/4 way through the thickness at the shell bottom. Again, yielding was more severe away from $\varphi = 0$. The same meridian points and their associated through-thickness Gauss point locations were evaluated as in Problem 3.

A graphical representation of the comparison between TSM and ABAQUS meridian and hoop stresses is given in Figures E-13 through E-19. Note that TSM meridian and hoop stresses up to the sixth Gauss point location (just beyond the midplane) in the middle of the hot spot underpredicted those calculated by ABAQUS. This area of underprediction was larger than the underpredicted area in Problem 3. This portion of the wall was very soft because of the temperature profile and the material definition. A small percentage of the total load was carried by this portion of the wall. Because of the softness of the wall, the radial component of stress up to the fourth Gauss point location from the inside surface maintained a magnitude higher than that of the hoop and meridian stresses. As in Problem 3, the underprediction of hoop and meridian stresses by TSM was largely due to neglecting the radial stress component in the calculations.

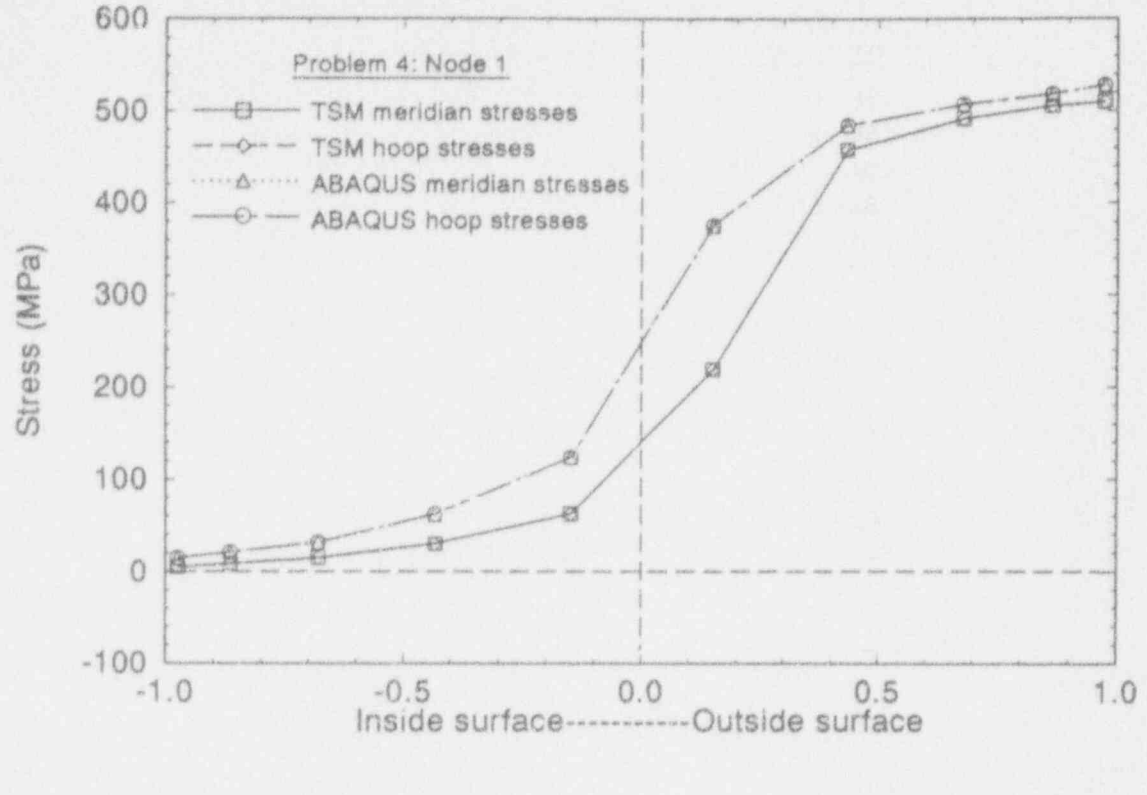

M756 as-1192-08

Figure E-13. Problem 4: node 1 stresses.

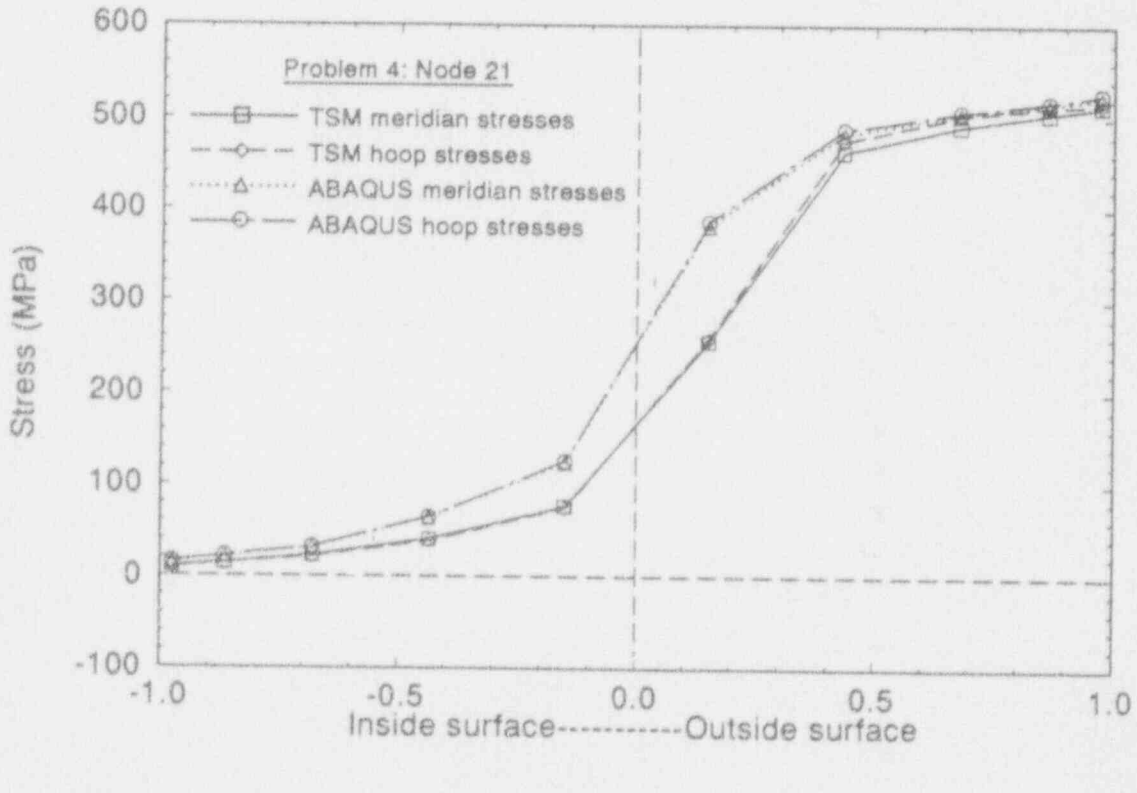

M756 as-1192-09

Figure E-14. Problem 4: node 21 stresses.

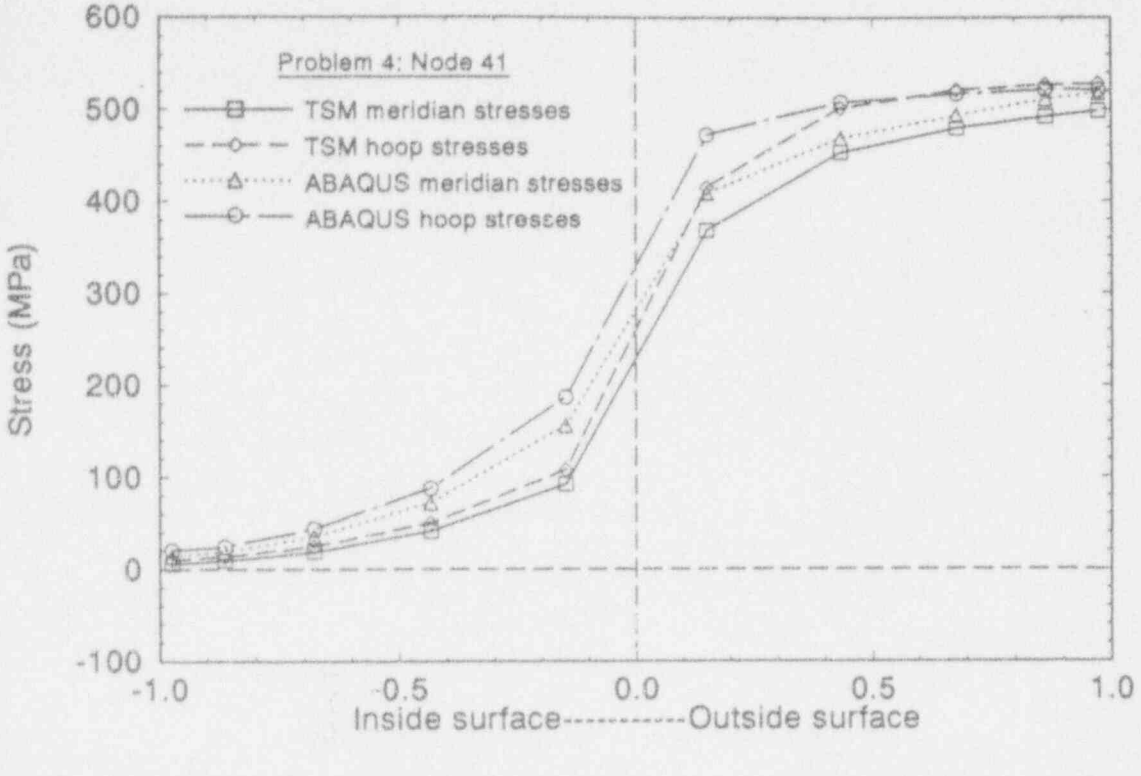

Figure E-15. Problem 4: node 41 stresses.

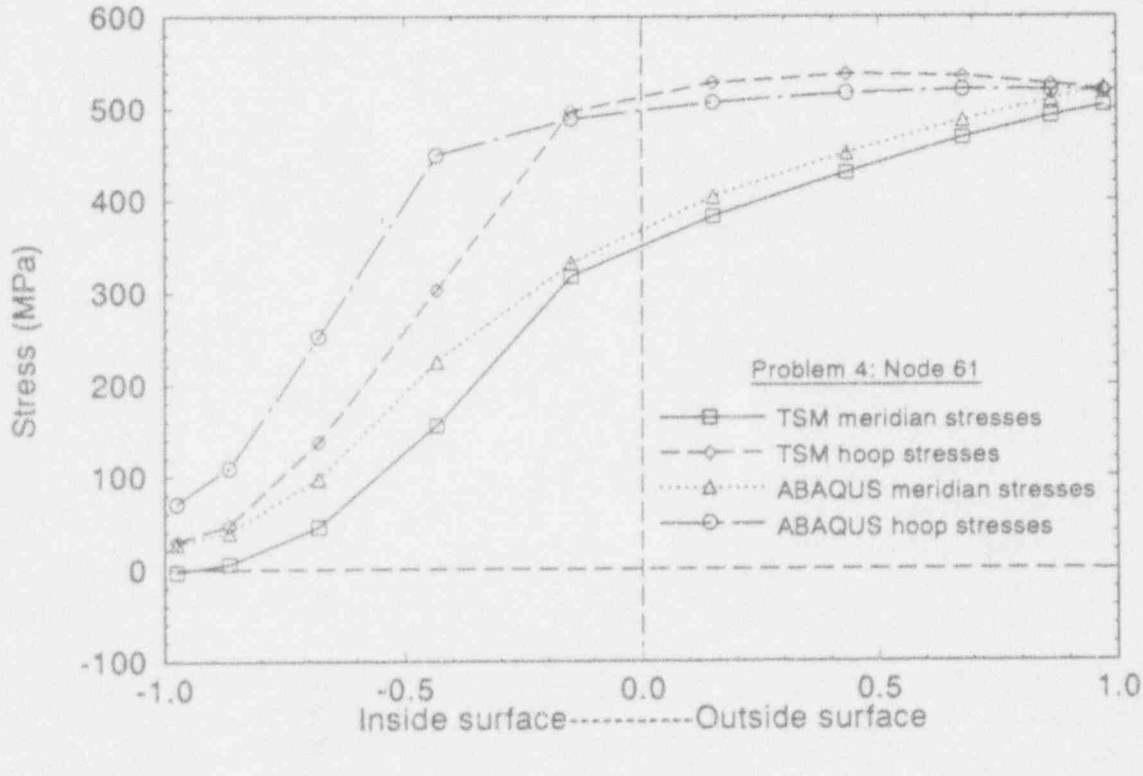

Figure E-16. Problem 4: node 61 stresses.

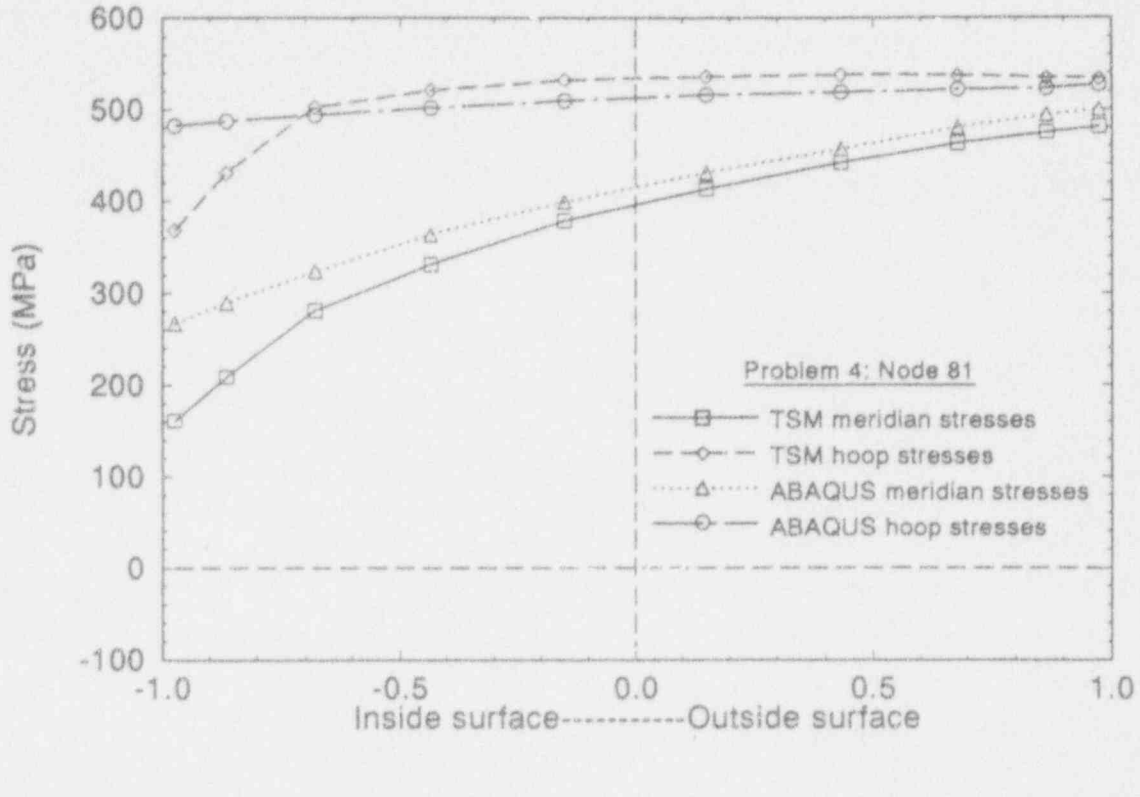

M756 ae-1192-12

Figure E-17. Problem 4: node 81 stresses.

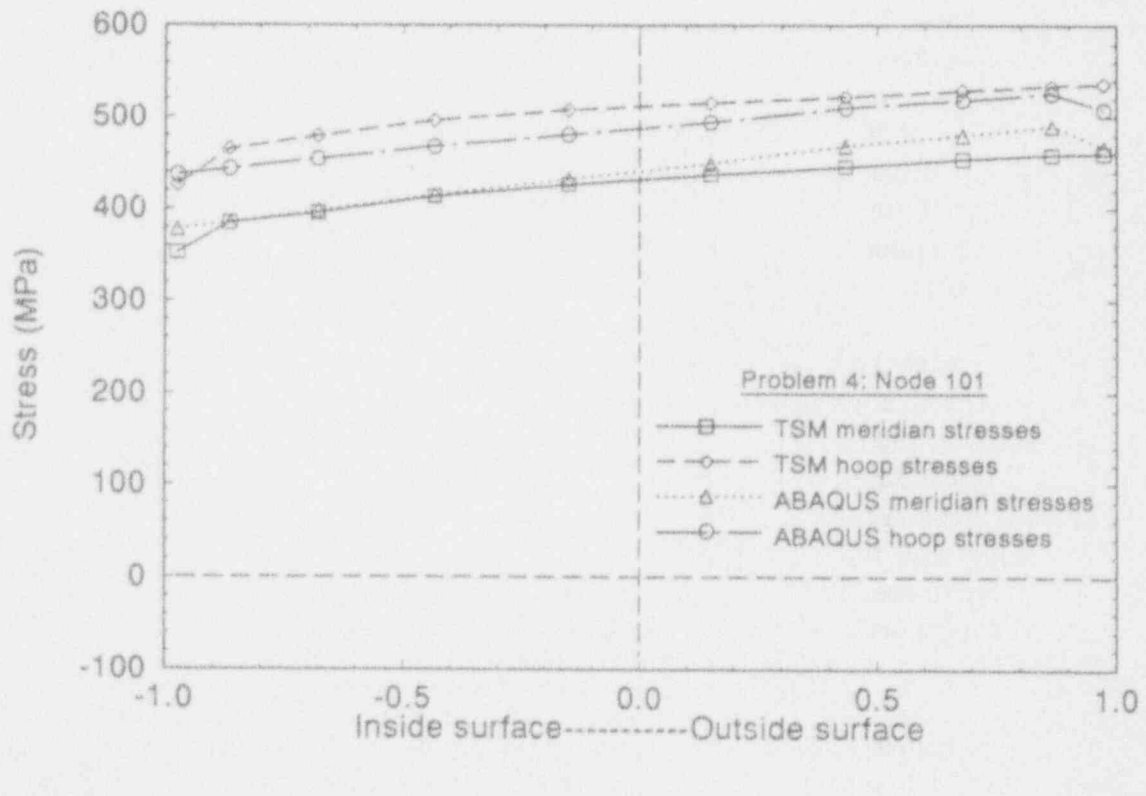

M756 ae-1192-13

Figure E-18. Problem 4: node 101 stresses.

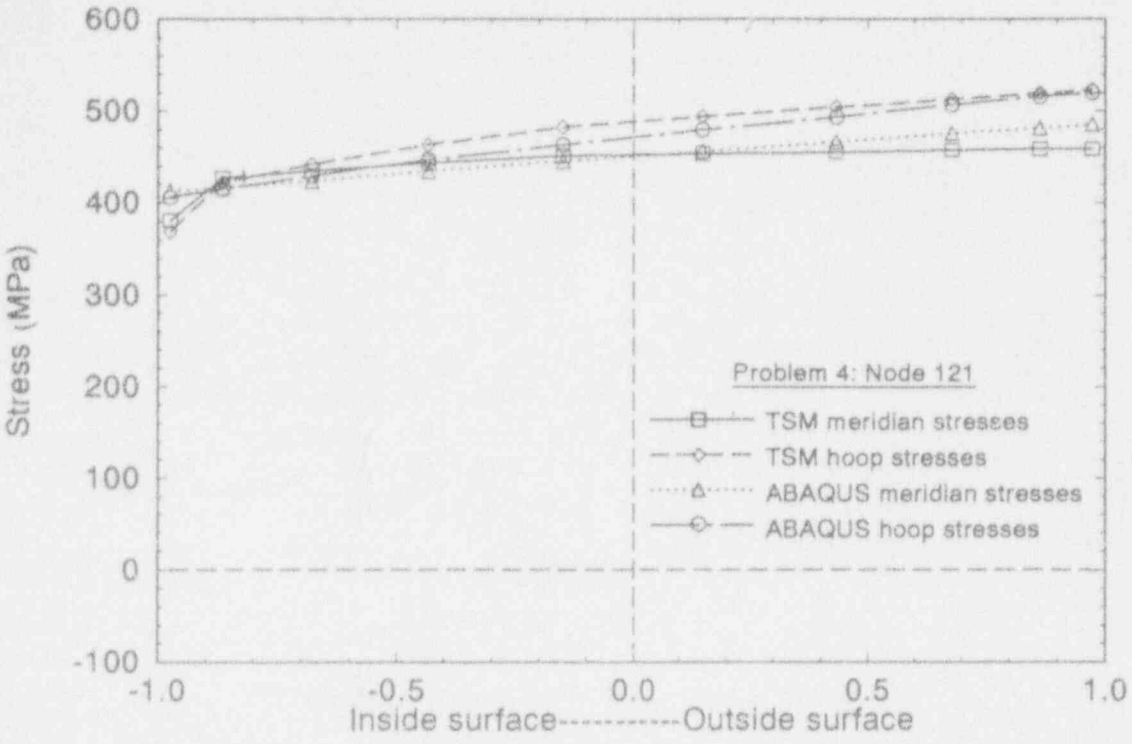

M756 98-1192-14

Figure E-19. Problem 4: node 121 stresses.

As discussed in Reference E-2, Section 4.2.2 and Appendix D, TSM solution scheme assumes that radial stresses are negligible. This was true beyond the sixth Gauss point in the hot spot, since the radial stresses quickly dropped off to zero at the outside surface while the hoop and meridian stresses rose by a factor of 50 to 100. TSM meridian and hoop stresses in this area underpredicted those calculated by ABAQUS by about 4%. This portion of the wall carried the majority of the load, and shell yielding propagated from the outer surface inward. The far-field (points 101 and 121) meridian and hoop stresses were within an average of 4% of ABAQUS values for the entire wall.

Next, TSM and ABAQUS models were evaluated with the severe localized thermal loading of Problem 4 applied with a maximum internal pressure of 15 MPa. Figure E-20 shows the comparison of the hoop and meridian stresses of the two models for node point 41 (located in the middle of the hot spot). TSM stresses throughout the wall were an average of 4% lower than those of ABAQUS. The agreement between ABAQUS and TSM in the more severe temperature gradient at 15 MPa pressure is comparable to the agreement between the two models in a moderate temperature gradient at 15 MPa pressure, indicating again that the absence of radial stress in TSM is primarily responsible for the differences between the two models at elevated pressures.

TSM total meridian and hoop strains in Benchmark Problem 4 underpredicted the values calculated by ABAQUS by up to 24% on the inside surface to near 10% on the outside for locations within the hot spot at elevated pressures. Away from the hot spot those values were reduced to 12% on the inside and 7% on the outside surfaces. For the condition including the

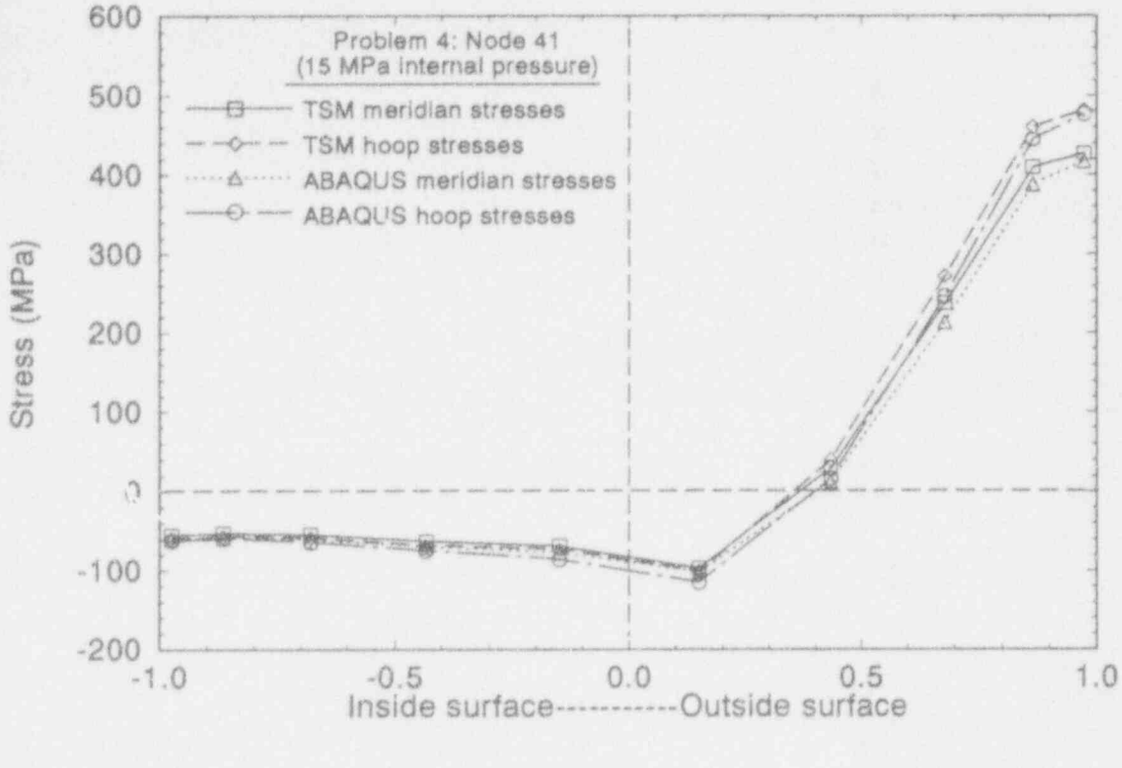

Figure E-20. Problem 4 thermal loading with only 15 MPa internal pressure: node 41 stresses.

Problem 4 thermal loading with a maximum pressure of 15 MPa, the total meridian and hoop strains in the hot spot were at most 16% lower than ABAQUS on the inside surface and within 2% on the outside. Outside of the hot spot all TSM total strains were within 5% of ABAQUS values. Figure E-21 compares the total strains of the two models for the Problem 4 thermal loading with an internal pressure of 15 MPa.

TSM results for Problem 4 showed that all plastic strains (meridian and hoop) occurred one or two Gauss point locations closer to the outer surface than ABAQUS. Those plastic strains increased towards the outer surface. As in Problem 3, TSM plastic meridian and hoop strains started at 100% lower values (at the smallest plastic strains), and steadily increased to, at most, 1% lower values than ABAQUS (where the plastic strains reached maximum values).

E.7 Conclusions

The verification of TSM has provided several insights into the applicability of this program for use in lower head severe accident structural response calculations. First of all, it must be remembered that the purpose for developing this program was to provide a fast-running solution to predict the collapse of a localized portion of the vessel wall resulting from hot spots in a debris bed resting on the lower head. Thus, the program would be appropriate for scoping parameter studies in various accident scenarios. Results of the benchmark problems used in this verification effort indicate that TSM performs well for its intended purpose.

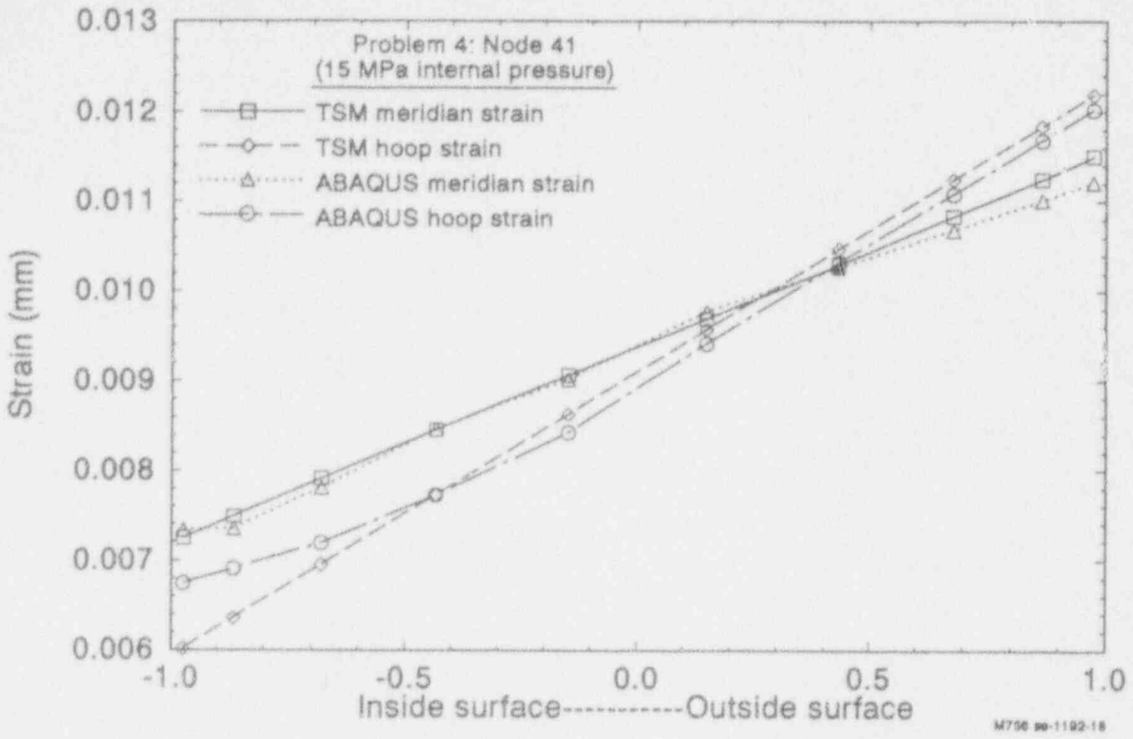

Figure E-21. Problem 4 thermal loading with only 15 MPa internal pressure: node 41 strains.

The two benchmark problems that applied a localized hot spot (Problems 3 and 4) with an internal pressure of 45 to 55 MPa identified that TSM does not accurately predict the stresses in the hottest regions. This was due to TSM assumption that the radial component of stress was negligible. However, it was pointed out that the hottest areas carry a very small percentage of the total pressure load. The assumption of negligible radial stresses was shown to be valid in the cooler regions under the hot spot, which is essentially the portion beyond the midplane and away from the hot spot. That portion of the wall carried the majority of the pressure load in these cases. It was noted that vessel wall material yielding eventually begins at the outer surface and propagates inward to final failure. Hoop and meridian stress levels are typically 35 times higher in the outer portions than the inner regions of the vessel wall. Thus, model accuracy in these areas is most crucial to accurate predictions of vessel failure margins.

Two additional load cases were evaluated that employed the thermal hot spot definitions from Problems 3 and 4 with a pressure of 15 MPa. This lower pressure was more representative of accident conditions on a reactor vessel. The evaluation of these two cases verified that TSM assumption of negligible radial stresses was acceptable for the more representative accident conditions.

TSM total strain comparisons ranged from underpredictions of 24% on the inside surface to 11% on the outside surface in the hot spot region for the severe thermal gradient load case at elevated pressures. In the cooler boundary areas, strain comparisons ranged from underpredictions of 13% on the inner surface to 7% on the outer surface. Examinations of the

plastic strains indicated that plasticity of the wall had propagated from the outside inward one Gauss point further in the ABAQUS model than in TSM model for the two hot spot load cases. The magnitude of total strains for Benchmark Problems 3 and 4 were 3 to 5 times lower than the plastic strain values. Use of TSM for predicting vessel response is considered acceptable for pressure levels at or below 15 MPa.

E.8 References

E-1. ABAQUS, Version 4-8-5, Providence Rhode Island: Hibbit, Karlsson, and Sorenson, Inc. 1990.

E-2. J. L. Rempe et al., *Light Water Reactor Lower Head Failure Analysis*, NUREG/CR-5642, EGG-2618, October 1993.

E-3. R. H. Bogaard et al., *Thermophysical Properties of Selected Manganese and Nickel Steels and High Nickel Iron, CINDAS Special Report (Part VI)*, Center for Information and Numerical Data Analysis and Synthesis, Purdue University, January 1978.

NRC FORM 335 (2-89) NRCM 1102, 3201, 3202

U.S. NUCLEAR REGULATORY COMMISSION

BIBLIOGRAPHIC DATA SHEET

(See instructions on the reverse)

1. REPORT NUMBER (Assigned by NRC, Add Vol., Supp., Rev., and Addendum Numbers, if any.)

NUREG/CR-6196
TMI V(93)EG01
EGG-2733

2. TITLE AND SUBTITLE

Calculations to Estimate the Margin to Failure in the TMI-2 Vessel

3. DATE REPORT PUBLISHED

MONTH	YEAR
March	1994

4. FIN OR GRANT NUMBER

A6899

5. AUTHOR(S)

L. A. Stickler, J. L. Rempe, S. A. Chávez, G. L. Thinnes, S. D. Snow,
R. J. Witt,* M. L. Corradini,* J. A. Kos*

6. TYPE OF REPORT

Technical

7. PERIOD COVERED (Inclusive Dates)

8. PERFORMING ORGANIZATION – NAME AND ADDRESS (If NRC, provide Division, Office or Region, U.S. Nuclear Regulatory Commission, and mailing address; if contractor, provide name and mailing address.)

EG&G Idaho, Inc.
Idaho Falls, ID 83415

* University of Wisconsin-Madison
1500 Johnson Drive
Madison, WI 53706

9. SPONSORING ORGANIZATION – NAME AND ADDRESS (If NRC, type "Same as above"; if contractor, provide NRC Division, Office or Region, U.S. Nuclear Regulatory Commission, and mailing address.)

Division of Systems Research
Office of Nuclear Regulatory Research
U.S. Nuclear Regulatory Commission
Washington, D.C. 20555-0001

10. SUPPLEMENTARY NOTES

11. ABSTRACT (200 words or less)

As part of the OECD-sponsored Three Mile Island Unit 2 (TMI-2) Vessel Investigation Project (VIP), margin-to-failure calculations for mechanisms having the potential to threaten the integrity of the vessel were performed to improve understanding of events that occurred during the TMI-2 accident. Analyses considered four failure mechanisms: tube rupture, tube ejection, global vessel failure, and localized vessel failure. Calculational input was based on data from the TMI-2 VIP examinations of the vessel steel samples, the instrument tube nozzles, and samples of the hard layer of debris found on the TMI-2 vessel lower head. Sensitivity studies were performed to investigate the uncertainties in key parameters for these analyses.

12. KEY WORDS/DESCRIPTORS (List words or phrases that will assist researchers in locating the report.)

TMI-2, Vessel Thermal Response, Vessel Structural Response, Melt-water Interactions, Tube Failure, Melt Penetration in Tubes

13. AVAILABILITY STATEMENT

Unlimited

14. SECURITY CLASSIFICATION

(This Page)

Unclassified

(This Report)

Unclassified

15. NUMBER OF PAGES

16. PRICE

NRC FORM 335 (2-89)

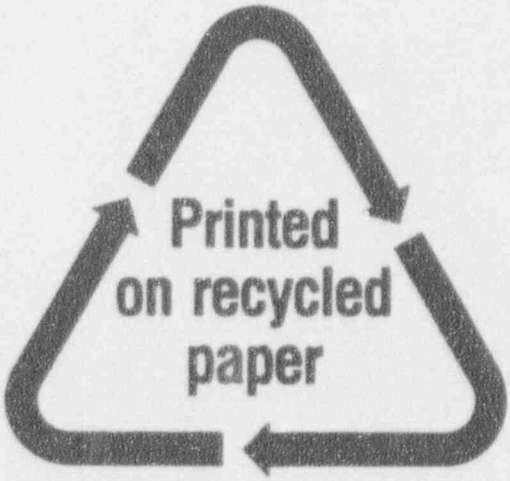

Federal Recycling Program

UNITED STATES
NUCLEAR REGULATORY COMMISSION
WASHINGTON, D.C. 20555-0001